Dipl.-Ing. Bernd Cermenek, BSc

Ethanol electrooxidation catalysts for the alkaline direct ethanol fuel cell

DOCTORAL THESIS

to achieve the university degree of

Doktor der technischen Wissenschaften

submitted to

Graz University of Technology

Supervisor

Assoc.Prof. Dipl.-Ing. Dr.techn. Viktor Hacker

Institute of Chemical Engineering and Environmental Technology

Faculty of Technical Chemistry, Chemical and Process Engineering and Biotechnology

Graz, March 2020

AFFIDAVIT

I declare that I have authored this thesis independently, that I have not used other than the declared sources/resources, and that I have explicitly indicated all material which has been quoted either literally or by content from the sources used. The text document uploaded to TUGRAZonline is identical to the present doctoral thesis.

Date

Signature

Abstract

The direct ethanol fuel cell (DEFC) is an energy converter with high volumetric energy density and is predestinate to be a promising candidate for small portable and mobile electronic devices. The doctoral thesis concentrates on the development and characterization of Pt-free anode catalysts for the alkaline ethanol oxidation reaction (EOR). This includes the investigation of the influence of adatoms and structure on the EOR performance (activity, stability and byproduct tolerance) of selected Pt-free electrocatalysts and the identification of a novel and applicable catalyst system with high EOR activity for the alkaline DEFC.

The 3d transition metal, Pd, is currently used as the state-of-the-art catalyst toward alkaline EOR. Carbon supported monometallic, binary and ternary Pd-based anode catalysts were synthesized by the instant reduction method. The addition of low-cost and oxophilic co-catalysts (adatoms), such as Ni and Bi, leads to an enhancement of the EOR performance on the developed Pd-based nanocatalysts. The electrochemical properties of these catalysts were characterized with cyclic voltammetry and chronoamperometry using a rotating disk electrode. The physico-chemical characterization methods, such as inductively coupled plasma optical emission spectrometry, transmission electron microscopy combined with energy dispersive X-ray spectroscopy, X-ray powder diffractometry and X-ray photoelectron spectroscopy, were used to analyze the elemental composition, morphology and (surface) structure characteristics of the Pd-based nanocatalysts.

The novel carbon supported ternary PdNiBi nanocatalyst with an atomic ratio of 85:10:5 ($Pd_{85}Ni_{10}Bi_5$/C) exhibits the highest EOR activity among all synthesized Pt-free catalysts. The modification of the instant reduction method for development of the $Pd_{85}Ni_{10}Bi_5$/C anode catalyst results in a homogeneously distributed spherical catalyst nanoparticles with an average particle diameter of 3.7 ± 0.8 nm on Vulcan XC72R carbon support. This ternary catalyst system shows a higher peak current density, a lower onset potential and an improved byproduct tolerance toward EOR in alkaline medium compared to the commercial mono-metallic Pd/C catalyst due to bifunctional, electronic and synergetic effects.

Kurzfassung

Die Direkt-Ethanol-Brennstoffzelle (engl. Abk.: DEFC) ist ein Energiewandler mit hoher volumetrischer Energiedichte und ist für kleine tragbare und mobile elektronische Geräte prädestiniert. Die Dissertation beschäftigt sich mit der Synthese und Charakterisierung von Pt-freien Anodenkatalysatoren für die alkalische Ethanoloxidationsreaktion (EOR). Diese beinhaltet die Untersuchung des Einflusses von Adatomen und der Struktur auf die EOR-Leistung (Aktivität, Stabilität und Nebenprodukttoleranz) von ausgewählten Pt-freien Elektrokatalysatoren, und die Identifizierung eines neuartigen und geeigneten Katalysatorsystems mit hoher EOR-Aktivität für die alkalische DEFC.

Der Einsatz des 3d-Übergangsmetalls, Pd, ist derzeit für die Entwicklung von EOR-Nanokatalysatoren Stand der Technik. Kohlenstoffgeträgerte monometallische, binäre und ternäre Pd-basierende Anodenkatalysatoren wurden mit der Instant-Reduktionsmethode hergestellt. Die Beimengung der kostengünstigen und oxophilen Co-Katalysatoren (Adatomen) wie Ni und Bi bewirken eine Erhöhung der EOR-Leistung der Pd-basierenden Elektrokatalysatoren. Die elektrochemischen Eigenschaften dieser Katalysatoren wurden mit Cyclovoltammetrie und Chronoamperometrie unter Verwendung einer rotierenden Scheibenelektrode charakterisiert. Physikochemische Charakterisierungsverfahren, wie die optische Emissionsspektrometrie mit induktiv gekoppeltem Plasma, Transmissionselektronenmikroskopie kombiniert mit energiedispersiver Röntgenspektroskopie, Röntgen-Pulverdiffraktometrie und Röntgenphotoelektronenspektroskopie wurden verwendet, um die Elementzusammensetzung, die Morphologie und die (Oberflächen-)Struktureigenschaften der Pd-basierenden Nanokatalysatoren zu analysieren.

Der neuartige kohlenstoffgeträgerte ternäre PdNiBi Nanokatalysator mit einem atomaren Verhältnis von 85:10:5 ($Pd_{85}Ni_{10}Bi_5/C$) weist die höchste EOR-Aktivität unter allen hergestellten Pt-freien Katalysatoren auf. Die Modifizierung der Instant-Reduktionsmethode zur Herstellung dieses $Pd_{85}Ni_{10}Bi_5/C$ Katalysators führt zu homogen verteilten sphärischen Katalysatornanopartikeln mit einem durchschnittlichen Partikeldurchmesser von 3,7 ± 0,8 nm auf dem Kohlenstoffträgermaterial Vulcan XC72R. Dieses ternäre Katalysatorsystem zeigt eine höhere Spitzenstromdichte, ein geringeres Startpotential und eine verbesserte Nebenprodukttoleranz gegenüber der EOR im alkalischen Medium – im Vergleich zum kommerziellen monometallischen Pd/C Katalysator – aufgrund bifunktioneller, elektronischer und synergetischer Effekte.

Acknowledgments

First of all, I would like to thank my supervisor Assoc. Prof. Viktor Hacker for the opportunity to write my doctoral thesis in the Fuel Cell and Hydrogen Systems Group at the Institute of Chemical Engineering and Technology at the Graz University of Technology. This is thanks to his critical proofreading, his professional competence and his great supervision and guidance of all my dissertation activities.

In addition, I would especially like to thank the Fuel Cell and Hydrogen Systems Group, whose active support made it possible for me to achieve and implement my desired goals successfully. I would particularly like to highlight the support of DI Stephan Weinberger, Dr. Alexander Schenk, Dr. Christoph Grimmer, Dr. Ilena Grimmer, DI Johanna Ranninger, DI Sigrid Wolf and Michaela Roschger, BSc, who have made a significant contribution to all of my publications and all those people (Dr. Chakkrapong Chaiburi, Dominic Leipold, BSc, DI Julia Raunicher, Thomas Winter, MSc, Robert Zacharias, MSc) who have supported me with catalyst synthesis and characterization.

Another thanks goes to Dr. Ilse Letofsky-Papst (TEM-EDX), Dr. Brigitte Bitschnau (XRD), DI Norbert Kienzl (ICP-OES) and Dr. Christian Palfinger (XPS) for performing the physico-chemical characterization of my catalyst samples. I would also like to thank Assist. Prof. Dr. Boštjan Genorio and Dr. Justin Grant Connell for their professional support with experimentation (XPS) and proofreading of a peer-reviewed article.

Many thanks to my family (Mama, Papa, Sabine, Dominik, Maximilian, Daniela, Hubert, Laura, Moritz, Maximilian, Brigitte, Hubert, Thomas, Konstantin, Philipp, Angelika, Sebastian, Aloisia) for their ongoing support throughout my studies. Above all, I want to express sincere thanks to the most important people in my life, my fiancée Christina and my two sons Alexander and Leopold who, thanks to their great support, motivation and love, have made an essential contribution to the completion of this doctoral thesis.

Preface

A part of the doctoral thesis was published in advance in the Journal Nano Research (Cermenek et al. *Nano Res.*, **2019**, *12*, 683–693.) and in the Journal Electrocatalysis (Cermenek et al. *Electrocatalysis*, **2020**, *11*, 203–214.). The peer-reviewed articles and also related master theses (T. Winter and J. Ranninger) were included in the continuous text of the doctoral thesis and cited accordingly.

Financial support by the Austrian Climate Energy Fund, Austrian Federal Ministry of Transport, Innovation and Technology (BMVIT), The Austrian Research Promotion Agency (FFG) through the program “e!MISSION.at - Energy Mission Austria” – **Project ‘e!Polycat’** – and by the Austrian Science Fund (FWF) – **International project I 3871 ‘GO DEFC’** – and also the IEA research cooperation are gratefully acknowledged.

Contents

Contents ..... **I**

List of Figures ..... **V**

List of Tables ..... **XII**

Abbreviations ..... **XVI**

1 Introduction **1**

1.1 Motivation and Basics 1
1.2 Aims and Objectives 5
1.3 Structure of Dissertation 6

2 State of the Art **8**

2.1 Alkaline Ethanol Oxidation Reaction 8
2.1.1 Challenges 8
2.1.2 Pt-free Anode Catalyst Systems 9
2.1.3 Structure Characteristics Effects 11
2.1.4 Electrochemical Characteristics Effects 12
2.2 Anode Catalyst Support Materials 15
2.3 Pt-free Anode Catalyst Performances 16
2.4 Alkaline Direct Ethanol Fuel Cell Performance 18

3 Methodology **19**

3.1 Pt-free Anode Catalyst Systems 20
3.1.1 Synthesis 20
3.1.2 Characterization 24
3.2 Polysaccharide Based Anion Exchange Membranes 28
3.2.1 Synthesis 28
3.2.2 Characterization 29
3.3 Electrode Development 30

3.3.1 Anode 30
3.3.2 Cathode 30
3.4 Preparation of Membrane Electrode Assemblies 31
3.5 Single Cell Tests 32
3.5.1 Current-Voltage Characteristics 32
3.5.2 Electrochemical Impedance Spectroscopy 33
3.6 Various Parameters used for Evaluation of Anode Catalyst Performance 33

4 Results and Discussion 36

4.1 PART I: The Effect of Various Characterization Parameters and Operating Conditions on the EOR Performance of Carbon Supported Pt-free Electrocatalysts in an Alkaline Medium 39
4.1.1 Electrochemical Parameters and Operating Conditions Effects 40
4.1.2 Adatoms / Alloying Effect 46
4.1.3 Further Approaches for Catalyst EOR Performance Enhancement 46
4.1.4 Conclusion 48
4.2 PART II: Effects of Ni and Bi on EOR Performance and Structure Characteristics of Carbon Supported Pd-Based Nanocatalysts 50
4.2.1 Physico-Chemical Characterization 51
4.2.2 Electrochemical Characterization 60
4.2.3 In-situ Characterization 65
4.2.4 Conclusion 67
4.3 PART III: Atomic Composition Optimization of Carbon Supported $Pd_xNi_yBi_z$ Nanocatalyst for the Alkaline EOR 69
4.3.1 Physico-Chemical Characterization 70
4.3.2 Electrochemical Characterization 78
4.3.3 In-situ Characterization 85
4.3.4 Conclusion 85
4.4 PART IV: Alkaline Ethanol Oxidation Reaction on Carbon Supported Ternary PdNiBi Nanocatalyst using Modified Instant Reduction Synthesis Method 87
4.4.1 Modified Instant Reduction Synthesis Method 88
4.4.2 Physico-Chemical Characterization 89
4.4.3 Electrochemical Characterization 94
4.4.4 Conclusion 99
4.5 PART V: In-plane Ionic Conductivity Measurements of Various Ion Exchange Membranes for Low Temperature Fuel Cells 101

5 Summary 103

6 Outlook 105

7 References 108

8 Appendix A: Supplementary Material 122

8.1 PART I: The Effect of Various Characterization Parameters and Operating Conditions on the EOR Performance of Carbon Supported Pt-free Electrocatalysts in an Alkaline Medium 122

8.1.1 Chemicals, Materials and Equipment 122

8.1.2 Calculations of the Catalyst Ink Preparation 124

8.1.3 Relevant Resulting Publications 126

8.2 PART II: Effects of Ni and Bi on EOR Performance and Structural Characteristics of Carbon Supported Pd-Based Nanocatalysts 139

8.2.1 Chemicals and Materials 139

8.2.2 Physico-Chemical Characterization 141

8.2.3 Electrochemical Characterization 182

8.3 PART III: Atomic Composition Optimization of Carbon Supported $Pd_xNi_yBi_z$ Nanocatalyst for the Alkaline EOR 187

8.3.1 Chemicals and Materials 187

8.3.2 Physico-Chemical Characterization 188

8.3.3 Electrochemical Characterization 212

8.4 PART IV: Alkaline Ethanol Oxidation Reaction on Carbon Supported Ternary PdNiBi Nanocatalyst using Modified Instant Reduction Synthesis Method 213

8.4.1 Chemicals and Materials 213

8.4.2 Physico-Chemical Characterization 214

8.4.3 Electrochemical Characterization 234

9 Appendix B: Resulting Scientific Publications during the Doctoral Study 237

9.1 Peer-Reviewed Articles 237

9.2 Lectures 239

9.3 Book Chapters 239

9.4 Commissioned Reports 240

9.5 Conference Contributions and Professional Articles 240

9.6 Scientific Posters 243

10 Appendix C: Other Research Activities 246

10.1 Involvement in the Preparation of Accepted Proposals.....246

10.2 Supervised Students 247

10.3 News and Stories 247

List of Figures

Figure 1: Comparison of fuels in terms of volumetric energy density; *stored in hydrogen tanks under pressure of 70 MPa [4–6,8]. 1

Figure 2: Schematic ADEFC system **(a)** with complete and **(b)** with incomplete EtOH oxidation. Reproduced from [25] with permission from Elsevier. 4

Figure 3: Various influencing factors on the catalyst performance include: [a]Improvement of the catalyst activity with high > than low index crystal planes (= Miller indices) and its particle shape is not crucial; [b]Increased compressive strain-lattice parameter (a) affects the electronic structure; [c]discussed in **section 2.1.4**; [d]Low particle size results in a high active surface area of the catalyst and consequently improves its catalytic performance, [e]described in **section 2.2**; [f]Influences the surface structure (crystal planes), particle size and degree of alloying [20]. ..12

Figure 4: Synthesis steps of the standardized instant reduction method for EOR catalyst systems. 21

Figure 5: Modified instant reduction synthesis method – changes are marked red compared to the common instant reduction synthesis method described previously [3,15]. 23

Figure 6: Electrochemical and physico-chemical characterization methods used. 24

Figure 7: CV/CA-RDE setup for electrochemical characterization of the Pt-free anode catalyst systems. 25

Figure 8: Standardized in-plane conductivity measurement process for fuel cell membranes [112–114]. 29

Figure 9: MEA preparation: **(a)** Anode: Catalyst on carbon cloth; **(b)** HTCC/QPVA membrane; **(c)** Drop coating process and **(d)** developed MEA [103,118]. 31

Figure 10: Single cell configuration: **(a)** Open single cell system without ADEFC components; **(b)** Cathode flow field; **(c)** Anode flow field and **(d)** ADEFC system [103,118]. 32

Figure 11: EOR activity determinations on the Pd_xNi_y/C catalyst with catalyst loadings of **(a)-(c)** 28 $\mu g_{Pd} \cdot cm^{-2}$, **(d)-(f)** 56 $\mu g_{Pd} \cdot cm^{-2}$ and **(g)-(i)** 112 $\mu g_{Pd} \cdot cm^{-2}$ in 1 M KOH electrolyte with increased EtOH concentrations at a scan rate of 10 $mV \cdot s^{-1}$ and at 30 °C [103]. 41

Figure 12: Determined byproduct tolerance of the Pd_xNi_y/C catalyst using the ratio of the peak current density of the forward and backward scan from the EOR measurements (see

Figure 11) toward poisoning by reaction intermediates of EtOH oxidation with increased EtOH concentrations and catalyst loadings of **(a)** 28 $\mu g_{Pd} \cdot cm^{-2}$, **(b)** 56 $\mu g_{Pd} \cdot cm^{-2}$ and **(c)** 112 $\mu g_{Pd} \cdot cm^{-2}$ at 30 °C [103].....42

Figure 13: Catalyst loading effect on EOR activity of the Pd_xNi_y/C catalyst at 30 °C: **(a)** CVs in 1 M KOH at different catalyst loadings (relating to Pd), **(b)** the resulting EASAs and **(c)** CVs in an electrolyte mixture of 1 M KOH and 1 M EtOH [103].....43

Figure 14: Effect of various rotation speeds of the RDE on the EOR activity of the Pd_xNi_y/C catalyst **(a)** in a mixture of 1 M KOH and 1 M EtOH with a scan rate of 10 $mV \cdot s^{-1}$ at rt, and **(b)** the resulting peak current densities of the forward and backward scan from the EOR measurements. **(c)** Magnification of the potential range between 0.4 to 0.43 V from **(a)** showing the effect of different rotation speeds on onset potential toward alkaline EtOH oxidation [103]. 43

Figure 15: Effect of various scan rates on the EOR activity of the **(a)-(c)** Pd_xNi_y/C catalyst in a mixture of 1 M KOH and 1 M EtOH with a rotation speed of 0 rpm at 30 °C [103].....44

Figure 16: Temperature effect on the EOR activity of the Pd_xNi_y/C catalyst in dependence of different catalyst loadings **(a)-(c)** 28 $\mu g_{Pd} \cdot cm^{-2}$, **(d)-(f)** 56 $\mu g_{Pd} \cdot cm^{-2}$ and **(g)-(i)** 112 $\mu g_{Pd} \cdot cm^{-2}$ with a scan rate of 10 $mV \cdot s^{-1}$ [103]. 45

Figure 17: CVs of carbon supported Au-based nanocatalysts **(a)** in a mixture of 1 M KOH and 1 M EtOH at rt with a scan rate of 10 $mV \cdot s^{-1}$ (inset: CVs in de-aerated 1.0 M KOH solution at rt with a scan rate of 10 $mV \cdot s^{-1}$); **(b)** Determined tolerances of carbon supported Au-based nanocatalysts toward EtOH reaction intermediates using the EOR measurements; Stability tests of carbon supported Au-based nanocatalysts **(c)** in a mixture of 1 M KOH and 1 M EtOH at an applied potential of 1.1 V for 3,600 s using the CA method and **(d)** their resulting current density decrease, given in percentage values. 47

Figure 18: TEM micrographs of the **(a)** Pd/C with the corresponding particle size distribution histogram including the determined average particle size, **(b)** $Pd_{60}Ni_{40}/C$, **(c)** $Pd_{60}Bi_{40}/C$ and **(d)** $Pd_{60}Ni_{20}Bi_{20}/C$ catalyst [15].....52

Figure 19: HRTEM micrographs including the determined inter-planar spacing of the **(a)** Pd/C, **(b)** $Pd_{60}Ni_{40}/C$, **(c)** $Pd_{60}Bi_{40}/C$ and **(d)** $Pd_{60}Ni_{20}Bi_{20}/C$ catalyst [15]. 53

Figure 20: XRD patterns of carbon supported Pd-based nanocatalysts [15]. 54

Figure 21: Pd 3d XPS spectra of the **(a)** Pd/C, **(b)** $Pd_{60}Ni_{40}/C$, **(c)** $Pd_{60}Bi_{40}/C$ and **(d)** $Pd_{60}Ni_{20}Bi_{20}/C$ catalyst [15].....56

Figure 22: Ni 2p XPS spectra of the **(a)** $Pd_{60}Ni_{40}/C$ and **(b)** $Pd_{60}Ni_{20}Bi_{20}/C$ catalyst [15]. 57

Figure 23: Bi 4f XPS spectra of the **(a)** $Pd_{60}Bi_{40}/C$ and **(b)** $Pd_{60}Ni_{20}Bi_{20}/C$ catalyst [15]. 57

Figure 24: CVs of carbon supported Pd-based nanocatalysts **(a)** in de-aerated 1.0 M KOH solution at 30 °C with a scan rate of 10 $mV \cdot s^{-1}$ and **(b)** their resulting determined EASA; **(c)** in a mixture of 1 M KOH and 1 M EtOH at 30 °C with a scan rate of 10 $mV \cdot s^{-1}$; **(d)** Determined tolerances of Pd-based nanocatalysts toward EtOH reaction intermediates using the EOR measurements [15,29].....61

Figure 25: CVs of **(a)** $Pd_{60}Ni_{40}/C$ and $Pd_{60}Ni_{20}Bi_{20}/C$ catalysts in de-aerated 1.0 M KOH at 30 °C with a scan rate of 10 $mV \cdot s^{-1}$ in the potential range of 0.05-1.5 V with **(b)** their resulting determined EASA and **(c)** a magnification of the Ni peaks (anodic scan: oxidation of $NiOH_2$ to NiOOH; cathodic scan: reduction of NiOOH to $NiOH_2$) [15,29].....61

Figure 26: Stability tests of carbon supported Pd-based electrocatalysts **(a)** in a mixture of 1 M KOH and 1 M EtOH at an applied potential of 0.83 V and at 30 °C for 3,600 s using the CA method and **(b)** their resulting current density decrease, given in percentage [15,29].....63

Figure 27: Polarization and their resulting maximum power density curves of MEA 1 and MEA 2 at (a) 40 °C and at (b) 60 °C (Anode: 1 M KOH + 1 M EtOH, 10 $mL \cdot min^{-1}$; Cathode: Dry pure O_2, ~10 $mL \cdot min^{-1}$). 65

Figure 28: Nyquist plots of the **(a)** MEA 1 with **(b)** a magnification of the electrolyte resistance region and **(c)** MEA 2 with **(d)** a magnification of the electrolyte resistance region at constant temperature of 40 °C and 60 °C at different applied currents (Anode: 1 M KOH + 1 M EtOH, 10 $mL \cdot min^{-1}$; Cathode: Pure O_2, ~10 $mL \cdot min^{-1}$). 66

Figure 29: HRTEM micrographs including the determined inter-planar spacing of the **(a)** $Pd_{70}Ni_{25}Bi_5/C$, **(b)** $Pd_{70}Ni_{20}Bi_{10}/C$, **(c)** $Pd_{80}Ni_{10}Bi_{10}/C$ and **(d)** $Pd_{40}Ni_{20}Bi_{40}/C$ catalyst [15]..71

Figure 30: XRD patterns of carbon supported $Pd_xNi_yBi_z$ nanocatalysts [15]. 72

Figure 31: Pd 3d XPS spectra of the **(a)** $Pd_{70}Ni_{25}Bi_5/C$, **(b)** $Pd_{70}Ni_{20}Bi_{10}/C$, **(c)** $Pd_{80}Ni_{10}Bi_{10}/C$ and **(d)** $Pd_{40}Ni_{20}Bi_{40}/C$ catalyst [15]. 74

Figure 32: Ni 2p XPS spectra of the **(a)** $Pd_{70}Ni_{25}Bi_5/C$, **(b)** $Pd_{70}Ni_{20}Bi_{10}/C$, **(c)** $Pd_{80}Ni_{10}Bi_{10}/C$ and **(d)** $Pd_{40}Ni_{20}Bi_{40}/C$ catalyst [15]. 75

Figure 33: Bi 4f XPS spectra of the **(a)** $Pd_{70}Ni_{25}Bi_5/C$, **(b)** $Pd_{70}Ni_{20}Bi_{10}/C$, **(c)** $Pd_{80}Ni_{10}Bi_{10}/C$ and **(d)** $Pd_{40}Ni_{20}Bi_{40}/C$ catalyst [15]. 76

Figure 34: Electrochemical characterization of $Pd_{60}Ni_{40}/C$, $Pd_{70}Ni_{20}Bi_{10}/C$, $Pd_{60}Ni_{20}Bi_{20}/C$ and $Pd_{40}Ni_{20}Bi_{40}/C$ catalysts: **(a)** in de-aerated 1.0 M KOH and **(b)** the resulting EASAs, **(c)** in an electrolyte mixture of 1 M KOH + 1 M EtOH and **(d)** the obtained byproduct tolerances resulting from EOR measurements (see **(c)**) – performed at 30 °C and with a scan rate of 10 $mV \cdot s^{-1}$ [15,29]. 78

Figure 35: CA-measurements of $Pd_{60}Ni_{40}$/C, $Pd_{70}Ni_{20}Bi_{10}$/C, $Pd_{60}Ni_{20}Bi_{20}$/C and $Pd_{40}Ni_{20}Bi_{40}$/C catalysts: **(a)** in an electrolyte mixture of 1 M KOH + 1 M EtOH and **(b)** the resulting current density decrease in percentage at an applied potential of 0.83 V and at 30 °C for 3,600 s [15,29]. 80

Figure 36: Electrochemical characterization of $Pd_{80}Ni_{10}Bi_{10}$/C, $Pd_{70}Ni_{20}Bi_{10}$/C and $Pd_{70}Ni_{25}Bi_5$/C catalysts: **(a)** in de-aerated 1.0 M KOH and **(b)** the resulting EASAs, **(c)** in an electrolyte mixture of 1 M KOH + 1 M EtOH and **(d)** the obtained byproduct tolerances resulting from EOR measurements (see **(c)**) - performed at 30 °C and with a scan rate of 10 $mV \cdot s^{-1}$ [15,29]. 81

Figure 37: CA-measurements of $Pd_{80}Ni_{10}Bi_{10}$/C, $Pd_{70}Ni_{20}Bi_{10}$/C and $Pd_{70}Ni_{25}Bi_5$/C catalysts: **(a)** in an electrolyte mixture of 1 M KOH + 1 M EtOH and **(b)** the resulting current density decrease in percentage at an applied potential of 0.83 V for 3,600 s [15,29]. 82

Figure 38: TEM micrographs and particle size distribution histograms including the determined average particle size of the **(a)** $Pd_{85}Ni_{10}Bi_5/C^{(II)}$ and **(b)** $Pd_{85}Ni_{10}Bi_5/C^{(III)}$ catalyst [3]. 90

Figure 39: HRTEM micrographs with determined *d*-spacing of the **(a)** $Pd_{85}Ni_{10}Bi_5/C^{(I)}$, **(b)** $Pd_{85}Ni_{10}Bi_5/C^{(II)}$ and **(c)** $Pd_{85}Ni_{10}Bi_5/C^{(III)}$ catalyst [3]. 91

Figure 40: (a) XRD patterns of all $Pd_{85}Ni_{10}Bi_5$/C nanocatalysts and **(b)** the corresponding position of Pd (111) diffraction peak compared to the commercial Pd/C nanocatalyst [3]. 92

Figure 41: Pd 3d core level XPS spectra of the **(a)** Pd/C comm., **(b)** $Pd_{85}Ni_{10}Bi_5/C^{(I)}$, **(c)** $Pd_{85}Ni_{10}Bi_5/C^{(II)}$ and **(d)** $Pd_{85}Ni_{10}Bi_5/C^{(III)}$ catalyst [3]. 93

Figure 42: Electrochemical characterization of Pd/C comm., $Pd_{85}Ni_{10}Bi_5/C^{(I)}$, $Pd_{85}Ni_{10}Bi_5/C^{(II)}$ and $Pd_{85}Ni_{10}Bi_5/C^{(III)}$ catalysts: **(a)** in de-aerated 1.0 M KOH and **(b)** the resulting EASAs, **(c)** in an electrolyte mixture of 1 M KOH + 1 M EtOH and **(d)** the obtained byproduct tolerances resulting from EOR measurements (see **(c)**) – performed at 30 °C and with a scan rate of 10 $mV \cdot s^{-1}$ [3]. 95

Figure 43: CA-measurements of Pd/C comm., $Pd_{85}Ni_{10}Bi_5/C^{(I)}$, $Pd_{85}Ni_{10}Bi_5/C^{(II)}$ and $Pd_{85}Ni_{10}Bi_5/C^{(III)}$ catalysts: **(a)** in an electrolyte mixture of 1 M KOH + 1 M EtOH and **(b)** the resulting current density decrease percentage at an applied potential of 0.83 V and at 30 °C for 3,600 s [3]. 96

Figure 44: TEM micrographs with low and high magnifications of the Pd/C catalyst [15]. ..142

Figure 45: STEM-HAADF micrograph **(a)** and the corresponding EDX spectra **(b)-(d)** of the Pd/C catalyst [15]. 143

Figure 46: TEM micrographs with low and high magnifications of the $Pd_{60}Ni_{40}$/C catalyst [15]. 144

Figure 47: STEM-HAADF micrograph **(a)** and the corresponding EDX spectra **(b)** and **(c)** of the $Pd_{60}Ni_{40}$/C catalyst [15]. 145

Figure 48: TEM micrographs with low and high magnifications of the $Pd_{60}Bi_{40}$/C catalyst [15]. 146

Figure 49: STEM-HAADF micrograph **(a)** and the corresponding EDX spectra **(b)-(f)** of the $Pd_{60}Bi_{40}$/C catalyst [15]. 147

Figure 50: TEM micrographs with low and high magnifications of the $Pd_{60}Ni_{20}Bi_{20}$/C catalyst [15]. 148

Figure 51: STEM-HAADF micrograph **(a)** and the corresponding EDX spectra **(b)** and **(c)** of the $Pd_{60}Ni_{20}Bi_{20}$/C catalyst [15]. 149

Figure 52: C 1s XPS spectra of the **(a)** Pd/C, **(b)** $Pd_{60}Ni_{40}$/C, **(c)** $Pd_{60}Bi_{40}$/C and **(d)** $Pd_{60}Ni_{20}Bi_{20}$/C catalyst [15]. 181

Figure 53: O 1s XPS spectra of the **(a)** Pd/C, **(b)** $Pd_{60}Ni_{40}$/C, **(c)** $Pd_{60}Bi_{40}$/C and **(d)** $Pd_{60}Ni_{20}Bi_{20}$/C catalyst [15]. 181

Figure 54: (a) Diffusion controlled process for the alkaline EOR takes place on carbon supported Pd-based catalysts in scan rates region of 100 to 1000 $mV \cdot s^{-1}$, showing by linear relationship between peak current density and square root of scan rate. The EOR measurements on the respective catalyst were performed in a mixture of 1 M KOH and 1 M EtOH and at 30 °C and **(b)** the number of electrons which are released during the EOR oxidation, were determined according to Randles-Sevcik equation. 182

Figure 55: Stability tests of carbon supported Pd-based electrocatalysts **(a)** in a mixture of 1 M KOH and 1 M EtOH at an applied potential of 0.5 V and at 30 °C for 3,600 s using the CA method and **(b)** their resulting current density decrease, given in percentage. 182

Figure 56: Nyquist plots of the MEA 1 consisting of $Pd_{60}Ni_{40}$/C based anode, Tokuyama A201 AEM and Ag-MnO_x/C based cathode at a constant current of **(a)** 20 mA, **(b)** 40 mA and **(c)** 80 mA with corresponding magnified electrolyte resistance region (right) at different temperatures (Anode: 1 M KOH + 1 M EtOH, 10 $mL \cdot min^{-1}$; Cathode: Pure O_2, ~10 $mL \cdot min^{-1}$). 183

Figure 57: Nyquist plots of the MEA 1 consisting of $Pd_{60}Ni_{40}$/C based anode, Tokuyama A201 AEM and Ag-MnO_x/C based cathode at a constant temperature of **(a)** 40 °C, **(b)** 50 °C, **(c)** 60 °C and **(d)** 70 °C with corresponding magnified electrolyte resistance region (right) at different applied currents (Anode: 1 M KOH + 1 M EtOH, 10 $mL \cdot min^{-1}$; Cathode: Pure O_2, ~10 $mL \cdot min^{-1}$). 184

Figure 58: Nyquist plots of the MEA 2 consisting of $Pd_{60}Ni_{20}Bi_{20}$/C based anode, Tokuyama A201 AEM and Ag-MnO_x/C based cathode at a constant current of **(a)** 20 mA, **(b)** 40 mA and **(c)** 80 mA with corresponding magnified electrolyte resistance region (right) at different temperatures (Anode: 1 M KOH + 1 M EtOH, 10 mL·min^{-1}; Cathode: Pure O_2, ~10 mL·min^{-1}). 185

Figure 59: Nyquist plots of the MEA 2 consisting of $Pd_{60}Ni_{20}Bi_{20}$/C based anode, Tokuyama A201 AEM and Ag-MnO_x/C based cathode at a constant temperature of **(a)** 40 °C, **(b)** 50 °C, **(c)** 60 °C and **(d)** 70 °C with corresponding magnified electrolyte resistance region (right) at different applied currents (Anode: 1 M KOH + 1 M EtOH, 10 mL·min^{-1}; Cathode: Pure O_2, ~10 mL·min^{-1}). 186

Figure 60: TEM micrographs with low and high magnifications of the $Pd_{70}Ni_{25}Bi_5$/C catalyst [15]. 189

Figure 61: TEM micrographs with low and high magnifications of the $Pd_{70}Ni_{20}Bi_{10}$/C catalyst [15]. 190

Figure 62: TEM micrographs with low and high magnifications of the $Pd_{80}Ni_{10}Bi_{10}$/C catalyst [15]. 191

Figure 63: TEM micrographs with low and high magnifications of the $Pd_{40}Ni_{20}Bi_{40}$/C catalyst [15]. 192

Figure 64: EDX spectra of the **(a)** $Pd_{70}Ni_{25}Bi_5$/C, **(b)** $Pd_{70}Ni_{20}Bi_{10}$/C, **(c)** $Pd_{80}Ni_{10}Bi_{10}$/C and **(d)** $Pd_{40}Ni_{20}Bi_{40}$/C catalyst [15]. 193

Figure 65: C 1s XPS spectra of the **(a)** $Pd_{70}Ni_{25}Bi_5$/C, **(b)** $Pd_{70}Ni_{20}Bi_{10}$/C, **(c)** $Pd_{80}Ni_{10}Bi_{10}$/C and **(d)** $Pd_{40}Ni_{20}Bi_{40}$/C catalyst [15]. 210

Figure 66: O 1s XPS spectra of the **(a)** $Pd_{70}Ni_{25}Bi_5$/C, **(b)** $Pd_{70}Ni_{20}Bi_{10}$/C, **(c)** $Pd_{80}Ni_{10}Bi_{10}$/C and **(d)** $Pd_{40}Ni_{20}Bi_{40}$/C catalyst [15]. 211

Figure 67: (a) Diffusion controlled process for the alkaline EOR takes place on carbon supported $Pd_xNi_yBi_z$ catalysts in scan rates region of 10 to 100 mV·s^{-1}, showing by linear relationship between peak current density and square root of scan rate. The EOR measurements on the respective catalyst were performed in a mixture of 1 M KOH and 1 M EtOH and at 30 °C and **(b)** the number of electrons which are released during the EOR oxidation, were determined according to Randles-Sevcik equation. 212

Figure 68: Stability tests of carbon supported $Pd_{60}Ni_{40}$ and $Pd_xNi_yBi_z$ electrocatalysts **(a)** and **(b)** in a mixture of 1 M KOH and 1 M EtOH at an applied potential of 0.5 V and at 30 °C for 3,600 s using the CA method and **(c)** and **(d)** their resulting current density decrease, given in percentage. 212

Figure 69: TEM micrographs with low and high magnifications of the $Pd_{85}Ni_{10}Bi_5/C^{(I)}$ catalyst [3]. 215

Figure 70: STEM-HAADF micrograph **(a)** and the corresponding EDX spectra **(b)-(g)** of the $Pd_{85}Ni_{10}Bi_5/C^{(I)}$ catalyst [3]. 216

Figure 71: TEM micrographs with low and high magnifications of the $Pd_{85}Ni_{10}Bi_5/C^{(II)}$ catalyst [3]. 218

Figure 72: STEM-HAADF micrograph **(a)** and the corresponding EDX spectra **(b)-(f)** of the $Pd_{85}Ni_{10}Bi_5/C^{(II)}$ catalyst [3]. 219

Figure 73: TEM micrographs with low and high magnifications of the $Pd_{85}Ni_{10}Bi_5/C^{(III)}$ catalyst [3]. 221

Figure 74: STEM-HAADF micrograph **(a)** and the corresponding EDX spectra **(b)-(f)** of the $Pd_{85}Ni_{10}Bi_5/C^{(III)}$ catalyst [3]. 222

Figure 75: Survey XPS spectra of the **(a)** Pd/C comm., **(b)** $Pd_{85}Ni_{10}Bi_5/C^{(I)}$, **(c)** $Pd_{85}Ni_{10}Bi_5/C^{(II)}$ and **(d)** $Pd_{85}Ni_{10}Bi_5/C^{(III)}$ catalyst [3]. 230

Figure 76: Ni 2p core level XPS spectra of the **(a)** $Pd_{85}Ni_{10}Bi_5/C^{(I)}$, **(b)** $Pd_{85}Ni_{10}Bi_5/C^{(II)}$ and **(c)** $Pd_{85}Ni_{10}Bi_5/C^{(III)}$ catalyst [3]. 233

Figure 77: Bi 4f core level XPS spectra of the **(a)** $Pd_{85}Ni_{10}Bi_5/C^{(I)}$, **(b)** $Pd_{85}Ni_{10}Bi_5/C^{(II)}$ and **(c)** $Pd_{85}Ni_{10}Bi_5/C^{(III)}$ catalyst [3]. 234

Figure 78: CVs of **(a)** $Pd_{85}Ni_{10}Bi_5/C$ catalysts in de-aerated 1.0 M KOH at 30 °C and with a scan rate of 10 $mV \cdot s^{-1}$ in the potential range of 0.05-1.5 V with **(b)** their resulting determined EASA [3]. 234

List of Tables

Table 1: State-of-the-art EOR performance relating to activity (onset potential, specific activity and mass activity) of different ternary Pd-based nanocatalysts compared to $Pd_xNi_yBi_z/C$ nanocatalysts using the common and the modified instant reduction synthesis method [3,15]. 17

Table 2: State-of-the-art ADEFC efficiency and power density compared to the counterparts acidic DEFC and acidic-alkaline DEFC [9,98–100]. 18

Table 3: Overview of all developed monometallic, binary, ternary and other Pt-free anode catalyst systems (incl. reference materials) showing the synthesis methods and carbon support materials used. 20

Table 4: ICP-OES analysis of carbon supported Au-based nanocatalysts. 47

Table 5: Elemental analysis of Pd-based nanocatalysts by ICP-OES [15,29]. 51

Table 6: Structure analysis of carbon supported Pd-based catalysts by XRD [15]. 55

Table 7: XPS characterization data of the carbon supported Pd-based catalysts including the determined metal contents [15]. 59

Table 8: Electrochemical characterization results of carbon supported Pd-based nanocatalysts [15]. 64

Table 9: Elemental analysis of $Pd_xNi_yBi_z/C$ nanocatalysts by ICP-OES [15,29]. 70

Table 10: Structure analysis of carbon supported $Pd_xNi_yBi_z$ nanocatalysts by XRD [15].....73

Table 11: XPS characterization data of $Pd_xNi_yBi_z/C$ catalysts including the determined metal contents [15]. 77

Table 12: Electrochemical results of all carbon supported Pd-based electrocatalysts from **sections 4.2.2** (grey shaded) and **4.3.2** [15,29]. 84

Table 13: Determined XRD analysis parameters of all catalyst samples. Average crystallite size estimation according to Scherrer assuming spherical crystallites with cubic crystal system of five diffraction peaks (peak pos.). Determination of half-width (FWHM; B_{obs}), *d*-spacing and lattice parameter by profile-fit and Rietveld refinement, $B_{standard}$ determined from LaB_6 [3]. ...92

Table 14: Electrochemical characterization results of carbon supported $Pd_{85}Ni_{10}Bi_5$/C nanocatalysts developed by instant reduction synthesis method with different modifications compared to commercial Pd/C catalyst [3].....98

Table 15: ICP-OES data of carbon supported Pd-based catalysts [15,29]. 141

Table 16: XRD data (Rietveld refinement) of Pd/C catalyst [15]. 150

Table 17: XRD data (Rietveld refinement) of $Pd_{60}Ni_{40}$/C catalyst [15]. 150

Table 18: XRD data (Rietveld refinement) of $Pd_{60}Bi_{40}$/C catalyst [15]. 151

Table 19: XRD data (Rietveld refinement) of $Pd_{60}Ni_{20}Bi_{20}$/C catalyst [15]. 167

Table 20: Determined crystal structure in all Pd-based catalyst samples and their corresponding data – adopted from Inorganic Crystal Structure Database (ICSD) – FIZ Karlsruhe - Leibniz Institute for Information Infrastructure with the ICSD Collection code of 64922 (https://icsd.fiz-karlsruhe.de/display/details.xhtml) [153]. 170

Table 21: Determined crystal structure in the $Pd_{60}Ni_{40}$/C catalyst and their corresponding data – adopted from Inorganic Crystal Structure Database (ICSD) – FIZ Karlsruhe - Leibniz Institute for Information Infrastructure with the ICSD Collection code of 106936 (https://icsd.fiz-karlsruhe.de/display/details.xhtml) [154]. 171

Table 22: Determined crystal structure in the $Pd_{60}Bi_{40}$/C catalyst and their corresponding data – adopted from Inorganic Crystal Structure Database (ICSD) – FIZ Karlsruhe - Leibniz Institute for Information Infrastructure with the ICSD Collection code of 53797 (https://icsd.fiz-karlsruhe.de/display/details.xhtml) [153]. 172

Table 23: Determined crystal structure (Bi: violet; O: red) in the $Pd_{60}Bi_{40}$/C catalyst and their corresponding data – adopted from Inorganic Crystal Structure Database (ICSD) – FIZ Karlsruhe - Leibniz Institute for Information Infrastructure with the ICSD Collection code of 189995 (https://icsd.fiz-karlsruhe.de/display/details.xhtml) [155].....173

Table 24: Determined crystal structure (Bi: violet; O: red, C: grey) in the $Pd_{60}Bi_{40}$/C, $Pd_{60}Ni_{20}Bi_{20}$/C, $Pd_{80}Ni_{10}Bi_{10}$/C and $Pd_{40}Ni_{20}Bi_{40}$/C catalysts and their corresponding data – adopted from Inorganic Crystal Structure Database (ICSD) – FIZ Karlsruhe - Leibniz Institute for Information Infrastructure with the ICSD Collection code of 252588 (https://icsd.fiz-karlsruhe.de/display/details.xhtml) [156]. 174

Table 25: Determined crystal structure (Pd: blue; Bi: violet) in the $Pd_{60}Bi_{40}$/C catalyst and their corresponding data – adopted from Inorganic Crystal Structure Database (ICSD) – FIZ Karlsruhe - Leibniz Institute for Information Infrastructure with the ICSD Collection code of 56279 (https://icsd.fiz-karlsruhe.de/display/details.xhtml) [157].....175

Table 26: Determined crystal structure in all Pd-based catalyst samples and their corresponding data – adopted from Inorganic Crystal Structure Database (ICSD) – FIZ Karlsruhe - Leibniz Institute for Information Infrastructure with the ICSD Collection code of 187640 (https://icsd.fiz-karlsruhe.de/display/details.xhtml) [158]. 176

Table 27: XPS data of the Pd/C catalyst [15]. 177

Table 28: XPS data of the $Pd_{60}Ni_{40}$/C catalyst [15]. 178

Table 29: XPS data of the $Pd_{60}Bi_{40}$/C catalyst [15]. 179

Table 30: XPS data of the $Pd_{60}Ni_{20}Bi_{20}$/C catalyst [15]. 180

Table 31: ICP-OES data of carbon supported $Pd_xNi_yB_z$ catalysts [15,29]. 188

Table 32: TEM-EDX results of the $Pd_{70}Ni_{25}Bi_5$/C, $Pd_{70}Ni_{20}Bi_{10}$/C, $Pd_{80}Ni_{10}Bi_{10}$/C and $Pd_{40}Ni_{20}Bi_{40}$/C catalyst [15]. 193

Table 33: XRD data (Rietveld refinement) of $Pd_{70}Ni_{25}Bi_5$/C catalyst [15]. 194

Table 34: XRD data (Rietveld refinement) of $Pd_{70}Ni_{20}Bi_{10}$/C catalyst [15]. 194

Table 35: XRD data (Rietveld refinement) of $Pd_{80}Ni_{10}Bi_{10}$/C catalyst [15]. 195

Table 36: XRD data (Rietveld refinement) of $Pd_{40}Ni_{20}Bi_{40}$/C catalyst [15]. 198

Table 37: XPS results of carbon supported Pd-based catalysts with the assignments of Pd 3d, Ni 2p and Bi 4f peaks [15]. 205

Table 38: XPS data of the $Pd_{70}Ni_{25}Bi_5$/C catalyst [15].....206

Table 39: XPS data of the $Pd_{70}Ni_{20}Bi_{10}$/C catalyst [15]. 207

Table 40: XPS data of the $Pd_{80}Ni_{10}Bi_{10}$/C catalyst [15]. 208

Table 41: XPS data of the $Pd_{40}Ni_{20}Bi_{40}$/C catalyst [15]. 209

Table 42: ICP-OES data of the commercial Pd/C catalyst and the carbon supported $Pd_{85}Ni_{10}B_5$ catalysts using the instant method with different modifications [3]. 214

Table 43: TEM-EDX results of the $Pd_{85}Ni_{10}Bi_5/C^{(I)}$ catalyst [3]. 217

Table 44: TEM-EDX results of the $Pd_{85}Ni_{10}Bi_5/C^{(II)}$ catalyst [3]. 220

Table 45: TEM-EDX results of the $Pd_{85}Ni_{10}Bi_5/C^{(III)}$ catalyst [3].....223

Table 46: XRD data (Rietveld refinement) of the commercial Pd/C catalyst [3]. 224

Table 47: XRD data (Rietveld refinement) of the $Pd_{85}Ni_{10}Bi_5/C^{(I)}$ catalyst [3]. 225

Table 48: XRD data (Rietveld refinement) of the $Pd_{85}Ni_{10}Bi_5/C^{(II)}$ catalyst [3].....226

Table 49: XRD data (Rietveld refinement) of the $Pd_{85}Ni_{10}Bi_5/C^{(III)}$ catalyst [3]. 227

Table 50: XRD analysis of the commercial Pd/C catalyst – average crystallite size estimation according to Scherrer, assuming spherical crystallites with cubic crystal system at five diffraction peaks (peak pos.) including the determination of half-width (B_{obs}) and lattice parameter by profile fit and Rietveld refinement, respectively [3]. 228

Table 51: XRD analysis of the $Pd_{85}Ni_{10}Bi_5/C^{(I)}$ catalyst – average crystallite size estimation according to Scherrer, assuming spherical crystallites with cubic crystal system at five diffraction peaks (peak pos.) including the determination of half-width (B_{obs}) and lattice parameter by profile fit and Rietveld refinement, respectively [3]. 228

Table 52: XRD analysis of the $Pd_{85}Ni_{10}Bi_5/C^{(II)}$ catalyst – average crystallite size estimation according to Scherrer assuming spherical crystallites with cubic crystal system at five diffraction peaks (peak pos.) including the determination of half-width (B_{obs}) and lattice parameter by profile fit and Rietveld refinement, respectively [3]. 229

Table 53: XRD analysis of the $Pd_{85}Ni_{10}Bi_5/C^{(III)}$ catalyst – average crystallite size estimation according to Scherrer, assuming spherical crystallites with cubic crystal system at five diffraction peaks (peak pos.) including the determination of half-width (B_{obs}) and lattice parameter by profile fit and Rietveld refinement, respectively [3]. 229

Table 54: XPS data (measured) of the commercial Pd/C catalyst [3]. 231

Table 55: XPS data (measured) of the $Pd_{85}Ni_{10}Bi_5/C^{(I)}$ catalyst [3]. 231

Table 56: XPS data (measured) of the $Pd_{85}Ni_{10}Bi_5/C^{(II)}$ catalyst [3]. 231

Table 57: XPS data (measured) of the $Pd_{85}Ni_{10}Bi_5/C^{(III)}$ catalyst [3]. 231

Table 58: XPS results (fitted) of carbon supported Pd-based catalysts with the assignments of Pd 3d, Ni 2p and Bi 4f peaks including the determined metal contents obtained from measured data [3]. 232

Abbreviations

AC	Alternating current
ADEFC(s)	Alkaline direct ethanol fuel cell(s)
AEM(s)	Anion exchange membrane(s)
AL	Active layer
ALT	Active layer thickness
ARRS	Slovenian Research Agency
AST	Accelerated stress test
CA	Chronoamperometry
CEET	Chemical Engineering and Environmental Technology
CEM(s)	Cation exchange membrane(s)
CV	Cyclic voltammetry
DEFC(s)	Direct ethanol fuel cell(s)
DEMS	Differential electrochemical mass spectrometry
DFT	Density functional theory
EASA	Electrochemical active surface area
EDX	Energy dispersive X-ray
EG	Ethylene glycol
EIS	Electrochemical impedance spectroscopy
EOR	Ethanol oxidation reaction
EtOH	Ethanol
fcc	Face-centered cubic
FFG	The Austrian Research Promotion Agency (in German: Österreichische Forschungsförderungsgesellschaft mbH)
FFT	Fast Fourier transformation

FTIR	Fourier-transform infrared
FWF	Austrian Science Fund (in German: Fonds zur Förderung der wissenschaftlichen Forschung)
FWHM	Full width half maximum
GC	Glassy carbon
GDL	Gas diffusion layer
HAADF	High-angle angular dark-field imaging
HFR	High frequency resistance
HPLC	High performance liquid chromatography
HRTEM	High resolution transmission electron microscopy
HTCC	N-[(2-Hydroxy-3-trimethylammonium) propyl] chitosan chloride
ICP-OES	Inductively coupled plasma optical emission spectrometry
ICSD	Inorganic crystal structure database
IEMs	Ion exchange membranes
IF	Impact factor
I-V	Current-voltage
JR	Joanneum Research
MA	Mass activity
MEA(s)	Membrane electrode assembly(ies)
MeOH	Methanol
MFP	Mean free path
MMO	Mercury-mercury oxide
n/a	Not applicable
NHE	Normal hydrogen electrode
NMR	Nuclear magnetic resonance
OCP	Open circuit potential
OeAD	Austrian Exchange Service Company (in German: Österreichische Austauschdienst-Gesellschaft)

ORR	Oxygen reduction reaction
PEEK	Polyether ether ketone
PM-IRRAS	Polarization modulation infrared reflection absorption
PTFE	Polytetrafluoroethylene
QPVA	Quaternized poly (vinyl alcohol)
RDE	Rotating disk electrode
RHE	Reversible hydrogen electrode
rms	Root mean square
rpm	Revolution per minute
RSF	Relative sensitivity factor
rt	Room temperature
SCE	Saturated calomel electrode
SHE	Standard hydrogen electrode
STEM	Scanning transmission electron microscopy
TEM	Transmission electron microscopy
TOC	Table of contents
UHV	Ultrahigh-vacuum
UL	University of Ljubljana
UM	University of Maribor
WTZ	Scientific & Technological Cooperation (in German: Wissenschaftlich-Technische Zusammenarbeit)
XPS	X-ray photoelectron spectroscopy
XRD	X-ray powder diffractometry

1 Introduction

1.1 Motivation and Basics

The demand for renewable energy has recently risen sharply due to the already visible ecological impact of the fossil age, with fuel cells identified as a key technology for the clean energy conversion of the future [1–3].

The direct conversion of a sustainable and easy-to-use liquid fuel into electricity using emission-free fuel cell technology is at the heart of the research efforts of electrochemists and engineers. Various liquid fuels such as sodium borohydride ($NaBH_4$, solution, 30 wt.%), methanol (MeOH), hydrazine hydrate ($N_2H_4 \cdot H_2O$), ethylene glycol (EG), ethanol (EtOH), glycerol ($C_3H_8O_3$), 1-propanol (C_3H_8O) and 2-propanol (C_3H_8O) have high volumetric energy densities and are comparable to gasoline and diesel. However, they exceed gaseous hydrogen H_2(g)*, liquid hydrogen H_2(l) (Figure 1) and batteries (e.g., Li ion batteries: 0.2 – 0.6 $kWh \cdot L^{-1}$) by a multiple [4–8].

Fuel cells with liquid fuels show a higher theoretical efficiency (η > 83%) compared to H_2 [5]. After applying exclusion criteria for a future fuel such as ‘renewable’, ‘available’, ‘non-toxic’ and ‘liquid’ [6], EtOH is classified as a promising fuel.

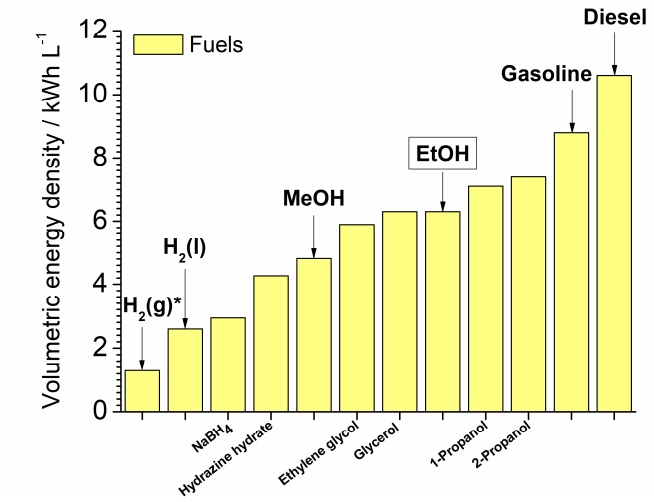


Figure 1: Comparison of fuels in terms of volumetric energy density;
*stored in hydrogen tanks under pressure of 70 MPa [4–6,8].

Ethanol is a sustainable, low-toxic, liquid fuel with high volumetric energy density (6.3 $kWh \cdot L^{-1}$) compared to MeOH (4.8 $kWh \cdot L^{-1}$) and H_2 (2.6 $kWh \cdot L^{-1}$), making it easy to handle, store and transport [8–15] and is available worldwide (largest producer: USA and Brazil [16]). The production of EtOH using enzymatic hydrolysis and fermentation processes depending on the raw material used from agricultural products or biomass such as straw, corn, sugar cane or wheat in comparison to MeOH and H_2 avoids the use of fossil fuels with limited availability as feedstocks [10,13,15,16].

The direct use of EtOH under alkaline conditions in a fuel cell is denoted as **alkaline direct ethanol fuel cell (ADEFC)**. The ADEFC using non-Pt-based electrocatalysts and cost-efficient materials for the production of anion exchange membranes (AEMs) is a low-cost, environment-friendly and easy-to-use energy source as an alternative to batteries for small portable applications [9,15].

The ADEFC directly converts the chemical energy of the EtOH solution into electrical energy under alkaline conditions, without a reforming step. The overall reaction of the ADEFC (Equation 3) is composed of the ethanol oxidation reaction (EOR) (Equation 1) and the oxygen reduction reaction (ORR) (Equation 2). Theoretically, the complete oxidation of EtOH to CO_2 in alkaline media occurs at an anode potential of -0.74 V (Equation 1) and the reduction of O_2 to hydroxide ions (OH^-) occurs at a cathode potential of 0.40 V (Equation 2), resulting in a reversible cell voltage of 1.14 V (Equation 3) [8–11].

$$C_2H_5OH + 12\ OH^- \rightarrow 2\ CO_2 + 9\ H_2O + 12\ e^- \qquad E^0 = -0.74\ V\ vs.\ SHE \qquad (1)$$

$$3\ O_2 + 6\ H_2O + 12\ e^- \rightarrow 12\ OH^- \qquad E^0 = 0.40\ V\ vs.\ SHE \qquad (2)$$

$$C_2H_5OH + 3\ O_2 \rightarrow 2\ CO_2 + 3\ H_2O \qquad E^0 = 1.14\ V\ vs.\ SHE \qquad (3)$$

The use of alkaline electrolytes compared to acidic counterparts has the following benefits for DEFCs [15]:

- The kinetics of EOR and ORR are enhanced [9–15].
- Non-noble elements (e.g., Ni, Fe, Co, Bi or Mn) as admetals or adatoms are used in the production of EOR and ORR catalysts to reduce catalytic material costs and to improve their catalytic performance [9–11,13–15,17,18].
- The use of the AEM instead of the cation exchange membrane (CEM) lowers the costs (AEM: 67.5 $\$ \cdot m^{-2}$ vs. CEM: 675 $\$ \cdot m^{-2}$) [9,15].

- Due to the reversed direction of ion conduction of AEMs (electro osmotic drag) compared to CEMs, the EtOH crossover is drastically reduced [11,15,19].
- Reduction of corrosion and simplified water management [20–23].

The main challenge of ADEFC is the incomplete oxidation of EtOH to different intermediates at the anode (Equations 4-6) [9–11]. The main products of the incomplete EOR in alkaline media are usually acetic acid (CH_3COOH) and acetate (CH_3COO^-) delivering of four electrons (Equations 4 and 6), which leads to a Faradaic efficiency loss of 66.7% in the ADEFC system [9,10]. Acetic acid is not stable in alkaline media, so it reacts with OH^- to CH_3COO^- (Equation 5), which is the final product of EtOH oxidation [9,10].

$$C_2H_5OH + 4\ OH^- \rightarrow CH_3COOH + 3\ H_2O + 4\ e^- \quad (4)$$

$$CH_3COOH + OH^- \rightarrow CH_3COO^- + H_2O \quad (5)$$

$$C_2H_5OH + 5\ OH^- \rightarrow CH_3COO^- + 4\ H_2O + 4\ e^- \quad (6)$$

To date, no catalyst has been identified that efficiently cleaves the strong carbon-carbon bond in EtOH molecules at low temperatures (< 100 °C) to completely oxidize EtOH to CO_2 (CO_2 current efficiency of 100%), H_2O, and release 12 electrons (Equation 1) [12,13,24]. The actual overall reaction (Equation 8) of state-of-the-art ADEFC consists of the electrochemical reactions of Equations 6 and 7 [9–11].

$$O_2 + 2\ H_2O + 4\ e^- \rightarrow 4\ OH^- \quad (7)$$

$$C_2H_5OH + O_2 + OH^- \rightarrow CH_3COO^- + 2\ H_2O \quad (8)$$

Figure 2 schematically shows the process in the ADEFC system under theoretical (a) and practical (b) conditions [25]. The substitution of liquid alkaline electrolyte by AEM prevents electrolyte leaks, but the carbonate problem in this fuel cell system remains unsolved [10,19,25]. The addition of KOH to the EtOH fuel improves the currently low ionic conductivities of AEMs in order to increase the performance of ADEFC. However, KOH reacts with CO_2, the product of EtOH oxidation at the anode, to form K_2CO_3 as precipitate[1]. This blocks the active sites of the electrodes and reduces the ADEFC performance continuously [9,10,19,25].

[1] The air containing CO_2 (0.039%), when used to supply the ADEFC, reacts with OH^-, the product of ORR at the cathode, to form carbonates (CO_3^{2-} or HCO_3^-) [10,19,25].

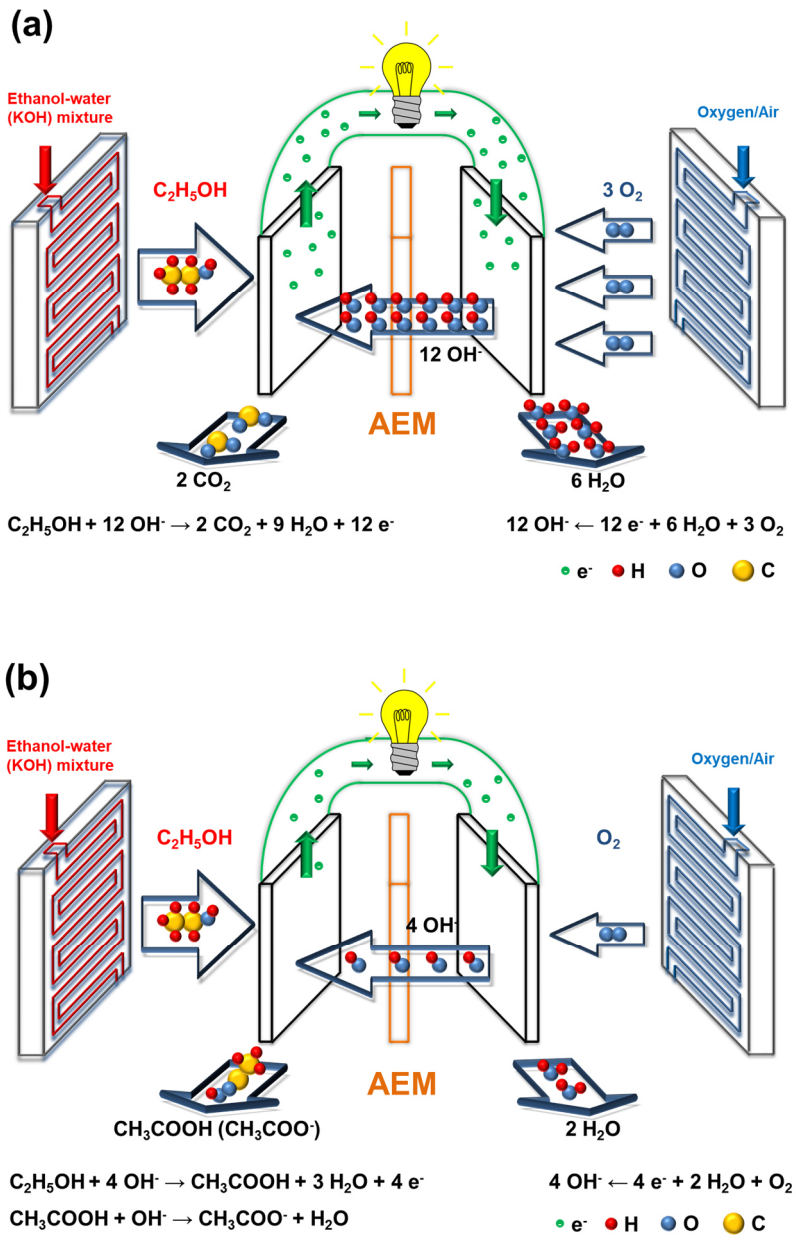


Figure 2: Schematic ADEFC system **(a)** with complete and **(b)** with incomplete EtOH oxidation. Reproduced from [25] with permission from Elsevier.

It is essential to develop electrodes with high activity as well as high stability and tolerance to the reaction intermediates of alkaline EtOH oxidation (e.g., CO and CH_x). These resulting poisoning species deactivate easily the carbon supported Pt-based catalysts and reduce their efficiencies over time for the use in ADEFCs [15,26–28]. Therefore, binary and ternary Pt-free catalysts are preferentially used for the alkaline EOR [15] and are at the top of the research agenda for DEFC development [8,25].

This doctoral thesis focuses on the investigation of the effects of (i) different electrochemical measuring parameters (e.g., rotation speed and scan rate), (ii) various operating conditions (e.g., at different temperatures and electrolyte concentrations), (iii) different catalyst

loadings, (iv) adatoms (alloying), (v) the structure and morphology, and (vi) the chemical composition on the EOR performance of carbon supported Pt-free electrocatalysts in an alkaline medium. Using different synthesis procedures, monometallic, binary and ternary, and other Pt-free anode catalyst systems were analyzed with electrochemical characterization methods for the alkaline EOR. The best performing anode catalyst was further optimized by both the atomic composition variations and the modification of the instant reduction synthesis method. It was then comprehensively characterized, electrochemically and physico-chemically, for the application in ADEFCs.

1.2 Aims and Objectives

The doctoral thesis was written within the framework of the already completed research project 'e!Polycat' entitled 'Pt-free anode catalyst systems and composite polysaccharide-membranes for the alkaline DEFC' – funded by The Austrian Research Promotion Agency (FFG) – in co-operation with University of Graz (KFU, Institute of Chemistry, Ao.Univ.-Prof.i.R. Dr.phil. Volker Ribitsch) and Joanneum Research Forschungsgesellschaft mbH (JR, Materials, Institute for Surface Technologies and Photonics, Ing.^{in} Birgit Feketeföldi) and the ongoing research project 'GO DEFC' entitled 'Graphene oxide based MEAs for the direct ethanol fuel cell' – funded by Austrian Science Fund (FWF) – in cooperation with University of Maribor (UM, Faculty of Electrical Engineering and Computer Science, Univ.-Prof. Dr.rer.nat. Karin Stana Kleinschek) and University of Ljubljana (UL, Faculty of Chemistry and Chemical Technology, Assist. Prof. Dr. Boštjan Genorio).

The following aims and objectives were pursued in terms of anode catalyst development and characterization for the ADEFC, and ionic conductivity measurements of various fuel cell membranes:

(1) The development of novel carbon supported Pt-free electrocatalysts using various synthesis methods with high EOR performances in an alkaline medium:
   - High specific and mass activity (→ High peak current with low onset potential), and
   - High catalytic stability / High byproduct tolerance.

(2) The research of material and measuring effects on the alkaline EOR performance of carbon supported monometallic, binary and ternary Pt-free anode catalyst systems:

   - Identification of the optimal catalyst ink preparation and fixing of the electrolyte concentration, temperature and catalyst loading to establish a standardized procedure for electrochemical characterization of the synthesized Pt-free EOR catalysts.

- Analysis of the influence of electrochemical characterization parameters (scan rate and rotation speed), adatoms (alloying) and the carbon support materials used on the alkaline EOR performance of synthesized Pt-free catalysts.
- Investigation of adatoms effect on alkaline EOR performance and structural characteristics of the identified novel carbon supported nanocatalyst using selected synthesis method.
- Optimization of the alkaline EOR performance on the novel carbon supported nano-catalyst by atomic composition variations.
- Modification of the selected synthesis method for particle size reduction of the novel carbon supported nanocatalyst achieving a high electrochemical active surface area (EASA) resulting in an EOR activity enhancement.

(3) The application of a simple and fast handling standardized procedure with a conductivity clamp using electrochemical impedance spectroscopy (EIS) to determine the in-plane ionic conductivity of AEMs and CEMs.

1.3 Structure of Dissertation

The dissertation is divided into six sections:

Section 2 describes the requirements of the EOR on Pt-free anode catalyst systems in the ADEFC. The influencing factors, such as, the addition of adatoms (alloying), the electrochemical and structure characteristics effects on the EOR performance of various selected monometallic, binary and ternary Pd-based electrocatalysts from the literature are discussed. Finally, the state-of-the-art anode catalyst support materials as well as DEFC systems with different membrane electrode assemblies (MEAs) are represented.

Section 3 deals with the experimental part, and includes the description of the catalyst synthesis and characterization methods used, the electrode development, the ionic conductivity measurement process for fuel cell membranes, the MEA preparation and the single cell testing.

Section 4 is structured in five parts and contains an intensive discussion on the electrochemical and physico-chemical characterization results of in-house carbon supported monometallic, binary and ternary Pt-free electrocatalysts and the function of material and measuring influences on their EOR performances.

- **Section 4.1** describes the influence of various electrochemical measuring conditions, varied characterization parameters used and various atomic compositions on the EOR activity of selected carbon supported Pt-free electrocatalysts.

- **Section 4.2** reports the effect of Ni and Bi on the EOR performance and the (surface) structural and morphological properties of carbon supported binary and ternary Pd-based nanocatalysts compared to the in-house carbon supported monometallic Pd catalyst. These catalysts were investigated ex-situ by using cyclic voltammetry (CV) and chronoamperometry (CA) with a rotating disk electrode (RDE), and by using various physico-chemical analysis methods, such as inductively coupled plasma optical emission spectrometry (ICP-OES), X-ray powder diffraction (XRD), X-ray photoelectron spectroscopy (XPS) and transmission electron microscopy - energy dispersive X-ray spectroscopy (TEM-EDX). Furthermore, this section discusses the differences between the in-situ characterizations (current-voltage (I-V) characteristics and EIS) of two selected catalysts ($Pd_{60}Ni_{40}$/C and $Pd_{60}Ni_{20}Bi_{20}$/C) in a single cell configuration under various operating conditions (e.g., at different temperatures and currents).

- **Section 4.3** deals with the optimization of the EOR performance based on the best performing, novel carbon supported ternary PdNiBi catalyst from **section 4.2**, that was developed by the common instant reduction synthesis method with variation of atomic compositions.

- **Section 4.4** depicts new synthesis approaches of the instant reduction method for the development of the carbon supported ternary PdNiBi catalyst for the alkaline EOR and compares them to the common instant reduction synthesis method. The differences between the resulting electrochemical and physico-chemical characterization results of these synthesized ternary catalysts using different synthesis approaches are intensively discussed.

- **Section 4.5** demonstrates further the measurement procedure for determining the in-plane ionic conductivity of various fuel cell membranes (AEMs and CEMs) whereby the obtained results contribute to some peer-reviewed journal articles.

Section 5 gives an overview of the catalyst, membrane and single cell test analyses discussed.

Section 6 discusses further possible research activities on the novel PdNiBi anode catalyst for the ADEFC.

2 State of the Art

Section 2 is partly based on the peer-reviewed articles published by Cermenek et al. [3,15] and on the master's thesis of Johanna Ranninger [29]. This section deals with the alkaline EOR on Pt-free anode catalysts. The electrochemical and structural characteristics of carbon supported monometallic, binary and ternary Pd-based electrocatalysts and support materials for the alkaline EOR are discussed. The EOR performance of carbon supported Pd-based nanocatalysts is used as reference for the synthesized anode catalysts in this doctoral thesis. The ADEFC, which currently has the highest power density, is compared with other DEFC systems at the end of the section.

2.1 Alkaline Ethanol Oxidation Reaction

2.1.1 Challenges

Critical technical barriers that restrict the commercialization of fuel cells include performance (activity), durability (stability), and costs of state-of-the-art catalysts [3,9,30]. DEFCs have attracted attention in the last decades due to their robustness, low cost, and environmental compatibility [3,31,32].

Commercialization of DEFCs is currently still hampered by slow kinetics of the anode electrochemical reactions and by the EtOH crossover through the membrane [3]. The latter is responsible for occurrence of a mixed potential which results in a reduction of the cathode potential and subsequently a decrease in power density of the DEFC system [3]. The use of an AEM in ADEFCs results in a reversed ion conduction mechanism relative to acidic DEFCs, which reduces the challenges of fuel crossover and additionally simplifies the water management [3,23].

Nevertheless, the greatest limited performance factor for the ADEFC system is the incomplete electrooxidation of EtOH, resulting in various EtOH intermediates (e.g., poisoning CO_{ads} or $CH_{x,\ ads}$), which deactivate the catalyst used. The development of a highly efficient anode catalyst for complete oxidation of EtOH to use the total chemical energy (Standard free Gibbs energy change $\Delta G_r^0 =$ -1325 kJ·moL^{-1} [9]) stored in EtOH molecule in electricity (Standard enthalpy change $\Delta H_r^0 =$ -1367 kJ·moL^{-1} [9]) is the main challenge of the ADEFC [15].

Currently, there is no catalyst which cleaves the carbon–carbon bond of EtOH resulting in a CO_2 efficiency of 100% according to C1 pathway (Scheme 1) at low temperatures (< 100 °C) due to mechanistic and/or sterical effects [15,24,33].

$$CH_3CH_2OH \rightarrow CH_3CHO_{ads} \rightarrow CO_{ads}, CH_{x,ads} \rightarrow CO_2 \text{ or } CO_3^{2-}$$

Scheme 1: Alkaline ethanol electrooxidation according to C1 pathway [15,33].

The reaction mechanism of the EtOH oxidation on the currently used catalysts predominantly takes place on the C2 pathway (Scheme 2), resulting in various reaction intermediate deposits on the active sites of the catalyst with a decrease of its performance [15]. The main products of alkaline EOR, generated by the reaction between adsorbed EtOH and adsorbed OH on the present catalysts, are acetic acid (CH_3COOH) and/or acetate (CH_3COO^-) [15,33].

$$CH_3CH_2OH \rightarrow CH_3CHO_{ads} \rightarrow CH_3CHO/CH_3COOH \text{ or } CH_3COO^-$$

Scheme 2: Alkaline ethanol electrooxidation according to C2 pathway [15,33].

The reaction products and intermediates, including the poisoning species of the EtOH oxidation on the catalyst used, can be identified by various characterization methods. These include in-situ Fourier-transform infrared (FTIR) spectroscopy [34,35], differential electrochemical mass spectrometry (DEMS) [36,37], nuclear magnetic resonance (NMR) spectroscopy [38], high performance liquid chromatography (HPLC) [39], CA coupled with in-situ polarization modulation infrared reflection absorption spectroscopy (PM-IRRAS) [40], or density functional theory (DFT) [40,41]. These characterization methods provide a better understanding of the EOR mechanism in alkaline media for designing and tuning an efficient anode catalyst for the ADEFC. The product selectivity and the reaction activity of EtOH oxidation on the catalyst under alkaline conditions depends on many influencing factors, such as temperature, concentration of the electrolyte and its pH, the applied potential and the catalyst type itself (e.g., degree of alloying, atomic composition, structure or morphology) [20,21,40,42–44].

2.1.2 Pt-free Anode Catalyst Systems

Pt is the most used catalyst for alcohol oxidation in acidic media, but high cost, low availability and prevalent poisoning by adsorbed CO-like intermediates formed during EtOH oxidation limits its application. The use of alkaline electrolytes significantly improves the kinetics of the EOR and of the ORR [3,23,45] and allows the replacement of expensive Pt catalysts by more abundant, inexpensive and non-noble metal containing catalysts [3,9,32,44].

Currently, Pd/C is the most suitable catalyst for the DEFC in alkaline solution, with significantly higher EOR activity relative to Pt/C [3,28]. This can be attributed to the more oxophilic character of, and improved C-C bond cleavage on, the Pd surface relative to Pt. Further, Pd is known to have higher stability and is less susceptible to poisoning effects than Pt [3,28,31,46].

Chatenet et al. [47] investigated the stability/durability/degradation of two commercial Pd/C catalysts firstly after a short and a long accelerated stress test (AST) of 150 and 1000 CV cycles in acidic and alkaline media and secondly in alkaline electrolytes in the absence/presence of strong reducing agents (hydrogen, hydrazine borane) [3,47]. It was found that the degradation of these two Pd/C catalysts in the acidic electrolyte is high, but their stability in the alkaline electrolyte is higher than Pt/C catalysts [3,47]. In addition, the carbon supported Pd nanoparticles in alkaline media with strong reducing agents have an insignificantly lower stability than without, whereby the instability of large particles is lower than that of smaller ones [3,47].

Another study in Chatenet and colleagues [48] also showed that after an AST of 150 CV cycles with different characterization methods, the Pd/C catalyst is less active against CO oxidation to carbonates and CO_2, leading to a lower degree of detachment of Pd nanoparticles from the carbon carrier Vulcan XC72 compared to PtRu/C and Pt/C catalysts [3,48]. This means that the corrosion resistance of the carbon carrier Vulcan XC72 in the presence of Pd nanoparticles is greater than that of PtRu and Pt nanoparticles, indicating that the Pd/C catalyst is more stable in alkaline media than the other two [3,48].

The reaction mechanism of EOR on Pd-based catalysts is still not fully understood. Wang et al. as well as other research groups [46,49,50] describe the generally accepted mechanism of EOR on Pd in alkaline media by Equations 9-13 [3]:

$$Pd^0 + OH^- \leftrightarrows Pd^0 - OH_{ads} + e^- \quad (9)$$

$$Pd^0 + CH_3CH_2OH \leftrightarrows Pd - (CH_3CHOH)_{ads} \quad (10)$$

$$Pd - (CH_3CHOH)_{ads} + 3\ OH^- \leftrightarrows Pd - (COCH_3)_{ads} + 3\ H_2O + 3\ e^- \quad (11)$$

$$Pd - (COCH_3)_{ads} + Pd - OH_{ads} \leftrightarrows Pd - (C(OH)_2CH_3)_{ads} + Pd^0 \quad (12)$$

$$Pd - (C(OH)_2CH_3)_{ads} + OH^- \leftrightarrows Pd^0 + CH_3COO^- + H_2O \quad (13)$$

The above mechanism points out the importance of the OH^- ions and the conversion of the acyl intermediates to acetate [3]. Liang et al. [50] described that the exchange of the adsorbed acyl $(COCH_3)_{ads}$ for the adsorbed hydroxyl is the rate determining step (Equation 12), while the dissociative adsorption of EtOH is a fast reaction [3,35,46,51].

Based on this understanding, much research has been done in recent years to improve the EOR performance of anode materials and to reduce costs by developing new synthesis methods for catalyst nanostructure preparation, specifically to alloy Pd with other metals like Ru, Pb, Sb, As, Ni or Bi, as well as to improve the active surface area of the catalyst material on its support [3,22,31,52,53]. The benefits of bi- and tri-metallic catalysts are that the additives are usually inexpensive and act as co-catalysts that improve catalytic activity and stability [1,3,23].

Since the diesel scandal, the price of Pd (Mar 4, 2020: 71.95 EUR/g [54]) has risen dramatically in recent years compared to Pt (Mar 4, 2020: 25.32 EUR/g [55]) and Au (Mar 4, 2020: 47.61 EUR/g [56]), due to low supply and high demand [57]. However, the precursor salt of Pd (price of $PdCl_2$ (59-60% Pd basis) [58]) which is used for catalyst synthesis in this doctoral thesis, is more inexpensive than Pt and Au precursor salts (price of $PtCl_4$ (57.5% Pt) [59] and of $HAuCl_4 \cdot aq$ (~52% Au basis) [60]). Pd is mainly produced in South Africa and Russia, while North America, Zimbabwe and other countries also contribute to the production of this precious metal [57]. However, the world mine production of Pd is higher than that of Pt [61].

Carbon supported Pd (Pd/C) as monometallic catalyst exhibits the best performance for the alkaline EOR compared to the other noble metals e.g. Pt and Au [15,28,62].

2.1.3 Structure Characteristics Effects

The review paper from Ozoemena [20] describes in detail the structure characteristics effects on the catalytic performance of catalyst nanoparticles. Some important factors, which are crucial for improving the electrochemical properties of a catalyst, are extracted and summarized here in Figure 3.

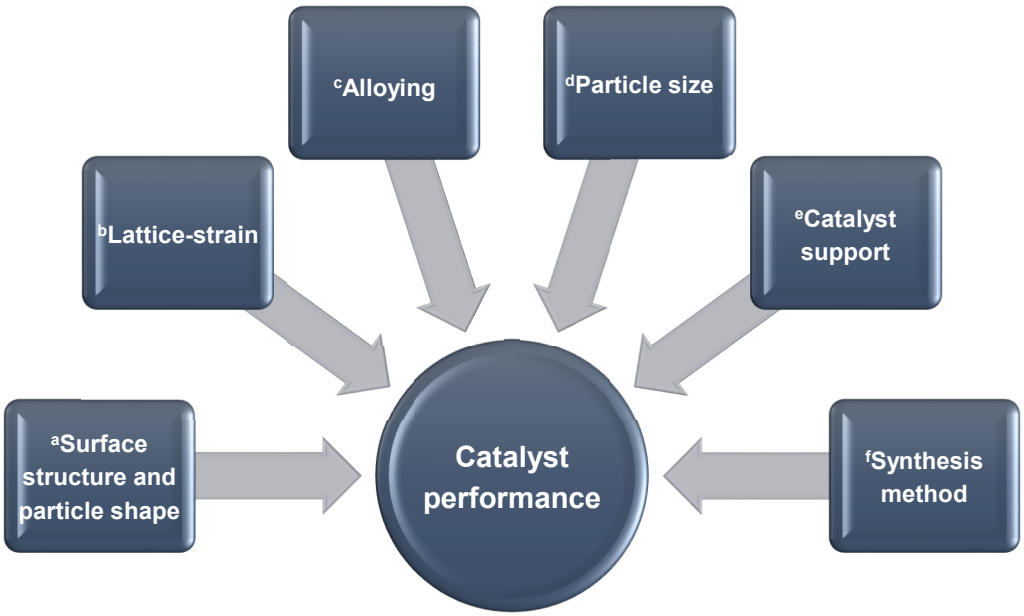


Figure 3: Various influencing factors on the catalyst performance include: [a]Improvement of the catalyst activity with high > than low index crystal planes (= Miller indices) and its particle shape is not crucial; [b]Increased compressive strain-lattice parameter (a) affects the electronic structure; [c]discussed in **section 2.1.4**; [d]Low particle size results in a high active surface area of the catalyst and consequently improves its catalytic performance, [e]described in **section 2.2**; [f]Influences the surface structure (crystal planes), particle size and degree of alloying [20].

The influencing factors mentioned above in Figure 3 are considered in the context of the electrochemical characterization results and discussion of the synthesized carbon supported monometallic, binary and ternary Pd-based nanocatalysts in the present doctoral thesis.

2.1.4 Electrochemical Characteristics Effects

Alloying or adatoms effect

The alloying process, or the addition of adatoms into a Pd lattice, affects the capability of Pd-based catalyst, as described in the journal article of Liao et al., in three dominating manners, by the geometric factor, the electronic factor and the synergy effect [63].

- The **geometric factor** refers to the adatom effect on Pd in different geometric variations. For example, when the bond length of Pd–Pd is prolonged or compressed, the size of Pd is decreased and the numbers of corner, edge and low-coordinated sites can be reduced, thus resulting in the promotion of catalytic properties [63].

- The **electronic factor** refers to the modification of the electronic structure of the element by the addition of a second element in the catalyst used. For example, the second element modifies the d-band structure in terms of transition metals such as Pd, thus influencing their catalytic ability [63].

- The **synergy effect** refers to the modification of the Pd lattice by the second element results in a stronger adsorption site for reactants and intermediates which enhance the interaction with the catalyst, thus leading to a catalytic improvement of binary nanoparticles [63].

The addition of oxophilic elements such as Ni, Bi, Ru, Sn, Zn or P improves the catalytic stability including tolerance to poisonous species such as CO resulting from the EtOH oxidation process (→ byproduct tolerance) and activity (onset potential and peak current density or mass activity) of Pd catalysts with bi- and polymetallic compositions due to bifunctional, electronic and synergetic effects [12,14,15,17,26,29,50,64–67]. The poisoning of catalysts by reaction intermediates of the incomplete EtOH oxidation thus depends in particular on the nature of the catalyst used [15,29].

The carbon supported bismuth (Bi/C) and nickel (Ni/C) electrocatalysts display no activities to alkaline EOR in the potential useful range [14,15,17,29,68,69]. A certain amount of Bi and Ni as elemental additives (oxophilic elements) however, improve the alkaline EOR performance of Pd-based catalysts considerably [15,17,29,69,70].

Nickel is often used as co-catalyst in Pd-based anode catalysts and promotes their alkaline EOR activities and stabilities for the ADEFC. One of many studies here, for example that of Shen and co-workers [12], confirms the performance improvement achieved by developing and testing of Pd_xNi_y/C (C = Vulcan XC72R) catalysts with various atomic ratios [12,15,29]. The enhancement of the alkaline EOR catalytic activities was explained due to the affinity of Ni to form Ni–OH_{ads} species which facilitate the oxidation process to CH_3COOH through a bifunctional mechanism and also by oxidative removal of poisonous EtOH species from the catalyst surface [12,15,29]. Furthermore, the alkaline EOR performance of Pd-based electrocatalysts depends on the Ni content which leads to a decrease in alkaline EOR activity when it is too high due to the presence of Ni oxide species with low conductivity [12,15,29].

Shen et al. [64] developed a carbon supported Pd-NiO catalyst with lower onset potential and higher current density toward the alkaline EOR compared to other Pd-oxide/C catalysts. The Pd-NiO/C anode catalyst shows higher byproduct tolerance of EtOH oxidation than Pt-based catalysts [2,15,29,64].

Nickel is a particularly promising co-catalyst candidate for Pd, as Ni/Pd alloys have shifted lattice constants that usually promote synergetic effects. For example, the surface binding energy for reaction intermediates is lower, and therefore, the effect of poisoning by different adsorbents like CO or CH_x species is reduced [3,42,71,72]. Moreover, Ni has a high OH^- affinity which is crucial for the EOR as described above [2,3].

Neto et al. [17] show the influence of Bi on the alkaline EOR performance of carbon supported binary Pd_xBi_y catalysts (Pd_xBi_y/C, C = Vulcan XC72R) with various atomic ratios of (95:05), (90:10), (80:20) and (70:30) using CV for determination of their catalytic activities in comparison to a carbon supported monometallic Pd/C catalyst [15,17,29]. The Bi content of 5 at.% and 10 at.% in Pd catalysts shifts the onset potentials toward the alkaline EOR to lower potentials in contrast with Pd/C. The PdBi/C with the atomic ratio of (95:5) exhibits the best results relating to electrocatalytic activity and stability compared to the other catalysts [15,17,29]. This study reveals that the kinetics of alkaline EOR and the byproduct tolerance on PdBi catalysts with low Bi content are improved by the oxidative removal of adsorbed ethoxy species (rate-determining step; see Scheme 2) from the catalytic sites of Pd [15,17,29].

Further, Neto et al. [17] reported that adding Bi to Pd has a positive impact on the performance of the anode catalyst, which has been proposed to yield additional oxide- and hydroxide-species that increase OH^- adsorption on the catalyst surface, thus improving the activity for EOR [3,17,73]. Cai et al. have also demonstrated that Pd has great affinity $Bi^{(III)}$-ion adsorption, which is important in the catalyst synthesis [3,53].

The third element in carbon supported ternary anode catalysts for the ADEFC can additionally improve or strengthen the alkaline EOR performances of the catalyst relating to catalytic activity (onset potential and current density), long-term stability and byproduct tolerance compared to carbon supported binary EOR catalysts [15,29,45,66,74–85]. For example, the addition of P and Zn to carbon supported PdNi catalyst (PdNi/C, C = Vulcan XC72R), forming ternary PdNiP/C and PdNiZn/C catalysts which exhibit higher EOR activity (lower onset potential and higher peak current) than the binary PdNi/C catalyst [14,15,78,86].

Zhu et al. [66] investigated the influence of elemental additives as Ni, Co and Ag on the electrocatalytic activities of binary PdSn-based catalysts for alkaline EOR [15,29,66]. This study demonstrated that the PdSn-based catalyst alloyed with Ag exhibited the best results related to intrinsic activity and stability toward alkaline EtOH oxidation [15,29,66].

Catalyst ink preparation effect

The catalyst ink preparation plays an important role for a homogeneous distribution on the GC substrate of RDE to obtain reproducible results for electrochemical characterization [15,29]. The addition of Nafion ionomer as binder shows according to Shinozaki et al. a better quality of catalyst dispersion than is the case without Nafion ionomer in the context of the reproducibility of the EASA, mass activity and the specific mass activity determination of the catalyst in RDE measurements [15,29,87].

The research group [87] has found that the optimal dispersion of catalyst particles was obtained if the Nafion ionomer with a concentration of 24 wt.% is used. Furthermore, it was

stated that the temperature of the catalyst slurry increased while sonication whereby the EASA decreased due to thermally induced degradation of smaller catalyst particles. This temperature increase can be counteracted by cooling of the catalyst slurry using an ice-water bath during the sonication process [15,29,87].

Pollet and co-workers [88] investigated the effect of the sonication parameters used in the distribution of catalyst inks based on Pt nanoparticles with Nafion ionomer as binder [15,29,88]. The frequency and power of the sonication bath or probe significantly influence the EASA, shown in a comparison of two samples with different sonication times, the one sonicated for 120 min thus results in an EASA decline of 45% compared to the other sonicated for 30 min [15,29,88]. It was also reported that the Nafion ionomer separated from the Pt nanoparticles which then also agglomerated and dissolved by longer sonication time [15,29,88]. Furthermore, Adamsky et al. [89] have recently investigated the effect of frequency power ultrasound on the viscosity, thermal degradation and glass transition temperature of Nafion ionomer dispersions with different concentrations.

In this context, the aforementioned effects were also considered in the catalyst ink preparation, especially for electrochemical characterization of carbon supported Pd-based nanocatalysts, in the present doctoral thesis [15].

Also important to the electrocatalytic activity of Pd catalysts is the uniform dispersion of the nanoparticles on a suitable support material [1,3,23], which results in a higher active surface area and enables lower total loading subsequently lower costs [3,90]. It is well known that the support material also influences the active component, particle size and distribution, morphology, and stability [3]. As a result, the most commonly used supports are carbon-based materials (e.g., Vulcan XC72R from CABOT Corporation) that show an excellent combination of surface properties, electronic conductivity and corrosion resistance [3,91,92].

Further details about anode catalyst support materials for the ADEFC are described in the following **section 2.2**.

2.2 Anode Catalyst Support Materials

A high electronic conductivity, an appropriate porosity, applicable surface functional groups, a large surface area and a high corrosion resistance (stability) of the catalyst support material with an intimate contact to active material and binder material are important requirements to guarantee a high performance of the catalyst used [20,21,43,93]. Carbon-based materials, such as carbon blacks (e.g., Acetylene black, Ketjen Black, Black Pearls 2000 or Vulcan

XC72), and carbon nanotubes and graphene-based materials (reduced graphene oxide (rGO) or N-, S-, P-, I-, B-doped graphene) are currently the state-of-the-art catalyst supports for ADEFCs [93–96].

The benefits of carbon as catalyst support material are its low-cost, easy of availability, high stability under acidic and alkaline environments and easy burning off. However, the great challenge of using carbon is corrosion which causes poor durability of the catalyst that separates from the carbon support material. These small, formed catalyst particles aggregate (Ostwald ripening) and lead to inhomogeneity of the catalyst structure over a certain period [20]. Alternative catalyst support materials are extensively investigated for anode catalysts in DEFCs [20,21,43,93,96] and are not discussed here further.

In this doctoral thesis, the amorphous Vulcan XC72R carbon black with an average particle size of 50 nm is used as catalyst support. It is developed using the well-known “furnace black” procedure and exhibits a satisfied surface area of approx. 250 $m^2 \cdot g^{-1}$ and a high electronic conductivity of 2.77 $S \cdot cm^{-1}$ [93,94,97].

2.3 Pt-free Anode Catalyst Performances

Table 1 shows carbon supported ternary Pd-based nanocatalysts, which display higher mass activities for the alkaline EOR than monometallic and binary benchmarks and are compared to the best performing catalysts ($Pd_{70}Ni_{20}Bi_{10}$/C and $Pd_{85}Ni_{10}Bi_5$/C) in this doctoral thesis. It is especially difficult to compare the EOR performance of these catalysts to the others, because each catalyst was characterized under different CV conditions and catalyst loadings. The catalysts with mass activities toward EtOH oxidation in alkaline media higher than $Pd_{70}Ni_{20}Bi_{10}$/C and $Pd_{85}Ni_{10}Bi_5$/C catalysts have been caused as a result of the performing of CV measurements at higher scan rate (50 $mV \cdot s^{-1}$ vs. 10 $mV \cdot s^{-1}$) [3,15].

These comprehensively characterized $Pd_{70}Ni_{20}Bi_{10}$/C and $Pd_{85}Ni_{10}Bi_5$/C catalysts that have achieved excellent current densities or mass activities for the alkaline EOR (see Table 1), have great potential as anode catalysts in ADEFCs and are intensively discussed in **sections 4.3** and **4.4** [3,15].

Table 1: State-of-the-art EOR performance relating to activity (onset potential, specific activity and mass activity) of different ternary Pd-based nanocatalysts compared to $Pd_xNi_yBi_z$/C nanocatalysts using the common and the modified instant reduction synthesis method [3,15].

Catalyst	Electrolyte	Scan rate ($mV \cdot s^{-1}$)	T[a] (°C)	Catalyst loading ($mg \cdot cm^{-2}$)	E_{onset}[b] (V)	i_f[c] ($mA \cdot cm^{-2}$)	MA[d] ($mA \cdot mg^{-1}$)	Ref.[e]
Pd-(NiZn)/C*	2 M KOH + 10 wt.% EtOH	50	rt[f]	0.022-0.025[#]	-0.6 vs. Ag/AgCl/KCl_{sat} [i] (0.423 vs. RHE)	79-90	3,600[#]	[86]
$Pd_{35}Cu_{14}Ni_2$/C**	1.0 M KOH + 1.0 M EtOH	50	25	0.108[#]	-0.67 vs. Ag/AgCl/KCl_{sat} [i] (0.352 vs. RHE)	337	3,120[#]	[85]
$Pd_8Ni_1P_1$/C*	0.5 M NaOH + 1 M EtOH	50	rt[f]	0.028[#]	-0.61 vs. SCE [ii] (0.446 vs. RHE)	71	2,533[#]	[78]
20%Pd10%Ni10%Sn/CB**	1 M KOH + 1 M EtOH	50	rt[f]	0.068[#]	-0.564 vs. Ag/AgCl [i] (0.458 vs. RHE)	146	2,151[#]	[83]
PdCuPb/C**	1 M KOH + 1 M EtOH	50	25	0.057[#]	~ -0.6 vs. MMO, 1 M KOH [iii] (0.323 vs. RHE)	105	1,847[#]	[77]
$Pd_{41}Au_{29}Ni_{30}$/C*	0.5 M NaOH + 1 M EtOH	50	rt[f]	0.77	~ -0.65 vs. MMO [iv] (0.315 vs. RHE)	160	1,403[#] [9]	[80]
Pd_7IrNi_{12}/C*	1.0 M KOH + 1.0 M EtOH	50	rt[f]	0.128	-0.71 vs. MMO, 1 M KOH [iii] (0.213 vs. RHE)	139[##]	1,250[#] [34]	[79]
$Pd_2Sn_2Ag_1$/C**	1.0 M KOH + 1.0 M EtOH	50	~25	n/a	-0.52 vs. MMO, 1 M KOH [iii] (0.403 vs. RHE)	3.37[###]	819[#]	[66]
$Pd_2Sn_2Ni_1$/C**	1.0 M KOH + 1.0 M EtOH	50	~25	n/a	-0.50 vs. MMO, 1 M KOH [iii] (0.423 vs. RHE)	2.23[###]	463[#]	[66]
$Pd_2Sn_2Co_1$/C**	1.0 M KOH + 1.0 M EtOH	50	~25	n/a	-0.47 vs. MMO, 1 M KOH [iii] (0.453 vs. RHE)	1.74[###]	370[#]	[66]
$Pd_{70}Ni_{20}Bi_{10}$/C**	1 M KOH + 1 M EtOH	**10**	30	0.056[#]	0.236 vs. RHE	106[##]	1,889[#]	**This work**
$Pd_{85}Ni_{10}Bi_5$/C**	1 M KOH + 1 M EtOH	**10**	30	0.056[#]	0.207 vs. RHE	150[##]	2,678[#]	**This work**

[a] T: temperature; [b] E_{onset}: onset potential of the ethanol oxidation; [c] i_f: peak current density of EOR forward scan; [d] MA: mass activity, [e] Ref.: reference, [f] rt: room temperature. *Vulcan XC72; **Vulcan XC72R; relating to [#] Pd loading; [##] geometric electrode area and [###] EASA; n/a: not applicable.

[i] 0.197 V vs. NHE → E(RHE) = E(Ag/AgCl/KCl_{sat}) + 0.197 + 0.059 × pH

[ii] 0.248 V vs. NHE → E(RHE) = E(SCE) + 0.248 + 0.059 × pH

[iii] 0.098 V vs. NHE → E(RHE) = E(MMO, 1 M KOH) + 0.098 + 0.059 × pH

[iv] 0.140 V vs. NHE → E(RHE) = E(MMO) + 0.140 + 0.059 × pH

The onset potentials of all listed catalysts in Table 1 were adapted to the potential of the Reversible Hydrogen Electrode (RHE), which used as reference electrode for the electrochemical characterization measurements in this doctoral thesis [15].

2.4 Alkaline Direct Ethanol Fuel Cell Performance

In Table 2 below different kinds of DEFC efficiency as well as the currently highest achieved power density of ADEFC are compared with counterparts acidic DEFC and acidic-alkaline DEFC under various operating conditions [9,98–100].

The DEFC performance depends on various influencing factors, such as the electrolyte used, the EtOH concentration, catalyst loading, temperature, the flow-rates of the anolyte and catholyte, bipolar plates with different flow field designs, the interconnection of electrodes, electrolyte (ionomer) and fuel (triple-phase boundary) and the component materials [33,101]. Therefore, it is difficult to compare the MEA performance of the three DEFC systems, regarding the EOR catalyst performance comparison, as explained in the previous **section 2.3**. The correlation between ex-situ and in-situ characterization is still not fully understood.

Table 2: State-of-the-art ADEFC efficiency and power density compared to the counterparts acidic DEFC and acidic-alkaline DEFC [9,98–100].

DEFC systems	[a]E^0_{Cell} (V)	[b]η_{th} (%)	[c]η_V (%)	[d]η_F (%)	[e]η_{FC} (%)	State-of-the-art Power density ($mW \cdot cm^{-2}$)	[f]Ref.
Alkaline DEFC	1.14	97	44	37 to 54	16 to 23	185* (@ 60 °C)	[9,98]
Acidic DEFC				25	11	96** (@ 90 °C)	[9,99]
Acidic-Alkaline DEFC	2.52	n/a	n/a	n/a	n/a	360*** (@ 60 °C)	[9,100]

[a]E^0_{Cell}: reversible cell voltage; [b]η_{th}: thermodynamic efficiency (= theoretical energy-conversion efficiency); [c]η_V: voltage efficiency: 44%; [d]η_F: Faradaic efficiency: 2 e^- (16%), 4 e^- (33%); [e]η_A: Actual energy-conversion efficiency (fuel cell) = $\eta_{th} \cdot \eta_V \cdot \eta_F$; [f]Ref.: reference; [f]not applicable.

*MEA: Anode: commercial non-Pt catalyst (from ACTA, is now Enapter [102]) on Ni foam, Fuel: 5 M KOH + 3 M EtOH with a flow rate of 1 $mL \cdot min^{-1}$; AEM: A201 (thickness: 28 µm) from Tokuyama Corporation; Cathode: m-Pd_3Au/CNT on carbon cloth, Oxidant: O_2 with a flow rate of 100 sccm.

**MEA: Anode: Pt_3Sn-PtRu catalyst on carbon paper, Fuel: 1.5 M EtOH with a flow rate of 1 $mL \cdot min^{-1}$; CEM: Nafion 115 (thickness: 127 µm); Cathode: Pt/C catalyst on carbon paper, Oxidant: O_2 with a flow rate of 240 $mL \cdot min^{-1}$ at 0.2 MPa.

***MEA: Anode: PdNi/C on Ni foam, Fuel: 5 M NaOH + 3 M EtOH with a flow rate of 2 $mL \cdot min^{-1}$; CEM: Nafion N211 (thickness: 25 µm); Cathode: commercial Pt/C catalyst (60 wt.%, Johnson-Matthey), Oxidant: 4 M H_2O_2 + 1 M H_2SO_4 with a flow rate of 2 $mL \cdot min^{-1}$.

3 Methodology

Section 3 describes the ADEFC component development and characterization procedures (**sections 3.1–3.5**) and the electrochemical and physico-chemical parameters used to evaluate the performance of the anode catalyst system (**section 3.6**). The sections are based on the following references:

[3] **Cermenek, B.**; Genorio, B.; Winter, T.; Wolf, S.; Connell, J.G.; Roschger, M.; Letofsky-Papst, I.; Kienzl, N.; Bitschnau, B.; Hacker, V. Alkaline Ethanol Oxidation Reaction on Carbon Supported Ternary PdNiBi Nanocatalyst using Modified Instant Reduction Synthesis Method. *Electrocatalysis*, **2020**, *11*, 203-214.

[15] **Cermenek, B.**; Ranninger, J.; Feketeföldi, B.; Letofsky-Papst, I.; Kienzl, N.; Bitschnau, B.; Hacker, V. Novel highly active carbon supported ternary PdNiBi nanoparticles as anode catalyst for the alkaline direct ethanol fuel cell. *Nano Res.*, **2019**, *12*, 683–693.

[29] Ranninger, J. Development and Characterization of Pd-based Catalysts for the alkaline Direct Ethanol Fuel Cell. *Master's thesis*, Graz University of Technology, **2017**, p. 85. (supervised **Cermenek, B**.)

[103] **Cermenek, B**.; Hacker, V.; Feketeföldi, B.; Ribtisch, V. Pt-free anode catalyst systems and composite polysaccharide-membranes for the alkaline DEFC. *End report*, **2017**, p. 73.

[118] Hacker, V.; **Cermenek, B**. IEA AFC Annex 35: Brennstoffzellen für portable Anwendungen: Arbeitsperiode 2014-2017. *End report*, **2017**, p. 34.

The chemicals, materials and equipment used for the experiments in each **section (4.1–4.4**) are listed in the Appendix A (**sections 8.1.1–8.4.1** based on the references above).

3.1 Pt-free Anode Catalyst Systems

The deposition of Pt-free nanoparticles on carbon-based support materials was carried out using different catalyst synthesis procedures, such as impregnation, instant, water-in-oil microemulsion and aqueous solution phase synthesis processes. This resulted in various corresponding carbon supported monometallic, binary and ternary Pt-free anode catalysts for the ADEFC. Precipitation and electrodeposition are further synthesis methods for the development of nitrogen containing nickel complexes as electrocatalysts for alkaline EOR. These different synthesis methods have been described in the end report of the FFG project 'e!Polycat' [103]. All synthesized Pt-free anode catalyst systems are given in Table 3. The catalysts shaded in grey have been shown to be potential candidates for the alkaline EOR and are discussed in detail in **section 4** of the doctoral thesis.

Table 3: Overview of all developed monometallic, binary, ternary and other Pt-free anode catalyst systems (incl. reference materials) showing the synthesis methods and carbon support materials used.

Type	Monometallic	Binary	Ternary	Other
	[a,d]Ni/C[vi]	Raney-Ni	[b]PdNiZn/C[vi]	[f]Ni(II)$(DMG)_2$
	[b]Au/C[vi]	[a]NiCo/C[vi]	[e]PdNiP/C[vi]	[f]Ni(II)$(DMG)_2$/C[vi]
	Cu/C	[a]NiMo/C[vi]	[b,c]$Pd_xNi_yBi_z$/C[vi]	[g]Ni-Cysteine
	Ru/C	[b]Au_xNi_y/C[vi]		[b]PdNi-Pyrrole/C[vi]
Catalysts	[b]Pd/C	[b]Au_xCo_y/C[vi]		*R-porphyrine-Pd(II) comm.
	*Pd/C comm.	[b]Au_xCu_y/C[vi]		
	*Pd/rGO[VII] comm.	[b]$Pd_xNi_y/C_{(i-vi)}$		
		[b]PdBi/C[vi]		
		*$Pt_{40}Ru_{20}$/C comm.		

[a]Impregnation method; [b]Instant method; [c]Modified instant method [d]Water-in-oil microemulsion method; [e]Aqueous solution phase synthesis method; [f]Precipitation method; [g]Electrodeposition method. Carbon supported materials used: [i]Acetylene Black; [ii]Carbon nanofiber; [iii]Black-Pearls 2000; [iv]Tungsten carbide; [v]Vulcan XC72; [vi]Vulcan XC72R. *Commercial catalysts: Pd/C (40 wt.%, Fuel Cell Store); Pd/rGO (rGO = reduced graphene oxide); $Pt_{40}Ru_{20}$/C (Alfa Aeasar), R-porphyrine-Pd(II) = (5,10,15,20-Tetrakis(2,4,6-trimethylphenyl)porphyrin-Pd(II) 98% (Porphyrin Systems).

3.1.1 Synthesis

The instant reduction method is a simultaneous currentless deposition procedure [15,29,104–107] and is selected as the standard method for the development of Pt-free anode catalysts, due to its ease of use compared to other synthesis methods. The standardized synthesis procedure of the instant reduction method is shown in Figure 4.

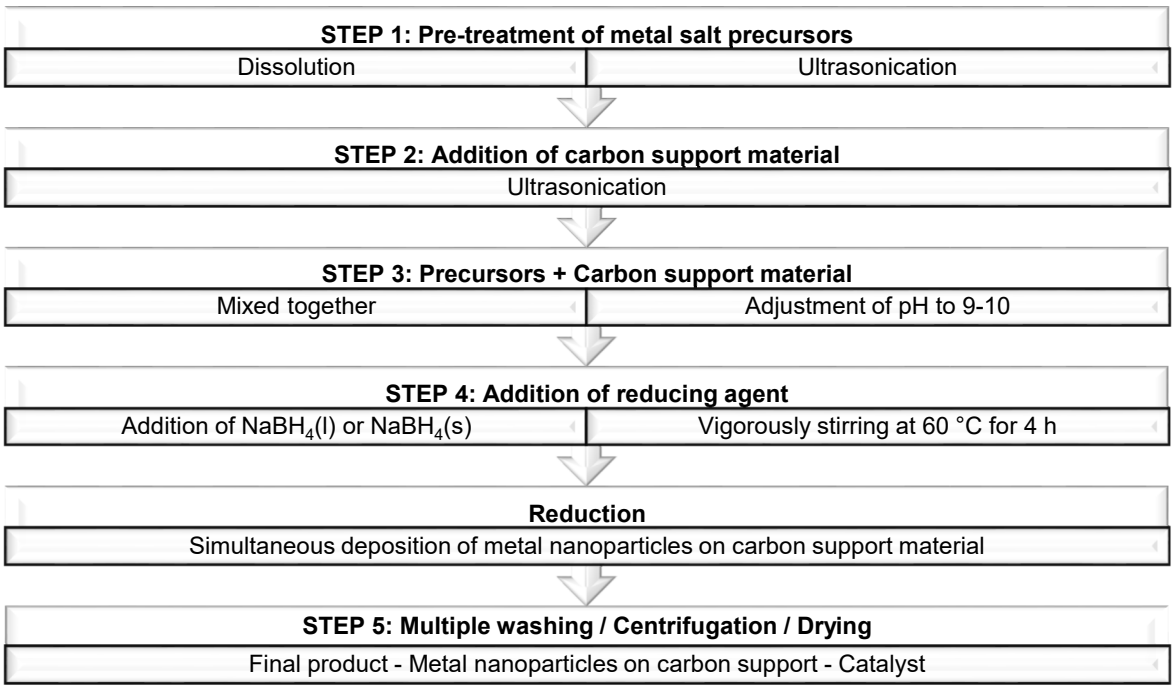


Figure 4: Synthesis steps of the standardized instant reduction method for EOR catalyst systems.

The syntheses of carbon supported Au- and Pd-based anode catalysts using the standardized instant reduction method [15,29,104–107] and their new synthesis approach (modified instant reduction method [3]) are described in detail below. These developed catalysts are comprehensively characterized using electrochemical and physico-chemical methods, and the obtained results are discussed in **sections 4.1–4.4**.

Instant reduction method for synthesis of Au-based anode catalysts (section 4.1)

The carbon supported Au_xCu_y anode catalysts were synthesized by means of the instant reduction method [15,29,104–107]. $Cu(NO_3)_2{\cdot}3H_2O$ (s) and $HAuCl_4$ (liquid, 10 g Au/L) were dissolved in a 20 mL 9:1 mixture of 2-propanol:ultra-pure water (~18 MΩ·cm) in various stoichiometry and suspended with pre-dispersed Vulcan XC72R carbon black (CABOT) as the catalyst support material using an ultrasonic bath and ultrasonic probe (catalyst composition: 40 wt.% of metals, 60 wt.% of carbon support material).

The pH of metal salt solution was increased to 9-10 using 1.0 M NaOH and the suspension was stirred overnight at 60 °C. An excess of solid sodium borohydride ($NaBH_4$ (s)) in 0.5 M NaOH was added dropwise to the salt suspension under vigorous stirring to reduce it to its respective metals, giving the corresponding Au_xCu_y/C electrocatalysts (denoted as $Au_{40}Cu_{60}$/C, $Au_{60}Cu_{40}$/C and $Au_{80}Cu_{20}$/C). After cooling of the reaction mixture, multiple washes of the catalyst suspension were performed with ultra-pure water including by centrifugation at 3,500 rpm for 40 min. Finally, the water was decanted from the product and the cleaned carbon supported Au_xCu_y nanoparticles were dried at 80 °C [15,29,104–107].

The synthesis of the carbon supported Au anode catalyst (40 wt.% of metal on Vulcan XC72R; denoted as Au/C) was carried out using the same procedure that was used for the development of the Au_xCu_y/C catalysts.

Instant reduction method for synthesis of Pd-based anode catalysts (sections 4.1–4.4)

The carbon supported $Pd_xNi_yBi_z$ nanocatalysts were synthesized by means of the instant reduction method using $NaBH_4$ as a reducing agent [15,29,104–107]. Firstly, $PdCl_2$ and NaCl were completely dissolved in 10 mL of ultra-pure water using an ultrasonic bath for several hours. The added NaCl causes a better solubility of $PdCl_2$ in ultra-pure water due to complex formation of sodium tetrachloropalladate ($Na_2[PdCl_4]$) (Equation 14) [15].

$$PdCl_2 + 2\ NaCl \rightarrow Na_2[PdCl_4] \qquad (14)$$

$Ni(NO_3)_2 \cdot 6H_2O$ and $BiCl_3$ were dissolved in 10 mL of ultra-pure water. A few drops of HCl were added to the $BiCl_3$ solution to dissolve the precipitated bismuth oxychloride (BiOCl). These dissolved precursor salts were added to the $Na_2[PdCl_4]$ solution in a definite stoichiometry. Vulcan XC72R carbon black as support material was suspended in 54 mL of 2-propanol and 6 mL of ultra-pure water for 0.5 h using an ultrasonic bath. The metal salt solutions were added with additional 40 mL of ultra-pure water to suspended carbon support material (catalyst composition: 40 wt.% of metals, 60 wt.% of carbon support material). The pH of the metal salts containing solution was adjusted to 10 using 5.0 M NaOH. After dropwise addition of the reducing agent solution (~3 equivalent of $NaBH_4$ (s) in 0.6 mL of 1 M NaOH and 6 mL of ultra-pure water) to the salt suspension, the reaction mixture was vigorously stirred at 60 °C for 4 h to reduce to respective metals on the carbon support material Vulcan XC72R, giving the corresponding $Pd_xNi_yBi_z$/C [15].

After cooling of the reaction mixture to room temperature (rt), multiple washing (three times) of the catalyst suspension was performed with ultra-pure water including by centrifugation at 3,500 rpm for 30 min. After each washing process, the water was decanted from the product. Finally, the obtained cleaned carbon supported $Pd_xNi_yBi_z$ nanoparticles were dried at 80 °C until constant weight was adjusted [15].

The syntheses of the other Pd-based nanocatalysts (Pd/C, Pd_xNi_y/C, PdBi/C) were performed by the same procedure as for the development of the $Pd_xNi_yBi_z$/C anode catalysts [15].

Modified instant reduction method (section 4.4)

The carbon supported ternary $Pd_{85}Ni_{10}Bi_5$ anode catalysts were synthesized by the common (see above, [15]) as well as the modified instant reduction method using Vulcan XC72R as catalyst support material (catalyst composition: 60 wt.% of carbon support and 40 wt.% of

metals). The modified instant method was developed based on the common instant method with the following modifications [3].

The precursor salt solution is prepared by dissolving $PdCl_2$ salt in 10 mL of ultra-pure water with additional 1.5 mL of 1 M HCl instead of NaCl. This results in a better solubility and faster dissolution time (Equation 15) [3].

$$PdCl_2 + 2\ HCl \rightarrow H_2[PdCl_4] \qquad (15)$$

The dissolution of $Ni(NO_3)_2{\cdot}6H_2O$ salt is carried out in 10 mL of ultra-pure water with additional 1.5 mL of 1 M HCl. The precursor salt solution $BiCl_3$ (aq.) is prepared similarly with a few drops of HCl (see common instant reduction method above) [3].

The overall synthesis process is performed under N_2 atmosphere in the ice bath. Vulcan XC72R carbon black is dispersed in 60 mL of ultra-pure water (without the addition of 2-propanol), and the suspension is sonicated two times for 5 min with a cycle of 0.6 and an amplitude of 40%, using an ultrasonic probe (Hilscher, UP400s). Afterward, the precursor salt solutions are added to the Vulcan XC72R carbon black dispersion under constant sonication and the pH of the mixture is adjusted to 10 with 1 M NaOH. The reducing agent $NaBH_4$ (~5 equivalent) is added to the catalyst dispersion in pieces (pure solid form) or dropwise in liquid form (0.6 mL of 1 M NaOH and 6 mL ultra-pure water) [3].

The reaction mixture is stirred vigorously for 4 h at 60 °C to obtain the $Pd_{85}Ni_{10}Bi_5/C^{(II)}$ ($NaBH_4$ (s)) and $Pd_{85}Ni_{10}Bi_5/C^{(III)}$ ($NaBH_4$ (l)) catalysts. After cooling to rt, multiple washing with ultra-pure water and centrifugation is performed. Finally, the purified catalyst samples are dried at 40 °C for 24 h. Figure 5 presents a schematic representation of the modified instant reduction synthesis method [3].

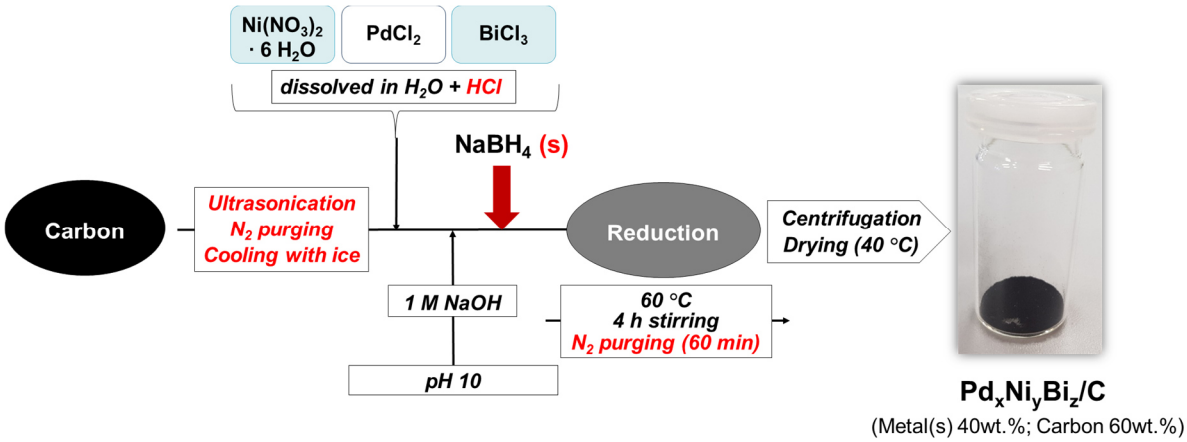


Figure 5: Modified instant reduction synthesis method – changes are marked red compared to the common instant reduction synthesis method described previously [3,15].

3.1.2 Characterization

The EOR performance (activity, stability and byproduct tolerance) of all synthesized catalysts was investigated using electrochemical analysis methods, such as CV and CA with a RDE. The anode catalyst with the best EOR performance, in this case PdNiBi/C, was comprehensively characterized by various physico-chemical analysis methods, such as ICP-OES, TEM-EDX, XRD and XPS, in comparison to benchmarks Pd/C, PdNi/C, PdBi/C and commercial Pd/C. The characterization procedure for the Pt-free anode catalyst systems is shown in Figure 6.

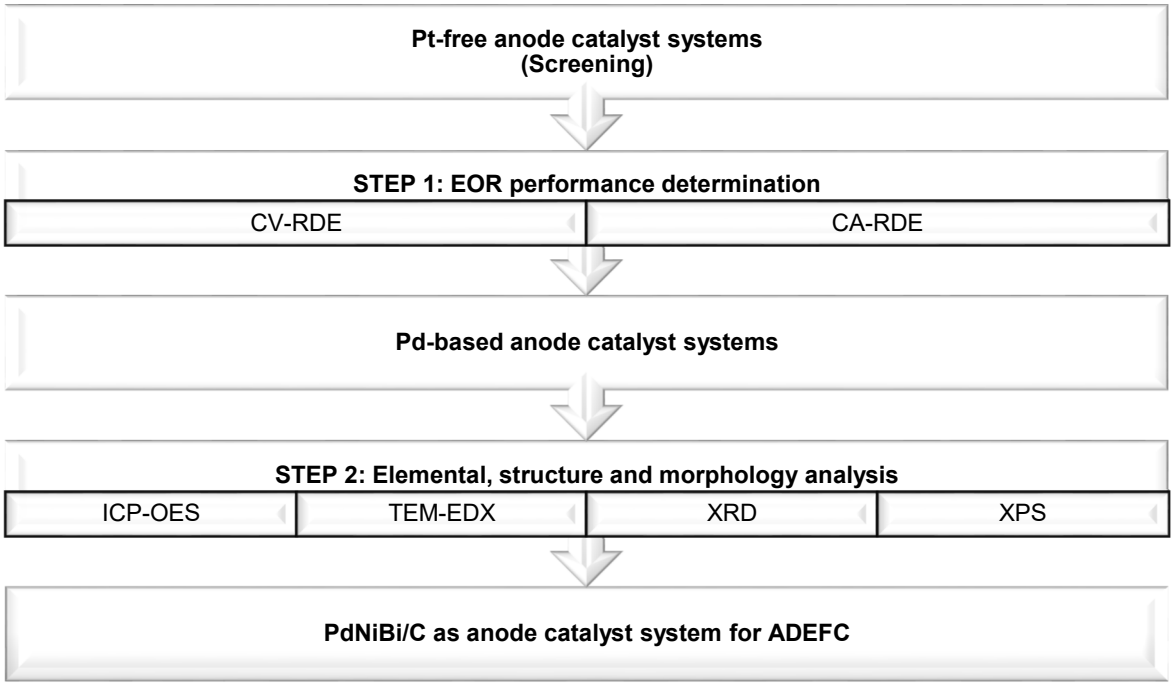


Figure 6: Electrochemical and physico-chemical characterization methods used.

Electrochemical Analysis Methods

The EOR activity and stability of carbon supported Pt-free electrocatalysts were determined by means of CV and CA using a RDE (Model AFE5T050GC from PINE Research Instrumentation), respectively [3,15,29,104,106,108–110].

The electrochemical measurements were performed in an electrochemical glass cell (Metrohm) with a three-electrode-arrangement consisting of platinized titanium rod (Bank Elektronik – Intelligent controls GmbH) as counter electrode, reversible hydrogen electrode (RHE; HydroFlex®, gaskatel) as reference electrode and RDE as working electrode. A GAMRY (bi-)potentiostat (Reference 600^{TM} Potentiostat/Galvanostat/ZRA, GAMRY Instruments Inc., Pennsylvania, USA) was used as control system (see Figure 7) [3,15].

Before starting the electrochemical measurement, the RDE with GC substrate (Ø = 5 mm; geometric area: 0.196 cm^2) was polished using 0.05 µm alumina suspension (MasterPrep® Polishing Suspension; Buehler) and was finally rinsed with ultra-pure water [3,15]. The synthesized catalysts were dissolved in a mixture of 2-propanol, ultra-pure water, with and without Nafion ionomer solution (5 wt.%, Quintech) as binder, and were sonicated in two manners (i) for 15 min in an ice-bath [15] and (ii) two times for 5 min with a cycle of 0.6 and an amplitude of 20% using an ultrasonic probe (Hilscher, UP400s) [3] until a homogeneous dispersion was formed. An appropriate amount of catalyst ink was dropped onto the RDE in order to achieve the desired loading of certain µg precious metal (Pd or Au) per cm^2 (see calculation of the catalyst ink preparation in **section 8.1.2**) [3,15].

The RDE with the catalyst ink was dried by rotation to air at a rotation speed of 700 rpm for approx. 1.5 h. In the meantime, the alkaline electrolyte (1.0 M potassium hydroxide standard solution; FIXANAL KA 180 mL, Sigma-Aldrich) was purged with nitrogen gas (N_2, purity of 5.0, Air Liquide) for 30 min to remove the dissolved oxygen out of it, before the measurements were started. After that, the RDE with the respective catalyst was immersed in the 1.0 M KOH, saturated with nitrogen and cyclic voltammograms (CVs) of each catalyst were recorded at a scan rate of 50 $mV \cdot s^{-1}$ (→ cleaning cycles are fast oxidation and reduction processes to remove the impurities from the surface of the catalyst) and finally at a scan rate of 10 $mV \cdot s^{-1}$ in a stationary condition, respectively. After the addition of 1.0 M EtOH (purchased from EtOH absolute, 99.999%, Aldrich) to 1.0 M KOH, further CVs of each catalyst was also recorded at a scan rate of 10 $mV \cdot s^{-1}$ to determine the specific activity toward the EtOH oxidation in alkaline medium [3,15].

Finally, all synthesized Pt-free catalysts were applied at a constant potential for 1 h to investigate their catalytic stability (= CA measurements) under the same operating conditions as those used for CV-measurements [3,15].

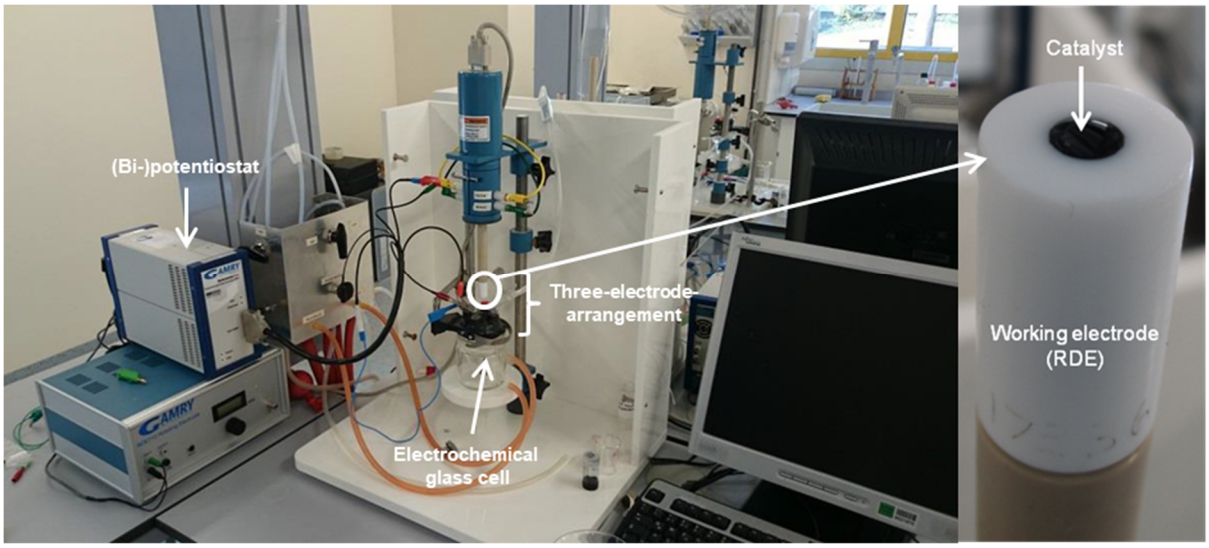


Figure 7: CV/CA-RDE setup for electrochemical characterization of the Pt-free anode catalyst systems.

By integration of the reduction peak (PdO to Pd → catalyst charge Q_{Pd}) with the Echem Analyst™ Software-Gamry, the charge was determined to calculate the EASA of each Pd-based catalyst according to Equation 16 [15].

$$\mathrm{EASA} = \frac{Q_{\mathrm{Pd}}}{Q^*_{\mathrm{Pd}}}\left(\frac{1}{c_{\mathrm{L}}}\right)\left(\frac{1}{A_{\mathrm{GC}}}\right) \tag{16}$$

The calculated EASAs (incl. standard deviation) of all catalysts using the parameters (Equation 16) such as Q^*_{Pd} (= reduction charge of 405 $\mu C \cdot cm^{-2}$ of PdO to Pd, assumed value according to Jongsomjit et al. [83]), c_L (= catalyst loading of 56 $\mu g_{Pd} \cdot cm^{-2}$ on the RDE) and the A_{GC} (= surface area of 0.196 cm^2 from the GC substrate on RDE) [15,27].

The active layer thicknesses (ALT) of the Pd/C (commercial) and $Pd_{85}Ni_{10}Bi_5/C^{(I)-(III)}$ catalysts on the GC-RDE are approx. 3 µm and 10 µm, respectively. Details for ALT calculations of the catalysts are given in the Appendix A (**section 8.4.3**) [3].

Physico-Chemical Analysis Methods

ICP-OES

The actual elemental compositions of carbon supported Pd-based catalysts were analyzed by ICP-OES (**sections 4.2.1** and **4.3.1**) [15,29]. Metal concentrations of catalysts were determined by this method after microwave-assisted pressurized acid digestion. A Multiwave 3000 microwave system (Anton Paar, Graz, Austria) was used for digestion. Each material was analyzed in triplicate by digesting 5-10 mg of catalyst with 7 mL of concentrated nitric acid and 0.2 mL of $HClO_4$ (Carl Roth, Karlsruhe, Germany). Temperature was ramped to 195 °C within 15 min with the application of 1,500 W of power, followed by a dwell time of 25 min at maximum temperature. Samples were diluted to 25 mL with deionized water. The ICP-OES system was an Arcos SOP by Spectro (Kleve, Germany). Following detection wavelengths were used for each element: Bi 223.061 nm, Ni 231.604 nm and Pd 340.458 nm. Sample blanks and spikes were included in all preparation procedures [15,29].

The ICP-OES analysis for the carbon supported ternary $Pd_{85}Ni_{10}Bi_5$ catalysts from **section 4.4.2** was almost identically performed as described above with an one difference – the digesting procedure of these catalysts occurred besides 7 mL of concentrated nitric acid and 0.2 mL of $HClO_4$ in additional 0.2 mL of hydrofluoric acid 40% (Merck, Darmstadt, Germany) [3].

The ICP-OES analysis for the carbon supported Au-based catalysts from **section 4.1.3** was carried out in a similar way as described above, with three differences – the digestion of these catalysts occurred in a mixture of HCl and HNO_3 (nitrohydrochloric acid) at a maximum temperature of 190 °C for 30 min.

TEM-EDX

The morphology, particle size distribution and the chemical composition (atomic ratio) of the carbon supported Pd-based catalysts (**sections 4.2–4.4**) were determined by means of the TEM-EDX, respectively [3,15]. The images were acquired using a monochromated TF20 TEM (FEI) equipped with a Schottky field emission gun and operated at a maximum accelerating voltage of 200 kV. The EDX spectra were detected with an EDAX Si(Li) detector. The TEM grids were prepared by the standard preparation procedure for powder samples by depositing a drop of in alcohol suspended sample particles onto a copper TEM grid which was covered with a holey carbon support-film. The evaluation of the TEM-EDX measurements of each catalyst (*d*-spacing determinations and element quantifications) was performed by Digital Micrograph software program [3,15].

For the particle size distribution and average particle diameter determination, 100 spherical-shaped particles of the TEM micrograph areas were chosen for in-house Pd/C, $Pd_{85}Ni_{10}Bi_5/C^{(II)}$ and $Pd_{85}Ni_{10}Bi_5/C^{(III)}$ catalysts and the diameter of particles were measured manually by FIJI (ImageJ)-free software program [3,111].

XRD

The structural composition from each synthesized carbon supported Pd-based catalyst was investigated with XRD using a Bruker D8-Advance diffractometer with Lynxeye detector. XRD measurements of catalysts from **sections 4.2.1** and **4.3.1** were performed from 20° to 100° 2θ, with a step size of 0.02°, and a scan time of 2 s·step^{-1} [15]. XRD measurements of catalysts from **section 4.4.2** were performed from 5° to 100° 2θ, a step size of 0.02° and a counting time of 3 s·step^{-1} [3]. Cu-K_α radiation (= 0.15418 nm) was used for the XRD analysis. Lattice parameters, half-widths ($B_{observed}$) and *d*-spacings were calculated with Rietveld method and profile fit, using PANalytical X'Pert Highscore Plus software. The average crystallite size (*L*) of located crystal structures in different catalyst powders was estimated according to Scherrer (Equation 17) assuming spherical crystallites with cubic crystal system [3,15].

$$L = \frac{K \cdot \lambda}{B_{2\Theta} \cdot cos\ \Theta} \tag{17}$$

K Constant which is assigned to the value of 0.94 for assumption of spherical crystallites with cubic crystal system.

λ Wavelength of the Cu $K_{\alpha1}$ radiation (= 1.54056 Å), only $K_{\alpha1}$ peaks were used.

B Difference between half width (full width half maximum FWHM, peak width = $B_{observed}$) and the device related width (= $B_{standard}$) using the measurement of the standard material LaB_6.

XPS

The XPS is a qualitative and quantitative method to find more information about the chemical composition from the binding energies of core-level-electrons of each contained element in the synthesized carbon supported Pd-based catalysts (**sections 4.2.1** and **4.3.1**). The X-ray photoelectron spectrometer works under ultrahigh-vacuum (UHV) conditions with a residual gas pressure below 10^{-10} mbar. Each catalyst sample was transferred into the analysis-chamber within several hours via load-lock. The system is also equipped with a UV-photo-electron spectrometer. The following instrumentation is used for XPS-analysis: "Multiprobe" UHV-surface-analysis system (Omicron Nanotechnology); X-ray source: DAR400 aluminium-anode; quartz-crystal monochromator XM 500; X-ray excitation energy: 1486.70 eV (Al $K_{\alpha 1}$-line); monochromated X-ray line width (FWHM): 0.3 eV; energy analyzer: hemispherical analyzer, type EA 125 signal-detection with pulse-counting channeltron [15].

Survey spectra / core level spectra of Pd 3d, Ni 2p and Bi 4f were measured using a pass energy of 80/20 eV at a resolution of 0.5/0.03 eV·step^{-1} and a total integration time of 0.2/0.1 s·point^{-1} (**sections 4.2.1** and **4.3.1**). The deconvolution of Pd 3d, Ni 2p and Bi 4f core level spectra was conducted by fitting with Gaussian-Lorentzian lines [3,15].

The XPS measurements of catalysts from **section 4.4.2** were performed using a SPECS PHOIBOS 150 Hemispherical Energy Analyzer with a monochromated Al K_{α} X-ray source. Indium-foil was used as substrate for the sample preparation. Survey spectra were measured using a pass energy of 40 eV at a resolution of 0.2 eV·step^{-1} and a total integration time of 0.1 s·point^{-1}. Data analysis was performed using CasaXPS software (http://www.casaxps.com/) with a Shirley-type background and 70–30 Gaussian–Lorentzian peak shapes, except for Pd metal, which was fit with an asymmetric line shape [3].

3.2 Polysaccharide Based Anion Exchange Membranes

3.2.1 Synthesis

Within the FFG project ‘e!Polycat’, the project partners JR in cooperation with KFU have successfully prepared and comprehensively characterized various polysaccharide based AEMs for the ADEFC. Details about the synthesis procedures of AEMs are described in the end report of the research project ‘e!Polycat’ [103].

3.2.2 Characterization

The membrane resistance of polysaccharide based AEMs provided by the project partners JR and KFU and commercial AEMs, and also the membrane resistance of commercial CEMs and different kinds of CEMs provided by the Institute of Solid State Physics (head of the institute: Assoc. Prof. Anna Maria Coclite, TU Graz) were determined by the EIS method (ex-situ). A Conductivity Clamp was used (Bekktech, BT110 LLC, Scribner Associates, Southern Pines, NC, USA) in electrical connection with Gamry Reference 600 (bi-)potentiostat to calculate their in-plane ionic conductivities in ultra-pure water (~18 MΩ·cm). A schema of the conductivity measurement process of membranes is shown in Figure 8 [112–114].

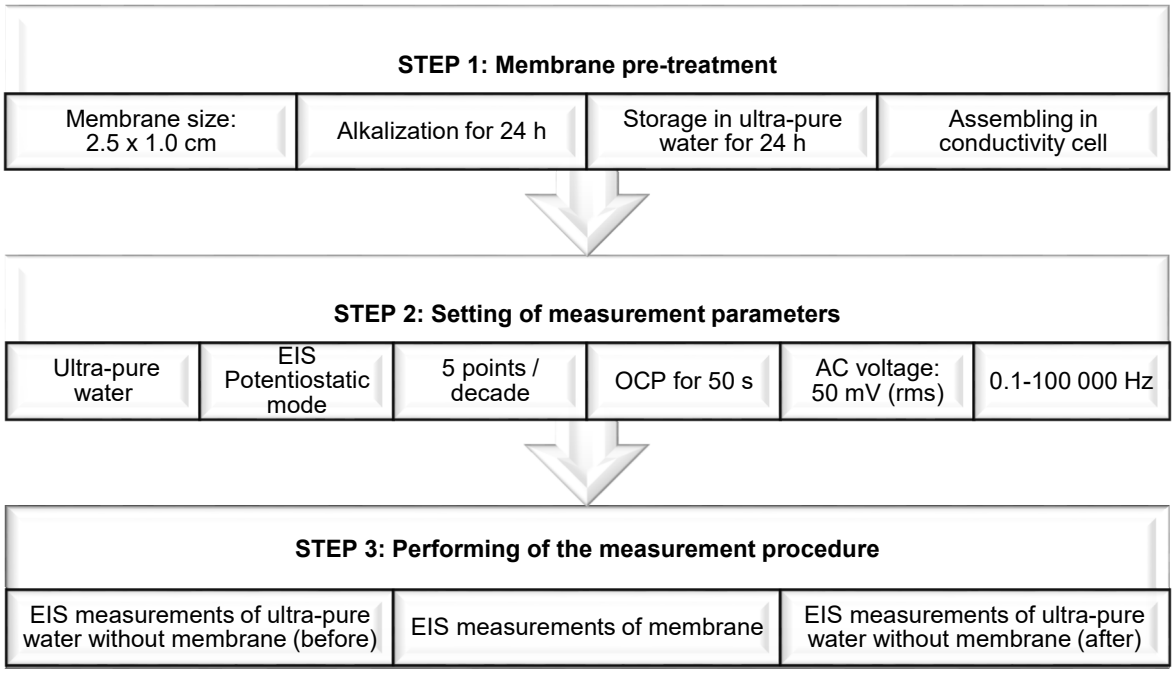


Figure 8: Standardized in-plane conductivity measurement process for fuel cell membranes [112–114].

Further details of the in-plane membrane conductivity measurements are described in the previous publications [112–114].

3.3 Electrode Development

3.3.1 Anode

For the preparation of anodes, the synthesized carbon supported catalysts (40 wt.% of metals on Vulcan XC72R carbon black) with an anionomer solution[2] as a binder, in the dependence of AEM used, was well dispersed in 1-propanol using an ultrasonic bath and ultrasound probe. 1.2 mL of the catalyst suspension was dripped using a micropipette on a 3x3 cm^2 carbon cloth (see Figure 9c), in order to achieve the desired loading of 1 $mg_{metal} \cdot cm^{-2}$ (see calculation of the catalyst ink preparation in **section 8.1.2**). Finally, the anode was dried in the oven for 24 h at 40 °C [103,104,106,108,109].

3.3.2 Cathode

According to Grimmer et al. [106,108,109], the cathode was manufactured by a cross-rolling, hot-pressing method. The cathode was composed of Toray carbon paper as the gas diffusion layer (GDL) and the active layer (AL), and using polytetrafluoroethylene (PTFE) powder (3M Dyneon, TF 2021Z) and anionomer solution[4] as binder materials. The AL consisted of the binder materials, the carbon supported Ag-MnO_x catalyst (see synthesis below) and 1-propanol. After mixing until a leathery texture was achieved, the AL was rolled onto the GDL and hot pressed at 120 °C with a pressure of 120 $kg \cdot cm^{-2}$. The thickness of the electrode was 0.75 mm with a catalyst loading of 13 $mg \cdot cm^{-2}$ [103].

The Ag-MnO_x cathode catalyst was synthesized according to Wu et al. [18]. The carbon support Vulcan XC72R was therefore dispersed in ultra-pure water with a few drops of 2-propanol to reduce the surface tension of the water. Equimolar aqueous solutions of $KMnO_4$ and $AgNO_3$ were added to the carbon suspension and were stirred at 60 °C in order to remove the solvent. The resulting impregnated carbon was ground to powder and heat-treated in a tubular furnace for 2 h at 400 °C in N_2 atmosphere, resulting in the Ag-MnO_x/C catalyst (10 wt.% Ag, 20 wt.% MnO_x). The Ag-MnO_x cathode catalysts were comprehensively ex-situ characterized for the alkaline ORR [115,116].

[2] 5 wt.%, Tokuyama AS-4 from Tokuyama Corporation (Japan) or FAA3 from Fumatech (Germany) or N-[(2-Hydroxy-3-trimethyl-ammonium) propyl] chitosan chloride/quaternized poly(vinyl alcohol) (HTCC/QPVA) mixture provided from project partners JR and KFU; 20 wt.% based on catalyst.

In the framework of the FFG project ‘e!Polycat’, ethanol tolerant perovskite based cathodes ($La_{0.7}Sr_{0.3}MnO_3$ and $La_{0.7}Sr_{0.3}(Fe_{0.2}Co_{0.8})O_3$) with high ORR performance for the ADEFC were developed [117].

3.4 Preparation of Membrane Electrode Assemblies

A (commercial) AEM, 4x4 cm^2 in size, was processed to MEA (Figure 9d) using both the carbon supported Pt-free based anode (Figure 9a), and the EtOH tolerant based cathode, in the following two ways: (1) by hot-pressing (adaptation of the parameters, such as pressure, temperature and time especially to the used AEM, and also to the electrode containing materials) and (2) by layered assembling in the in-house designed single cell. Prior to preparation of the synthesized MEAs, the used AEMs were immersed in a 1.0 M KOH solution for 24 h resulting in a hydroxide form (OH^-). The MEAs using the AEM (fumasep® FAA3-PK-130 PEEK reinforced, Fumatech, Germany) were developed at 110 °C and using a compacting pressure of 300 kg for 35 min according to method 1. The MEA production with the AEMs (A201 Tokuyama from Tokuyama Corporation, Japan; Polybenzimidazole Dapazol from Danish Power Systems, Denmark; HTCC/QPVA (MQ195b) provided from project partners, JR and KFU (Figure 9b)) was performed according to method 2. The MEA preparation is demonstrated in Figure 9 [103,118].

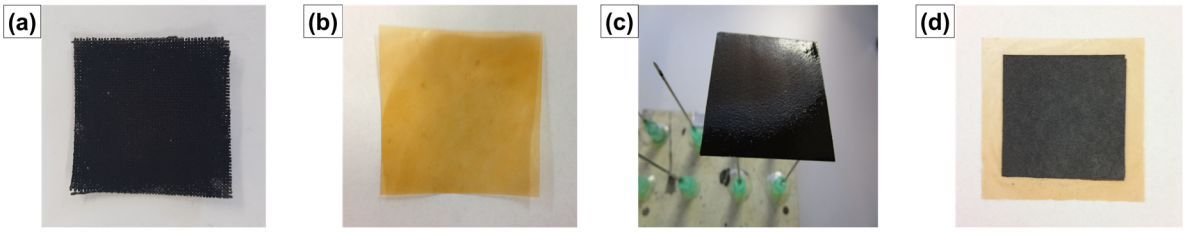


Figure 9: MEA preparation: **(a)** Anode: Catalyst on carbon cloth; **(b)** HTCC/QPVA membrane; **(c)** Drop coating process and **(d)** developed MEA [103,118].

The carbon supported $Pd_{60}Ni_{40}$ and $Pd_{60}Ni_{20}Bi_{20}$ based anodes, the A201 Tokuyama as semi-commercial AEMs and the carbon supported $AgMnO_x$ cathodes were assembled in layers (MEA 1 and MEA 2) in the in-house designed single cell (Figure 10) and were characterized by I-V characteristics and EIS. The in-situ characterization results of both MEAs are discussed in **section 4.2.3**.

3.5 Single Cell Tests

The maximum power density and the dynamic behavior of the developed MEAs were investigated by means of in-situ methods [106,108,109]. These included, I-V characteristics and EIS in single cell configuration (Figure 10) under various operating conditions, respectively. A mixture of 1 M EtOH (purchased from EtOH absolute, 99.999%, Aldrich) and 1 M KOH (standard solution; FIXANAL KA 180 mL, Sigma-Aldrich) were pumped with a flow rate of 10 mL·min^{-1} to the anode, where the cathode was supplied for single cell measurements with pure oxygen (O_2, purity of 5.0, Air Liquide) using a flow rate of approx. 10 mL·min^{-1} [103,118].

The **ADEFC system** (Figure 10d) includes all needed components in the following order: Steel end plate (Figure 10a); PTFE gasket; Cu current collector with carbon paper which is directed to the backside of the cathode flow field; **cathode flow field** (Figure 10b); silicon gasket; **MEA**; silicon gasket; **anode flow field** (Figure 10c); Cu current collector with carbon paper which is directed to the backside of the anode flow field; PTFE gasket; steel end plate.

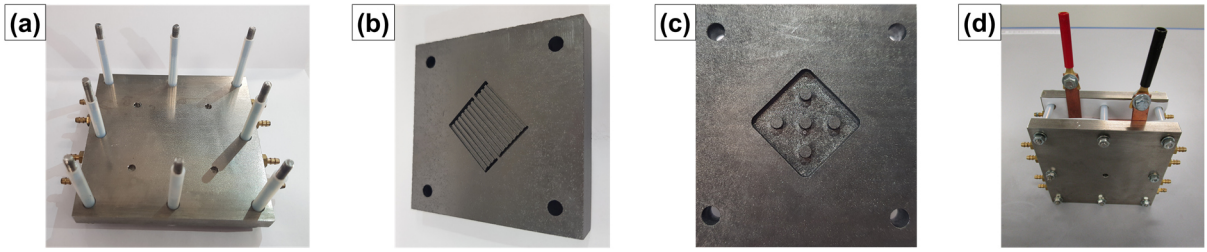


Figure 10: Single cell configuration[3]: **(a)** Open single cell system without ADEFC components; **(b)** Cathode flow field; **(c)** Anode flow field and **(d)** ADEFC system [103,118].

3.5.1 Current-Voltage Characteristics

Chronopotentiometric scans of MEAs were recorded at different temperatures to determine the power densities of the I-V characteristics. Thereby, a specific current was gradually applied for 60 s (MEA 1) and 120 s (MEA 2) using Gamry Reference 600 (bi-)potentiostat, and the resulting cell voltage was determined (active area: 4 cm^2) [103,118].

[3] Dr. Christoph Grimmer (CEET, TU Graz; now Chief of Executive Officer of Efficient Energy Technology GmbH) designed and manufactured the direct single cell in cooperation with Rene Fras (CEET, TU Graz) and Fabrication Laboratory (FabLab at Institute of Innovation and Industrial Management, TU Graz).

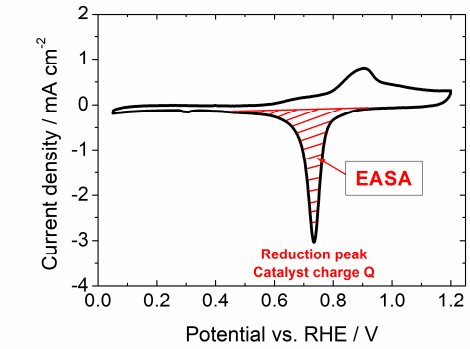
3.5.2 Electrochemical Impedance Spectroscopy

After each I-V characteristic of the respective MEA, the electrochemical impedance spectra were recorded at various constantly applied currents and at different temperatures in a frequency range of 0.1-10 000 Hz using the galvanostatic EIS method (additional measuring settings: AC current: 0.002 A·rms, Points/decade: 5). The individual losses of voltage were identified from the electrochemical impedance spectra [103,118].

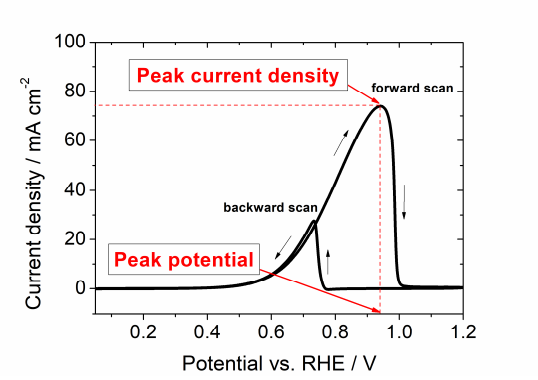
3.6 Various Parameters used for Evaluation of Anode Catalyst Performance

Section 3.6 explains the meaning of electrochemical parameters, which are used in the framework of this doctoral thesis for evaluation of the anode catalyst performance (activity, stability and byproduct tolerance) under consideration of structure characteristics (particle and crystallite size, shape, (surface) structure, chemical composition) for alkaline EOR.

The determination of the **EOR activity** of each synthesized electrocatalyst is described by following electrochemical characterization parameters with a corresponding example (marked in red):

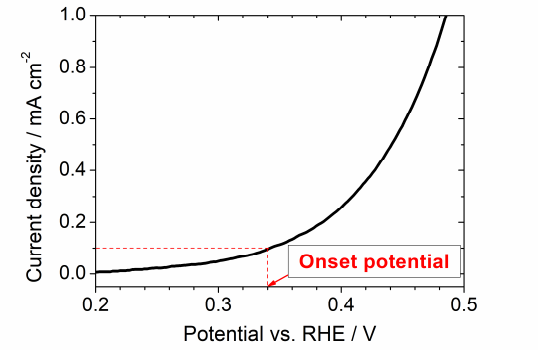
Electrochemical Active Surface Area (EASA)	
	• The integrated charge of the characteristic CV peak in respect to active material is used for the EASA calculation of each Pd-based catalyst. • There is another possible way to determine the EASA e.g. by CO stripping test [119]. • The EASA depends mostly on the particle size. The lower particle size the higher the EASA thus resulting in a high EOR activity of the catalyst used.

Peak current density (i_P) & Peak potential (E_P)



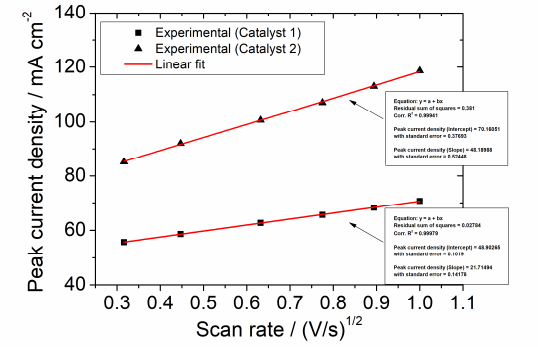
- Peak current density (i_P) is the maximal current density of the forward scan and is an indicator used for describing the EOR activity.
- Peak potential (E_P) is the maximal potential of the forward scan and is a further indicator used for describing the EOR activity.

Onset potential (E_{onset})



- The onset potential (E_{onset}) is the potential where the EtOH oxidation on the catalyst starts.
- The E_{onset} of each catalyst is determined at the current density of 0.1 mA·cm^{-2} due to the electro-chemical double layer charge influencing [3].
- There are other possibilities to determine the E_{onset} e.g. at the intersection between a linear along the EOR curve of the forward scan with the x-axis or, where the base CV overlaps with the EOR curve.
- The lower the E_{onset} the higher EOR activity.
- The E_{onset} depends mainly on the surface concentration and chemical composition of the catalyst used, respectively.
- Wang et al. use the half-wave potential ($E_{1/2}$) of the EtOH oxidation (forward scan) which is a further parameter for the comparison of the EOR kinetic on different catalysts [120].

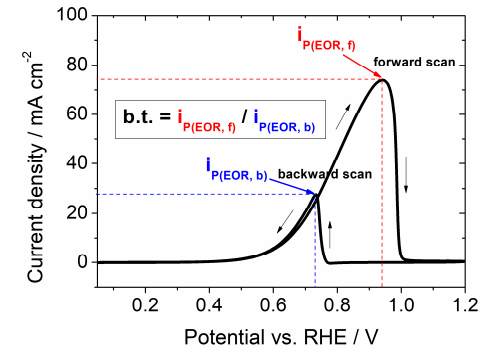
Number of electrons released during the alkaline EOR



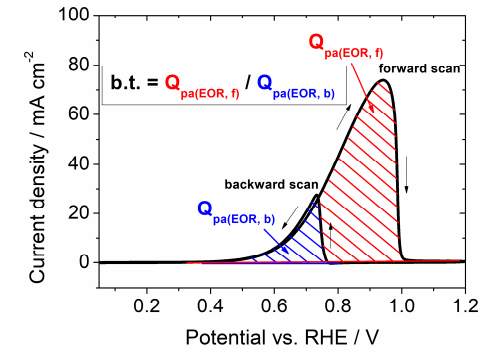
- Plotting of the peak current density against the square root of the scan rate.
- The higher the slope of the linear, the higher the number of electrons (n) that are generated from the alkaline EOR.
- Electron releasing determination by the Randles-Sevcik equation (see Equation 20).

The determination of the **EOR stability (byproduct tolerance)** of each electrocatalyst is described using the following approaches with corresponding examples (marked in red):

Byproduct tolerance relating to peak current density (i_P) & peak current density area (Q_{pa} - total charge)

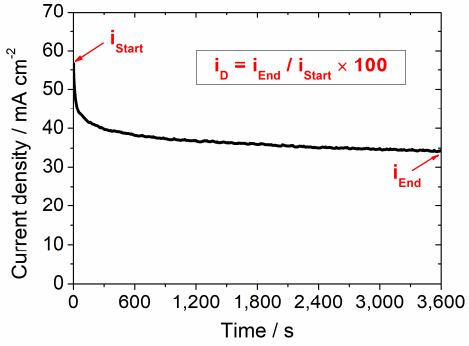


- The byproduct tolerance (b.t.) of each catalyst is determined by the ratio of the peak current density of the forward ($i_{P(EOR, f)}$) and backward scan ($i_{P(EOR, b)}$) [26].
- The higher the value, the higher the tolerance toward poisoning by intermediates of the EtOH oxidation (e.g., CO or CH_x).



- The byproduct tolerance (b.t.) of each catalyst is determined by the ratio of the integrated peak current density areas (total charge) of the forward ($Q_{pa(EOR, f)}$) and backward scan ($Q_{pa(EOR, b)}$) [121].
- The higher the value, the higher the tolerance toward poisoning by intermediates of the EtOH oxidation (e.g., CO or CH_x).

Current density decrease (i_D) using the ratio of i_{End} and i_{Start}



- The EOR stability is described by the current density decrease (i_D) using the CA method.
- Current density decrease (i_D) is the ratio of the resulting current density after 0 s (i_{Start}) and the current density after 3,600 s (i_{End}) from the CA measurements at an applied constant potential.
- There is another possible way to determine the EOR stability e.g. the height of the slope using a linear function through the resulting current density after 0 s (i_{Start}) and the current density after 3,600 s (i_{End}) from the CA measurements at an applied constant potential.
- The changing of the current density in dependency of time is described by the Cottrell equation which is valid if the EtOH oxidation is a diffusion controlled process [49,122,123].
- The linear current density decay of the CA measurement was used for describing the long-term poisoning rate of the catalyst according to Datta et al. [124].
- Performing of stepwise applied constant potential over time on the catalyst to analyze the EOR stability in the low and high potential.

4 Results and Discussion

In this doctoral thesis, an innovative carbon supported Pt-free anode catalyst system with higher EOR performance has been successfully developed using common and modified instant synthesis reduction methods for the ADEFC, compared to other synthesized carbon supported monometallic, binary and ternary as well as commercial EOR catalysts. This novel carbon supported ternary PdNiBi catalyst was comprehensively characterized with electro-chemical and various physico-chemical analysis methods for the alkaline EOR.

- The **sections 4.1** to **4.4** extend from profound insights of characterization effects on EOR performance of selected catalysts, to identifying and performance optimizing the novel carbon supported ternary PdNiBi catalyst for the alkaline EOR. Some parts of the electro-chemical characterization results of various carbon supported Pt-free anode catalyst systems, from the **commissioned end report** of the **FFG project 'e!Polycat'** entitled **'Pt-free anode catalyst systems and composite polysaccharide-membranes for the alkaline DEFC'** [103], were adopted, adapted and further intensively discussed in **section 4.1**. This section describes the electrochemical characterization effects using various measuring parameters and conditions on the catalyst EOR performance.

- **Sections 4.2** and **4.3** deal with electrochemical and physico-chemical characterization results and discussion of carbon supported Pd-based nanocatalysts (Pd/C, $Pd_{60}Ni_{40}$/C, $Pd_{60}Bi_{40}$/C and $Pd_xNi_yBi_z$/C) from the **peer-reviewed article** entitled **'Novel highly active carbon supported ternary PdNiBi nanoparticles as anode catalyst for the alkaline direct ethanol fuel cell'** of Cermenek et al. [15] which is based on the **master's thesis** entitled **'Development and Characterization of Pd-based Catalysts for the alkaline Direct Ethanol Fuel Cell'** of Johanna Ranninger [29].

- **Section 4.4** contains further EOR performance optimization results and discussion of the novel ternary PdNiBi anode catalyst, using the modified instant reduction synthesis method from the **peer-reviewed article** entitled **'Alkaline Ethanol Oxidation Reaction on Carbon Supported Ternary PdNiBi Nanocatalyst using Modified Instant Reduction Synthesis Method'** of Cermenek et al. [3], which is based on the **unpublished master project work** entitled **'Vorgänge während der Herstellung von Pd-basierenden Katalysatoren für die Direkt-Ethanol-Brennstoffzelle'** of Thomas Winter.

- The obtained electrochemical and physico-chemical characterization results of the carbon supported ternay PdNiBi anode catalysts from **sections 4.2–4.4** [3,15] are used for further research activities in the framework of the ongoing FWF project 'GO DEFC' (see **section 6** and details about the FWF project in **section 10.1** in the Appendix C).

- My scientific contribution to the characterization of the synthesized membranes (from project partners JR and KFU, and from the Institute of Solid State Physics, head of the institute: Assoc. Prof. Anna Maria Coclite; TU Graz) and of commercial membranes is discussed in brief in **section 4.5**.

Throughout the doctoral study from 10/2014 to 01/2020, all resulting **scientific publications**, such as **peer-reviewed articles**, **lectures**, **book chapters, commissioned reports**, **conference contributions**, **professional articles** and **scientific posters** are listed in Appendix B (**section 9**). Furthermore, the research works of students that I supervised, are described in **section 10.2** in Appendix C and contribute to the **sections 4.1–4.4**. Appendix C concludes with news and stories about me (**section 10.3**).

PART I

The Effect of Various Characterization Parameters and Operating Conditions on the EOR Performance of Carbon Supported Pt-free Electrocatalysts in an Alkaline Medium

Parts of the following **section 4.1** and the corresponding Appendix A (**section 8.1**) have been **published in advance** in:

[15] **Cermenek, B.**; Ranninger, J.; Feketeföldi, B.; Letofsky-Papst, I.; Kienzl, N.; Bitschnau, B.; Hacker, V. Novel highly active carbon supported ternary PdNiBi nanoparticles as anode catalyst for the alkaline direct ethanol fuel cell. *Nano Res*. **2019**, *12*, 683–693.

[131] Hacker, V.; Ranninger, J.; **Cermenek, B.**; Feketeföldi, B.; Spirk, C.; Hesse, J.; Ribitsch, V. Optimization of the Catalyst and Membrane Performance by addition of various Additives for the alkaline Direct Ethanol Fuel Cell. *Zenodo*, **2018**.

[29] Ranninger, J. Development and Characterization of Pd-based Catalysts for the alkaline Direct Ethanol Fuel Cell. *Master's thesis*, Graz University of Technology, **2017**, p. 85. (supervised **Cermenek, B.**)

[103] **Cermenek, B.**; Hacker, V.; Feketeföldi, B.; Ribtisch, V. Pt-free anode catalyst systems and composite polysaccharide-membranes for the alkaline DEFC. *End report*, **2017**, p. 73.

[118] Hacker, V.; **Cermenek, B.** IEA AFC Annex 35: Brennstoffzellen für portable Anwendungen: Arbeitsperiode 2014-2017. *End report*, **2017**, p. 34.

[132] **Cermenek, B.**; Feketeföldi, B.; Zacharias, R.; Ribitsch, V.; Hacker, V. Characterization of Platinum-free electrocatalysts and anion exchange membranes for direct ethanol fuel cell. in Proceedings of 6th European Fuel Cell - Piero Lunghi Conference, Cigolotti, V.; Barchiesi, C.; Chianella, M. (eds) **2015**, ENEA, Naples, Italy, 16/12/15–18/12/15, pp. 167–168.

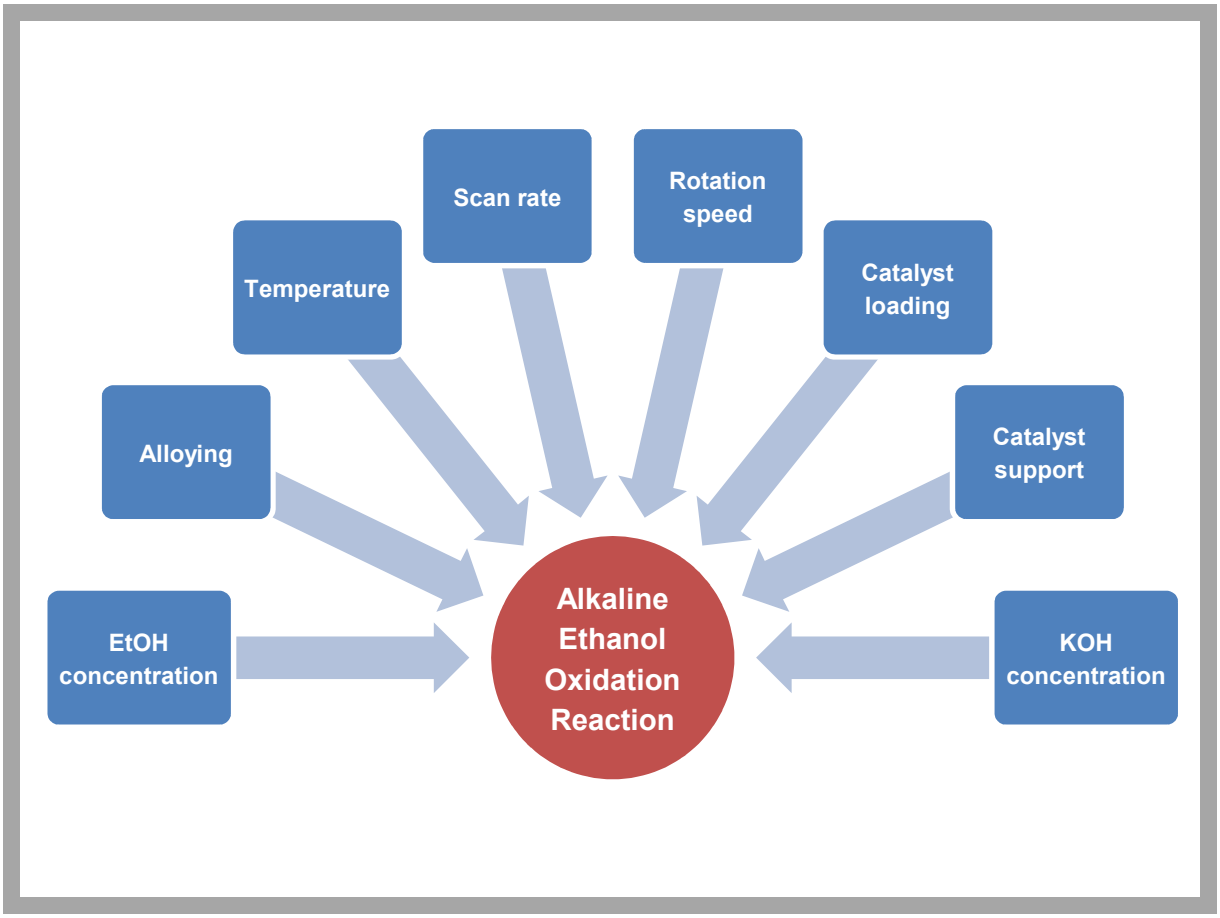
Acknowledgment

Dominic Leipold **2015**, Electrocatalysts for Alkaline Ethanol Oxidation Reaction and Oxygen Reduction Reaction, *Project Laboratory*, Graz University of Technology, 06/07/15 – 31/07/15. (unpublished; supervised **Cermenek, B.**)

4.1 PART I: The Effect of Various Characterization Parameters and Operating Conditions on the EOR Performance of Carbon Supported Pt-free Electrocatalysts in an Alkaline Medium

Abstract

Part I of the doctoral thesis shows the effect of various characterization parameters and operating conditions on the EOR performance (EASA, onset potential, peak potential, peak current density and byproduct tolerance) of selected catalyst samples in an alkaline medium. Carbon supported bimetallic Pd_xNi_y, bimetallic Au_xCu_y, ternary Pd-based and other Pt-free electrocatalysts were investigated by CV using RDE. The electrochemical aspects of interface between catalyst layer and electrolyte are intensively discussed.



Graphical abstract TOC: Effects of various characterization parameters and operating conditions on the alkaline EOR performance of selected carbon supported Pt-free electrocatalysts.

4.1.1 Electrochemical Parameters and Operating Conditions Effects

The effect of different (i) concentrations of electrolyte, (ii) catalyst loadings, (iii) operating temperatures, (iv) scan rates and (v) rotation speeds for the alkaline EOR were investigated on the synthesized carbon supported bimetallic PdNi catalyst using RDE-CV measurements, and were fixed as electrochemical characterization standard parameters and operating conditions for investigation of the other developed Pd-based catalysts discussed in this doctoral thesis (see **sections 4.2–4.4**).

Catalyst ink preparation effect

The described studies in **section 2.1.4** concerning the effects of Nafion binder and sonication parameters on the catalyst ink preparation and catalyst distribution on the GC-RDE were also considered in the experiments in this doctoral thesis (see experimental **section 3.1.2**) and improvements were implemented [15]. In this context, an optimum catalyst ink preparation procedure was thus developed resulting in a homogeneous catalyst ink and a homogeneous catalyst distribution on the GC substrate of the RDE for reproducible results of Pd-based nano-catalysts [15]. Details about the catalyst ink preparation are shown in the master's thesis of Johanna Ranninger [29].

Electrolyte concentration effect on EOR performance

The effect of an increased EtOH concentration on the EOR activity of the Pd_xNi_y/C catalyst with different catalyst loadings was investigated in 1 M KOH at 30 °C by CV using a RDE (Figure 11). Figures 11a, 11d and 11g show that the peak potential of the forward scan toward the alkaline EOR, increases with enhanced EtOH concentration resulting in peak potential increase that gets larger on this bimetallic catalyst with enhanced catalyst loadings [103].

Rivera-González et al. [125] report that the peak potential of alcohol oxidation in the forward scan suggests an energy barrier toward alcohol oxidation reaction. This occurs during charge transfer at the interface between catalyst layer and electrolyte and can be influenced by the electrical features of the catalyst used and by their various electrochemical oxidation processes (e.g., dissociative adsorption of the reactant, in that case EtOH, charge transfer or desorption of the reaction product as well as intermediates) [125].

The peak current density of the forward scan for the alkaline EOR on the catalyst increases up to a certain EtOH concentration in dependency on catalyst loading and then decreases with further enhancement of the EtOH concentration (see Figures 11b, 11e and 11h) [103].

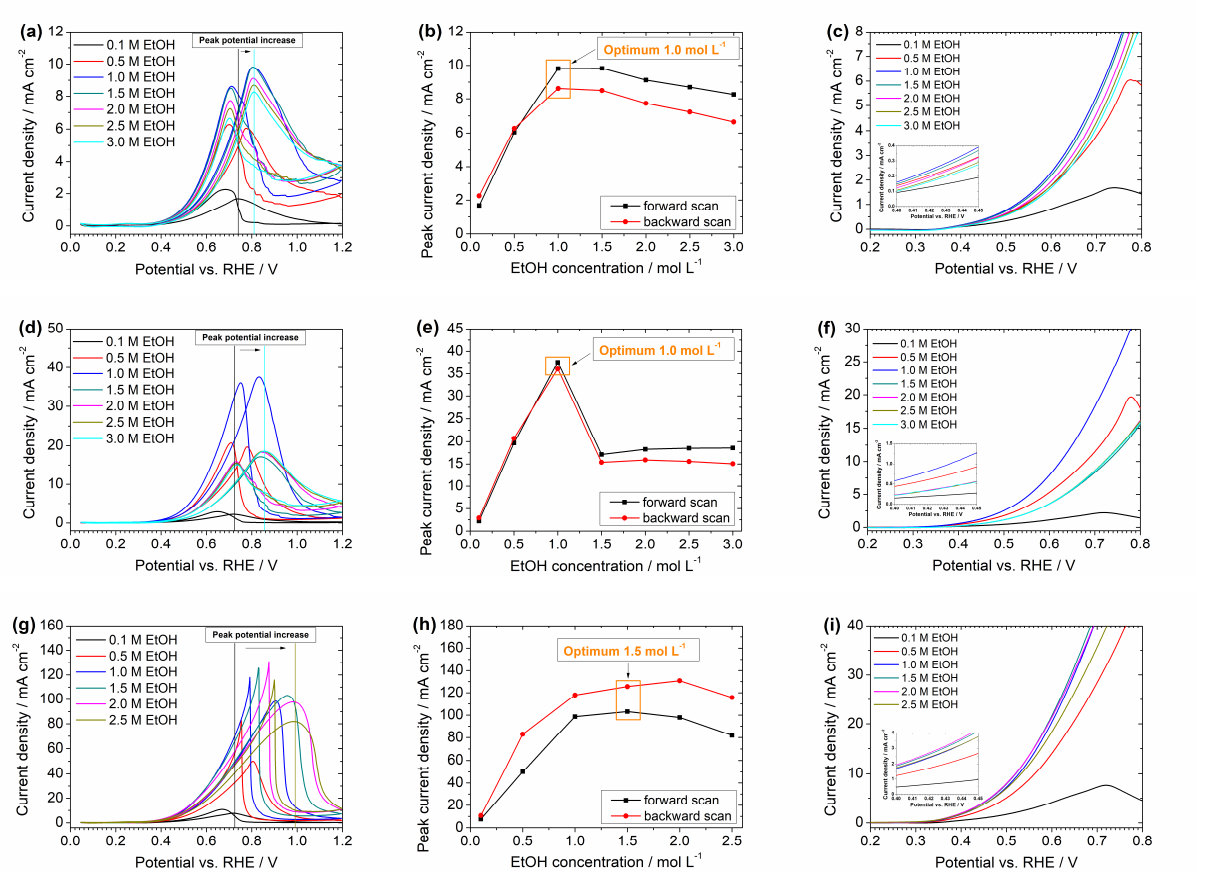


Figure 11: EOR activity determinations on the Pd_xNi_y/C catalyst with catalyst loadings of **(a)-(c)** 28 $\mu g_{Pd} \cdot cm^{-2}$, **(d)-(f)** 56 $\mu g_{Pd} \cdot cm^{-2}$ and **(g)-(i)** 112 $\mu g_{Pd} \cdot cm^{-2}$ in 1 M KOH electrolyte with increased EtOH concentrations at a scan rate of 10 $mV \cdot s^{-1}$ and at 30 °C [103].

The highest peak current density for the alkaline EOR on the catalysts with Pd loadings of 28, 56 and 112 $\mu g_{Pd} \cdot cm^{-2}$ was achieved at an EtOH concentration of 1.0 M and 1.5 M. The enhanced EtOH concentration has the same effect on the onset potential (see Figures 11c, 11f and 11i), which is similar to the peak current density toward alkaline EtOH oxidation on the Pd_xNi_y/C catalyst [103].

The rate limiting step of the alkaline EOR on this catalyst is the oxidation process between the adsorbed ethoxy groups and the adsorbed OH according to Equations 18 and 19 based on research group of Cerritos et al. thus resulting in acetic acid (unstable in alkaline media) and/or acetate as main products [103,126].

$$\begin{aligned} Pd - (COCH_3)_{ads} + Pd - OH_{ads} &\leftrightarrows Pd - (C(OH)_2CH_3)_{ads} + Pd^0 \\ Pd - (C(OH)_2CH_3)_{ads} + OH^- &\leftrightarrows Pd^0 + CH_3COO^- + H_2O \end{aligned} \quad (18)$$

$$\begin{aligned} Pd - (COCH_3)_{ads} + Ni - OH_{ads} &\leftrightarrows Pd - (C(OH)_2CH_3)_{ads} + Ni^0 \\ Pd - (C(OH)_2CH_3)_{ads} + OH^- &\leftrightarrows Pd^0 + CH_3COO^- + H_2O \end{aligned} \quad (19)$$

Cerritos et al. [126] report that enhanced EtOH concentration suppresses the hydrogen absorption-desorption process in the low potential region, thus resulting in a formation of a high amount of ethoxy species which adsorbed at the Pd surface, in such a way that the adsorbed OH groups are blocked by the ethoxy groups. The insufficient coverage of the OH^- ions is the reason for the EOR activity decrease as shown in Figures 11b, 11e and 11h. The balance of the amount of adsorbed ethoxy groups and OH^- ions on the catalyst used is crucial for high EOR activity in an alkaline medium [103,126].

The byproduct tolerance of the Pd_xNi_y/C catalyst with loadings of both 28 and 56 $\mu g_{Pd} \cdot cm^{-2}$ increases continuously with enhanced EtOH concentration (Figures 12a and 12b) but in contrast, the catalyst with the loading of 112 $\mu g_{Pd} \cdot cm^{-2}$ shows a changed curve progression (Figure 12c) [103]. It is assumed that the catalyst with the loading of 112 $\mu g_{Pd} \cdot cm^{-2}$ provides more active sites for alkaline EOR than the others. This results in an adsorption of more EtOH intermediates on the catalyst surface which are not all oxidized in the forward scan. The non-oxidized adsorbed EtOH intermediates are oxidized during the backward scan and cause a higher peak current density consequently in a low byproduct tolerance of the Pd_xNi_y/C catalyst (Figure 12c) [103].

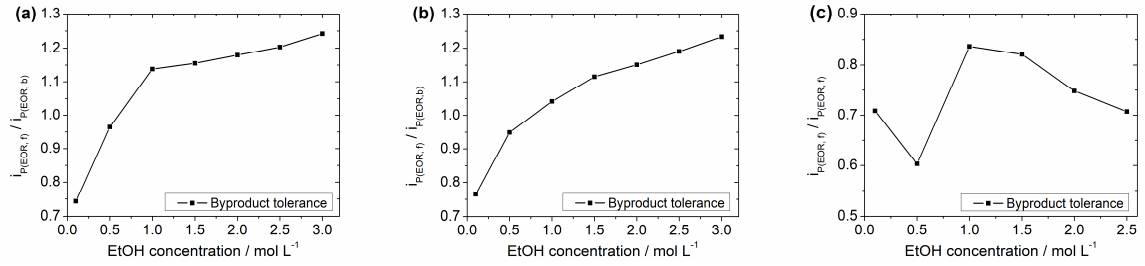


Figure 12: Determined byproduct tolerance of the Pd_xNi_y/C catalyst using the ratio of the peak current density of the forward and backward scan from the EOR measurements (see Figure 11) toward poisoning by reaction intermediates of EtOH oxidation with increased EtOH concentrations and catalyst loadings of **(a)** 28 $\mu g_{Pd} \cdot cm^{-2}$, **(b)** 56 $\mu g_{Pd} \cdot cm^{-2}$ and **(c)** 112 $\mu g_{Pd} \cdot cm^{-2}$ at 30 °C [103].

Effect of catalyst loading on EOR activity

The EOR activity (EASA, peak current density and onset potential) improves drastically on the Pd_xNi_y/C catalyst with increased catalyst loadings (see Figures 13a and 13c), but the determined EASAs relating to Pd (see calculation in Equation 16), decreases with loading of 112 $\mu g_{Pd} \cdot cm^{-2}$ (Figure 13b) [103]. The lower EASA of the Pd_xNi_y/C catalyst, with loading 112 $\mu g_{Pd} \cdot cm^{-2}$ compared to the others, is due to the formation of more Ni oxide than Pd oxide in the presence of KOH on the catalyst surface that covers the active site of Pd. This results in a lower reduction charge of PdO to Pd in alkaline medium [14,103].

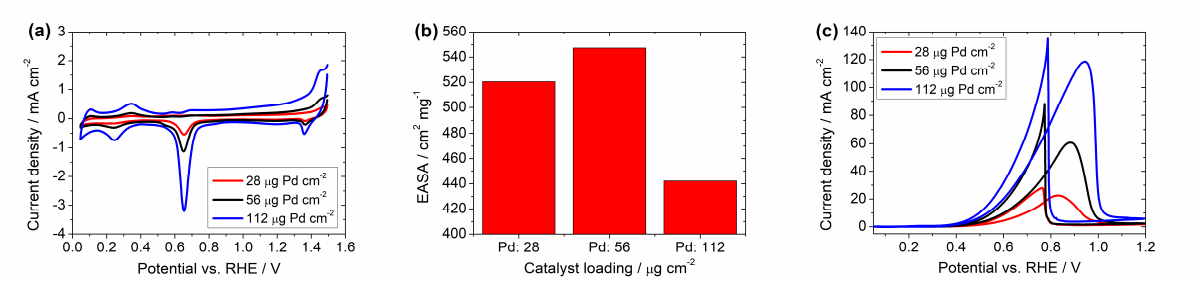


Figure 13: Catalyst loading effect on EOR activity of the Pd_xNi_y/C catalyst at 30 °C: **(a)** CVs in 1 M KOH at different catalyst loadings (relating to Pd), **(b)** the resulting EASAs and **(c)** CVs in an electrolyte mixture of 1 M KOH and 1 M EtOH [103].

Effect of rotation speed on EOR activity

The rotation speed ω of the RDE does not have a great impact regarding the improvement of EOR activity, neither in, for example, peak current density (Figures 14a and 14b) or onset potential (Figure 14c) of the Pd_xNi_y/C catalyst in the forward scan. However, the byproduct tolerance of the catalyst increases continuously with enhanced rotation speeds from 0 to 1600 rpm. As demonstrated in Figure 14b, the difference between the peak current densities of the forward and backward scan gets larger [103]. This is due to a faster oxidation of adsorbed poisonous EtOH species from the catalyst surface. The relationship between peak current densities and rotation speeds from 0 to 1600 rpm is non-linear. Consequently, the mass transport (diffusion) is not controlled toward the alkaline EOR on this bimetallic catalyst [103,127].

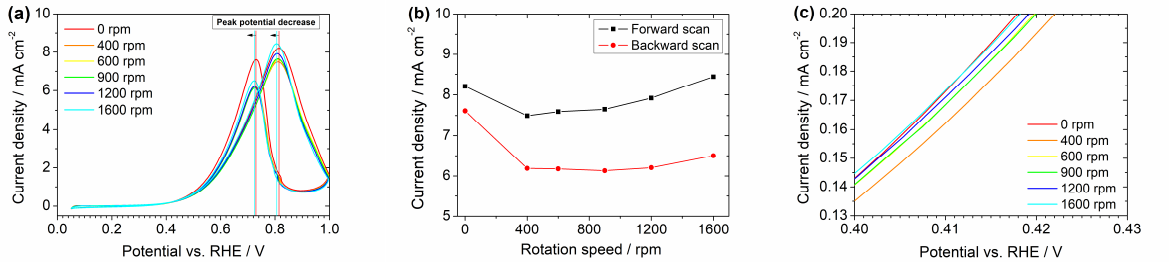


Figure 14: Effect of various rotation speeds of the RDE on the EOR activity of the Pd_xNi_y/C catalyst **(a)** in a mixture of 1 M KOH and 1 M EtOH with a scan rate of 10 $mV \cdot s^{-1}$ at rt, and **(b)** the resulting peak current densities of the forward and backward scan from the EOR measurements. **(c)** Magnification of the potential range between 0.4 to 0.43 V from **(a)** showing the effect of different rotation speeds on onset potential toward alkaline EtOH oxidation [103].

Effect of scan rate on EOR activity

The peak current density of the bimetallic Pd_xNi_y/C catalyst in the forward scan inreases with enhanced scan rates for the alkaline EOR, whereupon the peak potential also slightly increases (Figure 15a) [103]. This means that the anode reaction on this bimetallic Pd_xNi_y/C

catalyst is an irreversible charge-transfer electrode process [36,128]. The relationship between the peak current and the square root of the scan rates from 10 to 1000 mV·s^{-1} is non-linear at the catalyst Pd_xNi_y/C, which is shown in the comparison of experimental data with the linear fit in Figure 15b. The experimental data exhibits a logarithm behavior that can be split into two linear regressions in both scan rate regions of 10 to 100 mV·s^{-1} and 100 to 1000 mV·s^{-1}, respectively. Figure 15b shows clearly that the EOR kinetic process is controlled on this catalyst at both scan rates regions [103].

Therefore, the linear behavior of mono-, bi- and tri-metallic Pd-based catalysts from **sections 8.2.3** and **8.3.3** were also investigated at both scan rate regions. In this context, Figures 54a and 67a in Appendix A show in which scan rate region, the EtOH oxidation on the respective catalyst is diffusion-controlled [125,128]. This electrochemical characterization effect can be described using the Randles-Sevcik equation (Equation 20) by determining the number of electrons transferred during the EtOH oxidation process [125,128].

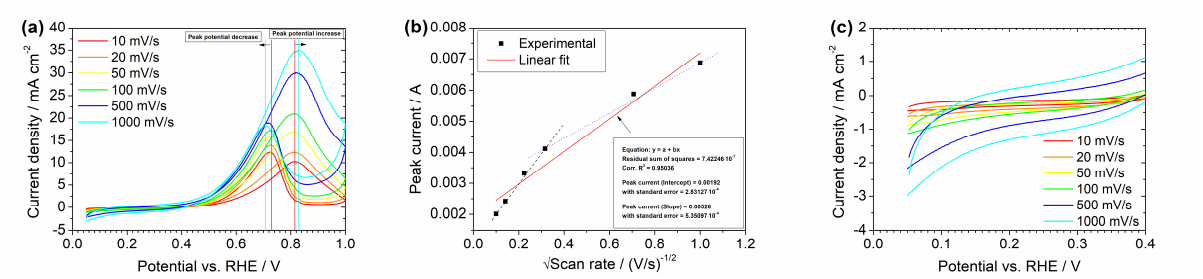


Figure 15: Effect of various scan rates on the EOR activity of the **(a)-(c)** Pd_xNi_y/C catalyst in a mixture of 1 M KOH and 1 M EtOH with a rotation speed of 0 rpm at 30 °C [103].

Furthermore, Figure 15c shows that the onset potential of the bimetallic Pd_xNi_y/C catalyst shifts to lower potentials as it moves toward alkaline EtOH oxidation with increased scan rates [103].

$$i_p = 0.4463 \cdot n \cdot F \cdot A \cdot c \left(\frac{n \cdot F \cdot \upsilon \cdot D}{R \cdot T}\right)^{\frac{1}{2}} \quad (20)$$

i_p	Peak current of the forward scan (A)
n	Number of electrons transferred during the EtOH oxidation process
A	Surface area of GC substrate on RDE (= 0.196 cm²)
F	Faraday constant (= 96,485 C·moL^{-1})
D	Diffusion coefficient of EtOH (= 8.40·10^{-6} cm²·s^{-1} [129])
C	Concentration of EtOH (= 0.001 moL·cm^{-3})
υ	Scan rate (mV·s^{-1})
R	Gas constant (= 8.31445 J·K^{-1}·moL^{-1})
T	Temperature (= 303.15 K)

Effect of temperature on EOR activity

As expected, the EOR kinetics on the Pd_xNi_y/C catalyst with different catalyst loadings, were enhanced at increased temperature. This is shown in Figure 16. Therefore, the peak current density, as well as the peak potential of the forward scan toward alkaline EOR, increases continuously (Figures 16a, 16d and 16g) [103].

The experimental data was applied as a logarithm of peak current density against the reciprocal value of the corresponding absolute temperature, resulting in a less than optimal linear form, confirmed by the linear fit (Figures 16b, 16e and 16h). The enhanced EOR activity on the Pd_xNi_y/C catalyst with different Pd loadings at increased temperatures is confirmed by the reduced onset potential (Figures 16c, 16f and 16i). The temperature increase not only promotes the EOR kinetics, but also the complete EtOH oxidation on this catalyst [103].

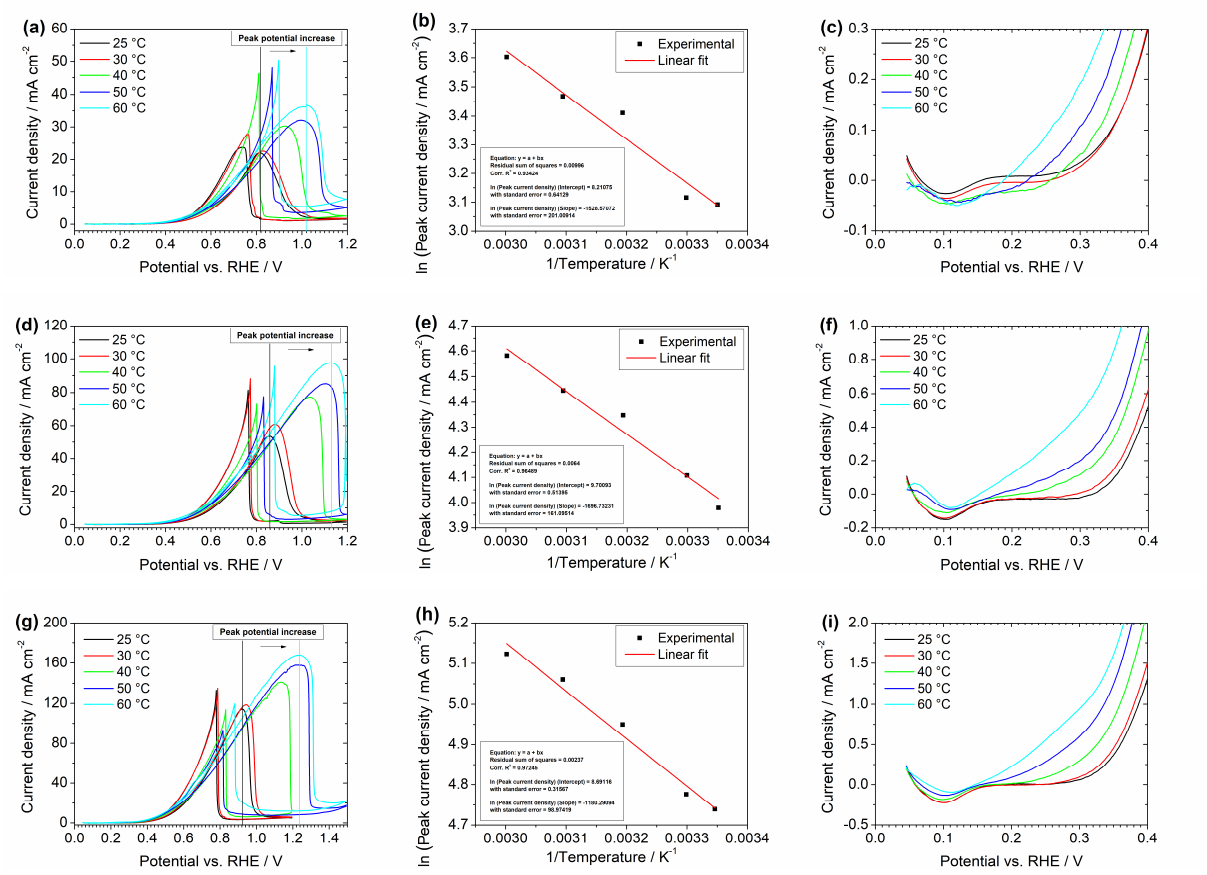


Figure 16: Temperature effect on the EOR activity of the Pd_xNi_y/C catalyst in dependence of different catalyst loadings **(a)-(c)** 28 $\mu g_{Pd} \cdot cm^{-2}$, **(d)-(f)** 56 $\mu g_{Pd} \cdot cm^{-2}$ and **(g)-(i)** 112 $\mu g_{Pd} \cdot cm^{-2}$ with a scan rate of 10 $mV \cdot s^{-1}$ [103].

The temperature effect can be described by the Arrhenius equation (Equation 21) in order to determine the reaction rate of the EtOH oxidation in an alkaline medium [130].

$$k = A \cdot e^{-\frac{E_A}{R \cdot T}} \quad (21)$$

k	Reaction rate constant
A	Pre-exponential factor
E_A	Activation energy ($J \cdot moL^{-1}$)
R	Gas constant (= 8.31445 $J \cdot K^{-1} \cdot moL^{-1}$)
T	Temperature (= 303.15 K)

4.1.2 Adatoms / Alloying Effect

The adatoms and alloying facilitates a catalytic activity and stability enhancement of binary and ternary compared to monometallic catalysts due to the bifunctional mechanism, electronic and synergetic effects [63]. Ni and Bi have an oxophilic character like Pd that generates adsorbed OH to oxidize the similar poisonous CO species from the catalyst surface, resulting in an improvement of the EOR performance. The effect of Ni and Bi on the electrochemical and physico-chemical properties of carbon supported binary and ternary Pd-based catalysts for the alkaline EOR, are described in **sections 4.2–4.4** [3,15,29]. One part of the full paper (see Appendix A in **section 8.1.3**) describes the influence of P on the EOR activity and stability of the PdNi catalyst compared to the commercial Pt/C catalyst [131].

4.1.3 Further Approaches for Catalyst EOR Performance Enhancement

Gold, copper and nickel dimethylglyoxime complex ($Ni(II)(DMG)_2$) enhance the catalytic stability and the byproduct tolerance to EtOH oxidation in an alkaline medium. The activity and stability of this nitrogen containing complex for the alkaline EOR were investigated by CV-RDE and CA-RDE (see Appendix A in **section 8.1.3**, [103,132]).

Table 4 and Figure 17 below show the ICP-OES analysis and the electrochemical characterization results of carbon supported bimetallic Au_xCu_y based (Au_xCu_y/C) catalysts, with different elemental compositions and the benchmark Au/C using Vulcan XC72R as the carbon support material for the alkaline EOR. The targeted values of the atomic ratios of the carbon supported Au-based catalysts are similar to the measured element concentrations by ICP-OES with small deviations (Table 4). The Au_xCu_y/C catalysts with atomic ratios of 60:40 and 40:60 exhibit almost the same peak current density and are more than twice that of Au/C and $Au_{80}Cu_{20}$/C catalysts (see Figure 17a).

Table 4: ICP-OES analysis of carbon supported Au-based nanocatalysts.

Catalysts		Au (g/kg)	Cu (g/kg)	Au (mol/kg)	Cu (mol/kg)	Sum (mol/kg)	Au (at.%)	Cu (at.%)
Au/C	Average	178	-	0.90	-	0.90	100	
$Au_{80}Cu_{20}$/C	Average	277	27.3	1.41	0.43	1.94	76.6	23.4
$Au_{60}Cu_{40}$/C	Average	255	70	1.29	1.10	2.40	54.0	46.0
$Au_{40}Cu_{60}$/C	Average	200	127	1.02	2.00	3.01	33.7	66.3

Atomic weight (AMU): Au = 196.97; Cu = 63.55

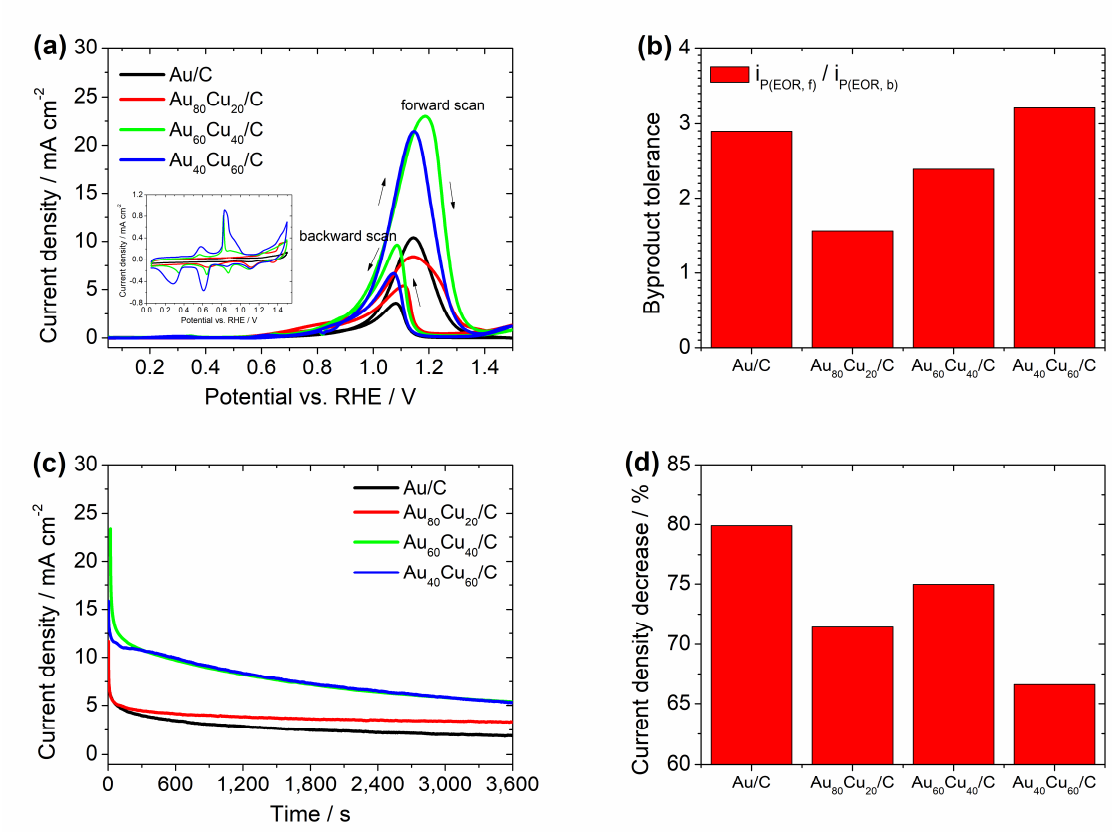


Figure 17: CVs of carbon supported Au-based nanocatalysts **(a)** in a mixture of 1 M KOH and 1 M EtOH at rt with a scan rate of 10 mV·s^{-1} (inset: CVs in de-aerated 1.0 M KOH solution at rt with a scan rate of 10 mV·s^{-1}); **(b)** Determined tolerances of carbon supported Au-based nanocatalysts toward EtOH reaction intermediates using the EOR measurements; Stability tests of carbon supported Au-based nanocatalysts **(c)** in a mixture of 1 M KOH and 1 M EtOH at an applied potential of 1.1 V for 3,600 s using the CA method and **(d)** their resulting current density decrease, given in percentage values.

It was stated that the Cu content is crucial for the enhancement of the EOR activity (Figure 17a), the byproduct tolerance against poisoning by intermediates resulting from the EOR process (Figure 17b) and the EOR stability (Figures 17c and 17d) on these synthesized Au_xCu_y/C catalysts compared to the Au/C. The low EOR activity of the Au_xCu_y/C catalysts could be increased by the addition of Pd. This would be the next promising research approach for these binary catalysts.

4.1.4 Conclusion

The settings parameter and measurement conditions were established from the electrochemical analysis of the Pd_xNi_y/C catalyst in consideration of their effects on the EOR activity and were fixed as follows: (i) scan rate: 10 $mV \cdot s^{-1}$; (ii) rotation speed: 0 rpm; (iii) catalyst loading: 56 $\mu g_{metal} \cdot cm^{-2}$; (iv) operating temperature: 30 °C and (v) concentration of the electrolyte mixture of KOH and EtOH: 1 M [103]. Those determined measuring parameters and conditions were also used for electrochemical characterization of the Pd-based synthesized catalysts in **sections 4.2–4.4**. The addition of cost-efficient co-catalysts, such as Ni and Bi to Pd and Cu to Au, were used to develop both novel ternary $Pd_xNi_yBi_z/C$ anode catalyst systems with high EOR performance, and stable binary Au_xCu_y/C anode catalysts with excellent by-product tolerance toward alkaline EtOH oxidation, respectively. Both are potential candidates for application in ADEFCs [103].

PART II

Effects of Ni and Bi on EOR Performance and Structure Characteristics of Carbon Supported Pd-Based Nanocatalysts

The following **section 4.2** and the corresponding Appendix A **(section 8.2)** have been **published in advance** in:

[15] **Cermenek, B.;** Ranninger, J.; Feketeföldi, B.; Letofsky-Papst, I.; Kienzl, N.; Bitschnau, B.; Hacker, V. Novel highly active carbon supported ternary PdNiBi nanoparticles as anode catalyst for the alkaline direct ethanol fuel cell. *Nano Res.* **2019**, *12*, 683-693.

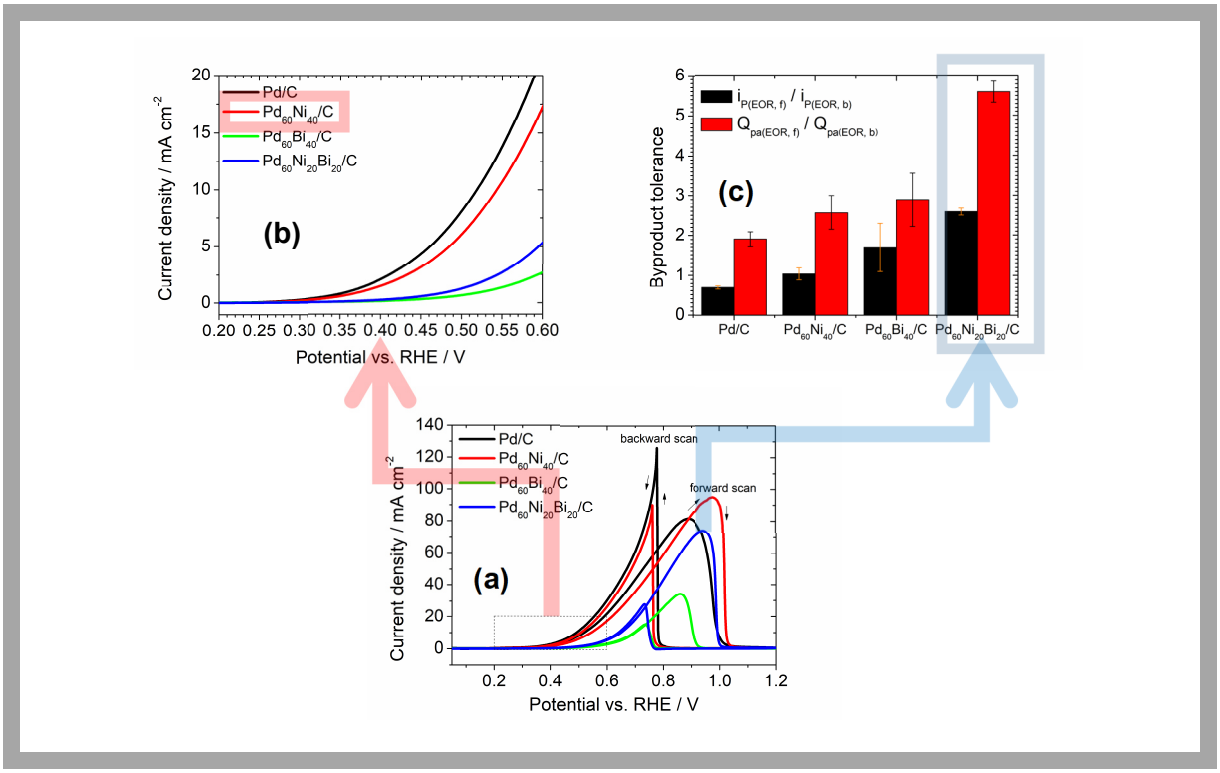
and are based on **master's thesis** of **Johanna Ranninger** (supervised **Cermenek, B.** – The ICP-OES analysis and electrochemical characterization (CV-RDE and CA-RDE) results and discussions were adopted and adapted):

[29] Ranninger, J. Development and Characterization of Pd-based Catalysts for the alkaline Direct Ethanol Fuel Cell. *Master's thesis*, Graz University of Technology, **2017**, p. 85.

4.2 PART II: Effects of Ni and Bi on EOR Performance and Structure Characteristics of Carbon Supported Pd-Based Nanocatalysts

Abstract

Part II of the doctoral thesis [15] focuses on the influence of Ni and Bi on alkaline EOR activities, stabilities and structure characteristics of carbon supported Pd-based nanocatalysts (Pd/C, $Pd_{60}Ni_{40}$/C, $Pd_{60}Bi_{40}$/C, $Pd_{60}Ni_{20}Bi_{20}$/C) by CV/CA using RDE and various physico-chemical methods such as XRD, XPS, TEM-EDX and ICP-OES. Nickel generates more adsorbed OH on the Pd catalyst surface than Bi and promotes the oxidation of adsorbed EtOH species. This results in a low onset potential toward EtOH oxidation with high current density. The presence of Bi facilitates high tolerance toward various reaction intermediates resulting from the incomplete EtOH oxidation, but might also initiate the agglomeration of Pd nanoparticles. From the electrochemical characterization, the binary $Pd_{60}Ni_{40}$/C exhibits the highest EOR activity and the novel ternary $Pd_{60}Ni_{20}Bi_{20}$/C displays exceptional byproduct tolerance toward EtOH oxidation in an alkaline medium compared to the other Pd-based nanocatalysts [15]. The results from I-V characteristics and EIS measurements confirm the performance of both anode catalysts in MEAs under various operating conditions in single cell configuration.



Graphical abstract TOC: (a) EOR activity determinations of carbon supported Pd-based nanocatalysts in an electrolyte mixture of 1 M KOH and 1 M EtOH at 30 °C with a scan rate of 10 $mV \cdot s^{-1}$ by CV using RDE. **(b)** $Pd_{60}Ni_{40}$/C: Highest peak current density with low onset potential and **(c)** $Pd_{60}Ni_{20}Bi_{20}$/C: Highest byproduct tolerance toward alkaline EOR [15].

4.2.1 Physico-Chemical Characterization

An extensive physico-chemical characterization is very important for a better interpretation and understanding of performances of all synthesized nanocatalysts for the alkaline EOR. Pd-based nanocatalysts were analyzed by various methods, such as, ICP-OES, TEM-EDX, XRD and XPS in this study [15].

ICP-OES

ICP-OES is an appropriate method for the quantitative determination of the elemental concentrations of the carbon supported Pd, Pd_xNi_y, Pd_xBi_y and $Pd_xNi_yBi_z$ catalysts with the calculated atomic ratio of (100), (60:40), (60:40) and (60:20:20). Analysis results by ICP-OES are in good agreement with calculated values (= subscripts of catalysts) from the preparation of nanocatalysts (Table 5, detailed in Table 15 in the Appendix A) [15,29].

Table 5: Elemental analysis of Pd-based nanocatalysts by ICP-OES [15,29].

Catalysts	Pd (at.%)	Ni (at.%)	Bi (at.%)
Pd/C	100	-	-
$Pd_{60}Ni_{40}$/C	60	40	-
$Pd_{60}Bi_{40}$/C	61	-	39
$Pd_{60}Ni_{20}Bi_{20}$/C	61	19	20

TEM-EDX

The particle size distribution of the synthesized carbon supported Pd-based catalysts in low and high magnifications are shown by TEM micrographs in Figure 18 and Figures 44, 46, 48 and 50 in Appendix A, respectively. Metal nanoparticles (black or dark grey) of the Pd/C catalyst are more evenly distributed on the carbon support material Vulcan XC72R (grey) than the binary and ternary Pd-based catalysts (Figure 18) [15]. It can be observed that the presence of Bi and Ni in carbon supported Pd-based catalysts apparently causes an agglomeration of the metal nanoparticles (Figures 18b–18d) [15].

In an attempt to determine the average particle diameter of all catalysts, 100 (for Pd/C) and 30 (for $Pd_{60}Ni_{40}$/C, $Pd_{60}Bi_{40}$/C and $Pd_{60}Ni_{20}Bi_{20}$/C) spherical-shaped particles of the TEM micrograph areas are taken, and the particles are measured manually by the FIJI ImageJ-free software program [3,111]. The average particle size determination of Pd/C catalyst is reproducible (Figure 18a), contrary to the other catalysts which tend to agglomerate (Figures 18b–18d). Therefore, a reproducible average particle size for the binary and ternary Pd-based catalysts was not determined.

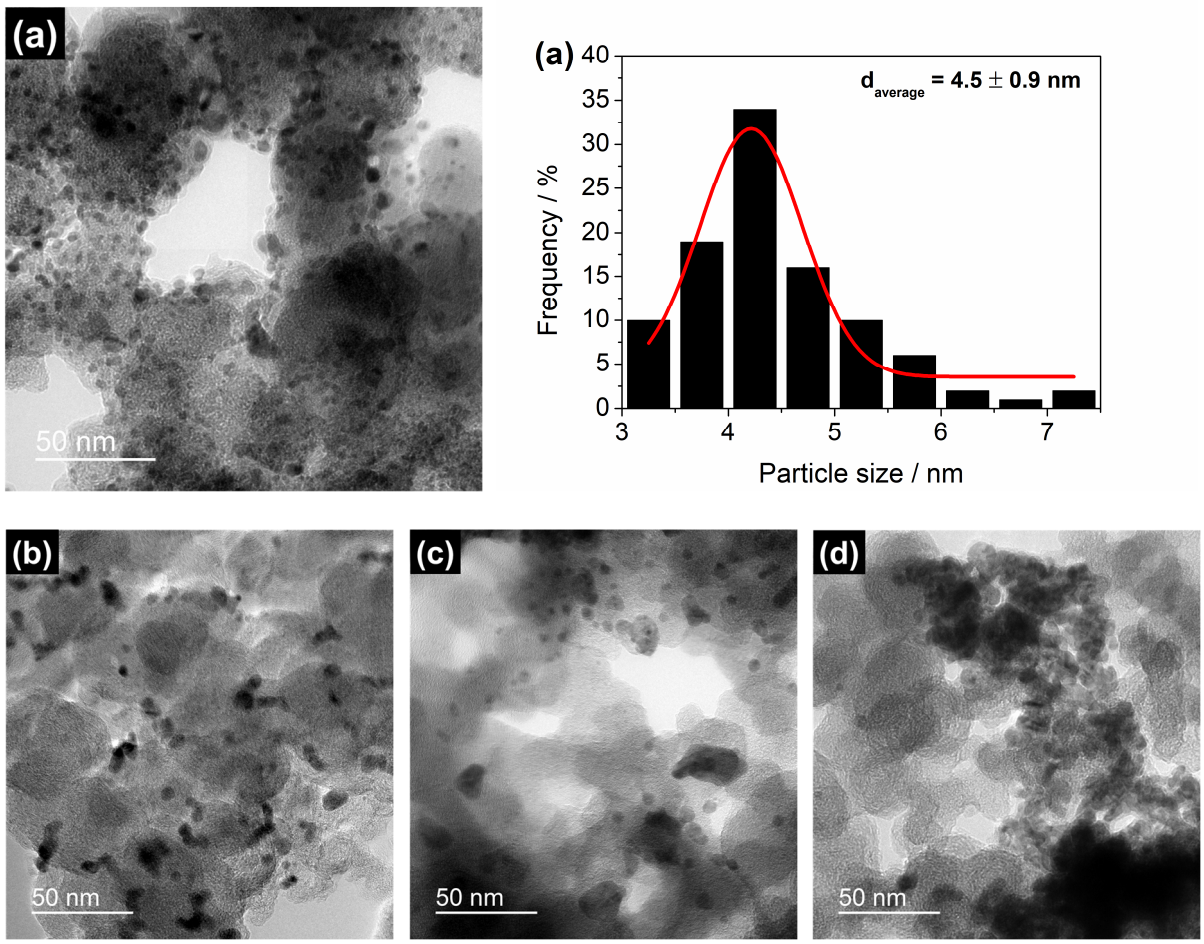


Figure 18: TEM micrographs of the **(a)** Pd/C with the corresponding particle size distribution histogram including the determined average particle size, **(b)** $Pd_{60}Ni_{40}$/C, **(c)** $Pd_{60}Bi_{40}$/C and **(d)** $Pd_{60}Ni_{20}Bi_{20}$/C catalyst [15].

Applying fast Fourier transformation (FFT) on high resolution TEM (HRTEM) micrographs show that all carbon supported Pd-based catalysts exhibit inter-planar (*d*) spacing of ~0.21 nm determined which complies with lattice spacing of Pd (111) (Figure 19) [15].

Furthermore, scanning transmission electron microscopy high-angle angular dark-field imaging (STEM-HAADF) was used to determine semi-quantitatively the metal contents of the carbon supported Pd-based catalysts at specific chosen areas by recording of EDX spectra (Figures 45, 47, 49 and 51 in the Appendix A). This analysis confirms that the metal nano-particles of binary and ternary Pd-based catalysts are not homogeneously distributed on the carbon support material [15].

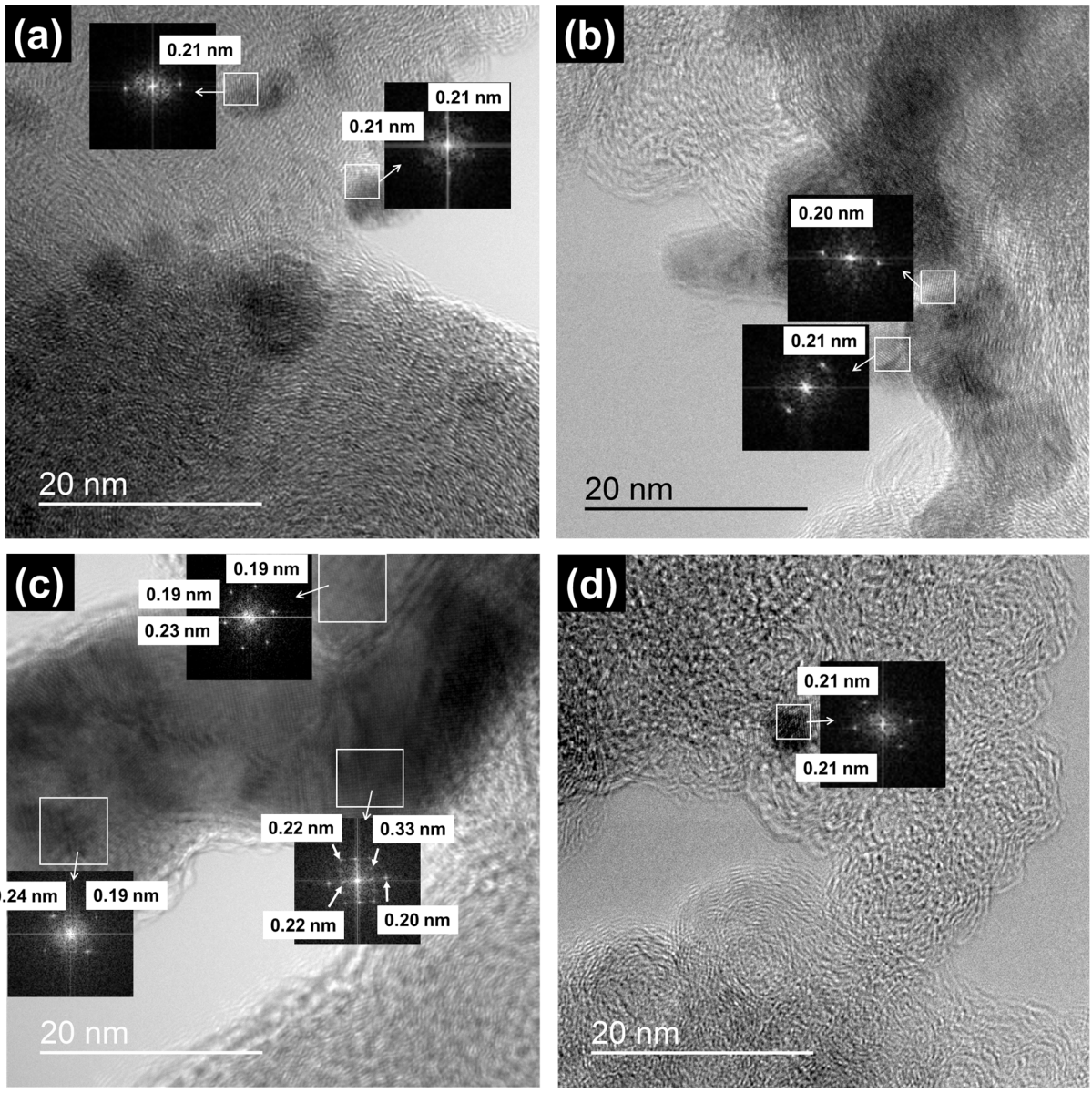


Figure 19: HRTEM micrographs including the determined inter-planar spacing of the **(a)** Pd/C, **(b)** $Pd_{60}Ni_{40}$/C, **(c)** $Pd_{60}Bi_{40}$/C and **(d)** $Pd_{60}Ni_{20}Bi_{20}$/C catalyst [15].

The instant reduction method using $NaBH_4$ as reducing agent is therefore not the optimal catalyst synthesis method especially for controlling the homogeneous deposition of bi- and tri-metallic nanoparticles on carbon support material [15]. New synthesis approaches for the instant reduction method were developed and optimized (see **section 4.4**).

Alternatively, nanocapsule, bromide anion exchange, aqueous solution phase synthesis or the polyol method are other synthesis procedures to minimize the agglomeration effect for polymetallic catalysts [14,15,78,126,133–136].

XRD

The XRD patterns of all carbon supported Pd-based catalysts exhibit the typical diffraction peaks approx. at the 2θ values of 40°, 47°, 68°, 82° and 86° which can be assigned to the Pd face-centered cubic (fcc) crystalline structure (Pd_64922-ICSD) with miller indices of (111), (200), (220), (311) and (222), respectively (Figure 20) [12,14,15]. The diffraction peak located approx. at the 2θ value of 25° attributes to carbon black Vulcan XC72R as crystalline structure of graphite (2H)_187640-ICSD with the miller indices of (002) for all catalyst samples (Figure 20) [12,14,15].

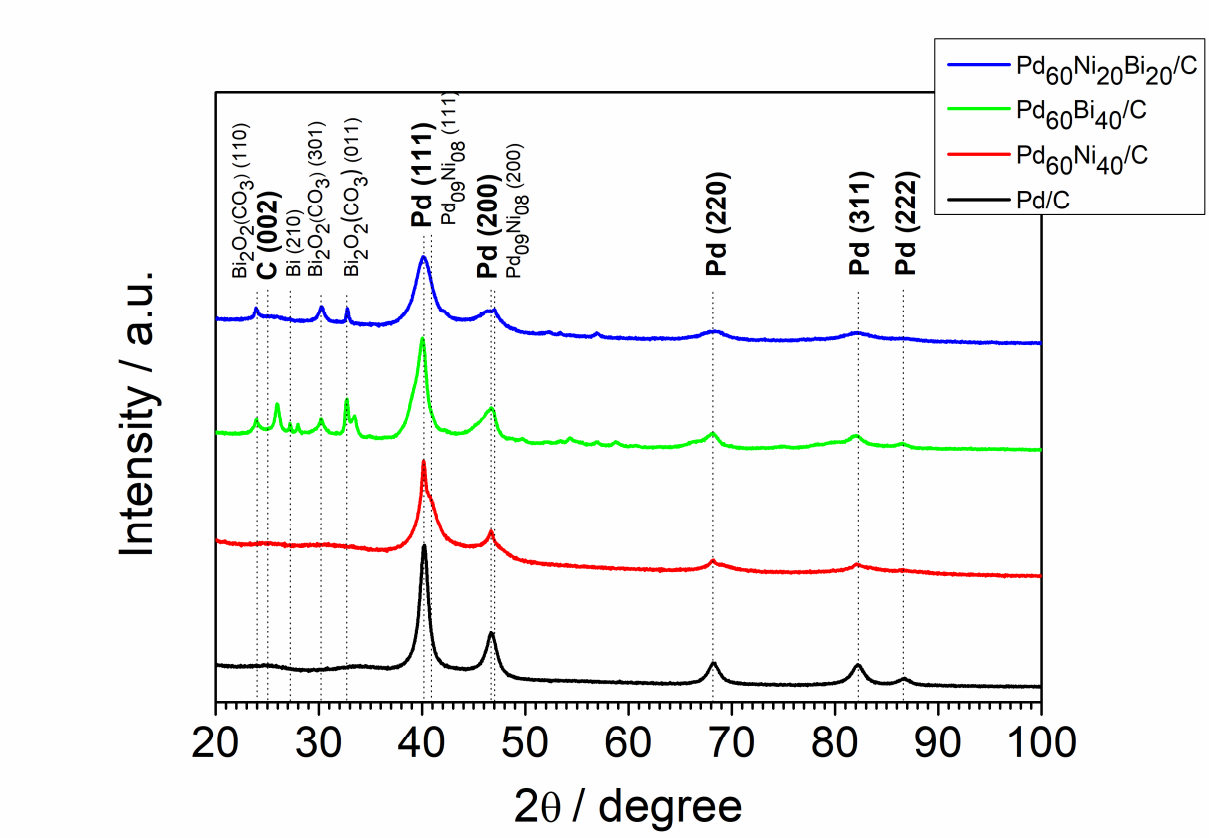


Figure 20: XRD patterns of carbon supported Pd-based nanocatalysts [15].

The 2θ values of the binary and ternary catalysts ($Pd_{60}Ni_{40}$/C, $Pd_{60}Bi_{40}$/C and $Pd_{60}Ni_{20}Bi_{20}$/C) are slightly lower (Tables 17–19 in the Appendix A) and their *d*-spacing values and lattice parameters (Table 6) are slightly higher than for the Pd/C catalyst (Table 16 in the Appendix A), which indicates that the Pd lattice expands and is modified by alloying with Ni and Bi. This statement is confirmed by various research groups [14,15,17,26,46,78,137].

The determined *d*-spacing for the catalysts in the recorded HRTEM micrographs (Figure 19) conforms to the XRD results (Table 6) [15]. Furthermore, the XRD pattern of the $Pd_{60}Ni_{40}$/C catalyst has additional diffraction peaks approx. at 41°, 48°, 70°, 84° and 89° close

to the diffraction peaks of Pd fcc crystalline structure, which is assigned to an alloying compound with a crystalline structure of $Pd_{09}Ni_{08}$_106936-ICSD with the same miller indices (Figure 20 and Table 17) [15].

The XRD patterns of $Pd_{60}Bi_{40}$/C and $Pd_{60}Ni_{20}Bi_{20}$/C catalysts also reveal additional diffraction peaks approx. at 24°, 30° and 33°, and were identified as crystalline structure of $Bi_2O_2(CO_3)$_252588-ICSD (Figure 20) [15]. The diffraction peak located at 27° is assigned to the crystalline structure of Bi_53797-ICSD with the miller indices of (210) for the $Pd_{60}Bi_{40}$/C catalyst (Figure 20) [15]. Also tetragonal PdBi alloy (PdBi_tetrag_56279-ICSD) is one of the main constituents of this catalyst (Figure 20 and Table 18 in the Appendix A) [15]. The XRD pattern of the $Pd_{60}Bi_{40}$/C catalyst exhibits a diffraction peak approx. at 28°, which is attributed to the crystalline structure of Bi_2O_3_beta_189995-ICSD with the miller indices of (120) (Table 18 in the Appendix A) [15]. The located crystalline structures of Pd, Ni, Bi and C, with their corresponding unit cells for all catalyst samples, are demonstrated in Tables 20–26 in Appendix A.

More details about XRD data with Rietveld-refinement for the carbon supported Pd-based catalysts are given in Tables 16–19 in the Appendix A [15]. The crystallite sizes of Pd and the alloyed compounds in the catalysts (Pd/C, $Pd_{60}Ni_{40}$/C, $Pd_{60}Bi_{40}$/C and $Pd_{60}Ni_{20}Bi_{20}$/C) were experimentally estimated in accordance with the Scherrer equation (Equation 17), assuming spherical crystallites with cubic crystal system. The crystallites are in the order of 5 to 12 nm (Table 6) [15].

Table 6: Structure analysis of carbon supported Pd-based catalysts by XRD [15].

Catalysts	*d*-spacing Pd (111) (nm)	Lattice parameter (nm)	Crystallite size (nm)
Pd/C	0.2244	Pd: a = 0.3891	Pd: 9
$Pd_{60}Ni_{40}$/C	0.2245	Pd: a = 0.3904 $Pd_{09}Ni_{08}$: a = 0.3816	Pd: 6-12 $Pd_{09}Ni_{08}$: 9
$Pd_{60}Bi_{40}$/C	0.2259	Pd: a = 0.3904 PdBi_tetrag: a = 0.4567; b = 0.726; c = 1.068	Pd: 9 PdBi_tetrag: 10
$Pd_{60}Ni_{20}Bi_{20}$/C	0.2247	Pd: a = 0.3894 $Bi_2O_2(CO_3)$: a = 0.385; b = 0.388; c = 1.3750	Pd: 5 $Bi_2O_2(CO_3)$: >10

XPS

XPS was used to investigate the surface oxidation states, chemical compositions and binding energies of Pd, Ni and Bi in all synthesized catalysts. The recorded XPS spectra of Pd/C,

$Pd_{60}Ni_{40}$/C, $Pd_{60}Bi_{40}$/C and $Pd_{60}Ni_{20}Bi_{20}$/C catalysts show different oxidation states for their elements (Figures 21–23) [15].

As expected, the XPS results relating to the atomic content determinations in the binary and ternary carbon supported Pd-based catalysts have a discrepancy to ICP-OES analysis due to predominant overlapping of Pd and Bi on Ni at the catalyst surface leading to lower Ni content (Table 7 and detailed in Tables 28–30 in the Appendix A: deconvolution results of the elements) [15].

The doublets of Pd $3d_{3/2}$ and Pd $3d_{5/2}$ peaks are attributed to Pd^0 (→ metallic Pd) and Pd^{II} species (→ PdO) on the surface of all catalysts (Figure 21) according to Su et al., Wang et al. and Simões et al. [15,26,78,138]. It is observed that the binding energy of the $3d_{5/2}$ peak of PdO for the Ni and Bi containing Pd catalysts shifts negatively compared to Pd/C catalyst (Table 7 and detailed in Tables 27–30 in the Appendix A) [15].

Wang et al. [78] explain this issue by a down-shift of the d-band center of Pd i.e. the down-shift of the core-level of Pd to the Fermi level of Pd due to alloying with oxophilic elements which enhance its EtOH reaction intermediate tolerance resulting in a weak-interaction with the active sites of the catalyst (see electrochemical characterization results in Figure 24d) [15,78,139].

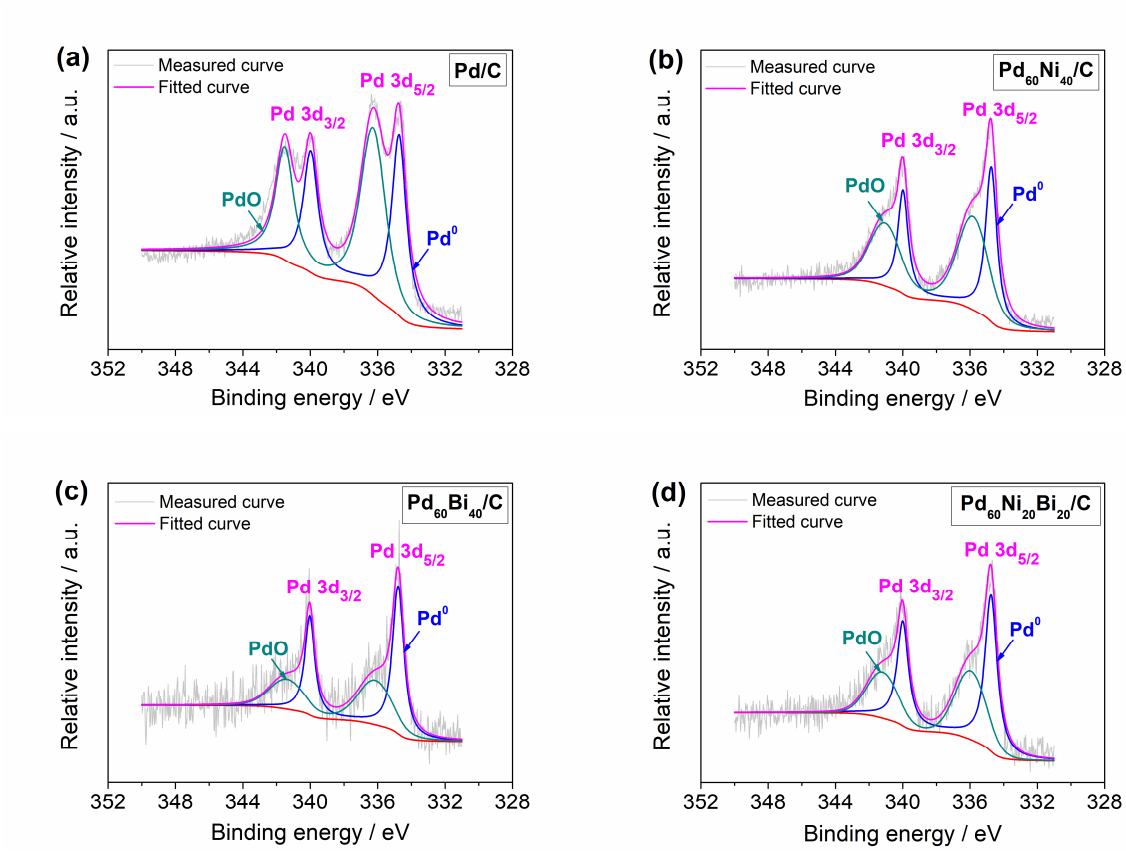


Figure 21: Pd 3d XPS spectra of the **(a)** Pd/C, **(b)** $Pd_{60}Ni_{40}$/C, **(c)** $Pd_{60}Bi_{40}$/C and **(d)** $Pd_{60}Ni_{20}Bi_{20}$/C catalyst [15].

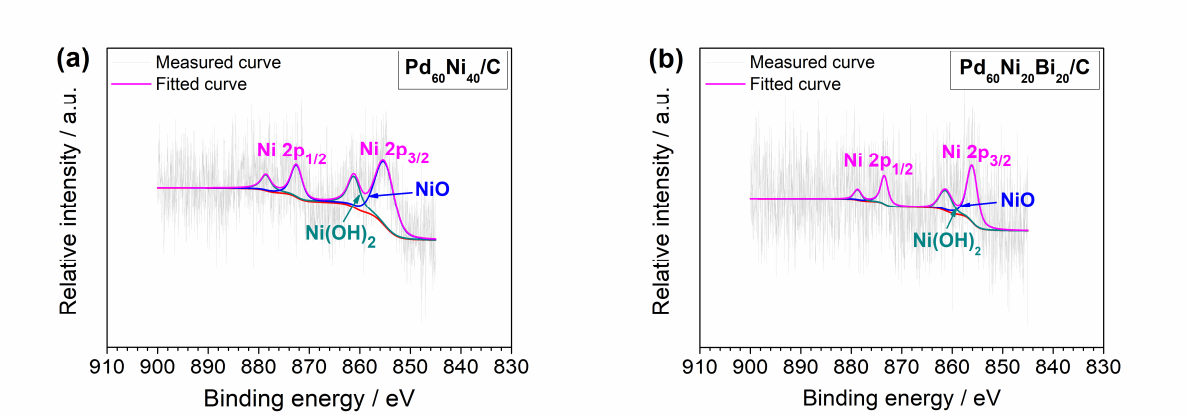


Figure 22: Ni 2p XPS spectra of the **(a)** $Pd_{60}Ni_{40}/C$ and **(b)** $Pd_{60}Ni_{20}Bi_{20}/C$ catalyst [15].

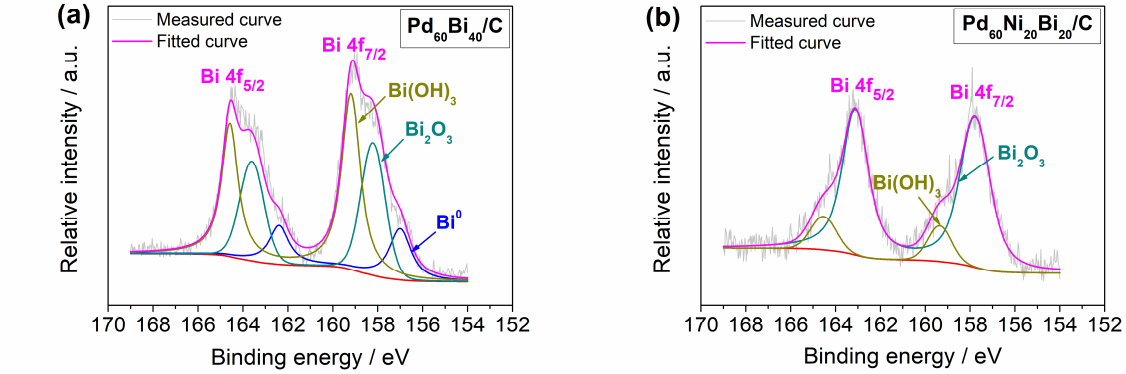


Figure 23: Bi 4f XPS spectra of the **(a)** $Pd_{60}Bi_{40}/C$ and **(b)** $Pd_{60}Ni_{20}Bi_{20}/C$ catalyst [15].

Furthermore, the decrease of Pd^{II} binding energies of 335.81, 336.14 and 335.95 eV for $Pd_{60}Ni_{40}/C$, $Pd_{60}Bi_{40}/C$ and $Pd_{60}Ni_{20}Bi_{20}/C$ catalysts compared to the Pd^{II} binding energy of 336.27 eV for Pd/C catalyst suggests a suppression of the PdO formation due to alloying with Ni and Bi on the surface of binary and ternary Pd-based catalysts as reported by Su et al. (Table 7 and detailed in Tables 27–30 in the Appendix A) [15,26].

Figures 22a and 22b show the doublets of Ni $2p_{1/2}$ and Ni $2p_{3/2}$ which assigned to Ni^{II} species such as NiO and $Ni(OH)_2$ can be formed on the catalyst surfaces of $Pd_{60}Ni_{40}/C$ and $Pd_{60}Ni_{20}Bi_{20}/C$ according to Wang et al. [15,78]. The measured values of the Ni 2p XPS spectra for $Pd_{60}Ni_{40}/C$ and $Pd_{60}Ni_{20}Bi_{20}/C$ catalysts are undefined – most likely due to the inhomogeneous distribution of the metal nanoparticles on the carbon support material (see TEM-EDX results: Figures 44–51 in the Appendix A) [15]. A further hypothesis for the cause of the noising effect in the measured values of the Ni 2p XPS spectra is that the metallic and oxide species of Ni on the catalysts are covered mainly by metallic and oxide species of Pd and Bi. This was identified by XPS (Figure 22), as well as by XRD (Figure 20, and Tables 17 and 19 in Appendix A) and may have been the reason that noise was present in the Ni $2p_{1/2}$ XPS

spectra obtained [15]. Nevertheless, the fitting of the undefined Ni 2p XPS signals of both catalysts by Gaussian and Lorentzian lines enable us to show the surface oxidation states, binding energies and content (at.%) of Ni (Figure 22 and Table 7, and Tables 28 and 30 in Appendix A) [15].

The doublets of Bi $4f_{5/2}$ and Bi $4f_{7/2}$ peaks (Figure 23a) for the $Pd_{60}Bi_{40}$/C catalyst can be attributed to Bi^0 and Bi^{III} species such as metallic Bi, Bi_2O_3 and $Bi(OH)_3$ located at 157, 158.21 and 159.19 eV [15,138]. Metallic Bi and Bi_2O_3 species were also identified by XRD (Table 29 in the Appendix A) in $Pd_{60}Bi_{40}$/C catalyst, which confirmed the XPS results [15]. By contrast, the doublets of Bi $4d_{5/2}$ and Bi $4d_{7/2}$ peaks (Figure 23b) for the $Pd_{60}Ni_{20}Bi_{20}$/C catalyst are attributed to Bi_2O_3 and $Bi(OH)_3$ located at 157.78 and 159.35 eV [15,138]. It is assumed that no complete reduction of Bi oxide species to Bi has occurred for the synthesis of the $Pd_{60}Ni_{20}Bi_{20}$/C catalyst, because the Bi peak (Bi^0) in the XPS spectrum of $Pd_{60}Ni_{20}Bi_{20}$/C catalyst is absent (Figure 23b) compared to the XPS spectrum of $Pd_{60}Bi_{40}$/C catalyst, which conforms to the XRD results (Tables 18 and 19) [15].

Furthermore, the XPS spectra obtained for C and O are demonstrated in Figures 52 and 53 in the Appendix A [15]. The measured Pd 3d, Bi 4f, C 1s and O 1s XPS spectra of the synthesized catalysts showed good agreement to their fitted XPS spectra (Figures 21 and 23, and Figures 52 and 53 in the Appendix A) [15].

Subsequently, the results of the physico-chemical characterization will be used to interpret the electrochemical characterization results of all Pd-based electrocatalysts [15].

Table 7: XPS characterization data of the carbon supported Pd-based catalysts including the determined metal contents [15].

Catalysts	Pd 3d (eV)	Ni 2p (eV)	Bi 4f (eV)	O 1s (eV)	C 1s (eV)	Pd (at.%)	Ni (at.%)	Bi (at.%)	O (at.%)	C (at.%)	Pd / metal	Ni / metal	Bi / metal
	334.73			530.11	283.76	1.28			2.99	59.48			
	336.27			531.52	284.61	1.56			2.99	10.33			
Pd/C				532.96	285.21				0	16.62			
				535.21	288.37				0.79	3.94			
					Total	**2.84**			**6.77**	**90.37**	**100**		
	334.74	861.14		530.22	283.8	0.86	0.1		2.24	48.93			
	335.81	855.13		531.76	284.45	1.16	0.23		3.64	31.84			
$Pd_{60}Ni_{40}/C$				533.17	286.32				0	5.54			
				535.2	288.67				0.5	4.96			
					Total	**2.02**	**0.33**		**6.38**	**91.27**	**86**	**14**	
	334.78		157	530.27	283.81	0.19		0.06	0.86	59.42			
	336.14		158.21	531.79	284.74	0.14		0.14	3.33	19.91			
$Pd_{60}Bi_{40}/C$			159.19	533.2	285.88			0.18	0	9.5			
					288.56					6.28			
					Total	**0.33**		**0.38**	**4.19**	**95.11**	**46**		**54**
	334.75	856.06	157.78	529.91	283.88	0.41	0.08	0.15	0.85	62.14			
	335.95	861.33	159.35	531.75	284.8	0.34	0.03	0.03	4.02	10.28			
$Pd_{60}Ni_{20}Bi_{20}/C$				533.15	285.46				0	16.24			
					288.54					5.43			
					Total	**0.75**	**0.11**	**0.18**	**4.87**	**94.09**	**72**	**11**	**17**

4.2.2 Electrochemical Characterization

Cyclic Voltammetry

Cyclic voltammograms of Pd/C, $Pd_{60}Ni_{40}$/C, $Pd_{60}Bi_{40}$/C and $Pd_{60}Ni_{20}Bi_{20}$/C catalysts were recorded stationary (without rotation) in a de-aerated 1.0 M KOH electrolyte at 30 °C in a potential range of 0.05-1.2 V (Figure 24a) [15]. By the presence of Bi in carbon supported Pd electrocatalysts, the hydrogen adsorption/and absorption region (0.05-0.5 V) in the anodic scan and cathodic scan of the CVs of $Pd_{60}Bi_{40}$/C and $Pd_{60}Ni_{20}Bi_{20}$/C is drastically reduced (no distinct visible characteristic peaks) compared to the CVs of Pd/C and $Pd_{60}Ni_{40}$/C electrocatalysts (Figure 24a) [15]. Therefore, the changing of the Pd crystal structure, inducing by insertion of H, is also minimized. Neto et al. show the same effect of Bi in CVs of Pd_xBi_y/C catalysts in various atomic ratios [15,17]. Simões et al. confirm the suppression of the hydrogen adsorption/absorption processes by Bi on Pd and Pt containing Bi catalysts compared to monometallic Pd/C and Pt/C catalysts [15,138]. This suppression depends on the height of the amount of Bi atoms which are covered on the surface of the Pd catalyst and have strong interaction with Pd [15,138].

Furthermore, another distinctive peak in the anodic scan for the Bi containing catalysts appears at approx. 0.9 V (Figures 24a and 25a), which attributed to Bi_2O_3 species from the reaction of Bi in the presence of an alkaline solution [15,73]. The Bi oxide species were also identified by XRD (Tables 18 and 19 in the Appendix A). The oxidation of Bi in KOH electrolyte starts at approx. 0.5 V to $Bi(OH)_3$ as a non-soluble compound, identified in the Bi_2O_3 phase according to Simões et al. (Figures 24a and 25a) [15,138].

The reduction current peak in the cathodic scan between the potential of 0.5 and 0.9 V can be attributed to the formation of Pd and/or Bi oxide species for in the study synthesized catalysts (Figures 24a and 25a) [15,17,27].

The charge of the reduction of Bi oxide to Bi could not be considered for the EASA calculation (see Equation 16) of the Bi containing catalysts because the Bi oxide reduction arises in the same potential range as the Pd oxide reduction [15]. Therefore, the excellent EASA result of the $Pd_{60}Ni_{20}Bi_{20}$/C catalyst compared to the other carbon supported Pd-based electrocatalysts (Figures 24b and 25b, and Table 8) is only comparable with the $Pd_{60}Bi_{40}$/C catalyst. The $Pd_{60}Ni_{20}Bi_{20}$/C catalyst with a 2.6-fold higher EASA than the $Pd_{60}Bi_{40}$/C catalyst depends on the Bi content [15]. Neto et al. report that the increased addition of Bi to Pd catalysts causes more agglomerations whereby the active sites of Pd are blocked resulting in decreasing of the EASA (Figure 24b) and consequently the catalytic activity (Figure 24c) [15,17].

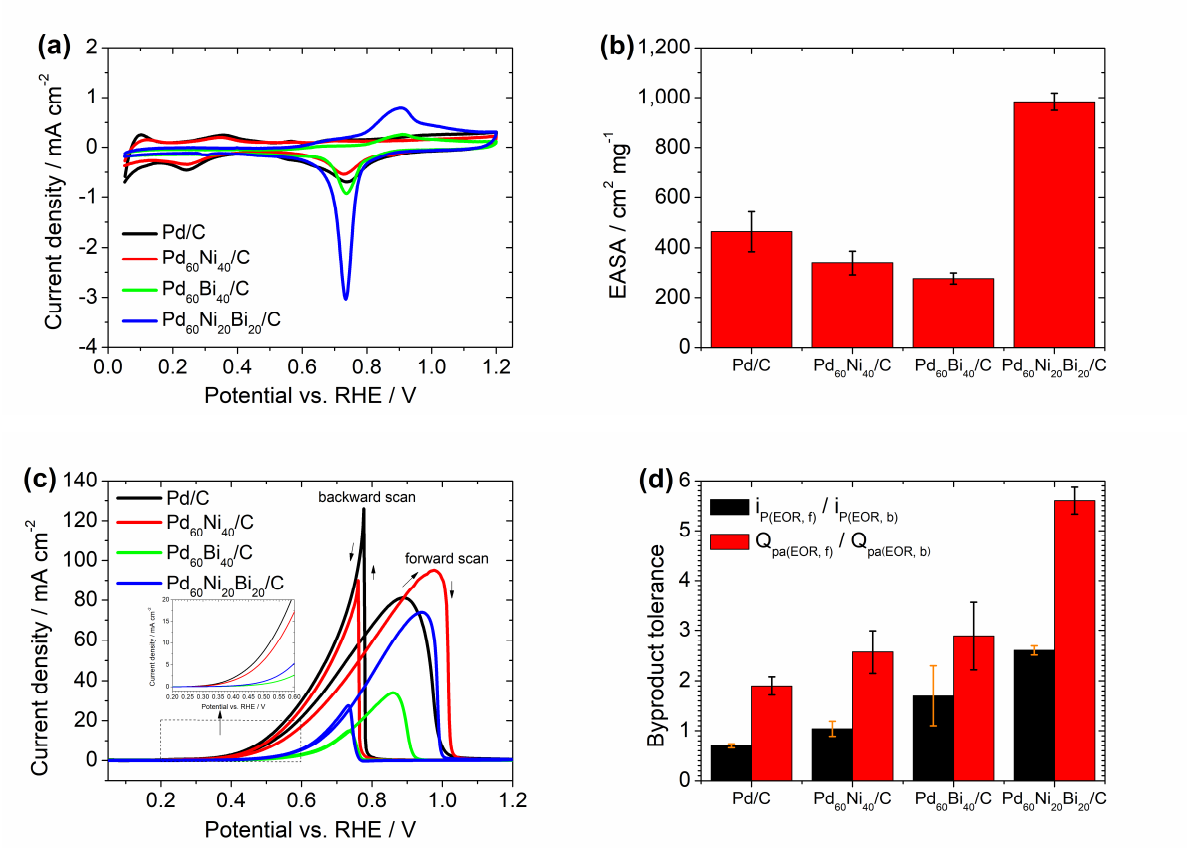


Figure 24: CVs of carbon supported Pd-based nanocatalysts **(a)** in de-aerated 1.0 M KOH solution at 30 °C with a scan rate of 10 mV·s^{-1} and **(b)** their resulting determined EASA; **(c)** in a mixture of 1 M KOH and 1 M EtOH at 30 °C with a scan rate of 10 mV·s^{-1}; **(d)** Determined tolerances of Pd-based nanocatalysts toward EtOH reaction intermediates using the EOR measurements [15,29].

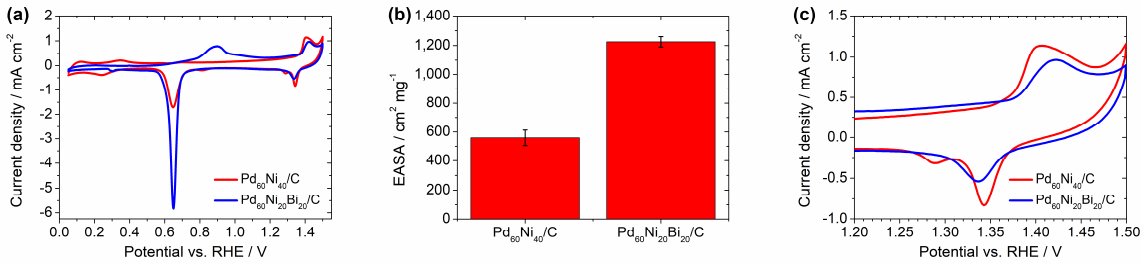


Figure 25: CVs of **(a)** $Pd_{60}Ni_{40}$/C and $Pd_{60}Ni_{20}Bi_{20}$/C catalysts in de-aerated 1.0 M KOH at 30 °C with a scan rate of 10 mV·s^{-1} in the potential range of 0.05-1.5 V with **(b)** their resulting determined EASA and **(c)** a magnification of the Ni peaks (anodic scan: oxidation of $NiOH_2$ to NiOOH; cathodic scan: reduction of NiOOH to $NiOH_2$) [15,29].

Additionally, $Pd_{60}Ni_{40}$/C and $Pd_{60}Ni_{20}Bi_{20}$/C catalysts were investigated under the same measurement conditions in Figure 25a, but using the potential range of 0.05-1.5 V to find out if Ni is present in the catalysts [15]. Figure 25c shows that the peak in the anodic scan at the potential range of 1.3-1.5 V as the oxidation of $Ni(OH)_2$ to NiOOH whereas the peak in the cathodic scan at the potential range of 1.2-1.4 V as the reduction of NiOOH to $Ni(OH)_2$ are represented for both catalysts $Pd_{60}Ni_{40}$/C and $Pd_{60}Ni_{20}Bi_{20}$/C according to Zhang et al. [14,15].

It is evident and also as expected that the current density of the Ni oxidation and reduction peaks of $Pd_{60}Ni_{40}$/C catalyst are higher than for the $Pd_{60}Ni_{20}Bi_{20}$/C catalyst (Figure 25) [15].

The determination of the catalytic activity and stability toward EOR of Pd/C, $Pd_{60}Ni_{40}$/C, $Pd_{60}Bi_{40}$/C and $Pd_{60}Ni_{20}Bi_{20}$/C catalysts takes place in a mixture of 1 M KOH and 1 M EtOH by means of CV using RDE (without rotation) at 30 °C. The $Pd_{60}Ni_{40}$/C catalyst exhibits the best result relating to EOR activity compared to the other carbon supported Pd-based catalysts (Figure 24c and Table 8) [15].

Nickel as an additive is more oxophilic than Bi in the resulting low onset potential of $Pd_{60}Ni_{40}$/C catalyst with a high produced current density toward EtOH oxidation in alkaline medium compared to catalysts containing Bi (see small Figure in Figure 24c and Table 8) [15,121]. This means that Ni generates more adsorbed OH on the Pd catalyst surface than Bi to oxidize the adsorbed EtOH species quickly. Zhang et al. report that onset potentials of Pd_xNi_y/C based catalysts toward EtOH oxidation depend significantly on the surface concentration of Ni [14,15].

Furthermore, in the synthesized Pd-based electrocatalysts Bi facilitates an essential improvement of the tolerance toward EtOH intermediates from the EOR in the electrolyte mixture of 1 M KOH and 1 M EtOH (Figure 24d and Table 8), but their onset potentials shift to higher potentials (see small Figure in Figure 24c and Table 8) and their catalytic activities decrease (Figure 24c and Table 8) compared to Pd/C and $Pd_{60}Ni_{40}$/C catalysts, respectively [15]. The higher onset potential and the lower specific activity of the $Pd_{60}Bi_{40}$/C catalyst toward the EtOH oxidation compared to the $Pd_{60}Ni_{20}Bi_{20}$/C catalyst (Figure 24c and Table 8) are due to its higher Bi content thus formed Bi oxide species block multiple active sites of Pd [15,17].

The tolerance toward EOR intermediates was determined by two different methods (Figure 24d): 1) using the ratio of the peak current density of the forward ($i_{P(EOR,f)}$) and backward scan ($i_{P(EOR,b)}$) [26], and 2) using the ratio of the integrated oxidation peak current density area (total charge) of forward ($Q_{pa(EOR,f)}$) and backward scan ($Q_{pa(EOR,b)}$) from EOR measurements in alkaline medium (Figure 24c), respectively [15,121]. Sekol et al. identified the second method as being a more accurate method than the first one for determining the catalyst tolerance toward reaction intermediates resulting from the EOR [15,121]. The higher the value the better is the tolerance of the catalyst toward the reaction intermediates of EtOH. This means that the EtOH reaction intermediates or poisonous species which are not oxidized in the forward scan, are oxidatively removed in the backward scan [15,26,121].

Figure 24d shows that the $Pd_{60}Ni_{20}Bi_{20}/C$ catalyst exhibits the best tolerance by far toward the reaction intermediates of EtOH compared to the other catalysts [15]. The excellent results relating to the byproduct tolerance of the Bi containing catalysts can be explained by the study of Paschos et al. [15,140]. In a CO stripping test was stated that one Bi adatom blocked three Pd surface atoms for avoiding the poisoning of the Pd active sites in the BiPd-based catalyst [15,140].

It should be noted, the i_f/i_b or Q_f/Q_b ratio is not a sufficient but a necessary indicator for evaluation of anti-poisoning tolerance of a catalyst as it has been discussed in Refs. [15,141,142].

Chronoamperometry

After the Pd/C, $Pd_{60}Ni_{40}/C$, $Pd_{60}Bi_{40}/C$ and $Pd_{60}Ni_{20}Bi_{20}/C$ nanocatalysts were subjected to 1 h stress at an applied potential of 0.83 V, the novel $Pd_{60}Ni_{20}Bi_{20}/C$ catalyst showed the best result in terms of electrocatalytic stability toward alkaline EOR (Figure 26a and Table 8) [15]. The order of the decrease of produced current density in percentage of all catalysts from the start (i_{Start}) until to the end (i_{End}) of CA measurement is given in Figure 26b [15]. The decrease of current densities of all catalysts after 1 h stress at 0.83 V is listed in following order: $Pd_{60}Bi_{40}/C$ > $Pd_{60}Ni_{40}/C$ > Pd/C > $Pd_{60}Ni_{20}Bi_{20}/C$ (Figure 26b) [15].

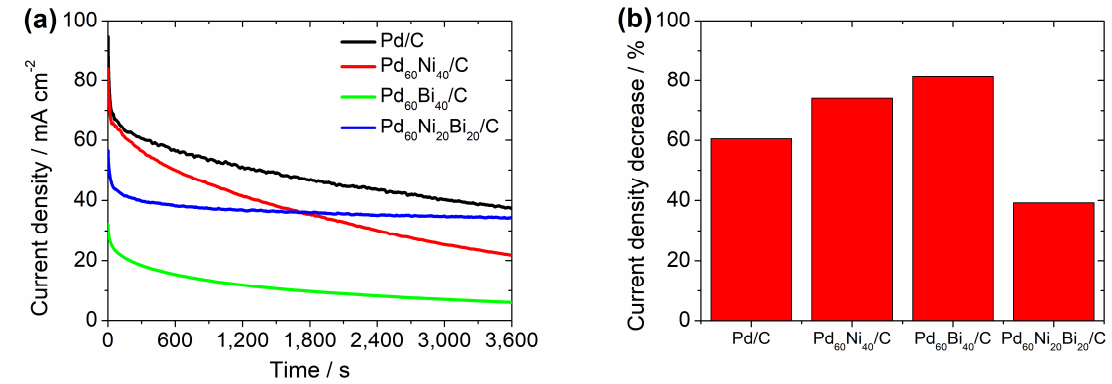


Figure 26: Stability tests of carbon supported Pd-based electrocatalysts **(a)** in a mixture of 1 M KOH and 1 M EtOH at an applied potential of 0.83 V and at 30 °C for 3,600 s using the CA method and **(b)** their resulting current density decrease, given in percentage [15,29].

The electrochemical characterization results of the carbon supported Pd-based nanocatalysts are summarized in Table 8 [15]. Additional electrochemical characterizations, such as the determination of the number of electrons during EtOH oxidation and the CA measurements of all Pd-based catalysts at an applied potential of 0.5 V, are demonstrated in Figures 54 and 55.

Table 8: Electrochemical characterization results of carbon supported Pd-based nanocatalysts [15].

Catalysts	EASA[a] ($cm^2 \cdot mg^{-1}$)	i_f[b] ($mA \cdot cm^{-2}$)	i_b[b] ($mA \cdot cm^{-2}$)	i_f / i_b[c]	$Q_{pa,f}$ / $Q_{pa,b}$[d]	E_{onset}[e] (V)	i_{Start}[f] ($mA \cdot cm^{-2}$)	i_{End}[f] ($mA \cdot cm^{-2}$)	i_D[g] (%)
Pd/C	463 ± 78	81.17	125.95	0.70 ± 0.04	1.90 ± 0.18	0.280 ± 0.015	94.97	37.37	61
$Pd_{60}Ni_{40}$/C	339 ± 49	95.11	90.05	1.04 ± 0.15	2.57 ± 0.42	0.290 ± 0.018	84.14	21.77	74
$Pd_{60}Bi_{40}$/C	276 ± 22	34.03	14.96	1.70 ± 0.60	2.89 ± 0.67	0.352 ± 0.015	32.16	6.02	81
$Pd_{60}Ni_{20}Bi_{20}$/C	983 ± 35	73.93	27.60	2.60 ± 0.09	5.60 ± 0.27	0.348 ± 0.007	56.59	34.39	39

[a]Electrochemical active surface area (EASA) determination; [b]i_f and i_b: peak current density of forward and backward scan; [c]i_f / i_b: byproduct tolerance using peak current density of forward and backward scan; [d]$Q_{pa,f}$ / $Q_{pa,b}$: byproduct tolerance using the charge of the integrated peak current density area of the forward and backward scan; [e]E_{onset}: onset potential of the EtOH oxidation; [f]i_{Start} and i_{End}: resulting current densities at an applied potential of 0.83 V after 0 s and 3,600 s; [g]i_D: loss of current density after stress test at an applied of 0.83 V for 3,600 s.

4.2.3 In-situ Characterization

Current-Voltage Characteristics

The carbon supported based $Pd_{60}Ni_{40}$ and $Pd_{60}Ni_{20}Bi_{20}$ anodes, the A201 Tokuyama as semi-commercial AEMs and the carbon supported $AgMnO_x$ cathodes were layered assembled in the in-house designed single cell, respectively. Prior to preparation of the MEA 1 and MEA 2, two A201 Tokuyama AEMs were immersed in a 1.0 M KOH solution for 24 h resulting in a hydroxide form (OH^-). The MEA 1 and MEA 2 were investigated in a single cell configuration under various operating conditions (Figures 27 and 28, and Figures 56–59 in the Appendix A), respectively.

The polarization curves of MEA 1 and MEA 2 differ in particular at higher current densities, where MEA 1 exhibits a superior performance for both temperatures (Figures 27a and 27b). The power densities of MEA 1 and MEA 2 increase slightly with increased temperature due to enhanced kinetics of both electrode reactions EOR and ORR [66]. Nevertheless, in this case MEA 2 exhibits a lower tendency toward the formation of mixed potentials and therefore results in higher cell potentials at low current densities (Figures 27a and 27b). Simultaneously, the activation overvoltage can be reduced with increasing temperature, whereby this is identified by the flat rising voltage drop of the polarization curves of both MEAs at low current densities (Figures 27a and 27b) [18].

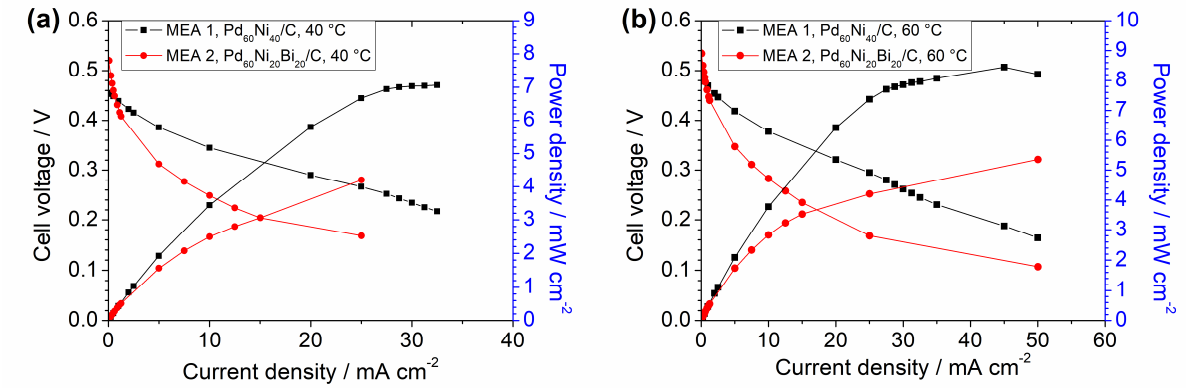


Figure 27: Polarization and their resulting maximum power density curves of MEA 1 and MEA 2 at **(a)** 40 °C and at **(b)** 60 °C (Anode: 1 M KOH + 1 M EtOH, 10 mL·min^{-1}; Cathode: Dry pure O_2, ~10 mL·min^{-1}).

Electrochemical Impedance Spectroscopy

After each I-V characteristic of the MEA 1 and MEA 2, the electrochemical impedance spectra were recorded at various constant applied currents (20, 40 and 60 mA) and at different temperatures (30-70 °C) in a frequency range of 0.1-10 000 Hz using the galvanostatic EIS method (Figure 28, detailed in Figures 56–59 in the Appendix A). The impedance spectra indicate three distinguishable loss mechanisms. We attribute the high frequency intercept and high frequency resistance (HFR) respectively to the ohmic losses within the test setup. By far the major share of the HFR originates from the membrane resistance.

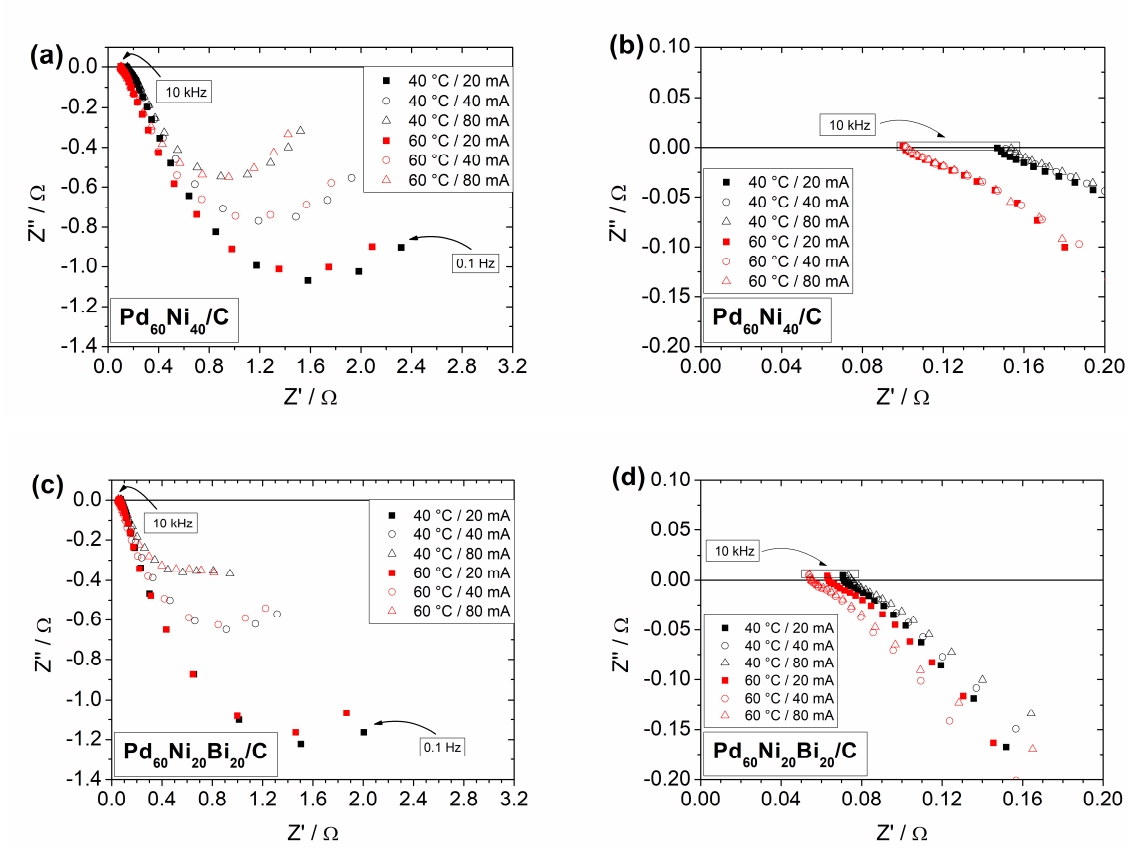


Figure 28: Nyquist plots of the **(a)** MEA 1 with **(b)** a magnification of the electrolyte resistance region and **(c)** MEA 2 with **(d)** a magnification of the electrolyte resistance region at constant temperature of 40 °C and 60 °C at different applied currents (Anode: 1 M KOH + 1 M EtOH, 10 mL·min^{-1}; Cathode: Pure O_2, ~10 mL·min^{-1}).

The membrane resistance for both MEAs decreases with increasing temperature as expected (Figures 28b and 28d, detailed in Figures 56b, 56d, 58b and 58d in the Appendix A) and indicates a slight dependency on the applied direct current density, which is attributed to the measurement set-up. MEA 1 shows a generally increased electrolyte resistance which indicates an increased distance between the reactive zones. This is plausible since the cathodes were relatively thick making it possible that the 3-phase boundary layer moves along the electrodes z-axis. Thereby, the effective distance between the reactive zones and the

electrolyte resistance is affected. Furthermore, the impedance spectra exhibits one semicircle, which is attributed to activation overpotential of the kinetically hindered anode reaction (Figure 28a, and Figures 56 and 57 in the Appendix A).

In the case of MEA 2 at higher currents, the beginning of a second semicircle becomes observable (Figure 28c and Figure 59c in the Appendix A), which is due to limited diffusion rate. Generally, MEA 2 shows decreased activation overpotentials compared to MEA 1 at the investigated operating points, although the polarization curve indicates increased activation overpotentials close to the open circuit potential (Figure 28).

4.2.4 Conclusion

Carbon supported Pd-based nanocatalysts (Pd/C, $Pd_{60}Ni_{40}$/C, $Pd_{60}Bi_{40}$/C and $Pd_{60}Ni_{20}Bi_{20}$/C) were successfully developed using the instant reduction synthesis method with $NaBH_4$ as reducing agent, comprehensively characterized and the influence of the admetals Ni and Bi in the carbon supported binary and ternary Pd-based EOR catalysts was determined [15].

From the ex-situ characterization, the novel $Pd_{60}Ni_{20}Bi_{20}$/C catalyst exhibits the highest electrocatalytic stability and tolerance toward EtOH intermediates resulting from the alkaline EOR compared to the other carbon supported Pd-based anode catalysts. The $Pd_{60}Ni_{40}$/C catalyst shows the highest specific activity with low onset potential (0.29 V vs. RHE) toward EtOH oxidation in alkaline medium among all investigated carbon supported Pd-based catalysts.

The good performances relating to the respective catalytic properties of both catalysts in the electrochemical characterization were confirmed by single cell tests. The resulting MEA performances (MEA 1 vs. MEA 2: 5.5 $mW \cdot cm^{-2}$ vs. 8.5 $mW \cdot cm^{-2}$ at 60 °C) were demonstrated for fuel with low concentration (1 M KOH + 1 M EtOH) and with low metal loading (1 $mg_{Pd} \cdot cm^{-2}$) at the anode.

The novel ternary $Pd_{60}Ni_{20}Bi_{20}$/C catalyst showed excellent byproduct tolerance toward alkaline EOR. Future work will focus on one hand on the optimization of the atomic composition to further decrease the onset potential and to enhance the current density for the alkaline EOR. On the other hand, the alkaline EOR performance and the structural characteristics of the ternary $Pd_{60}Ni_{20}Bi_{20}$/C catalyst will be improved by more homogeneous distribution of the spherical metal nanoparticles with defined particle sizes on the carbon support material in consideration of the presence of oxide species with different oxidation states (XPS), the various crystal structures with the respective miller indices (XRD) and the local concentrations (ICP-OES) of Pd, Ni and Bi (see **sections 4.3** and **4.4**).

PART III

Atomic Composition Optimization of Carbon Supported $Pd_xNi_yBi_z$ Nanocatalyst for the Alkaline EOR

The following **section 4.3** and the corresponding Appendix A (**section 8.3**) have been **published in advance** in:

[15] **Cermenek, B.**; Ranninger, J.; Feketeföldi, B.; Letofsky-Papst, I.; Kienzl, N.; Bitschnau, B.; Hacker, V. Novel highly active carbon supported ternary PdNiBi nanoparticles as anode catalyst for the alkaline direct ethanol fuel cell. *Nano Res*. **2019**, *12*, 683–693.

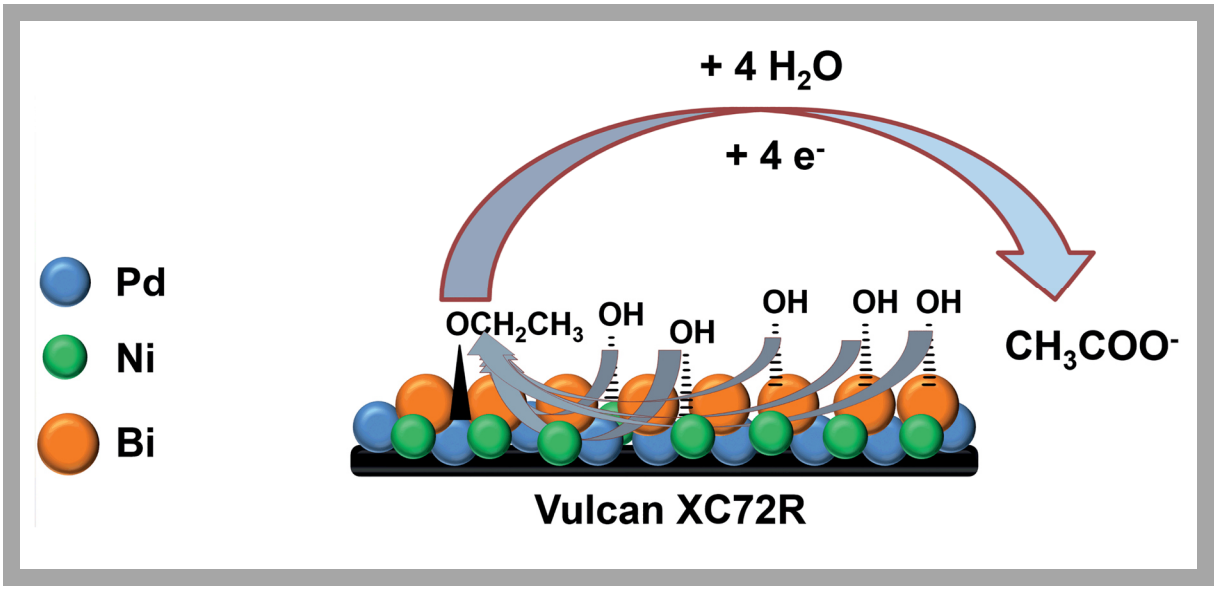
and are based on **master's thesis** of **Johanna Ranninger** (supervised **Cermenek, B.** – The ICP-OES analysis and electrochemical characterization (CV-RDE and CA-RDE) results and discussions were 1:1 adopted and adapted):

[29] Ranninger, J. Development and Characterization of Pd-based Catalysts for the alkaline Direct Ethanol Fuel Cell. *Master's thesis*, Graz University of Technology, **2017**, p. 85.

4.3 PART III: Atomic Composition Optimization of Carbon Supported $Pd_xNi_yBi_z$ Nanocatalyst for the Alkaline EOR

Abstract

Part III of the doctoral thesis deals with the development and characterization of novel carbon supported ternary $Pd_xNi_yBi_z$ anode catalysts ($Pd_{70}Ni_{25}Bi_5$/C, $Pd_{70}Ni_{20}Bi_{10}$/C, $Pd_{80}Ni_{10}Bi_{10}$/C and $Pd_{40}Ni_{20}Bi_{40}$/C) with various atomic variations using the well-known current less $NaBH_4$ reduction synthesis method ('instant') for the ADEFC. ICP-OES, XPS, XRD and TEM-EDX methods determine the accurate element concentrations, surface oxidation states, binding energies and morphology/structure of Pd, Ni and Bi from the synthesized anode catalysts [15]. The carbon supported Pd:Ni:Bi nanocatalyst with atomic ratio of 70:20:10 displays outstanding catalytic activity (highest current density with lowest onset potential) for the alkaline EOR using CV and CA on a RDE compared to the other $Pd_xNi_yBi_z$/C nanocatalysts as well as to the benchmarks Pd/C, $Pd_{60}Ni_{40}$/C and $Pd_{60}Ni_{20}Bi_{20}$/C from **section 4.2**. The synergy and the optimal content in consideration of the oxide species of Pd, Ni and Bi are crucial for the EOR kinetic enhancement in alkaline medium [15].



Graphical abstract TOC: The Ni-OH_{ads} and Bi-OH_{ads} species on carbon supported $Pd_{70}Ni_{20}Bi_{10}$ nanocatalyst facilitate the EOR process to CH_3COO^- by bifunctional mechanism and also by oxidative removal of poisonous EtOH species from the catalyst surface. This results in a catalytic activity enhancement of $Pd_{70}Ni_{20}Bi_{10}$/C with lower onset potential (0.236 V) for alkaline EOR compared to Pd/C (0.280 V) and $Pd_{60}Ni_{40}$/C (0.290 V) nanocatalysts [15].

4.3.1 Physico-Chemical Characterization

ICP-OES

The ICP-OES method was used to determine the elemental concentrations of the carbon supported $Pd_xNi_yBi_z$ catalysts with the calculated atomic ratio of 70:25:5, 70:20:10, 80:10:10 and 40:20:40. Analysis results by ICP-OES are in good agreement with calculated values (= subscripts of catalysts) from the preparation of nanocatalysts (Table 9). The chemical compositions of carbon supported $Pd_xNi_yBi_z$ catalysts are given accurately and precisely in Table 31 in Appendix A [15,29].

Table 9: Elemental analysis of $Pd_xNi_yBi_z$/C nanocatalysts by ICP-OES [15,29].

Catalysts	Pd (at.%)	Ni (at.%)	Bi (at.%)
$Pd_{70}Ni_{25}Bi_5$/C	71	24	5
$Pd_{70}Ni_{20}Bi_{10}$/C	70	19	11
$Pd_{80}Ni_{10}Bi_{10}$/C	78	10	12
$Pd_{40}Ni_{20}Bi_{40}$/C	46	17	37

TEM-EDX

The structure and morphology of the synthesized carbon supported $Pd_xNi_yBi_z$ catalysts in low and high magnification are shown by TEM micrographs in Figure 29 and Figures 60–63 in Appendix A, respectively. It can be observed that the agglomeration of the metal nanoparticles (black or dark grey) occurs also on the carbon support material (grey) of $Pd_xNi_yBi_z$/C catalysts with varying atomic ratios, which as mentioned in **section 4.2.1,** makes determining the particle sizes difficult due to the absence of sufficient spherical particles for showing reproducible results [15].

Applying FFT on HRTEM micrographs show that all carbon supported $Pd_xNi_yBi_z$ catalysts exhibit *d*-spacing of ~0.21 nm determined which complies with lattice spacing of Pd (111) (Figure 29). The metal contents of the $Pd_{70}Ni_{25}Bi_5$/C, $Pd_{70}Ni_{20}Bi_{10}$/C, $Pd_{80}Ni_{10}Bi_{10}$/C and $Pd_{40}Ni_{20}Bi_{40}$/C catalysts were determined at specific chosen areas by recording EDX spectra (Figure 64). This analysis confirms that the metal nanoparticles of the ternary $Pd_xNi_yBi_z$/C catalysts are not homogeneously distributed on the carbon support material [15].

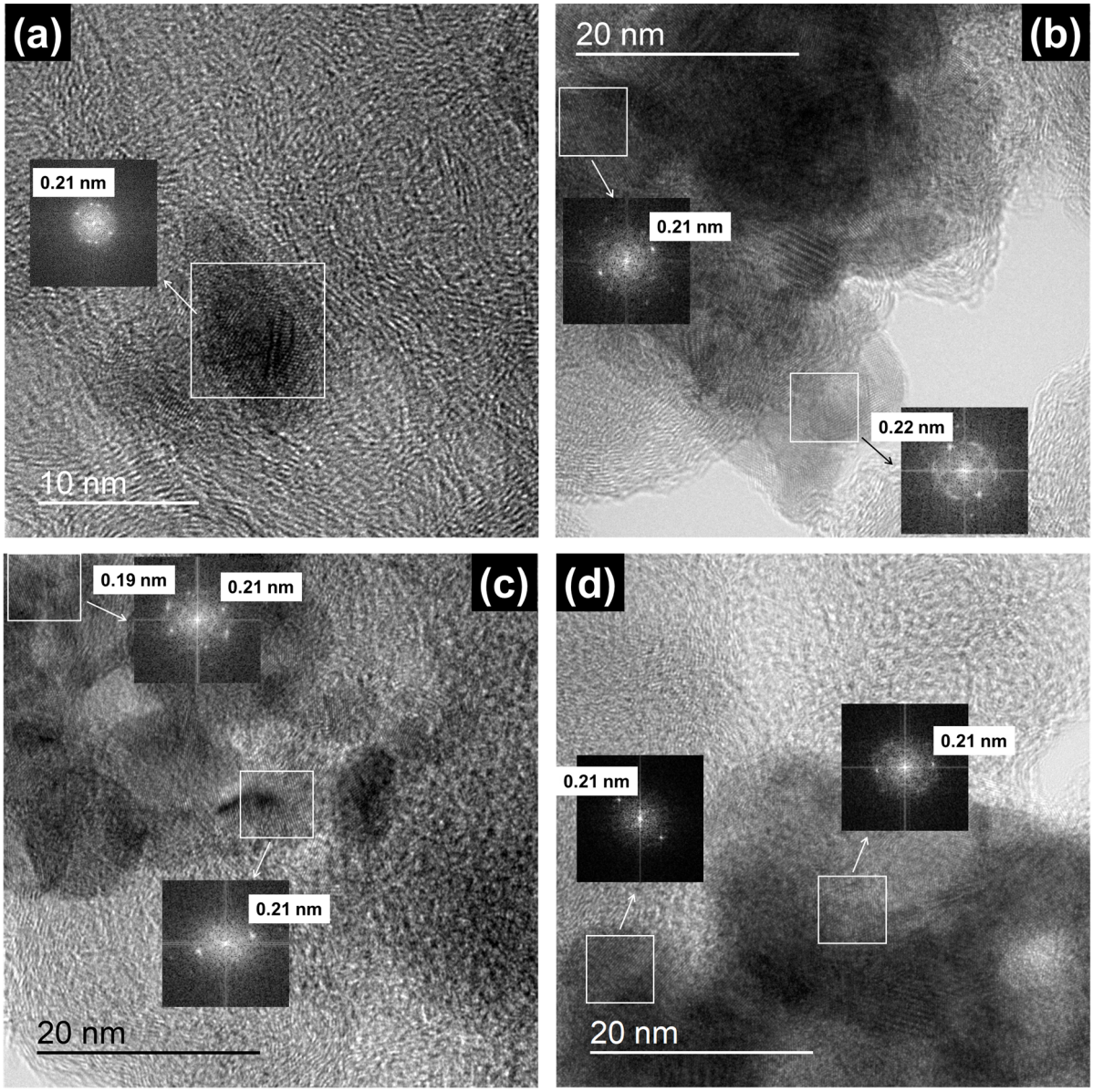


Figure 29: HRTEM micrographs including the determined inter-planar spacing of the **(a)** $Pd_{70}Ni_{25}Bi_5/C$, **(b)** $Pd_{70}Ni_{20}Bi_{10}/C$, **(c)** $Pd_{80}Ni_{10}Bi_{10}/C$ and **(d)** $Pd_{40}Ni_{20}Bi_{40}/C$ catalyst [15].

The obtained TEM-EDX results of one specific area of each ternary $Pd_xNi_yBi_z/C$ catalyst (Figure 64) were summarized in Table 32 and are in good agreement with the ICP-OES results (Table 9 and Table 31 in the Appendix A) [15].

STEM-HAADF investigations of the $Pd_{70}Ni_{25}Bi_5/C$, $Pd_{70}Ni_{20}Bi_{10}/C$, $Pd_{80}Ni_{10}Bi_{10}/C$ and $Pd_{40}Ni_{20}Bi_{40}/C$ catalysts would not have given any additional information about the structure and morphology as confirmed for the catalysts in **section 8.2.2** (Figures 45, 47, 49 and 51). To get more details of the structures, sizes and shapes of the $Pd_xNi_yBi_z/C$ catalysts, XRD analyses were performed (see Figure 30 and Table 10) [15].

XRD

The XRD patterns of all carbon supported $Pd_xNi_yBi_z$ catalysts exhibit the typical diffraction peaks approx. at the 2θ values of 40°, 47°, 68°, 82° and 86° which can be assigned to the Pd fcc crystalline structure (Pd_64922-ICSD) with miller indices of (111), (200), (220), (311) and (222), respectively (Figure 30). The diffraction peak located approx. at the 2θ value of 25° attributes to carbon black Vulcan XC72R as crystalline structure of graphite (2H)_187640-ICSD with the miller indices of (002) for all catalyst samples (Figure 30). These diffraction peaks assignments were also confirmed in the previous **section 4.2.1** [15].

The 2θ values of the ternary catalysts ($Pd_{70}Ni_{20}Bi_{10}$/C and $Pd_{40}Ni_{20}Bi_{40}$/C) are slightly lower (Tables 34 and 36 in the Appendix A) and their *d*-spacing values and lattice parameters (Table 10) are slightly higher than for the Pd/C catalyst (Table 6 and Table 16 in the Appendix A), which indicates that the Pd lattice expands and is modified by alloying with Ni and Bi [15]. This statement is already confirmed in the previous **section 4.2.1** and also by various research groups [14,15,17,26,46,78,137]. The determined inter-planar spacing for the catalysts in the recorded HRTEM micrographs (Figure 29) conforms to the XRD results (Table 10) [15].

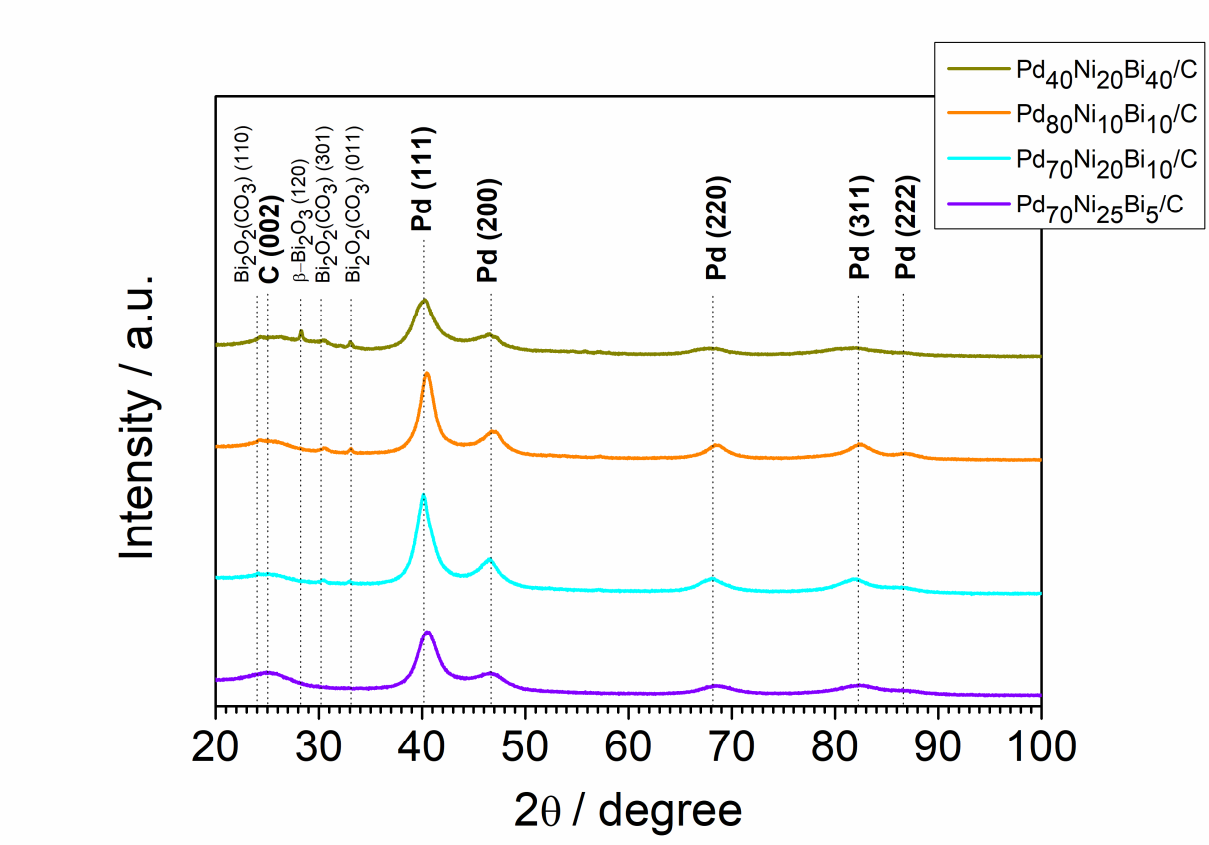


Figure 30: XRD patterns of carbon supported $Pd_xNi_yBi_z$ nanocatalysts [15].

Furthermore, the XRD patterns of $Pd_{80}Ni_{10}Bi_{10}$/C and $Pd_{40}Ni_{20}Bi_{40}$/C catalysts reveal additional diffraction peaks approx. at 24°, 30°, and 33° and were identified as crystalline structure of $Bi_2O_2(CO_3)$_252588-ICSD (Figure 30, Tables 35 and 36 in the Appendix A) [15].

The XRD pattern of the $Pd_{40}Ni_{20}Bi_{40}$/C catalyst exhibits a diffraction peak approx. at 28°, which is attributed to the crystalline structure of Bi_2O_3_beta_189995-ICSD with the miller indices of (120) (Figure 30 and Table 36 in the Appendix A). This crystalline structure was also found for the $Pd_{60}Bi_{40}$/C catalyst, as confirmed in **section 4.2.1** (see Table 18 in the Appendix). More details about XRD data with Rietveld-refinement for the carbon supported $Pd_xNi_yBi_z$ catalysts are given in Tables 33–36 in the Appendix A [15]. Furthermore, the located crystalline structures of Pd, Ni, Bi and C with their corresponding unit cells for all catalyst samples are demonstrated in Table 20 and Tables 23–26 in the Appendix A. The crystallite sizes of Pd in all $Pd_xNi_yBi_z$/C catalysts and $Bi_2O_2(CO_3)$ in the $Pd_{40}Ni_{20}Bi_{40}$/C catalyst were experimentally estimated in accordance with the Scherrer equation (Equation 17), assuming spherical crystallites with cubic crystal system. The crystallites are in the order of 4 to 8 nm (Table 10) [15].

The crystallite sizes of the located crystalline structures of $Bi_2O_2(CO_3)$_252588-ICSD and Bi2O3_beta_189995-ICSD in the $Pd_{80}Ni_{10}Bi_{10}$/C and $Pd_{40}Ni_{20}Bi_{40}$/C catalysts could not be determined due to their low amount, respectively. But these Bi species as crystal structures were not found in the $Pd_{70}Ni_{25}Bi_5$/C and $Pd_{70}Ni_{20}Bi_{10}$/C catalysts. No Ni crystalline structures were identified in all of the $Pd_xNi_yBi_z$/C catalysts [15].

Table 10: Structure analysis of carbon supported $Pd_xNi_yBi_z$ nanocatalysts by XRD [15].

Catalysts	*d*-spacing Pd (111) (nm)	Lattice parameter (nm)	Crystallite size (nm)
$Pd_{70}Ni_{25}Bi_5$/C	0.2230	Pd: *a* = 0.3863	Pd: 4
$Pd_{70}Ni_{20}Bi_{10}$/C	0.2247	Pd: *a* = 0.3892	Pd: 4
$Pd_{80}Ni_{10}Bi_{10}$/C	0.2229	Pd: *a* = 0.3894	Pd: 5
$Pd_{40}Ni_{20}Bi_{40}$/C	0.2248	Pd: *a* = 0.3894	Pd: 5 $Bi_2O_2(CO_3)$: 8

XPS

The surface oxidation states, chemical compositions and binding energies of Pd, Ni and Bi from the synthesized $Pd_xNi_yBi_z$/C catalysts were determined by XPS. As expected, the XPS results relating to the atomic content determinations in all ternary catalysts have a discrepancy to ICP-OES analysis due to predominant overlapping of Pd and Bi on Ni at the catalyst surface leading to lower Ni content (Table 11 and detailed in Tables 38–41 in the Appendix A: deconvolution results of the elements) [15].

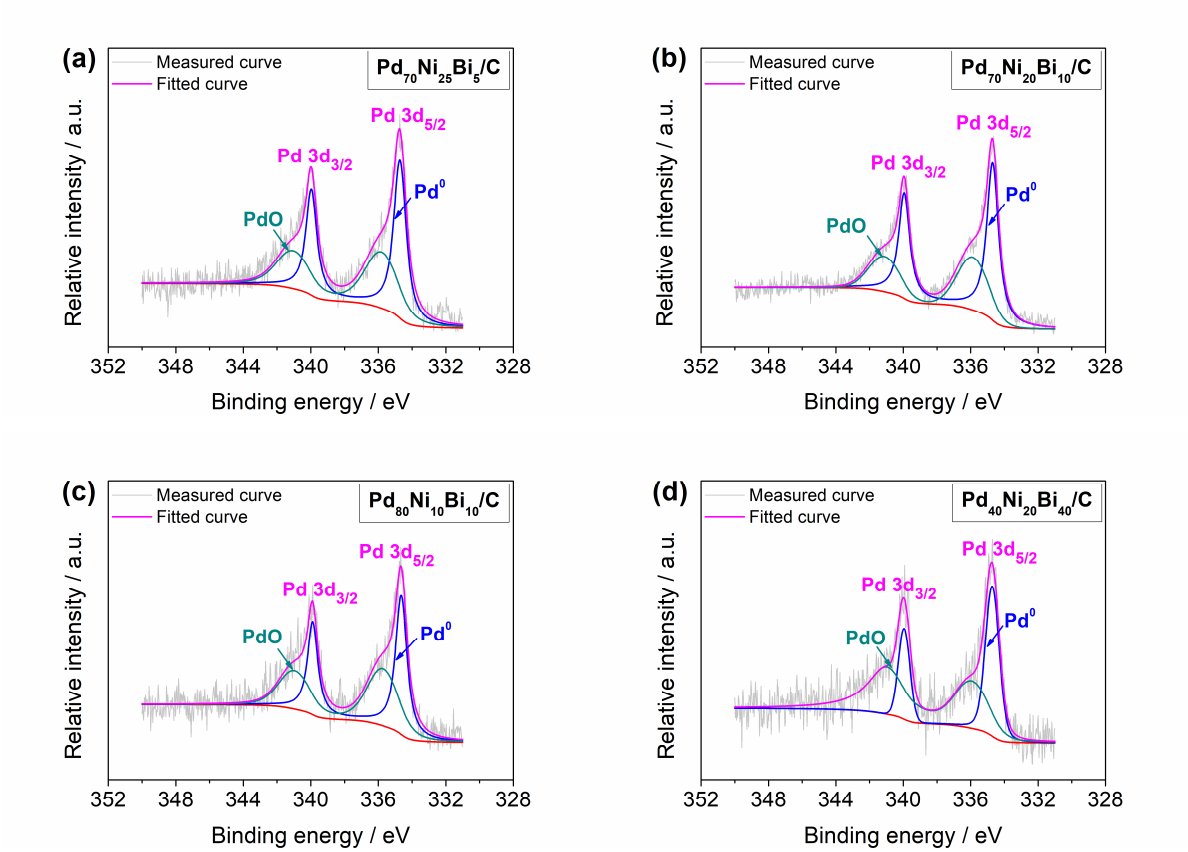


Figure 31: Pd 3d XPS spectra of the **(a)** $Pd_{70}Ni_{25}Bi_5/C$, **(b)** $Pd_{70}Ni_{20}Bi_{10}/C$, **(c)** $Pd_{80}Ni_{10}Bi_{10}/C$ and **(d)** $Pd_{40}Ni_{20}Bi_{40}/C$ catalyst [15].

Two oxidation states of Pd were identified in the Pd $3d_{5/2}$ and Pd $3d_{3/2}$ regions of the Pd 3d XPS spectra as metallic Pd (Pd^0) and PdO (Pd^{II}) species on all $Pd_xNi_yBi_z/C$ catalyst surfaces (Figures 31a–31d), as also confirmed by the previous study as described in **section 4.2.1** in this doctoral thesis [3,15]. The shifting of the PdO peak of all $Pd_xNi_yBi_z/C$ catalysts to lower binding energy compared to Pd/C catalyst (Table 37) results on the one hand in an improvement of the byproduct tolerance toward alkaline EOR and on the other hand in a suppression of the PdO formation as already explained in **section 4.2.1** [15].

The surface of the $Pd_{80}Ni_{10}Bi_{10}/C$ catalyst contains the most oxide species of Pd, Ni and Bi (Table 11 and detailed in Tables 37 and 40 in the Appendix A), but limits its catalytic activity for the alkaline EOR (Figure 36c). The presence of the lower Ni oxide content (lower electron and proton conductivity) of the $Pd_{80}Ni_{10}Bi_{10}/C$ catalyst is the main limiting factor for its lower EOR activity compared to the other catalysts (Table 11 and Tables 37–41 in the Appendix A). It has been shown literature that Ni oxide promotes significantly the EOR performance of the catalysts used [12,15,64].

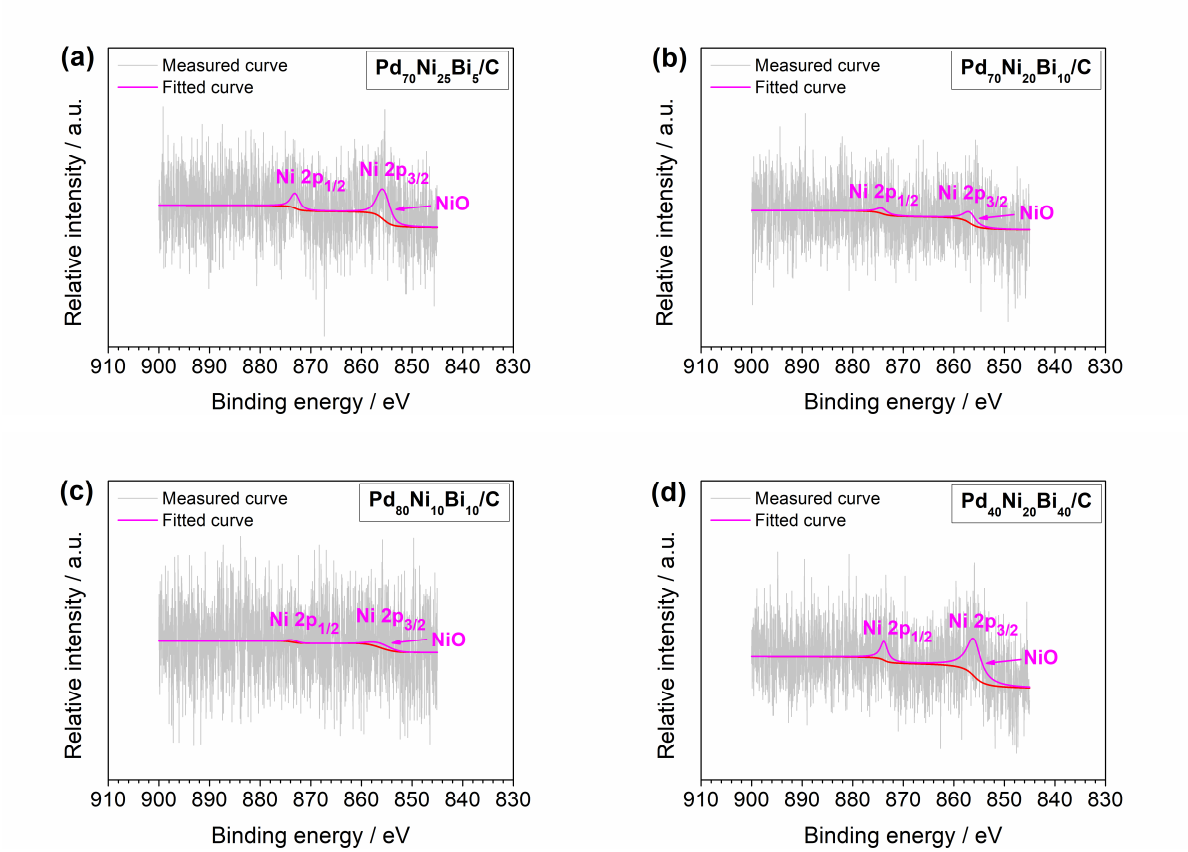


Figure 32: Ni 2p XPS spectra of the **(a)** $Pd_{70}Ni_{25}Bi_5/C$, **(b)** $Pd_{70}Ni_{20}Bi_{10}/C$, **(c)** $Pd_{80}Ni_{10}Bi_{10}/C$ and **(d)** $Pd_{40}Ni_{20}Bi_{40}/C$ catalyst [15].

The Ni 2p XPS spectra of all $Pd_xNi_yBi_z/C$ catalysts show that in the doublets of Ni $2p_{1/2}$ and Ni $2p_{3/2}$ only one Ni^{II} species is observed which is attributable to NiO (Figures 32a–32d) compared to the previous XPS results of the $Pd_{60}Ni_{20}Bi_{20}/C$ catalyst (Figure 22) where $Ni(OH)_2$ as the second Ni^{II} species was identified [15]. The measured values of the Ni 2p XPS spectra are undefined (Figure 32) and have a similar appearance to the Ni 2p XPS spectra (Figure 22). This noising effect arises as already mentioned in **section 4.2.1** from the inhomogeneous catalyst particle distribution on the carbon support material (see TEM-EDX results: Figure 64 and Table 32). The other reason for the undefined Ni 2p XPS spectra was also described previously in **section 4.2.1** [15].

The resulting Bi 4f XPS spectra show that metallic Bi and Bi oxide species are distributed on the surfaces of $Pd_{70}Ni_{25}Bi_5/C$, $Pd_{70}Ni_{20}Bi_{10}/C$ and $Pd_{40}Ni_{20}Bi_{40}/C$ catalysts (Figures 33a, 33b and 33d). It can be observed, however, that the doublets of Bi $4f_{5/2}$ and Bi $4f_{7/2}$ peak from the $Pd_{80}Ni_{10}Bi_{10}/C$ catalyst shift by more than 1 eV to higher binding energies, due to the increased measured oxygen content compared to the other catalysts (Table 11) and the peak of metallic Bi is absent. The explanation for the absence of Bi peak is already commented previously (**section 4.2.1**) [15,138].

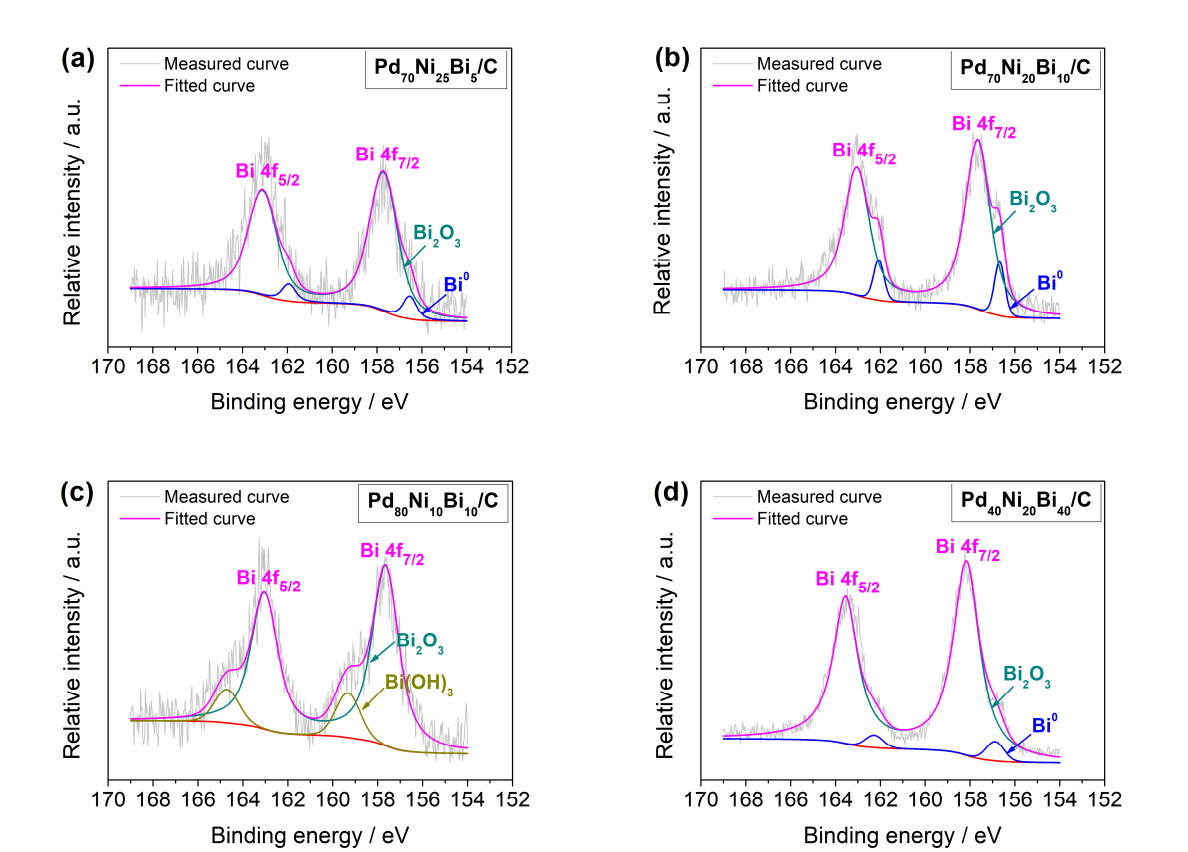


Figure 33: Bi 4f XPS spectra of the **(a)** $Pd_{70}Ni_{25}Bi_5/C$, **(b)** $Pd_{70}Ni_{20}Bi_{10}/C$, **(c)** $Pd_{80}Ni_{10}Bi_{10}/C$ and **(d)** $Pd_{40}Ni_{20}Bi_{40}/C$ catalyst [15].

An additional Bi oxide species on the $Pd_{80}Ni_{10}Bi_{10}/C$ catalyst surface, such as $Bi(OH)_3$, was identified (Figure 33c) as in $Pd_{60}Ni_{40}/C$ and $Pd_{60}Ni_{20}Bi_{20}/C$ catalysts (see Figure 23) [15,138]. Furthermore, the XPS spectra obtained for C and O are demonstrated in Figures 65 and 66 in the Appendix A [15]. The measured Pd 3d, Bi 4f, C 1s and O 1s XPS spectra of the synthesized catalysts also showed good agreements to their fitted XPS spectra, as mentioned in **section 4.2.1** (Figures 31 and 33; and Figures 65 and 66 in the Appendix A) [15].

Additionally, Table 37 shows the assignments of the metallic and oxide species to the Pd 3d, Ni 2p and Bi 4f peaks and their corresponding peak positions and atomic percentages. Details about the effects of the Pd, Ni and Bi species/ions on the catalytic properties and surface structures of all synthesized catalysts from **sections 4.2.1** and **4.3.1** are discussed in Appendix A (see **section 8.3.3**, pp. 204) [15].

Table 11: XPS characterization data of $Pd_xNi_yBi_z/C$ catalysts including the determined metal contents [15].

Catalysts	Pd 3d (eV)	Ni 2p (eV)	Bi 4f (eV)	O 1s (eV)	C 1s (eV)	Pd (at.%)	Ni (at.%)	Bi (at.%)	O (at.%)	C (at.%)	Pd / metal	Ni / metal	Bi / metal
	334.72	855.69	156.54	529.48	283.76	0.32	0.04	0	0.34	45.36			
	335.8		157.72	531.41	284.24	0.26		0.05	1.96	35.82			
$Pd_{70}Ni_{25}Bi_5/C$				532.78	285.89				3.26	7.57			
					288.33					5.01			
					Total	**0.58**	**0.04**	**0.05**	**5.56**	**93.76**	**87**	**6**	**7**
	334.69	856.83	156.68	529.64	283.8	0.63	0.02	0.02	0.76	63.96			
	335.86		157.66	531.48	284.72	0.41		0.14	2.5	15.57			
$Pd_{70}Ni_{20}Bi_{10}/C$				532.91	285.94				3.56	7.58			
					288.39					4.85			
					Total	**1.04**	**0.02**	**0.16**	**6.82**	**91.96**	**85**	**2**	**13**
	334.64	856.24	157.65	531.79	283.71	0.24	0.01	0.07	5.44	24.5			
	335.72		159.32	533.21	284.42	0.22		0.01	4.77	52.22			
$Pd_{80}Ni_{10}Bi_{10}/C$					286.18					6.09			
					288.46					6.43			
					Total	**0.46**	**0.01**	**0.08**	**10.21**	**89.24**	**84**	**2**	**14**
	334.71	856.04	156.88	530.06	283.78	0.17	0.07	0.02	1.03	47.43			
	335.93		158.16	531.76	284.38	0.2		0.33	2.42	34.96			
$Pd_{40}Ni_{20}Bi_{40}/C$				533.2	286.19				2.02	6.1			
					288.6					5.27			
					Total	**0.37**	**0.07**	**0.35**	**5.47**	**93.76**	**47**	**9**	**44**

4.3.2 Electrochemical Characterization

The electrocatalytic activities and stabilities of the synthesized carbon supported $Pd_xNi_yBi_z$ catalysts ($Pd_{70}Ni_{25}Bi_5$/C, $Pd_{70}Ni_{20}Bi_{10}$/C, $Pd_{80}Ni_{10}Bi_{10}$/C, $Pd_{40}Ni_{20}Bi_{40}$/C) were characterized by CV and CA using the RDE in static mode with metal loading of 56 $\mu g_{Pd} \cdot cm^{-2}$ (Figures 34–37) under the same operating conditions as for the catalysts (Pd/C, $Pd_{60}Ni_{40}$/C, $Pd_{60}Bi_{40}$/C and $Pd_{60}Ni_{20}Bi_{20}$/C) described in **section 4.2.2** (see Figures 25 and 26) [15,29].

The influence of varied Bi content on the EOR performances of the synthesized catalysts $Pd_{40}Ni_{20}Bi_{40}$/C and $Pd_{70}Ni_{20}Bi_{10}$/C were investigated by means of the aforementioned electrochemical characterization methods and compared to the benchmarks $Pd_{60}Ni_{40}$/C and $Pd_{60}Ni_{20}Bi_{20}$/C (Figures 34 and 35), which possessed the best catalytic performances in terms of alkaline EOR activity and stability (byproduct tolerance) in the previous experiments (see **section 4.2.2**: Figures 24c and 24d) [15,29].

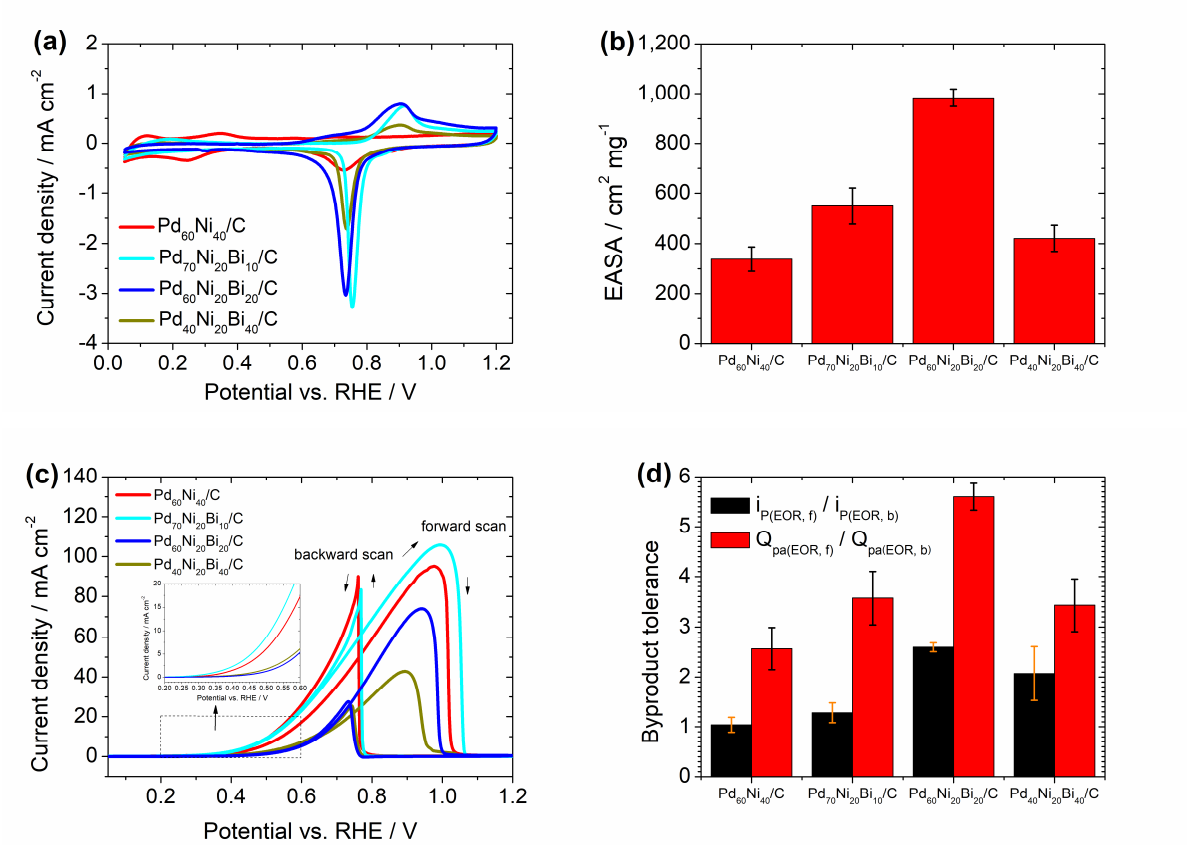


Figure 34: Electrochemical characterization of $Pd_{60}Ni_{40}$/C, $Pd_{70}Ni_{20}Bi_{10}$/C, $Pd_{60}Ni_{20}Bi_{20}$/C and $Pd_{40}Ni_{20}Bi_{40}$/C catalysts: **(a)** in de-aerated 1.0 M KOH and **(b)** the resulting EASAs, **(c)** in an electrolyte mixture of 1 M KOH + 1 M EtOH and **(d)** the obtained byproduct tolerances resulting from EOR measurements (see **(c)**) – performed at 30 °C and with a scan rate of 10 $mV \cdot s^{-1}$ [15,29].

The recorded CV of the $Pd_{70}Ni_{20}Bi_{10}$/C catalyst in de-aerated 1.0 M KOH shows a peak in the potential region between 0.1 and 0.2 V indicating an occurring hydrogen sorption reaction (Figure 34a). It was confirmed that $Pd_xNi_yBi_z$/C catalysts with more than 10 at.% of Bi ($Pd_{60}Ni_{20}Bi_{20}$/C and $Pd_{40}Ni_{20}Bi_{40}$/C) lead to a suppression of the hydrogen adsorption and the absorption process itself compared to the CVs of $Pd_{60}Ni_{40}$/C and $Pd_{70}Ni_{20}Bi_{10}$/C catalysts (Figure 34a). This effect was observed by adding a specific quantity of Bi to Pd as well as to Pt-based catalysts [17,68,138]. Neto et al. improved the alkaline EOR activities of carbon supported Pd catalysts by adding of decreased Bi contents [17], whereupon the Pt_xBi_y based catalysts were enhanced by increasing of Bi contents [68]. Further distinctive peaks in the potential regions of the anodic scan between 0.8 and 1.0 V and of the cathodic scan between 0.5 and 0.9 V are attributed to the oxidized and reduced Bi and Pd species, respectively (Figure 34a) [15,29].

From the obtained XPS and XRD data we suggest that the peak around 0.9 V in the anodic scan (Figure 34a) mainly originates from the oxidation of Bi and Bi oxide species. Simões et al. observed that this characteristic peak became higher in the CVs of carbon supported binary Pd_xBi_y catalysts by increasing of Bi content [15,29,138].

The former statement does not coincide with our RDE-CV measurements because this peak of $Pd_{40}Ni_{20}Bi_{40}$/C is lower than for $Pd_{60}Ni_{20}Bi_{20}$/C catalyst (Figure 34a). Here, many cleaning cycles (= recorded CVs at a scan rate of 50 mV s^{-1}) of the $Pd_{40}Ni_{20}Bi_{40}$/C catalyst had to be conducted until a stable CV was obtained, because the peak, which was assigned to Bi oxide species, decreased with increased cycles. This decreased trend can be thus explained by the presence of impurities which undergo an oxidative removal or other species that are dissolved with increasing potential. As this phenomenon was also observed in the previous RDE-CV measurements of the $Pd_{60}Bi_{40}$/C catalyst (see **section 4.2.2**). It is assumed that Bi^0-agglomerates, mentioned by Simões et al., are oxidized and dissolved into the electrolyte [15,29,138].

Our studies are supported by the observation that the current densities in the EOR measurements of $Pd_{60}Bi_{40}$/C and $Pd_{40}Ni_{20}Bi_{40}$/C catalysts increased when more cycles were performed. The proven Bi^0-agglomerates in the $Pd_{60}Bi_{40}$/C which block the active sites of Pd are gradually dissolved and lead to higher activities after multiple CV cycles and it is assumed that this is also valid for the $Pd_{40}Ni_{20}Bi_{40}$/C catalyst. The study of Simões et al. reported that Bi^0 agglomerates in catalysts with a Bi content as high as 20% or higher by EDX analysis. However, the agglomerations were not identified in carbon supported Pd_xBi_y catalysts with Bi content lower than 20% [138]. The prior statement cannot be confirmed by our TEM results (Figures 18c and 18d; Figures 48–51 and Figures 62–64 in the Appendix A) [15,29].

The $Pd_{60}Ni_{20}Bi_{20}$/C catalyst as benchmark exhibits the highest EASA among all in this doctoral thesis synthesized carbon supported $Pd_xNi_yBi_z$ catalysts, followed by $Pd_{70}Ni_{20}Bi_{10}$/C catalyst (Table 12 and Figure 34b). These results are conclusive in respect to the findings of Simões et al., that the reduction peak approx. at 0.75 V not only originates from Pd oxide species alone but also that other oxidized species are reduced in this region [15,29,138]. As more Bi is incorporated in the $Pd_{60}Ni_{20}Bi_{20}$/C catalyst and more Bi species can be oxidized, the reduction peak approx. at 0.75 V in the cathodic sweep is also more distinct compared to $Pd_{70}Ni_{20}Bi_{10}$/C catalyst (Figure 34a). The EASA of the $Pd_{40}Ni_{20}Bi_{40}$/C is assumed to be lower due to the low Pd content and the high Bi content leading to agglomerations [15,29].

The $Pd_{70}Ni_{20}Bi_{10}$/C catalyst exceeded the alkaline EOR performance of $Pd_{60}Ni_{40}$/C in terms of peak current density and onset potential (Figure 34c and Table 12). The onset potential for the alkaline EOR was decreased by 54 mV using the $Pd_{70}Ni_{20}Bi_{10}$/C and the peak current density could be increased by 10 $mA \cdot cm^{-2}$ compared to $Pd_{60}Ni_{40}$/C (Figure 34c and Table 12). This result proves that small amounts of Bi in the carbon supported $Pd_xNi_yBi_z$ catalyst enhance the activity and kinetics toward the EOR in an alkaline medium [15,29].

Even though $Pd_{70}Ni_{20}Bi_{10}$/C catalyst shows the best results in respect to the onset potential and peak current density toward alkaline EOR (Table 12), the byproduct tolerance is not as good as for $Pd_{60}Ni_{20}Bi_{20}$/C catalyst. However, $Pd_{70}Ni_{20}Bi_{10}$/C is the second best catalyst among all of those tested if the total current for the calculation of the byproduct tolerance is used (Figure 34d and Table 12). An explanation for this result could be that in the $Pd_{60}Ni_{20}Bi_{20}$/C catalyst containing 20 at.% of Bi, more Pd active sites are protected by Bi atoms. However, the reactant is hindered from reaching the active sites leading to lower activity and higher stability than $Pd_{70}Ni_{20}Bi_{10}$/C catalyst. By contrast, in the $Pd_{70}Ni_{20}Bi_{10}$/C catalyst only 10 at.% of Bi protects the active sites of Pd from poisoning resulting in a lower byproduct tolerance than for $Pd_{60}Ni_{20}Bi_{20}$/C catalyst. However, the active sites are better accessible for EtOH and a higher EOR activity is observed in an alkaline medium (Figure 34c) [15,29].

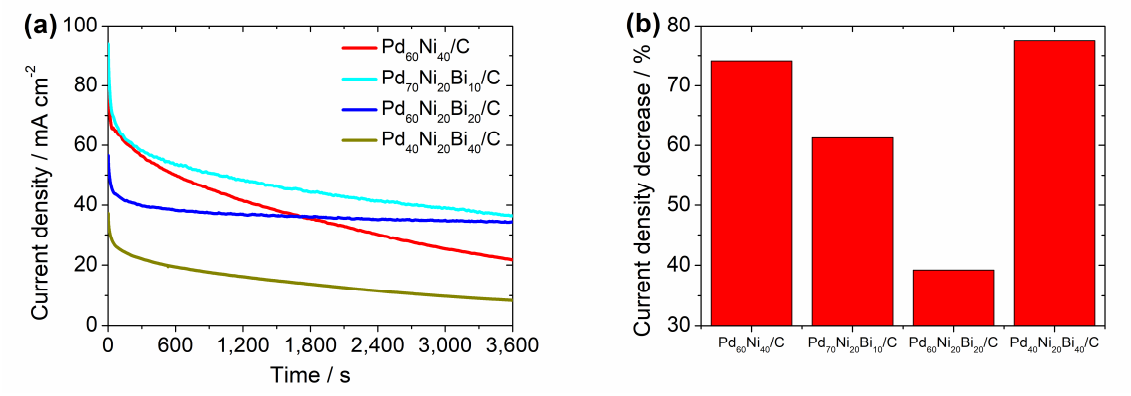


Figure 35: CA-measurements of $Pd_{60}Ni_{40}$/C, $Pd_{70}Ni_{20}Bi_{10}$/C, $Pd_{60}Ni_{20}Bi_{20}$/C and $Pd_{40}Ni_{20}Bi_{40}$/C catalysts: **(a)** in an electrolyte mixture of 1 M KOH + 1 M EtOH and **(b)** the resulting current density decrease in percentage at an applied potential of 0.83 V and at 30 °C for 3,600 s [15,29].

The CA results of $Pd_{70}Ni_{20}Bi_{10}/C$ catalyst (Figure 35) correlate with the results obtained from the byproduct tolerance determinations (Figure 34d). The $Pd_{60}Ni_{20}Bi_{20}/C$ catalyst, which exhibits the highest byproduct tolerance was also found to be the most stable one in the CA measurement followed by $Pd_{70}Ni_{20}Bi_{10}/C$, which still had almost 40% of the starting current density after 1 h at an applied potential of 0.83 V (Figure 35b and Table 12). Since the previous studies on the influence of Ni and Bi in carbon supported ternary $Pd_xNi_yBi_z$ catalysts have shown that a low Bi content enhances the alkaline EOR activity of the catalyst, the attempt was made to decrease the Bi content even further than 10 at.% to 5 at.%. Additionally, the Pd content was increased to test whether the alkaline EOR activity would rise further with a higher Pd content. The catalysts $Pd_{70}Ni_{25}Bi_5/C$ and $Pd_{80}Ni_{10}Bi_{10}/C$ were therefore synthesized, electrochemically characterized and the obtained results were compared with $Pd_{70}Ni_{20}Bi_{10}/C$ catalyst (Figures 36 and 37) [15,29].

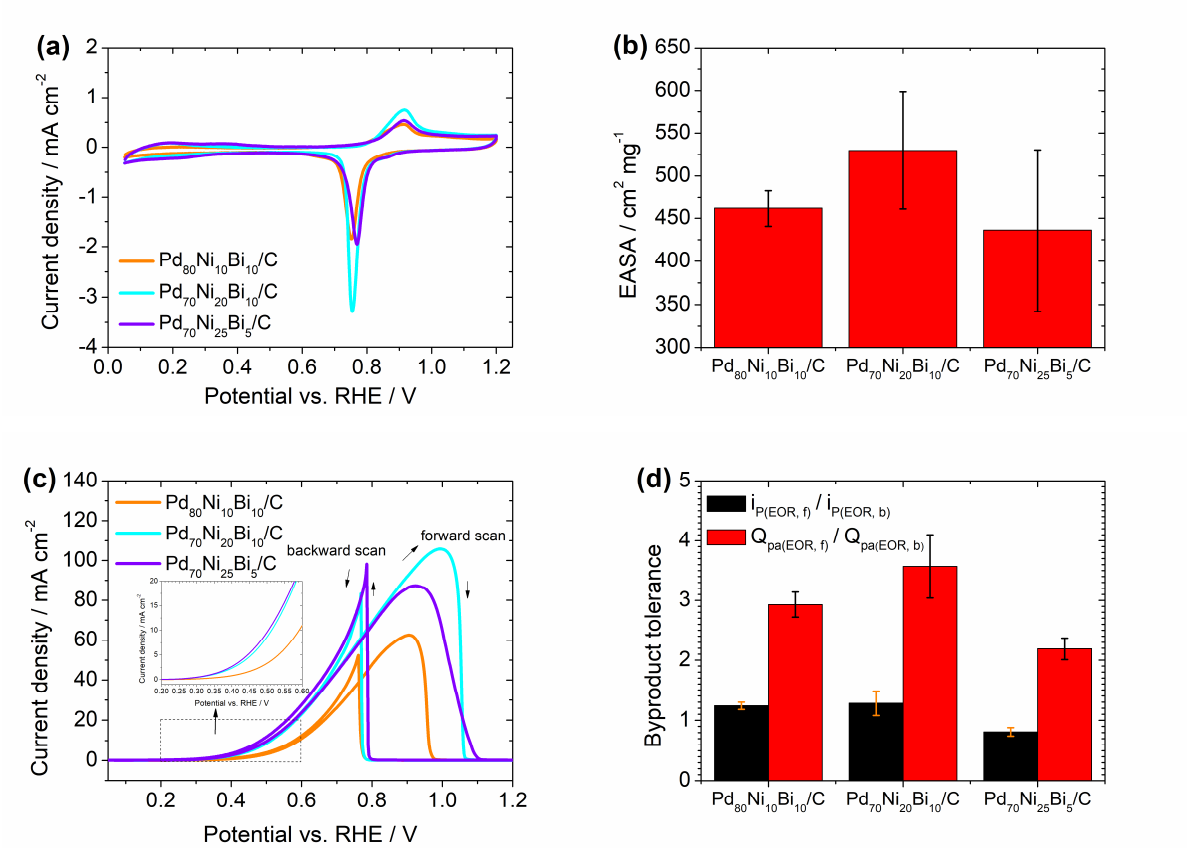


Figure 36: Electrochemical characterization of $Pd_{80}Ni_{10}Bi_{10}/C$, $Pd_{70}Ni_{20}Bi_{10}/C$ and $Pd_{70}Ni_{25}Bi_5/C$ catalysts: **(a)** in de-aerated 1.0 M KOH and **(b)** the resulting EASAs, **(c)** in an electrolyte mixture of 1 M KOH + 1 M EtOH and **(d)** the obtained byproduct tolerances resulting from EOR measurements (see **(c)**) - performed at 30 °C and with a scan rate of 10 $mV \cdot s^{-1}$ [15,29].

In the EOR measurements, the $Pd_{70}Ni_{25}Bi_5/C$ and $Pd_{80}Ni_{10}Bi_{10}/C$ catalysts could not exceed the peak current density of the $Pd_{70}Ni_{20}Bi_{10}/C$ catalyst (Figure 36c). However, $Pd_{70}Ni_{25}Bi_5/C$ has a low onset potential (0.239 V), very close to that of $Pd_{70}Ni_{20}Bi_{10}/C$ (0.236 V) (see small Figure in Figure 36c and Table 12). This supports the study that low amounts of Bi enhance the kinetics at the anode for the EOR in alkaline medium but the increase in peak current density could not be confirmed [15,29].

The onset potential and the peak current density of the $Pd_{80}Ni_{10}Bi_{10}/C$ catalyst were both reduced compared to $Pd_{70}Ni_{20}Bi_{10}/C$ (Figure 36c). This result is also conclusive when taking into account that the Ni content was reduced and the addition of higher amounts of Ni are necessary for a catalyst with high activity [14]. As expected, the byproduct tolerance of $Pd_{70}Ni_{25}Bi_5/C$ decreases when the Bi content is reduced from 10 at.% to 5 at.%. Also for the $Pd_{80}Ni_{10}Bi_{10}/C$ catalyst the byproduct tolerance is lower compared to $Pd_{70}Ni_{20}Bi_{10}/C$ but still higher than for $Pd_{70}Ni_{25}Bi_5/C$ (Figure 36d and Table 12) [15,29].

The CVs of the $Pd_{70}Ni_{25}Bi_5/C$, $Pd_{80}Ni_{10}Bi_{10}/C$ and $Pd_{70}Ni_{20}Bi_{10}/C$ catalysts exhibit similar curve progressions in 1.0 M KOH solution (Figure 36a). The EASAs of $Pd_{70}Ni_{25}Bi_5/C$ and $Pd_{80}Ni_{10}Bi_{10}/C$ catalysts are lower than the EASA of $Pd_{70}Ni_{20}Bi_{10}/C$ (Figure 36b and Table 12). The $Pd_{70}Ni_{25}Bi_5/C$ and $Pd_{80}Ni_{10}Bi_{10}/C$ catalysts also show lower stability than $Pd_{70}Ni_{20}Bi_{10}/C$ in the CA measurements (Figure 37 and Table 12). However, the results are still better than for $Pd_{60}Ni_{40}/C$ (Table 12) showing the positive effect of Bi on the stability toward alkaline EOR [15,29].

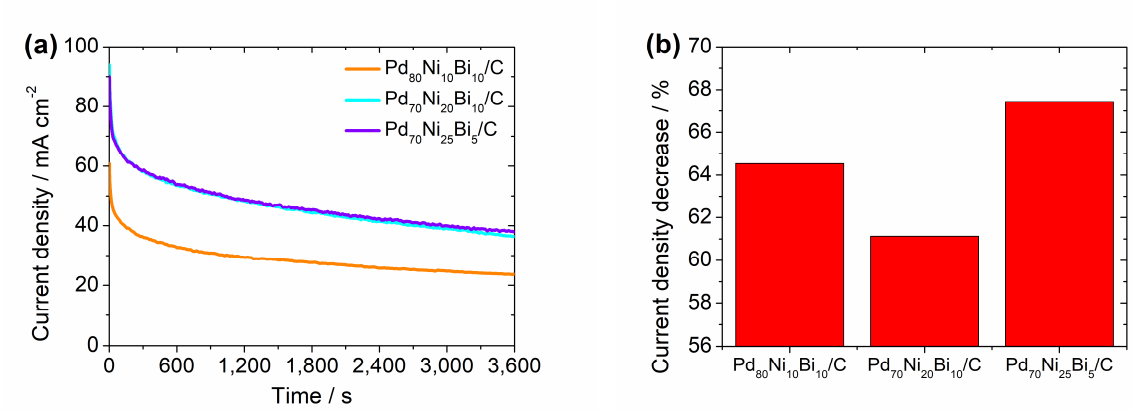


Figure 37: CA-measurements of $Pd_{80}Ni_{10}Bi_{10}/C$, $Pd_{70}Ni_{20}Bi_{10}/C$ and $Pd_{70}Ni_{25}Bi_5/C$ catalysts: **(a)** in an electrolyte mixture of 1 M KOH + 1 M EtOH and **(b)** the resulting current density decrease in percentage at an applied potential of 0.83 V for 3,600 s [15,29].

It can be concluded that higher amounts of Ni in Pd-based anode catalysts for the ADEFC enhance the activity for the EOR. In case of Bi, it is confirmed that lower amounts of Bi enhance the activity and kinetics at the anode for the EOR in an alkaline medium. This was observed as a low onset potential and high peak current density for catalysts with low Bi concentration. It was also found that a higher concentration of Bi (20 at.%) improves the byproduct tolerance and the stability of the catalyst [15,29].

The $Pd_{70}Ni_{20}Bi_{10}/C$ catalyst is the most active catalyst toward alkaline EOR among all tested catalysts (Figures 34c and 36c) and exhibits the second best results in terms of byproduct tolerance (Table 12). The maximum current density of 106 $mA \cdot cm^{-2}$ (mass activity: 1,889 $mA \cdot mg^{-1}$ – relating to Pd loading) from the novel ternary $Pd_{70}Ni_{20}Bi_{10}/C$ catalyst is, despite agglomerations, an outstanding value for the alkaline EOR compared to Ref. [143] as well as to Table 1. Considerably higher maximum current densities of the ternary $Pd_{70}Ni_{20}Bi_{10}/C$ catalyst could be achieved under the CV measurement conditions (e.g., with a scan rate of 50 $mV \cdot s^{-1}$ instead of $10 \cdot mV \cdot s^{-1}$) applied in Ref. [143] and Table 1 [15,29].

The electrochemical characterization results of all carbon supported Pd-based nano-catalysts (**sections 4.2.2** and **4.3.2**) are summarized in Table 12. Further details about the effects of the Pd, Ni and Bi species/ions on the catalytic properties and surface structures are discussed in the Appendix A (**section 8.3.3**, pp. 204) [15,29].

Additional electrochemical characterizations, such as the determination of the number of electrons during EtOH oxidation and the CA measurements of all Pd-based catalysts at an applied potential of 0.5 V, are demonstrated in Figures 67 and 68.

Table 12: Electrochemical results of all carbon supported Pd-based electrocatalysts from **sections 4.2.2** (grey shaded) and **4.3.2** [15,29].

Catalysts	EASA[a] ($cm^2 \cdot mg^{-1}$)	i_f[b] ($mA \cdot cm^{-2}$)	i_b[b] ($mA \cdot cm^{-2}$)	i_f / i_b[c]	$Q_{pa,f} / Q_{pa,b}$[d]	E_{onset}[e] (V)	i_{Start}[f] ($mA \cdot cm^{-2}$)	i_{End}[f] ($mA \cdot cm^{-2}$)	i_D[g] (%)
$Pd_{70}Ni_{25}Bi_5/C$	436 ± 94	87.28	98.19	0.81 ± 0.07	2.19 ± 0.18	0.239 ± 0.009	90.01	37.88	58
$Pd_{70}Ni_{20}Bi_{10}/C$	549 ± 72	105.77	83.39	1.28 ± 0.20	3.57 ± 0.53	0.236 ± 0.005	93.88	36.34	61
$Pd_{80}Ni_{10}Bi_{10}/C$	462 ± 21	62.55	52.30	1.24 ± 0.06	2.93 ± 0.53	0.274 ± 0.008	60.87	23.67	61
$Pd_{40}Ni_{20}Bi_{40}/C$	421 ± 52	42.79	25.37	2.07 ±0.54	3.43 ± 0.52	0.323 ± 0.033	37.14	8.36	77
Pd/C	463 ± 78	81.17	125.95	0.70 ± 0.04	1.90 ± 0.18	0.280 ± 0.015	94.97	37.37	61
$Pd_{60}Ni_{40}/C$	339 ± 49	95.11	90.05	1.04 ± 0.15	2.57 ± 0.42	0.290 ± 0.018	84.14	21.77	74
$Pd_{60}Bi_{40}/C$	276 ± 22	34.03	14.96	1.70 ± 0.60	2.89 ± 0.67	0.352 ± 0.015	32.16	6.02	81
$Pd_{60}Ni_{20}Bi_{20}/C$	983 ± 35	73.93	27.60	2.60 ± 0.09	5.60 ± 0.27	0.348 ± 0.007	56.59	34.39	39

[a]Electrochemical active surface area (EASA) determination; [b]i_f and i_b: peak current density of forward and backward scan; [c]i_f / i_b: byproduct tolerance using peak current density of forward and backward scan; [d]$Q_{pa,f} / Q_{pa,b}$: byproduct tolerance using the charge of the integrated peak current density area of the forward and backward scan; [e]E_{onset}: onset potential of the EtOH oxidation; [f]i_{Start} and i_{End}: resulting current densities at an applied potential of 0.83 V after 0 s and 3,600 s; [g]i_D: loss of current density after stress test at an applied of 0.83 V for 3,600 s.

4.3.3 In-situ Characterization

The $Pd_{70}Ni_{20}Bi_{10}/C$ anode catalyst with the best EOR activity among all synthesized carbon supported Pd-based catalysts (**sections 4.2** and **4.3**) was investigated in a liquid electrolyte ADEFC system in comparison to benchmarks, such as Pd/C and $Pd_{60}Ni_{20}Bi_{20}/C$ catalysts. The power density of the single cell test with $Pd_{70}Ni_{20}Bi_{10}/C$ anode catalyst is higher than the other two and confirms the ex-situ electrochemical characterizations (CV). Details about results and discussion of the membrane-less single cell tests are described in the master's thesis of Johanna Ranninger [29].

4.3.4 Conclusion

The alkaline EOR performance (catalytic activity, byproduct tolerance, and stability) of the novel carbon supported ternary $Pd_xNi_yBi_z$ catalyst was optimized by varying the atomic ratios of Pd, Ni and Bi for the application in ADEFCs. The carbon supported Pd:Ni:Bi catalyst with the atomic ratio of 70:20:10 exhibits the highest catalytic activity compared to the other synthesized $Pd_xNi_yBi_z/C$ catalysts as well as to the benchmarks Pd/C, $Pd_{60}Ni_{40}/C$, $Pd_{60}Bi_{40}/C$ and $Pd_{60}Ni_{20}Bi_{20}/C$. The maximum onset potential reduction of 116 mV and the peak current density enhancement of 71 $mA \cdot cm^{-2}$ were achieved for the alkaline EOR on the $Pd_{70}Ni_{20}Bi_{10}/C$ catalyst. The low Bi content (≤ 10 at.%) in the synthesized ternary $Pd_xNi_yBi_z$ catalysts promotes the alkaline EOR kinetics leading to high current densities and low onset potentials, whereas the use of high amounts of Bi (> 20 at.%) blocks the active sites of the used catalysts resulting in a decrease of the EOR activities. For further improvement of the EOR performance of the $Pd_{70}Ni_{20}Bi_{10}/C$ catalyst, an another catalyst composition using a modified instant reduction synthesis method for spherical metal nanoparticles with defined particle size and low tendency to agglomeration are investigated (see **section 4.4**) [15,29].

PART IV

Alkaline Ethanol Oxidation Reaction on Carbon Supported Ternary PdNiBi Nanocatalyst using Modified Instant Reduction Synthesis Method

The following **section 4.4** and the corresponding Appendix A (**section 8.4**) have been **published in advance** in:

[3] **Cermenek, B.**; Genorio, B.; Winter, T.; Wolf, S.; Connell, J.G.; Roschger, M.; Letofsky-Papst, I.; Kienzl, N.; Bitschnau, B.; Hacker, V. Alkaline Ethanol Oxidation Reaction on Carbon Supported Ternary PdNiBi Nanocatalyst using Modified Instant Reduction Synthesis Method. *Electrocatalysis*, **2020**, 11, 203-214.

and based on the **master project work** of **Thomas Winter** (supervised **Cermenek, B.** – The electrochemical characterization (RDE-CV and RDE-CA) and physico-chemical (ICP-OES and XRD) results were adopted and discussed in this part of the doctoral thesis.):

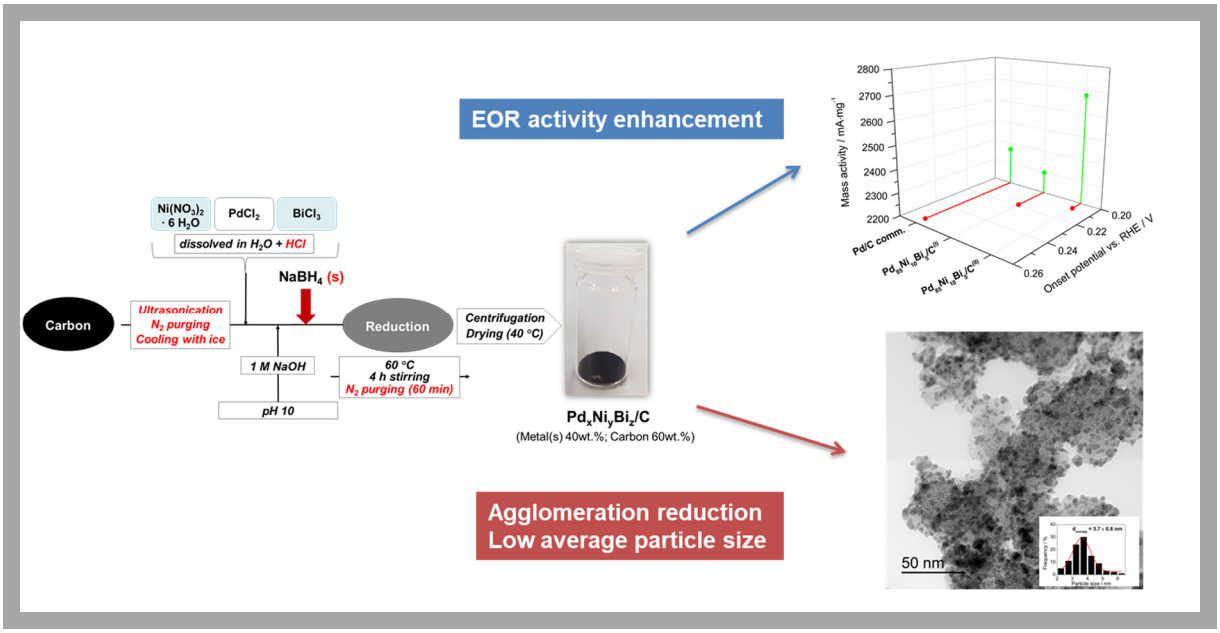
Winter, T. Vorgänge während der Herstellung von Pd-basierenden Katalysatoren für die Direkt-Ethanol-Brennstoffzelle. *Master project work*, Graz University of Technology, **2018**, p. 138. (unpublished)

4.4 PART IV: Alkaline Ethanol Oxidation Reaction on Carbon Supported Ternary PdNiBi Nanocatalyst using Modified Instant Reduction Synthesis Method

Part IV of the doctoral thesis describes the peer-reviewed article of Cermenek et al. [3] which is based on the master project work of master student, Thomas Winter, from Duisburg. The aim of the work is to further optimize the alkaline EOR performance of the novel carbon supported ternary PdNiBi electrocatalyst, which is based on the results of the master's thesis from Johanna Ranninger [29], as well as on the results of the peer-reviewed article from Cermenek et al. [15], by modification of the common instant reduction synthesis method.

Abstract

Direct ethanol fuel cells (DEFC) still lack active and efficient electrocatalysts for the alkaline ethanol oxidation reaction (EOR). In this work, a new instant reduction synthesis method was developed to prepare carbon supported ternary PdNiBi nanocatalysts with improved EOR activity [3]. Synthesized catalysts were characterized with a variety of structural and compositional analysis techniques in order to correlate their morphology and surface chemistry with electrochemical performance. The modified instant reduction synthesis results in well-dispersed, spherical $Pd_{85}Ni_{10}Bi_5$ nanoparticles on Vulcan XC72R support ($Pd_{85}Ni_{10}Bi_5/C^{(II\text{-}III)}$), with sizes ranging from 3.7 ± 0.8 to 4.7 ± 0.7 nm. On the other hand, the common instant reduction synthesis method leads to significantly agglomerated nanoparticles ($Pd_{85}Ni_{10}Bi_5/C^{(I)}$). EOR activity and stability of these three different carbon supported PdNiBi anode catalysts with a nominal atomic ratio of 85:10:5 were probed via cyclic voltammetry and chrono-amperometry using the rotating disk electrode method. $Pd_{85}Ni_{10}Bi_5/C^{(II)}$ showed the highest electrocatalytic activity (150 $mA \cdot cm^{-2}$; 2,678 $mA \cdot mg^{-1}$) with low onset potential (0.207 V) for EOR in alkaline medium, as compared to a commercial Pd/C and to the other synthesized ternary nanocatalysts $Pd_{85}Ni_{10}Bi_5/C^{(I)}$ and $Pd_{85}Ni_{10}Bi_5/C^{(III)}$. This new synthesis approach provides a new avenue to developing efficient, carbon supported ternary nanocatalysts for future energy conversion devices [3].



Graphical abstract TOC: The modified instant reduction method for synthesis of ternary $Pd_{85}Ni_{10}Bi_5/C^{(II)}$ nano-catalyst using Vulcan XC72R as carbon support initiates an agglomeration reduction, provides low average particle size, and enables enhanced activity for the alkaline ethanol oxidation reaction (EOR) compared to the common instant reduction method and to a commercial Pd/C catalyst [3].

4.4.1 Modified Instant Reduction Synthesis Method

Herein, we introduce a new synthesis approach in order to enhance the EOR activity/stability and to improve the dispersion of ternary PdNiBi/C nanocatalyst on Vulcan XC72R carbon support. This method improves upon the approach developed in our previous study [15] (**sections 4.2** and **4.3**), which yielded $Pd_xNi_yBi_z/C$ anode catalysts with high activity and high byproduct tolerance toward alkaline EOR but resulted in nanoparticles with inhomogeneous morphology that tended to agglomerate and provided a nonuniform distribution on the carbon support. The new synthesis method utilized the following modifications of the common instant reduction method: (i) using HCl instead of NaCl for dissolution of the $PdCl_2$, (ii) performing the synthesis process under N_2 inert atmosphere and ice-bath cooling, and (iii) addition of solid $NaBH_4$ as a reducing agent. Catalysts prepared by our new synthesis method were fully characterized and compared to catalysts obtained by previously used method [15] (**sections 4.2** and **4.3**). Electrochemical analysis revealed that the above modifications in the synthesis approach are crucial for improved activity and selectivity of ternary PdNiBi/C nanocatalyst toward alkaline EOR. This modified approach points to a new route to developing novel catalysts for energy conversion devices of the future [3].

4.4.2 Physico-Chemical Characterization

Differences in synthesis between $Pd_{85}Ni_{10}Bi_5/C^{(I)}$, $Pd_{85}Ni_{10}Bi_5/C^{(II)}$ and $Pd_{85}Ni_{10}Bi_5/C^{(III)}$ nano-catalysts are summarized in the experimental **section 3.1.1**, but are briefly discussed here again. In all cases the common instant reduction method was modified as follows to generate $Pd_{85}Ni_{10}Bi_5/C^{(II)}$ and $Pd_{85}Ni_{10}Bi_5/C^{(III)}$ catalysts: (a) HCl was used instead of NaCl for improved dissolution of the $PdCl_2$, and (b) the synthesis procedure was performed under N_2 inert atmosphere and with ice-bath cooling. Furthermore, solid or liquid $NaBH_4$ was used for the synthesis of $Pd_{85}Ni_{10}Bi_5/C^{(II)}$ and $Pd_{85}Ni_{10}Bi_5/C^{(III)}$, respectively. $Pd_{85}Ni_{10}Bi_5/C^{(I)}$ was prepared by the common instant reduction method according to catalysts from **section 4.2** and **4.3** [15]. The elemental composition, crystal structure, and morphology (i.e., particle size, crystallinity and shape) of all developed carbon supported ternary PdNiBi nanoparticles on Vulcan XC72R support were comprehensively analyzed by various physico-chemical characterization methods, such as ICP-OES, TEM-EDX, XRD and XPS [3].

The elemental concentrations of the carbon supported $Pd_xNi_yBi_z$ nanocatalysts and commercial Pd/C catalyst were determined using ICP-OES (summarized in Table 42), which revealed that atomic concentrations of synthesized anode catalysts agree with targeted values for $Pd_{85}Ni_{10}Bi_5$. As expected, quantitative analysis for commercial Pd/C catalyst revealed that material is pure with no other contaminants [3]. The morphology, particle size distribution, and the chemical composition of each synthesized carbon supported $Pd_{85}Ni_{10}Bi_5$ catalyst were also characterized by TEM with low and high magnification (Figures 38 and 39, and Figures 69, 71 and 73 in the Appendix A) [3].

Results on Figures 38a and 38b revealed that the agglomeration of the $Pd_{85}Ni_{10}Bi_5/C^{(II)}$ and $Pd_{85}Ni_{10}Bi_5/C^{(III)}$ nanoparticles on Vulcan XC72R carbon support was drastically reduced compared to the $Pd_{85}Ni_{10}Bi_5/C^{(I)}$ nanoparticles on Figure 69 in the Appendix A and the other $Pd_xNi_yBi_z/C$ catalysts from **sections 4.2** and **4.3** [15], which were developed by the common instant reduction synthesis method [3]. EDX spectra from chosen areas of corresponding STEM-HAADF micrograph (see Figure 70 in the Appendix A) further demonstrate that the Pd, Ni, and Bi nanoparticles of all ternary $Pd_{85}Ni_{10}Bi_5/C$ catalysts are homogeneously distributed on carbon support material. The obtained TEM-EDX results of the $Pd_{85}Ni_{10}Bi_5/C$ catalysts (atomic concentrations of Pd, Ni, and Bi) are summarized in Tables 43–45, and are in good agreement with the ICP-OES results (Table 42) [3].

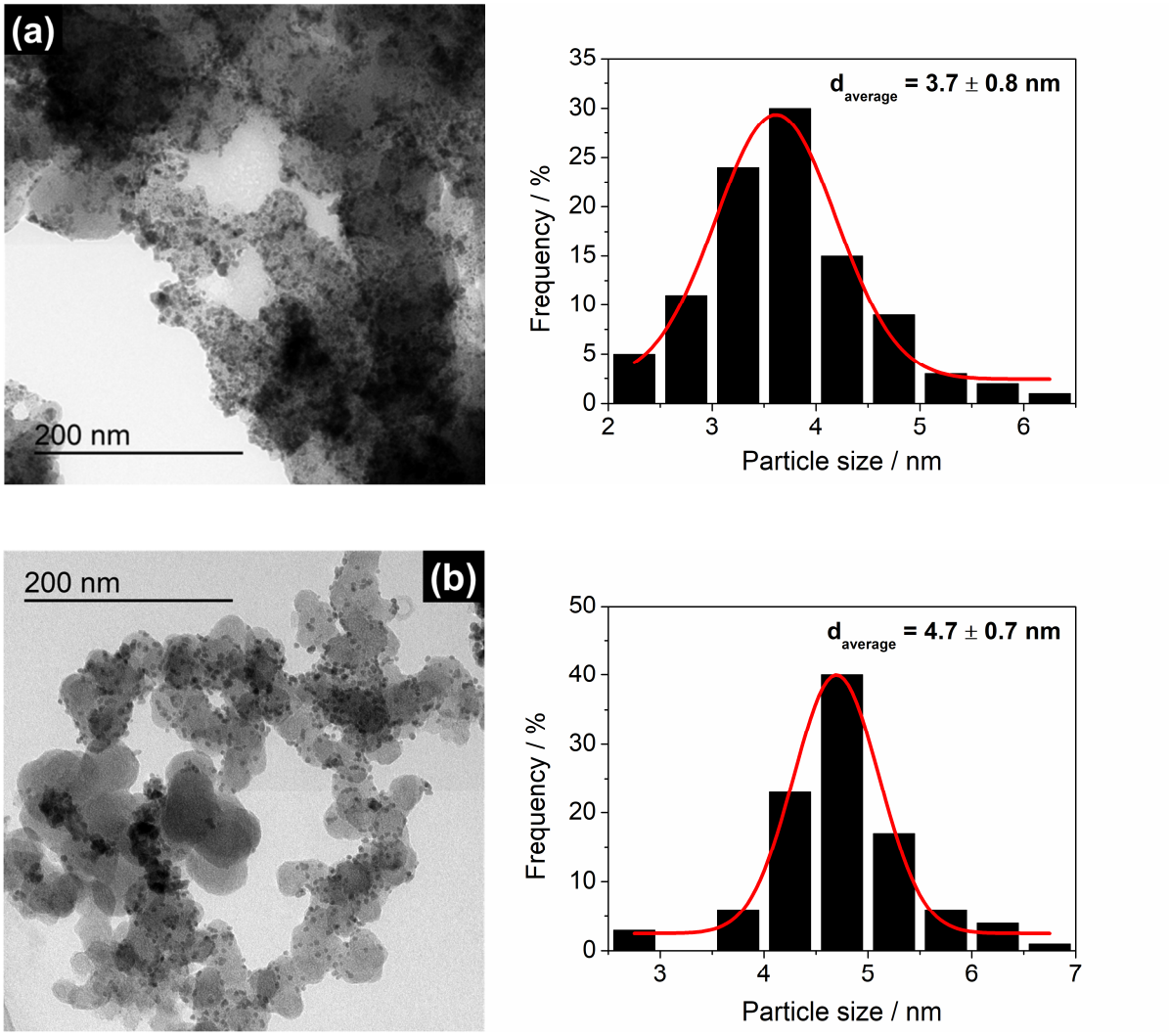


Figure 38: TEM micrographs and particle size distribution histograms including the determined average particle size of the **(a)** $Pd_{85}Ni_{10}Bi_5/C^{(II)}$ and **(b)** $Pd_{85}Ni_{10}Bi_5/C^{(III)}$ catalyst [3].

Particle size distribution and average particle diameter ($d_{average}$) were evaluated from TEM images (Figures 38a and 38b), with $Pd_{85}Ni_{10}Bi_5/C^{(II)}$ catalyst exhibiting smaller particles ($d_{average}$ = 3.7 ± 0.8 nm) as compared to $Pd_{85}Ni_{10}Bi_5/C^{(III)}$ ($d_{average}$ = 4.7 ± 0.7 nm). This difference is attributed to the use of solid $NaBH_4$ during the synthesis of $Pd_{85}Ni_{10}Bi_5/C^{(III)}$ as compared to the use of liquid $NaBH_4$ for $Pd_{85}Ni_{10}Bi_5/C^{(II)}$. In both cases the nanoparticles are significantly more evenly dispersed on the carbon support, which we attribute in part to the inert N_2 atmosphere used in synthesis. Synthesis of the $Pd_{85}Ni_{10}Bi_5/C^{(I)}$ under ambient atmosphere most likely results in the formation of various undesired oxide species, which easily tend to agglomerate with metal ions on the carbon support material (see catalysts from **sections 4.2** and **4.3** in Figure 50 and Figures 60–63 in the Appendix A [15]). Improved dispersion of $Pd_{85}Ni_{10}Bi_5/C^{(II)}$ and $Pd_{85}Ni_{10}Bi_5/C^{(III)}$ is likely also driven by improved solubility of the precursor salt $PdCl_2$ due to the substitution of HCl for the NaCl used to synthesize $Pd_{85}Ni_{10}Bi_5/C^{(I)}$ [3].

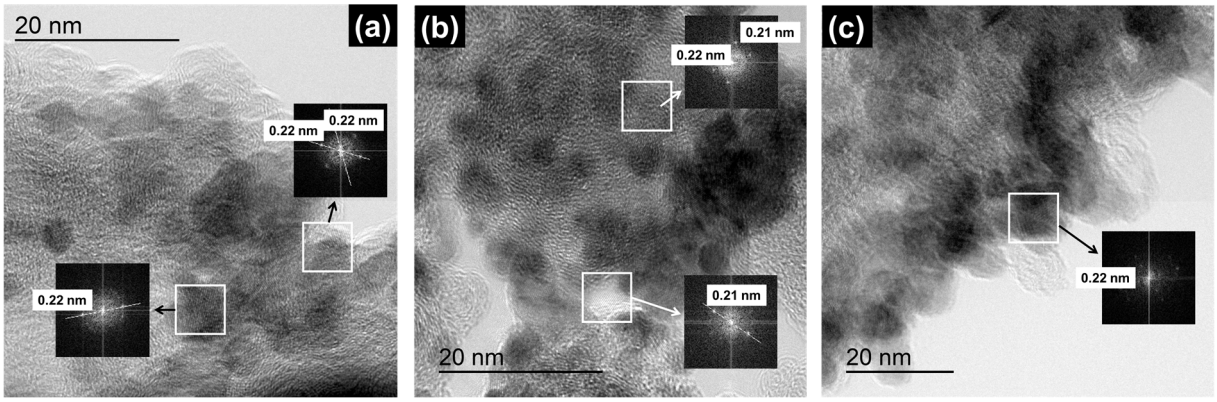


Figure 39: HRTEM micrographs with determined *d*-spacing of the **(a)** $Pd_{85}Ni_{10}Bi_5/C^{(I)}$, **(b)** $Pd_{85}Ni_{10}Bi_5/C^{(II)}$ and **(c)** $Pd_{85}Ni_{10}Bi_5/C^{(III)}$ catalyst [3].

This is supported by the presence of chloride in the $Pd_{85}Ni_{10}Bi_5/C^{(I)}$ catalyst identified by TEM-EDX (Figure 70) as well as XPS analysis (Figure 75b), whereas no chlorides were detected in the other ternary catalyst samples (Figures 72, 74, 75c and 75d). The use of ice-bath cooling during the catalyst synthesis using the modified instant method likely further contributes to more homogeneous reduction of the precursor salts to metals on the carbon support material, thus resulting in better dispersibility of the PdNiBi nanoparticles [3].

Fast Fourier transforms of catalyst particles in the HRTEM micrographs in Figure 39 reveal intensity consistent with an interplanar spacing of ~0.22 nm for all ternary $Pd_{85}Ni_{10}Bi_5/C$ catalysts, which corresponds to the (111) plane spacing of the fcc crystalline structure of Pd [3].

XRD analysis of all carbon supported $Pd_{85}Ni_{10}Bi_5$ catalysts, as well as the commercial Pd/C catalyst, also show the characteristic diffraction peaks at 2θ values of 40°, 47°, 68°, 82° and 87° (Figure 40a), which are further consistent with the (111), (200), (220), (311) and (222) spacings of the fcc Pd crystalline structure (Pd_64922-ICSD) (Tables 46–49). The Pd (111) *d*-spacing of all ternary catalysts (Table 13) are also in good agreement with those measured from HRTEM analysis (Figure 39). The diffraction peak at ~25° for all catalyst samples is identified as the (002) plane of graphite (2H_187640-ICSD) from the carbon black Vulcan XC72R (Figure 40a and Tables 46–49 in the Appendix A) and is consistent with the previous observation in Figures 20 and 30 [15]. The additional diffraction peak present in the commercial Pd/C catalyst at 2θ of 31.6° (Figure 40a and Table 46 in the Appendix A) is attributed to the (002) plane of NaCl (NaCl_655785-ICSD) [3].

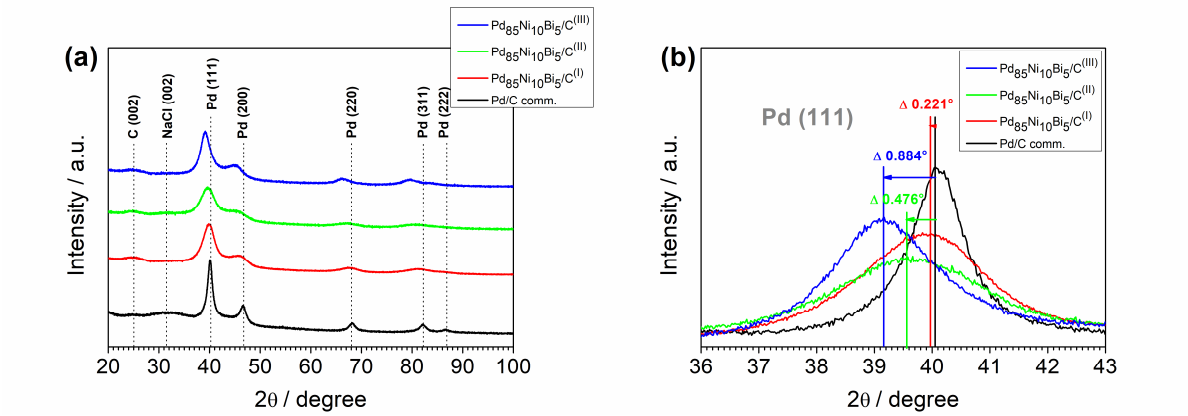


Figure 40: (a) XRD patterns of all $Pd_{85}Ni_{10}Bi_5/C$ nanocatalysts and **(b)** the corresponding position of Pd (111) diffraction peak compared to the commercial Pd/C nanocatalyst [3].

Figure 40b shows that the typical diffraction peaks for all $Pd_{85}Ni_{10}Bi_5/C$ nanocatalysts shift to lower 2θ values compared to the commercial Pd/C catalyst, with peak shifts increasing in following order: $Pd_{85}Ni_{10}Bi_5/C^{(I)}$ (Δ 0.221°) < $Pd_{85}Ni_{10}Bi_5/C^{(II)}$ (Δ 0.476°) < $Pd_{85}Ni_{10}Bi_5/C^{(III)}$ (Δ 0.884°). The precise peak positions of all catalyst samples are given in the Tables 46–53 (see Appendix A). The higher lattice parameters and *d*-spacings of all $Pd_{85}Ni_{10}Bi_5/C$ nanocatalysts compared to the commercial Pd/C catalyst (Table 13) are consistent with an expansion of Pd lattice due to the incorporation of the Ni and Bi co-catalysts to form an alloy, as has been observed before [14,15,17,26,46,78,137]. The half widths of the typical diffraction peaks for all $Pd_{85}Ni_{10}Bi_5/C$ nanocatalysts are broader than for the commercial Pd/C catalyst, indicating a smaller crystallite size. Average crystallite size for all catalyst samples are estimated in Table 13 according to the Scherrer equation (Equation 17), with crystallite size increasing as follows: $Pd_{85}Ni_{10}Bi_5/C^{(I)}$ < $Pd_{85}Ni_{10}Bi_5/C^{(II)}$ < $Pd_{85}Ni_{10}Bi_5/C^{(III)}$ < Pd/C comm. Details about the determined XRD parameters for evaluation of crystallite size (see Tables 50–53) and XRD data fitted using Rietveld refinement (Tables 46–49) of all catalysts are provided in the Appendix A [3].

Table 13: Determined XRD analysis parameters of all catalyst samples. Average crystallite size estimation according to Scherrer assuming spherical crystallites with cubic crystal system of five diffraction peaks (peak pos.). Determination of half-width (FWHM; B_{obs}), *d*-spacing and lattice parameter by profile-fit and Rietveld refinement, $B_{standard}$ determined from LaB_6 [3].

Catalysts	Lattice parameter (nm)	*d*-spacing Pd (111) (nm)	Crystallite size Pd (nm)
Pd/C comm.	a = 0.3890	0.225	9
$Pd_{85}Ni_{10}Bi_5/C^{(I)}$	a = 0.3953	0.226	3
$Pd_{85}Ni_{10}Bi_5/C^{(II)}$	a = 0.3957	0.228	4
$Pd_{85}Ni_{10}Bi_5/C^{(III)}$	a = 0.4024	0.229	5

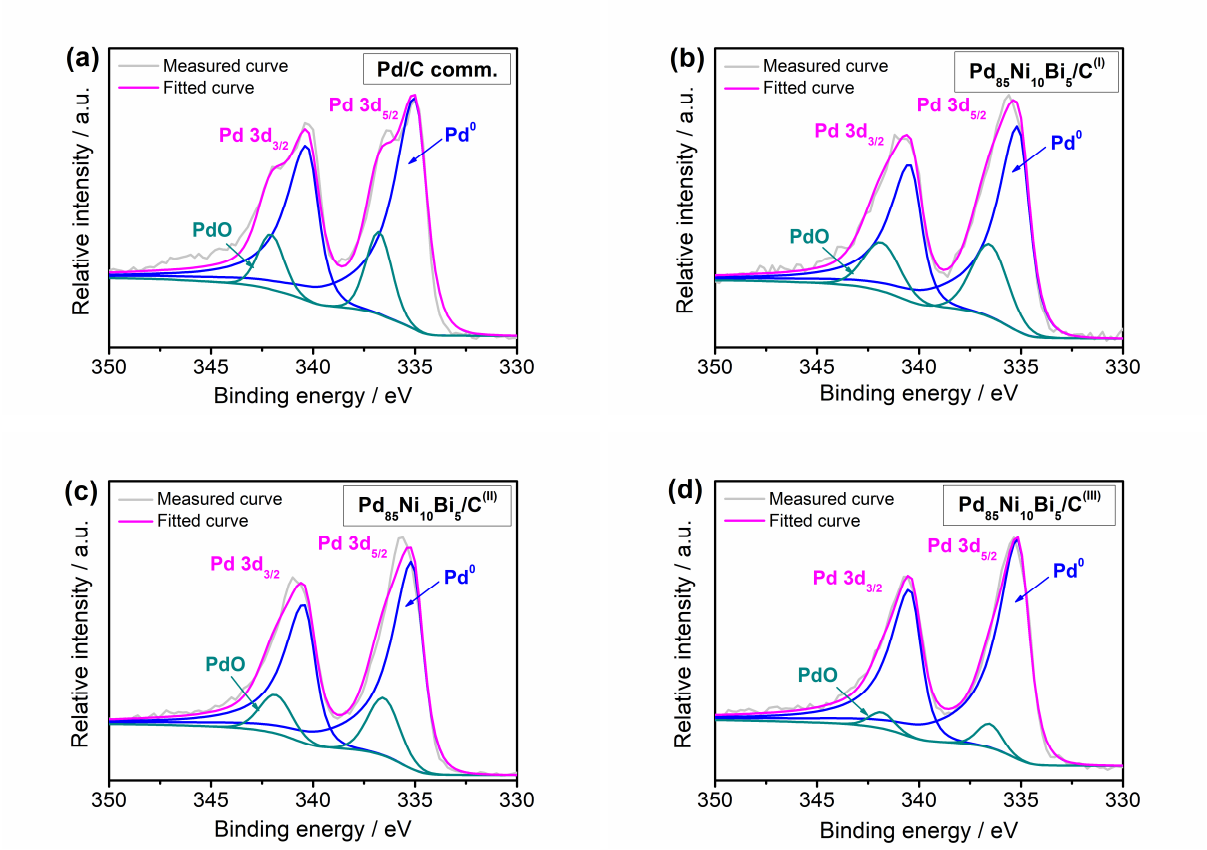


Figure 41: Pd 3d core level XPS spectra of the **(a)** Pd/C comm., **(b)** $Pd_{85}Ni_{10}Bi_5/C^{(I)}$, **(c)** $Pd_{85}Ni_{10}Bi_5/C^{(II)}$ and **(d)** $Pd_{85}Ni_{10}Bi_5/C^{(III)}$ catalyst [3].

The surface oxidation states, chemical compositions and binding energies of Pd, Ni and Bi in the synthesized $Pd_{85}Ni_{10}Bi_5/C$ catalysts and commercial Pd/C catalyst were determined by XPS. Survey spectra and extracted elemental concentrations for all catalysts are summarized in Figure 75 and Tables 54–58, respectively. The $Pd_{85}Ni_{10}Bi_5/C^{(I)}$ catalysts exhibit a slightly higher oxygen content as compared to the others, which is likely due to synthesis in non-inert atmosphere. Core level spectra of Pd 3d, Ni 2p and Bi 4f were analyzed directly from the survey XPS spectra, and deconvolution of the Pd 3d, Ni 2p and Bi 4f spectra was performed to understand the speciation of the different alloy species (see Figure 41, and Figures 76 and 77 in the Appendix A) [3].

Two oxidation states of Pd were identified in the Pd 3d region (Figure 41) – metallic (Pd^0) and PdO (Pd^{II}) – similar to observations in Figures 21 and 31 [3,15]. Figure 41d shows that the $Pd_{85}Ni_{10}Bi_5/C^{(III)}$ catalyst contains the most metallic Pd on the surface relative to PdO as compared with the other ternary catalysts (Figures 41b and 41c), which is likely due to the excess surface Ni content on these samples (Table 58) and may also contribute to the overall lower durability of these catalysts (Figure 42d). The $Pd_{85}Ni_{10}Bi_5/C^{(III)}$ catalyst was found to contain the highest overall Ni content of all three ternary alloys, and fitting of the Ni 2p core

level (Figure 76) reveals that $Ni(OH)_2$ is the main Ni species present on all $Pd_xNi_yBi_z/C$ catalysts. In contrast, $Pd_{85}Ni_{10}Bi_5/C^{(I)}$ catalyst exhibits a slightly higher surface Bi content compared to the $Pd_{85}Ni_{10}Bi_5/C^{(II)}$ and $Pd_{85}Ni_{10}Bi_5/C^{(III)}$ catalysts (Table 58) [3].

Deconvolution of the Bi 4f core levels (Figure 77) reveals similar Bi speciation for all $Pd_{85}Ni_{10}Bi_5/C$ catalysts. The primary peak is consistent with alloyed Bi metal (Bi^0), with the peak position shifted to higher binding energy relative to pure Bi metal due to the strong binding interaction between Bi and platinum-group metals [144,145]. All alloys also contain a small, secondary peak at higher binding energy that is consistent with Bi_2O_3 [3].

4.4.3 Electrochemical Characterization

The EOR performance of the various $Pd_{85}Ni_{10}Bi_5/C$ catalysts synthesized via different procedures was characterized by CV-RDE and CA-RDE and compared to the commercial Pd/C as a benchmark for the alkaline EOR in Figures 42, 43 and 78 [3].

Cyclic voltammograms in the potential range of 0.05-1.2 V were recorded without rotation in de-aerated 1.0 M KOH, as well as in a mixture of 1 M KOH and 1 M EtOH at 30 °C (Figures 42a and 42c) and demonstrate key differences between the different catalyst materials. As expected, in the absence of EtOH the hydrogen adsorption and desorption peaks in the potential region between 0.05 V and 0.5 V (Figure 42c) are suppressed for the ternary catalysts relative to commercial Pd/C. This suppression is due to the presence of bismuth, which lowers the degree of H insertion into the Pd crystal structure due to modified electronic properties as shown previously [3,15,17,138].

The characteristic peak at 0.9 V in CV of the forward scan (Figure 42a) is attributed to the oxidation of $Bi(OH)_3$ in the presence of KOH to form Bi_2O_3 [15,73,138]. Opening the potential window further to 1.5 V (Figure 78a) reveals the oxidation of $Ni(OH)_2$ to NiOOH in the positive scan and subsequent reduction of NiOOH to $Ni(OH)_2$ in the negative scan for all three catalysts, indicating the presence of $Ni(OH)_2$ on the surface of the catalysts that is consistent with the XPS analysis in **sections 4.2.1** and **4.3.1** [15]. Ni redox is more pronounced on $Pd_{85}Ni_{10}Bi_5/C^{(II)}$ and $Pd_{85}Ni_{10}Bi_5/C^{(III)}$ relative to $Pd_{85}Ni_{10}Bi_5/C^{(I)}$ catalyst, which is likely due to the lower overall concentration of Ni on these samples as measured by XPS (Tables 55–58). The $Pd_{85}Ni_{10}Bi_5/C^{(II)}$ catalyst exhibits the highest EASA compared to the other catalysts (Figures 42b and 78b, see experimental methods for details), which may be due to a higher surface Pd content (Table 58) and/or the more homogeneously distributed metal nanoparticles with lower average particle diameter on the carbon support material (Figure 38) [3].

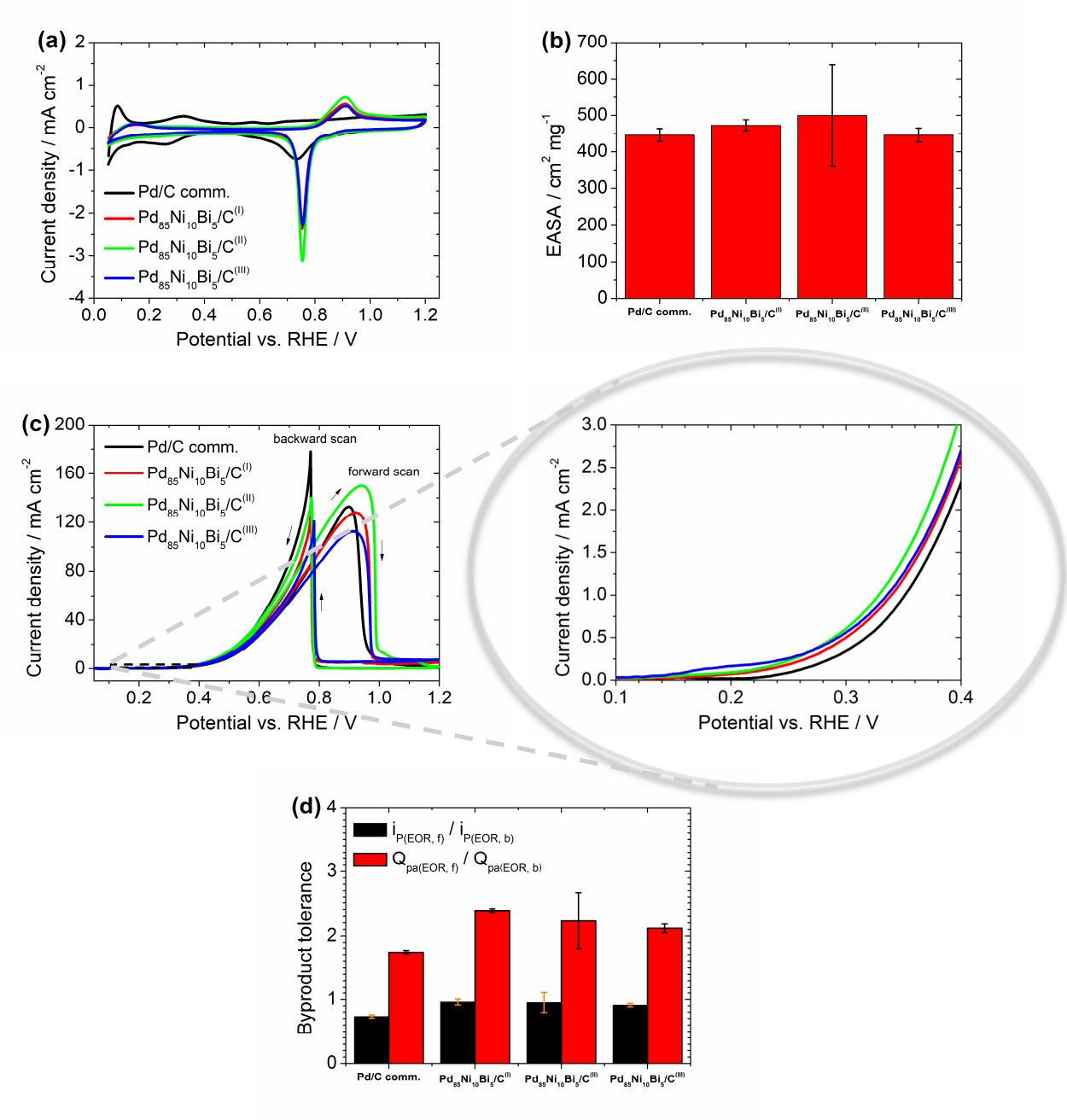


Figure 42: Electrochemical characterization of Pd/C comm., $Pd_{85}Ni_{10}Bi_5/C^{(I)}$, $Pd_{85}Ni_{10}Bi_5/C^{(II)}$ and $Pd_{85}Ni_{10}Bi_5/C^{(III)}$ catalysts: **(a)** in de-aerated 1.0 M KOH and **(b)** the resulting EASAs, **(c)** in an electrolyte mixture of 1 M KOH + 1 M EtOH and **(d)** the obtained byproduct tolerances resulting from EOR measurements (see **(c)**) – performed at 30 °C and with a scan rate of 10 $mV \cdot s^{-1}$ [3].

Cyclic voltammograms measured in the presence of EtOH (Figure 42c) can be used to evaluate differences in the kinetics of the alkaline EOR on the various catalysts by measuring the slope from the onset to the peak potential. Note that here the onset potential of the EtOH oxidation for all catalyst samples was determined at 0.1 $mA \cdot cm^{-2}$ due to electrochemical double layer charging effects, and the maximum current in the forward scan was utilized as an indicator for the EOR activity of each catalyst. In that context, Figure 42c and the corresponding zoomed in section show that the EOR activities at low and high potential are different, which

is likely due to the various catalyst surface compositions hindering or promoting the dissociation step of the EtOH oxidation. The $Pd_{85}Ni_{10}Bi_5/C^{(II)}$ catalyst shows the highest peak current density and the lowest onset potential for the alkaline EOR compared to the other catalysts, indicating these catalysts exhibit an optimal content and synergy between the Pd, Ni and Bi species. The $Pd_{85}Ni_{10}Bi_5/C^{(III)}$ catalyst exhibits the lowest EOR activity, which is likely due to excess Ni on the catalyst surface as measured by XPS (Table 58). Indeed, the oxophilic character of Ni leads to additional adsorbed OH on the catalyst surface, which aids in the rapid oxidation of various EtOH species and enhances the byproduct tolerance. However, Ni itself is inactive to alkaline EOR in the useful potential range, hindering the dissociative EtOH adsorption on the active material due to covering of active sites with excess OH, leading to overall lower activity of $Pd_{85}Ni_{10}Bi_5/C^{(III)}$ for the alkaline EOR [3,14,15].

As shown in Figure 42c, the commercial Pd/C catalyst exhibits a higher onset potential toward alkaline EtOH oxidation relative to the other catalysts, which is likely due to the faster poisoning of the Pd active sites by CO-like species at low potentials [26]. In order to assess the relative extent of surface poisoning by intermediates, the ratio of peak current density on the forward and backward scans, as well as the ratio of integrated charge, can serve as a measure of byproduct tolerance (i.e., resistance to surface poisoning) [26,121]. A comparison of these values (Figure 42d) reveals that indeed all $Pd_{85}Ni_{10}Bi_5/C$ catalysts exhibit higher byproduct tolerance relative to commercial Pd/C. The higher Bi content on the surface of $Pd_{85}Ni_{10}Bi_5/C^{(I)}$ compared to $Pd_{85}Ni_{10}Bi_5/C^{(III)}$ (Table 58) likely leads to the improved byproduct tolerance on these catalysts, as Bi affords higher protection of Pd active sites against poisoning of CO-like species from the alkaline EOR [3,140].

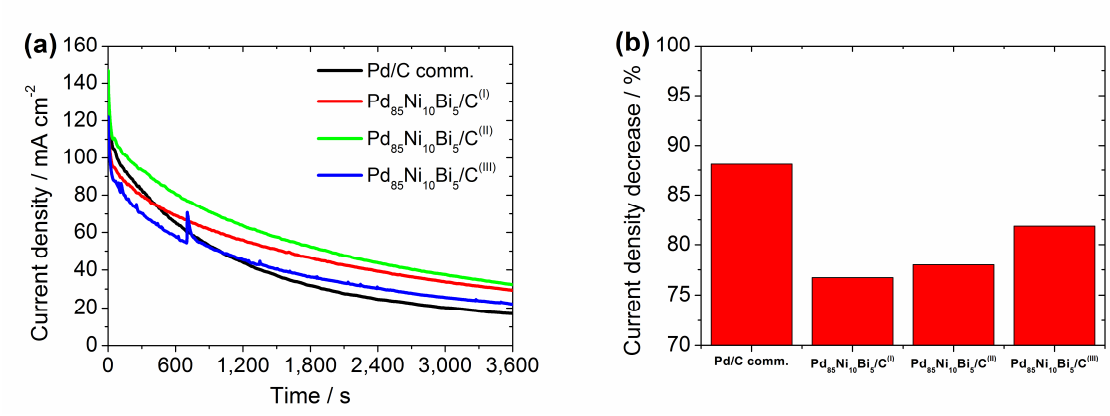


Figure 43: CA-measurements of Pd/C comm., $Pd_{85}Ni_{10}Bi_5/C^{(I)}$, $Pd_{85}Ni_{10}Bi_5/C^{(II)}$ and $Pd_{85}Ni_{10}Bi_5/C^{(III)}$ catalysts: **(a)** in an electrolyte mixture of 1 M KOH + 1 M EtOH and **(b)** the resulting current density decrease percentage at an applied potential of 0.83 V and at 30 °C for 3,600 s [3].

The EOR stabilities of all catalyst samples were further evaluated using CA-RDE at an applied potential of 0.83 V at 30 °C for 1 h (Figure 43) and reveal that stability decreases in the order: $Pd_{85}Ni_{10}Bi_5/C^{(II)}$ ~ $Pd_{85}Ni_{10}Bi_5/C^{(I)}$ < $Pd_{85}Ni_{10}Bi_5/C^{(III)}$ < Pd/C comm., consistent with the byproduct tolerance results (see Figure 42c) [3].

Table 14 summarizes the electrochemical results of all carbon supported $Pd_{85}Ni_{10}Bi_5/C$ nanocatalysts and of the commercial Pd/C catalyst [3].

Table 14: Electrochemical characterization results of carbon supported $Pd_{85}Ni_{10}Bi_5/C$ nanocatalysts developed by instant reduction synthesis method with different modifications compared to commercial Pd/C catalyst [3].

Catalysts	EASA[a] ($cm^2 \cdot mg^{-1}$)	EASA[b] ($cm^2 \cdot mg^{-1}$)	i_f[c] ($mA \cdot cm^{-2}$)	i_b[c] ($mA \cdot cm^{-2}$)	i_f / i_b[d]	$Q_{pa,f}$ / $Q_{pa,b}$[e]	E_{onset}[f] (V)	i_{Start}[g] ($mA \cdot cm^{-2}$)	i_{End}[g] ($mA \cdot cm^{-2}$)	i_D[h] (%)
Pd/C comm.	446 ± 18	-	132.73	178.21	0.732 ± 0.026	1.736 ± 0.029	0.249 ± 0.010	143.25	17.05	88
$Pd_{85}Ni_{10}Bi_5/C^{(I)}$	473 ± 15	746 ± 29	127.83	126.91	0.960 ± 0.047	2.381 ± 0.028	0.206 ± 0.018	125.79	29.29	77
$Pd_{85}Ni_{10}Bi_5/C^{(II)}$	500 ± 139	806 ± 239	149.96	140.04	0.951 ± 0.157	2.229 ± 0.439	0.199 ± 0.052	146.68	32.29	78
$Pd_{85}Ni_{10}Bi_5/C^{(III)}$	446 ± 19	687 ± 35	112.52	120.74	0.911 ± 0.028	2.116 ± 0.066	0.185 ± 0.027	121.92	22.11	82

[a]0.05-1.2 V; [b]0.05-1.5 V; [c]i_f and i_b: peak current density of forward and backward scan; [d]i_f / i_b: byproduct tolerance using peak current density of forward and backward scan; [e]$Q_{pa,f}$ / $Q_{pa,b}$: byproduct tolerance using the charge of the integrated peak current density area of the forward and backward scan; [f]E_{onset}: onset potential of the EtOH oxidation; [g]i_{start} and i_{End}: resulting current densities at an applied potential of 0.83 V after 0 s and 3,600 s. [h]i_D: loss of current density after stress test at an applied potential of 0.83 V for 3,600 s.

4.4.4 Conclusion

In this work, a new synthesis method for carbon supported PdNiBi alloy nanocatalysts has been successfully developed, with modifications in the synthesis method resulting in catalysts with smaller particle size and a more homogeneous distribution on the carbon support. The $Pd_{85}Ni_{10}Bi_5/C^{(II)}$ catalyst displays outstanding specific and mass activity (150 $mA \cdot cm^{-2}$; 2,678 $mA \cdot mg^{-1}$) with a low onset potential (0.207 V) for the alkaline EOR. It was found that the synthesis of the $Pd_{85}Ni_{10}Bi_5/C^{(II)}$ catalyst in N_2 atmosphere, the use of HCl, and the addition of solid $NaBH_4$ result in the highest EOR performance among all catalyst samples, with activity decreasing as: $Pd_{85}Ni_{10}Bi_5/C^{(II)}$ > Pd/C comm. > $Pd_{85}Ni_{10}Bi_5/C^{(I)}$ > $Pd_{85}Ni_{10}Bi_5/C^{(III)}$. We further demonstrate that the addition of Ni and Bi to monometallic Pd improves the EOR stability and byproduct tolerance of all ternary $Pd_{85}Ni_{10}Bi_5/C$ catalysts compared to commercial Pd/C catalyst. However, the durability of catalysts prepared by our modified instant reduction approach was not enhanced when compared to $Pd_xNi_yBi_z/C$ catalysts synthesized via the common instant reduction approach, suggesting there is room for further optimization of this process. Ongoing research is focused on advanced catalyst support materials such as reduced graphene oxide and N-doped graphene that may lead to overall improvements EOR stability and durability. Nevertheless, our synthesis scheme points to a new strategy for optimizing the structure, homogeneity and overall performance of ternary PdNiBi catalysts on carbon supports [3].

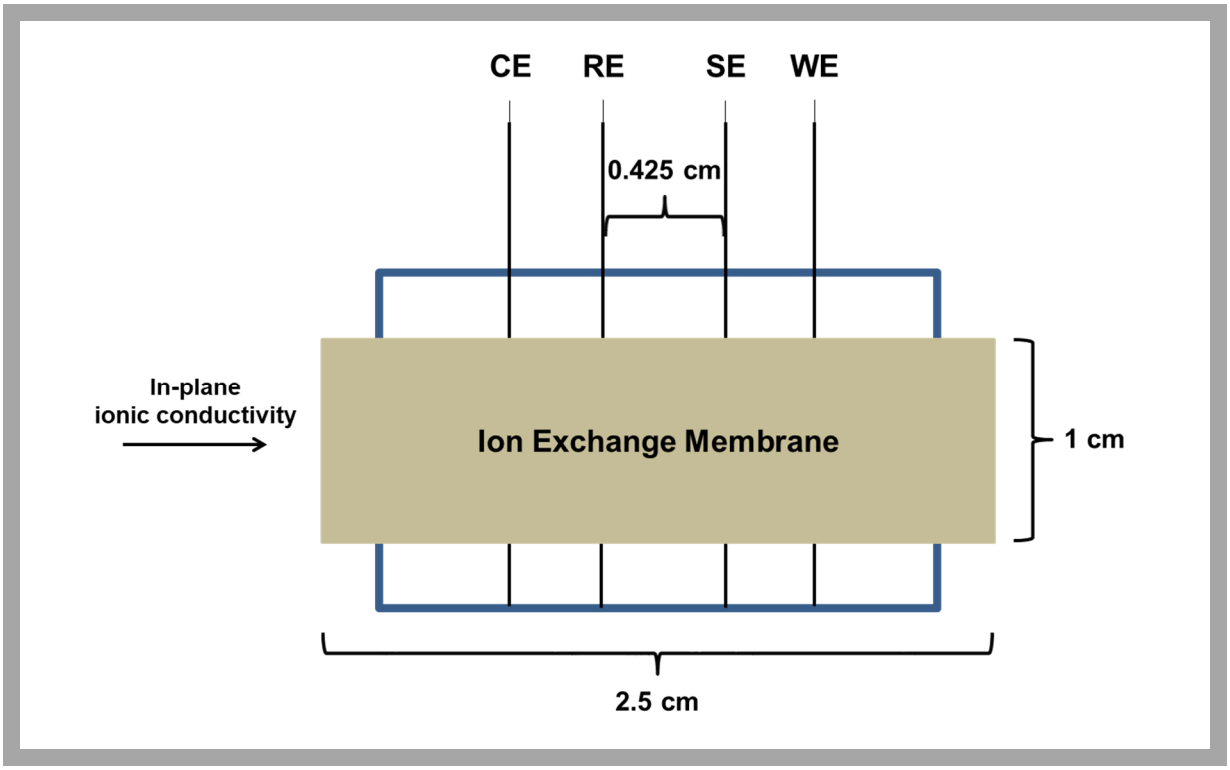
PART V

In-plane Ionic Conductivity Measurements of Various Ion Exchange Membranes for Low Temperature Fuel Cells

4.5 PART V: In-plane Ionic Conductivity Measurements of Various Ion Exchange Membranes for Low Temperature Fuel Cells

Abstract

Part V of the doctoral thesis deals with in-plane ionic conductivity measurements of poly-saccharides-based and commercial AEMs, as well as other CEMs with a conductivity clamp using EIS. This ex-situ analysis method is an appropriate and easy to handle characterization tool for determining the ionic conductivities of fuel cell membranes. Some of these obtained results from the aforementioned kinds of membranes, AEMs for application in ADEFCs and CEMs in polymer electrolyte membrane fuel cells, contribute to four peer-reviewed articles and one conference proceedings article.



Graphical abstract TOC: Schematic of the measurement setup for in-plane ionic conductivity determination of ion exchange membranes using conductivity clamp BT110 with a four-electrode configuration (CE = counter electrode, RE = reference electrode, SE = sensing electrode, WE = working electrode).

Ex-situ EIS Characterization

The ex-situ EIS characterization of ion exchange membranes (IEMs) using the conductivity clamp BT110 is a rapid and easy measurement tool for determining in-plane ionic conductivities. The use of ultra-pure water for the membrane conductivity measurements is required in order to obtain reproducible results and to minimize measurement errors [112–114].

The ionic conductivity of the following IEMs was investigated in the framework of the doctoral thesis:

- AEMs (provided by project partners JR and KFU) with various polymers, such as chitosan, hydroxyethylcellulose ethoxylate and poly (vinyl alcohol), used as backbones quaternized with (2,3 Epoxypropyl)trimethylammonium chloride, acting as a functional conductive group. Various cross-linkers, such as, Ethylene glycol diglycidyl ether, Glutaraldehyde, Methyltriethoxysilane and Tetraethylorthosilicate were utilized for membrane stability [103,114,132].
- Commercial AEMs: FAA3 PEEK130 non-reinforced (Fumatech, Germany) and polybenzimidazole (PBI, Dapazol®, Danish Power Systems®, Denmark)
- Semi-commercial AEM: A201 (Tokuyama Corporation, Japan)
- CEMs (Proton conductive copolymers of 1H,1H,2H,2H-perfluorodecyl acrylate and methacrylic acid, as well as ionomers of hexamethyldisiloxane and methacrylic acid) provided by the research group of Assoc. Prof. Anna-Maria Coclite [112,146].
- Commercial CEMs: Nafion 115 (DuPont, Wilmington, USA) and Nafion XL (QuinTech, Germany) [113]

Ultra-pure water (~18 MΩ·cm, Barnstead NANOpure Water Purification System) was used for all ionic conductivity measurements. Further details about the ex-situ EIS characterization method for ionic conductivity determination of fuel cell membranes are comprehensively described in the publications [112–114,132,146].

The above mentioned AEMs are convenient for application in ADEFCs as well as CEMs in polymer electrolyte membrane fuel cells.

5 Summary

The direct power generation of liquid EtOH in fuel cells without connection on the electricity network and without reforming the process of the fuel used, makes DEFC an alternative energy source to batteries and hydrogen fuel cells. Making it accessible on the fuel cell market requires further intensive research into catalyst and membrane development. The existing challenge of incomplete EtOH oxidation at low temperatures (< 100 °C), which results in a low faradaic efficiency on the present catalysts, is still one of the most critical performance losses of DEFC. However, the alkaline conditions enable an enhancement of EOR and ORR kinetics at the electrodes, a reduction of the EtOH permeability using AEMs, a simplified water management and the use of low-cost materials (e.g., non-noble metals as catalysts) with high stability, leading to performance improvement of this fuel cell type.

Novel ternary $Pd_xNi_yBi_z$ nanoparticles supported on Vulcan XC72R carbon black were successfully developed and proved to be the best performing anode catalysts. They were further optimized by (i) the variation of their atomic ratios and by (ii) the modification of the instant reduction synthesis method for application in ADEFCs. The specific/mass activity, catalytic stability and byproduct tolerance toward alkaline EOR on these ternary nanocatalysts were each determined with electrochemical methods (RDE-CV and RDE-CA) and their elemental composition, structural and morphological properties were characterized with various physicochemical analysis methods (ICP-OES, XRD, XPS and TEM-EDX) in comparison to in-house Pd/C, $Pd_{60}Ni_{40}$/C, $Pd_{60}Bi_{40}$/C catalysts and to a commercial Pd/C catalyst.

The EOR performance of the synthesized carbon supported Pd-based nanocatalysts are influenced by (i) the synthesis method itself, (ii) the content of Ni and Bi, (iii) the crystalline structures present with different shapes and sizes on the catalyst surface and (iv) the homogeneity and nanoparticle distribution on the carbon support material Vulcan XC72R.

- Ni promotes the improvement of EOR kinetic in the synthesized Pd-based anode catalysts by generating more adsorbed OH, which oxidizes rapidly adsorbed EtOH species from the catalyst surface at lower potential than with Bi.
- Bi promotes the byproduct tolerance of alkaline EtOH oxidation and suppresses the hydrogen adsorption/absorption region in binary and ternary Pd-based catalysts. The hydrogen adsorption/absorption process takes place on Pd-based catalysts in the low potential region. The insertion of hydrogen into the crystal structure of Pd changes the

electronic properties of the catalyst and influences the catalytic activity. In this context, the electrochemical phenomenon is reduced by blocking of Bi depending on its content in the carbon supported $Pd_xNi_yBi_z$ anode catalysts.

- The synergy of the oxophilic elements Ni and Bi with Pd depending on the contents significantly facilitates the reaction kinetic and the tolerance to the poisonous byproducts (e.g., CO) of the alkaline EOR on the synthesized ternary $Pd_xNi_yBi_z$/C catalysts.
- The new synthesis approach using the instant reduction method promotes a higher EOR activity (higher peak current densities with lower onset potential) of the $Pd_xNi_yBi_z$ nanoparticles with smaller particle size, more homogeneous distribution and without tendency to agglomeration on the Vulcan XC72R support, compared to the conventional instant reduction method.

The optimal Ni and Bi concentrations and the synergy between the two elements in relation to Pd in these novel carbon supported ternary $Pd_xNi_yBi_z$ nanocatalysts depending on the synthesis method used, are very crucial for the promotion of EOR performance in the alkaline medium. The three $Pd_xNi_yBi_z$/C anode catalysts such as **$Pd_{60}Ni_{20}Bi_{20}$/C** with the **highest EOR stability** (i_D = 39%) and **high byproduct tolerance** toward poisonous species of the EtOH oxidation (i_f/i_b = 2.60 ± 0.09; $Q_{pa,f}/Q_{pa,b}$ = 5.60 ± 0.27), **$Pd_{70}Ni_{20}Bi_{10}$/C** with **high EOR activity** (106 mA cm^{-2}; 1889 mA·mg^{-1}) and **low onset potential** (0.236 ± 0.005 V), and **$Pd_{85}Ni_{10}Bi_5$/C$^{(II)}$** with the **highest EOR activity** (150 mA·cm^{-2}; 2,678 mA·mg^{-1}) and **lowest onset potential** (0.199 ± 0.052 V), are potential candidates among all the synthesized carbon supported Pt-free catalysts for the ADEFC discussed in this dissertation.

The catalytic performance of the selected ex-situ characterized Pd-based catalysts, such as Pd/C, $Pd_{60}Ni_{40}$/C, $Pd_{60}Ni_{20}Bi_{20}$/C and $Pd_{70}Ni_{20}Bi_{10}$/C, correlated with the results of in-situ measurements that were performed in two different single cell configurations under different operating conditions. In addition to intensive catalyst development and characterization for the ADEFC, the in-plane conductivity of various ion exchange membranes was determined by EIS using the BT110 conductivity clamp, which was carried out by a self-established measurement procedure.

In summary, PdNiBi nanoparticle deposition on Vulcan XC72R carbon black with various atomic compositions, using a modified instant reduction synthesis method under defined ex-situ electrochemical characterization parameters and conditions (T = 30 °C, electrolyte = 1 M KOH + 1 M EtOH, catalyst loading = 56 $\mu g_{Pd} \cdot cm^{-2}$, scan rate = 10 mV·s^{-1}, rotation speed = 0 rpm), leads to highly active and stable EOR nanocatalysts in consideration of different influencing factors such as structure, morphology, catalyst composition and support material for use in ADEFC anodes.

6 Outlook

The international project 'GO DEFC', funded by FWF from January 2019 (details in the Appendix C; **section 10.1**), is based on the present doctoral thesis in relation to electro-catalysis. The ongoing research project at CEET (TU Graz), in collaboration with the University of Maribor (UM) and the University of Ljubljana (UL), continues to focus on optimizing the EOR performance of this novel carbon supported ternary PdNiBi nanocatalyst in an alkaline medium by (i) use of other synthesis methods (e.g., bromide anion exchange, nanocapsule, core-shell or polyol method), (ii) insertion of advanced catalyst support materials such as reduced graphene oxide (rGO), N-doped graphene or functionalized GO instead of the state-of-the-art catalyst support Vulcan XC72R and by (iii) more detailed and intensive catalyst characterization regarding the physico-chemical and electrochemical properties for application in DEFCs.

These graphene-based materials, provided from project partner UL, are used due to their approx. 10-fold higher surface area, higher electronic conductivity and higher corrosion resistance compared to conventional Vulcan XC72R [96], with the aim of increasing the catalytic efficiency of the active metal surface, as well as improving the long-term catalytic stability against alkaline EtOH oxidation on the novel carbon supported ternary PdNiBi anode catalyst system.

The following new approaches to further improve the EOR performance of the carbon supported ternary PdNiBi anode catalyst for the ADEFC are listed below:

- The reduction of the metal precursor salts to the respective metals on the catalyst support material could be carried out according to the size of the ion radius of containing elements in the ternary anode catalyst (order of reduction of the precursor salts: $BiCl_3$ > $PdCl_2$ > $Ni(NO_3)_2 \cdot 6H_2O$), for controlling and utilizing its excellent catalytic properties. It would be reasonable if all precursor salts are used as chloride form for the further synthesis of the $Pd_xNi_yBi_z$/C catalyst.
- The addition of Au, Cu or $Ni(II)(DMG)_2$ complex, which were already electrochemically tested for the alkaline EOR in the present doctoral thesis, would be the next approach to further improve the EOR performance of this ternary PdNiBi/C catalyst. Polyaniline is another additive that could enhance the catalytic ability for the alkaline EOR [147] and especially the byproduct tolerance toward poisonous CO species [38].

- Enlargement of the surface area of Vulcan XC72R by thermal and/or acidic pre-treatment for an enhancement efficient catalytic utilization of the active material used [148,149].
- In addition to the insertion of advanced graphene-based materials as catalyst supports, instead of the common Vulcan XC72R, other chemicals will also be used for synthesis of the ternary PdNiBi/C nanocatalysts in order to further investigate the influence on their catalytic ability toward the alkaline EOR. For example, the addition of another reducing agent (e.g., ascorbic acid) instead of $NaBH_4$ [133] or $NaBH_4$ under ice-cooling to the precursor solutions is reduced the hydrogen evolution. Furthermore, the direct use of Na_2PdCl_4 [91,150] and K_2PdCl_4 [134,136] as Pd precursors, instead of $PdCl_2$ for the synthesis of the carbon supported PdNiBi catalyst, is also possible.

The following analyses could provide more information and new insights about the electro-chemical and physico-chemical properties of the novel carbon supported ternary PdNiBi anode catalyst:

- The use of a teflon cell is preferred over a glass cell for the electrochemical characterization of catalysts in alkaline media due to the glass corrosion that occurs, as demonstrated by Mayrhofer et al. [151]. The catalysts are particularly deactivated in the long-term stability tests (RDE-CA measurements) by the contaminations leached out of the glass used. This could be one of many possible reasons for the decrease of the current density after 1 h stress test at a constant potential of 0.83 V. Therefore, future work will include the influence of impurities from dissolved glass on the ternary PdNiBi/C catalyst [3].
- The EASA determination of the catalyst with another method, such as CO stripping tests [119], enhances the reproducibility of the results. The CO tolerance of the catalyst used could also be determined by CO stripping tests [76,83].
- The catalyst layer on RDE might be investigated with light microscopy before electro-chemical characterization is carried out. In addition, the localized distribution of Pd, Ni and Bi on the Vulcan XC72R carbon black could analyze by STEM-EDX mapping [150] to gain a better understanding of their electrochemical results.
- The influence of a reduced metal loading from 40 to 20 wt.% or lower on the catalyst support material, as well as the catalyst loading on the GC-RDE, will be electro-chemically characterized toward the alkaline EOR on this novel catalyst in future studies.
- A RDE-CV study on a thinner catalyst layer of the PdNiBi/C (i.e. lower catalyst loading) could provide detailed information about its intrinsic behavior.

- TEM-EDX, XRD and XPS characterizations of the ternary anode catalyst, before and after fuel cell tests (in-situ) or long-term stability tests (ex-situ: e.g., CA measurements at different applied potentials over 24 h or recording of 1000 CV cycles in 1.0 M KOH and in a mixture of 1 M KOH and 1 M EtOH), would certainly provide additional information about its physico-chemical properties.
- The possible resulting EtOH oxidation intermediates during the EtOH oxidation process on the catalyst used can be identified by investigation of pH change from anodic to cathodic scan in the CV measurements [152]. The resulting intermediates of the EtOH oxidation on the PdNiBi/C catalyst can also be determined by other various characterization methods (e.g., DEMS, HPLC, NMR spectroscopy, online in-situ FTIR spectroscopy or in-situ PM-IRRAS) after fuel cell tests in the anode exhaust or during/after RDE measurements.

This novel highly active carbon supported ternary PdNiBi anode catalyst would undoubtedly be patentable for the application in DEFCs if new features are implemented in future works.

7 References

[1] Zhang, L.; Wang, H.; Li, X.; Xia, F.; Liu, Y.; Xu, X.; Gao, J.; Xing, F. One-step synthesis of palladium-gold-silver ternary nanoparticles supported on reduced graphene oxide for the electrooxidation of methanol and ethanol. *Electrochim. Acta*, **2015**, *172*, 42–51.

[2] Antolini, E. Catalysts for direct ethanol fuel cells. *J. Power Sources*, **2007**, *170*, 1–12.

[3] Cermenek, B.; Genorio, B.; Winter, T.; Wolf, S.; Connell, J.G.; Roschger, M.; Letofsky-Papst, I.; Kienzl, N.; Bitschnau, B.; Hacker, V. Alkaline Ethanol Oxidation Reaction on Carbon Supported Ternary PdNiBi Nanocatalyst using Modified Instant Reduction Synthesis Method. *Electrocatalysis*, **2020**, *11*, 203–214.

[4] Ong, B.C.; Kamarudin, S.K.; Basri, S. Direct liquid fuel cells: A review. *Int. J. Hydrogen Energy*, **2017**, *42*, 10142–10157.

[5] Soloveichik, G.L. Liquid fuel cells. *Beilstein J. Nanotechnol.*, **2014**, *5*, 1399–1418.

[6] Nacef, M.; Affoune, A.M. Comparison between direct small molecular weight alcohols fuel cells' and hydrogen fuel cell's parameters at low and high temperature. Thermodynamic study. *Int. J. Hydrogen Energy*, **2011**, *36*, 4208–4219.

[7] Ferreira, H.L.; Garde, R.; Fulli, G.; Kling, W.; Lopes, J.P. Characterisation of electrical energy storage technologies. *Energy*, **2013**, *53*, 288–298.

[8] Schenk, A.; Cermenek, B.; Hacker, V. Chapter 5 - Other Polymer Electrolyte Fuel Cells. In *Fuel Cells and Hydrogen: From Fundamentals to Applied Research*; Hacker, V.; Mitsushima, S., Eds.; Elsevier Inc.: Amsterdam, **2018**; pp. 91–115.

[9] An, L.; Zhao, T.S.; Li, Y.S. Carbon-neutral sustainable energy technology: Direct ethanol fuel cells. *Renew. Sustain. Energy Rev.*, **2015**, *50*, 1462–1468.

[10] Zhao, T.S.; Li, Y.S.; Shen, S.Y. Anion-exchange membrane direct ethanol fuel cells: Status and perspective. *Front. Energy Power Eng. China*, **2010**, *4*, 443–458.

[11] An, L.; Zhao, T.S. Transport phenomena in alkaline direct ethanol fuel cells for sustainable energy production. *J. Power Sources*, **2017**, *341*, 199–211.

[12] Shen, S.Y.; Zhao, T.S.; Xu, J.B.; Li, Y.S. Synthesis of PdNi catalysts for the oxidation of ethanol in alkaline direct ethanol fuel cells. *J. Power Sources*, **2010**, *195*, 1001–1006.

[13] Shen, S.Y.; Zhao, T.S.; Wu, Q.X. Product analysis of the ethanol oxidation reaction on

palladium-based catalysts in an anion-exchange membrane fuel cell environment. *Int. J. Hydrogen Energy*, **2012**, *37*, 575–582.

[14] Zhang, Z.; Xin, L.; Sun, K.; Li, W. Pd-Ni electrocatalysts for efficient ethanol oxidation reaction in alkaline electrolyte. *Int. J. Hydrogen Energy*, **2011**, *36*, 12686–12697.

[15] Cermenek, B.; Ranninger, J.; Feketeföldi, B.; Letofsky-Papst, I.; Kienzl, N.; Bitschnau, B.; Hacker, V. Novel highly active carbon supported ternary PdNiBi nanoparticles as anode catalyst for the alkaline direct ethanol fuel cell. *Nano Res.*, **2019**, *12*, 683–693.

[16] Bušić, A.; Mardetko, N.; Kundas, S.; Morzak, G.; Belskaya, H.; Šantek, M.I.; Komes, D.; Novak, S.; Šantek, B. Bioethanol Production from Renewable Raw Materials and Its Separation and Purification: A Review. *Food Technol. Biotechnol.*, **2018**, *56*, 289–311.

[17] Neto, A.O.; Tusi, M.M.; de Oliveira Polanco, N.S.; da Silva, S.G.; Santos, M.C.; Spinacé, E. V. PdBi/C electrocatalysts for ethanol electro-oxidation in alkaline medium. *Int. J. Hydrogen Energy*, **2011**, *36*, 10522–10526.

[18] Wu, Q.; Jiang, L.; Qi, L.; Yuan, L.; Wang, E.; Sun, G. Electrocatalytic activity and stability of Ag-MnO_x/C composites toward oxygen reduction reaction in alkaline solution. *Electrochim. Acta*, **2014**, *123*, 167–175.

[19] Yu, E.H.; Wang, X.; Krewer, U.; Li, L.; Scott, K. Direct oxidation alkaline fuel cells: from materials to systems. *Energy Environ. Sci.*, **2012**, *5*, 5668–5680.

[20] Ozoemena, K.I. Nanostructured platinum-free electrocatalysts in alkaline direct alcohol fuel cells: catalyst design, principles and applications. *RSC Adv.*, **2016**, *6*, 89523–89550.

[21] Monyoncho, E.A.; Woo, T.K.; Baranova, E.A. Ethanol electrooxidation reaction in alkaline media for direct ethanol fuel cells. In *SPR Electrochemistry*; Banks, C.; McIntosh, S., Eds.; **2019**; *Vol. 15*, pp. 1–57.

[22] Antolini, E.; Gonzalez, E.R. Alkaline direct alcohol fuel cells. *J. Power Sources*, **2010**, *195*, 3431–3450.

[23] Kakaei, K.; Dorraji, M. One-pot synthesis of Palladium Silver nanoparticles decorated reduced graphene oxide and their application for ethanol oxidation in alkaline media. *Electrochim. Acta*, **2014**, *143*, 207–215.

[24] Song, S.; Wang, Y.; Shen, P. Thermodynamic and Kinetic Considerations for Ethanol Electrooxidation in Direct Ethanol Fuel Cells. *Chinese J. Catal.*, **2007**, *28*, 752–754.

[25] Cermenek, B.; Ranninger, J.; Hacker, V. Alkaline Direct Ethanol Fuel Cell. In *Ethanol Science and Engineering*; Basile, A.; Iulianelli, A.; Dalena, F.; Veziroglu, N.T., Eds.; Elsevier Inc.: Amsterdam, **2019**; pp. 383–405.

[26] Su, P.-C.; Chen, H.-S.; Chen, T.-Y.; Liu, C.-W.; Lee, C.-H.; Lee, J.-F.; Chan, T.-S.; Wang, K.-W. Enhancement of electrochemical properties of Pd/C catalysts toward ethanol oxidation reaction in alkaline solution through Ni and Au alloying. *Int. J. Hydrogen Energy*, **2013**, *38*, 4474–4482.

[27] Singh, R.N.; Singh, A.; Anindita. Electrocatalytic activity of binary and ternary composite films of Pd, MWCNT, and Ni for ethanol electro-oxidation in alkaline solutions. *Carbon*, **2009**, *47*, 271–278.

[28] Ma, L.; Chu, D.; Chen, R. Comparison of ethanol electro-oxidation on Pt/C and Pd/C catalysts in alkaline media. *Int. J. Hydrogen Energy*, **2012**, *37*, 11185–11194.

[29] Ranninger, J. Development and Characterization of Pd-based Catalysts for the alkaline direct ethanol fuel cell, Graz University of Technology, **2017,** p. 85.

[30] Badwal, S.P.S.; Giddey, S.; Kulkarni, A.; Goel, J.; Basu, S. Direct ethanol fuel cells for transport and stationary applications - A comprehensive review. *Appl. Energy*, **2015**, *145*, 80–103.

[31] Tan, J.L.; De Jesus, A.M.; Chua, S.L.; Sanetuntikul, J.; Shanmugam, S.; Tongol, B.J. V.; Kim, H. Preparation and characterization of palladium-nickel on graphene oxide support as anode catalyst for alkaline direct ethanol fuel cell. *Appl. Catal. A Gen.*, **2017**, *531*, 29–35.

[32] Fathirad, F.; Mostafavi, A.; Afzali, D. Bimetallic Pd–Mo nanoalloys supported on Vulcan XC-72R carbon as anode catalysts for direct alcohol fuel cell. *Int. J. Hydrogen Energy*, **2017**, *42*, 3215–3221.

[33] Kamarudin, M.Z.F.; Kamarudin, S.K.; Masdar, M.S.; Daud, W.R.W. Review: Direct ethanol fuel cells. *Int. J. Hydrogen Energy*, **2013**, *38*, 9438–9453.

[34] Zhao, F.; Li, C.; Yuan, Q.; Yang, F.; Luo, B.; Xie, Z.; Yang, X.; Zhou, Z.; Wang, X. Trimetallic palladium–copper–cobalt alloy wavy nanowires improve ethanol electrooxidation in alkaline medium. *Nanoscale*, **2019**, *11*, 19448–19454.

[35] Fang, X.; Wang, L.; Shen, P.K.; Cui, G.; Bianchini, C. An in situ Fourier transform infrared spectroelectrochemical study on ethanol electrooxidation on Pd in alkaline solution. *J. Power Sources*, **2010**, *195*, 1375–1378.

[36] Hassan, K.M.; Hathoot, A.A.; Maher, R.; Abdel Azzem, M. Electrocatalytic oxidation of ethanol at Pd, Pt, Pd/Pt and Pt/Pd nano particles supported on poly 1,8-diaminonaphthalene film in alkaline medium. *RSC Adv.*, **2018**, *8*, 15417–15426.

[37] Bayer, D.; Cremers, C.; Baltruschat, H.; Tübke, J. The Electro-Oxidation of Ethanol in Alkaline Medium at Different Catalyst Metals. *ECS Trans.*, **2011**, *41*, 1669–1680.

[38] Prodromidis, M.I.; Zahran, E.M.; Tzakos, A.G.; Bachas, L.G. Preorganized composite material of polyaniline-palladium nanoparticles with high electrocatalytic activity to methanol and ethanol oxidation. *Int. J. Hydrogen Energy*, **2015**, *40*, 6745–6753.

[39] Santasalo-Aarnio, A.; Kwon, Y.; Ahlberg, E.; Kontturi, K.; Kallio, T.; Koper, M.T.M. Comparison of methanol, ethanol and iso-propanol oxidation on Pt and Pd electrodes in alkaline media studied by HPLC. *Electrochem. commun.*, **2011**, *13*, 466–469.

[40] Monyoncho, E.A.; Steinmann, S.N.; Michel, C.; Baranova, E.A.; Woo, T.K.; Sautet, P. Ethanol Electro-Oxidation on Palladium Revisited Using Polarization Modulation Infrared Reflection Absorption Spectroscopy (PM-IRRAS) and Density Functional Theory (DFT): Why Is It Difficult To Break the C-C Bond? *ACS Catal.*, **2016**, *6*, 4894–4906.

[41] Wu, Z.-P.; Miao, B.; Hopkins, E.; Park, K.; Chen, Y.; Jiang, H.; Zhang, M.; Zhong, C.-J.; Wang, L. Poisonous Species in Complete Ethanol Oxidation Reaction on Palladium Catalysts. *J. Phys. Chem. C*, **2019**, *123*, 20853–20868.

[42] Wang, Y.; Zou, S.; Cai, W.-B. Recent Advances on Electro-Oxidation of Ethanol on Pt- and Pd-Based Catalysts: From Reaction Mechanisms to Catalytic Materials. *Catalysts*, **2015**, *5*, 1507–1534.

[43] Bai, J.; Liu, D.; Yang, J.; Chen, Y. Nanocatalysts for Electrocatalytic Oxidation of Ethanol. *ChemSusChem*, **2019**, *12*, 2117–2132.

[44] Akhairi, M.A.F.; Kamarudin, S.K. Catalysts in direct ethanol fuel cell (DEFC): An overview. *Int. J. Hydrogen Energy*, **2016**, *41*, 4214–4228.

[45] Modibedi, R.M.; Masombuka, T.; Mathe, M.K. Carbon supported Pd-Sn and Pd-Ru-Sn nanocatalysts for ethanol electro-oxidation in alkaline medium. *Int. J. Hydrogen Energy*, **2011**, *36*, 4664–4672.

[46] Wang, L.; Lavacchi, A.; Bevilacqua, M.; Bellini, M.; Fornasiero, P.; Filippi, J.; Innocenti, M.; Marchionni, A.; Miller, H.A.; Vizza, F. Energy Efficiency of Alkaline Direct Ethanol Fuel Cells Employing Nanostructured Palladium Electrocatalysts. *ChemCatChem*, **2015**, *7*, 2214–2221.

[47] Zadick, A.; Dubau, L.; Demirci, U.B.; Chatenet, M. Effects of Pd Nanoparticle Size and Solution Reducer Strength on Pd/C Electrocatalyst Stability in Alkaline Electrolyte. *J. Electrochem. Soc.*, **2016**, *163*, F781–F787.

[48] Lafforgue, C.; Maillard, F.; Martin, V.; Dubau, L.; Chatenet, M. Degradation of Carbon-Supported Platinum-Group-Metal Electrocatalysts in Alkaline Media Studied by in Situ Fourier Transform Infrared Spectroscopy and Identical-Location Transmission Electron Microscopy. *ACS Catal.*, **2019**, *9*, 5613–5622.

[49] Carrera-Cerritos, R.; Salazar-Hernandez, C.; Galindo-Esquivel, I.R.; Fuentes-Ramirez, R. Effect of the Reduction Temperature of PdAg Nanoparticles during the Polyol Process in the Ethanol Electrooxidation Reaction. *J. Nanomater.*, **2018**, *2018*, Article ID 9451421.

[50] Liang, Z.X.; Zhao, T.S.; Xu, J.B.; Zhu, L.D. Mechanism study of the ethanol oxidation reaction on palladium in alkaline media. *Electrochim. Acta*, **2009**, *54*, 2203–2208.

[51] Bianchini, C.; Shen, P.K. Palladium-Based Electrocatalysts for Alcohol Oxidation in Half Cells and in Direct Alcohol Fuel Cells. *Chem. Rev.*, **2009**, *109*, 4183–4206.

[52] Guo, J.; Chen, R.; Zhu, F.C.; Sun, S.G.; Villullas, H.M. New understandings of ethanol oxidation reaction mechanism on Pd/C and Pd_2Ru/C catalysts in alkaline direct ethanol fuel cells. *Appl. Catal. B Environ.*, **2018**, *224*, 602–611.

[53] Cai, J.; Huang, Y.; Guo, Y. Bi-modified Pd/C catalyst via irreversible adsorption and its catalytic activity for ethanol oxidation in alkaline medium. *Electrochim. Acta*, **2013**, *99*, 22–29.

[54] Price history of palladium https://www.gold.de/kurse/palladiumpreis/ (accessed Mar 4, 2020).

[55] Price history of platinum https://www.gold.de/kurse/platinpreis/ (accessed Mar 4, 2020).

[56] Price history of gold https://www.gold.de/kurse/goldpreis/ (accessed Mar 4, 2020).

[57] Palladium price https://www.businesslive.co.za/bd/markets/2019-01-11-palladium-prices-are-still-not-high-enough/ (accessed Sep 12, 2019).

[58] Price of $PdCl_2$ https://www.sigmaaldrich.com/catalog/product/aldrich/14814 (accessed Sep 15, 2019).

[59] Price of $PtCl_4$ https://www.sigmaaldrich.com/catalog/product/mm/807347 (accessed Dec 29, 2019).

[60] Price of $HAuCl_4$·aq https://www.sigmaaldrich.com/catalog/product/aldrich/50780 (accessed Dec 29, 2019).

[61] Annual palladium and platinum mine production in 2017 and 2018 https://seekingalpha.com/article/4270121-platinum-vs-palladium-key-factor-holding-back-platinum-demand-and-price (accessed Oct 4, 2019).

[62] Geraldes, A.N.; Silva, D.F.; Silva, J.C.M.; Souza, R.F.B.; Spinacé, E. V.; Neto, A.O.; Linardi, M.; Santos, M.C. Glycerol Electrooxidation in Alkaline Medium Using Pd/C, Au/C and PdAu/C Electrocatalysts Prepared by Electron Beam Irradiation. *J. Braz. Chem. Soc.*, **2014**, *25*, 831–840.

[63] Liao, F.; Lo, T.W.B.; Tsang, S.C.E. Recent Developments in Palladium-Based Bimetallic Catalysts. *ChemCatChem*, **2015**, *7*, 1998–2014.

[64] Shen, P.K.; Xu, C. Alcohol oxidation on nanocrystalline oxide Pd/C promoted electrocatalysts. *Electrochem. commun.*, **2006**, *8*, 184–188.

[65] Ma, L.; He, H.; Hsu, A.; Chen, R. PdRu/C catalysts for ethanol oxidation in anion-exchange membrane direct ethanol fuel cells. *J. Power Sources*, **2013**, *241*, 696–702.

[66] Zhu, F.; Wang, M.; He, Y.; Ma, G.; Zhang, Z.; Wang, X. A comparative study of elemental additives (Ni, Co and Ag) on electrocatalytic activity improvement of PdSn-based catalysts for ethanol and formic acid electro-oxidation. *Electrochim. Acta*, **2014**, *148*, 291–301.

[67] Moraes, L.P.R.; Matos, B.R.; Radtke, C.; Santiago, E.I.; Fonseca, F.C.; Amico, S.C.; Malfatti, C.F. Synthesis and performance of palladium-based electrocatalysts in alkaline direct ethanol fuel cell. *Int. J. Hydrogen Energy*, **2016**, *41*, 6457–6468.

[68] Tusi, M.M.; Polanco, N.S.O.; da Silva, S.G.; Spinacé, E. V.; Neto, A.O. The high activity of PtBi/C electrocatalysts for ethanol electro-oxidation in alkaline medium. *Electrochem. commun.*, **2011**, *13*, 143–146.

[69] Nikiforova, T.G.; Datskevich, O.A.; Maleev, V. V. Palladium catalysts on porous nickel substrates for alcohol fuel cells. *Russ. J. Appl. Chem.*, **2012**, *85*, 1871–1878.

[70] Yang, H.; Wang, H.; Li, H.; Ji, S.; Davids, M.W.; Wang, R. Effect of stabilizers on the synthesis of palladium-nickel nanoparticles supported on carbon for ethanol oxidation in alkaline medium. *J. Power Sources*, **2014**, *260*, 12–18.

[71] Bidwell, L.R.; Speiser, R. Unit-cell dimensions of Ni-Pd alloys at 25 and 900°C. *Acta Crystallogr.*, **1964**, *17*, 1473–1474.

[72] Vegard, L. Die Konstitution der Mischkristalle und die Raumfüllung der Atome. *Zeitschrift für Phys.*, **1921**, *5*, 17–26.

[73] Casella, I.G.; Contursi, M. Characterization of bismuth adatom-modified palladium electrodes: The electrocatalytic oxidation of aliphatic aldehydes in alkaline solutions. *Electrochim. Acta*, **2006**, *52*, 649–657.

[74] Yang, H.; Yu, Z.; Li, S.; Zhang, Q.; Jin, J.; Ma, J. Ultrafine palladium-gold-phosphorus ternary alloyed nanoparticles anchored on ionic liquids-noncovalently functionalized carbon nanotubes with excellent electrocatalytic property for ethanol oxidation reaction in alkaline media. *J. Catal.*, **2017**, *353*, 256–264.

[75] Zhang, Y.; Yi, Q.; Deng, Z.; Zhou, X.; Nie, H. Excellent Electroactivity of Ternary Pd–Ag–Sn Nanocatalysts for Ethanol Oxidation. *Catal. Letters*, **2018**, *148*, 1190–1201.

[76] Shu, Y.; Shi, X.; Ji, Y.; Wen, Y.; Guo, X.; Ying, Y.; Wu, Y.; Yang, H. Hollow Echinus-like PdCuCo Alloy for Superior Efficient Catalysis of Ethanol. *ACS Appl. Mater. Interfaces*, **2018**, *10*, 4743–4749.

[77] Huang, Y.; Guo, Y.; Wang, Y.; Yao, J. Synthesis and performance of a novel PdCuPb/C nanocatalyst for ethanol electrooxidation in alkaline medium. *Int. J. Hydrogen Energy*, **2014**, *39*, 4274–4281.

[78] Wang, Y.; Shi, F.-F.; Yang, Y.-Y.; Cai, W.-B. Carbon supported Pd-Ni-P nanoalloy as an efficient catalyst for ethanol electro-oxidation in alkaline media. *J. Power Sources*, **2013**, *243*, 369–373.

[79] Shen, S.; Zhao, T.S.; Xu, J.; Li, Y. High performance of a carbon supported ternary PdIrNi catalyst for ethanol electro-oxidation in anion-exchange membrane direct ethanol fuel cells. *Energy Environ. Sci.*, **2011**, *4*, 1428–1433.

[80] Dutta, A.; Datta, J. Outstanding Catalyst Performance of PdAuNi Nanoparticles for the Anodic Reaction in an Alkaline Direct Ethanol (with Anion-Exchange Membrane) Fuel Cell. *J. Phys. Chem. C*, **2012**, *116*, 25677–25688.

[81] Jiang, R.; Tran, D.T.; McClure, J.P.; Chu, D. A Class of (Pd-Ni-P) Electrocatalysts for the Ethanol Oxidation Reaction in Alkaline Media. *ACS Catal.*, **2014**, *4*, 2577–2586.

[82] Yi, Q.; Chu, H.; Chen, Q.; Yang, Z.; Liu, X. High Performance Pd, PdNi, PdSn and PdSnNi Nanocatalysts Supported on Carbon Nanotubes for Electrooxidation of C2-C4 Alcohols. *Electroanalysis*, **2015**, *27*, 388–397.

[83] Jongsomjit, S.; Prapainainar, P.; Sombatmankhong, K. Synthesis and characterisation of Pd-Ni-Sn electrocatalyst for use in direct ethanol fuel cells. *Solid State Ionics*, **2016**, *288*, 147–153.

[84] Jana, R.; Dhiman, S.; Peter, S.C. Facile solvothermal synthesis of highly active and robust $Pd_{1.87}Cu_{0.11}Sn$ electrocatalyst towards direct ethanol fuel cell applications. *Mater. Res. Express*, **2016**, *3*, 084001.

[85] Rostami, H.; Abdollahi, T.; Mehdipour, P.; Rostami, A.A.; Farmanzadeh, D. Effect of Ni addition on electrocatalytic activity of PdCu catalysts for ethanol electrooxidation: An experimental and theoretical study. *Int. J. Hydrogen Energy*, **2017**, *42*, 24713–24725.

[86] Bambagioni, V.; Bianchini, C.; Filippi, J.; Oberhauser, W.; Marchionni, A.; Vizza, F.; Psaro, R.; Sordelli, L.; Foresti, M.L.; Innocenti, M. Ethanol Oxidation on Electrocatalysts Obtained by Spontaneous Deposition of Palladium onto Nickel-Zinc Materials. *ChemSusChem*, **2009**, *2*, 99–112.

[87] Shinozaki, K.; Zack, J.W.; Richards, R.M.; Pivovar, B.S.; Kocha, S.S. Oxygen Reduction

Reaction Measurements on Platinum Electrocatalysts Utilizing Rotating Disk Electrode Technique. *J. Electrochem. Soc.*, **2015**, *162*, F1144–F1158.

[88] Pollet, B.G.; Goh, J.T.E. The importance of ultrasonic parameters in the preparation of fuel cell catalyst inks. *Electrochim. Acta*, **2014**, *128*, 292–303.

[89] Adamsky, M.; Peressin, N.; Holdcroft, S.; Pollet, B.G. Does power ultrasound affect Nafion® dispersions?. *Ultrason. Sonochem.*, **2020**, *60*, 104758.

[90] Acres, G.J.K.; Hards, G.A. Electrocatalysts for Fuel Cells. *Philos. Trans. R. Soc. A Math. Phys. Eng. Sci.*, **1996**, *354*, 1671–1680.

[91] Kim, M.; Park, J.-N.; Kim, H.; Song, S.; Lee, W.-H. The preparation of Pt/C catalysts using various carbon materials for the cathode of PEMFC. *J. Power Sources*, **2006**, *163*, 93–97.

[92] Yu, X.; Ye, S. Recent advances in activity and durability enhancement of Pt/C catalytic cathode in PEMFC: Part I. Physico-chemical and electronic interaction between Pt and carbon support, and activity enhancement of Pt/C catalyst. *J. Power Sources*, **2007**, *172*, 133–144.

[93] Gwebu, S.S.; Nomngongo, P.N.; Maxakato, N.W. Platinum-Based Carbon Nanodots Nanocatalysts for Direct Alcohol Fuel Cells. In *Nanocatalysts*; Sinha, I.; Shukla, M., Eds.; IntechOpen; **2019**; pp. 1–18.

[94] Pérez-Rodríguez, S.; Pastor, E.; Lázaro, M.J. Electrochemical Behavior of the Carbon Black Vulcan XC-72R: Influence of the Surface Chemistry. *Int. J. Hydrogen Energy*, **2018**, *43*, 7911–7922.

[95] TANG, S.; SUN, G.; QI, J.; SUN, S.; GUO, J.; XIN, Q.; HAARBERG, G.M. Review of New Carbon Materials as Catalyst Supports in Direct Alcohol Fuel Cells. *Chinese J. Catal.*, **2010**, *31*, 12–17.

[96] Liu, M.; Zhang, R.; Chen, W. Graphene-Supported Nanoelectrocatalysts for Fuel Cells: Synthesis, Properties, and Applications. *Chem. Rev.*, **2014**, *114*, 5117–5160.

[97] Vulcan XC72R Carbon Black https://www.fuelcellstore.com/vulcan-xc-72r (accessed Sep 21, 2019).

[98] Xu, J.B.; Zhao, T.S.; Li, Y.S.; Yang, W.W. Synthesis and characterization of the Au-modified Pd cathode catalyst for alkaline direct ethanol fuel cells. *Int. J. Hydrogen Energy*, **2010**, *35*, 9693–9700.

[99] Wang, Q.; Sun, G.Q.; Cao, L.; Jiang, L.H.; Wang, G.X.; Wang, S.L.; Yang, S.H.; Xin, Q. High performance direct ethanol fuel cell with double-layered anode catalyst layer. *J. Power Sources*, **2008**, *177*, 142–147.

[100] An, L.; Zhao, T.S.; Chen, R.; Wu, Q.X. A novel direct ethanol fuel cell with high power density. *J. Power Sources*, **2011**, *196*, 6219–6222.

[101] Li, X.; Sabir, I. Review of bipolar plates in PEM fuel cells: Flow-field designs. *Int. J. Hydrogen Energy*, **2005**, *30*, 359–371.

[102] Company ENAPTER https://www.enapter.com/ (accessed Sep 11, 2019).

[103] Cermenek, B.; Hacker, V.; Feketeföldi, B.; Ribitsch, V. Pt-free anode catalyst systems and composite polysaccharide-membranes for the alkaline DEFC. *End report*, **2017**, p. 73.

[104] Grimmer, C.; Grandi, M.; Zacharias, R.; Cermenek, B.; Weber, H.; Morais, C.; Napporn, T.W.; Weinberger, S.; Schenk, A.; Hacker, V. The electrooxidation of borohydride: A mechanistic study on palladium (Pd/C) applying RRDE, ^{11}B-NMR and FTIR. *Appl. Catal. B Environ.*, **2016**, *180*, 614–621.

[105] Piasentin, R.M.; Spinacé, E.V.; Tusi, M.M.; Neto, A.O. Preparation of PdPtSn/C-Sb_2O_5.SnO_2 electrocatalysts by Borohydride Reduction for Ethanol Electro-Oxidation in Alkaline Medium. *Int. J. Electrochem. Sci.*, **2011**, *6*, 2255–2263.

[106] Grimmer, C.; Zacharias, R.; Grandi, M.; Cermenek, B.; Schenk, A.; Weinberger, S.; Mautner, F.-A.; Bitschnau, B.; Hacker, V. Carbon Supported Ruthenium as Anode Catalyst for Alkaline Direct Borohydride Fuel Cells. *J. Phys. Chem. C*, **2015**, *119*, 23839–23844.

[107] Reetz, M.T.; Lopez, M. Method for in situ immobilization of water-soluble nanodispersed metal oxide colloids. U.S. Patent 7,244,688, July 17, **2007**.

[108] Grimmer, C.; Zacharias, R.; Grandi, M.; Pichler, B.; Kaltenboeck, I.; Gebetsroither, F.; Wagner, J.; Cermenek, B.; Weinberger, S.; Schenk, A.; Hacker, V. A Membrane-Free and Practical Mixed Electrolyte Direct Borohydride Fuel Cell. *J. Electrochem. Soc.*, **2016**, *163*, F278–F283.

[109] Grimmer, C.; Grandi, M.; Zacharias, R.; Weinberger, S.; Schenk, A.; Aksamija, E.; Mautner, F.-A.; Bitschnau, B.; Hacker, V. Carbon Supported Nanocrystalline Manganese Oxide: Surpassing Platinum as Oxygen Reduction Catalyst in Direct Borohydride Fuel Cells. *J. Electrochem. Soc.*, **2016**, *163*, F885–F890.

[110] Sayadi, A.; Pickup, P.G. Evaluation of ethanol oxidation catalysts by rotating disc voltammetry. Electrochim. Acta, **2016**, *215*, 84–92.

[111] Schindelin, J.; Arganda-Carreras, I.; Frise, E.; Kaynig, V.; Longair, M.; Pietzsch, T.; Preibisch, S.; Rueden, C.; Saalfeld, S.; Schmid, B.; Tinevez, J.-Y.; White, D.J.; Harten-

stein, V.; Eliceiri, K.; Tomancak, P.; Cardona, A. Fiji: an open-source platform for biological-image analysis. *Nat. Methods*, **2012**, *9*, 676–682.

[112] Ranacher, C.; Resel, R.; Moni, P.; Cermenek, B.; Hacker, V.; Coclite, A.M. Layered Nanostructures in Proton Conductive Polymers Obtained by Initiated Chemical Vapor Deposition. *Macromolecules*, **2015**, *48*, 6177–6185.

[113] Bodner, M.; Cermenek, B.; Rami, M.; Hacker, V. The Effect of Platinum Electrocatalyst on Membrane Degradation in Polymer Electrolyte Fuel Cells. *Membranes*, **2015**, *5*, 888–902.

[114] Feketeföldi, B.; Cermenek, B.; Spirk, C.; Schenk, A.; Grimmer, C.; Bodner, M.; Koller, M.; Ribitsch, V.; Hacker, V. Chitosan-Based Anion Exchange Membranes for Direct Ethanol Fuel Cells. *J. Membr. Sci. Technol.*, **2016**, *6*, 145.

[115] Chaiburi, C.; Cermenek, B.; Pichler, B.E.; Grimmer, C.; Hacker, V. Ethanol: Tolerant Oxygen Reduction Reaction Catalysts in Alkaline Media. *J. Electrochem. En. Con. Stor.*, **2019**, *16*, 021004.

[116] Chaiburi, C.; Cermenek, B.; Pichler, B.E.; Grimmer, C.; Schenk, A.; Hacker, V. Ethanol - Tolerant Pt-free Cathode Catalysts for the Alkaline Direct Ethanol Fuel Cell. *J. New Mater. Electrochem. Syst.*, **2017**, *19*, 199–207.

[117] Grimmer, I.; Zorn, P.; Weinberger, S.; Grimmer, C.; Pichler, B.; Cermenek, B.; Gebetsroither, F.; Schenk, A.; Mautner, F.-A.; Bitschnau, B.; Hacker, V. Ethanol tolerant precious metal free cathode catalyst for alkaline direct ethanol fuel cells. *Electrochim. Acta*, **2017**, *228*, 325–331.

[118] Hacker, V.; Cermenek, B. IEA AFC Annex 35: Brennstoffzellen für portable Anwendungen: Arbeitsperiode 2014-2017. *End report,* **2017**, p. 34.

[119] Mittermeier, T.; Weiß, A.; Hasché, F.; Gasteiger, H.A. Activity, Stability and Degradation of Carbon Supported Palladium (Pd/C) Fuel Cell Electrocatalysts for the Oxygen Reduction. *ECS Trans.*, **2015**, *69*, 303–313.

[120] Wang, J.; Cheng, N.; Banis, M.N.; Xiao, B.; Riese, A.; Sun, X. Comparative study to understand the intrinsic properties of Pt and Pd catalysts for methanol and ethanol oxidation in alkaline media. *Electrochim. Acta*, **2015**, *185*, 267–275.

[121] Sekol, R.C.; Carmo, M.; Kumar, G.; Gittleson, F.; Doubek, G.; Sun, K.; Schroers, J.; Taylor, A.D. Pd-Ni-Cu-P metallic glass nanowires for methanol and ethanol oxidation in alkaline media. *Int. J. Hydrogen Energy*, **2013**, *38*, 11248–11255.

[122] Wang, Y.; Chen, W.; Pan, D.; Xu, Q.; Ma, J.; Zheng, J.; Li, R. Methanol Electrooxidation Reaction in Alkaline Medium on Glassy Carbon Electrode Modified with Ordered

Mesoporous Ni/Al_2O_3. *Int. J. Electrochem. Sci.*, **2017**, *12*, 2194–2206.

[123] Danaee, I.; Jafarian, M.; Forouzandeh, F.; Gobal, F.; Mahjani, M.G. Electrocatalytic oxidation of methanol on Ni and NiCu alloy modified glassy carbon electrode. *Int. J. Hydrogen Energy*, **2008**, *33*, 4367–4376.

[124] Datta, J.; Dutta, A.; Mukherjee, S. The Beneficial Role of the Cometals Pd and Au in the Carbon-Supported PtPdAu Catalyst Toward Promoting Ethanol Oxidation Kinetics in Alkaline Fuel Cells: Temperature Effect and Reaction Mechanism. *J. Phys. Chem. C*, **2011**, *115*, 15324–15334.

[125] Rivera-González, H.; Torres-Pacheco, L.; Álvarez-Contreras, L.; Olivas, A.; Guerra-Balcázar, M.; Valdez, R.; Arjona, N. Synthesis of Pd–Fe_3O_4 nanoparticles varying the stabilizing agent and additive and their effect on the ethanol electro-oxidation in alkaline media. *J. Electroanal. Chem.*, **2019**, *835*, 301–312.

[126] Cerritos, R.C.; Guerra-Balcázar, M.; Ramírez, R.F.; Ledesma-García, J.; Arriaga, L.G. Morphological Effect of Pd Catalyst on Ethanlol Electro-Oxidation Reaction. *Materials*, **2012**, *5*, 1686–1697.

[127] Bach Delpeuch, A.; Jacquot, M.; Chatenet, M.; Cremers, C. The influence of mass-transport conditions on the ethanol oxidation reaction (EOR) mechanism of Pt/C electrocatalysts. *Phys. Chem. Chem. Phys.*, **2016**, *18*, 25169–25175.

[128] Wang, D.; Chen, S.; Liu, J.; Xu, C. Determination of Diffusion Coefficient of Isopropanol in Alkaline Medium using electrochemical methods on Pd Electrode. *Open Electrochem. J.*, **2010**, *2*, 11–14.

[129] Tosun, İ. *Modelling in Transport Phenomena: A Conceptual Approach*, 2nd ed.; Elsevier B.V: Amsterdam, **2007**.

[130] Barbosa, A.F.B.; Oliveira, V.L.; van Drunen, J.; Tremiliosi-Filho, G. Ethanol electro-oxidation reaction using a polycrystalline nickel electrode in alkaline media: Temperature influence and reaction mechanism. *J. Electroanal. Chem.*, **2015**, *746*, 31–38.

[131] Hacker, V.; Ranninger, J.; Cermenek, B.; Feketeföldi, B.; Spirk, C.; Hesse, J.; Ribitsch, V. Optimization of the Catalyst and Membrane Performance by addition of various Additives for the alkaline Direct Ethanol Fuel Cell. *Zenodo*, **2018**.

[132] Cermenek, B.; Feketeföldi, B.; Zacharias, R.; Ribitsch, V.; Hacker, V. Characterization of Platinum-free electrocatalysts and anion exchange membranes for direct ethanol fuel cell. in *Proceedings of 6th European Fuel Cell - Piero Lunghi Conference, Cigolotti, V.; Barchiesi, C.; Chianella, M. (eds)* **2015**, ENEA, Neapel, Italy, 16/12/15–18/12/15, pp. 167–168.

[133] Holade, Y.; Servat, K.; Napporn, T.W.; Kokoh, K.B. Electrocatalytic properties of nanomaterials synthesized from “Bromide Anion Exchange” method - investigations of glucose and glycerol oxidation. *Electrochim. Acta*, **2015**, *162*, 205–214.

[134] Holade, Y.; Morais, C.; Arrii-Clacens, S.; Servat, K.; Napporn, T.W.; Kokoh, K.B. New Preparation of PdNi/C and PdAg/C Nanocatalysts for Glycerol Electrooxidation in Alkaline Medium. *Electrocatalysis*, **2013**, *4*, 167–178.

[135] Tonda-Mikiela, P.; Napporn, T.W.; Morais, C.; Servat, K.; Chen, A.; Kokoh, K.B. Synthesis of Gold-Platinum Nanomaterials Using Bromide Anion Exchange-Synergistic Electroactivity toward CO and Glucose Oxidation. *J. Electrochem. Soc.*, **2012**, *159*, H828–H833.

[136] Holade, Y.; Morais, C.; Napporn, T.W.; Servat, K.; Kokoh, K.B. Electrochemical Behavior of Organics Oxidation on Palladium-Based Nanocatalysts Synthesized from Bromide Anion Exchange. *ECS Trans.*, **2014**, *58*, 25–35.

[137] Amin, R.S.; Abdel Hameed, R.M.; El-Khatib, K.M.; Elsayed Youssef, M. Electrocatalytic activity of nanostructured Ni and Pd-Ni on Vulcan XC-72R carbon black for methanol oxidation in alkaline medium. *Int. J. Hydrogen Energy*, **2014**, *39*, 2026–2041.

[138] Simões, M.; Baranton, S.; Coutanceau, C. Influence of bismuth on the structure and activity of Pt and Pd nanocatalysts for the direct electrooxidation of $NaBH_4$. *Electrochim. Acta*, **2010**, *56*, 580–591.

[139] Obradović, M.D.; Stančić, Z.M.; Lačnjevac, U.Č; Radmilović, V.V.; Gavrilović-Wohlmuther, A.; Radmilović, V.R.; Gojković, S.L. Electrochemical oxidation of ethanol on palladium-nickel nanocatalyst in alkaline media. *Appl. Catal. B Environ.*, **2016**, *189*, 110–118.

[140] Paschos, O.; Simonov, A.N.; Bobrovskaya, A.N.; Hantel, M.; Rzepka, M.; Dotzauer, P.; Popov, A.N.; Simonov, P.A.; Parmon, V.N.; Stimming, U. Bismuth modified Pd/C as catalysts for hydrogen related reactions. *Electrochem. commun.*, **2010**, *12*, 1490–1492.

[141] Hofstead-Duffy, A.M.; Chen, D.-J.; Sun, S.-G.; Tong, Y.J. Origin of the current peak of negative scan in the cyclic voltammetry of methanol electro-oxidation on Pt-based electro-catalysts: a revisit to the current ratio criterion. *J. Mater. Chem.*, **2012**, *22*, 5205–5208.

[142] Zhao, Y.; Li, X.; Schechter, J.M.; Yang, Y. Revisiting the oxidation peak in the cathodic scan of the cyclic voltammogram of alcohol oxidation on noble metal electrodes. *RSC Adv.*, **2016**, *6*, 5384–5390.

[143] Brouzgou, A.; Podias, A.; Tsiakaras, P. PEMFCs and AEMFCs directly fed with ethanol:

a current status comparative review. *J. Appl. Electrochem.*, **2013**, *43*, 119–136.

[144] Hamm, U.W.; Kramer, D.; Zhai, R.S.; Kolb, D.M. On the valence state of bismuth adsorbed on a Pt(111) electrode: an electrochemistry, LEED and XPS study. *Electrochim. Acta*, **1998**, *43*, 2969–2978.

[145] Paffett, M.T.; Campbell, C.T.; Taylor, T.N. Adsorption and growth modes of Bi on Pt(111). *J. Chem. Phys.*, **1986**, *85*, 6176–6185.

[146] Urstöger, G.; Resel, R.; Koller, G.; Coclite, A.M. Deposition kinetics and characterization of stable ionomers from hexamethyldisiloxane and methacrylic acid by plasma enhanced chemical vapor deposition. *J. Appl. Phys.*, **2016**, *119*, 135307.

[147] Kim, H.C.; Kim, Y.; Bando, Y.; Yamauchi, Y.; Hong, J.W. Shape-controlled Pd nanocrystal-polyaniline heteronanostructures with modulated polyaniline thickness for efficient electrochemical ethanol oxidation. *J. Mater. Chem. A*, **2019**, *7*, 22029–22035.

[148] Holade, Y.; Morais, C.; Servat, K.; Napporn, T.W.; Kokoh, K.B. Enhancing the available specific surface area of carbon supports to boost the electroactivity of nanostructured Pt catalysts. *Phys. Chem. Chem. Phys.*, **2014**, *16*, 25609–25620.

[149] Thepkaew, J.; Therdthianwong, S.; Therdthianwong, A. Effect of pre-treatment approach of a carbon support on activity of PtSn/C electrocatalysts for direct ethanol fuel cells. *J. Appl. Electrochem.*, **2011**, *41*, 435–444.

[150] Shi, Q.; Zhu, C.; Bi, C.; Xia, H.; Engelhard, M.H.; Du, D.; Lin, Y. Intermetallic Pd_3Pb nanowire networks boost ethanol oxidation and oxygen reduction reactions with significantly improved methanol tolerance. *J. Mater. Chem. A*, **2017**, *5*, 23952–23959.

[151] Mayrhofer, K.J.J.; Wiberg, G.K.H.; Arenz, M. Impact of Glass Corrosion on the Electrocatalysis on Pt Electrodes in Alkaline Electrolyte. *J. Electrochem. Soc.*, **2008**, *155*, P1–P5.

[152] Figueiredo, M.C.; Arán-Ais, R.M.; Climent, V.; Kallio, T.; Feliu, J.M. Evidence of Local pH Changes during Ethanol Oxidation at Pt Electrodes in Alkaline Media. *ChemElectroChem*, **2015**, *2*, 1254–1258.

[153] Davey, W.P. Precision Measurements of the Lattice Constants of Twelve Common Metals. *Phys. Rev.*, **1925**, *25*, 753–761.

[154] Flanagan, T.B.; Wang, D.; Clewley, J.D.; Noh, H. Hydrogen solubility in ternary $Pd_{0.90}Rh_{0.1-x}Ni_x$ and $Pd_{0.90}Rh_{0.1-x}Co_x$ alloys. *J. Alloys Compd.*, **2000**, *305*, 172–182.

[155] Hull, S.; Norberg, S.T.; Tucker, M.G.; Eriksson, S.G.; Mohn, C.E.; Stølen, S. Neutron total scattering study of the δ and β phases of Bi_2O_3. *Dalton Trans.*, **2009**, 8737–8745.

[156] Huang, H.; Tian, N.; Jin, S.; Zhang, Y.; Wang, S. Syntheses, characterization and non-linear optical properties of a bismuth subcarbonate $Bi_2O_2CO_3$. *Solid State Sc.*, **2014**, *30*, 1–5.

[157] Zhuravlev, N.N. Structure of Superconductors, X. Thermal, Microscopic, and X-ray Investigation of the Bismuth-Palladium System. *J. Exp. Theor. Phys.*, **1957**, *5*, 1064–1072.

[158] Lian, C.-S.; Wang, X.-Q.; Wang, J.-T. Hydrogenated K_4 carbon: A new stable cubic gauche structure of carbon hydride. *J. Chem. Phys.*, **2013**, *138*, 024702.

[159] Mondal, A.; De, A.; Datta, J. Cost effective and energy efficient catalytic support of Co and Ni in Pd matrix toward ethanol oxidation reaction: Product analysis and mechanistic interpretation. *Appl. Catal. A: Gen.*, **2018**, *561*, 87–95.

[160] Mayrhofer, K.J.J.; Strmcnik, D.; Blizanac, B.B.; Stamenkovic, V.; Arenz, M.; Markovic, N.M. Measurement of oxygen reduction activities via the rotating disc electrode method: From Pt model surfaces to carbon-supported high surface area catalysts. *Electrochim. Acta*, **2008**, *53*, 3181–3188.

8 Appendix A: Supplementary Material

8.1 PART I: The Effect of Various Characterization Parameters and Operating Conditions on the EOR Performance of Carbon Supported Pt-free Electrocatalysts in an Alkaline Medium

8.1.1 Chemicals, Materials and Equipment

Anode Catalysts

Pd_xNi_y/C:

- Palladium(II) chloride ($PdCl_2$, anhydrous, 59-60% palladium (Pd) basis, Aldrich),
- sodium chloride (NaCl, ≥99.5%, Aldrich),
- nickel(II) nitrate hexahydrate ($Ni(NO_3)_2 \cdot 6H_2O$, Aldrich),
- Vulcan XC72R carbon black (CABOT Corporation, USA),
- sodium borohydride ($NaBH_4$, Sigma-Aldrich),
- 2-propanol (ASC ≥ 99.8%, Sigma-Aldrich),
- sodium hydroxide (NaOH, Aldrich) and
- ultra-pure water (~18 MΩ·cm, Barnstead NANOpure Water Purification System) were used for the development of Pd_xNi_y/C anode catalysts.

Au/C and Au_xCu_y/C:

- Copper(II) nitrate trihydrate ($Cu(NO_3)_2 \cdot 3H_2O$),
- hydrogen tetrachloroaurate(III) ($HAuCl_4$),
- Vulcan XC72R carbon black (CABOT Corporation, USA),
- sodium hydroxide (NaOH, Aldrich),
- sodium borohydride ($NaBH_4$, Sigma-Aldrich) and
- ultra-pure water (~18 MΩ·cm, Barnstead NANOpure Water Purification System) were used for the development of Au/C and Au_xCu_y/C anode catalysts.

$Pd_{80}Ni_{10}P_{10}$/C:

- Palladium chloride ($PdCl_2$, anhydrous, 59-60% palladium (Pd) basis, Aldrich),
- sodium chloride (NaCl, ≥99.5%, Sigma-Aldrich),

- sodium hypophosphite monohydrate ($NaH_2PO_2 \cdot H_2O$, ≥99, Sigma-Aldrich),
- nickel(II) sulfate hexahydrate ($NiSO_4 \cdot 6H_2O$, 99%, Sigma-Aldrich),
- Vulcan XC72R carbon black (CABOT Corporation, USA),
- sodium borohydride ($NaBH_4$, Sigma-Aldrich),
- sodium hydroxide (NaOH, Aldrich) and
- ultra-pure water (~18 MΩ·cm, Barnstead NANOpure Water Purification System) were used for development of the $Pd_{80}Ni_{10}P_{10}$/C anode catalyst [131].

Equipment[4]

- (Bi-)potentiostat (Reference 600™Potentiostat/Galvanostat/ZRA, GAMRY Instruments Inc., Pennsylvania, USA)
- Rotator (RDE710, GAMRY Instruments)
- Rotating Disk Electrode (RDE – Model AFE5T050GC according to producer: Glassy carbon RDE Tip: 5.0 mm disk OD; 15.0 mm OD PTFE shroud, Pine Research Instrument)
- Reversible Hydrogen Electrode (RHE – Gaskatel, HydroFlex)
- Platinized titanium rod (Bank Elektronik – Intelligent controls GmbH)
- Ultrasonic baths (Bandelin Sonorex, Type RK 31 H and Elma/Elmasonic S 300)
- Ultrasonic probe (Hilscher, UP400s)
- Julabo (model MC, class: III, Julabo Labortechniken GmbH)
- Analytical balance (Sartorius BP 110S max. 110 g, Sartorius AG)
- Magnetic stirrer (Roth, MH 15, Rotilabo)
- Centrifuge (Labofuge 400, Heraeus)
- Drying oven (DRY-line, VWR, S/N: 15-14/969)
- Laboratory platen press (‘hot press’) for MEA production (Fontijne Vlaardingen Holland TP200)
- Pump for Fuel Cell Tests: Fluid Metering Inc. (FMI) Lap Pump Model RHV, Syosset, NY, Made in US; Model: PM6014 #110473-2; PIN: 911-30-0510-7; FMI Stroke Rate Controller Model V200

[4] The listed equipment were used for the experiments at CEET in **sections 4.1–4.4**.

8.1.2 Calculations of the Catalyst Ink Preparation

Anode synthesis

The catalyst ink consists of catalyst, 5 wt.% anionomer, ultra-pure water and 1-propanol. The determination of the catalyst weight and the volume of anionomer are performed according to the equations 22 and 23[5] for the catalyst ink preparation. The following specifications are taken into account in the calculation: Catalyst composition: 40 wt.% of metal(s) (relating to Pd) and 60 wt.% of carbon support material.

$$m_{catalyst} = \frac{c_L \cdot A_{GDL} \cdot M_{catalyst} \cdot V_{1-propanol}}{M_{Pd} \cdot \omega_{metal(s)} \cdot V_d \cdot X_{\mathrm{Pd}}} \quad (22)$$

$$m_{Anionomer} = \frac{\mathrm{m}_{catalyst} \cdot 0.2}{0.05} \quad (23)$$

m_{catalyst}	Mass of catalyst for weighing (mg)
c_{L}	Catalyst loading on the carbon cloth (= 1 $mg_{Pd} \cdot cm^{-2}$)
A_{GDL}	Surface area from the carbon cloth (GDL) (= 9 cm^2)
M_{catalyst}	Molecular weight of the catalyst ($g \cdot moL^{-1}$)
$\omega_{\mathrm{metal(s)}}$	Mass fraction of the metal(s) of the catalyst used (40 wt.% = 0.4)
X_{Pd}	Atomic percentage of Pd in the catalyst used (at.%)
M_{Pd}	Molecular weight of Pd ($g \cdot moL^{-1}$)
V_{d}	Catalyst volume for dripping on GDL (= 1.2 mL)
$V_{\mathrm{1\text{-}propanol}}$	Volume of catalyst dispersion = Mixture of 1-propanol and ultra-pure water in a ratio of 7:3 (= 1.5 mL)
$m_{\mathrm{anionomer}}$	Mass of 5 wt.% (= 0.05) anionomer (20 wt.% from catalyst = 0.2)

[5] The calculations were used for the catalyst ink preparation in **sections 4.2** and **4.3**.

Anode Catalyst Characterization (RDE-CV and RDE-CA)

The catalyst ink consists of catalyst, 5 wt.% Nafion ionomer solution (optional), ultra-pure water and 2-propanol. The determination of the catalyst weight and the volume of Nafion ionomer are performed according to the equations 24**–**26[6] for the catalyst ink preparation. The following specifications are taken into account in the calculation: Catalyst composition: 40 wt.% of metal(s) (e.g., relating to Pd for Pd-based catalysts) and 60 wt.% of carbon support material.

$$\mathrm{m}_{catalyst} = \frac{c_L \cdot A_{GC} \cdot M_{catalyst} \cdot V_{cd}}{M_{Pd} \cdot \omega_{metal(s)} \cdot V_d \cdot X_{\mathrm{Pd}}} \tag{24}$$

$$\mathrm{m}_{Pd} = \frac{c_L \cdot A_{GC}}{V_d} \cdot V_{cd} \tag{25}$$

$$V_{Nafion} = \frac{\mathrm{m}_{Pd} \cdot 0.2}{0.05} \cdot \frac{1}{\rho_{Nafion}} \tag{26}$$

m_{catalyst}	Mass of catalyst for weighing (mg)
c_{L}	Catalyst loading on the RDE ($\mu g_{Pd} \cdot cm^{-2}$)
A_{GC}	Surface area from the GC substrate on RDE (= 0.196 cm^2)
M_{catalyst}	Molecular weight of the catalyst ($g \cdot moL^{-1}$)
$\omega_{\mathrm{metal(s)}}$	Mass fraction of the metal(s) of the catalyst used (40 wt.% = 0.4)
X_{Pd}	Atomic percentage of Pd in the catalyst used (at.%)
M_{Pd}	Molecular weight of Pd ($g \cdot moL^{-1}$)
V_{d}	Catalyst volume for dripping on RDE (= 10 µL)
V_{cd}	Volume of catalyst dispersion = Mixture of 2-propanol and ultra-pure water in a ratio of 7:3 (= 2.5 or 5.0 mL)
m_{Pd}	Mass of Pd (g)
V_{Nafion}	Volume of 5 wt.% (= 0.05) Nafion ionomer (20 wt.% from catalyst = 0.2)
ρ_{Nafion}	Density of the Nafion ionomer (= 0.94 $g \cdot cm^{-3}$)

[6] The calculations were used for the catalyst ink preparation in **sections 4.1–4.4**.

8.1.3 Relevant Resulting Publications

VIENNA 2018 TRA
A digital era for transport
solutions for society, economy and environment

Proceedings of 7th Transport Research Arena TRA 2018, April 16-19, 2018, Vienna, Austria

Optimization of the Catalyst and Membrane Performance by addition of various Additives for the alkaline Direct Ethanol Fuel Cell

Viktor Hacker[a], Johanna Ranninger[a], Bernd Cermenek[a*]
Birgit Feketeföldi[b], Christina Spirk[b], Jan Hesse[b]
Volker Ribitsch[c]

[a] *Institute of Chemical Engineering and Environmental Technology, Graz University of Technology, Inffeldgasse 25C; 8010 Graz, Austria.*
[b] *JOANNEUM RESEARCH Forschungsgesellschaft mbH/Materials, Institute for Surface Technologies and Photonics, Franz-Pichler-Straße 30, 8160 Weiz, Austria.*
[c] *University of Graz, Institute of Chemistry, Heinrichstraße 28, 8010 Graz, Austria.*

Abstract

Alcohol fuel cells are promising energy converters especially for portable applications. Ethanol as fuel is an attractive candidate for fuel cells due to the high volumetric energy density and to the easy handling, transport and storing. The chemical energy of ethanol is converted directly in electricity without any treatment step. The operation of the direct ethanol fuel cell (DEFC) in alkaline media compared to acidic media includes the advantages of the use of non-precious metals e.g. nickel or manganese as catalysts, the improved water management and reduced ethanol-crossover using anion exchange membranes (AEMs) which conduct the hydrated anions in the opposite direction than the electro-osmotic drag and the kinetic enhancement of the ethanol oxidation reaction (EOR) and oxygen reduction reaction (ORR).

Keywords: Direct fuel cell; decentralized electricity generation; auxiliary power unit

[*] Corresponding author. Bernd Cermenek, Viktor Hacker
E-mail address: bernd.cermenek@tugraz.at, viktor.hacker@tugraz.at

Nomenclature

AEM	Anion exchange membrane
CA	Chronoamperometry
CV	Cyclic voltammetry
DAFC	Direct alcohol fuel cell
DC	Degree of cross-linking
DEFC	Direct ethanol fuel cell
DQ	Degree of quaternization
EGDGE	Ethylene glycol diglycidyl ether
EOR	Ethanol oxidation reaction
EPTMAC	(2,3-Epoxypropyl) trimethylammonium chloride
GA	Glutaraldehyde
HTCC	N-[(2-Hydroxy-3-trimethylammonium)propyl] chitosan chloride
IEC	Ion exchange capacity
IPN	Interpenetrating polymer network
MEA	Membrane electrode assembly
MWCO	Molecular weight cut off
ORR	Oxygen reduction reaction
PEI	Polyethylene imine
PTFE	Polytetrafluorethylene
QPEI	Quaternized polyethylene imine
RDE	Rotating disk electrode

1. Introduction

In the alkaline DEFC, ethanol is directly oxidized by hydroxide (OH^-) ions at the anode and 12 e^- are released. Oxygen reacts at the cathode with the electrons and water to form the hydroxide ions, which are transported through the membrane to the anode. Alkaline solution along with ethanol fuel is provided at the anode to facilitate the oxidation of ethanol.

Anode reaction:	$CH_3CH_2OH + 12\ OH^- \rightarrow 2\ CO_2 + 9\ H_2O + 12\ e^-$
Cathode reaction:	$3\ O_2 + 6\ H_2O + 12\ e^- \rightarrow 12\ OH^-$
Cell reaction:	$CH_3CH_2OH + 3\ O_2 \rightarrow 3\ H_2O + 2\ CO_2$

The complete oxidation of ethanol at the anode is not reached with state-of-the-art catalysts in the alkaline DEFC at ambient temperature. Instead of CO_2, the main product of the ethanol oxidation reaction (EOR) is acetic acid – (acetate). In the incomplete oxidation pathway, only four electrons instead of 12, for the complete oxidation, are released. This loss in electrons leads to a reduction of the theoretical efficiency (97%) to 11% [1,2]. Therefore, anode catalysts with high activity, stability and byproduct tolerance have to be developed. The most promising catalysts are Pd-based catalysts which outperform Pt-based catalysts in alkaline medium [3]. The performance of Pd-based anode catalysts is improved by alloying Pd with co-catalysts which can also be non-noble metals like Ni, Bi, P or Zn [4-8].

In the alkaline DEFC, the direction of the ion mobility through the membrane is in the opposite direction than the electro-osmotic drag leading to reduced ethanol-crossover [9]. However, ethanol-crossover through the membrane cannot be totally prevented which makes the development of ethanol tolerant cathode catalysts also an important research topic. In acidic medium, mainly Pt is used as catalyst for the ORR. Ag, Mn_xO_y and Ag/Mn_xO_y have been reported as Pt-free cathode catalyst materials with high activity, stability and higher ethanol tolerance in alkaline cells than Pt [10].

Aside from the advantages of the alkaline DEFC, one challenge concerning alkaline fuel cells represents the carbonation of the electrolyte. The OH^- ions react with CO_2 in the air and the CO_2 formed during the ethanol oxidation to carbonate (CO_3^{2-}) ions [9].

$$2\ OH^- + CO_2 \rightarrow CO_3^{2-} + H_2O$$

The carbonate ions form solid precipitation which blocks the pores of the electrodes and increase the pH value. Hence, the activity of the oxidation and reduction reactions is reduced as well as the conductivity of the electrolyte [9].

With the development of polymer electrolyte membranes like Nafion, the development of direct alcohol fuel cells (DAFCs) was mainly focused on acidic DAFCs, however, in previous years, the synthesis of anion exchange membranes (AEM) lead to new research interests in alkaline DAFCs. When an AEM is applied instead of liquid alkaline electrolyte, the formation of carbonate can be drastically decreased [9,11].

Within the scope of the Austrian Research Promotion Agency (FFG) project "e!Polycat", Pt-free catalysts with high activities and stabilities toward alkaline EOR and ORR and high anion conductive and chemically, mechanically, thermally stable polysaccharide-based membranes (-> performance improvement by addition of various "additives" e.g. ad-metals for catalysts and cross-linkers for membranes) were developed for the alkaline DEFC.

A series of novel bi- and tri-metallic Pt-free anode catalysts were synthesized by means of the simultaneous reduction method. The addition of one or two metals to monometallic anode catalysts results to high EOR activities and stabilities due to bifunctional, electronic and synergistic effects in an alkaline electrolyte containing ethanol. Additionally, novel perovskite cathode catalysts for the alkaline DEFC have been developed. Those catalysts exhibit high activity toward the ORR, high stability and excellent ethanol tolerance [12]. Within the framework of the project, ethanol tolerant cathode catalysts based on manganese oxide and silver were also synthesized and characterized for the alkaline DEFC [13].

Furthermore, a series of novel AEMs based on chitosan were blended with water-soluble polyethylene imine. Chitosan can be modified due to its exchangeable functional groups[14] and polyethylene imine (PEI) is an inexpensive polymer with a high density of reactive amino groups. In order to use the polymers as solid polyelectrolytes in alkaline fuel cells both polymers were quaternized. A common strategy of introducing ionic conductive groups into polymeric matrices is the quaternization with trimethylammonium ($-N(CH_3)_3$) groups onto the backbone or side chains of the polymers [15-19,26] or in case of polyethylene imine the N-alkylation with iodomethane or with the less toxic reagents iodoethane [20]. To our best knowledge there is very little data available on the usage of quaternized polyethylene imine (QPEI) for alkaline fuel cells. Due to the high mass of the amino groups of PEI a high degree of quaternization (DQ) was obtained, thus resulting in a high hydrophilic polymer matrix with a high degree of swelling and subsequently modest membrane stability. To prepare durable membranes with improved chemical, mechanical and thermal properties, a cross-linking method consisting of a combination of different network was developed. The characteristics of the composite membranes were evaluated for potential application in alkaline DEFCs.

2. Experimental

2.1. Preparation of HTCC

N-[(2-Hydroxy-3-trimethylammonium) propyl] chitosan chloride (HTCC) was synthesized according to Wu *et al.* and Feketeföldi *et al.* [21,26].

2.2. Preparation of QPEI

Branched quaternized polyethylene imine (QPEI) was prepared by a method similar to those described elsewhere[20]. Briefly, PEI (1.0 g, 23 mmol of monomer unit) was dissolved in 15 ml of absolute ethanol. N-alkylation was conducted as follows: iodoethane (19.4 g, 124.4 mmol) was added and the reaction was carried out under reflux conditions for 24 hours at 72 °C. An excess of potassium carbonate (K_2CO_3) was added to neutralize the released acid. The reaction was continued for 72 hours at the same conditions. Formed KI and unreacted K_2CO_3 were discarded by filtration. Ethanol was removed by evaporation and the product was lyophilized. To remove traces of inorganic salts, the product was dialyzed (MWCO 3,5 kDa) against water for three days and the product was lyophilized again.

2.3. Preparation of the cross-linked HTCC/QPEI membrane

HTCC was dissolved in 1wt.% acetic acid solution, yielding a 5wt.% solution, a prescribed amount of 10wt.% ethylene glycol diglycidyl ether (EGDGE) in ethanol was added (see Table 1) under stirring at 60 °C for one hour. QPEI was dissolved in deionized water in order to prepare a 5wt.% solution. HTCC (5 g) and QPEI (5 g)

were mixed. To this solution, 0.3 mL of 10wt.% glutaraldehyde (GA) was added under stirring for 0.5 h. The solution was filtered with a 5 µm PTFE membrane filter and coated onto the surface of a plexiglass petri dish and dried at 60 °C overnight. Afterwards, the membrane was dried at 130 °C for 2 min [26].
A series of HTCC/QPEI membranes was prepared. The membranes were cross-linked with varying amounts of EGDGE, while the amount of the second cross-linking reagent (GA) was maintained constant. These series are referred to as HTCC/QPEI-i (i = 1, 2, 3, 4 and 5) [26].

2.4. Anode catalyst synthesis

Different binary and ternary anode catalysts were prepared via the simultaneous reduction method [27]. Therefore, various metal precursor salts are dissolved in aqueous media and mixed with carbon black Vulcan XC72R as support material. These metal precursor salts are reduced to respective metals on the support material by adding e.g. sodium borohydride ($NaBH_4$) or other reducing agents. As additives e.g.: Ni, Bi, P or Zn was used to improve the activities and stabilities of Pd based catalysts [30-32].

2.5. Methods

2.5.1. Degree of membrane cross-inking

The degree of membrane cross-linking for QPEI and HTCC with EGDGE was calculated according to Equation 1[22, 26].

$$DC(\%) = \frac{10\% \times V_{Agent}/Mw_{Agent}}{5\% \times V_{Q-Polymer}/Mw_{Q-Polymer}} \times 100\% \quad (1)$$

Where, DC (%) is the molar ratio of EGDGE to the composite membrane in repeat units, V_{Agent} is the volume [mL] of cross-linking agent (EGDGE, 10wt.%), $V_{Q\text{-}Polymer}$ is the volume [mL] of quaternized polymer solution (QPEI and HTCC, 5wt.%), $M_{w,\ Agent}$ is the molecular weight of EGDGE (174.19 g mol^{-1}). $M_{w,\ Q\text{-}Polymer}$ is corresponding to the averaged molecular weight of HTCC/QPEI monomers (361.0 g mol^{-1}) [26].

2.5.2. Alkaline water uptake

The alkaline water uptake (WU) of the membranes was performed by measuring the change in mass of the membranes before and after hydration [26]. The membranes were immersed in 1 M KOH at room temperature for 24 h. The surplus aqueous alkaline solution was wiped with filter paper and weighted immediately. The alkaline water uptake was calculated using the following relation (see Equation 2) [26]:

$$\mathrm{WU}(\%) = \frac{m_w - m_d}{m_d} \times 100 \quad (2)$$

where m_w is the mass [g] of wet membrane and m_d is the mass [g] of dry membrane [26].

2.5.3. Ion exchange capacity

The ion exchange capacity (IEC) was determined by back titration [26]. The membranes (0.2 g) were soaked in 1.0 M KOH for 24 h, washed with deionized water and equilibrated with 40 mL of 0.01 M HCl standard solution for 24 h, followed by potentiometric titration with 0.01 M NaOH standard solution. 40 mL of 0.01 M HCl standard solution was used as blank sample. The IEC value was calculated by the following Equation 3 [26]:

$$\mathrm{IEC} = \frac{(V_{blank} - V_{membrane}) \cdot C_{HCl}}{m_d} \times 1000 \quad (3)$$

where V_{blank} and $V_{membrane}$ were the consumed volumes [mL] of the NaOH solution for the blank sample and the HTCC/QPEI membrane sample, respectively, C_{HCl} was the concentration [M] of HCl solution, and m_w is the mass [g] of dry membrane sample [26].

2.5.4. Product and membrane characterizations

The content of surface charge was determined by streaming potential method using Mütek PCD system. The chemical stability in alkaline medium was evaluated by immersing the membranes in 1.0 M KOH solution at 60 °C for different periods of time [26]. The compactness and appearance of leaks of the membranes were visually observed. The structure of the unmodified PEI and quaternized QPEI was characterized by Fourier transform infrared spectroscopy (FT-IR) [26]. The infrared spectrometer (Bruker Tensor 27) was used to obtain spectra in the range from 4000 to 600 cm^{-1} with a wavenumber resolution of 4 cm^{-1} [26]. Thermal gravimetric analysis (TGA) was conducted using a TGA/DSC system (NETZSCH STA 449, Germany) [26]. Samples were heated from 25 to 600 °C at a heating rate of 10 °C min^{-1} using a flow of 20 mL min^{-1} nitrogen as inert gas [26].

2.6. Anode catalyst investigation

Different binary and ternary Pd-based anode catalysts were tested in a rotating disk electrode (RDE) experiment via cyclic voltammetry (CV) and chronoamperometry (CA) to get an impression of their activities and stabilities. The RDE experiments were carried out in aqueous solution containing 1 M KOH and 1 M ethanol at 30 °C with a scan rate of 10 mV s^{-1}. The CA was performed at 0.83 V for one hour. The elemental composition, structure and the morphology of the catalysts were investigated by different physical methods such as ICP-OES, XRD, XPS and TEM-EDX [30-32].

3. Results and Discussion

3.1. Synthesis of HTCC and QPEI

Anion exchange membranes with chitosan and PEI as polymer matrix and polyelectrolytes were prepared. Chitosan was quaternized with (2,3-Epoxypropyl) trimethylammonium chloride resulting in a high degree of quaternization of 80% averagely. PEI has a high mass of amine groups on its polymer chain and can provide a high ion exchange capacity after modification by N-alkylation (see Fig. 1). The resulting degree of quaternization for QPEI was 82.4%. The ^{1}H-NMR spectra of QPEI and HTCC are not shown.

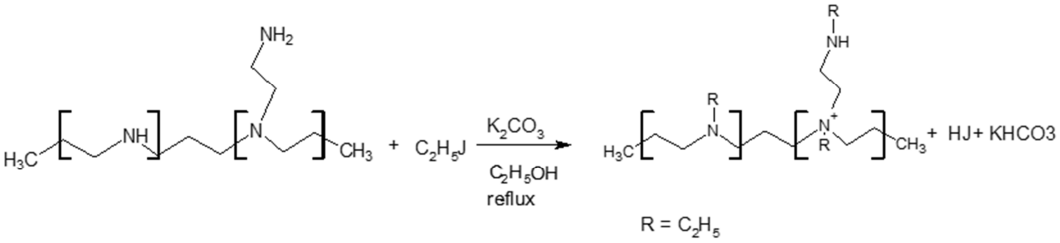


Fig. 1 Schematic representation of preparing QPEI

It was found, that quaternized chitosan with a degree of quaternization (DQ) of 80.2% had an average amount of surface charge of 3830 C/g. Compared to the HTCC-product, the quaternized PEI exhibited an average amount of surface charge of 575 C/g. The previous result was obtained from a dialyzed QPEI-product with a DQ of 82.4% and an ion conductivity of 740 µS cm^{-1}.

3.1.1 Fourier transform infrared spectroscopy

The FT-IR spectra of PEI and QPEI are shown in Fig. 2. The two peaks at 1020 and 1250 cm^{-1} in the spectra of the materials are characteristic for C-N bonds. The signal at 1650 cm^{-1} for unmodified PEI is assigned to the N-H bending of primary amines (R-NH2)[23]. QPEI consists of secondary (R2-NH) and tertiary (R3-N) amines, although the expected peak at 1650 cm^{-1} could not be observed. Absorption bands between 3250 and 3500 cm^{-1} were recorded, corresponding to the N-H bending of primary and secondary amines. The unmodified PEI offered two peaks at 3265 and 3355 cm^{-1}, attributed to the N-H bending of primary amines. A broad band around 3430 cm^{-1} was attributed to the secondary amines of the modified QPEI. It is noted that the absorption peaks of the primary amines could also not be observed for the QPEI-product.

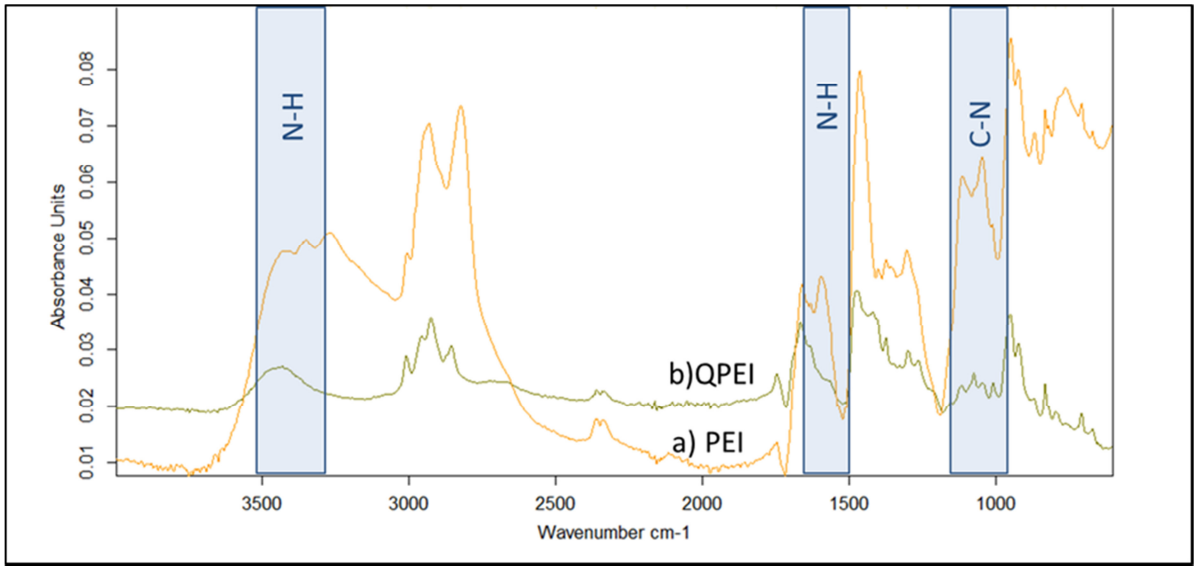


Fig. 2 FT-IR spectra of PEI and QPEI

3.2. Membrane Preparation

3.2.1. Cross-linking HTCC/QPEI membranes

To increase chemical, mechanical and thermal stability, the composite materials were cross-linked in order to form three-dimensional polymer networks. The effect of the degree of cross-linking on the membrane structure and the chemical/physical properties were investigated [26]. In this work, we used GA and EGDGE to cross-link the polymer membranes. The amount of the first cross-linking agent (GA) was constant, whereas the amount of the second cross-linker (EGDGE) was varied [26].

Table 1. Cross-linking conditions for HTCC/QPEI composite membrane with EGDGE [26].

Membrane [a,b,c]	Molar ratio of EGDGE to membrane [mmol mmol^{-1}]	Degree of cross-linking QPEI [%]
HTCC/QPEI-1	1.1/2.2	69,1
HTCC/QPEI-2	1.2/2.2	78,9
HTCC/QPEI-3	1.3/2.2	88,8
HTCC/QPEI-4	1.4/2.2	98,6
HTCC/QPEI-5	1.7/2.2	118,4

a All membranes were prepared using a same kind of HTCC and QPEI, the degree of quaternization (DQ) was 80,2% and 82,4%, respectively, determined by elemental analysis.
b The molar ratio of GA to composite membrane was 0.3/2.2 mmol mmol^{-1}, with a degree of crosslinking (DC) of 13.7%.
c The thickness of membranes was 85 nm, +/- 4 nm dry state.

GA and EGDGE are common cross-linking agents for PEI and chitosan [24,26]. The network formation takes place between the amino groups of the blend materials (HTCC and QPEI) and the aldehyde groups of GA. For gaining the highest possible mechanical and chemical stability, a second cross-linking agent - EGDGE - was used in this work [26]. Due to the presence of two reactive epoxy groups, EGDGE facilitates the cross-linking reaction with two amino groups of two different quaternized chitosan molecules and quaternized PEI molecules during drying process [25,26]. The blend materials form an interpenetrating polymer network (IPN), wherein both polymers are cross-linked independently in the presence of the other and do not interfere with one another (see Fig. 3).

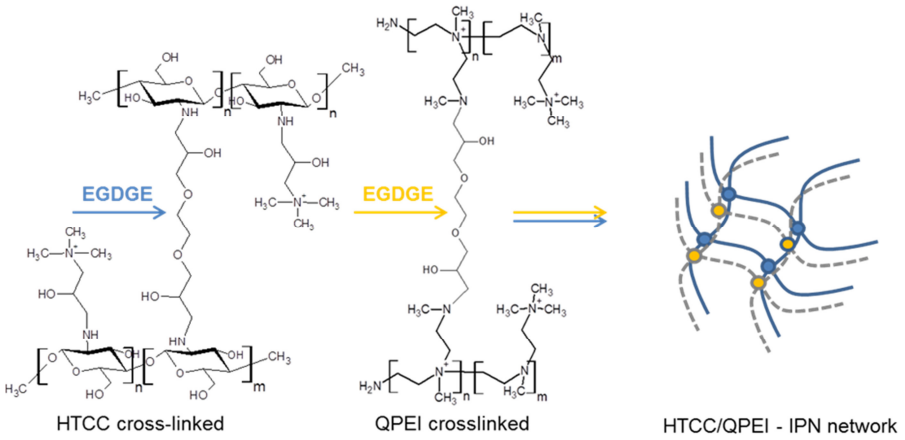


Fig. 3 HTCC/QPEI – IPN network

The cross-linking conditions for these membranes are summarized in Table 1. In the present study, all cross-linked membranes were prepared using HTCCs and QPEIs with a DQ higher than 80%. The stability of the membranes toward alkaline media was observed visually from physical appearance of fragmented membranes after immersion in 1.0 M KOH solution for a certain period of time [26]. By increasing the amount of cross-linker, the membranes became more stable with an optimum range of 0.3/2.2 mmol $mmol^{-1}$ for GA and 1.4/2.2 mmol $mmol^{-1}$ for EGDGE [26]. At a degree of cross-linking of 88.8%, the alkaline stability of the membrane sustained for 360 h in 1.0 M KOH solution at 60 °C.

3.3. Water uptake and ion exchange capacity

The presence of water in the solid electrolyte affects the chemical and mechanical stability of the membranes [26]. The degree of water uptake is related to the amount of polymer cross-linking agents and the hydrophilic properties due to the quaternary ammonium groups. In the present study, the amount of the ammonium groups of the HTCC/QPEI membranes was approximately the same (DQ of HTCC and QPEI higher than 80%). The parameter that primary influenced the swelling of the membranes was the degree of cross-linking. The water uptake of the composite membranes cross-linked with GA and EGDGE is given in Fig. 4.
The results indicate that with an increased DC, the water uptake of the membranes gradually decreased from around 168% to 120%. The differences in water uptake can be assigned to the interactions in the polymer matrix of the cross-linkers [26]. With increased amount of cross-linking reagents, the IPN-networks became more dense. The heating procedure during the membrane preparation (60-130 °C) resulted only in a higher mechanical and chemical stability, the swelling properties of the membranes (60 °C) remained the same [26].
The composite membranes exhibit the same behavior in terms of water uptake and ion exchange capacity [26]. A higher water uptake in membranes forms transferring channels and creates a higher accessibility for ammonium ions, whereas a high amount of cross-linking reagents reduces the ion transport [26]. It was found that, at a constant DQ, an increase of the amount of cross-linkers leads to a gradually decreased IEC of the HTCC/QPEI membranes from 1.6 meq g^{-1} to 0.9 meq g^{-1}. The IEC of anion exchange membranes describes the amount of exchangeable ammonium groups in the membrane [26].

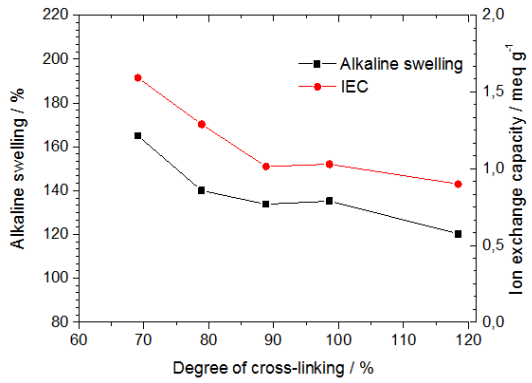


Fig. 4 Water uptake and ion exchange capacity of the cross-linked HTCC/QPEI membranes vs. degree of cross-linking

3.4. Thermogravimetric analysis (TGA)

The thermal degradation behavior of HTCC/QPEI composite membranes cross-linked by EGDGE is shown in comparison to HTCC/QPVA membranes in Fig. 5. The preparation and properties of the HTCC/QPVA membranes are described in a previous paper [26]. The mass decrease at around 100 °C is due to the bonded water evaporation of all membranes. The HTCC/QPVA and the HTCC/QPEI composite membranes cross-linked with EGDGE were stable up to 260 °C and 190 °C, respectively. The thermal stability of the membranes was mainly determined by QPVA and QPEI. Pure chitosan is thermally not stable enough and starts to degrade continuously at around 120 °C. Two stages of thermal degradation were found for the cross-linked membranes. The weight loss of the two composite membranes that occurs within a range of 180-280 °C is due to the degradation of quaternary ammonium groups. At the degradation stage in the range of 260-480 °C, the mass degradation is attributed to the break of the C-C backbone of the main polymer chains of HTCC, QPVA and QPEI [26].

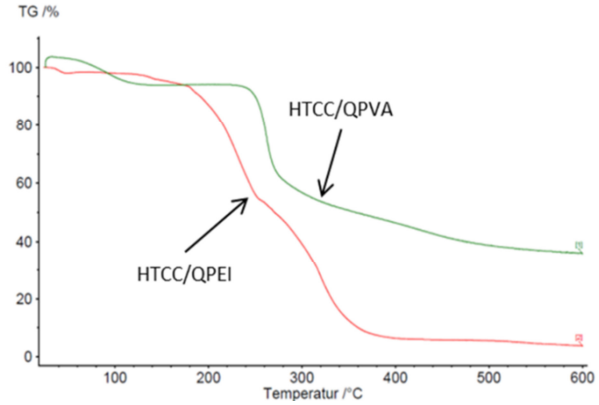


Fig. 5 TGA curve of HTCC/QPVA – and HTCC/QPEI composite membranes [26]

3.5. Anode Catalyst Testing

Carbon supported binary and ternary Pd based anode catalysts were successfully synthesized by the instant reduction method ($Pd_{80}Ni_{20}/C$) [27] and by the "aqueous solution phase synthesis method" ($Pd_{80}Ni_{10}P_{10}/C$) [28]. The activities and stabilities of the catalysts were investigated by CV/CA using a RDE. Fig. 6 shows that the EOR performances (activity and stability) of both Pd based catalysts are higher than the Pt/C catalyst (benchmark).
The poisoning of CO similar species on Pd based catalysts is drastically reduced thus results in an improvement in terms of activity and stability toward the alkaline EOR [5,7,28].

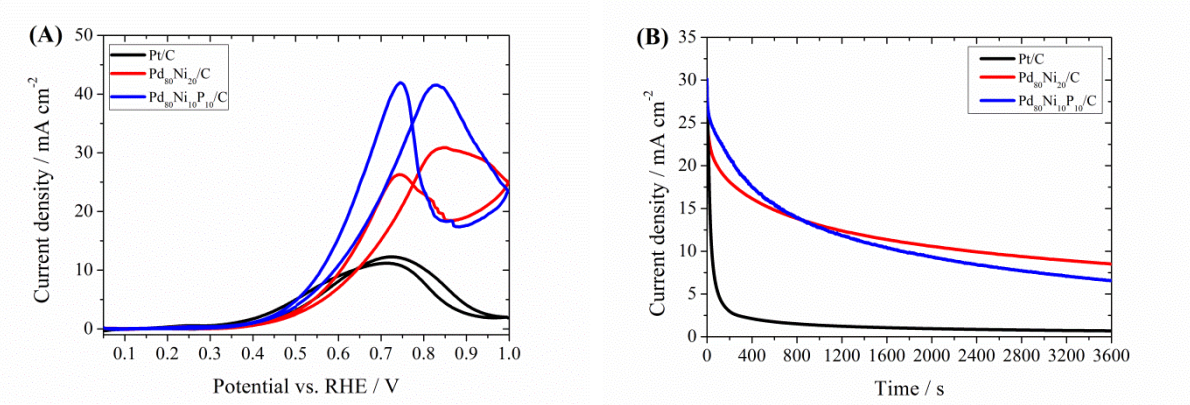


Fig. 6 (A) EOR activity of Pt/C, $Pd_{80}Ni_{20}/C$ and $Pd_{80}Ni_{10}P_{10}/C$ in an aqueous solution containing 1 M ethanol and 1 M KOH recorded with a scan rate of 10 mV s^{-1} at 30 °C; (B) EOR stability of Pt/C, $Pd_{80}Ni_{20}/C$ and $Pd_{80}Ni_{10}P_{10}/C$ in an aqueous solution containing 1 M ethanol and 1 M KOH recorded at 0.83 V for one hour at 30 °C

But the tolerances of the synthesized Pd based catalysts toward the intermediates of ethanol oxidation are not good enough by half for use in a long term operation. The byproduct tolerance is evaluated by the ratio of the current density of the forward scan and the backward scan according to Lee et al. [29]. Therefore, Pd catalysts with

further “additives” were investigated for the alkaline EOR. Within the scope of the project, a ternary Pd based catalyst system with high EOR performance (high byproduct tolerance, low onset-potential for the alkaline ethanol oxidation reaction, high produced peak current density) was developed for the alkaline DEFC [30,31]. The EOR performance of the ternary Pd based catalyst system outperformed the results of the in-house carbon supported Pd and binary Pd based catalysts, respectively. With the optimized catalysts, anodes are fabricated via drop-coating on a carbon cloth which were further processed to a membrane electrode assembly (MEA) and characterized in an in-house designed direct single cell at various operating conditions (see Fig. 7) [31,32].

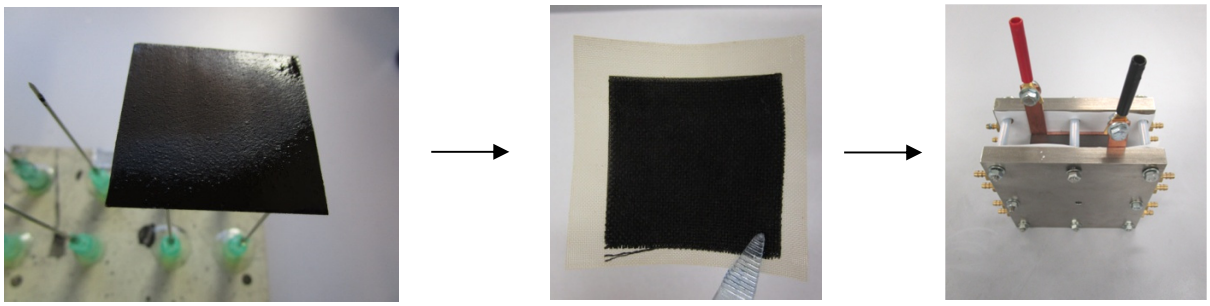


Fig. 7 Drop-coating process for anode preparation; Membrane electrode assembly (MEA); In-house direct single cell (left to right) [31,32]

4. Conclusion

A series of novel quaternized chitosan/PEI membranes were prepared. The chitosan and QPEI molecules were cross-linked with the cross-linking agents GA and EGDGE. During the polymerization procedure the quaternized polymers formed an IPN-network, wherein HTCC and QPEI were not connected with each other. The composite membranes showed ionic properties for anions and concurrently mechanical and chemical stability in alkaline environment. The IPN-network was stable up to 190 °C. This study demonstrates that the resulting membranes are suitable for direct ethanol fuel cells. Future investigations will focus on the screening of improvement of ionic conductivity and reduction of chemical degradation of the quaternized matrix.
A novel ternary anode catalyst with high EOR performance has been prepared by alloying of Pd with other metals. The results have been confirmed via CV and CA measurements using RDE and also in single cell tests using an in-house designed cell. The characterization results of the novel ternary Pd-based anode catalyst and the novel quaternized chitosan/PEI AEMs for the alkaline DEFC will be presented and discussed in detail.

Acknowledgements

Financial support by the Austrian Climate Energy Fund, Austrian Federal Ministry of Transport, Innovation and Technology (BMVIT), The Austrian Research Promotion Agency (FFG) through the program “Energy Mission Austria” and the IEA research cooperation is gratefully acknowledged.

5. References

(1) Liang, Z. X.; Zhao, T. S.; Xu, J. B.; Zhu, L. D. Mechanism study of the ethanol oxidation reaction on palladium in alkaline media. *Electrochim. Acta* **2009**, *54* (8), 2203–2208.

(2) An, L.; Zhao, T. S.; Li, Y. S. Carbon-neutral sustainable energy technology: Direct ethanol fuel cells. *Renew. Sustain. Energy Rev.* **2015**, *50*, 1462–1468.

(3) Xu, C.; Cheng, L.; Shen, P.; Liu, Y. Methanol and ethanol electrooxidation on Pt and Pd supported on carbon microspheres in alkaline media. *Electrochem. commun.* **2007**, *9* (5), 997–1001.

(4) Shen, P. K.; Xu, C. Alcohol oxidation on nanocrystalline oxide Pd/C promoted electrocatalysts. *Electrochem. commun.* **2006**, *8* (1), 184–188.

(5) Shen, S. Y.; Zhao, T. S.; Xu, J. B.; Li, Y. S. Synthesis of PdNi catalysts for the oxidation of ethanol in alkaline direct ethanol fuel cells. *J. Power Sources* **2010**, *195*, 1001–1006.

(6) Neto, A. O.; Tusi, M. M.; De Oliveira Polanco, N. S.; Da Silva, S. G.; Coelho Dos Santos, M.; Spinacé, E. V. PdBi/C electrocatalysts for ethanol electro-oxidation in alkaline medium. *Int. J. Hydrogen Energy* **2011**, *36* (17), 10522–10526.

(7) Jiang, R.; Tran, D. T.; McClure, J. P.; Chu, D. A Class of (Pd − Ni − P) Electrocatalysts for the Ethanol Oxidation Reaction in Alkaline Media. *ACS Catalysis* **2014**, *4*, 2577-2586.

(8) Bianchini, C.; Bambagioni, V.; Filippi, J.; Marchionni, A.; Vizza, F.; Bert, P.; Tampucci, A. Selective oxidation of ethanol to acetic acid in highly efficient polymer electrolyte membrane-direct ethanol fuel cells. *Electrochem. commun.* **2009**, *11* (5), 1077–1080.

(9) Yu, E. H.; Krewer, U.; Scott, K. Principles and materials aspects of direct alkaline alcohol fuel cells. *Energies* **2010**, *3* (8), 1499–1528.

(10) Tang, Q.; Jiang, L.; Qi, J.; Jiang, Q.; Wang, S.; Sun, G. One step synthesis of carbon-supported Ag/MnyOx composites for oxygen reduction reaction in alkaline media. *Appl. Catal. B Environ.* **2011**, *104* (3–4), 337–345.

(11) Kamarudin, M. Z. F.; Kamarudin, S. K.; Masdar, M. S.; Daud, W. R. W. Review: Direct ethanol fuel cells. *Int. J. Hydrogen Energy* **2013**, *38* (22), 9438–9453.

(12) Grimmer, I.; Zorn, P.; Weinberger, S.; Grimmer, C.; Pichler, B.; Cermenek, B.; Gebetsroither, F.; Schenk, A.; Mautner, F.-A.; Bitschnau, B.; Hacker V. Ethanol tolerant precious metal free cathode catalyst for alkaline direct ethanol fuel cells. *Electrochim. Acta* **2017**, *228*, 325–331.

(13) Chaiburi, C.; Cermenek, B.; Pichler, B. E.; Grimmer, C.; Schenk, A.; Hacker, V. Ethanol - Tolerant Pt-free Cathode Catalysts for the Alkaline Direct Ethanol Fuel Cell. *Journal of New Materials for Electrochemical Systems* **2017**, *19* (4), 199–207.

(14) Merle, G.; Wessling, M.; Nijmeijer, K. Anion exchange membranes for alkaline fuel cells: A review. *J. Memb. Sci.* **2011**, *377* (1–2), 1–35.

(15) Wan, Y.; Peppley, B.; Creber, K. A. M.; Bui, V. T.; Halliop, E. Preliminary evaluation of an alkaline chitosan-based membrane fuel cell. *J. Power Sources* **2006**, *162* (1), 105–113.

(16) Wan, Y.; Creber, K. A. M.; Peppley, B.; Bui, V. T. Chitosan-based electrolyte composite membranes. II. Mechanical properties and ionic conductivity. *J. Memb. Sci.* **2006**, *284* (1–2), 331–338.

(17) Wan, Y.; Creber, K. A. M.; Peppley, B.; Tam Bui, V. Chitosan-based solid electrolyte composite membranes. I. Preparation and characterization. *J. Memb. Sci.* **2006**, *280* (1–2), 666–674.

(18) Xiong, Y.; Liu, Q. L.; Zhang, Q. G.; Zhu, A. M. Synthesis and characterization of cross-linked quaternized poly(vinyl alcohol)/chitosan composite anion exchange membranes for fuel cells. *J. Power Sources* **2008**, *183* (2), 447–453.

(19) Xiong, Y.; Fang, J.; Zeng, Q. H.; Liu, Q. L. Preparation and characterization of cross-linked quaternized poly(vinyl alcohol) membranes for anion exchange membrane fuel cells. *J. Memb. Sci.* **2008**, *311* (1–2), 319–325.

(20) Domb, A. J.; Yudovin-Farber, I.; Golenser, J.; Beyth, N.; Weiss, E. I. Quaternary ammonium polyethyleneimine: Antibacterial activity. *J. Nanomater.* **2010**, *2010*, Article ID 826343.

(21) Wu, J.; Su, Z. G.; Ma, G. H. A thermo- and pH-sensitive hydrogel composed of quaternized chitosan/glycerophosphate. *Int. J. Pharm.* **2006**, *315* (1–2), 1–11.

(22) Tian, G.; Liu, L.; Meng, Q.; Cao, B. Preparation and characterization of cross-linked quaternised polyvinyl alcohol membrane/activated carbon composite electrode for membrane capacitive deionization. *Desalination* **2014**, *354*, 107–115.

(23) Peng, Z. X.; Wang, L.; Du, L.; Guo, S. R.; Wang, X. Q.; Tang, T. T. Adjustment of the antibacterial activity and biocompatibility of hydroxypropyltrimethyl ammonium chloride chitosan by varying the degree of substitution of quaternary ammonium. *Carbohydr. Polym.* **2010**, *81* (2), 275–283.

(24) Aeshala, L. M.; Uppaluri, R.; Verma, A. Electrochemical conversion of CO_2 to fuels: tuning of the reaction zone using suitable functional groups in a solid polymer electrolyte. *Phys. Chem. Chem. Phys.* **2014**, *16* (33), 17588–17594.

(25) Merle, G.; Hosseiny, S. S.; Wessling, M.; Nijmeijer, K. New cross-linked PVA based polymer electrolyte membranes for alkaline fuel cells. *J. Memb. Sci.* **2012**, *409–410*, 191–199.

(26) Feketeföldi, B.; Cermenek, B.; Spirk, C.; Schenk, A.; Grimmer, C.; Bodner, M.; Koller, M.; Ribitsch, V., Hacker, V. Chitosan-Based Anion Exchange Membranes for Direct Ethanol Fuel Cells. *J. Membr. Sci. Technol.* **2016**, *6* (1), 145.

(27) Grimmer, C.; Zacharias, R.; Grandi, M.; Cermenek, B.; Schenk, A.; Weinberger, S.; Mautner, F. A.; Bitschnau, B.; Hacker, V. Carbon Supported Ruthenium as Anode Catalyst for Alkaline Direct Borohydride Fuel Cells. *J. Phys. Chem. C.* **2015**, *119*, 23839-23844.

(28) Wang, Y.; Shi, F.-F.; Yang, Y.-Y.; Cai, W.-B. Carbon supported Pd-Ni-P nanoalloy as an efficient catalyst for ethanol electro-oxidation in alkaline media. *J. Power Sources* **2013**, *243*, 369-373.

(29) Lee, Y. W.; Han, S. B.; Park, K. W. Electrochemical properties of Pd nanostructures in alkaline solution. *Electrochem. commun.* **2009**, *11* (10), 1968–1971.

(30) Ranninger, J. Development and Characterization of Pd-based Catalysts for the alkaline Direct Ethanol Fuel Cell. *Masterarbeit* **2017**, Graz University of Technology, Graz.

(31) Cermenek, B.; Hacker, V.; Feketeföldi, B; & Ribitsch, V. e!Polycat - Pt-freie Katalysatorsysteme und ethanolbeständige Polysaccharid-Membranen für die alkalische DEFC. *Final report* **2017**, FFG Austrian Research Promotion Agency, Climate and energy funds, Vienna. https://www.energieforschung.at/assets/project/final-report/ePolycat-publizierbarer-Endbericht.pdf

(32) Hacker, V.; Cermenek, B. IEA AFC Annex 35: Brennstoffzellen für portable Anwendungen: Arbeitsperiode 2014-2017. *Nachhaltig Wirtschaften* vol. Berichte aus Energie- und Umweltforschung 28/**2017** edn, Bundesministerium für Verkehr, Innovation und Technologie, Vienna. https://nachhaltigwirtschaften.at/resources/iea_pdf/endbericht_201728_afc-annex-35-848118.pdf

Proceedings of EFC2015
European Fuel Cell Technology & Applications Conference - Piero Lunghi Conference
December 16-18, 2015, Naples, Italy

EFC15143

CHARACTERIZATION OF PLATINUM-FREE ELECTROCATALYSTS AND ANION EXCHANGE MEMBRANES FOR DIRECT ETHANOL FUEL CELL

B. Cermenek*, B. Feketeföldi**, R. Zacharias*, V. Ribitsch*** and V. Hacker*
*Institute of Chemical Engineering and Environmental Technology, Graz University of Technology, NAWI Graz, Inffeldgasse 25C, 8010 Graz, (*Austria*)
**Institute for Surface Technologies and Photonics, JOANNEUM RESEARCH Forschungsgesellschaft mbH/Materials, Franz-Pichler-Straße, 8160 Weiz, (*Austria*)
***Institute of Chemistry, University of Graz, Heinrichstraße 28, 8010 Graz, (*Austria*)

***Abstract* – Nickel dimethylglyoxime ($Ni(II)(DMG)_2$) complex was synthesized with precipitation method and the electrochemical properties were characterized by means of cyclic voltammetry and chronoamperometry. This catalyst exhibits superior long-term stability. A series of membranes based on quaternized chitosan (HTCC) and quaternized poly(vinyl alcohol) (QPVA) with various degrees of silica content were synthesized using a mixture of tetraethoxysilane / methyltriethyloxysilane (TEOS/MTES) by sol-gel method. The chemical properties of the organic/inorganic hybrids were characterized by means of electrochemical impedance spectroscopy (EIS) method and permeability-cell method. These membranes show an ion conductivity between $4.1 \cdot 10^{-3}$ and $5.3 \cdot 10^{-3}$ $S \cdot cm^{-1}$ and low ethanol permeability from $1.5 \cdot 10^{-7}$ to $7.3 \cdot 10^{-7}$ $cm^2 \cdot s^{-1}$ at 60 °C.**

***Index Terms* – Anion Exchange Membrane, EtOH-permeability, Pt-free electrocatalyst, long-term stability.**

I. INTRODUCTION

The alkaline direct ethanol fuel cell (DEFC) is a promising energy technology for portable applications [1]. Main challenges are their low power density and high costs of the components. Hence, the optimization of the membrane and the electrocatalyst is very important. Ethanol as renewable fuel is converted directly into electricity without reforming within fuel cells. However, the whole Gibbs free energy of this oxidation reaction may not be converted into electric energy so far, since the C-C bond is thermodynamically stable. Therefore, the great challenge is to develop a highly active catalyst for breaking the C-C bond of ethanol to achieve the complete oxidation to carbon dioxide and water releasing 12 electrons (see Eq. 1) [2]. Different reaction intermediate products, which are generated during ethanol oxidation reaction (EOR) in alkaline medium (see Eq. 2), deactivate the catalyst resulting in only 33.3% of Faradic efficiency [2].

$$C_2H_5OH + 12OH^- \rightarrow 2CO_2 + 9H_2O + 12e^- \quad (1)$$

$$C_2H_5OH + 5OH^- \rightarrow CH_3COO^- + 4H_2O + 4e^- \quad (2)$$

Various nickel-complexes [3-5] were established as catalysts for EOR in alkaline medium in order to substitute noble metal containing catalysts (for example: Pt, Pd, Au etc.) and enhance their long-term stability, respectively. Anion exchange membranes (AEMs) are used in DEFCs to transport the OH^- ions from the cathode to the anode and to reduce the so-called ethanol crossover due the reversed ion direction [6].

In this study, the catalytic activity and stability of the synthesized $Ni(II)(DMG)_2$ complex are compared to Pd/C and $Pd_{80}Ni_{20}$/C catalyst as references [7]. Furthermore, HTCC/QPVA membranes are prepared by blending and chemical cross-linking with ethylene glycol diglycidyl ether (EGDE) for chitosan and glutaraldehyde (GA) for QPVA. Nanoscale particles are introduced into the blend matrix leading to a hybrid system of organic/inorganic membranes. A sol-gel process with tetraethoxysilane (TEOS) as precursor and couple agent, such as methyltriethyloxysilane (MTES), is chosen and hydrolysis and condensation reactions cause polymerization of nano-silicon dioxide particles [8, 9].

II. EXPERIMENTAL

A. Synthesis of anion exchange membranes

All reagents were supplied by Sigma-Aldrich Handels Gmbh. Austria. QPVA and HTCC were dissolved in water and cross-linking reagents and quantitative amount of TEOS/MTES solution were added. The solutions were poured into plastic Petri dishes and dried.

Copyright © 2015

B. Synthesis of Pt-free electrocatalysts

$Ni(II)(DMG)_2$ complex was synthesized by a precipitation method [4,5]. An appropriate amount of $(NH_4)_2SO_4$ and $NiSO_4 \cdot 6H_2O$ in the ratio of 1:1 was dissolved in 14 ml HCl (2.5 M) and filled up to 200 ml with ultra-pure water. The solution was vigorously stirred at 70-80 °C. Then dimethylglyoxime (DMG) in 20 ml EtOH (99.9%) was added to the solution under stirring at 70-80 °C for approx. 1-1.5 h. After that 6.0 M KOH was added to the solution until pH = 8 was reached resulting a red-rose complex. After 24 h reaction time the $Ni(II)(DMG)_2$-complex was centrifuged and washed several times and dried at 70 °C.

C. Characterization of anion exchange membranes

The OH^--conductivity was determined using EIS [10] and the ethanol permeability was measured by the permeability-cell method.

D. Characterization of Pt-free electrocatalysts

The catalytic activity and stability of $Ni(II)(DMG)_2$ complex (without carbon as support material) toward EOR in alkaline medium were analyzed using cyclic voltammetry (CV) and chronoamperometry (CA) technique using Rotating Disc Electrode (RDE).

III. Results and Discussion

A limiting factor in operation of DEFC is the transport of ethanol through the membrane from anode to cathode. In Table I the ethanol permeability of the synthesized hybrid membranes at a temperature of 60 °C in 1.0 M ethanol mixture is presented. The addition of silica into the blend membranes changed the ethanol transport properties. The silica content led to the increase of aggregate pores, thus to a higher mass/ethanol transport [9].

TABLE I: SiO_2-content and Ethanol permeability (P) for membranes

Membrane	HM-0	HM-5	HM-10	HM-15	HM-20	HM-25
SiO_2 (wt %)	0	5	10	15	20	25
$Px10^{-7}$ (cm^2s^{-1}), 60°C	1.46	2.56	3.50	4.70	5.90	7.32

Fig. 1. shows the OH^--conductivity of the hybrid membranes. The ion conductivity increases with higher SiO_2 contents. The ion conductivity of these hybrid membranes depends on water uptake and quaternization degree of chitosan (88%) and QPVA (15%). The addition of silica facilitated the formation of small ion channels for OH^--transfer, resulting in a higher conductivity.

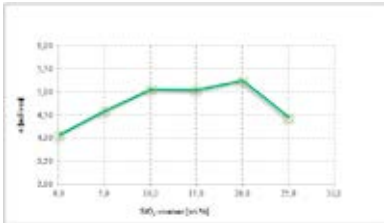


Fig. 1. Effect of SiO_2 content on OH^--conductivity.

The drawbacks of alkaline DEFC catalysis are on the one hand the sluggish kinetics of EOR on standard materials and on the other hand the insufficient long-term stability under operating conditions of these standard catalysts. Fig. 2a. shows that $Ni(II)(DMG)_2$ complex possesses a dissatisfactory catalytic activity toward EOR, due to high onset-potential and large anodic overpotential. However, the $Ni(II)(DMG)_2$ complex exhibits the highest stability in comparison with Pd-based catalysts due to the ligand (see Fig. 2b) [4].

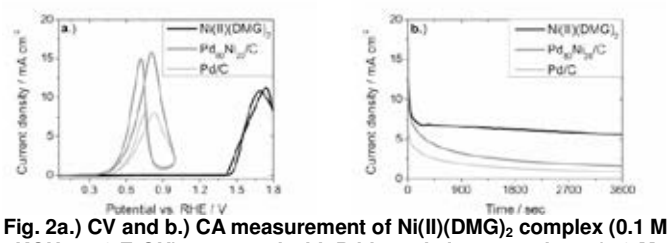


Fig. 2a.) CV and b.) CA measurement of $Ni(II)(DMG)_2$ complex (0.1 M KOH + 1.0 EtOH) compared with Pd-based electrocatalysts (1.0 M KOH + 1.0 M EtOH) [7].

IV. Conclusion

Hybrid AEMs were successfully prepared with HTCC/QPVA and TEOS/MTES by sol-gel method. Membrane properties were highly dependent on SiO_2 content. The highlight of the electrochemical investigation of $Ni(II)(DMG)_2$ complex was their superior long-term stability.

The components as $Ni(II)(DMG)_2$ complex as well as Pd-based electrocatalysts and HM-20 will be further processed to membrane electrode assemblies (MEAs) and operated in single cell DEFC.

Acknowledgment

Financial support by the Austrian Federal Ministry of Transport, Innovation and Technology (BMVIT), The Austrian Research Promotion Agency (FFG) and the IEA research cooperation is gratefully acknowledged.

References

[1] An, T.S. Zhao, Y.S. Li, Renew. Sustain. Energy Rev. 50 (2015) 1462–1468.
[2] M.Z.F. Kamarudin, S.K. Kamarudin, M.S. Masdar, W.R.W. Daud, Int. J. Hydrogen Energy (2012) 1.
[3] M. Revenga-Parra, T. García, E. Lorenzo, F. Pariente, Sens. Actuators B Chem. 130 (2008) 730.
[4] W.S. Cardoso, V.L.N. Dias, W.M. Costa, I. de Araujo Rodrigues, E.P. Marques, A.G. Sousa, J. Boaventura, C.W.B. Bezerra, C. Song, H. Liu, J. Zhang, A.L.B. Marques, J. Appl. Electrochem. 39 (2008) 55–64.
[5] M.A. Malati, Experimental Inorganic/Physical Chemistry, 1999.
[6] E.H. Yu, U. Krewer, K. Scott, Energies 3 (2010) 1499.
[7] B. Cermenek, R. Zacharias, M. Grandi, C. Grimmer, A. Schenk, V. Hacker, 1st International Workshop on Hydrogen and Fuel Cells, Yokohama National University, Japan, 2015.
[8] Y. Xiong, Q.L. Liu, Q.G. Zhang, A.M. Zhu, J. Power Sources 183 (2008) 447–453.
[9] B.P. Tripathi, M. Kumar, V.K. Shahi, J. Memb. Sci. 360 (2010) 90–101.
[10] C. Ranacher, R. Resel, P. Moni, B. Cermenek, V. Hacker, A.M. Coclite, Macromolecules (2015).

Copyright © 2015

8.2 PART II: Effects of Ni and Bi on EOR Performance and Structural Characteristics of Carbon Supported Pd-Based Nanocatalysts

8.2.1 Chemicals and Materials

Anode Catalysts

- Palladium(II) chloride ($PdCl_2$, anhydrous, 59-60% Pd basis, Aldrich),
- nickel(II) nitrate hexahydrate ($Ni(NO_3)_2 \cdot 6H_2O$, Aldrich),
- bismuth(III) chloride ($BiCl_3$, reagent grade, ≥ 98%, Aldrich),
- sodium chloride (NaCl, ≥ 99.5%, Aldrich),
- hydrochloric acid (HCl p.a. ≥ 32%, Fluka Analytics),
- Vulcan XC72R carbon black (CABOT Corporation, USA),
- sodium borohydride ($NaBH_4$, Sigma-Aldrich),
- 2-propanol (ASC ≥ 99.8%, Sigma-Aldrich),
- sodium hydroxide (NaOH, Aldrich),
- ultra-pure water (~18 MΩ·cm, Barnstead NANOpure Water Purification System) were used for the development of Pd/C, $Pd_{60}Ni_{40}$/C, $Pd_{60}Bi_{40}$/C and $Pd_{60}Ni_{20}Bi_{20}$/C anode catalysts [15].

Anode

- Carbon cloth (P/N: ELAT-H; Hydrophilic Plain Cloth, Fuel Cell Store / FuelCellsEtc., USA),
- AS4 ionomer solution (5 wt.%, Tokuyama Corporation, Japan),
- 1-propanol (Sigma-Aldrich) were used for the development of $Pd_{60}Ni_{40}$/C and $Pd_{60}Ni_{20}Bi_{20}$/C based anodes.

Anode 1: (AL = $Pd_{60}Ni_{40}$/C; C = Vulcan XC72R; GDL = carbon cloth)

Anode 2: (AL = $Pd_{60}Ni_{20}Bi_{20}$/C; C = Vulcan XC72R; GDL = carbon cloth)

Cathode

- Silver nitrate ($AgNO_3$, Alfa Aesar, USA),
- Vulcan XC72R carbon black (CABOT Corporation, USA),
- 2-propanol (ASC ≥ 99.8%, Sigma-Aldrich),
- potassium permanganate ($KMnO_4$, Merck),
- Carbon paper (Toray paper: P/N: T-090, FuelCellsEtc, USA),

- PTFE powder (3M Dyneon, TF 2021Z),
- AS4 ionomer solution (5 wt.%, Tokuyama Corporation, Japan),
- 1-propanol (Sigma-Aldrich) and
- ultra-pure water (~18 MΩ·cm, Barnstead NANOpure Water Purification System) were used for the development of the Ag-MnO_x/C based cathode.

Cathode: (AL = Ag-MnO_x/C; C = Vulcan XC72R; GDL = carbon paper)

MEA 1

- $Pd_{60}Ni_{40}$/C based anode (in-house)
- A201 AEM (27 µm, quaternary ammonium groups, Tokuyama Corporation)
- Ag-MnO_x/C based cathode (in-house)

MEA 2

- $Pd_{60}Ni_{20}Bi_{20}$/C based anode (in-house)
- A201 AEM (27 µm, quaternary ammonium groups, Tokuyama Corporation)
- Ag-MnO_x/C based cathode (in-house)

Electrochemical characterizations / Single cell tests

- Nafion ionomer solution (5 wt.%, Quintech),
- 1.0 M potassium hydroxide standard solution (KOH, FIXANAL KA 180 mL, Sigma-Aldrich),
- ethanol abs. (99.999%, Aldrich) and
- ultra-pure water (~18 MΩ·cm, Barnstead NANOpure Water Purification System) were used for electrochemical characterizations of Pd/C, $Pd_{60}Ni_{40}$/C, $Pd_{60}Bi_{40}$/C and $Pd_{60}Ni_{20}Bi_{20}$/C catalysts [15], and for single cell tests of the $Pd_{60}Ni_{40}$/C and $Pd_{60}Ni_{20}Bi_{20}$/C based anodes.

8.2.2 Physico-Chemical Characterization

ICP-OES analysis

Table 15: ICP-OES data of carbon supported Pd-based catalysts [15,29].

Catalysts		Pd (g/kg)	Ni (g/kg)	Bi (g/kg)	Pd (mol/kg)	Ni (mol/kg)	Bi (mol/kg)	Sum (mol/kg)	Pd (at.%)	Ni (at.%)	Bi (at.%)
PdC	Average	138.1	-	-	1.30	-	-	1.30	100	-	-
	SD	2.0	-	-	0.02	-	-	0.02	-	-	-
$Pd_{60}Ni_{40}/C$	Average	117.5	42.9	-	1.10	0.73	-	1.84	60.2	39.8	-
	SD	2.0	1.2	-	0.02	0.02	-	0.03	1.4	1.3	-
$Pd_{60}Bi_{40}/C$	Average	111.9	-	141.1	1.05	-	0.675	1.73	60.9	-	39.1
	SD	2.4	-	0.9	0.02	-	0.004	0.02	1.5	-	0.6
$Pd_{60}Ni_{20}Bi_{20}/C$	Average	110.6	18.5	70.4	1.04	0.315	0.34	1.69	61.4	18.6	19.9
	SD	1.8	0.2	1.5	0.02	0.003	0.01	0.02	1.2	0.3	0.5

SD … standard deviation
Atomic weight (AMU): Pd = 106.42; Ni = 58.69; Bi = 208.98

TEM-EDX analysis

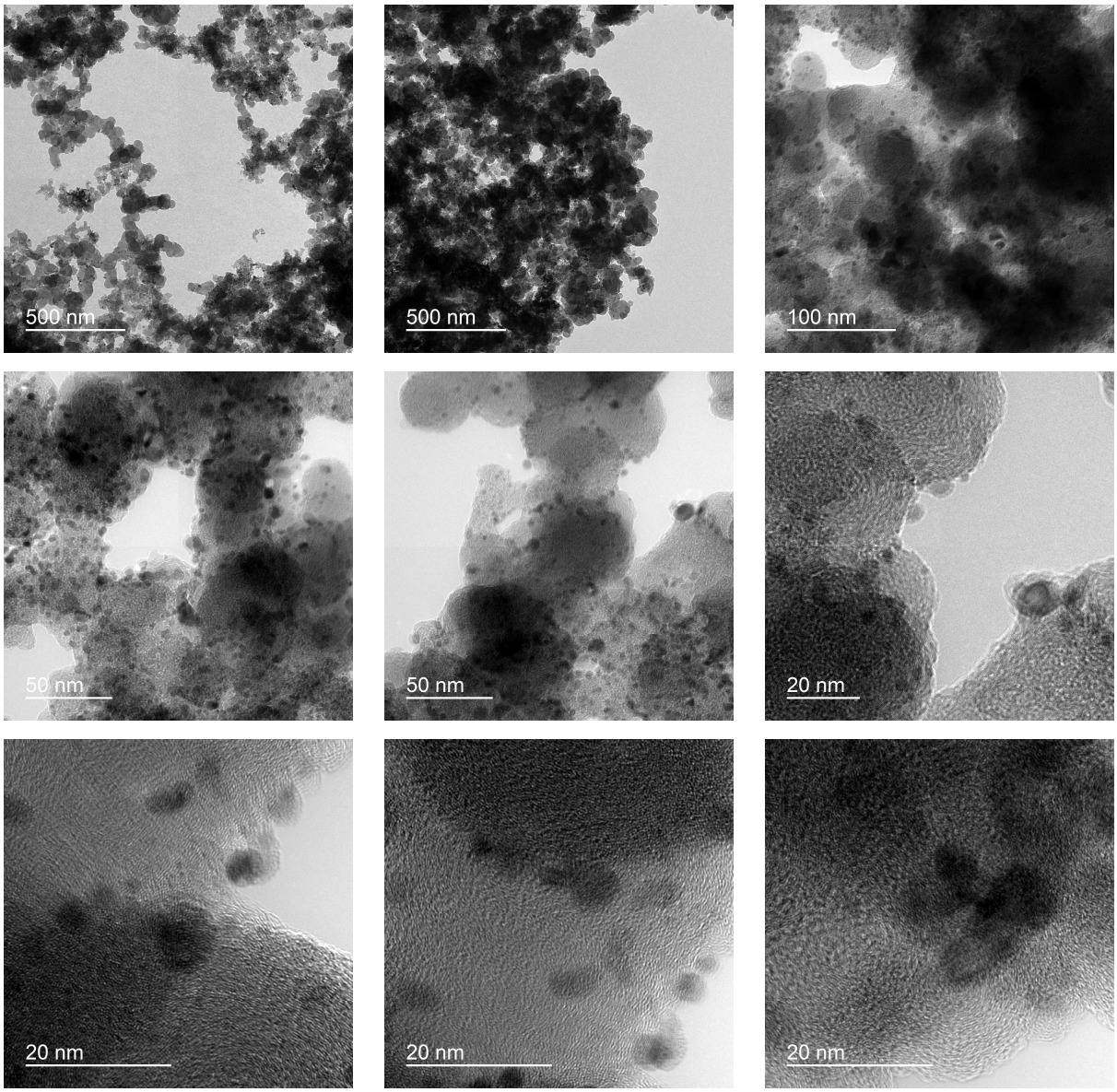


Figure 44: TEM micrographs with low and high magnifications of the Pd/C catalyst [15].

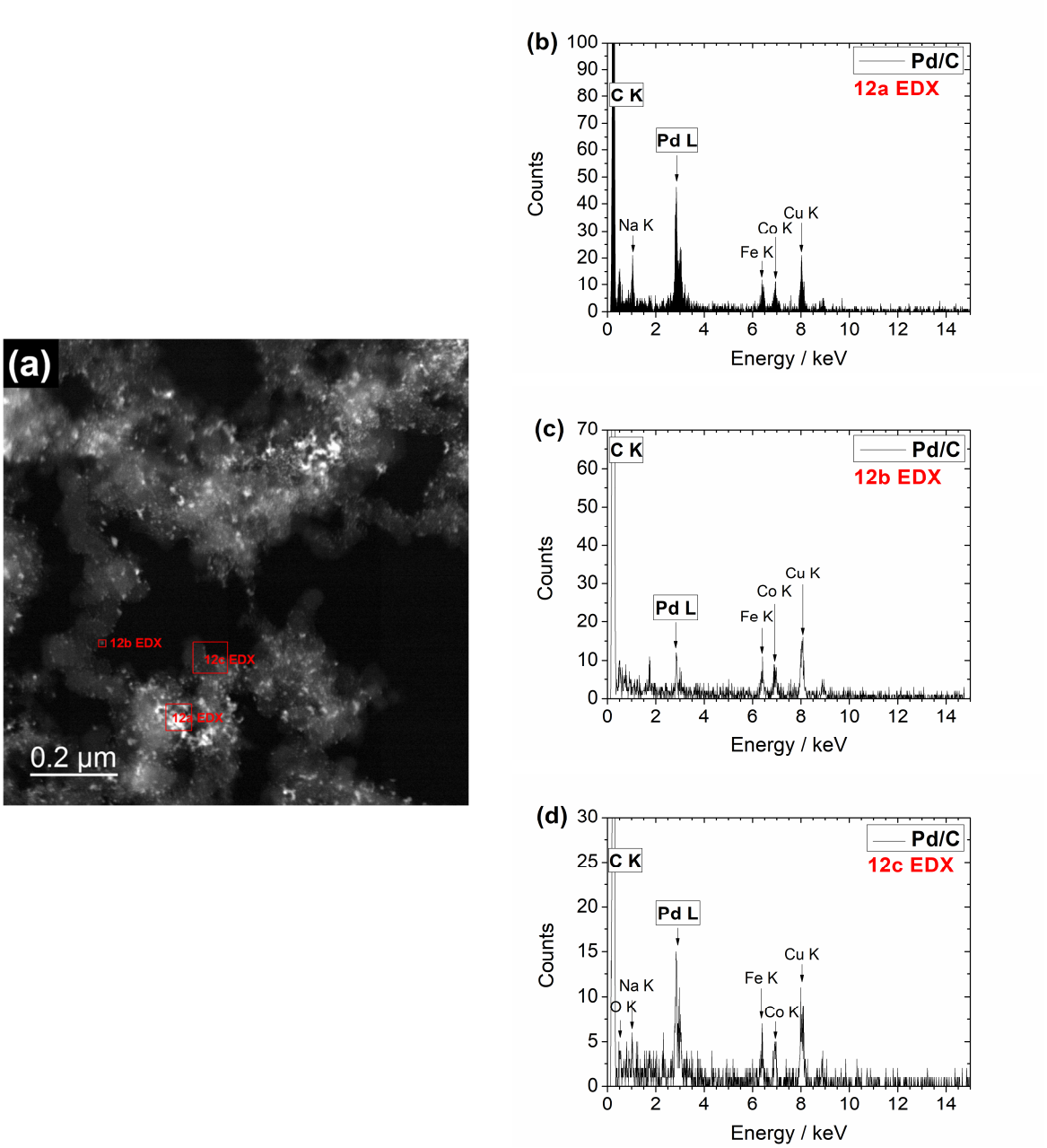


Figure 45: STEM-HAADF micrograph **(a)** and the corresponding EDX spectra **(b)-(d)** of the Pd/C catalyst [15].

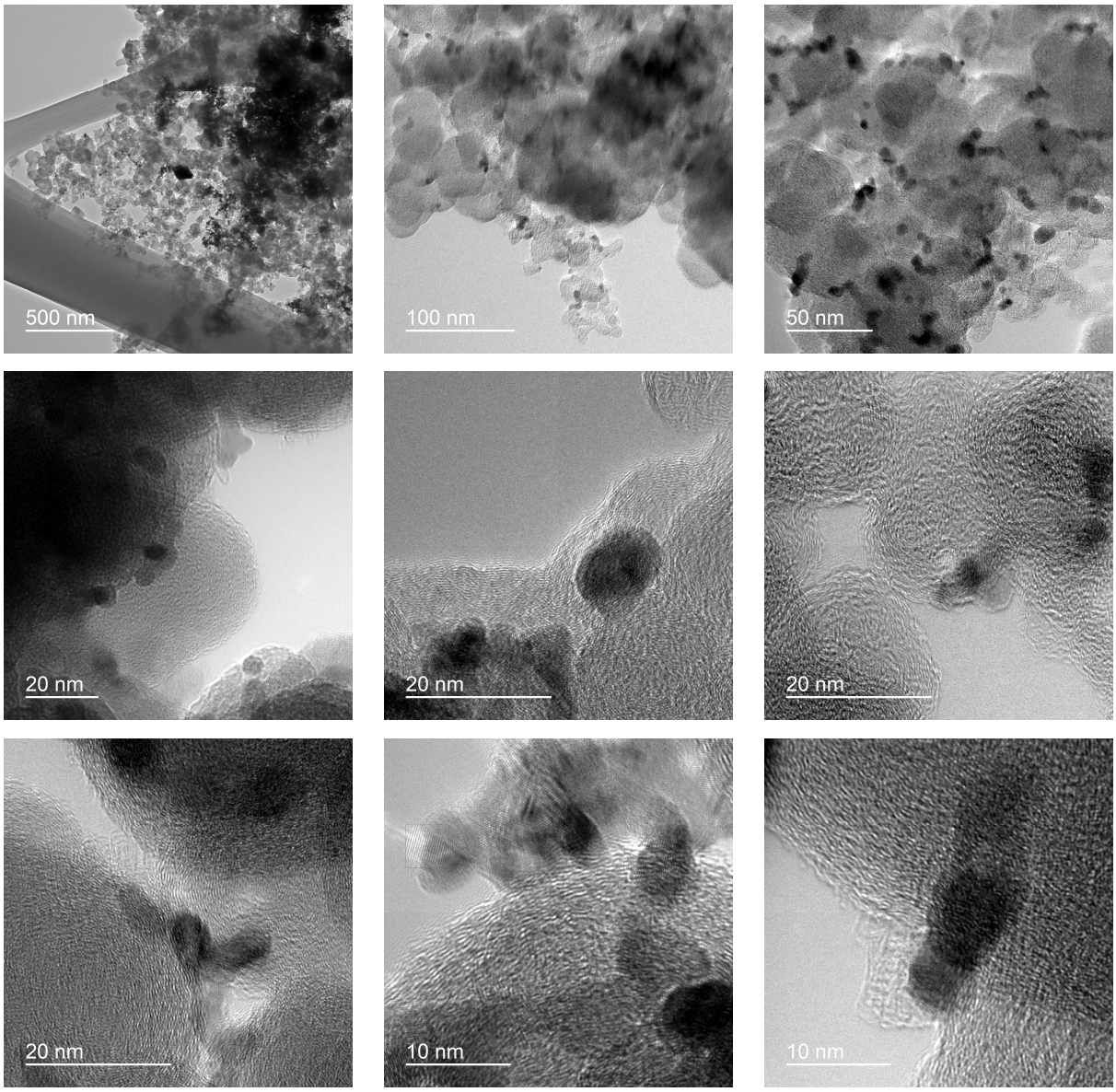


Figure 46: TEM micrographs with low and high magnifications of the $Pd_{60}Ni_{40}$/C catalyst [15].

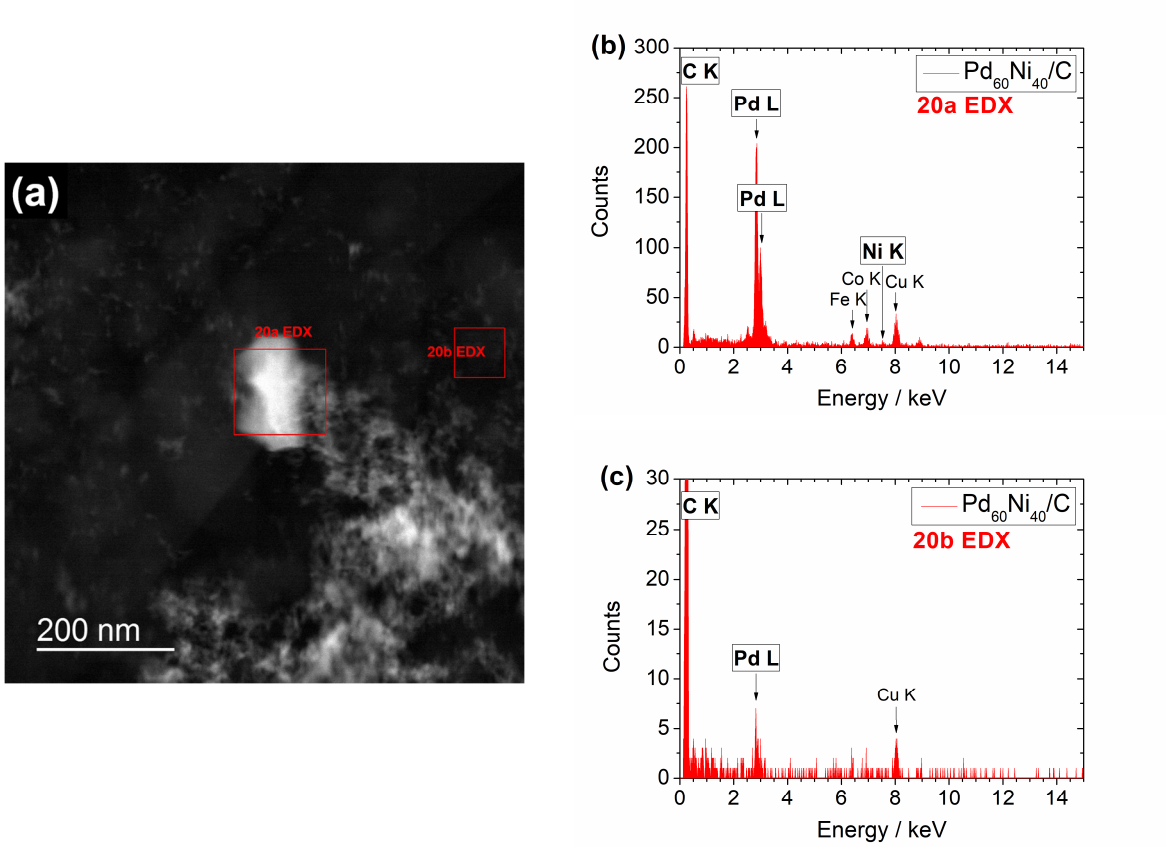


Figure 47: STEM-HAADF micrograph **(a)** and the corresponding EDX spectra **(b)** and **(c)** of the $Pd_{60}Ni_{40}/C$ catalyst [15].

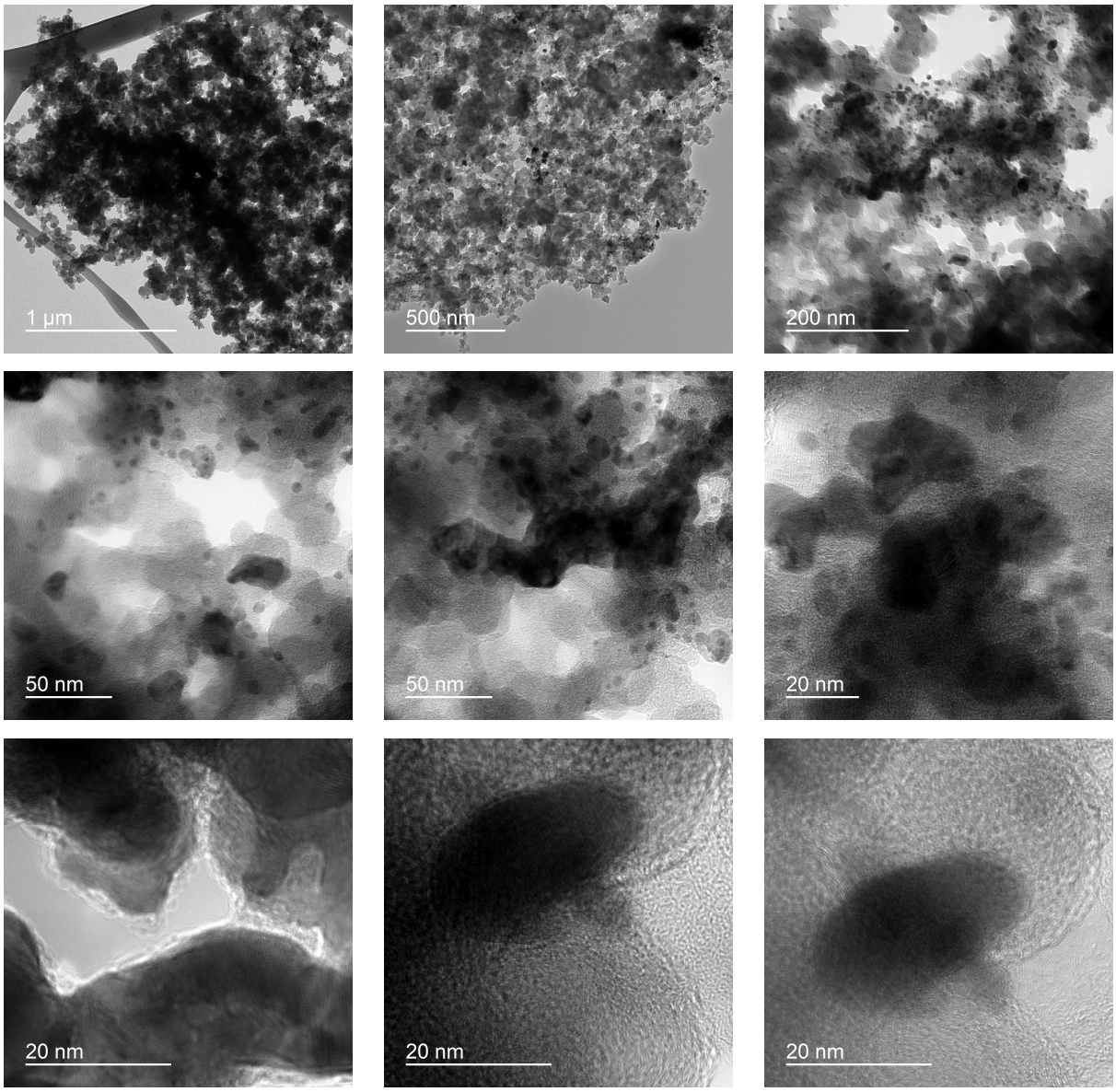


Figure 48: TEM micrographs with low and high magnifications of the $Pd_{60}Bi_{40}$/C catalyst [15].

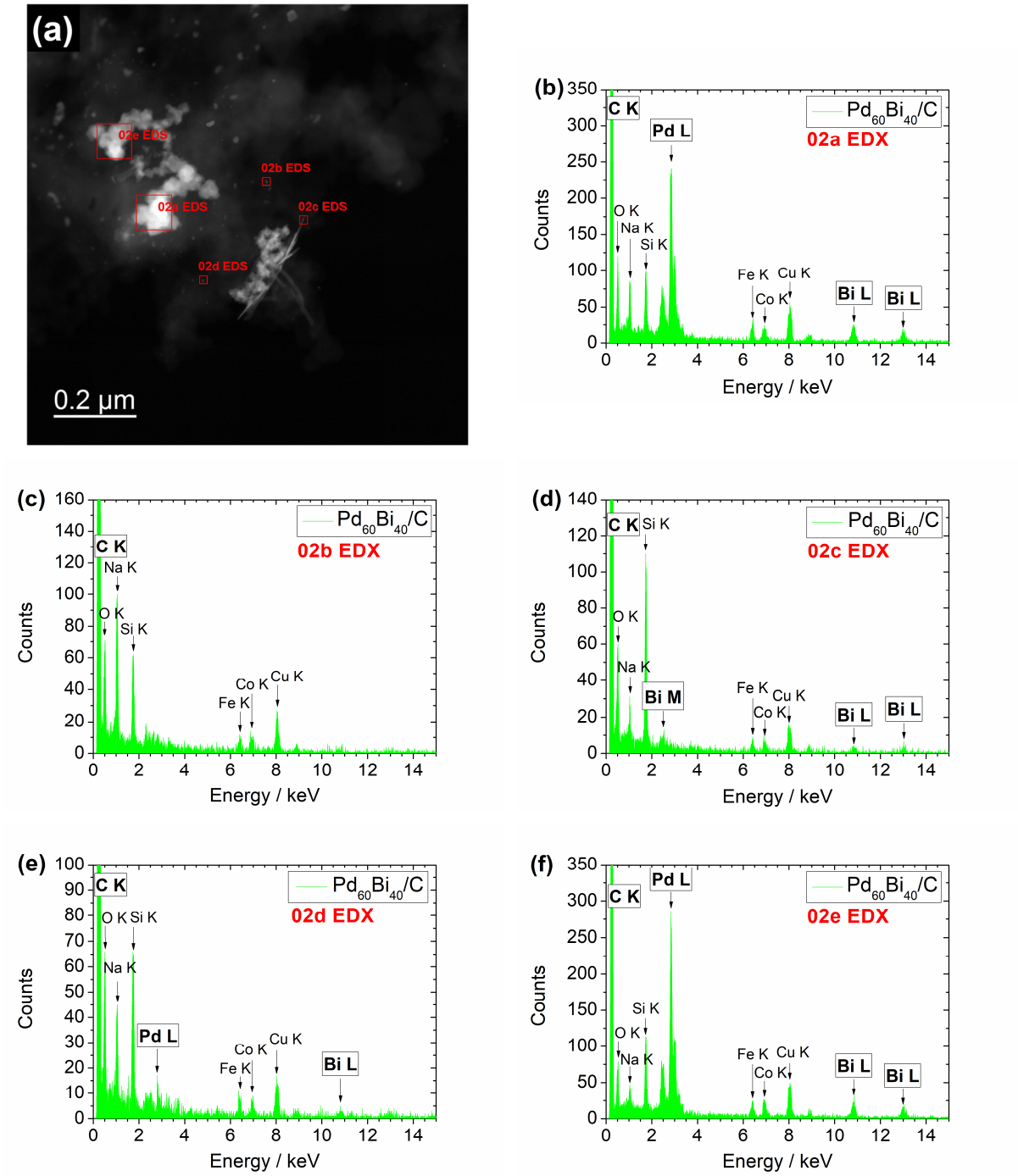


Figure 49: STEM-HAADF micrograph **(a)** and the corresponding EDX spectra **(b)-(f)** of the $Pd_{60}Bi_{40}/C$ catalyst [15].

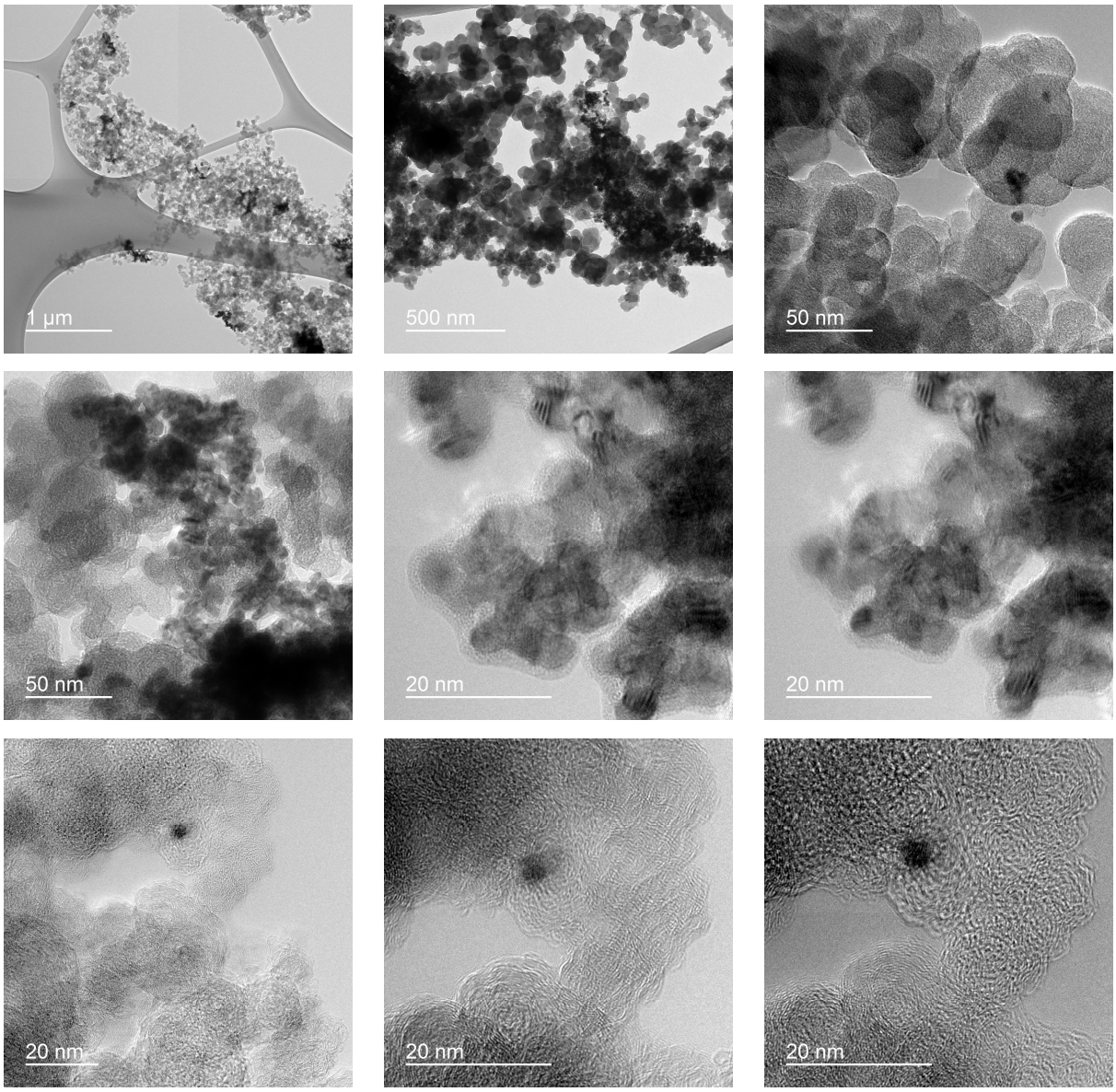


Figure 50: TEM micrographs with low and high magnifications of the $Pd_{60}Ni_{20}Bi_{20}$/C catalyst [15].

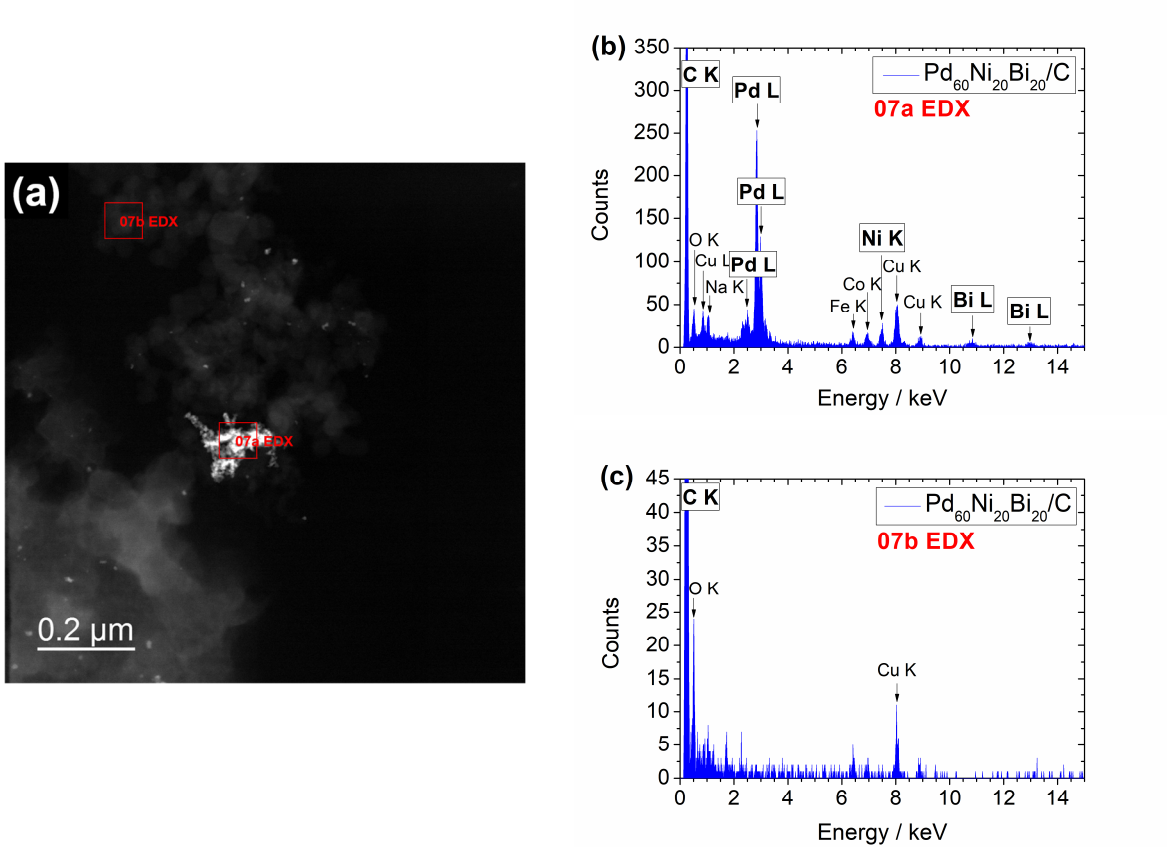


Figure 51: STEM-HAADF micrograph **(a)** and the corresponding EDX spectra **(b)** and **(c)** of the $Pd_{60}Ni_{20}Bi_{20}/C$ catalyst [15].

XRD analysis

Table 16: XRD data (Rietveld refinement) of Pd/C catalyst [15].

Catalyst	Peak No.	Peak Pos. (° 2θ)	*d*-spacing (Å)	Rel. Int. (%)	Height (cts)	h	k	l	Assignment
Pd/C	1	25.6883	3.46513	2.44	269(444)	0	0	2	Graphite(2H)_187640-ICSD
	2	40.15036	2.24412	100	11046(1137)	1	1	1	Pd_64922-ICSD
	3	44.50528	2.03411	0.06	7(10)	0	1	0	Graphite(2H)_187640-ICSD
	4	46.48519	1.95198	0.31	34(26)	0	1	1	Graphite(2H)_187640-ICSD
	5	46.69292	1.94378	41.72	4608(787)	0	0	2	Pd_64922-ICSD
	6	52.07588	1.7548	0.06	7(13)	0	1	2	Graphite(2H)_187640-ICSD
	7	52.74353	1.73415	0.16	18(33)	0	0	4	Graphite(2H)_187640-ICSD
	8	60.5655	1.52756	0.1	11(22)	0	1	3	Graphite(2H)_187640-ICSD
	9	68.14725	1.3749	17.17	1896(611)	0	2	2	Pd_64922-ICSD
	10	71.39799	1.32007	0.02	2(3)	0	1	4	Graphite(2H)_187640-ICSD
	11	81.92817	1.17498	0.09	10(6)	1	1	0	Graphite(2H)_187640-ICSD
	12	82.12421	1.17267	16.18	1787(629)	1	1	3	Pd_64922-ICSD
	13	83.52741	1.1565	0.03	3(2)	0	0	6	Graphite(2H)_187640-ICSD
	14	84.4146	1.14659	0.03	4(3)	0	1	5	Graphite(2H)_187640-ICSD
	15	86.6384	1.12278	4.45	491(330)	2	2	2	Pd_64922-ICSD
	16	87.59822	1.11294	0.16	17(18)	1	1	2	Graphite(2H)_187640-ICSD
	17	98.38704	1.01767	0	0(1)	0	2	0	Graphite(2H)_187640-ICSD
	18	99.8158	1.00691	0.02	3(6)	0	2	1	Graphite(2H)_187640-ICSD
	19	99.99369	1.0056	0.01	1(2)	0	1	6	Graphite(2H)_187640-ICSD

Table 17: XRD data (Rietveld refinement) of $Pd_{60}Ni_{40}$/C catalyst [15].

Catalyst	Peak No.	Peak Pos. (° 2θ)	*d*-spacing (Å)	Rel. Int. (%)	Height (cts)	h	k	l	Assignment
$Pd_{60}Ni_{40}$/C	1	25.49438	3.49105	3.8	425(790)	0	0	2	Graphite(2H)_187640-ICSD
	2	38.86749	2.31518	0.16	18(23)	0	1	0	Graphite(2H)_187640-ICSD
	3	40.14334	2.24449	100	11184(990)	1	1	1	Pd_64922-ICSD
	4	41.01806	2.19862	0.78	87(66)	0	1	1	Graphite(2H)_187640-ICSD
	5	41.07087	2.19592	14.15	1582(414)	1	1	1	Pd09Ni01_106936-ICSD
	6	46.66	1.94507	29.43	3291(799)	0	0	2	Pd_64922-ICSD
	7	46.98032	1.93255	0.15	17(13)	0	1	2	Graphite(2H)_187640-ICSD
	8	47.75606	1.90295	5.9	660(285)	0	0	2	Pd09Ni01_106936-ICSD
	9	52.16239	1.7521	0.26	29(72)	0	0	4	Graphite(2H)_187640-ICSD
	10	55.8115	1.64587	0.22	25(69)	0	1	3	Graphite(2H)_187640-ICSD

11	66.8222	1.39891	0.04	4(5)	0	1	4	Graphite(2H)_187640-ICSD
12	68.0186	1.37719	8.78	982(657)	0	2	2	Pd_64922-ICSD
13	69.74018	1.34734	2.42	270(204)	0	2	2	Pd09Ni01_106936-ICSD
14	70.19932	1.33965	0.24	26(33)	1	1	0	Graphite(2H)_187640-ICSD
15	75.958	1.25176	0.36	40(79)	1	1	2	Graphite(2H)_187640-ICSD
16	79.78585	1.20105	0.06	6(9)	0	1	5	Graphite(2H)_187640-ICSD
17	81.9195	1.17508	7.71	862(683)	1	1	3	Pd_64922-ICSD
18	82.37596	1.16972	0.05	5(4)	0	0	6	Graphite(2H)_187640-ICSD
19	83.15676	1.16071	0.01	1(1)	0	2	0	Graphite(2H)_187640-ICSD
20	84.1423	1.14961	2.29	256(199)	1	1	3	Pd09Ni01_106936-ICSD
21	84.54067	1.14521	0.05	5(5)	0	2	1	Graphite(2H)_187640-ICSD
22	86.40569	1.12521	2.09	233(288)	2	2	2	Pd_64922-ICSD
23	88.67592	1.10218	0.01	2(3)	0	2	2	Graphite(2H)_187640-ICSD
24	88.81417	1.10082	0.63	71(101)	2	2	2	Pd09Ni01_106936-ICSD
25	92.60956	1.06538	0.21	24(53)	1	1	4	Graphite(2H)_187640-ICSD
26	94.97817	1.04497	0.01	1(4)	0	1	6	Graphite(2H)_187640-ICSD
27	95.56118	1.04013	0.04	4(11)	0	2	3	Graphite(2H)_187640-ICSD

Table 18: XRD data (Rietveld refinement) of $Pd_{60}Bi_{40}$/C catalyst [15].

Catalyst	Peak No.	Peak Pos. (° 2θ)	*d*-spacing (Å)	Rel. Int. (%)	Height (cts)	h	k	l	Assignment
$Pd_{60}Bi_{40}$/C	1	22.78376	3.89988	0.18	15(16)	1	1	2	PdBi_tetrag_56279-ICSD
	2	22.90073	3.88023	0.02	2(1)	0	2	0	Bi2O3_beta_189995-ICSD
	3	23.07864	3.85072	0.52	43(16)	0	0	3	Bi_53797-ICSD
	4	23.62549	3.76281	0.17	14(2)	1	0	1	Bi_53797-ICSD
	5	23.75021	3.74333	4.48	369(117)	0	1	1	Bi2O2(CO3)_252588-ICSD
	6	23.76185	3.74152	0.14	12(3)	0	2	0	SiO2_Keatite_34889-ICSD
	7	23.9399	3.7141	8.22	677(124)	0	1	2	SiO2_Keatite_34889-ICSD
	8	23.98752	3.70683	2.6	214(55)	1	0	1	Bi2O2(CO3)_252588-ICSD
	9	24.342	3.65365	0.02	2(1)	0	2	0	PdBi_tetrag_56279-ICSD
	10	25.38503	3.50584	7.76	639(617)	0	0	2	Graphite(2H)_187640-ICSD
	11	25.66562	3.46815	0.38	31(3)	1	2	0	Bi2O3_beta_189995-ICSD
	12	25.74292	3.45791	0.56	46(11)	0	2	1	PdBi_tetrag_56279-ICSD
	13	25.78099	3.45289	2.07	170(32)	0	0	4	Bi2O2(CO3)_252588-ICSD
	14	25.86106	3.44238	5.56	458(96)	2	0	2	PdBi_tetrag_56279-ICSD
	15	25.9845	3.4263	20.96	1726(195)	0	2	1	SiO2_Keatite_34889-ICSD
	16	26.63363	3.34425	0.1	8(2)	1	2	0	SiO2_Keatite_34889-ICSD
	17	26.79389	3.32461	4.29	353(95)	1	1	2	SiO2_Keatite_34889-ICSD
	18	27.21277	3.27438	17.39	1431(154)	0	1	2	Bi_53797-ICSD

19	27.92182	3.19282	15.99	1316(159)	0	2	1	Bi2O3_beta_189995-ICSD
20	28.64995	3.11331	3.25	267(134)	1	2	1	SiO2_Keatite_34889-ICSD
21	29.51675	3.02382	0.23	19(17)	1	1	3	PdBi_tetrag_56279-ICSD
22	29.57796	3.01771	0	0.2(2)	0	2	2	PdBi_tetrag_56279-ICSD
23	30.09069	2.96744	8.53	702(215)	0	1	3	Bi2O2(CO3)_252588-ICSD
24	30.26284	2.95095	0.31	25(2)	1	2	1	Bi2O3_beta_189995-ICSD
25	30.28193	2.94914	9.75	803(230)	1	0	3	Bi2O2(CO3)_252588-ICSD
26	31.59842	2.8292	0.02	2(1)	2	2	0	PdBi_tetrag_56279-ICSD
27	31.76948	2.81436	2.41	199(44)	0	0	2	Bi2O3_beta_189995-ICSD
28	31.79675	2.81201	0.07	6(3)	0	2	2	SiO2_Keatite_34889-ICSD
29	32.36185	2.76418	1.2	99(33)	3	1	0	PdBi_tetrag_56279-ICSD
30	32.67549	2.73836	4.19	345(18)	2	2	0	Bi2O3_beta_189995-ICSD
31	32.71416	2.73522	23.63	1945(406)	2	2	1	PdBi_tetrag_56279-ICSD
32	32.77198	2.73052	6.16	507(77)	1	1	0	Bi2O2(CO3)_252588-ICSD
33	33.39274	2.68117	8.37	689(208)	0	0	4	PdBi_tetrag_56279-ICSD
34	33.45498	2.67632	0.95	78(25)	3	1	1	PdBi_tetrag_56279-ICSD
35	33.66189	2.66034	0.01	0.41(9)	0	1	3	SiO2_Keatite_34889-ICSD
36	33.87086	2.64441	0.01	0.8(1)	0	1	2	Bi2O3_beta_189995-ICSD
37	33.92049	2.64065	0.07	6(2)	2	2	0	SiO2_Keatite_34889-ICSD
38	34.04954	2.63094	0.06	5(2)	1	2	2	SiO2_Keatite_34889-ICSD
39	35.12859	2.55255	5.99	493(244)	0	2	3	PdBi_tetrag_56279-ICSD
40	35.33729	2.53795	0.93	76(31)	1	1	2	Bi2O2(CO3)_252588-ICSD
41	35.56392	2.5223	0	0.15(5)	2	2	1	SiO2_Keatite_34889-ICSD
42	35.81129	2.50544	0.33	27(11)	1	1	3	SiO2_Keatite_34889-ICSD
43	35.86374	2.5019	0.03	2(1)	1	1	2	Bi2O3_beta_189995-ICSD
44	35.8772	2.50099	0	0.2(1)	2	2	2	PdBi_tetrag_56279-ICSD
45	36.5619	2.45571	0.05	4(3)	3	1	2	PdBi_tetrag_56279-ICSD
46	36.68076	2.44802	0.01	0.8(2)	1	3	0	Bi2O3_beta_189995-ICSD
47	36.95571	2.43044	0.39	32(40)	0	1	0	Graphite(2H)_187640-ICSD
48	37.09372	2.42171	0.1	8(6)	1	1	4	PdBi_tetrag_56279-ICSD
49	37.61896	2.3891	0.04	3(1)	0	3	1	SiO2_Keatite_34889-ICSD
50	38.08869	2.36071	0.03	2(1)	1	3	0	SiO2_Keatite_34889-ICSD
51	38.34689	2.34541	0.5	41(15)	1	3	0	PdBi_tetrag_56279-ICSD
52	38.35366	2.34501	0.07	6(1)	0	3	1	Bi2O3_beta_189995-ICSD
53	38.58535	2.33146	6.49	534(45)	1	0	4	Bi_53797-ICSD
54	39.1516	2.29903	3.73	307(55)	2	0	4	PdBi_tetrag_56279-ICSD
55	39.1821	2.29731	1.42	117(16)	0	0	6	Bi2O2(CO3)_252588-ICSD
56	39.21629	2.29539	1.88	155(83)	0	1	1	Graphite(2H)_187640-ICSD
57	39.27715	2.29197	6.89	567(25)	1	1	0	Bi_53797-ICSD
58	39.295	2.29097	0.52	43(7)	1	3	1	PdBi_tetrag_56279-ICSD

59	39.58296	2.27497	0.17	14(1)	1	3	1	SiO2_Keatite_34889-ICSD
60	39.58938	2.27461	0.01	0.77(2)	0	2	2	Bi2O3_beta_189995-ICSD
61	39.80901	2.26257	0.01	0.46(2)	0	2	3	SiO2_Keatite_34889-ICSD
62	39.88209	2.25859	100	8232(922)	1	1	1	Pd_64922-ICSD
63	40.09853	2.2469	0.24	20(1)	0	1	5	Bi2O2(CO3)_252588-ICSD
64	40.14539	2.24438	0.72	59(3)	2	2	2	SiO2_Keatite_34889-ICSD
65	40.15511	2.24386	0.04	3.36(8)	1	3	1	Bi2O3_beta_189995-ICSD
66	40.2478	2.23891	0.19	15(1)	1	0	5	Bi2O2(CO3)_252588-ICSD
67	40.26372	2.23806	5.4	444(48)	4	0	0	PdBi_tetrag_56279-ICSD
68	40.67568	2.21634	10.57	870(135)	2	2	3	PdBi_tetrag_56279-ICSD
69	41.29289	2.18462	0.51	42(12)	3	1	3	PdBi_tetrag_56279-ICSD
70	41.34595	2.18194	0.28	23(2)	1	2	2	Bi2O3_beta_189995-ICSD
71	41.68666	2.16489	0.76	63(13)	1	2	3	SiO2_Keatite_34889-ICSD
72	41.81928	2.15833	0.01	0.5(2)	0	2	4	PdBi_tetrag_56279-ICSD
73	42.01067	2.14894	0	0.23(6)	0	3	2	SiO2_Keatite_34889-ICSD
74	42.03218	2.14789	0.01	1(1)	1	3	2	PdBi_tetrag_56279-ICSD
75	42.07288	2.14591	0.08	6(1)	2	3	0	Bi2O3_beta_189995-ICSD
76	42.22551	2.1385	3.31	272(108)	1	1	4	Bi2O2(CO3)_252588-ICSD
77	42.33333	2.13331	0.27	22(6)	0	0	4	SiO2_Keatite_34889-ICSD
78	43.70672	2.0694	0.04	3(2)	2	3	0	SiO2_Keatite_34889-ICSD
79	43.81114	2.06471	0.39	32(15)	1	3	2	SiO2_Keatite_34889-ICSD
80	43.81577	2.06451	0.03	3(2)	4	0	2	PdBi_tetrag_56279-ICSD
81	44.12322	2.05083	0.16	13(6)	0	1	4	SiO2_Keatite_34889-ICSD
82	45.04729	2.01089	0.01	1.1(4)	2	3	1	SiO2_Keatite_34889-ICSD
83	45.20295	2.00432	0.19	16(2)	2	3	1	Bi2O3_beta_189995-ICSD
84	45.22976	2.0032	0	0.16(9)	1	1	5	PdBi_tetrag_56279-ICSD
85	45.43448	1.99464	0.35	29(26)	0	1	2	Graphite(2H)_187640-ICSD
86	45.5037	1.99177	0.72	59(7)	0	1	5	Bi_53797-ICSD
87	45.85748	1.97722	0.14	12(2)	1	1	4	SiO2_Keatite_34889-ICSD
88	46.11042	1.96697	0.52	43(2)	1	1	3	Bi_53797-ICSD
89	46.28875	1.9598	4.19	345(14)	2	2	2	Bi2O3_beta_189995-ICSD
90	46.30072	1.95932	0.31	26(5)	1	3	3	PdBi_tetrag_56279-ICSD
91	46.41086	1.95493	41.8	3441(774)	0	0	2	Pd_64922-ICSD
92	46.41148	1.9549	0.03	2.4(1)	0	2	1	Bi_53797-ICSD
93	46.70455	1.94332	0.01	0.6(1)	2	2	4	PdBi_tetrag_56279-ICSD
94	46.83367	1.93826	1.07	88(15)	0	2	0	Bi2O2(CO3)_252588-ICSD
95	46.95278	1.93362	0	0.18(2)	2	2	3	SiO2_Keatite_34889-ICSD
96	46.9545	1.93355	1.94	160(10)	0	4	0	Bi2O3_beta_189995-ICSD
97	47.25852	1.92182	0.41	33(12)	3	1	4	PdBi_tetrag_56279-ICSD
98	47.33506	1.91889	1.06	87(9)	0	0	6	Bi_53797-ICSD

99	47.35984	1.91795	1.32	109(32)	2	0	0	Bi2O2(CO3)_252588-ICSD
100	47.67375	1.90605	0	0.3(2)	4	2	0	PdBi_tetrag_56279-ICSD
101	47.84681	1.89956	0	0.08(1)	0	3	2	Bi2O3_beta_189995-ICSD
102	48.29488	1.88298	0.01	0.4(3)	3	3	0	PdBi_tetrag_56279-ICSD
103	48.47332	1.87646	0.15	12(8)	4	2	1	PdBi_tetrag_56279-ICSD
104	48.49627	1.87563	0.17	14(2)	1	4	0	Bi2O3_beta_189995-ICSD
105	48.50748	1.87522	3.71	306(50)	2	0	2	Bi_53797-ICSD
106	48.60877	1.87155	1.35	111(32)	0	3	3	SiO2_Keatite_34889-ICSD
107	48.77547	1.86554	0.41	34(18)	0	2	2	Bi2O2(CO3)_252588-ICSD
108	48.8005	1.86464	1.65	136(42)	0	4	0	SiO2_Keatite_34889-ICSD
109	48.89645	1.86121	0.53	44(15)	2	3	2	SiO2_Keatite_34889-ICSD
110	49.08687	1.85443	0.01	1(1)	3	3	1	PdBi_tetrag_56279-ICSD
111	49.18348	1.85101	0.01	0.9(4)	0	2	4	SiO2_Keatite_34889-ICSD
112	49.286	1.8474	0.22	18(12)	2	0	2	Bi2O2(CO3)_252588-ICSD
113	49.32044	1.84619	0.06	5(4)	0	2	5	PdBi_tetrag_56279-ICSD
114	49.3676	1.84454	0.02	1.6(4)	1	3	2	Bi2O3_beta_189995-ICSD
115	49.84422	1.82801	0.01	0.6(1)	0	4	1	Bi2O3_beta_189995-ICSD
116	50.00236	1.8226	0.01	1.1(2)	3	3	0	Bi2O3_beta_189995-ICSD
117	50.03551	1.82147	0.07	6(2)	0	4	1	SiO2_Keatite_34889-ICSD
118	50.05014	1.82097	2.37	195(158)	0	4	0	PdBi_tetrag_56279-ICSD
119	50.07014	1.82029	0.04	4(1)	0	1	3	Bi2O3_beta_189995-ICSD
120	50.22381	1.81508	1.41	116(41)	1	3	3	SiO2_Keatite_34889-ICSD
121	50.41101	1.80878	0.14	11(4)	1	4	0	SiO2_Keatite_34889-ICSD
122	50.78507	1.79633	0.28	23(11)	1	2	4	SiO2_Keatite_34889-ICSD
123	50.8157	1.79532	0	0.05(5)	4	2	2	PdBi_tetrag_56279-ICSD
124	50.82194	1.79512	0	0.4(4)	0	4	1	PdBi_tetrag_56279-ICSD
125	51.14341	1.78459	0	0.2(2)	0	0	6	PdBi_tetrag_56279-ICSD
126	51.32124	1.77882	0.4	33(9)	1	4	1	Bi2O3_beta_189995-ICSD
127	51.40871	1.776	0.08	7(6)	3	3	2	PdBi_tetrag_56279-ICSD
128	51.61784	1.76929	0.01	0.7(3)	1	4	1	SiO2_Keatite_34889-ICSD
129	51.81598	1.76299	0.21	17(14)	1	3	4	PdBi_tetrag_56279-ICSD
130	51.98509	1.75765	0.01	0.9(3)	3	3	0	SiO2_Keatite_34889-ICSD
131	52.04977	1.75562	2.52	207(116)	1	1	6	Bi2O2(CO3)_252588-ICSD
132	52.09771	1.75412	0.75	62(34)	0	1	7	Bi2O2(CO3)_252588-ICSD
133	52.21977	1.75031	0.78	64(35)	1	0	7	Bi2O2(CO3)_252588-ICSD
134	52.30964	1.74751	0.52	43(50)	0	0	4	Graphite(2H)_187640-ICSD
135	52.6444	1.73718	0.17	14(9)	5	1	0	PdBi_tetrag_56279-ICSD
136	52.9204	1.72877	0.01	0.8(1)	2	4	0	Bi2O3_beta_189995-ICSD
137	53.08889	1.72368	0.01	1(1)	0	4	2	PdBi_tetrag_56279-ICSD
138	53.16645	1.72135	0	0.006(2)	3	3	1	SiO2_Keatite_34889-ICSD

139	53.17191	1.72119	0	0.2(1)	0	0	8	Bi2O2(CO3)_252588-ICSD
140	53.34658	1.71596	2.27	187(116)	4	0	4	PdBi_tetrag_56279-ICSD
141	53.35268	1.71578	0.71	59(29)	1	2	1	Bi2O2(CO3)_252588-ICSD
142	53.38939	1.71469	0.16	13(8)	5	1	1	PdBi_tetrag_56279-ICSD
143	53.61607	1.70797	0.21	17(5)	0	4	2	SiO2_Keatite_34889-ICSD
144	53.67951	1.7061	1.59	131(79)	2	2	5	PdBi_tetrag_56279-ICSD
145	53.71231	1.70514	0.58	48(23)	2	1	1	Bi2O2(CO3)_252588-ICSD
146	53.73967	1.70433	0.1	8(1)	2	3	2	Bi2O3_beta_189995-ICSD
147	53.83991	1.7014	0.02	2(1)	1	1	6	PdBi_tetrag_56279-ICSD
148	54.18085	1.69149	0.07	6(4)	3	1	5	PdBi_tetrag_56279-ICSD
149	54.29103	1.68832	0.47	38(20)	0	2	4	Bi2O2(CO3)_252588-ICSD
150	54.36726	1.68613	0.01	0.7(5)	2	4	0	PdBi_tetrag_56279-ICSD
151	54.40177	1.68514	2.33	192(29)	0	2	3	Bi2O3_beta_189995-ICSD
152	54.55583	1.68075	0.49	41(46)	0	1	3	Graphite(2H)_187640-ICSD
153	54.5575	1.6807	1.83	151(105)	4	2	3	PdBi_tetrag_56279-ICSD
154	54.76455	1.67484	0.34	28(17)	2	0	4	Bi2O2(CO3)_252588-ICSD
155	54.86146	1.67211	0.13	11(4)	2	3	3	SiO2_Keatite_34889-ICSD
156	55.03749	1.66717	0	0.05(2)	2	4	0	SiO2_Keatite_34889-ICSD
157	55.09623	1.66554	0.01	0.5(4)	2	4	1	PdBi_tetrag_56279-ICSD
158	55.12225	1.66481	0.2	16(13)	3	3	3	PdBi_tetrag_56279-ICSD
159	55.12565	1.66472	0.4	33(13)	1	4	2	SiO2_Keatite_34889-ICSD
160	55.21426	1.66225	0	0.016(6)	0	1	5	SiO2_Keatite_34889-ICSD
161	55.38955	1.65741	0	0.17(7)	2	2	4	SiO2_Keatite_34889-ICSD
162	55.40031	1.65711	0.95	78(69)	2	0	6	PdBi_tetrag_56279-ICSD
163	55.58307	1.65209	0.07	5(5)	5	1	2	PdBi_tetrag_56279-ICSD
164	55.58405	1.65207	3.97	327(60)	2	4	1	Bi2O3_beta_189995-ICSD
165	55.79353	1.64636	0.15	12(3)	1	2	3	Bi2O3_beta_189995-ICSD
166	56.17468	1.63609	0.39	32(16)	2	4	1	SiO2_Keatite_34889-ICSD
167	56.31185	1.63243	2.21	182(45)	0	2	4	Bi_53797-ICSD
168	56.60814	1.62459	0.12	10(5)	3	3	2	SiO2_Keatite_34889-ICSD
169	56.69522	1.6223	0.01	0.6(3)	1	1	5	SiO2_Keatite_34889-ICSD
170	56.72651	1.62148	0	0.4(4)	0	4	3	PdBi_tetrag_56279-ICSD
171	56.86276	1.61792	1.6	131(99)	1	2	3	Bi2O2(CO3)_252588-ICSD
172	56.8675	1.61779	0	0.3(1)	0	3	4	SiO2_Keatite_34889-ICSD
173	57.20754	1.60898	1.68	138(107)	2	1	3	Bi2O2(CO3)_252588-ICSD
174	57.24598	1.60799	0.56	46(49)	2	4	2	PdBi_tetrag_56279-ICSD
175	57.48141	1.60196	0	0.04(5)	0	2	6	PdBi_tetrag_56279-ICSD
176	57.88036	1.59187	1.69	140(39)	0	4	2	Bi2O3_beta_189995-ICSD
177	58.32111	1.58088	0.22	18(15)	1	3	4	SiO2_Keatite_34889-ICSD
178	58.35212	1.58012	0.05	4(7)	1	3	5	PdBi_tetrag_56279-ICSD

179	59.11855	1.56145	0.23	19(38)	5	1	3	PdBi_tetrag_56279-ICSD
180	59.21864	1.55905	0.21	17(8)	1	4	2	Bi2O3_beta_189995-ICSD
181	59.24947	1.55831	0.01	0.5(4)	0	4	3	SiO2_Keatite_34889-ICSD
182	59.50101	1.55232	0.01	1(1)	2	4	2	SiO2_Keatite_34889-ICSD
183	59.52513	1.55175	0	0.2(5)	4	2	4	PdBi_tetrag_56279-ICSD
184	59.58541	1.55032	0.6	50(40)	0	2	5	SiO2_Keatite_34889-ICSD
185	59.78076	1.54572	0.11	9(4)	3	4	0	Bi2O3_beta_189995-ICSD
186	60.05955	1.53921	0.11	9(17)	3	3	4	PdBi_tetrag_56279-ICSD
187	60.53866	1.52817	0.01	0.8(3)	3	3	2	Bi2O3_beta_189995-ICSD
188	60.66737	1.52524	0	0.2(2)	1	4	3	SiO2_Keatite_34889-ICSD
189	60.71982	1.52405	0.01	1(1)	2	4	3	PdBi_tetrag_56279-ICSD
190	60.97764	1.51822	0.57	47(18)	1	0	7	Bi_53797-ICSD
191	60.9986	1.51775	0.03	3(2)	1	2	5	SiO2_Keatite_34889-ICSD
192	61.09345	1.51562	0.02	1.3(4)	1	5	0	Bi2O3_beta_189995-ICSD
193	61.15282	1.51429	0.01	0.6(2)	0	3	3	Bi2O3_beta_189995-ICSD
194	61.44415	1.50781	0	0.06(9)	2	2	6	PdBi_tetrag_56279-ICSD
195	61.58195	1.50476	1.3	107(148)	0	4	4	PdBi_tetrag_56279-ICSD
196	61.72202	1.50168	0.3	24(8)	2	0	5	Bi_53797-ICSD
197	61.90473	1.49769	0.01	1(2)	3	1	6	PdBi_tetrag_56279-ICSD
198	62.06592	1.49419	0.08	7(4)	3	3	3	SiO2_Keatite_34889-ICSD
199	62.22899	1.49066	0.02	2(1)	3	4	0	SiO2_Keatite_34889-ICSD
200	62.25309	1.49014	0	0.22(7)	0	5	1	Bi2O3_beta_189995-ICSD
201	62.25309	1.49014	0.16	13(4)	3	4	1	Bi2O3_beta_189995-ICSD
202	62.26061	1.48998	0.04	3(4)	6	0	0	PdBi_tetrag_56279-ICSD
203	62.4485	1.48595	0.03	2(1)	1	3	3	Bi2O3_beta_189995-ICSD
204	62.46127	1.48567	0.02	2(1)	2	1	1	Bi_53797-ICSD
205	62.55543	1.48366	0.62	51(26)	2	3	4	SiO2_Keatite_34889-ICSD
206	62.73946	1.47975	0.45	37(35)	0	2	6	Bi2O2(CO3)_252588-ICSD
207	62.93694	1.47559	0.03	3(3)	1	1	7	PdBi_tetrag_56279-ICSD
208	63.12938	1.47155	0.01	0.4(1)	2	4	2	Bi2O3_beta_189995-ICSD
209	63.17267	1.47065	0.47	38(35)	2	0	6	Bi2O2(CO3)_252588-ICSD
210	63.2197	1.46967	2.73	224(53)	1	1	6	Bi_53797-ICSD
211	63.28491	1.46831	0	0.05(2)	0	5	1	SiO2_Keatite_34889-ICSD
212	63.28491	1.46831	0.05	4(2)	3	4	1	SiO2_Keatite_34889-ICSD
213	63.50425	1.46376	0.09	7(7)	1	2	5	Bi2O2(CO3)_252588-ICSD
214	63.53596	1.46311	0.02	1.2(4)	1	5	1	Bi2O3_beta_189995-ICSD
215	63.6078	1.46163	0.08	6(3)	1	5	0	SiO2_Keatite_34889-ICSD
216	63.82716	1.45713	0.08	6(6)	2	1	5	Bi2O2(CO3)_252588-ICSD
217	63.86304	1.4564	0.19	15(17)	5	1	4	PdBi_tetrag_56279-ICSD
218	63.95358	1.45456	0.01	1(1)	1	1	8	Bi2O2(CO3)_252588-ICSD

219	64.19136	1.44974	3.26	268(58)	1	2	2	Bi_53797-ICSD
220	64.65123	1.44054	0.15	12(5)	1	5	1	SiO2_Keatite_34889-ICSD
221	64.71576	1.43926	0.25	21(19)	5	3	0	PdBi_tetrag_56279-ICSD
222	64.81119	1.43737	0.1	8(3)	2	4	3	SiO2_Keatite_34889-ICSD
223	64.84062	1.43679	0.07	5(5)	1	5	0	PdBi_tetrag_56279-ICSD
224	64.9204	1.43521	0.14	11(10)	6	0	2	PdBi_tetrag_56279-ICSD
225	64.93854	1.43486	0.03	3(1)	2	5	0	Bi2O3_beta_189995-ICSD
226	65.13048	1.43109	0	0.03(1)	2	2	5	SiO2_Keatite_34889-ICSD
227	65.37264	1.42638	0.25	21(15)	5	3	1	PdBi_tetrag_56279-ICSD
228	65.39695	1.4259	0.78	65(48)	2	4	4	PdBi_tetrag_56279-ICSD
229	65.49684	1.42397	0.03	3(2)	1	5	1	PdBi_tetrag_56279-ICSD
230	65.56721	1.42261	0.03	2(2)	4	2	5	PdBi_tetrag_56279-ICSD
231	65.58749	1.42222	0.43	35(19)	0	1	9	Bi2O2(CO3)_252588-ICSD
232	65.69339	1.42019	0.4	33(17)	1	0	9	Bi2O2(CO3)_252588-ICSD
233	65.77128	1.41869	0.01	0.4(3)	1	3	6	PdBi_tetrag_56279-ICSD
234	65.84221	1.41734	0.08	6(6)	0	1	4	Graphite(2H)_187640-ICSD
235	66.07364	1.41293	0	0.2(1)	3	3	5	PdBi_tetrag_56279-ICSD
236	66.17749	1.41097	1.21	99(56)	4	4	0	PdBi_tetrag_56279-ICSD
237	66.24987	1.4096	0.06	5(1)	2	3	3	Bi2O3_beta_189995-ICSD
238	66.26716	1.40927	1.39	114(63)	0	2	7	PdBi_tetrag_56279-ICSD
239	66.39716	1.40683	0.77	63(13)	0	5	2	SiO2_Keatite_34889-ICSD
240	66.39716	1.40683	0.01	1.2(3)	3	4	2	SiO2_Keatite_34889-ICSD
241	66.47656	1.40534	0.21	17(4)	0	3	5	SiO2_Keatite_34889-ICSD
242	66.57096	1.40358	0.31	26(3)	0	0	4	Bi2O3_beta_189995-ICSD
243	66.63375	1.40241	0.28	23(5)	0	4	4	SiO2_Keatite_34889-ICSD
244	66.73348	1.40055	0.59	48(35)	1	1	0	Graphite(2H)_187640-ICSD
245	66.82694	1.39882	0	0.2(1)	4	4	1	PdBi_tetrag_56279-ICSD
246	67.02716	1.39513	0.1	8(1)	0	1	6	SiO2_Keatite_34889-ICSD
247	67.09862	1.39382	0	0.3(1)	4	0	6	PdBi_tetrag_56279-ICSD
248	67.30436	1.39006	0.03	2.1(2)	2	5	1	Bi2O3_beta_189995-ICSD
249	67.32335	1.38971	0.01	0.5(2)	5	3	2	PdBi_tetrag_56279-ICSD
250	67.44573	1.38749	0.03	3(1)	1	5	2	PdBi_tetrag_56279-ICSD
251	67.52031	1.38613	0	0.05(2)	0	4	5	PdBi_tetrag_56279-ICSD
252	67.65229	1.38375	0	0.18(2)	2	5	0	SiO2_Keatite_34889-ICSD
253	67.73047	1.38234	0.39	32(4)	1	5	2	SiO2_Keatite_34889-ICSD
254	67.80912	1.38093	0.15	13(1)	1	3	5	SiO2_Keatite_34889-ICSD
255	67.81009	1.38091	0.03	2.4(2)	0	1	4	Bi2O3_beta_189995-ICSD
256	67.81421	1.38084	17.18	1415(535)	0	2	2	Pd_64922-ICSD
257	67.93911	1.37861	0	0.07(3)	6	2	0	PdBi_tetrag_56279-ICSD
258	67.96479	1.37815	0.01	0.46(6)	1	4	4	SiO2_Keatite_34889-ICSD

259	68.08371	1.37603	0.18	15(4)	0	0	10	Bi2O2(CO3)_252588-ICSD
260	68.35445	1.37124	0.03	2.1(3)	1	1	6	SiO2_Keatite_34889-ICSD
261	68.58037	1.36727	0.85	70(34)	6	2	1	PdBi_tetrag_56279-ICSD
262	68.66398	1.36581	0.38	31(6)	2	5	1	SiO2_Keatite_34889-ICSD
263	68.66715	1.36575	0.49	40(4)	4	4	0	Bi2O3_beta_189995-ICSD
264	68.75712	1.36419	0.01	0.4(2)	4	4	2	PdBi_tetrag_56279-ICSD
265	68.89165	1.36185	0.45	37(16)	2	2	0	Bi2O2(CO3)_252588-ICSD
266	69.03846	1.35931	0	0.011(1)	1	1	4	Bi2O3_beta_189995-ICSD
267	69.28351	1.3551	0.26	22(6)	3	3	4	SiO2_Keatite_34889-ICSD
268	69.3716	1.3536	0	0.13(2)	0	5	2	Bi2O3_beta_189995-ICSD
269	69.3716	1.3536	0.16	14(2)	3	4	2	Bi2O3_beta_189995-ICSD
270	69.49853	1.35143	0.84	69(12)	0	1	8	Bi_53797-ICSD
271	69.69841	1.34805	0.03	2(2)	5	1	5	PdBi_tetrag_56279-ICSD
272	69.94391	1.34392	0	0.25(5)	0	4	3	Bi2O3_beta_189995-ICSD
273	69.94722	1.34386	0.25	21(18)	2	2	7	PdBi_tetrag_56279-ICSD
274	70.34192	1.33728	0.09	7(7)	0	0	8	PdBi_tetrag_56279-ICSD
275	70.37844	1.33668	0.04	3(3)	3	1	7	PdBi_tetrag_56279-ICSD
276	70.42802	1.33586	0.17	14(11)	2	2	2	Bi2O2(CO3)_252588-ICSD
277	70.48792	1.33487	0	0.01(1)	6	2	2	PdBi_tetrag_56279-ICSD
278	70.51571	1.33441	0.19	15(15)	5	3	3	PdBi_tetrag_56279-ICSD
279	70.58748	1.33323	0.02	2.0(5)	1	5	2	Bi2O3_beta_189995-ICSD
280	70.63553	1.33244	0.07	5(6)	1	5	3	PdBi_tetrag_56279-ICSD
281	70.88787	1.32832	2.26	186(41)	2	1	4	Bi_53797-ICSD
282	70.97403	1.32692	0	0.0011(4)	0	2	6	SiO2_Keatite_34889-ICSD
283	71.10051	1.32487	0.01	1.0(2)	3	5	0	Bi2O3_beta_189995-ICSD
284	71.15548	1.32398	0.11	9(2)	1	4	3	Bi2O3_beta_189995-ICSD
285	71.16977	1.32375	0	0.09(9)	2	4	5	PdBi_tetrag_56279-ICSD
286	71.34837	1.32087	0.62	51(12)	0	3	0	Bi_53797-ICSD
287	71.34837	1.32087	0.62	51(12)	3	0	0	Bi_53797-ICSD
288	71.43116	1.31954	0.03	2(1)	0	5	3	SiO2_Keatite_34889-ICSD
289	71.43116	1.31954	0.31	25(10)	3	4	3	SiO2_Keatite_34889-ICSD
290	71.46621	1.31898	0.01	0.4(1)	0	2	4	Bi2O3_beta_189995-ICSD
291	71.58326	1.31711	0.07	6(2)	4	4	0	SiO2_Keatite_34889-ICSD
292	71.65951	1.3159	0	0.08(4)	2	5	2	SiO2_Keatite_34889-ICSD
293	71.7362	1.31468	0.06	5(2)	2	3	5	SiO2_Keatite_34889-ICSD
294	71.88803	1.31228	0.02	2(1)	2	4	4	SiO2_Keatite_34889-ICSD
295	71.92047	1.31176	0	0.3(3)	4	4	3	PdBi_tetrag_56279-ICSD
296	72.18399	1.30762	0.19	15(16)	3	5	0	PdBi_tetrag_56279-ICSD
297	72.26825	1.30631	0	0.3(1)	1	2	6	SiO2_Keatite_34889-ICSD
298	72.57042	1.30161	0.01	0.5(2)	4	4	1	SiO2_Keatite_34889-ICSD

299	72.58655	1.30136	0	0.03(3)	4	2	6	PdBi_tetrag_56279-ICSD
300	72.59514	1.30123	0.23	19(19)	6	0	4	PdBi_tetrag_56279-ICSD
301	72.60035	1.30115	0.01	1(1)	1	1	8	PdBi_tetrag_56279-ICSD
302	72.66707	1.30012	0.06	5(1)	1	2	4	Bi2O3_beta_189995-ICSD
303	72.69618	1.29967	0.86	71(92)	1	1	2	Graphite(2H)_187640-ICSD
304	72.72203	1.29927	0.1	8(3)	1	5	3	SiO2_Keatite_34889-ICSD
305	72.80869	1.29794	0.12	10(10)	3	5	1	PdBi_tetrag_56279-ICSD
306	72.82496	1.29769	0.4	33(26)	1	2	7	Bi2O2(CO3)_252588-ICSD
307	73.07029	1.29393	0.05	4(4)	3	3	6	PdBi_tetrag_56279-ICSD
308	73.12775	1.29306	0.39	32(25)	2	1	7	Bi2O2(CO3)_252588-ICSD
309	73.37284	1.28934	0.02	1.9(4)	3	5	1	Bi2O3_beta_189995-ICSD
310	73.49925	1.28744	0	0.14(3)	0	6	0	Bi2O3_beta_189995-ICSD
311	73.61693	1.28567	0	0.08(6)	0	2	8	Bi2O2(CO3)_252588-ICSD
312	73.61946	1.28563	0.64	53(54)	6	2	3	PdBi_tetrag_56279-ICSD
313	73.6675	1.28491	0.07	6(5)	0	3	1	Bi2O2(CO3)_252588-ICSD
314	73.93026	1.28099	0.57	47(49)	2	0	8	PdBi_tetrag_56279-ICSD
315	74.01891	1.27968	0	0.10(8)	2	0	8	Bi2O2(CO3)_252588-ICSD
316	74.02483	1.27959	0.02	2(2)	1	3	7	PdBi_tetrag_56279-ICSD
317	74.15391	1.27768	0.17	14(3)	0	0	9	Bi_53797-ICSD
318	74.15402	1.27768	0	0.21(9)	3	5	0	SiO2_Keatite_34889-ICSD
319	74.18422	1.27724	0.04	3(1)	2	5	2	Bi2O3_beta_189995-ICSD
320	74.45567	1.27325	0	0.1(2)	0	4	6	PdBi_tetrag_56279-ICSD
321	74.57062	1.27157	0.06	5(4)	3	0	1	Bi2O2(CO3)_252588-ICSD
322	74.67069	1.27012	0	0.2(2)	3	5	2	PdBi_tetrag_56279-ICSD
323	74.68738	1.26987	0.11	9(2)	1	6	0	Bi2O3_beta_189995-ICSD
324	74.74132	1.26909	1.5	124(27)	2	4	3	Bi2O3_beta_189995-ICSD
325	74.88485	1.26701	0.19	15(18)	5	3	4	PdBi_tetrag_56279-ICSD
326	74.95642	1.26598	0.26	21(19)	2	2	4	Bi2O2(CO3)_252588-ICSD
327	75.00188	1.26533	0.09	8(9)	1	5	4	PdBi_tetrag_56279-ICSD
328	75.05795	1.26452	0.32	26(7)	0	2	7	Bi_53797-ICSD
329	75.12818	1.26351	0.13	11(5)	3	5	1	SiO2_Keatite_34889-ICSD
330	75.50176	1.25819	0	0.3(1)	4	4	2	SiO2_Keatite_34889-ICSD
331	75.56298	1.25732	0.12	10(12)	7	1	0	PdBi_tetrag_56279-ICSD
332	75.57696	1.25712	0.01	0.5(2)	0	4	5	SiO2_Keatite_34889-ICSD
333	75.72888	1.25498	0	0.03(4)	0	2	8	PdBi_tetrag_56279-ICSD
334	75.7335	1.25491	0.33	27(7)	1	2	5	Bi_53797-ICSD
335	75.74386	1.25477	0.65	54(13)	0	6	1	Bi2O3_beta_189995-ICSD
336	76.09894	1.24979	0.49	41(17)	2	2	6	SiO2_Keatite_34889-ICSD
337	76.17744	1.2487	0.11	9(10)	7	1	1	PdBi_tetrag_56279-ICSD
338	76.18275	1.24863	0.06	5(1)	0	3	3	Bi_53797-ICSD

339	76.18275	1.24863	0.06	5(1)	3	0	3	Bi_53797-ICSD
340	76.22584	1.24803	0.76	63(13)	2	2	4	Bi2O3_beta_189995-ICSD
341	76.2584	1.24758	0.88	72(82)	4	4	4	PdBi_tetrag_56279-ICSD
342	76.54442	1.24362	0.37	31(13)	2	5	3	SiO2_Keatite_34889-ICSD
343	76.55114	1.24353	0.04	4(4)	5	1	6	PdBi_tetrag_56279-ICSD
344	76.64913	1.24219	0.28	23(20)	0	3	3	Bi2O2(CO3)_252588-ICSD
345	76.69273	1.24159	0	0.0009(4)	0	6	0	SiO2_Keatite_34889-ICSD
346	76.84189	1.23955	0.06	5(2)	1	4	5	SiO2_Keatite_34889-ICSD
347	76.91992	1.23849	0.17	14(3)	1	6	1	Bi2O3_beta_189995-ICSD
348	77.36114	1.23252	0.01	1.1(5)	0	3	6	SiO2_Keatite_34889-ICSD
349	77.39956	1.23201	0.01	1.0(2)	0	3	4	Bi2O3_beta_189995-ICSD
350	77.54041	1.23012	0.28	23(20)	3	0	3	Bi2O2(CO3)_252588-ICSD
351	77.65625	1.22857	0.09	8(3)	0	6	1	SiO2_Keatite_34889-ICSD
352	77.71299	1.22782	0.31	25(22)	1	1	10	Bi2O2(CO3)_252588-ICSD
353	77.71861	1.22774	0.62	51(11)	4	4	2	Bi2O3_beta_189995-ICSD
354	77.73896	1.22747	0.09	8(9)	3	5	3	PdBi_tetrag_56279-ICSD
355	77.92357	1.22503	0	0.08(9)	6	2	4	PdBi_tetrag_56279-ICSD
356	77.95197	1.22465	0.17	14(6)	1	6	0	SiO2_Keatite_34889-ICSD
357	77.97299	1.22437	0.41	33(37)	2	4	6	PdBi_tetrag_56279-ICSD
358	78.01158	1.22386	0.01	1(1)	7	1	2	PdBi_tetrag_56279-ICSD
359	78.02597	1.22367	0.11	9(4)	3	5	2	SiO2_Keatite_34889-ICSD
360	78.08717	1.22287	0.26	22(19)	1	3	0	Bi2O2(CO3)_252588-ICSD
361	78.1004	1.22269	0.03	2(1)	3	3	5	SiO2_Keatite_34889-ICSD
362	78.2143	1.2212	0.56	47(10)	2	6	0	Bi2O3_beta_189995-ICSD
363	78.24783	1.22076	0.01	0.4(2)	0	5	4	SiO2_Keatite_34889-ICSD
364	78.24783	1.22076	0.01	1.2(5)	3	4	4	SiO2_Keatite_34889-ICSD
365	78.56801	1.21659	0.01	0.7(2)	1	3	4	Bi2O3_beta_189995-ICSD
366	78.61722	1.21595	0.02	1(1)	1	3	6	SiO2_Keatite_34889-ICSD
367	78.87534	1.21261	0.23	19(16)	3	1	0	Bi2O2(CO3)_252588-ICSD
368	78.88153	1.21253	0	0.1(1)	0	6	0	PdBi_tetrag_56279-ICSD
369	78.88875	1.21244	0.02	2(2)	0	2	0	Graphite(2H)_187640-ICSD
370	78.91099	1.21216	0.08	6(3)	1	6	1	SiO2_Keatite_34889-ICSD
371	79.06544	1.21017	0.12	10(12)	0	1	5	Graphite(2H)_187640-ICSD
372	79.22831	1.2081	0	0.05(5)	2	2	8	PdBi_tetrag_56279-ICSD
373	79.37938	1.20618	0.02	2.0(4)	4	5	0	Bi2O3_beta_189995-ICSD
374	79.48827	1.2048	0.02	1(1)	0	6	1	PdBi_tetrag_56279-ICSD
375	79.49999	1.20465	0.18	15(5)	1	5	4	SiO2_Keatite_34889-ICSD
376	79.55625	1.20394	0.04	3(2)	1	3	2	Bi2O2(CO3)_252588-ICSD
377	79.6411	1.20287	0.02	2(1)	3	1	8	PdBi_tetrag_56279-ICSD
378	79.79475	1.20094	0.05	4(1)	0	1	7	SiO2_Keatite_34889-ICSD

379	80.04823	1.19777	0	0.057(9)	3	5	2	Bi2O3_beta_189995-ICSD
380	80.30732	1.19456	0.02	1.8(5)	4	4	3	SiO2_Keatite_34889-ICSD
381	80.31041	1.19452	0.12	10(9)	0	2	1	Graphite(2H)_187640-ICSD
382	80.34063	1.19415	0.05	4(2)	3	1	2	Bi2O2(CO3)_252588-ICSD
383	80.3777	1.19369	0.05	4(3)	5	3	5	PdBi_tetrag_56279-ICSD
384	80.41721	1.1932	0.01	1.2(2)	2	6	1	Bi2O3_beta_189995-ICSD
385	80.49233	1.19228	0.01	0.6(4)	1	5	5	PdBi_tetrag_56279-ICSD
386	80.52707	1.19185	0.02	1.2(3)	0	6	2	SiO2_Keatite_34889-ICSD
387	80.55732	1.19148	1.05	86(58)	4	2	7	PdBi_tetrag_56279-ICSD
388	80.59287	1.19104	0.01	0.52(6)	0	5	3	Bi2O3_beta_189995-ICSD
389	80.59287	1.19104	0.07	5(1)	3	4	3	Bi2O3_beta_189995-ICSD
390	80.60092	1.19095	0.36	30(6)	2	4	5	SiO2_Keatite_34889-ICSD
391	80.68624	1.1899	0	0.4(2)	0	1	11	Bi2O2(CO3)_252588-ICSD
392	80.78405	1.18871	0	0.11(5)	1	0	11	Bi2O2(CO3)_252588-ICSD
393	81.02571	1.18577	0.12	10(5)	3	3	7	PdBi_tetrag_56279-ICSD
394	81.04086	1.18559	0.02	2.0(3)	1	1	7	SiO2_Keatite_34889-ICSD
395	81.04229	1.18557	0.12	10(5)	7	1	3	PdBi_tetrag_56279-ICSD
396	81.30177	1.18244	0	0.02(1)	0	6	2	PdBi_tetrag_56279-ICSD
397	81.57448	1.17918	0.1	8(1)	4	5	1	Bi2O3_beta_189995-ICSD
398	81.6975	1.17771	0.01	0.68(9)	2	6	0	SiO2_Keatite_34889-ICSD
399	81.72468	1.17739	0	0.05(2)	4	4	5	PdBi_tetrag_56279-ICSD
400	81.74959	1.17709	0.01	0.59(4)	1	5	3	Bi2O3_beta_189995-ICSD
401	81.75063	1.17708	16.12	1327(609)	1	1	3	Pd_64922-ICSD
402	81.77064	1.17684	0.03	2.1(3)	1	6	2	SiO2_Keatite_34889-ICSD
403	81.97804	1.17439	0.15	12(6)	3	5	4	PdBi_tetrag_56279-ICSD
404	82.04704	1.17358	0.04	3.5(2)	2	3	4	Bi2O3_beta_189995-ICSD
405	82.31138	1.17048	0.32	26(9)	2	2	6	Bi2O2(CO3)_252588-ICSD
406	82.34459	1.17009	0	0.16(8)	2	6	0	PdBi_tetrag_56279-ICSD
407	82.35535	1.16996	0.03	2.7(4)	2	3	6	SiO2_Keatite_34889-ICSD
408	82.36157	1.16989	0.01	0.92(7)	0	6	2	Bi2O3_beta_189995-ICSD
409	82.37042	1.16979	0	0.10(5)	0	4	7	PdBi_tetrag_56279-ICSD
410	82.5132	1.16812	0.01	1.0(4)	0	3	5	Bi2O2(CO3)_252588-ICSD
411	82.64603	1.16658	0.01	0.6(1)	2	6	1	SiO2_Keatite_34889-ICSD
412	82.792	1.1649	0.22	18(3)	3	5	3	SiO2_Keatite_34889-ICSD
413	82.90029	1.16365	0.09	8(5)	0	0	6	Graphite(2H)_187640-ICSD
414	82.93744	1.16322	0.03	3(1)	4	5	0	SiO2_Keatite_34889-ICSD
415	82.94458	1.16314	0.53	44(5)	2	0	8	Bi_53797-ICSD
416	82.9456	1.16313	0.43	36(21)	2	6	1	PdBi_tetrag_56279-ICSD
417	82.97978	1.16274	0	0.004(2)	1	1	9	PdBi_tetrag_56279-ICSD
418	83.15398	1.16074	0.01	1(1)	1	3	8	PdBi_tetrag_56279-ICSD

419	83.22913	1.15989	0.12	10(2)	2	5	4	SiO2_Keatite_34889-ICSD
420	83.36202	1.15837	0.19	15(10)	6	2	5	PdBi_tetrag_56279-ICSD
421	83.38883	1.15807	0.01	0.9(5)	3	0	5	Bi2O2(CO3)_252588-ICSD
422	83.51342	1.15666	0.18	15(2)	1	6	2	Bi2O3_beta_189995-ICSD
423	83.52111	1.15657	0.16	13(3)	0	2	7	SiO2_Keatite_34889-ICSD
424	83.88344	1.1525	0.01	0.5(1)	4	5	1	SiO2_Keatite_34889-ICSD
425	83.92291	1.15205	0.01	1(1)	6	4	0	PdBi_tetrag_56279-ICSD
426	83.9267	1.15201	0.2	16(10)	1	3	4	Bi2O2(CO3)_252588-ICSD
427	84.00123	1.15118	0.06	5(1)	3	6	0	Bi2O3_beta_189995-ICSD
428	84.30611	1.14779	0.15	12(10)	0	6	3	PdBi_tetrag_56279-ICSD
429	84.3789	1.14699	0.08	6(5)	4	0	8	PdBi_tetrag_56279-ICSD
430	84.41347	1.14661	0.1	8(6)	5	1	7	PdBi_tetrag_56279-ICSD
431	84.45653	1.14613	0.06	5(3)	0	0	12	Bi2O2(CO3)_252588-ICSD
432	84.52207	1.14541	0	0.10(8)	6	4	1	PdBi_tetrag_56279-ICSD
433	84.54361	1.14517	0.03	3(2)	0	2	2	Graphite(2H)_187640-ICSD
434	84.6023	1.14453	0.33	27(18)	1	2	9	Bi2O2(CO3)_252588-ICSD
435	84.69877	1.14347	0.81	67(11)	2	2	0	Bi_53797-ICSD
436	84.70302	1.14342	0.2	17(11)	3	1	4	Bi2O2(CO3)_252588-ICSD
437	84.74432	1.14297	0	0.04(3)	2	6	2	PdBi_tetrag_56279-ICSD
438	84.75649	1.14284	0.06	5(1)	1	2	7	SiO2_Keatite_34889-ICSD
439	84.77339	1.14265	0.12	10(8)	6	0	6	PdBi_tetrag_56279-ICSD
440	84.89322	1.14135	0.31	26(17)	2	1	9	Bi2O2(CO3)_252588-ICSD
441	85.20181	1.138	0.03	2.7(4)	2	5	3	Bi2O3_beta_189995-ICSD
442	85.24582	1.13753	0.12	10(9)	7	1	4	PdBi_tetrag_56279-ICSD
443	85.26338	1.13734	0	0.03(1)	0	6	3	SiO2_Keatite_34889-ICSD
444	85.48083	1.135	0.01	0.4(1)	2	6	2	SiO2_Keatite_34889-ICSD
445	85.49731	1.13482	0.51	42(7)	0	4	4	Bi2O3_beta_189995-ICSD
446	85.80591	1.13153	0	0.2(2)	2	4	7	PdBi_tetrag_56279-ICSD
447	86.00497	1.12942	0	0.2(1)	0	2	9	PdBi_tetrag_56279-ICSD
448	86.01716	1.12929	0.02	2(1)	7	3	0	PdBi_tetrag_56279-ICSD
449	86.06161	1.12882	0.01	1.0(3)	0	4	6	SiO2_Keatite_34889-ICSD
450	86.1305	1.1281	0	0.0000007(6)	5	5	0	PdBi_tetrag_56279-ICSD
451	86.17451	1.12763	0.17	14(2)	3	6	1	Bi2O3_beta_189995-ICSD
452	86.2499	1.12684	4.42	364(305)	2	2	2	Pd_64922-ICSD
453	86.31628	1.12614	0.08	6(6)	6	4	2	PdBi_tetrag_56279-ICSD
454	86.49558	1.12427	0.02	1.5(4)	1	6	3	SiO2_Keatite_34889-ICSD
455	86.61456	1.12303	0.02	1(1)	7	3	1	PdBi_tetrag_56279-ICSD
456	86.64327	1.12273	0.08	7(1)	1	4	4	Bi2O3_beta_189995-ICSD
457	86.71272	1.12201	0.26	22(6)	4	5	2	SiO2_Keatite_34889-ICSD
458	86.72783	1.12185	0.01	0.4(4)	5	5	1	PdBi_tetrag_56279-ICSD

459	86.7857	1.12126	0	0.33(9)	0	5	5	SiO2_Keatite_34889-ICSD
460	86.7857	1.12126	0.04	3(1)	3	4	5	SiO2_Keatite_34889-ICSD
461	86.80895	1.12102	0.12	10(7)	0	2	10	Bi2O2(CO3)_252588-ICSD
462	86.93027	1.11976	0.08	6(2)	4	4	4	SiO2_Keatite_34889-ICSD
463	86.95545	1.1195	0.85	70(11)	2	6	2	Bi2O3_beta_189995-ICSD
464	86.97846	1.11927	0	0.4(4)	5	3	6	PdBi_tetrag_56279-ICSD
465	87.09169	1.1181	0.03	2(2)	1	5	6	PdBi_tetrag_56279-ICSD
466	87.19578	1.11703	0.14	12(9)	2	0	10	Bi2O2(CO3)_252588-ICSD
467	87.2371	1.11661	0.13	11(11)	8	0	0	PdBi_tetrag_56279-ICSD
468	87.29275	1.11604	0	0.11(4)	1	4	6	SiO2_Keatite_34889-ICSD
469	87.36836	1.11527	0.03	2(3)	3	5	5	PdBi_tetrag_56279-ICSD
470	87.38618	1.11509	0.68	56(12)	1	1	9	Bi_53797-ICSD
471	87.73189	1.11159	0.35	29(34)	2	6	3	PdBi_tetrag_56279-ICSD
472	87.78795	1.11102	0.02	1.5(3)	3	3	4	Bi2O3_beta_189995-ICSD
473	87.84005	1.1105	0.01	1.2(3)	0	1	5	Bi2O3_beta_189995-ICSD
474	87.8707	1.11019	0.03	3(1)	3	6	0	SiO2_Keatite_34889-ICSD
475	88.01606	1.10873	0.03	2(1)	1	5	5	SiO2_Keatite_34889-ICSD
476	88.09986	1.10789	0.05	4(1)	4	5	2	Bi2O3_beta_189995-ICSD
477	88.25895	1.1063	0.44	36(10)	2	1	7	Bi_53797-ICSD
478	88.31056	1.10579	0	0.02(3)	4	4	6	PdBi_tetrag_56279-ICSD
479	88.4049	1.10485	0.02	2(3)	7	3	2	PdBi_tetrag_56279-ICSD
480	88.45073	1.1044	0.01	0.5(2)	2	2	7	SiO2_Keatite_34889-ICSD
481	88.48845	1.10403	0	0.1(2)	0	6	4	PdBi_tetrag_56279-ICSD
482	88.49861	1.10393	0.35	29(8)	1	0	10	Bi_53797-ICSD
483	88.51803	1.10373	0.03	3(3)	5	5	2	PdBi_tetrag_56279-ICSD
484	88.5227	1.10369	0.02	2(1)	3	3	6	SiO2_Keatite_34889-ICSD
485	88.81106	1.10085	0.14	12(6)	3	6	1	SiO2_Keatite_34889-ICSD
486	89.29981	1.09609	0	0.1(2)	6	4	3	PdBi_tetrag_56279-ICSD
487	89.34942	1.09561	0.09	7(2)	2	2	3	Bi_53797-ICSD
488	89.38997	1.09521	0.01	0.7(4)	3	5	4	SiO2_Keatite_34889-ICSD
489	89.42547	1.09487	0.1	8(13)	2	2	9	PdBi_tetrag_56279-ICSD
490	89.54191	1.09375	0	0.04(6)	4	2	8	PdBi_tetrag_56279-ICSD
491	89.56747	1.0935	0.01	0.8(3)	1	3	1	Bi_53797-ICSD
492	89.62304	1.09297	0.01	1(1)	8	0	2	PdBi_tetrag_56279-ICSD
493	89.68007	1.09242	0.07	5(3)	0	3	7	SiO2_Keatite_34889-ICSD
494	89.72864	1.09196	0	0.14(4)	1	7	0	Bi2O3_beta_189995-ICSD
495	89.72864	1.09196	0	0.21(6)	5	5	0	Bi2O3_beta_189995-ICSD
496	89.73842	1.09186	0.47	38(65)	1	1	4	Graphite(2H)_187640-ICSD
497	89.83147	1.09097	0	0(1)	3	1	9	PdBi_tetrag_56279-ICSD
498	89.93474	1.08999	0	0.01(2)	6	2	6	PdBi_tetrag_56279-ICSD

499	90.00445	1.08932	0.05	4(6)	3	3	8	PdBi_tetrag_56279-ICSD
500	90.0753	1.08865	0	0.04(1)	2	4	4	Bi2O3_beta_189995-ICSD
501	90.18516	1.08761	0.02	1(1)	2	6	3	SiO2_Keatite_34889-ICSD
502	90.24317	1.08706	0.56	46(14)	0	3	6	Bi_53797-ICSD
503	90.24317	1.08706	0.56	46(14)	3	0	6	Bi_53797-ICSD
504	90.61712	1.08355	0.03	2(4)	7	1	5	PdBi_tetrag_56279-ICSD
505	90.75085	1.0823	0	0.15(4)	0	7	1	Bi2O3_beta_189995-ICSD
506	90.90936	1.08082	0.02	2(1)	1	3	7	SiO2_Keatite_34889-ICSD
507	90.92421	1.08069	0.02	2(1)	3	5	3	Bi2O3_beta_189995-ICSD
508	90.98133	1.08016	0	0.16(8)	2	4	6	SiO2_Keatite_34889-ICSD
509	91.11548	1.07892	1.38	114(32)	3	1	2	Bi_53797-ICSD
510	91.14686	1.07863	0.29	24(30)	1	3	6	Bi2O2(CO3)_252588-ICSD
511	91.18475	1.07828	0.09	7(9)	0	3	7	Bi2O2(CO3)_252588-ICSD
512	91.27095	1.07748	0.48	39(11)	0	2	5	Bi2O3_beta_189995-ICSD
513	91.3357	1.07689	0.06	5(8)	0	4	8	PdBi_tetrag_56279-ICSD
514	91.38653	1.07642	0.07	6(10)	7	3	3	PdBi_tetrag_56279-ICSD
515	91.41458	1.07616	0.02	1(1)	4	5	3	SiO2_Keatite_34889-ICSD
516	91.49967	1.07539	0.06	5(8)	5	5	3	PdBi_tetrag_56279-ICSD
517	91.54605	1.07496	0.08	7(12)	0	2	3	Graphite(2H)_187640-ICSD
518	91.63145	1.07418	0.02	1(1)	3	6	2	SiO2_Keatite_34889-ICSD
519	91.70436	1.07352	0.04	3(2)	2	5	5	SiO2_Keatite_34889-ICSD
520	91.84881	1.07221	0.01	0.6(3)	0	6	4	SiO2_Keatite_34889-ICSD
521	91.8947	1.07179	0.01	1.1(3)	1	7	1	Bi2O3_beta_189995-ICSD
522	91.90663	1.07169	0	0.2(4)	2	6	4	PdBi_tetrag_56279-ICSD
523	91.91988	1.07157	0.28	23(30)	3	1	6	Bi2O2(CO3)_252588-ICSD
524	92.01605	1.0707	0	0.03(1)	4	6	0	Bi2O3_beta_189995-ICSD
525	92.05445	1.07035	0.09	7(10)	3	0	7	Bi2O2(CO3)_252588-ICSD
526	92.18272	1.0692	0.02	2(3)	0	0	10	PdBi_tetrag_56279-ICSD
527	92.39354	1.06731	0	0.02(4)	8	2	0	PdBi_tetrag_56279-ICSD
528	92.41511	1.06712	0.04	3(1)	1	2	5	Bi2O3_beta_189995-ICSD
529	92.42727	1.06701	0	0.05(7)	2	2	8	Bi2O2(CO3)_252588-ICSD
530	92.47588	1.06657	0.06	5(7)	2	3	1	Bi2O2(CO3)_252588-ICSD
531	92.61997	1.06529	0	0.1(2)	4	6	0	PdBi_tetrag_56279-ICSD
532	92.67507	1.0648	0.1	8(3)	3	6	2	Bi2O3_beta_189995-ICSD
533	92.71857	1.06442	0.06	5(3)	0	0	8	SiO2_Keatite_34889-ICSD
534	92.95942	1.06229	0.08	7(10)	3	2	1	Bi2O2(CO3)_252588-ICSD
535	92.99053	1.06202	0.05	4(7)	8	2	1	PdBi_tetrag_56279-ICSD
536	93.07934	1.06124	0.02	2(1)	1	6	4	SiO2_Keatite_34889-ICSD
537	93.16082	1.06052	0.01	0.4(1)	2	7	0	Bi2O3_beta_189995-ICSD
538	93.21297	1.06007	0.39	32(10)	0	6	3	Bi2O3_beta_189995-ICSD

539	93.21708	1.06003	0.01	1(2)	4	6	1	PdBi_tetrag_56279-ICSD
540	93.30772	1.05924	0	0(1)	1	3	9	PdBi_tetrag_56279-ICSD
541	93.36773	1.05871	0.05	4(7)	5	1	8	PdBi_tetrag_56279-ICSD
542	93.47604	1.05777	0.14	12(22)	6	4	4	PdBi_tetrag_56279-ICSD
543	93.66727	1.05612	0.16	14(20)	1	1	12	Bi2O2(CO3)_252588-ICSD
544	93.73095	1.05556	0.06	5(3)	0	7	1	SiO2_Keatite_34889-ICSD
545	93.85817	1.05447	0	0(1)	0	6	5	PdBi_tetrag_56279-ICSD
546	93.93142	1.05384	0	0.2(3)	3	5	6	PdBi_tetrag_56279-ICSD
547	93.95009	1.05368	0.01	0.5(3)	0	1	8	SiO2_Keatite_34889-ICSD
548	94.02086	1.05307	0.02	1(1)	1	7	0	SiO2_Keatite_34889-ICSD
549	94.02086	1.05307	0.07	6(4)	5	5	0	SiO2_Keatite_34889-ICSD
550	94.18531	1.05167	0.68	56(17)	4	6	1	Bi2O3_beta_189995-ICSD
551	94.32971	1.05044	0	0(1)	1	1	10	PdBi_tetrag_56279-ICSD
552	94.35914	1.05019	0.13	11(4)	1	6	3	Bi2O3_beta_189995-ICSD
553	94.52234	1.0488	0.03	2(4)	0	1	6	Graphite(2H)_187640-ICSD
554	94.60241	1.04813	0.03	2(1)	2	3	7	SiO2_Keatite_34889-ICSD
555	94.73694	1.04699	0.02	2(3)	5	3	7	PdBi_tetrag_56279-ICSD
556	94.75914	1.04681	0.4	33(63)	2	4	8	PdBi_tetrag_56279-ICSD
557	94.78382	1.0466	0	0.01(1)	8	2	2	PdBi_tetrag_56279-ICSD
558	94.85045	1.04604	0.05	4(7)	1	5	7	PdBi_tetrag_56279-ICSD
559	94.96399	1.04509	0.04	3(2)	1	7	1	SiO2_Keatite_34889-ICSD
560	94.96399	1.04509	0.02	2(1)	5	5	1	SiO2_Keatite_34889-ICSD
561	95.01089	1.0447	0	0.02(5)	4	6	2	PdBi_tetrag_56279-ICSD
562	95.18351	1.04326	0	0.15(9)	1	1	8	SiO2_Keatite_34889-ICSD
563	95.33297	1.04202	0.02	2(1)	2	7	1	Bi2O3_beta_189995-ICSD
564	95.36728	1.04173	0.26	22(32)	2	3	3	Bi2O2(CO3)_252588-ICSD
565	95.40037	1.04146	0	0.2(1)	4	4	5	SiO2_Keatite_34889-ICSD
566	95.56965	1.04006	0.06	5(10)	7	3	4	PdBi_tetrag_56279-ICSD
567	95.60938	1.03974	0.19	16(31)	2	0	10	PdBi_tetrag_56279-ICSD
568	95.68332	1.03913	0.05	4(8)	5	5	4	PdBi_tetrag_56279-ICSD
569	95.80324	1.03815	0.01	0.8(3)	0	5	4	Bi2O3_beta_189995-ICSD
570	95.80324	1.03815	0.07	6(2)	3	4	4	Bi2O3_beta_189995-ICSD
571	95.85265	1.03774	0.23	19(28)	3	2	3	Bi2O2(CO3)_252588-ICSD
572	96.01052	1.03645	0.83	69(22)	1	2	8	Bi_53797-ICSD
573	96.07433	1.03593	0	0.1(2)	4	4	7	PdBi_tetrag_56279-ICSD
574	96.34515	1.03374	0	0.03(2)	3	6	3	SiO2_Keatite_34889-ICSD
575	96.49048	1.03257	0	0.03(2)	4	6	0	SiO2_Keatite_34889-ICSD
576	96.56338	1.03198	0	0.07(4)	0	7	2	SiO2_Keatite_34889-ICSD
577	96.57098	1.03192	0.03	3(6)	1	7	0	PdBi_tetrag_56279-ICSD
578	96.78218	1.03023	0.01	1(1)	2	6	4	SiO2_Keatite_34889-ICSD

579	96.79513	1.03013	0.14	11(23)	8	0	4	PdBi_tetrag_56279-ICSD
580	96.95416	1.02886	0.02	1.4(5)	1	5	4	Bi2O3_beta_189995-ICSD
581	97.00663	1.02844	0.02	2(1)	0	3	5	Bi2O3_beta_189995-ICSD
582	97.14705	1.02733	0.09	8(5)	0	5	6	SiO2_Keatite_34889-ICSD
583	97.14705	1.02733	0.02	1(1)	3	4	6	SiO2_Keatite_34889-ICSD
584	97.17174	1.02714	0.06	5(10)	1	7	1	PdBi_tetrag_56279-ICSD
585	97.19604	1.02694	0.02	1(3)	7	1	6	PdBi_tetrag_56279-ICSD
586	97.26841	1.02637	0	0.0026(8)	0	7	2	Bi2O3_beta_189995-ICSD
587	97.29342	1.02618	0.13	10(23)	2	6	5	PdBi_tetrag_56279-ICSD
588	97.32819	1.0259	1.17	96(31)	1	3	4	Bi_53797-ICSD
589	97.35823	1.02567	0	0.01(2)	0	2	10	PdBi_tetrag_56279-ICSD
590	97.4378	1.02504	0.01	0.5(3)	4	6	1	SiO2_Keatite_34889-ICSD
591	97.65838	1.02331	0	0.2(1)	0	2	8	SiO2_Keatite_34889-ICSD
592	97.71071	1.0229	0.07	6(14)	6	2	7	PdBi_tetrag_56279-ICSD
593	97.72965	1.02276	0.06	5(3)	2	7	0	SiO2_Keatite_34889-ICSD
594	97.78434	1.02233	0.14	12(28)	8	2	3	PdBi_tetrag_56279-ICSD
595	97.80275	1.02219	0	0.09(6)	1	7	2	SiO2_Keatite_34889-ICSD
596	97.80275	1.02219	0.03	2(1)	5	5	2	SiO2_Keatite_34889-ICSD
597	97.81041	1.02213	0.01	0.6(2)	2	6	3	Bi2O3_beta_189995-ICSD
598	97.87634	1.02162	0.1	8(5)	3	5	5	SiO2_Keatite_34889-ICSD
599	98.01278	1.02056	0.14	12(29)	4	6	3	PdBi_tetrag_56279-ICSD
600	98.02217	1.02048	0.03	2(1)	4	5	4	SiO2_Keatite_34889-ICSD
601	98.05604	1.02022	0.1	8(15)	0	1	13	Bi2O2(CO3)_252588-ICSD
602	98.15365	1.01947	0.11	9(17)	1	0	13	Bi2O2(CO3)_252588-ICSD
603	98.16058	1.01942	0.01	0.9(3)	1	3	5	Bi2O3_beta_189995-ICSD
604	98.31536	1.01822	0	0.03(2)	0	4	7	SiO2_Keatite_34889-ICSD
605	98.38812	1.01767	0.02	2(1)	1	5	6	SiO2_Keatite_34889-ICSD
606	98.4231	1.0174	0.01	1.2(5)	1	7	2	Bi2O3_beta_189995-ICSD
607	98.4231	1.0174	0.01	1.1(4)	5	5	2	Bi2O3_beta_189995-ICSD
608	98.67975	1.01544	0	0.02(2)	2	7	1	SiO2_Keatite_34889-ICSD
609	98.87724	1.01394	0	0.03(8)	6	4	5	PdBi_tetrag_56279-ICSD
610	98.90104	1.01376	0.03	2(2)	1	2	8	SiO2_Keatite_34889-ICSD
611	98.91396	1.01366	0.01	0.5(2)	3	7	0	Bi2O3_beta_189995-ICSD
612	98.96669	1.01326	0.07	6(2)	4	5	3	Bi2O3_beta_189995-ICSD
613	98.97918	1.01317	0	0(1)	1	7	2	PdBi_tetrag_56279-ICSD
614	99.06831	1.01249	0.01	1(1)	1	2	11	Bi2O2(CO3)_252588-ICSD
615	99.36198	1.01029	0	0(1)	2	1	11	Bi2O2(CO3)_252588-ICSD
616	99.37787	1.01017	0.39	32(15)	0	1	11	Bi_53797-ICSD
617	99.56022	1.00881	0	0.02(1)	1	4	7	SiO2_Keatite_34889-ICSD
618	99.72712	1.00757	0	0(1)	4	2	9	PdBi_tetrag_56279-ICSD

Table 19: XRD data (Rietveld refinement) of $Pd_{60}Ni_{20}Bi_{20}$/C catalyst [15].

Catalyst	Peak No.	Peak Pos. (° 2θ)	*d*-spacing (Å)	Rel. Int. (%)	Height (cts)	h	k	l	Assignment
$Pd_{60}Ni_{20}Bi_{20}$/C	1	23.85107	3.72773	5.04	294(105)	1	0	1	Bi2O2(CO3)_252588-ICSD
	2	23.97149	3.70928	8.33	485(163)	0	1	1	Bi2O2(CO3)_252588-ICSD
	3	25.20714	3.53018	6.37	371(487)	0	0	2	Graphite(2H)_187640-ICSD
	4	25.93282	3.43301	3.84	223(97)	0	0	4	Bi2O2(CO3)_252588-ICSD
	5	30.19592	2.95734	17.85	1039(241)	1	0	3	Bi2O2(CO3)_252588-ICSD
	6	30.2928	2.9481	15.12	880(197)	0	1	3	Bi2O2(CO3)_252588-ICSD
	7	32.75027	2.73228	10.84	631(259)	1	1	0	Bi2O2(CO3)_252588-ICSD
	8	35.32378	2.53889	1.57	91(58)	1	1	2	Bi2O2(CO3)_252588-ICSD
	9	38.28704	2.34893	0.28	16(16)	0	1	0	Graphite(2H)_187640-ICSD
	10	39.32093	2.28952	2.21	128(14)	0	0	6	Bi2O2(CO3)_252588-ICSD
	11	40.09861	2.24689	100	5819(1162)	1	1	1	Pd_64922-ICSD
	12	40.20333	2.24128	0.29	17(1)	1	0	5	Bi2O2(CO3)_252588-ICSD
	13	40.27884	2.23725	0.37	21(2)	0	1	5	Bi2O2(CO3)_252588-ICSD
	14	40.43458	2.22899	1.34	78(35)	0	1	1	Graphite(2H)_187640-ICSD
	15	42.22684	2.13844	4.9	285(85)	1	1	4	Bi2O2(CO3)_252588-ICSD
	16	45.99342	1.9717	-9.71	-565(43)	1	1	1	Ni_191753-ICSD
	17	46.38225	1.95607	0.26	15(10)	0	1	2	Graphite(2H)_187640-ICSD
	18	46.63483	1.94606	39.42	2294(802)	0	0	2	Pd_64922-ICSD
	19	46.84748	1.93772	1.84	107(13)	2	0	0	Bi2O2(CO3)_252588-ICSD
	20	47.11434	1.92737	1.39	81(11)	0	2	0	Bi2O2(CO3)_252588-ICSD
	21	48.79074	1.86499	0.29	17(7)	2	0	2	Bi2O2(CO3)_252588-ICSD
	22	49.04957	1.85575	0.51	29(14)	0	2	2	Bi2O2(CO3)_252588-ICSD
	23	51.71789	1.7661	0.44	25(41)	0	0	4	Graphite(2H)_187640-ICSD
	24	52.06048	1.75529	2.93	171(78)	1	1	6	Bi2O2(CO3)_252588-ICSD
	25	52.1959	1.75105	0.91	53(24)	1	0	7	Bi2O2(CO3)_252588-ICSD
	26	52.25761	1.74913	0.86	50(23)	0	1	7	Bi2O2(CO3)_252588-ICSD
	27	53.28393	1.71783	0.68	40(23)	2	1	1	Bi2O2(CO3)_252588-ICSD
	28	53.29597	1.71747	0	0.2(1)	0	0	8	Bi2O2(CO3)_252588-ICSD
	29	53.46625	1.7124	0.8	46(27)	1	2	1	Bi2O2(CO3)_252588-ICSD
	30	53.62544	1.70769	-4.38	-255(72)	0	0	2	Ni_191753-ICSD
	31	54.30859	1.68782	0.39	23(14)	2	0	4	Bi2O2(CO3)_252588-ICSD
	32	54.54844	1.68096	0.5	29(18)	0	2	4	Bi2O2(CO3)_252588-ICSD
	33	55.17869	1.66324	0.38	22(39)	0	1	3	Graphite(2H)_187640-ICSD
	34	56.79808	1.6196	1.78	104(53)	2	1	3	Bi2O2(CO3)_252588-ICSD
	35	56.97277	1.61505	1.63	95(47)	1	2	3	Bi2O2(CO3)_252588-ICSD
	36	62.7562	1.4794	0.43	25(14)	2	0	6	Bi2O2(CO3)_252588-ICSD

37	62.97539	1.47478	0.4	23(13)	0	2	6	Bi2O2(CO3)_252588-ICSD
38	63.44353	1.46502	0.07	4(2)	2	1	5	Bi2O2(CO3)_252588-ICSD
39	63.60697	1.46165	0.08	5(3)	1	2	5	Bi2O2(CO3)_252588-ICSD
40	63.96438	1.45434	0.01	0.7(4)	1	1	8	Bi2O2(CO3)_252588-ICSD
41	65.67338	1.42057	0.34	20(9)	1	0	9	Bi2O2(CO3)_252588-ICSD
42	65.72689	1.41954	0.36	21(9)	0	1	9	Bi2O2(CO3)_252588-ICSD
43	66.12866	1.41189	0.06	4(5)	0	1	4	Graphite(2H)_187640-ICSD
44	68.06575	1.37635	11.69	680(503)	0	2	2	Pd_64922-ICSD
45	68.18986	1.37415	0.15	9(2)	0	0	10	Bi2O2(CO3)_252588-ICSD
46	68.60879	1.36677	0.39	23(5)	2	2	0	Bi2O2(CO3)_252588-ICSD
47	69.19489	1.35662	0.41	24(25)	1	1	0	Graphite(2H)_187640-ICSD
48	70.14699	1.34052	0.15	9(3)	2	2	2	Bi2O2(CO3)_252588-ICSD
49	72.76301	1.29864	0.37	21(9)	2	1	7	Bi2O2(CO3)_252588-ICSD
50	72.91611	1.29629	0.37	21(8)	1	2	7	Bi2O2(CO3)_252588-ICSD
51	73.56564	1.28644	0.06	4(1)	3	0	1	Bi2O2(CO3)_252588-ICSD
52	73.62653	1.28553	0	0.07(3)	2	0	8	Bi2O2(CO3)_252588-ICSD
53	73.82973	1.28249	0	0.06(2)	0	2	8	Bi2O2(CO3)_252588-ICSD
54	74.02267	1.27962	0.07	4(2)	0	3	1	Bi2O2(CO3)_252588-ICSD
55	74.67856	1.27	0.29	17(6)	2	2	4	Bi2O2(CO3)_252588-ICSD
56	74.92087	1.26649	0.61	36(59)	1	1	2	Graphite(2H)_187640-ICSD
57	76.54578	1.24361	0.74	43(9)	3	0	3	Bi2O2(CO3)_252588-ICSD
58	76.9966	1.23745	4.19	244(16)	0	3	3	Bi2O2(CO3)_252588-ICSD
59	77.71332	1.22781	4.53	264(17)	1	1	10	Bi2O2(CO3)_252588-ICSD
60	77.91223	1.22518	3.46	202(12)	3	1	0	Bi2O2(CO3)_252588-ICSD
61	78.31087	1.21993	3.67	213(12)	1	3	0	Bi2O2(CO3)_252588-ICSD
62	78.99757	1.21104	0.1	6(9)	0	1	5	Graphite(2H)_187640-ICSD
63	79.25593	1.20774	-2.27	-132(35)	0	2	2	Ni_191753-ICSD
64	79.38047	1.20616	0.68	40(3)	3	1	2	Bi2O2(CO3)_252588-ICSD
65	79.77709	1.20116	0.49	29(2)	1	3	2	Bi2O2(CO3)_252588-ICSD
66	80.75295	1.18909	0.02	0.98(4)	1	0	11	Bi2O2(CO3)_252588-ICSD
67	80.80236	1.18848	0.05	3.2(2)	0	1	11	Bi2O2(CO3)_252588-ICSD
68	81.70199	1.17766	0.08	5(5)	0	0	6	Graphite(2H)_187640-ICSD
69	81.9304	1.17495	0.01	1(1)	0	2	0	Graphite(2H)_187640-ICSD
70	82.02408	1.17385	8.24	479(459)	1	1	3	Pd_64922-ICSD
71	82.0322	1.17375	3.69	215(7)	2	2	6	Bi2O2(CO3)_252588-ICSD
72	82.40468	1.16939	0.13	7.4(3)	3	0	5	Bi2O2(CO3)_252588-ICSD
73	82.84717	1.16426	0.13	7.6(3)	0	3	5	Bi2O2(CO3)_252588-ICSD
74	83.30299	1.15904	0.08	5(5)	0	2	1	Graphite(2H)_187640-ICSD
75	83.74705	1.15403	2.22	129(6)	3	1	4	Bi2O2(CO3)_252588-ICSD
76	84.1393	1.14964	1.98	115(7)	1	3	4	Bi2O2(CO3)_252588-ICSD

77	84.52926	1.14533	3.16	184(8)	2	1	9	Bi2O2(CO3)_252588-ICSD
78	84.53894	1.14522	0.59	34(2)	0	0	12	Bi2O2(CO3)_252588-ICSD
79	84.67618	1.14372	3.28	191(11)	1	2	9	Bi2O2(CO3)_252588-ICSD
80	86.53142	1.1239	2.05	119(170)	2	2	2	Pd_64922-ICSD
81	86.80183	1.12109	1.26	73(5)	2	0	10	Bi2O2(CO3)_252588-ICSD
82	86.99714	1.11907	1.04	61(4)	0	2	10	Bi2O2(CO3)_252588-ICSD
83	87.40081	1.11494	0.02	1(2)	0	2	2	Graphite(2H)_187640-ICSD
84	90.95629	1.08039	1.98	115(9)	3	1	6	Bi2O2(CO3)_252588-ICSD
85	91.06316	1.0794	0.62	36(3)	3	0	7	Bi2O2(CO3)_252588-ICSD
86	91.34642	1.07679	1.94	113(8)	1	3	6	Bi2O2(CO3)_252588-ICSD
87	91.42866	1.07604	0.35	21(36)	1	1	4	Graphite(2H)_187640-ICSD
88	91.50207	1.07536	0.59	34(3)	0	3	7	Bi2O2(CO3)_252588-ICSD
89	92.07545	1.07016	0.56	33(3)	3	2	1	Bi2O2(CO3)_252588-ICSD
90	92.13389	1.06964	0	0.25(2)	2	2	8	Bi2O2(CO3)_252588-ICSD
91	92.3194	1.06797	0.4	24(2)	2	3	1	Bi2O2(CO3)_252588-ICSD
92	93.64289	1.05633	0.98	57(5)	1	1	12	Bi2O2(CO3)_252588-ICSD
93	94.04098	1.0529	0.02	1(2)	0	1	6	Graphite(2H)_187640-ICSD
94	94.21096	1.05145	0.06	4(7)	0	2	3	Graphite(2H)_187640-ICSD
95	94.95975	1.04513	1.31	76(6)	3	2	3	Bi2O2(CO3)_252588-ICSD
96	95.20448	1.04308	1.45	84(7)	2	3	3	Bi2O2(CO3)_252588-ICSD
97	96.80546	1.03005	-2.69	-156(48)	1	1	3	Ni_191753-ICSD
98	98.09193	1.01995	0.53	31(2)	1	0	13	Bi2O2(CO3)_252588-ICSD
99	98.14117	1.01957	0.47	27(2)	0	1	13	Bi2O2(CO3)_252588-ICSD
100	98.96719	1.01326	0.02	1.13(8)	2	1	11	Bi2O2(CO3)_252588-ICSD
101	99.11528	1.01214	0.03	1.6(1)	1	2	11	Bi2O2(CO3)_252588-ICSD

Table 20: Determined crystal structure in all Pd-based catalyst samples and their corresponding data – adopted from Inorganic Crystal Structure Database (ICSD) – FIZ Karlsruhe - Leibniz Institute for Information Infrastructure with the ICSD Collection code of 64922 (https://icsd.fiz-karlsruhe.de/display/details.xhtml) [153].

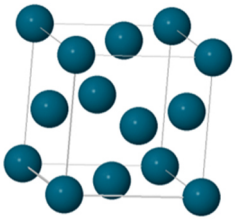
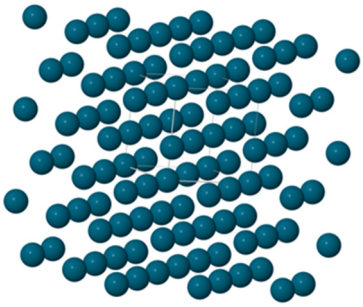
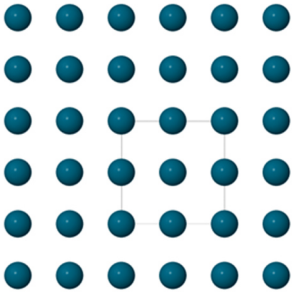
Pd_64922-ICSD		
		
(a)	**(b)**	**(c)**
Unit cell	Crystal lattice	Crystal lattice (view: top)
Chemistry		
Sum formula	Pd1	
Molecular weight	106.4000 [u]	
ANX formula	N	
Chemical name	Palladium	
Mineral name	Palladium	
Mineral origin	synthetic (from Heraeus)	
Structure formula	Pd	
AB formula	A	
Mineral group	Platinum	
Standardized Crystal Structure Data		
Structure formula	Pd	
Cell parameter	*a* = 3.8670 Å *b* = 3.8670 Å *c* = 3.8670 Å	*α* = 90.000 ° *β* = 90.000 ° *γ* = 90.000 °
Cell volume	57.83 [Å³]	
Crystal system	Cubic	
Structure type	fcc(ccp)-Cu	
Space group	F m -3 m (225)	
Coordination number Z	4	

Table 21: Determined crystal structure in the $Pd_{60}Ni_{40}$/C catalyst and their corresponding data – adopted from Inorganic Crystal Structure Database (ICSD) – FIZ Karlsruhe - Leibniz Institute for Information Infrastructure with the ICSD Collection code of 106936 (https://icsd.fiz-karlsruhe.de/display/details.xhtml) [154].

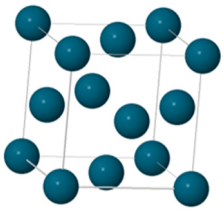
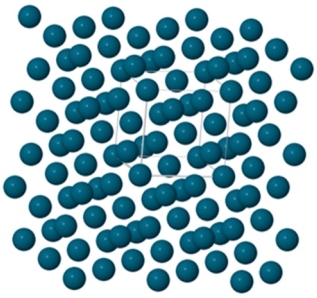
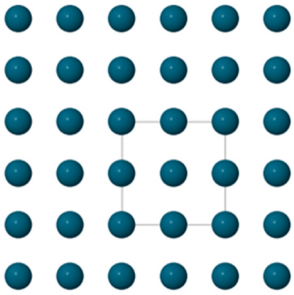
Pd09Ni08_106936-ICSD		
		
(a)	**(b)**	**(c)**
Unit cell	Crystal lattice	Crystal lattice (view: top)
Chemistry		
Sum formula	Ni0.1 Pd0.9	
Molecular weight	101.6310 [u]	
ANX formula	N	
Chemical name	Palladium nickel (0.9/0.1)	
Mineral name	-	
Mineral origin	-	
Structure formula	(Pd0.9 Ni0.1)	
AB formula	A	
Mineral group	-	
Standardized Crystal Structure Data		
Structure formula	(Pd0.9 Ni0.1)	
Cell parameter	a = 3.8660 Å b = 3.8660 Å c = 3.8660 Å	α = 90.000 ° β = 90.000 ° γ = 90.000 °
Cell volume	57.78 [Å³]	
Crystal system	Cubic	
Structure type	fcc(ccp)-Cu	
Space group	F m -3 m (225)	
Coordination number Z	4	

Table 22: Determined crystal structure in the $Pd_{60}Bi_{40}$/C catalyst and their corresponding data – adopted from Inorganic Crystal Structure Database (ICSD) – FIZ Karlsruhe - Leibniz Institute for Information Infrastructure with the ICSD Collection code of 53797 (https://icsd.fiz-karlsruhe.de/display/details.xhtml) [153].

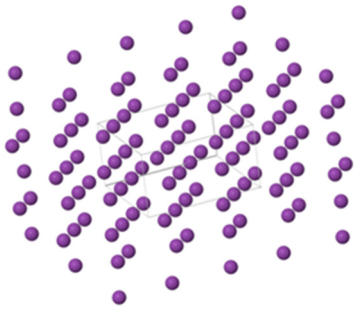
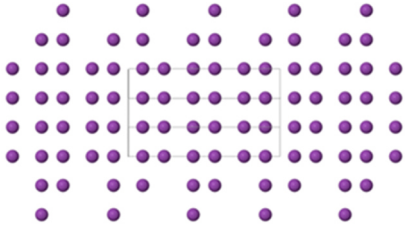
Bi_53797-ICSD		
		
(a)	**(b)**	**(c)**
Unit cell	Crystal lattice	Crystal lattice (view: top)
	Chemistry	
Sum formula	Bi1	
Molecular weight	208.9800 [u]	
ANX formula	N	
Chemical name	Bismuth	
Mineral name	Bismuth	
Mineral origin	-	
Structure formula	Bi	
AB formula	A	
Mineral group	Arsenic	
	Standardized Crystal Structure Data	
Structure formula	Bi	
Cell parameter	a = 4.5480 Å b = 4.5480 Å c = 11.8520 Å	α = 90.000 ° β = 90.000 ° γ = 120.000 °
Cell volume	212.31 [Å³]	
Crystal system	Trigonal	
Structure type	As	
Space group	R -3 m H (166)	
Coordination number Z	6	

Table 23: Determined crystal structure (Bi: violet; O: red) in the $Pd_{60}Bi_{40}$/C catalyst and their corresponding data – adopted from Inorganic Crystal Structure Database (ICSD) – FIZ Karlsruhe - Leibniz Institute for Information Infrastructure with the ICSD Collection code of 189995 (https://icsd.fiz-karlsruhe.de/display/details.xhtml) [155].

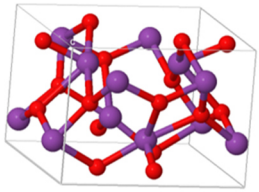
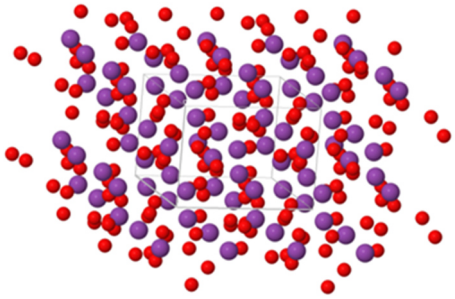
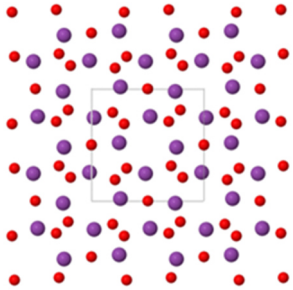
Bi2O3_beta_189995-ICSD		
		
(a)	**(b)**	**(c)**
Unit cell	Crystal lattice	Crystal lattice (view: top)
Chemistry		
Sum formula	Bi2 O3	
Molecular weight	465.9570 [u]	
ANX formula	A2X3	
Chemical name	Dibismuth trioxide	
Mineral name	-	
Mineral origin	-	
Structure formula	Bi2 O3	
AB formula	A2B3	
Mineral group	-	
Standardized Crystal Structure Data		
Structure formula	Bi2 O3	
Cell parameter	a = 7.7439 Å b = 7.7439 Å c = 5.6287 Å	α = 90.000 ° β = 90.000 ° γ = 90.000 °
Cell volume	337.54 [Å³]	
Crystal system	Tetragonal	
Structure type	Bi2O3(tP20)	
Space group	P -4 21 c (114)	
Coordination number Z	4	

Table 24: Determined crystal structure (Bi: violet; O: red, C: grey) in the $Pd_{60}Bi_{40}$/C, $Pd_{60}Ni_{20}Bi_{20}$/C, $Pd_{80}Ni_{10}Bi_{10}$/C and $Pd_{40}Ni_{20}Bi_{40}$/C catalysts and their corresponding data – adopted from Inorganic Crystal Structure Database (ICSD) – FIZ Karlsruhe - Leibniz Institute for Information Infrastructure with the ICSD Collection code of 252588 (https://icsd.fiz-karlsruhe.de/display/details.xhtml) [156].

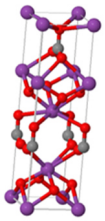
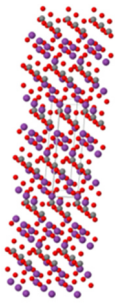
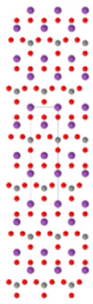
Bi2O2(CO3)_252588-ICSD		
		
(a)	**(b)**	**(c)**
Unit cell	Crystal lattice	Crystal lattice (view: top)
	Chemistry	
Sum formula	C1 Bi2 O5	
Molecular weight	509.9660 [u]	
ANX formula	AB2X5	
Chemical name	Dibismuth carbonate dioxide	
Mineral name	Bismutite	
Mineral origin	Synthetic	
Structure formula	Bi2 O2 (C O3)	
AB formula	AB2C5	
Mineral group	-	
	Standardized Crystal Structure Data	
Structure formula	Bi2 O2 (C O3)	
Cell parameter	a = 3.8658 Å b = 3.8648 Å c = 13.6757 Å	α = 90.000 ° β = 90.000 ° γ = 90.000 °
Cell volume	204.32 [Å³]	
Crystal system	orthorhombic	
Structure type	-	
Space group	I m m 2 (44)	
Coordination number Z	2	

Table 25: Determined crystal structure (Pd: blue; Bi: violet) in the $Pd_{60}Bi_{40}$/C catalyst and their corresponding data – adopted from Inorganic Crystal Structure Database (ICSD) – FIZ Karlsruhe - Leibniz Institute for Information Infrastructure with the ICSD Collection code of 56279 (https://icsd.fiz-karlsruhe.de/display/details.xhtml) [157].

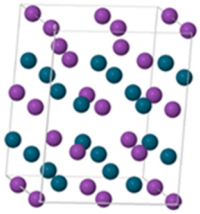
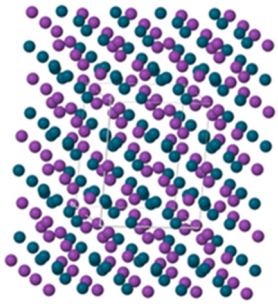
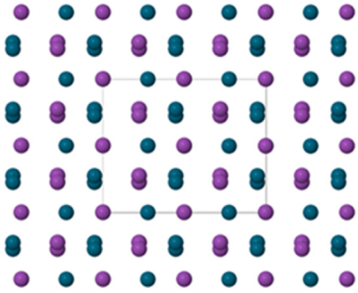
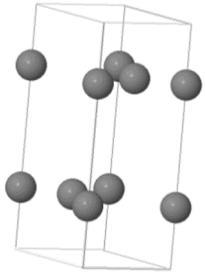
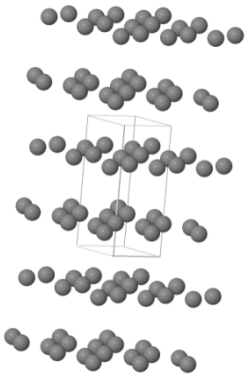
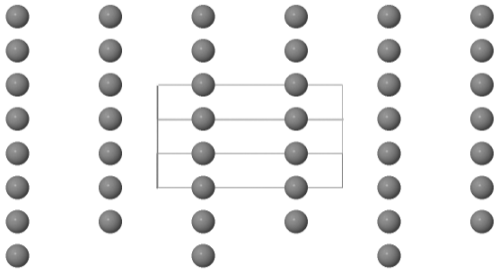
PdBi_tetrag_56279-ICSD		
		
(a)	**(b)**	**(c)**
Unit cell	Crystal lattice	Crystal lattice (view: top)
	Chemistry	
Sum formula	Bi1 Pd1	
Molecular weight	315.3800 [u]	
ANX formula	NO	
Chemical name	Palladium bismuthide (1/1)	
Mineral name	Polarite (Pb-free)	
Mineral origin	Synthetic	
Structure formula	Pd Bi	
AB formula	AB	
Mineral group	-	
	Standardized Crystal Structure Data	
Structure formula	Pd Bi	
Cell parameter	a = 8.7070 Å b = 7.2030 Å c = 10.6620 Å	α = 90.000 ° β = 90.000 ° γ = 90.000 °
Cell volume	668.68 [Å³]	
Crystal system	orthorhombic	
Structure type	BiPbPd2	
Space group	C m c 21 (36)	
Coordination number Z	16	

Table 26: Determined crystal structure in all Pd-based catalyst samples and their corresponding data – adopted from Inorganic Crystal Structure Database (ICSD) – FIZ Karlsruhe - Leibniz Institute for Information Infrastructure with the ICSD Collection code of 187640 (https://icsd.fiz-karlsruhe.de/display/details.xhtml) [158].

Graphite (2H)_187640-ICSD		
		
(a)	**(b)**	**(c)**
Unit cell	Crystal lattice	Crystal lattice (view: top)

Chemistry		
Sum formula	C1	
Molecular weight	12.0110 [u]	
ANX formula	N	
Chemical name	Graphite	
Mineral name	Graphite 2H	
Mineral origin	-	
Structure formula	C	
AB formula	A	
Mineral group	-	

Standardized Crystal Structure Data		
Structure formula	C	
Cell parameter	a = 2.4460 Å	α = 90.000 °
	b = 2.4460 Å	β = 90.000 °
	c = 6.6480 Å	γ = 120.000 °
Cell volume	34.45 [Å³]	
Crystal system	Hexagonal	
Structure type	Graphite(2H)	
Space group	P 63/m m c (194)	
Coordination number Z	4	

XPS analysis

Table 27: XPS data of the Pd/C catalyst [15].

Catalyst	Peak name	Area (cps·eV)	E_{bin}[a] (eV)	Sigma	Lambda	IERF[b]	Sens. Fact.[c]	Norm. Area[d] (cps·eV)	Quant. (at.%)	[e]Sum (at.%)
Pd/C	C1s_2 Peak 1	4069.7704	283.76	1	20.31	0.913	18.543	219.47745	59.48	90.37
	C1s_2 Peak 2	706.35839	284.61	1	20.29	0.913	18.525	38.130008	10.33	
	C1s_2 Peak 3	1137.5140	285.21	1	20.29	0.914	18.545	61.338045	16.62	
	C1s_2 Peak 4	269.62020	288.37	1	20.25	0.915	18.529	14.551254	3.94	
	O1s_3 Peak 1	565.11169	530.11	2.93	17.12	1.022	51.265	11.023343	2.99	6.77
	O1s_3 Peak 2	564.74893	531.52	2.93	17.1	1.023	51.255	11.018416	2.99	
	O1s_3 Peak 3	1068.8054	532.96	10000	17.08	1.024	174899	0.0061109	0	
	O1s_3 Peak 4	149.45891	535.21	2.93	17.05	1.025	51.205	2.9188343	0.79	
	Pd3d_4 Doublet 1	1391.3131	334.73	16.04	19.66	0.932	293.90	4.7339196	1.28	2.84
	Pd3d_4 Doublet 2	1695.1762	336.27	16.04	19.64	0.933	293.91	5.7674946	1.56	

[a]E_{bin}: binding energy; [b]IERF: intensity/energy response factor, [c]Sens. Fact.: sensitivity factor, [d]Norm. Area: Product of Area and Sens. Fact.; [e]Sum: Gaussian-Lorentzian lines.

Table 28: XPS data of the $Pd_{60}Ni_{40}$/C catalyst [15].

Catalyst	Peak name	Area (cps·eV)	E_{bin}[a] (eV)	Sigma	Lambda	IERF[b]	Sens. Fact.[c]	Norm. Area[d] (cps·eV)	Quant. (at.%)	[e]Sum (at.%)
$Pd_{60}Ni_{40}$/C	C1s_2 Peak 1	2289.5422	283.8	1	20.31	0.913	18.543	123.47205	48.93	91.27
	C1s_2 Peak 2	1489.0192	284.45	1	20.3	0.913	18.534	80.339876	31.84	
	C1s_2 Peak 3	259.23786	286.32	1	20.27	0.914	18.527	13.992436	5.54	
	C1s_2 Peak 4	232.04678	288.67	1	20.24	0.915	18.52	12.529523	4.96	
	O1s_3 Peak 1	289.40099	530.22	2.93	17.12	1.022	51.265	5.6451964	2.24	6.38
	O1s_3 Peak 2	471.29767	531.76	2.93	17.1	1.023	51.255	9.1951550	3.64	
	O1s_3 Peak 3	442.53722	533.17	10000	17.08	1.024	174899	0.0025302	0	
	O1s_3 Peak 4	64.916508	535.2	2.93	17.05	1.025	51.205	1.2677767	0.5	
	Pd3d_4 Doublet 1	637.25394	334.74	16.04	19.66	0.932	293.90	2.1682457	0.86	2.02
	Pd3d_4 Doublet 2	860.11626	335.81	16.04	19.65	0.933	294.06	2.9248790	1.16	
	Ni2p_5 Doublet 1	85.676351	861.14	22.18	12.48	1.27	351.54	0.2437144	0.1	0.33
	Ni2p_5 Doublet 2	203.37931	855.13	22.18	12.56	1.264	352.12	0.5775753	0.23	

[a]E_{bin}: binding energy; [b]IERF: intensity/energy response factor, [c]Sens. Fact.: sensitivity factor, [d]Norm. Area: Product of Area and Sens. Fact.; [e]Sum: Gaussian-Lorentzian lines.

Table 29: XPS data of the $Pd_{60}Bi_{40}$/C catalyst [15].

Catalyst	Peak name	Area (cps·eV)	E_{bin}[a] (eV)	Sigma	Lambda	IERF[b]	Sens. Fact.[c]	Norm. Area[d] (cps·eV)	Quant. (at.%)	[e]Sum (at.%)
$Pd_{60}Bi_{40}$/C	C1s_2 Peak 1	3953.8952	283.81	1	20.31	0.913	18.543	213.22845	59.42	95.11
	C1s_2 Peak 2	1323.2849	284.74	1	20.29	0.913	18.525	71.432384	19.91	
	C1s_2 Peak 3	631.72100	285.88	1	20.28	0.914	18.536	34.080762	9.5	
	C1s_2 Peak 4	417.40309	288.56	1	20.25	0.915	18.529	22.527016	6.28	
	O1s_3 Peak 1	157.73022	530.27	2.93	17.12	1.022	51.265	3.0767623	0.86	4.19
	O1s_3 Peak 2	612.33465	531.79	2.93	17.1	1.023	51.255	11.946827	3.33	
	O1s_3 Peak 3	641.89857	533.2	10000	17.08	1.024	174899	0.0036701	0	
	Pd3d_4 Doublet 1	200.69425	334.78	16.04	19.66	0.933	294.21	0.6821277	0.19	0.33
	Pd3d_4 Doublet 2	151.20054	336.14	16.04	19.64	0.933	293.91	0.5144292	0.14	
	Bi4f_5 Doublet 1	104.37947	157	24.83	21.88	0.87	472.65	0.2208369	0.06	0.38
	Bi4f_5 Doublet 2	236.77777	158.21	24.83	21.86	0.87	472.22	0.5014119	0.14	
	Bi4f_5 Doublet 3	307.29802	159.19	24.83	21.85	0.87	472.00	0.6510468	0.18	

[a]E_{bin}: binding energy; [b]IERF: intensity/energy response factor, [c]Sens. Fact.: sensitivity factor, [d]Norm. Area: Product of Area and Sens. Fact.; [e]Sum: Gaussian-Lorentzian lines.

Table 30: XPS data of the $Pd_{60}Ni_{20}Bi_{20}/C$ catalyst [15].

Catalyst	Peak name	Area (cps·eV)	E_{bin}[a] (eV)	Sigma	Lambda	IERF[b]	Sens. Fact.[c]	Norm. Area[d] (cps·eV)	Quant. (at.%)	[e]Sum (at.%)
	C1s_2 Peak 1	3022.1428	283.88	1	20.3	0.913	18.534	163.05939	62.14	94.09
	C1s_2 Peak 2	499.95624	284.8	1	20.29	0.913	18.525	26.988191	10.28	
	C1s_2 Peak 3	790.09587	285.46	1	20.28	0.914	18.536	42.624939	16.24	
	C1s_2 Peak 4	263.78597	288.54	1	20.25	0.915	18.529	14.236385	5.43	
	O1s_3 Peak 1	113.87625	529.91	2.93	17.12	1.022	51.265	2.2213256	0.85	4.87
	O1s_3 Peak 2	540.60367	531.75	2.93	17.1	1.023	51.255	10.547335	4.02	
$Pd_{60}Ni_{20}Bi_{20}/C$	O1s_3 Peak 3	555.29835	533.15	10000	17.08	1.024	174899	0.0031749	0	
	Pd3d_4 Doublet 1	313.94532	334.75	16.04	19.66	0.933	294.21	1.0670500	0.41	0.75
	Pd3d_4 Doublet 2	265.05043	335.95	16.04	19.65	0.933	294.06	0.9013205	0.34	
	Bi4f_5 Doublet 1	187.12291	157.78	24.83	21.87	0.87	472.43	0.3960793	0.15	0.18
	Bi4f_5 Doublet 2	31.799922	159.35	24.83	21.85	0.87	472.00	0.0673718	0.03	
	Ni2p_6 Doublet 1	74.412448	856.06	22.18	12.55	1.265	352.12	0.2113245	0.08	0.11
	Ni2p_6 Doublet 2	28.757929	861.33	22.18	12.47	1.27	351.26	0.0818703	0.03	

[a]E_{bin}: binding energy; [b]IERF: intensity/energy response factor, [c]Sens. Fact.: sensitivity factor, [d]Norm. Area: Product of Area and Sens. Fact.; [e]Sum: Gaussian-Lorentzian lines.

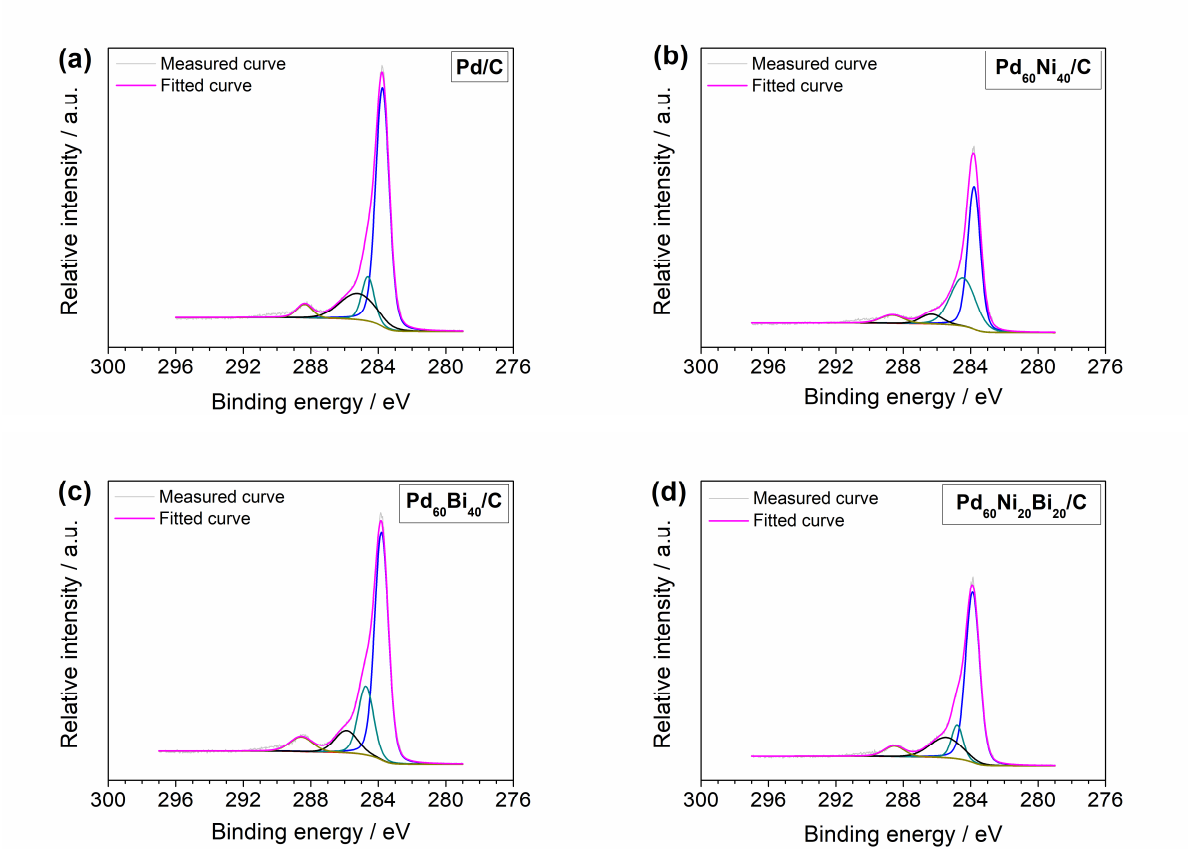


Figure 52: C 1s XPS spectra of the **(a)** Pd/C, **(b)** $Pd_{60}Ni_{40}$/C, **(c)** $Pd_{60}Bi_{40}$/C and **(d)** $Pd_{60}Ni_{20}Bi_{20}$/C catalyst [15].

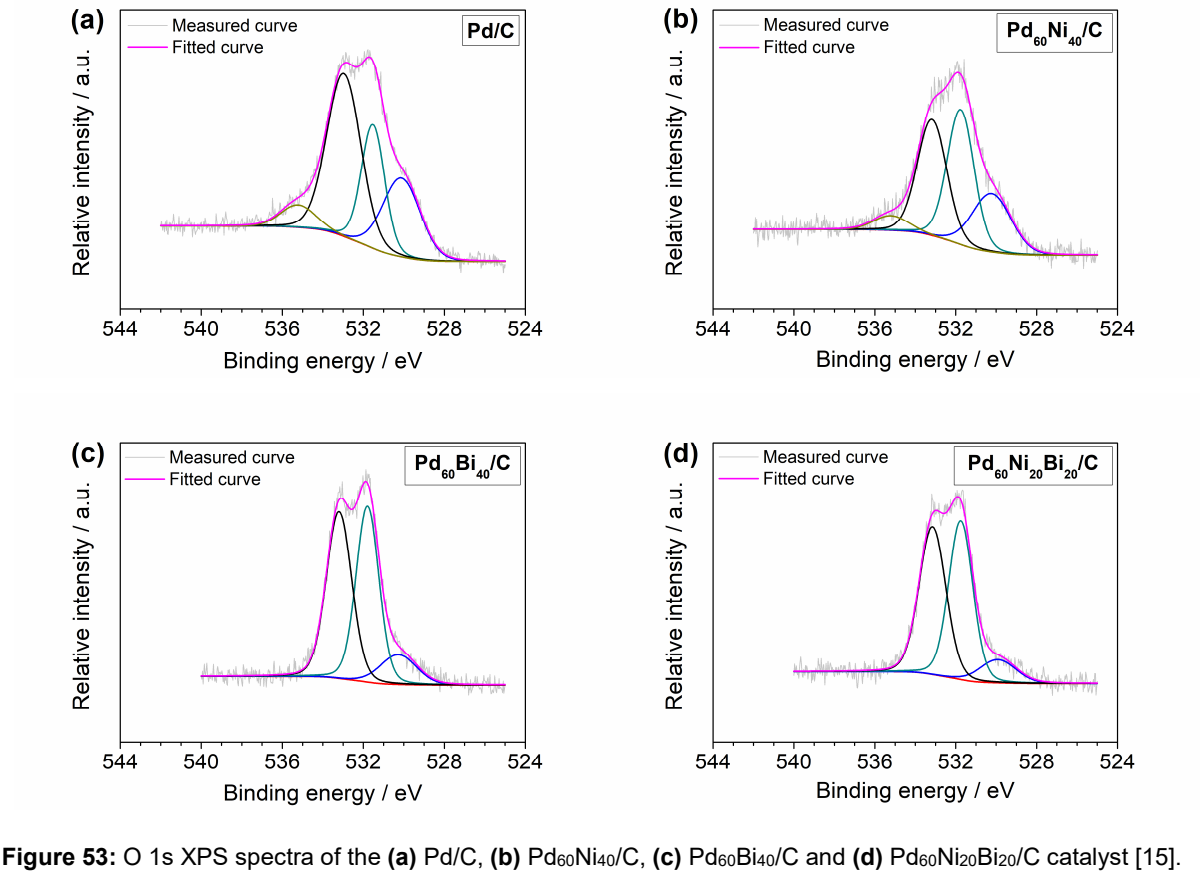


Figure 53: O 1s XPS spectra of the **(a)** Pd/C, **(b)** $Pd_{60}Ni_{40}$/C, **(c)** $Pd_{60}Bi_{40}$/C and **(d)** $Pd_{60}Ni_{20}Bi_{20}$/C catalyst [15].

8.2.3 Electrochemical Characterization

CV and CA analysis

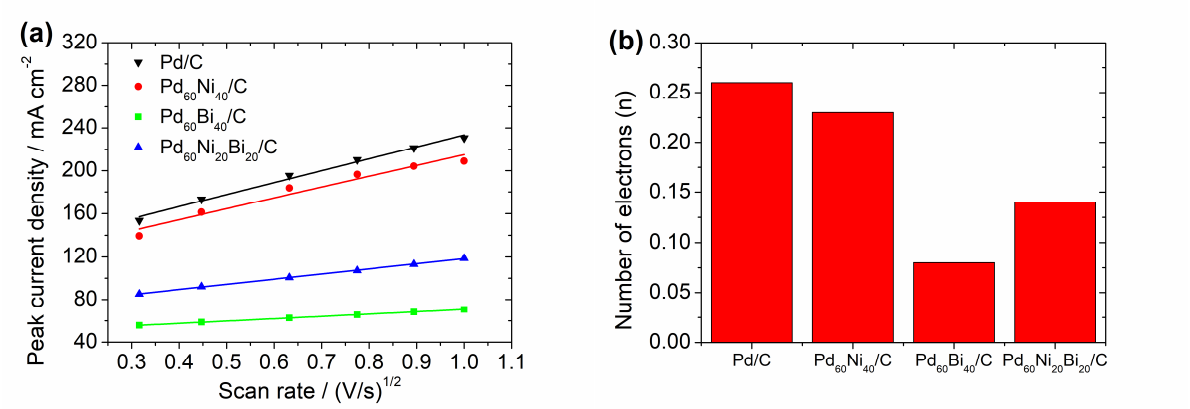


Figure 54: (a) Diffusion controlled process for the alkaline EOR takes place on carbon supported Pd-based catalysts in scan rates region of 100 to 1000 mV·s^{-1}, showing by linear relationship between peak current density and square root of scan rate. The EOR measurements on the respective catalyst were performed in a mixture of 1 M KOH and 1 M EtOH and at 30 °C and **(b)** the number of electrons which are released during the EOR oxidation, were determined according to Randles-Sevcik equation.

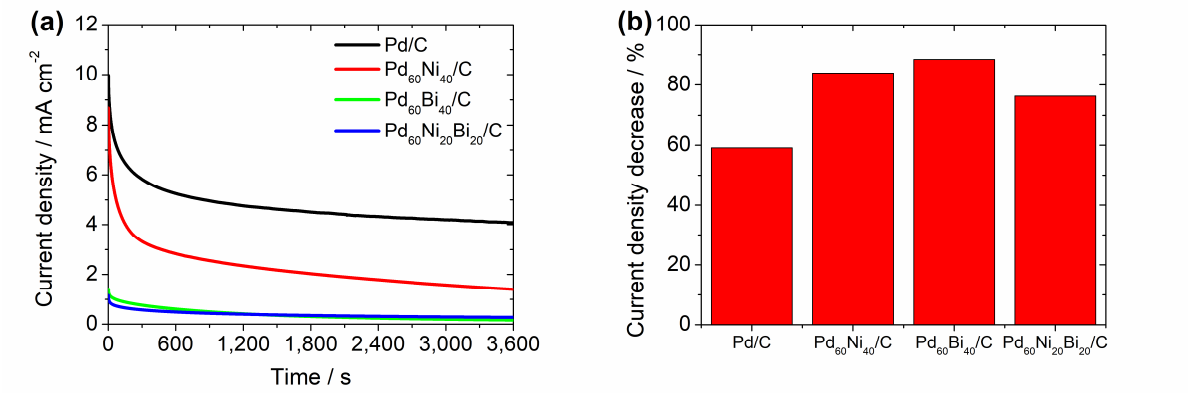


Figure 55: Stability tests of carbon supported Pd-based electrocatalysts **(a)** in a mixture of 1 M KOH and 1 M EtOH at an applied potential of 0.5 V and at 30 °C for 3,600 s using the CA method and **(b)** their resulting current density decrease, given in percentage.

EIS analysis

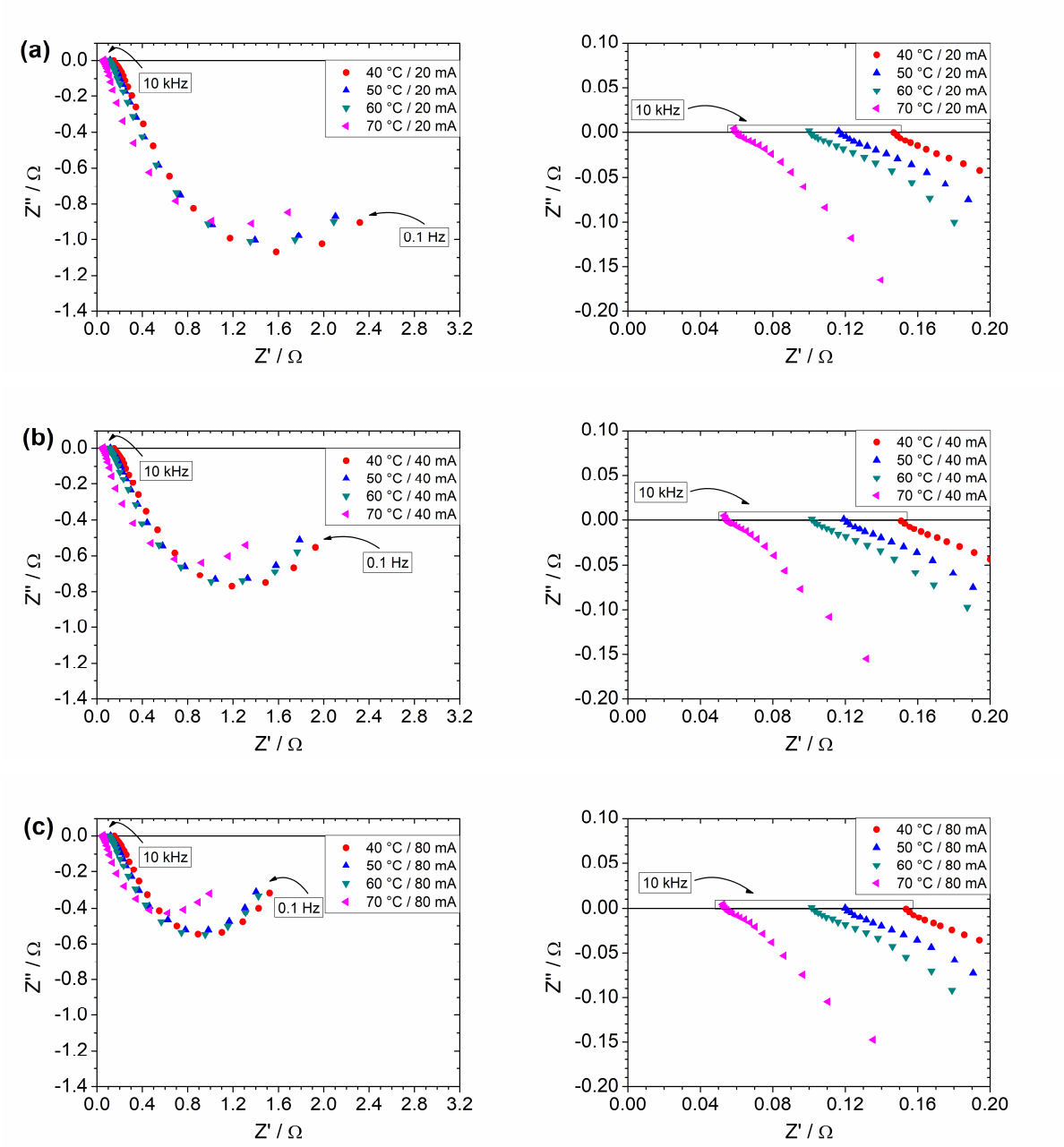


Figure 56: Nyquist plots of the MEA 1 consisting of $Pd_{60}Ni_{40}$/C based anode, Tokuyama A201 AEM and Ag-MnO_x/C based cathode at a constant current of **(a)** 20 mA, **(b)** 40 mA and **(c)** 80 mA with corresponding magnified electrolyte resistance region (right) at different temperatures (Anode: 1 M KOH + 1 M EtOH, 10 mL·min^{-1}; Cathode: Pure O_2, ~10 mL·min^{-1}).

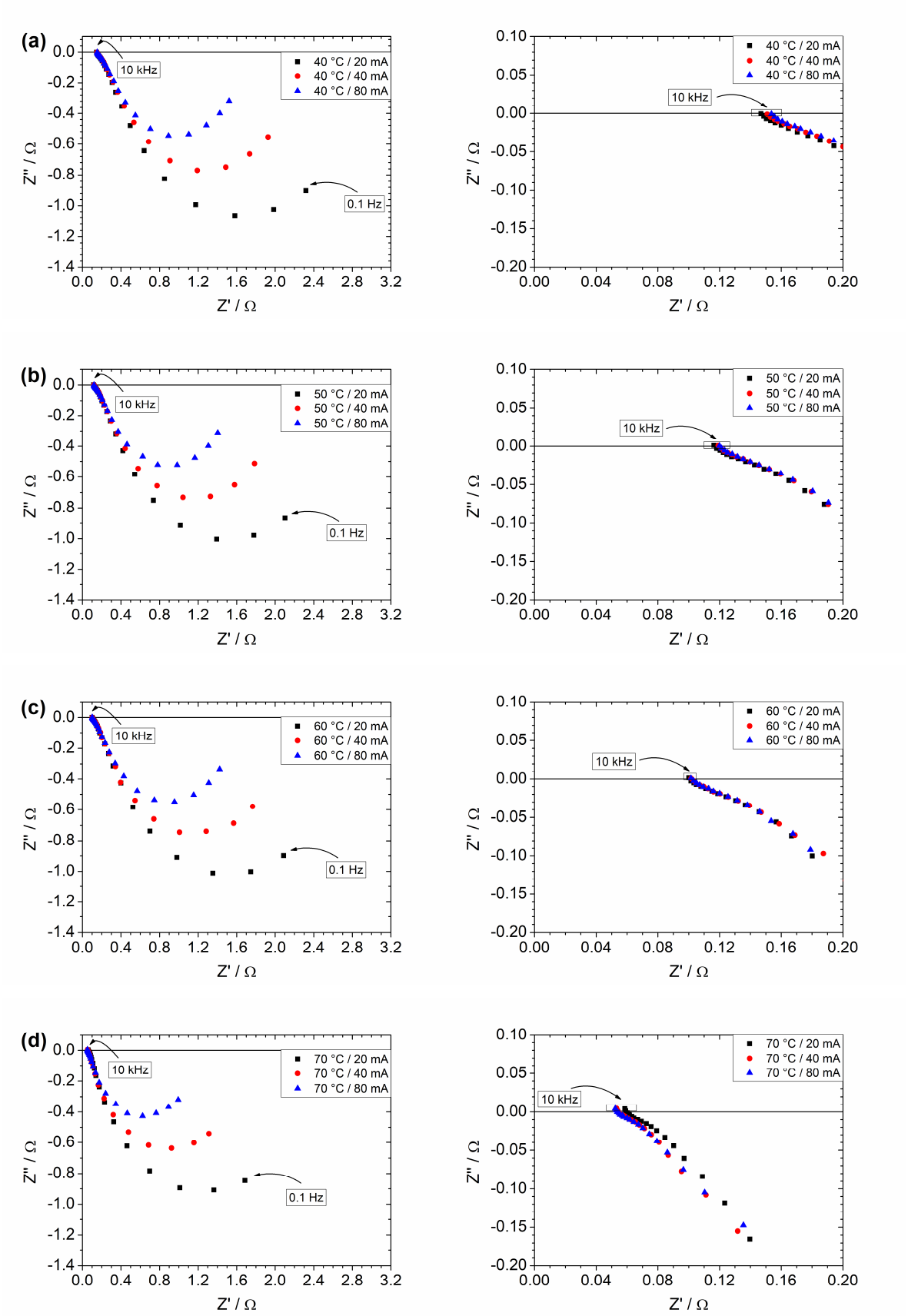


Figure 57: Nyquist plots of the MEA 1 consisting of $Pd_{60}Ni_{40}$/C based anode, Tokuyama A201 AEM and Ag-MnO_x/C based cathode at a constant temperature of **(a)** 40 °C, **(b)** 50 °C, **(c)** 60 °C and **(d)** 70 °C with corresponding magnified electrolyte resistance region (right) at different applied currents (Anode: 1 M KOH + 1 M EtOH, 10 mL·min^{-1}; Cathode: Pure O_2, ~10 mL·min^{-1}).

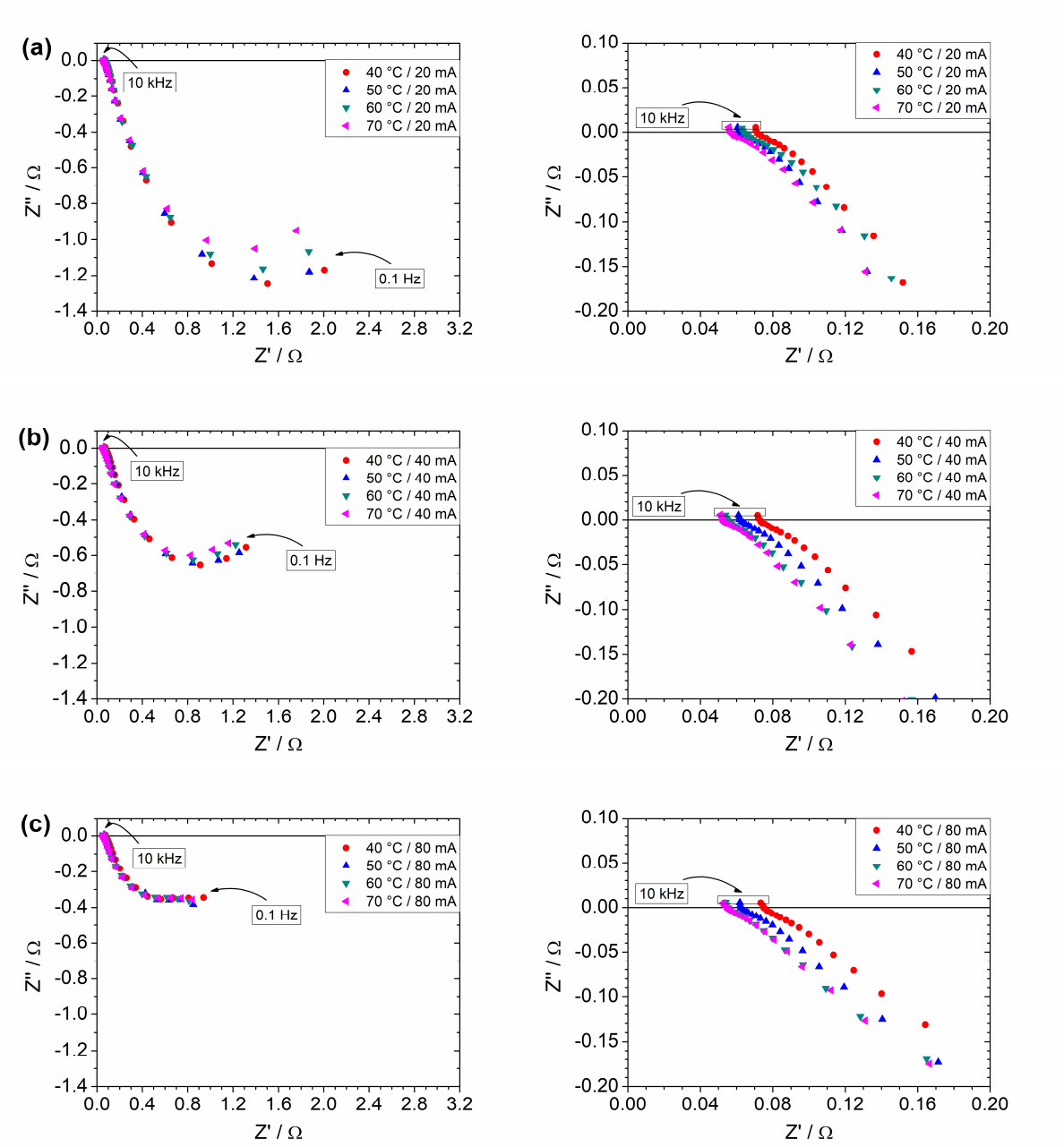


Figure 58: Nyquist plots of the MEA 2 consisting of $Pd_{60}Ni_{20}Bi_{20}$/C based anode, Tokuyama A201 AEM and Ag-MnO_x/C based cathode at a constant current of **(a)** 20 mA, **(b)** 40 mA and **(c)** 80 mA with corresponding magnified electrolyte resistance region (right) at different temperatures (Anode: 1 M KOH + 1 M EtOH, 10 mL·min^{-1}; Cathode: Pure O_2, ~10 mL·min^{-1}).

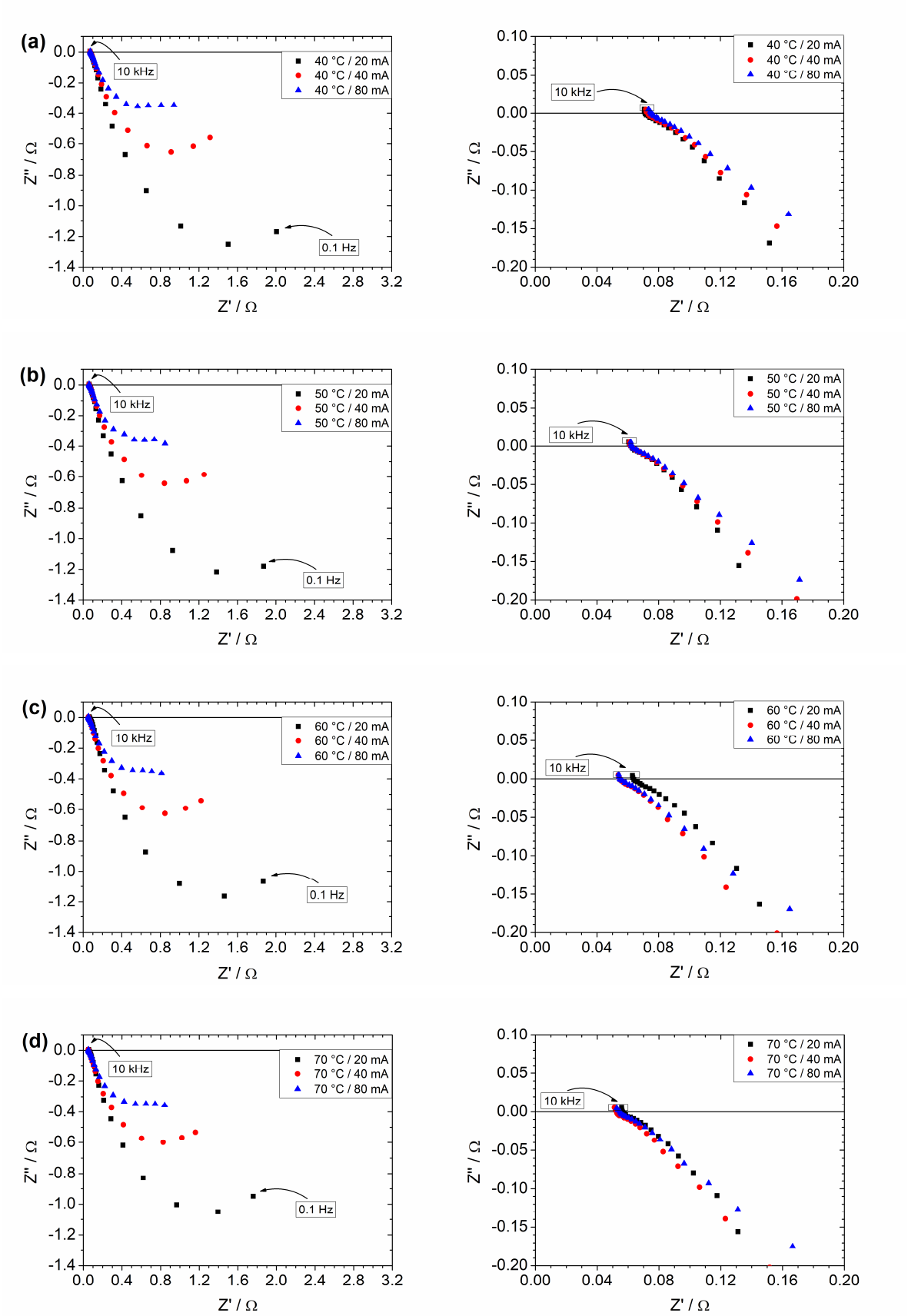


Figure 59: Nyquist plots of the MEA 2 consisting of $Pd_{60}Ni_{20}Bi_{20}$/C based anode, Tokuyama A201 AEM and Ag-MnO_x/C based cathode at a constant temperature of **(a)** 40 °C, **(b)** 50 °C, **(c)** 60 °C and **(d)** 70 °C with corresponding magnified electrolyte resistance region (right) at different applied currents (Anode: 1 M KOH + 1 M EtOH, 10 mL·min^{-1}; Cathode: Pure O_2, ~10 mL·min^{-1}).

8.3 PART III: Atomic Composition Optimization of Carbon Supported $Pd_xNi_yBi_z$ Nanocatalyst for the Alkaline EOR

8.3.1 Chemicals and Materials

Anode Catalysts

- Palladium(II) chloride ($PdCl_2$, anhydrous, 59-60% Pd basis, Aldrich),
- nickel(II) nitrate hexahydrate ($Ni(NO_3)_2 \cdot 6H_2O$, Aldrich),
- bismuth(III) chloride ($BiCl_3$, reagent grade, ≥ 98%, Aldrich),
- sodium chloride (NaCl, ≥ 99.5%, Aldrich),
- hydrochloric acid (HCl p.a. ≥ 32%, Fluka Analytics),
- Vulcan XC72R carbon black (CABOT Corporation, USA),
- sodium borohydride ($NaBH_4$, Sigma-Aldrich),
- 2-propanol (ASC ≥ 99.8%, Sigma-Aldrich),
- sodium hydroxide (NaOH, Aldrich) and
- ultra-pure water (~18 MΩ·cm, Barnstead NANOpure Water Purification System) were used for the development of $Pd_xNi_yBi_z$/C anode catalysts [15].

Electrochemical Characterizations (RDE-CV and RDE-CA)

- 1.0 M potassium hydroxide solution (KOH, FIXANAL KA 180 mL, Sigma-Aldrich),
- Nafion ionomer solution (5 wt.%, Quintech),
- ethanol abs. (99.999%, Aldrich) and
- ultra-pure water (~18 MΩ·cm, Barnstead NANOpure Water Purification System) were used for electrochemical characterizations of $Pd_xNi_yBi_z$/C anode catalysts [15].

8.3.2 Physico-Chemical Characterization

ICP-OES analysis

Table 31: ICP-OES data of carbon supported $Pd_xNi_yB_z$ catalysts [15,29].

Catalysts		Pd (g/kg)	Ni (g/kg)	Bi (g/kg)	Pd (mol/kg)	Ni (mol/kg)	Bi (mol/kg)	Sum (mol/kg)	Pd (at.%)	Ni (at.%)	Bi (at.%)
$Pd_{70}Ni_{25}Bi_5/C$	Average	131.7	25.2	17.4	1.24	0.43	0.083	1.75	70.7	24.5	4.8
	SD	3.2	0.6	0.4	0.03	0.01	0.002	0.03	2.1	0.7	0.1
$Pd_{70}Ni_{20}Bi_{10}/C$	Average	124.5	19.1	39.2	1.17	0.325	0.188	1.68	69.5	19.3	11.1
	SD	2.7	0.1	1.0	0.03	0.002	0.005	0.03	1.8	0.3	0.3
$Pd_{80}Ni_{10}Bi_{10}/C$	Average	143.4	10.4	43.2	1.35	0.177	0.207	1.73	77.8	10.2	11.9
	SD	1.4	0.1	0.5	0.01	0.002	0.002	0.01	1.0	0.1	0.2
$Pd_{40}Ni_{20}Bi_{40}/C$	Average	92.5	18.4	143.5	0.87	0.314	0.69	1.87	46.5	16.8	36.7
	SD	1.0	0.1	1.3	0.01	0.002	0.01	0.01	0.6	0.1	0.4

SD … standard deviation

Atomic weight (AMU): Pd = 106.42; Ni = 58.69; Bi = 208.98

TEM analysis

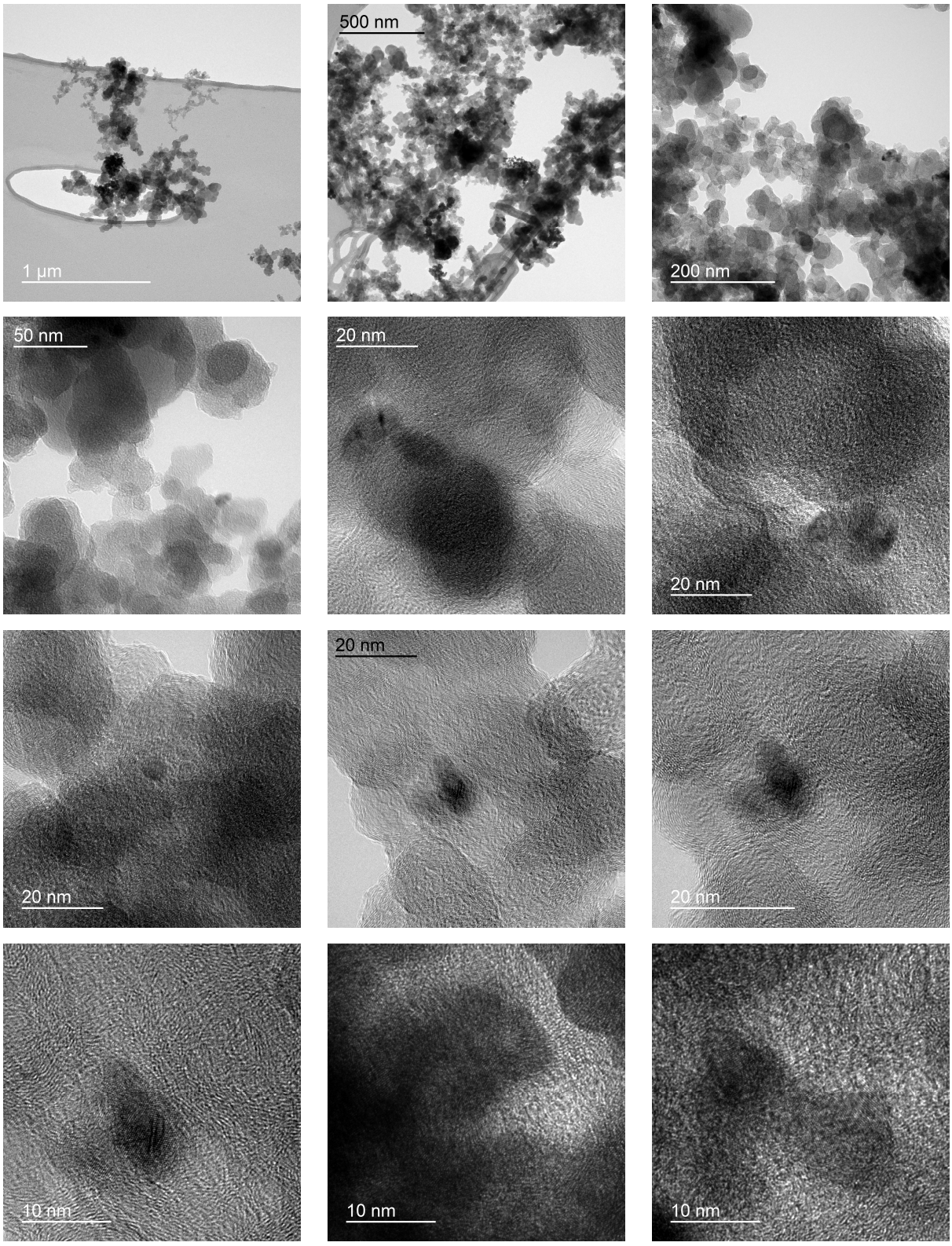


Figure 60: TEM micrographs with low and high magnifications of the $Pd_{70}Ni_{25}Bi_5/C$ catalyst [15].

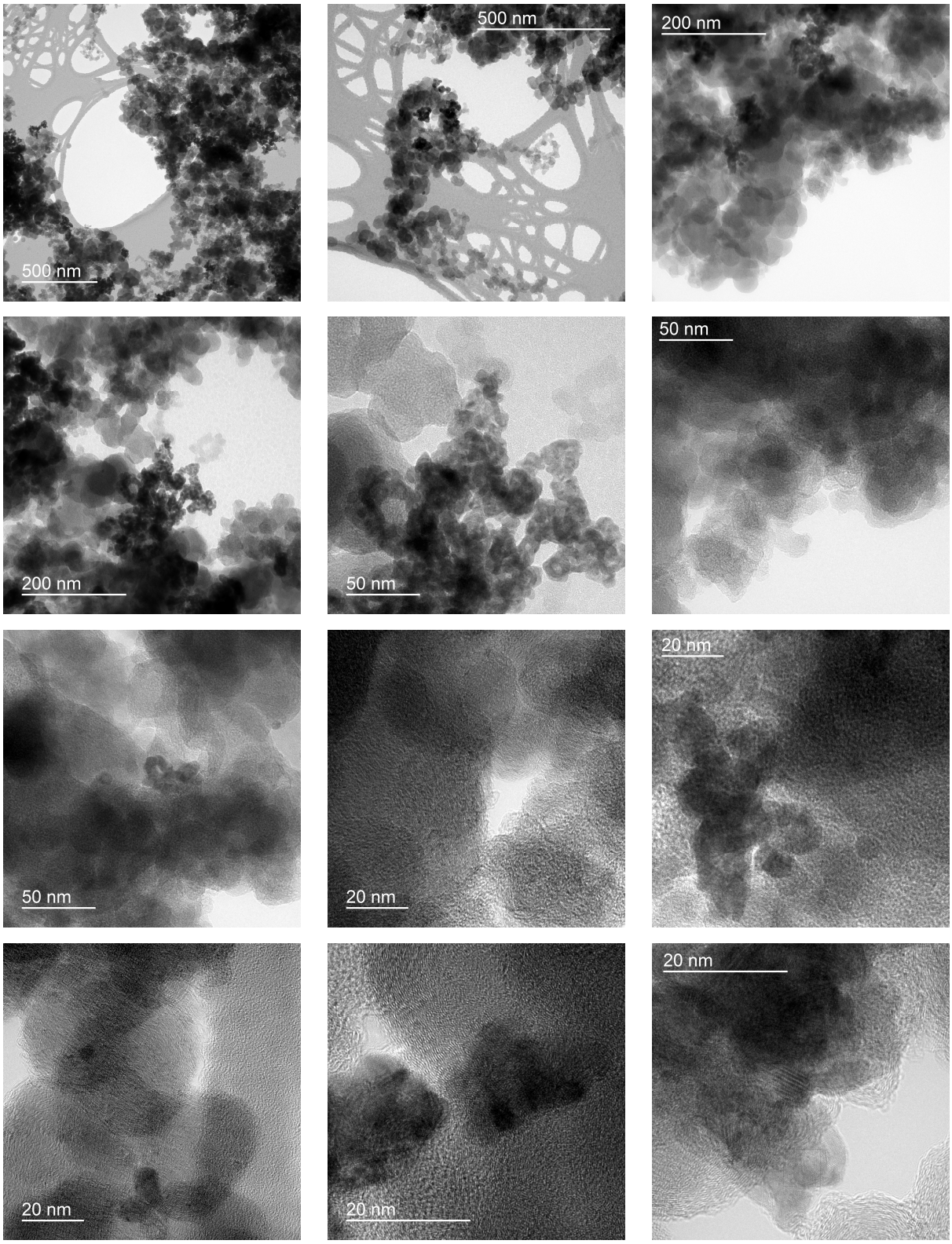


Figure 61: TEM micrographs with low and high magnifications of the $Pd_{70}Ni_{20}Bi_{10}$/C catalyst [15].

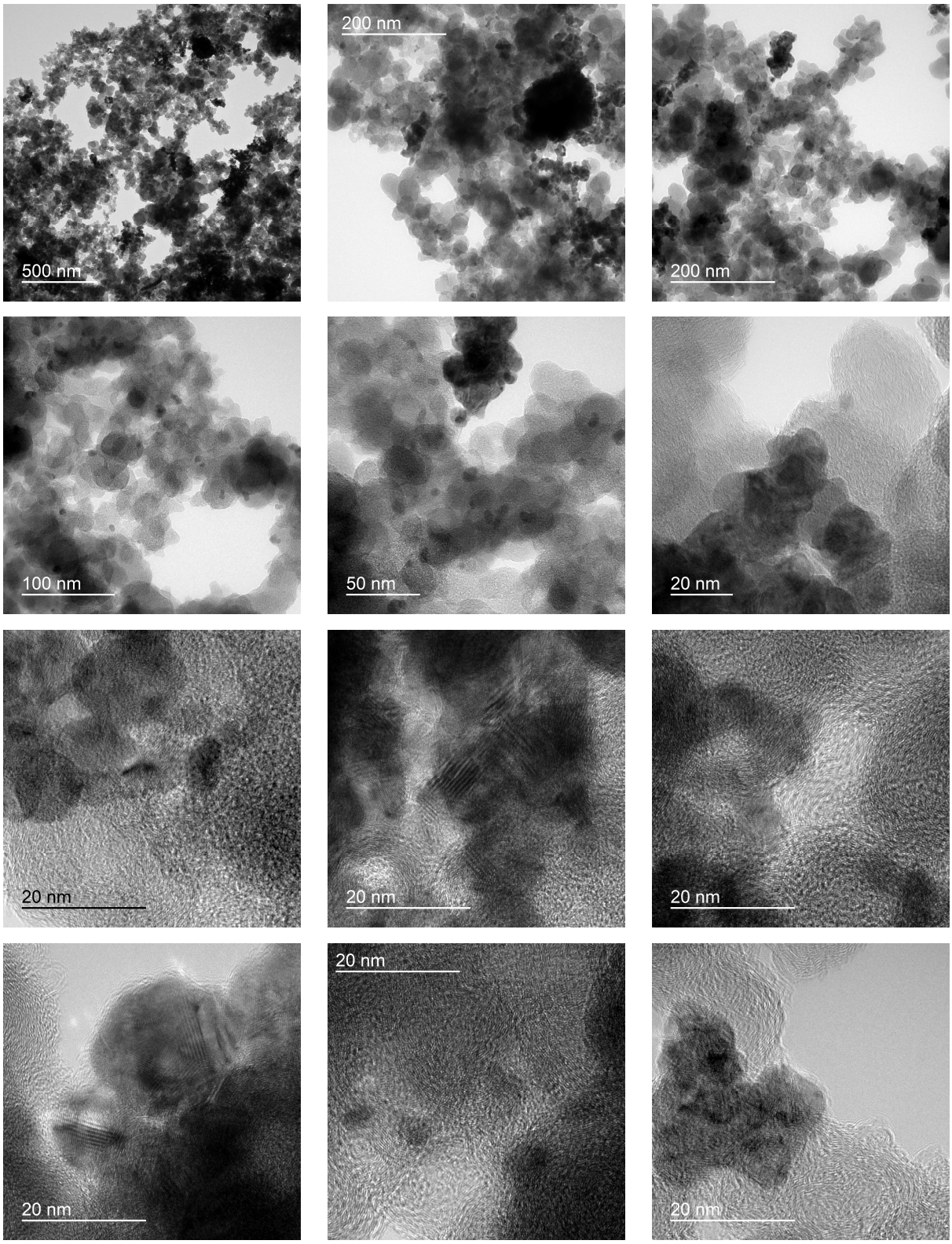


Figure 62: TEM micrographs with low and high magnifications of the $Pd_{80}Ni_{10}Bi_{10}$/C catalyst [15].

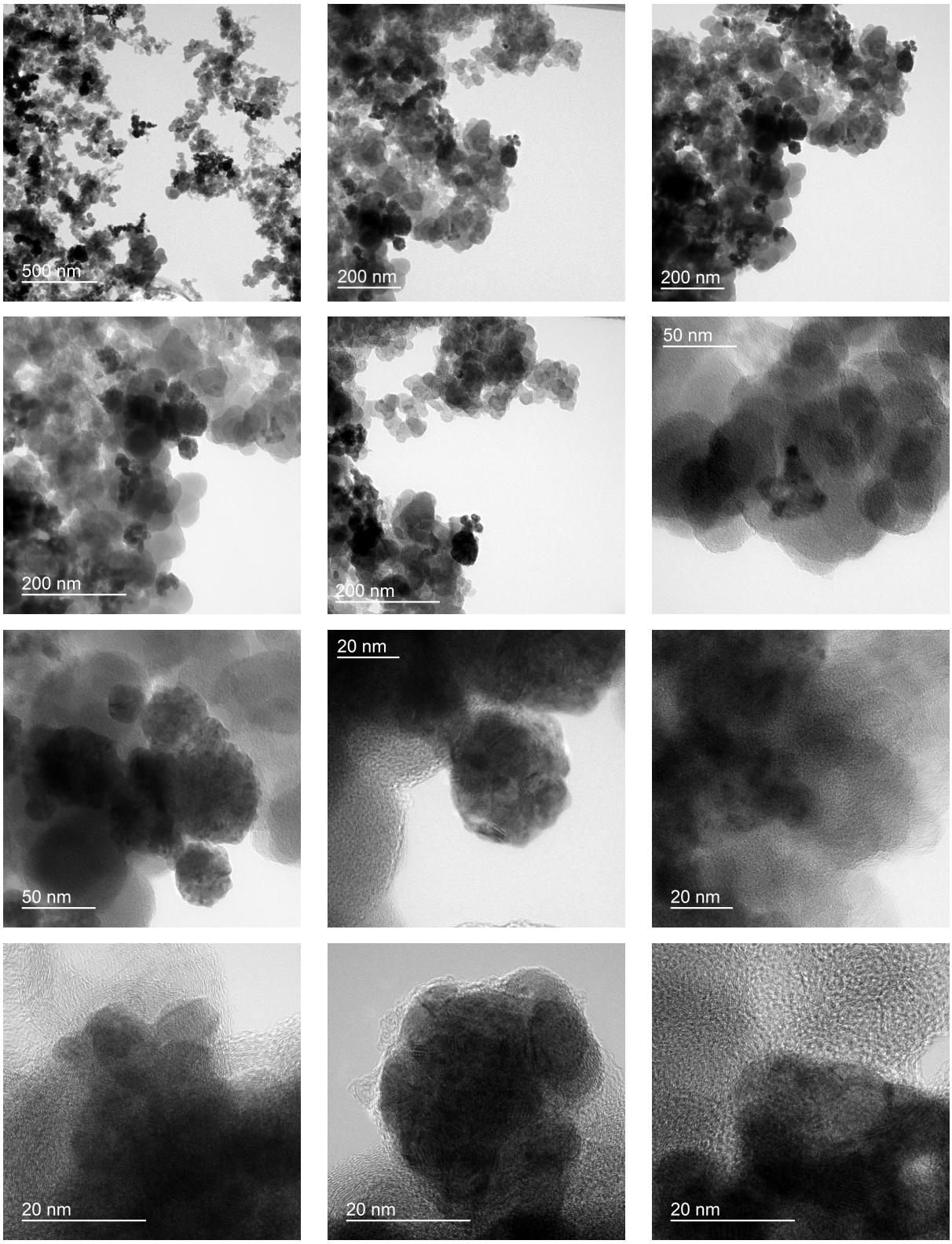


Figure 63: TEM micrographs with low and high magnifications of the $Pd_{40}Ni_{20}Bi_{40}$/C catalyst [15].

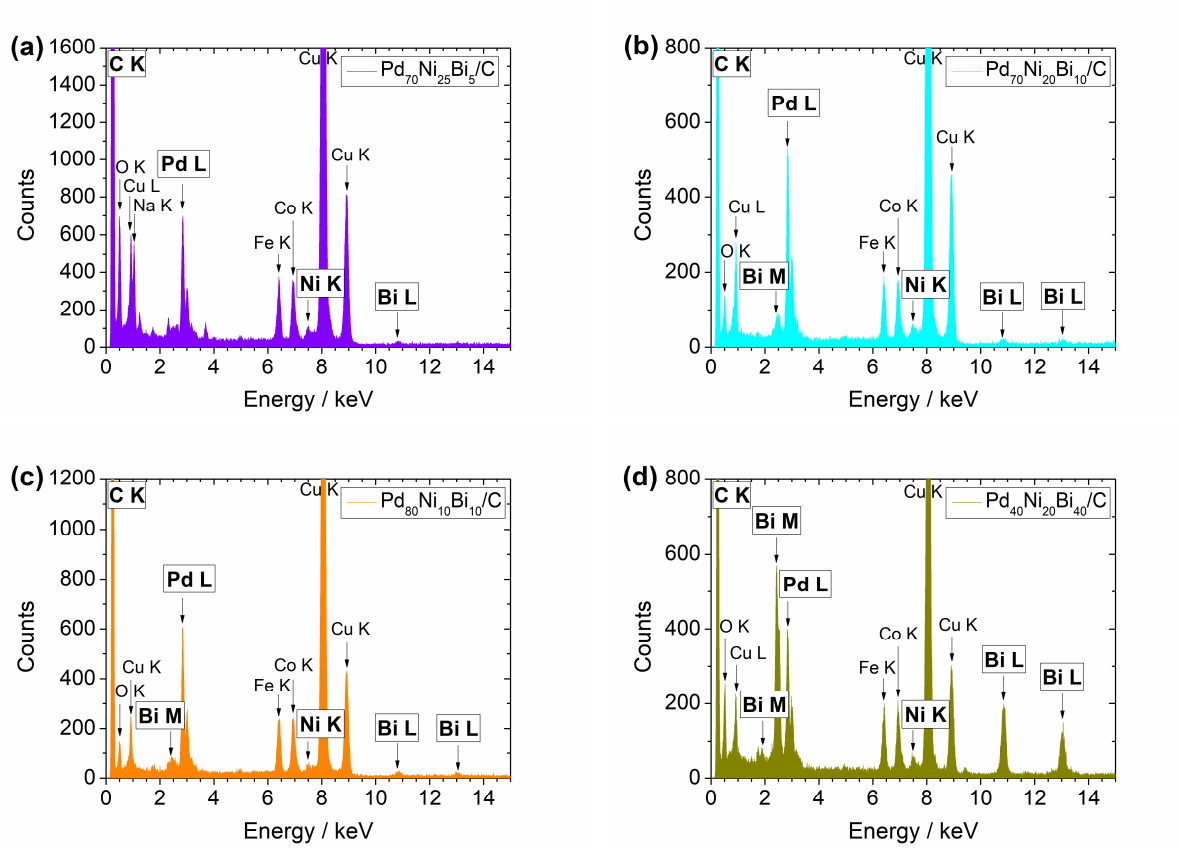


Figure 64: EDX spectra of the **(a)** $Pd_{70}Ni_{25}Bi_5/C$, **(b)** $Pd_{70}Ni_{20}Bi_{10}/C$, **(c)** $Pd_{80}Ni_{10}Bi_{10}/C$ and **(d)** $Pd_{40}Ni_{20}Bi_{40}/C$ catalyst [15].

Table 32: TEM-EDX results of the $Pd_{70}Ni_{25}Bi_5/C$, $Pd_{70}Ni_{20}Bi_{10}/C$, $Pd_{80}Ni_{10}Bi_{10}/C$ and $Pd_{40}Ni_{20}Bi_{40}/C$ catalyst [15].

Catalysts	3 elements	net counts	k-factor (Si)	rel. (wt.%)	wt.% (norm.)	at.%	rel. (at.%)
$Pd_{70}Ni_{25}Bi_5/C$	Pd-L	7429	2.651	1.000	80.26	74.01	1.000
	Ni-K	2237	1.525	0.173	13.90	23.24	0.314
	Bi-L	223	6.425	0.073	5.84	2.74	0.037
$Pd_{70}Ni_{20}Bi_{10}/C$	Pd-L	5834	2.651	1.000	78.21	74.42	1.000
	Ni-K	1570	1.525	0.155	12.11	20.89	0.281
	Bi-L	298	6.425	0.124	9.68	4.69	0.063
$Pd_{80}Ni_{10}Bi_{10}/C$	Pd-L	14490	2.651	1.000	84.98	86.90	1.000
	Ni-K	1173	1.525	0.047	3.96	7.34	0.084
	Bi-L	778	6.425	0.130	11.06	5.76	0.066
$Pd_{40}Ni_{20}Bi_{40}/C$	Pd-L	4642	2.651	1.000	32.16	44.22	1.000
	Ni-K	1161	1.525	0.144	4.63	11.53	0.261
	Bi-L	3764	6.425	1.965	63.21	44.25	1.001

XRD analysis

Table 33: XRD data (Rietveld refinement) of $Pd_{70}Ni_{25}Bi_5/C$ catalyst [15].

Catalyst	Peak No.	Peak Pos. (° 2θ)	*d*-spacing (Å)	Rel. Int. (%)	Height (cts)	h	k	l	Assignment
$Pd_{70}Ni_{25}Bi_5/C$	1	25.13032	3.54079	28.71	1330(747)	0	0	2	Graphite(2H)_187640-ICSD
	2	40.4127	2.23015	100	4632(970)	1	1	1	Pd_64922-ICSD
	3	41.29583	2.18447	0.92	42(13)	0	1	0	Graphite(2H)_187640-ICSD
	4	43.31041	2.08742	4.54	210(116)	0	1	1	Graphite(2H)_187640-ICSD
	5	47.01088	1.93137	43.11	1997(616)	0	0	2	Pd_64922-ICSD
	6	48.95464	1.85913	0.92	42(27)	0	1	2	Graphite(2H)_187640-ICSD
	7	51.58326	1.7704	1.97	91(93)	0	0	4	Graphite(2H)_187640-ICSD
	8	57.42953	1.60329	1.42	66(79)	0	1	3	Graphite(2H)_187640-ICSD
	9	68.11846	1.37541	0.24	11(7)	0	1	4	Graphite(2H)_187640-ICSD
	10	68.67123	1.36568	17.65	817(416)	0	2	2	Pd_64922-ICSD
	11	75.28943	1.26121	1.35	62(71)	1	1	0	Graphite(2H)_187640-ICSD
	12	80.80975	1.18839	0.4	19(16)	0	1	5	Graphite(2H)_187640-ICSD
	13	80.83486	1.18809	2.15	100(85)	1	1	2	Graphite(2H)_187640-ICSD
	14	81.48331	1.18026	0.35	16(12)	0	0	6	Graphite(2H)_187640-ICSD
	15	82.81269	1.16466	15.68	726(371)	1	1	3	Pd_64922-ICSD
	16	87.38765	1.11508	4.22	195(162)	2	2	2	Pd_64922-ICSD
	17	89.69928	1.09224	0.05	2(3)	0	2	0	Graphite(2H)_187640-ICSD
	18	91.05518	1.07947	0.3	14(17)	0	2	1	Graphite(2H)_187640-ICSD
	19	95.12951	1.04371	0.09	4(5)	0	2	2	Graphite(2H)_187640-ICSD
	20	95.77317	1.03839	0.09	4(5)	0	1	6	Graphite(2H)_187640-ICSD
	21	97.16269	1.02721	1.44	67(80)	1	1	4	Graphite(2H)_187640-ICSD

Table 34: XRD data (Rietveld refinement) of $Pd_{70}Ni_{20}Bi_{10}/C$ catalyst [15].

Catalyst	Peak No.	Peak Pos. (° 2θ)	*d*-spacing (Å)	Rel. Int. (%)	Height (cts)	h	k	l	Assignment
$Pd_{70}Ni_{20}Bi_{10}/C$	1	25.08724	3.54678	8.53	663(547)	0	0	2	Graphite(2H)_187640-ICSD
	2	40.09831	2.24691	100	7772(1078)	1	1	1	Pd_64922-ICSD
	3	41.26541	2.18602	0.28	22(8)	0	1	0	Graphite(2H)_187640-ICSD
	4	43.27447	2.08907	1.4	109(70)	0	1	1	Graphite(2H)_187640-ICSD
	5	46.63944	1.94588	41.93	3259(717)	0	0	2	Pd_64922-ICSD
	6	48.90377	1.86095	0.29	22(18)	0	1	2	Graphite(2H)_187640-ICSD
	7	51.48988	1.77339	0.62	48(55)	0	0	4	Graphite(2H)_187640-ICSD
	8	57.35688	1.60515	0.46	35(45)	0	1	3	Graphite(2H)_187640-ICSD

9	68.018	1.3772	0.08	6(3)	0	1	4	Graphite(2H)_187640-ICSD
10	68.08848	1.37594	15.58	1211(524)	0	2	2	Pd_64922-ICSD
11	75.22716	1.2621	0.46	36(40)	1	1	0	Graphite(2H)_187640-ICSD
12	80.67365	1.19006	0.14	11(7)	0	1	5	Graphite(2H)_187640-ICSD
13	80.75534	1.18906	0.75	58(36)	1	1	2	Graphite(2H)_187640-ICSD
14	81.31692	1.18226	0.12	9(5)	0	0	6	Graphite(2H)_187640-ICSD
15	82.06123	1.17341	12.83	997(499)	1	1	3	Pd_64922-ICSD
16	86.57388	1.12345	3.36	261(218)	2	2	2	Pd_64922-ICSD
17	89.61898	1.09301	0.02	1(2)	0	2	0	Graphite(2H)_187640-ICSD
18	90.97031	1.08026	0.11	8(10)	0	2	1	Graphite(2H)_187640-ICSD
19	95.03056	1.04453	0.03	3(3)	0	2	2	Graphite(2H)_187640-ICSD
20	95.58766	1.03992	0.03	3(3)	0	1	6	Graphite(2H)_187640-ICSD
21	97.02831	1.02827	0.53	41(49)	1	1	4	Graphite(2H)_187640-ICSD

Table 35: XRD data (Rietveld refinement) of $Pd_{80}Ni_{10}Bi_{10}$/C catalyst [15].

Catalyst	Peak No.	Peak Pos. (° 2θ)	*d*-spacing (Å)	Rel. Int. (%)	Height (cts)	h	k	l	Assignment
$Pd_{80}Ni_{10}Bi_{10}$/C	1	13.25495	6.67425	0.96	69(32)	0	0	2	Bi2O2(CO3)_252588-ICSD
	2	24.17697	3.67821	0.55	39(7)	1	0	1	Bi2O2(CO3)_252588-ICSD
	3	24.25652	3.66633	0.91	65(11)	0	1	1	Bi2O2(CO3)_252588-ICSD
	4	25.46052	3.49562	11.71	839(573)	0	0	2	Graphite(2H)_187640-ICSD
	5	26.32122	3.38323	0.44	31(5)	0	0	4	Bi2O2(CO3)_252588-ICSD
	6	30.54839	2.92402	2.34	167(39)	1	0	3	Bi2O2(CO3)_252588-ICSD
	7	30.61232	2.91806	1.99	143(32)	0	1	3	Bi2O2(CO3)_252588-ICSD
	8	33.03814	2.70913	1.56	111(31)	1	1	0	Bi2O2(CO3)_252588-ICSD
	9	35.62561	2.51807	0.25	18(5)	1	1	2	Bi2O2(CO3)_252588-ICSD
	10	39.7424	2.26621	0.4	29(1)	0	0	6	Bi2O2(CO3)_252588-ICSD
	11	40.43174	2.22914	100	7170(922)	1	1	1	Pd_64922-ICSD
	12	40.59106	2.22076	0.05	3.9(1)	1	0	5	Bi2O2(CO3)_252588-ICSD
	13	40.64085	2.21816	0.07	5.0(2)	0	1	5	Bi2O2(CO3)_252588-ICSD
	14	41.5366	2.17237	0.39	28(11)	0	1	0	Graphite(2H)_187640-ICSD
	15	42.56164	2.12239	1.01	72(10)	1	1	4	Bi2O2(CO3)_252588-ICSD
	16	43.55157	2.07642	1.93	139(93)	0	1	1	Graphite(2H)_187640-ICSD
	17	46.96881	1.933	43.51	3119(616)	0	0	2	Pd_64922-ICSD
	18	47.1612	1.92556	0.46	33(2)	2	0	0	Bi2O2(CO3)_252588-ICSD
	19	47.33753	1.9188	0.35	25(1)	0	2	0	Bi2O2(CO3)_252588-ICSD
	20	49.11363	1.85348	0.08	6(1)	2	0	2	Bi2O2(CO3)_252588-ICSD
	21	49.19537	1.85059	0.4	28(22)	0	1	2	Graphite(2H)_187640-ICSD
	22	49.28461	1.84745	0.14	10(2)	0	2	2	Bi2O2(CO3)_252588-ICSD

23	51.88349	1.76086	0.85	61(63)	0	0	4	Graphite(2H)_187640-ICSD
24	52.43587	1.7436	0.92	66(15)	1	1	6	Bi2O2(CO3)_252588-ICSD
25	52.62249	1.73785	0.29	21(5)	1	0	7	Bi2O2(CO3)_252588-ICSD
26	52.66317	1.73661	0.27	19(5)	0	1	7	Bi2O2(CO3)_252588-ICSD
27	53.57698	1.70912	0.23	16(4)	2	1	1	Bi2O2(CO3)_252588-ICSD
28	53.69743	1.70557	0.27	19(5)	1	2	1	Bi2O2(CO3)_252588-ICSD
29	53.75508	1.70388	0	0.08(2)	0	0	8	Bi2O2(CO3)_252588-ICSD
30	54.65608	1.6779	0.13	10(3)	2	0	4	Bi2O2(CO3)_252588-ICSD
31	54.81444	1.67343	0.18	13(4)	0	2	4	Bi2O2(CO3)_252588-ICSD
32	57.10829	1.61154	0.69	49(12)	2	1	3	Bi2O2(CO3)_252588-ICSD
33	57.22366	1.60857	0.64	46(11)	1	2	3	Bi2O2(CO3)_252588-ICSD
34	57.6662	1.59727	0.63	45(51)	0	1	3	Graphite(2H)_187640-ICSD
35	63.13887	1.47135	0.21	15(4)	2	0	6	Bi2O2(CO3)_252588-ICSD
36	63.28353	1.46834	0.2	14(4)	0	2	6	Bi2O2(CO3)_252588-ICSD
37	63.7842	1.45801	0.04	3(1)	2	1	5	Bi2O2(CO3)_252588-ICSD
38	63.8921	1.45581	0.04	3(1)	1	2	5	Bi2O2(CO3)_252588-ICSD
39	64.38502	1.44585	0.01	0.5(1)	1	1	8	Bi2O2(CO3)_252588-ICSD
40	66.14438	1.41159	0.18	13(3)	1	0	9	Bi2O2(CO3)_252588-ICSD
41	66.17966	1.41092	0.2	14(3)	0	1	9	Bi2O2(CO3)_252588-ICSD
42	68.34556	1.37139	0.11	8(4)	0	1	4	Graphite(2H)_187640-ICSD
43	68.40282	1.37039	19.51	1399(482)	0	2	2	Pd_64922-ICSD
44	68.69459	1.36528	0.09	6.3(5)	0	0	10	Bi2O2(CO3)_252588-ICSD
45	68.84291	1.3627	0.23	16(1)	2	2	0	Bi2O2(CO3)_252588-ICSD
46	70.38903	1.3365	0.09	6(1)	2	2	2	Bi2O2(CO3)_252588-ICSD
47	73.14403	1.29281	0.21	15(4)	2	1	7	Bi2O2(CO3)_252588-ICSD
48	73.24508	1.29128	0.21	15(4)	1	2	7	Bi2O2(CO3)_252588-ICSD
49	73.87057	1.28188	0.03	2(1)	3	0	1	Bi2O2(CO3)_252588-ICSD
50	74.05298	1.27918	0	0.05(1)	2	0	8	Bi2O2(CO3)_252588-ICSD
51	74.17239	1.27741	0.04	3(1)	0	3	1	Bi2O2(CO3)_252588-ICSD
52	74.18706	1.27719	0	0.036(9)	0	2	8	Bi2O2(CO3)_252588-ICSD
53	74.94312	1.26617	0.14	10(2)	2	2	4	Bi2O2(CO3)_252588-ICSD
54	75.40984	1.25949	0.63	45(45)	1	1	0	Graphite(2H)_187640-ICSD
55	76.8645	1.23924	0.16	12(3)	3	0	3	Bi2O2(CO3)_252588-ICSD
56	77.16218	1.2352	0.16	11(3)	0	3	3	Bi2O2(CO3)_252588-ICSD
57	78.18684	1.22156	0.18	13(3)	1	1	10	Bi2O2(CO3)_252588-ICSD
58	78.19623	1.22144	0.14	10(2)	3	1	0	Bi2O2(CO3)_252588-ICSD
59	78.45947	1.218	0.15	11(2)	1	3	0	Bi2O2(CO3)_252588-ICSD
60	79.67136	1.20249	0.03	2.2(4)	3	1	2	Bi2O2(CO3)_252588-ICSD
61	79.93325	1.19921	0.02	1.6(3)	1	3	2	Bi2O2(CO3)_252588-ICSD
62	80.94906	1.1867	1.03	74(38)	1	1	2	Graphite(2H)_187640-ICSD

63	81.01976	1.18584	0.19	14(7)	0	1	5	Graphite(2H)_187640-ICSD
64	81.27936	1.18271	0	0.058(5)	1	0	11	Bi2O2(CO3)_252588-ICSD
65	81.31194	1.18232	0	0.19(2)	0	1	11	Bi2O2(CO3)_252588-ICSD
66	81.74003	1.17721	0.17	12(5)	0	0	6	Graphite(2H)_187640-ICSD
67	82.3315	1.17024	0.2	14(1)	2	2	6	Bi2O2(CO3)_252588-ICSD
68	82.36362	1.16987	18.94	1358(497)	1	1	3	Pd_64922-ICSD
69	82.75001	1.16538	0.01	0.50(4)	3	0	5	Bi2O2(CO3)_252588-ICSD
70	83.04212	1.16202	0.01	0.53(4)	0	3	5	Bi2O2(CO3)_252588-ICSD
71	84.05813	1.15055	0.13	10(1)	3	1	4	Bi2O2(CO3)_252588-ICSD
72	84.31708	1.14767	0.12	9(1)	1	3	4	Bi2O2(CO3)_252588-ICSD
73	84.96076	1.14061	0.2	14(2)	2	1	9	Bi2O2(CO3)_252588-ICSD
74	85.05773	1.13956	0.21	15(2)	1	2	9	Bi2O2(CO3)_252588-ICSD
75	85.10419	1.13906	0.04	2.7(4)	0	0	12	Bi2O2(CO3)_252588-ICSD
76	86.87186	1.12036	5.25	376(239)	2	2	2	Pd_64922-ICSD
77	87.28347	1.11614	0.09	7(1)	2	0	10	Bi2O2(CO3)_252588-ICSD
78	87.41238	1.11482	0.08	6(1)	0	2	10	Bi2O2(CO3)_252588-ICSD
79	89.75165	1.09174	0.03	2(2)	0	2	0	Graphite(2H)_187640-ICSD
80	91.10481	1.07901	0.15	11(11)	0	2	1	Graphite(2H)_187640-ICSD
81	91.30021	1.07721	0.2	14(3)	3	1	6	Bi2O2(CO3)_252588-ICSD
82	91.44763	1.07586	0.06	5(1)	3	0	7	Bi2O2(CO3)_252588-ICSD
83	91.55772	1.07486	0.21	15(3)	1	3	6	Bi2O2(CO3)_252588-ICSD
84	91.73734	1.07322	0.06	5(1)	0	3	7	Bi2O2(CO3)_252588-ICSD
85	92.3042	1.06811	0.06	4(1)	3	2	1	Bi2O2(CO3)_252588-ICSD
86	92.46522	1.06667	0.05	3(1)	2	3	1	Bi2O2(CO3)_252588-ICSD
87	92.47932	1.06654	0	0.034(8)	2	2	8	Bi2O2(CO3)_252588-ICSD
88	94.18558	1.05166	0.12	9(2)	1	1	12	Bi2O2(CO3)_252588-ICSD
89	95.16981	1.04337	0.05	3(4)	0	2	2	Graphite(2H)_187640-ICSD
90	95.20135	1.04311	0.18	13(3)	3	2	3	Bi2O2(CO3)_252588-ICSD
91	95.36286	1.04177	0.2	15(4)	2	3	3	Bi2O2(CO3)_252588-ICSD
92	95.95427	1.03691	0.05	3(4)	0	1	6	Graphite(2H)_187640-ICSD
93	97.24531	1.02656	0.73	52(56)	1	1	4	Graphite(2H)_187640-ICSD
94	98.69719	1.01531	0.09	7(2)	1	0	13	Bi2O2(CO3)_252588-ICSD
95	98.72971	1.01506	0.08	6(1)	0	1	13	Bi2O2(CO3)_252588-ICSD
96	99.4658	1.00951	0	0.26(7)	2	1	11	Bi2O2(CO3)_252588-ICSD
97	99.5636	1.00878	0.01	0.36(9)	1	2	11	Bi2O2(CO3)_252588-ICSD

Table 36: XRD data (Rietveld refinement) of $Pd_{40}Ni_{20}Bi_{40}$/C catalyst [15].

Catalyst	Peak No.	Peak Pos. (° 2θ)	*d*-spacing (Å)	Rel. Int. (%)	Height (cts)	h	k	l	Assignment
$Pd_{40}Ni_{20}Bi_{40}$/C	1	12.77746	6.92258	4.36	207(145)	0	0	2	Bi2O2(CO3)_252588-ICSD
	2	16.37355	5.40938	4.95	235(18)	1	1	0	Bi2O3_beta_189995-ICSD
	3	19.69843	4.5032	0.03	1.3(1)	0	1	1	Bi2O3_beta_189995-ICSD
	4	23.223	3.82711	0.04	2(1)	0	2	0	Bi2O3_beta_189995-ICSD
	5	23.90992	3.71869	3.16	150(74)	0	1	1	Bi2O2(CO3)_252588-ICSD
	6	24.32887	3.65559	1.8	85(38)	1	0	1	Bi2O2(CO3)_252588-ICSD
	7	25.68614	3.46542	1.5	71(23)	0	0	4	Bi2O2(CO3)_252588-ICSD
	8	26.00577	3.42355	0.56	27(4)	1	2	0	Bi2O3_beta_189995-ICSD
	9	26.18939	3.39996	16.84	798(537)	0	0	2	Graphite(2H)_187640-ICSD
	10	28.26146	3.15522	19.9	950(143)	0	2	1	Bi2O3_beta_189995-ICSD
	11	30.13583	2.9631	6.03	285(122)	0	1	3	Bi2O2(CO3)_252588-ICSD
	12	30.47501	2.93089	6.78	321(136)	1	0	3	Bi2O2(CO3)_252588-ICSD
	13	30.619	2.91744	0.33	16(3)	1	2	1	Bi2O3_beta_189995-ICSD
	14	32.09553	2.78651	2.39	113(39)	0	0	2	Bi2O3_beta_189995-ICSD
	15	33.06192	2.70724	3.95	185(50)	2	2	0	Bi2O3_beta_189995-ICSD
	16	33.08668	2.70527	4.21	200(108)	1	1	0	Bi2O2(CO3)_252588-ICSD
	17	34.21402	2.61866	0.01	0.4(2)	0	1	2	Bi2O3_beta_189995-ICSD
	18	35.59231	2.52035	0.64	30(20)	1	1	2	Bi2O2(CO3)_252588-ICSD
	19	36.22293	2.47791	0.02	1.0(4)	1	1	2	Bi2O3_beta_189995-ICSD
	20	37.09437	2.42167	0.01	0.3(1)	1	3	0	Bi2O3_beta_189995-ICSD
	21	38.76728	2.32093	0.05	2.4(3)	0	3	1	Bi2O3_beta_189995-ICSD
	22	38.93669	2.31123	1.02	48(10)	0	0	6	Bi2O2(CO3)_252588-ICSD
	23	39.97822	2.25338	0.01	0.31(2)	0	2	2	Bi2O3_beta_189995-ICSD
	24	39.98855	2.25282	0.17	8(1)	0	1	5	Bi2O2(CO3)_252588-ICSD
	25	40.06665	2.24861	100	4736(888)	1	1	1	Pd_64922-ICSD
	26	40.25408	2.23857	0.13	6(1)	1	0	5	Bi2O2(CO3)_252588-ICSD
	27	40.58173	2.22125	0.03	1.3(1)	1	3	1	Bi2O3_beta_189995-ICSD
	28	40.87297	2.20609	0.66	31(11)	0	1	0	Graphite(2H)_187640-ICSD
	29	41.74871	2.16182	0.18	9(1)	1	2	2	Bi2O3_beta_189995-ICSD
	30	42.33773	2.1331	2.28	108(39)	1	1	4	Bi2O2(CO3)_252588-ICSD
	31	42.52412	2.12418	0.05	2(1)	2	3	0	Bi2O3_beta_189995-ICSD
	32	43.06831	2.09859	3.21	152(99)	0	1	1	Graphite(2H)_187640-ICSD
	33	45.66658	1.98505	0.11	5(1)	2	3	1	Bi2O3_beta_189995-ICSD
	34	46.5966	1.94757	41.11	1947(577)	0	0	2	Pd_64922-ICSD
	35	46.73076	1.94229	2.4	111(13)	2	2	2	Bi2O3_beta_189995-ICSD
	36	47.0117	1.93134	0.73	35(8)	0	2	0	Bi2O2(CO3)_252588-ICSD

37	47.44102	1.91485	1.08	50(8)	0	4	0	Bi2O3_beta_189995-ICSD
38	47.94025	1.89607	0.88	41(15)	2	0	0	Bi2O2(CO3)_252588-ICSD
39	48.30127	1.88274	0	0.025(7)	0	3	2	Bi2O3_beta_189995-ICSD
40	48.91412	1.86058	0.28	13(8)	0	2	2	Bi2O2(CO3)_252588-ICSD
41	48.99422	1.85772	0.09	4(2)	1	4	0	Bi2O3_beta_189995-ICSD
42	49.18037	1.85112	0.63	30(27)	0	1	2	Graphite(2H)_187640-ICSD
43	49.81586	1.82899	0.14	7(5)	2	0	2	Bi2O2(CO3)_252588-ICSD
44	49.83429	1.82835	0.01	0.5(2)	1	3	2	Bi2O3_beta_189995-ICSD
45	50.34288	1.81107	0	0.16(8)	0	4	1	Bi2O3_beta_189995-ICSD
46	50.49575	1.80594	0.02	1(1)	0	1	3	Bi2O3_beta_189995-ICSD
47	50.51158	1.80542	0.01	0.3(2)	3	3	0	Bi2O3_beta_189995-ICSD
48	51.81438	1.76304	0.53	25(18)	0	1	7	Bi2O2(CO3)_252588-ICSD
49	51.83129	1.76251	0.2	9(4)	1	4	1	Bi2O3_beta_189995-ICSD
50	51.98346	1.7577	1.75	83(59)	1	1	6	Bi2O2(CO3)_252588-ICSD
51	52.0317	1.75619	0.55	26(18)	1	0	7	Bi2O2(CO3)_252588-ICSD
52	52.75542	1.73379	0	0.10(7)	0	0	8	Bi2O2(CO3)_252588-ICSD
53	53.4519	1.71283	0	0.2(1)	2	4	0	Bi2O3_beta_189995-ICSD
54	53.61401	1.70803	0.48	23(17)	1	2	1	Bi2O2(CO3)_252588-ICSD
55	53.85277	1.70102	1.17	56(58)	0	0	4	Graphite(2H)_187640-ICSD
56	54.24197	1.68973	0.05	2(1)	2	3	2	Bi2O3_beta_189995-ICSD
57	54.2489	1.68953	0.39	18(14)	2	1	1	Bi2O2(CO3)_252588-ICSD
58	54.32297	1.6874	0.32	15(12)	0	2	4	Bi2O2(CO3)_252588-ICSD
59	54.86541	1.672	1.08	50(25)	0	2	3	Bi2O3_beta_189995-ICSD
60	55.16094	1.66373	0.23	11(8)	2	0	4	Bi2O2(CO3)_252588-ICSD
61	56.1277	1.63735	1.78	82(41)	2	4	1	Bi2O3_beta_189995-ICSD
62	56.26947	1.63356	0.07	3(2)	1	2	3	Bi2O3_beta_189995-ICSD
63	57.04988	1.61305	1.08	51(40)	1	2	3	Bi2O2(CO3)_252588-ICSD
64	57.65933	1.59744	1.12	53(41)	2	1	3	Bi2O2(CO3)_252588-ICSD
65	58.29171	1.58161	0.97	46(49)	0	1	3	Graphite(2H)_187640-ICSD
66	58.41721	1.57851	0.72	33(17)	0	4	2	Bi2O3_beta_189995-ICSD
67	59.76687	1.54605	0.09	4(2)	1	4	2	Bi2O3_beta_189995-ICSD
68	60.367	1.53211	0.05	2(1)	3	4	0	Bi2O3_beta_189995-ICSD
69	61.09822	1.51551	0	0.2(1)	3	3	2	Bi2O3_beta_189995-ICSD
70	61.67673	1.50268	0	0.14(9)	0	3	3	Bi2O3_beta_189995-ICSD
71	61.6906	1.50237	0.01	0.3(2)	1	5	0	Bi2O3_beta_189995-ICSD
72	62.61695	1.48235	0.31	15(14)	0	2	6	Bi2O2(CO3)_252588-ICSD
73	62.85189	1.47738	0	0.05(3)	0	5	1	Bi2O3_beta_189995-ICSD
74	62.85189	1.47738	0.06	3(2)	3	4	1	Bi2O3_beta_189995-ICSD
75	62.98419	1.47459	0.01	0.4(3)	1	3	3	Bi2O3_beta_189995-ICSD
76	63.38482	1.46623	0.32	15(14)	2	0	6	Bi2O2(CO3)_252588-ICSD

77	63.55822	1.46265	0.06	3(3)	1	2	5	Bi2O2(CO3)_252588-ICSD
78	63.68552	1.46003	0.01	0.5(4)	1	1	8	Bi2O2(CO3)_252588-ICSD
79	63.71156	1.4595	0	0.09(6)	2	4	2	Bi2O3_beta_189995-ICSD
80	64.1299	1.45098	0.05	2(2)	2	1	5	Bi2O2(CO3)_252588-ICSD
81	64.14578	1.45066	0.01	0.3(2)	1	5	1	Bi2O3_beta_189995-ICSD
82	65.10444	1.4316	0.3	14(13)	0	1	9	Bi2O2(CO3)_252588-ICSD
83	65.29285	1.42793	0.28	13(11)	1	0	9	Bi2O2(CO3)_252588-ICSD
84	65.56853	1.42259	0.01	0.5(3)	2	5	0	Bi2O3_beta_189995-ICSD
85	66.82074	1.39894	0.02	0.9(4)	2	3	3	Bi2O3_beta_189995-ICSD
86	67.09003	1.39397	0.11	5(2)	0	0	4	Bi2O3_beta_189995-ICSD
87	67.4604	1.38722	0.13	6(3)	0	0	10	Bi2O2(CO3)_252588-ICSD
88	67.94747	1.37846	0.01	0.4(1)	2	5	1	Bi2O3_beta_189995-ICSD
89	68.00432	1.37744	14.01	664(385)	0	2	2	Pd_64922-ICSD
90	68.34137	1.37147	0.01	0.5(1)	0	1	4	Bi2O3_beta_189995-ICSD
91	69.33035	1.3543	0.17	8(3)	4	4	0	Bi2O3_beta_189995-ICSD
92	69.38809	1.35332	0.3	14(9)	2	2	0	Bi2O2(CO3)_252588-ICSD
93	69.58193	1.35002	0	0.0022(9)	1	1	4	Bi2O3_beta_189995-ICSD
94	69.7389	1.34736	0.17	8(6)	0	1	4	Graphite(2H)_187640-ICSD
95	70.01054	1.3428	0	0.02(1)	0	5	2	Bi2O3_beta_189995-ICSD
96	70.01054	1.3428	0.05	3(1)	3	4	2	Bi2O3_beta_189995-ICSD
97	70.54997	1.33385	0	0.05(3)	0	4	3	Bi2O3_beta_189995-ICSD
98	70.88995	1.32828	0.12	6(5)	2	2	2	Bi2O2(CO3)_252588-ICSD
99	71.2379	1.32265	0.01	0.4(2)	1	5	2	Bi2O3_beta_189995-ICSD
100	71.77335	1.31409	0.04	2(1)	1	4	3	Bi2O3_beta_189995-ICSD
101	71.78621	1.31389	0	0.2(1)	3	5	0	Bi2O3_beta_189995-ICSD
102	72.03403	1.30998	0	0.08(5)	0	2	4	Bi2O3_beta_189995-ICSD
103	72.70026	1.2996	0.27	13(12)	1	2	7	Bi2O2(CO3)_252588-ICSD
104	73.23688	1.2914	0.26	12(12)	2	1	7	Bi2O2(CO3)_252588-ICSD
105	73.2471	1.29125	0.02	1(1)	1	2	4	Bi2O3_beta_189995-ICSD
106	73.29966	1.29045	0	0.03(3)	0	2	8	Bi2O2(CO3)_252588-ICSD
107	73.8378	1.28237	0.05	2(2)	0	3	1	Bi2O2(CO3)_252588-ICSD
108	74.01257	1.27977	0	0.04(4)	2	0	8	Bi2O2(CO3)_252588-ICSD
109	74.07268	1.27888	0.01	0.3(2)	3	5	1	Bi2O3_beta_189995-ICSD
110	74.20782	1.27689	0	0.02(1)	0	6	0	Bi2O3_beta_189995-ICSD
111	74.3946	1.27414	1.07	51(54)	1	1	0	Graphite(2H)_187640-ICSD
112	74.86955	1.26724	0.01	0.5(3)	2	5	2	Bi2O3_beta_189995-ICSD
113	75.31951	1.26078	0.17	8(8)	2	2	4	Bi2O2(CO3)_252588-ICSD
114	75.39492	1.2597	0.45	21(13)	2	4	3	Bi2O3_beta_189995-ICSD
115	75.40754	1.25952	0.03	2(1)	1	6	0	Bi2O3_beta_189995-ICSD
116	75.43412	1.25915	0.04	2(2)	3	0	1	Bi2O2(CO3)_252588-ICSD

117	76.46708	1.24469	0.19	9(6)	0	6	1	Bi2O3_beta_189995-ICSD
118	76.75855	1.24069	0.19	9(9)	0	3	3	Bi2O2(CO3)_252588-ICSD
119	76.84277	1.23954	0.22	10(7)	2	2	4	Bi2O3_beta_189995-ICSD
120	77.20716	1.2346	0.22	10(10)	1	1	10	Bi2O2(CO3)_252588-ICSD
121	77.65501	1.22859	0.05	2(2)	1	6	1	Bi2O3_beta_189995-ICSD
122	78.02894	1.22364	0	0.2(1)	0	3	4	Bi2O3_beta_189995-ICSD
123	78.33485	1.21962	0.18	9(8)	3	0	3	Bi2O2(CO3)_252588-ICSD
124	78.3412	1.21954	0.18	8(8)	1	3	0	Bi2O2(CO3)_252588-ICSD
125	78.43978	1.21825	0.17	8(5)	4	4	2	Bi2O3_beta_189995-ICSD
126	78.97002	1.2114	0.16	7(4)	2	6	0	Bi2O3_beta_189995-ICSD
127	79.20991	1.20833	0	0.11(7)	1	3	4	Bi2O3_beta_189995-ICSD
128	79.73479	1.20169	0.15	7(6)	3	1	0	Bi2O2(CO3)_252588-ICSD
129	79.77974	1.20113	0.03	1(1)	1	3	2	Bi2O2(CO3)_252588-ICSD
130	79.95351	1.19895	0	0.1(1)	0	1	11	Bi2O2(CO3)_252588-ICSD
131	80.12714	1.19679	0	0.05(3)	1	0	11	Bi2O2(CO3)_252588-ICSD
132	80.14726	1.19654	0.01	0.3(2)	4	5	0	Bi2O3_beta_189995-ICSD
133	80.41155	1.19327	1.7	81(62)	1	1	2	Graphite(2H)_187640-ICSD
134	80.79393	1.18859	0	0.009(4)	3	5	2	Bi2O3_beta_189995-ICSD
135	81.16701	1.18406	0.03	2(1)	3	1	2	Bi2O2(CO3)_252588-ICSD
136	81.18878	1.1838	0	0.17(7)	2	6	1	Bi2O3_beta_189995-ICSD
137	81.30794	1.18237	0	0.08(3)	0	5	3	Bi2O3_beta_189995-ICSD
138	81.30794	1.18237	0.02	0.8(3)	3	4	3	Bi2O3_beta_189995-ICSD
139	81.94421	1.17479	10.78	511(335)	1	1	3	Pd_64922-ICSD
140	82.35853	1.16993	0.03	1.2(5)	4	5	1	Bi2O3_beta_189995-ICSD
141	82.47734	1.16854	0	0.09(3)	1	5	3	Bi2O3_beta_189995-ICSD
142	82.50413	1.16823	0.01	0.4(2)	0	3	5	Bi2O2(CO3)_252588-ICSD
143	82.52016	1.16804	0.21	10(6)	2	2	6	Bi2O2(CO3)_252588-ICSD
144	82.72718	1.16564	0.01	0.5(2)	2	3	4	Bi2O3_beta_189995-ICSD
145	83.13245	1.16099	0	0.13(6)	0	6	2	Bi2O3_beta_189995-ICSD
146	83.34992	1.15851	0.29	14(10)	0	1	5	Graphite(2H)_187640-ICSD
147	83.56016	1.15613	0.04	2(1)	0	0	12	Bi2O2(CO3)_252588-ICSD
148	84.05391	1.15059	0.01	0.3(3)	3	0	5	Bi2O2(CO3)_252588-ICSD
149	84.06017	1.15052	0.13	6(5)	1	3	4	Bi2O2(CO3)_252588-ICSD
150	84.2512	1.1484	0.23	11(8)	1	2	9	Bi2O2(CO3)_252588-ICSD
151	84.29714	1.14789	0.05	2(1)	1	6	2	Bi2O3_beta_189995-ICSD
152	84.76658	1.14273	0.21	10(8)	2	1	9	Bi2O2(CO3)_252588-ICSD
153	84.81945	1.14215	0.02	0.7(4)	3	6	0	Bi2O3_beta_189995-ICSD
154	85.43403	1.1355	0.13	6(5)	3	1	4	Bi2O2(CO3)_252588-ICSD
155	85.54824	1.13428	0.24	12(10)	0	0	6	Graphite(2H)_187640-ICSD
156	85.96862	1.12981	0.01	0.4(2)	2	5	3	Bi2O3_beta_189995-ICSD

157	86.21694	1.12719	0.13	6(3)	0	4	4	Bi2O3_beta_189995-ICSD
158	86.24355	1.12691	0.08	4(3)	0	2	10	Bi2O2(CO3)_252588-ICSD
159	86.44475	1.1248	2.75	130(124)	2	2	2	Pd_64922-ICSD
160	86.92879	1.11978	0.1	5(4)	2	0	10	Bi2O2(CO3)_252588-ICSD
161	87.01046	1.11894	0.04	2(1)	3	6	1	Bi2O3_beta_189995-ICSD
162	87.37643	1.11519	0.02	1(1)	1	4	4	Bi2O3_beta_189995-ICSD
163	87.77895	1.11111	0.2	9(6)	2	6	2	Bi2O3_beta_189995-ICSD
164	88.52258	1.10369	0	0.2(1)	0	1	5	Bi2O3_beta_189995-ICSD
165	88.53481	1.10357	0	0.2(1)	3	3	4	Bi2O3_beta_189995-ICSD
166	88.53899	1.10353	0.04	2(2)	0	2	0	Graphite(2H)_187640-ICSD
167	88.93707	1.09961	0.01	0.6(4)	4	5	2	Bi2O3_beta_189995-ICSD
168	90.00634	1.08931	0.25	12(13)	0	2	1	Graphite(2H)_187640-ICSD
169	90.61468	1.08357	0	0.02(1)	1	7	0	Bi2O3_beta_189995-ICSD
170	90.61468	1.08357	0	0.03(2)	5	5	0	Bi2O3_beta_189995-ICSD
171	90.85023	1.08137	0	0.006(4)	2	4	4	Bi2O3_beta_189995-ICSD
172	90.99908	1.07999	0.06	3(3)	0	3	7	Bi2O2(CO3)_252588-ICSD
173	91.13209	1.07876	0.2	9(11)	1	3	6	Bi2O2(CO3)_252588-ICSD
174	91.6425	1.07408	0	0.02(1)	0	7	1	Bi2O3_beta_189995-ICSD
175	91.76032	1.07301	0.01	0.2(2)	3	5	3	Bi2O3_beta_189995-ICSD
176	91.99596	1.07088	0.11	5(4)	0	2	5	Bi2O3_beta_189995-ICSD
177	92.42784	1.067	0	0.02(2)	2	2	8	Bi2O2(CO3)_252588-ICSD
178	92.50079	1.06635	0.18	9(10)	3	1	6	Bi2O2(CO3)_252588-ICSD
179	92.53883	1.06601	0.06	3(3)	3	0	7	Bi2O2(CO3)_252588-ICSD
180	92.80098	1.06369	0	0.1(1)	1	7	1	Bi2O3_beta_189995-ICSD
181	92.84941	1.06326	0.11	5(6)	1	1	12	Bi2O2(CO3)_252588-ICSD
182	92.93112	1.06254	0	0.004(3)	4	6	0	Bi2O3_beta_189995-ICSD
183	92.94448	1.06242	0.04	2(2)	2	3	1	Bi2O2(CO3)_252588-ICSD
184	93.15475	1.06057	0.01	0.4(3)	1	2	5	Bi2O3_beta_189995-ICSD
185	93.56982	1.05696	0.02	1(1)	3	6	2	Bi2O3_beta_189995-ICSD
186	93.80094	1.05496	0.06	3(3)	3	2	1	Bi2O2(CO3)_252588-ICSD
187	94.07864	1.05258	0.08	4(3)	0	6	3	Bi2O3_beta_189995-ICSD
188	94.09089	1.05247	0	0.05(4)	2	7	0	Bi2O3_beta_189995-ICSD
189	94.41217	1.04974	0.08	4(4)	0	2	2	Graphite(2H)_187640-ICSD
190	95.12183	1.04377	0.14	7(5)	4	6	1	Bi2O3_beta_189995-ICSD
191	95.24006	1.04279	0.03	1(1)	1	6	3	Bi2O3_beta_189995-ICSD
192	95.77728	1.03836	0.18	8(10)	2	3	3	Bi2O2(CO3)_252588-ICSD
193	96.28514	1.03423	0	0.2(2)	2	7	1	Bi2O3_beta_189995-ICSD
194	96.63727	1.03139	0.15	7(9)	3	2	3	Bi2O2(CO3)_252588-ICSD
195	96.65298	1.03127	0	0.10(8)	0	5	4	Bi2O3_beta_189995-ICSD
196	96.65298	1.03127	0.01	1(1)	3	4	4	Bi2O3_beta_189995-ICSD

197	96.96886	1.02874	0.07	3(4)	0	1	13	Bi2O2(CO3)_252588-ICSD
198	97.14116	1.02738	0.08	4(5)	1	0	13	Bi2O2(CO3)_252588-ICSD
199	97.80749	1.02215	0	0.2(1)	0	3	5	Bi2O3_beta_189995-ICSD
200	97.81982	1.02205	0	0.2(1)	1	5	4	Bi2O3_beta_189995-ICSD
201	98.0894	1.01996	1.18	56(68)	1	1	4	Graphite(2H)_187640-ICSD
202	98.22592	1.01891	0	0.0003(2)	0	7	2	Bi2O3_beta_189995-ICSD
203	98.41299	1.01748	0	0.2(3)	1	2	11	Bi2O2(CO3)_252588-ICSD
204	98.73921	1.01499	0	0.06(6)	2	6	3	Bi2O3_beta_189995-ICSD
205	98.93188	1.01352	0	0.1(2)	2	1	11	Bi2O2(CO3)_252588-ICSD
206	98.97756	1.01318	0	0.1(1)	1	3	5	Bi2O3_beta_189995-ICSD
207	99.39728	1.01003	0	0.1(1)	1	7	2	Bi2O3_beta_189995-ICSD
208	99.39729	1.01003	0	0.1(1)	5	5	2	Bi2O3_beta_189995-ICSD
209	99.54775	1.0089	0.07	3(5)	0	1	6	Graphite(2H)_187640-ICSD
210	99.91225	1.0062	0.01	1(1)	4	5	3	Bi2O3_beta_189995-ICSD
211	99.92464	1.00611	0	0.06(7)	3	7	0	Bi2O3_beta_189995-ICSD

XPS analysis

Effects of the Pd, Ni and Bi species/ions on the catalytic properties and surface structures

The electronic charge transfer in the ternary $Pd_xNi_yBi_z$/C catalysts occurs according to the order of the ionization energy of the elements (Pd (8.34 eV) > Ni (7.64 eV) > Bi (7.29 eV)) from Bi to Pd, Ni to Pd and Bi to Ni to Pd [159]. This charge distribution causes additional positive charge on Bi and Ni atoms facilitating the formation of the Bi and Ni oxides and hydroxides (Table 37). The Pd active sites with δ^- charges enable the easy access of the EtOH molecule for EtOH oxidation [15,159].

The optimal surface concentrations of Ni and Bi oxide species (NiO, $Ni(OH)_2$, Bi_2O_3 and $Bi(OH)_3$) (Table 37) promote the onset potential of EtOH oxidation for $Pd_{70}Ni_{20}Bi_{10}$/C, $Pd_{75}Ni_{20}Bi_5$/C, $Pd_{80}Ni_{10}Bi_{10}$/C, Pd/C, $Pd_{60}Ni_{40}$/C, $Pd_{40}Ni_{20}Bi_{40}$/C, $Pd_{60}Ni_{20}Bi_{20}$/C and $Pd_{60}Bi_{40}$/C catalysts in the following order: 0.236 ± 0.005 < 0.239 ± 0.009 < 0.274 ± 0.008 < 0.280 ± 0.015 < 0.290 ± 0.018 < 0.323 ± 0.033 < 0.348 ± 0.007 < 0.352 ± 0.015 V. Both oxygenated Ni and Bi species facilitate the quick oxidative removal of CH_3CO_{ads}, poisonous CO_{ads} and other intermediates of EtOH oxidation by bifunctional mechanism to refresh the active sites of Pd for further EtOH oxidation. The height of the amount of metallic Pd (Pd^0) in relation to amount of the co-species (Table 37) is crucial for a high peak current density toward alkaline EOR (Table 12). The identified PdO is not a promoter for the alkaline EOR [15].

The Bi species (Bi^0, Bi_2O_3 and $Bi(OH)_3$) affect significantly the EOR stability and the byproduct tolerance to EtOH oxidation (the details are explained in the **sections 4.2.2** and **4.3.2**) but also initiate the agglomeration of Pd nanoparticles. The agglomerations of the catalyst particles might have been caused also by the rapid reduction process [83]. The unstable ions such as Ni^{2+} and Bi^{3+} tend to form on the surface different large crystal structures (e.g., tetragonal, cubic or hexagonal) and species with various shapes, which have a change in the electron state, the inter-planar spacing and the lattice parameters of Pd (Tables 6, 10 and 37). The large crystal structures (e.g., Bi2O2(CO3) and PdBi_tetrag) of the $Pd_{60}Bi_{40}$/C, $Pd_{60}Ni_{20}Bi_{20}$/C and $Pd_{40}Ni_{20}Bi_{40}$/C catalysts block the active sites of Pd and influence the alkaline EOR performances (onset potential and peak current density) drastically (Table 12) [15].

Table 37: XPS results of carbon supported Pd-based catalysts with the assignments of Pd 3d, Ni 2p and Bi 4f peaks [15].

Catalyst	Pd 3d (eV)	Pd (at.%)	Assignment	Ni 2p (eV)	Ni (at.%)	Assignment	Bi 4f (eV)	Bi (at.%)	Assignment
Pd/C	334.73	1.28	Pd^0	-	-	-	-	-	-
	336.27	1.56	PdO	-	-	-	-	-	-
$Pd_{60}Ni_{40}/C$	334.74	0.86	Pd^0	855.13	0.23	NiO	-	-	-
	335.81	1.16	PdO	861.14	0.1	$Ni(OH)_2$	-	-	-
$Pd_{60}Bi_{40}/C$	334.78	0.19	Pd^0	-	-	-	157	0.06	Bi^0
	336.14	0.14	PdO	-	-	-	158.21	0.14	Bi_2O_3
	-	-	-	-	-	-	159.19	0.18	$Bi(OH)_3$
$Pd_{60}Ni_{20}Bi_{20}/C$	334.75	0.41	Pd^0	856.06	0.08	NiO	157.78	0.15	Bi_2O_3
	335.95	0.34	PdO	861.33	0.03	$Ni(OH)_2$	159.35	0.03	$Bi(OH)_3$
$Pd_{70}Ni_{25}Bi_5/C$	334.72	0.32	Pd^0	855.69	0.04	NiO	156.54	0	Bi^0
	335.8	0.26	PdO	-	-	-	157.72	0.05	Bi_2O_3
$Pd_{70}Ni_{20}Bi_{10}/C$	334.69	0.63	Pd^0	856.83	0.02	NiO	156.68	0.02	Bi_0
	335.86	0.41	PdO	-	-	-	157.66	0.14	Bi_2O_3
$Pd_{80}Ni_{10}Bi_{10}/C$	334.64	0.24	Pd^0	856.24	0.01	NiO	157.65	0.07	Bi_2O_3
	335.72	0.22	PdO	-	-	-	159.32	0.01	$Bi(OH)_3$
$Pd_{40}Ni_{20}Bi_{40}/C$	334.71	0.17	Pd^0	856.04	0.07	NiO	156.88	0.02	Bi^0
	335.93	0.2	PdO	-	-	-	158.16	0.33	Bi_2O_3

Table 38: XPS data of the $Pd_{70}Ni_{25}Bi_5/C$ catalyst [15].

Catalyst	Peak name	Area (cps·eV)	E_{bin}[a] (eV)	Sigma	Lambda	IERF[b]	Sens. Fact.[c]	Norm. Area[d] (cps·eV)	Quant. (at.%)	[e]Sum (at.%)
$Pd_{70}Ni_{25}Bi_5/C$	C1s_2 Peak 1	2881.0722	283.76	1	20.31	0.913	18.543	155.37249	45.36	93.76
	C1s_2 Peak 2	2273.8229	284.24	1	20.3	0.913	18.534	122.68387	35.82	
	C1s_2 Peak 3	480.44136	285.89	1	20.28	0.914	18.536	25.919366	7.57	
	C1s_2 Peak 4	318.11235	288.33	1	20.25	0.915	18.529	17.168349	5.01	
	O1s_3 Peak 1	59.561557	529.48	2.93	17.13	1.022	51.295	1.1611571	0.34	5.56
	O1s_3 Peak 2	344.56608	531.41	2.93	17.1	1.023	51.255	6.7225848	1.96	
	O1s_3 Peak 3	572.96026	532.78	2.93	17.08	1.024	51.245	11.180803	3.26	
	Pd3d_4 Doublet 1	324.15930	334.72	16.04	19.66	0.932	293.90	1.1029465	0.32	0.58
	Pd3d_4 Doublet 2	260.57055	335.8	16.04	19.65	0.933	294.06	0.8860864	0.26	
	Bi4f_5 Doublet 1	6.3096851	156.54	24.83	21.88	0.87	472.65	0.0133494	0	0.05
	Bi4f_5 Doublet 2	73.406036	157.72	24.83	21.87	0.87	472.43	0.1553770	0.05	
	Ni2p_6 Doublet 1	47.129185	855.69	22.18	12.56	1.264	352.12	0.1338418	0.04	0.04

[a]E_{bin}: binding energy; [b]IERF: intensity/energy response factor, [c]Sens. Fact.: sensitivity factor, [d]Norm. Area: Product of Area and Sens. Fact.; [e]Sum: Gaussian-Lorentzian lines.

Table 39: XPS data of the $Pd_{70}Ni_{20}Bi_{10}/C$ catalyst [15].

Catalyst	Peak name	Area (cps·eV)	E_{bin}[a] (eV)	Sigma	Lambda	IERF[b]	Sens. Fact.[c]	Norm. Area[d] (cps·eV)	Quant. (at.%)	[e]Sum (at.%)
$Pd_{70}Ni_{20}Bi_{10}/C$	C1s_2 Peak 1	3398.0833	283.8	1	20.31	0.913	18.543	183.25423	63.96	91.96
	C1s_2 Peak 2	826.15929	284.72	1	20.29	0.913	18.525	44.596993	15.57	
	C1s_2 Peak 3	402.61511	285.94	1	20.28	0.914	18.536	21.720711	7.58	
	C1s_2 Peak 4	257.31780	288.39	1	20.25	0.915	18.529	13.887301	4.85	
	O1s_3 Peak 1	111.81839	529.64	2.93	17.13	1.022	51.295	2.1799082	0.76	6.82
	O1s_3 Peak 2	366.67858	531.48	2.93	17.1	1.023	51.255	7.1540061	2.5	
	O1s_3 Peak 3	522.96437	532.91	2.93	17.08	1.024	51.245	10.205178	3.56	
	Pd3d_4 Doublet 1	528.92407	334.69	16.04	19.66	0.932	293.90	1.7996552	0.63	1.04
	Pd3d_4 Doublet 2	348.00972	335.86	16.04	19.65	0.933	294.06	1.1834288	0.41	
	Bi4f_5 Doublet 1	21.717727	156.68	24.83	21.88	0.87	472.65	0.0459484	0.02	0.16
	Bi4f_5 Doublet 2	189.31813	157.66	24.83	21.87	0.87	472.43	0.4007258	0.14	
	Ni2p_6 Doublet 1	23.955247	856.83	22.18	12.54	1.265	351.84	0.0680848	0.02	0.02

[a]E_{bin}: binding energy; [b]IERF: intensity/energy response factor, [c]Sens. Fact.: sensitivity factor, [d]Norm. Area: Product of Area and Sens. Fact.; [e]Sum: Gaussian-Lorentzian lines.

Table 40: XPS data of the $Pd_{80}Ni_{10}Bi_{10}/C$ catalyst [15].

Catalyst	Peak name	Area (cps·eV)	E_{bin}[a] (eV)	Sigma	Lambda	IERF[b]	Sens. Fact.[c]	Norm. Area[d] (cps·eV)	Quant. (at.%)	[e]Sum (at.%)
	C1s_2 Peak 1	1372.9714	283.71	1	20.31	0.913	18.543	74.042574	24.5	89.24
	C1s_2 Peak 2	2924.7593	284.42	1	20.3	0.913	18.534	157.80507	52.22	
	C1s_2 Peak 3	340.91435	286.18	1	20.28	0.914	18.536	18.392013	6.09	
	C1s_2 Peak 4	360.16451	288.46	1	20.25	0.915	18.529	19.437882	6.43	
	O1s_3 Peak 1	841.96442	531.79	2.93	17.1	1.023	51.255	16.426971	5.44	10.21
$Pd_{80}Ni_{10}Bi_{10}/C$	O1s_3 Peak 2	738.77528	533.21	2.93	17.08	1.024	51.245	14.416534	4.77	
	Pd3d_4 Doublet 1	211.96762	334.64	16.04	19.66	0.932	293.90	0.7212162	0.24	0.46
	Pd3d_4 Doublet 2	195.49642	335.72	16.04	19.65	0.933	294.06	0.6647978	0.22	
	Bi4f_5 Doublet 1	99.903287	157.65	24.83	21.87	0.87	472.43	0.2114632	0.07	0.08
	Bi4f_5 Doublet 2	18.226782	159.32	24.83	21.85	0.87	472.00	0.0386155	0.01	
	Ni2p_6 Doublet 1	6.7783168	856.24	22.18	12.55	1.265	352.12	0.0192498	0.01	0.01

[a]E_{bin}: binding energy; [b]IERF: intensity/energy response factor, [c]Sens. Fact.: sensitivity factor, [d]Norm. Area: Product of Area and Sens. Fact.; [e]Sum: Gaussian-Lorentzian lines.

Table 41: XPS data of the $Pd_{40}Ni_{20}Bi_{40}$/C catalyst [15].

Catalyst	Peak name	Area (cps·eV)	E_{bin}[a] (eV)	Sigma	Lambda	IERF[b]	Sens. Fact.[c]	Norm. Area[d] (cps·eV)	Quant. (at.%)	[e]Sum (at.%)
$Pd_{40}Ni_{20}Bi_{40}$/C	C1s_2 Peak 1	2920.4508	283.78	1	20.31	0.913	18.543	157.49613	47.43	93.76
	C1s_2 Peak 2	2151.8750	284.38	1	20.3	0.913	18.534	116.10418	34.96	
	C1s_2 Peak 3	375.49201	286.19	1	20.28	0.914	18.536	20.257445	6.1	
	C1s_2 Peak 4	323.99665	288.6	1	20.24	0.915	18.52	17.494419	5.27	
	O1s_3 Peak 1	174.83248	530.06	2.93	17.12	1.022	51.265	3.4103674	1.03	5.47
	O1s_3 Peak 2	412.10641	531.76	2.93	17.1	1.023	51.255	8.0403163	2.42	
	O1s_3 Peak 3	343.12680	533.2	2.93	17.08	1.024	51.245	6.6958103	2.02	
	Pd3d_4 Doublet 1	163.91842	334.71	16.04	19.66	0.932	293.90	0.5577296	0.17	0.37
	Pd3d_4 Doublet 2	198.44316	335.93	16.04	19.65	0.933	294.06	0.6748183	0.2	
	Bi4f_5 Doublet 1	25.624664	156.88	24.83	21.88	0.87	472.65	0.0542144	0.02	0.35
	Bi4f_5 Doublet 2	510.70735	158.16	24.83	21.87	0.87	472.43	1.0810039	0.33	
	Ni2p_6 Doublet 2	77.013884	856.04	22.18	12.55	1.265	352.12	0.2187123	0.07	0.07

[a]E_{bin}: binding energy; [b]IERF: intensity/energy response factor, [c]Sens. Fact.: sensitivity factor, [d]Norm. Area: Product of Area and Sens. Fact.; [e]Sum: Gaussian-Lorentzian lines.

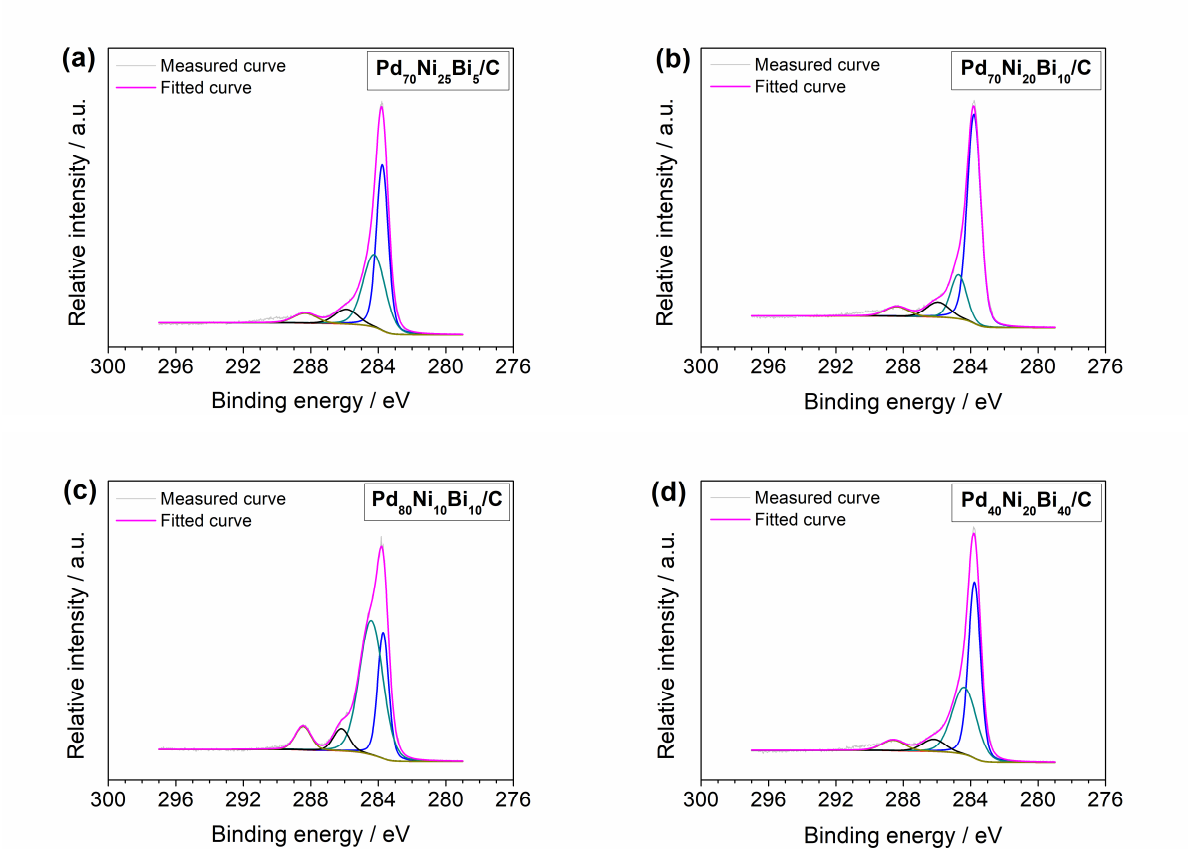


Figure 65: C 1s XPS spectra of the **(a)** $Pd_{70}Ni_{25}Bi_5/C$, **(b)** $Pd_{70}Ni_{20}Bi_{10}/C$, **(c)** $Pd_{80}Ni_{10}Bi_{10}/C$ and **(d)** $Pd_{40}Ni_{20}Bi_{40}/C$ catalyst [15].

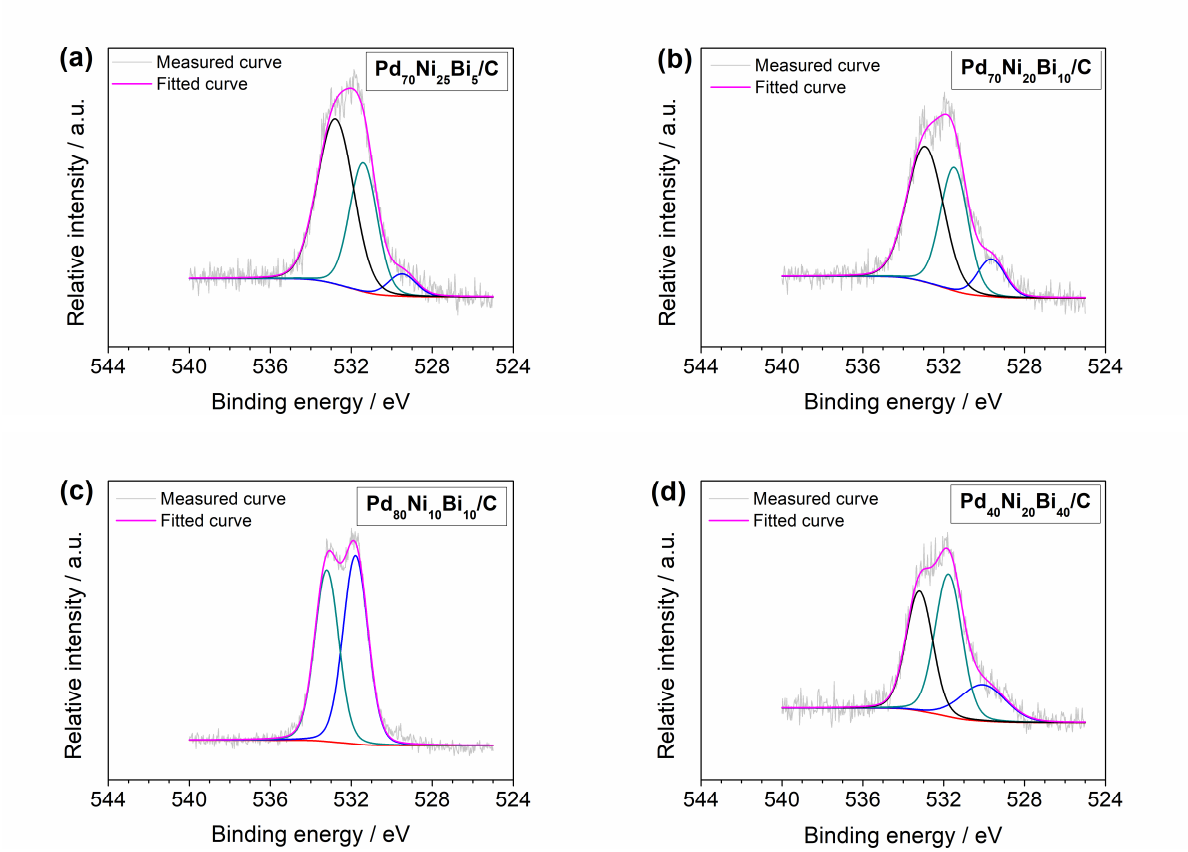


Figure 66: O 1s XPS spectra of the **(a)** $Pd_{70}Ni_{25}Bi_5/C$, **(b)** $Pd_{70}Ni_{20}Bi_{10}/C$, **(c)** $Pd_{80}Ni_{10}Bi_{10}/C$ and **(d)** $Pd_{40}Ni_{20}Bi_{40}/C$ catalyst [15].

8.3.3 Electrochemical Characterization

CV and CA analysis

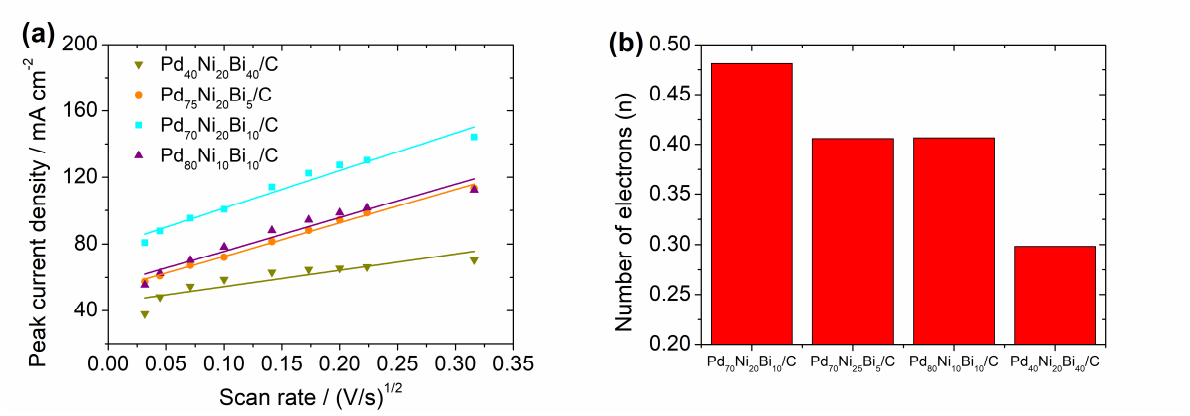


Figure 67: (a) Diffusion controlled process for the alkaline EOR takes place on carbon supported $Pd_xNi_yBi_z$ catalysts in scan rates region of 10 to 100 mV·s^{-1}, showing by linear relationship between peak current density and square root of scan rate. The EOR measurements on the respective catalyst were performed in a mixture of 1 M KOH and 1 M EtOH and at 30 °C and **(b)** the number of electrons which are released during the EOR oxidation, were determined according to Randles-Sevcik equation.

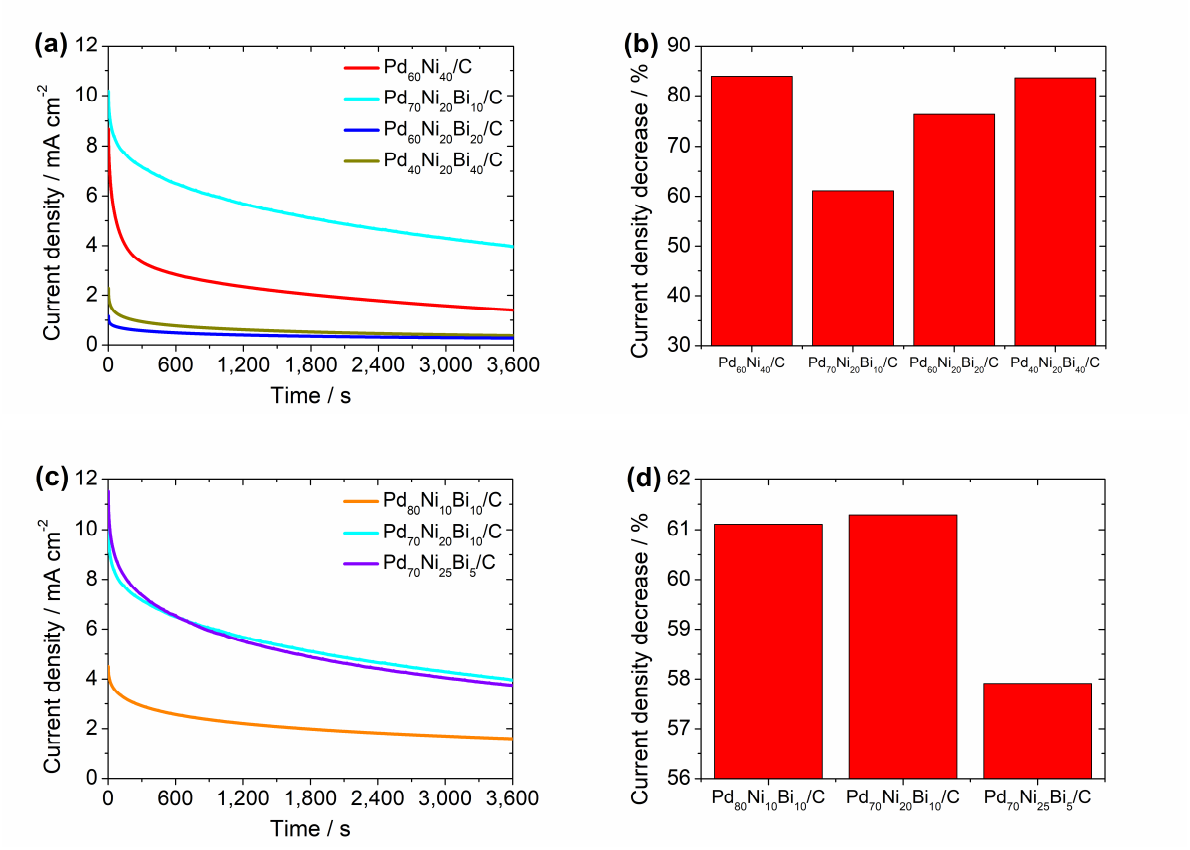


Figure 68: Stability tests of carbon supported $Pd_{60}Ni_{40}$ and $Pd_xNi_yBi_z$ electrocatalysts **(a)** and **(b)** in a mixture of 1 M KOH and 1 M EtOH at an applied potential of 0.5 V and at 30 °C for 3,600 s using the CA method and **(c)** and **(d)** their resulting current density decrease, given in percentage.

8.4 PART IV: Alkaline Ethanol Oxidation Reaction on Carbon Supported Ternary PdNiBi Nanocatalyst using Modified Instant Reduction Synthesis Method

8.4.1 Chemicals and Materials

Anode Catalysts

- Palladium chloride ($PdCl_2$, anhydrous, 59-60% palladium (Pd) basis, Aldrich),
- sodium chloride (NaCl, ≥ 99.5%, Carl Roth),
- nickel(II) nitrate hexahydrate ($Ni(NO_3)_2 \cdot 6H_2O$, Aldrich),
- bismuth(III) chloride ($BiCl_3$, reagent grade, ≥ 98%, Aldrich),
- hydrochloric acid (HCl (aq), Carl Roth),
- Vulcan XC72R carbon black (CABOT Corporation, USA),
- sodium borohydride ($NaBH_4$, purity of 97%, Alfa Aesar),
- 2-propanol (ASC ≥ 99.8%, Honeywell),
- sodium hydroxide (NaOH, Fluka) and
- ultra-pure water (~18 MΩ·cm, Barnstead NANOpure Water Purification System) were used for the development of $Pd_{85}Ni_{10}Bi_5$/C nanoparticles on the Vulcan XC72R carbon support material as anode catalysts. A commercial Pd/C (40 wt.%, Fuel Cell Store) catalyst was used as reference material [3].

Electrochemical Characterizations (RDE-CV and RDE-CA)

- 1.0 M potassium hydroxide solution (KOH, FIXANAL KA 180 mL, Sigma-Aldrich),
- Nafion ionomer solution (5 wt.%, Quintech),
- ethanol abs. (99.999%, Aldrich) and
- ultra-pure water (~18 MΩ·cm, Barnstead NANOpure Water Purification System) were used for electrochemical characterizations of the commercial Pd/C and $Pd_{85}Ni_{10}Bi_5$/C anode catalysts [3].

8.4.2 Physico-Chemical Characterization

ICP-OES analysis

Table 42: ICP-OES data of the commercial Pd/C catalyst and the carbon supported $Pd_{85}Ni_{10}B_5$ catalysts using the instant method with different modifications [3].

Catalysts		Pd (g/kg)	Ni (g/kg)	Bi (g/kg)	Pd (mol/kg)	Ni (mol/kg)	Bi (mol/kg)	Sum (mol/kg)	Pd (at.%)	Ni (at.%)	Bi (at.%)
Pd/C comm.	Average	406			3.82			3.82	100		
$Pd_{85}Ni_{10}Bi_5/C^{(I)}$	Average	173	11.9	21.3	1.63	0.20	0.10	1.93	84.2	10.5	5.3
$Pd_{85}Ni_{10}Bi_5/C^{(II)}$	Average	335	21.3	41.6	3.15	0.36	0.20	3.71	84.9	9.8	5.4
$Pd_{85}Ni_{10}Bi_5/C^{(III)}$	Average	339	21.2	36.8	3.19	0.36	0.18	3.72	85.6	9.7	4.7

Atomic weight (AMU): Pd = 106.42; Ni = 58.69; Bi = 208.98

TEM analysis

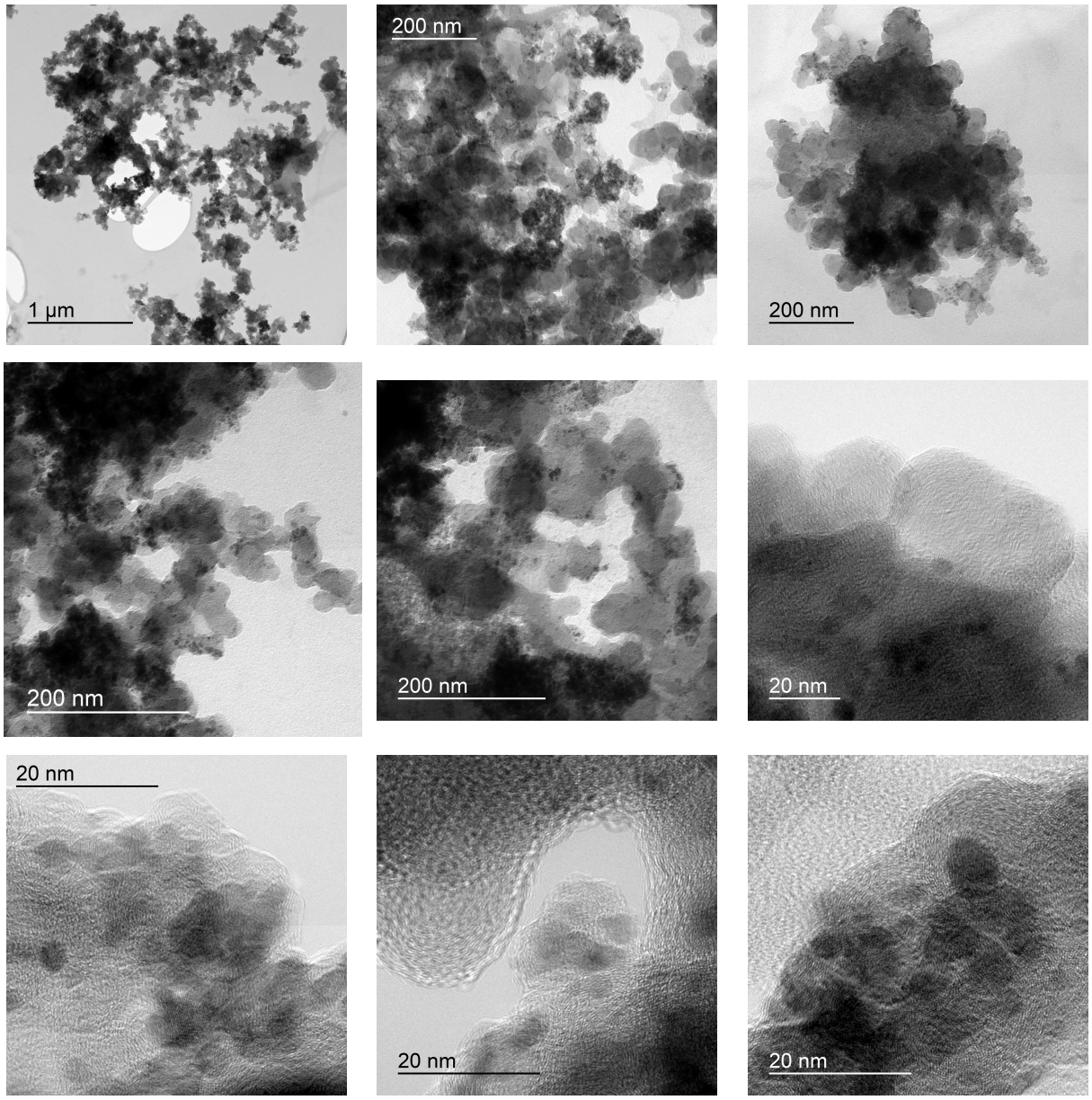


Figure 69: TEM micrographs with low and high magnifications of the $Pd_{85}Ni_{10}Bi_5/C^{(I)}$ catalyst [3].

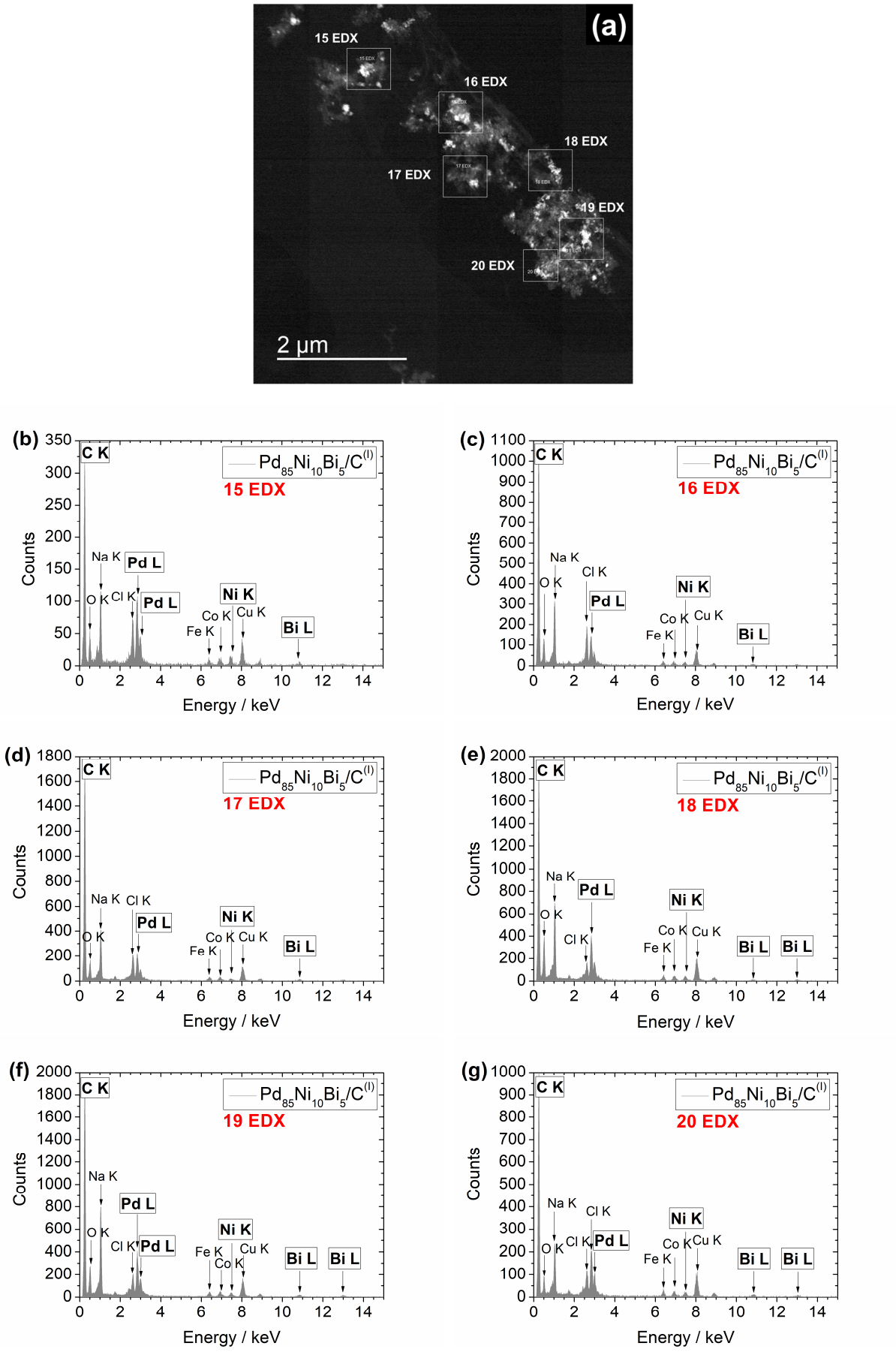


Figure 70: STEM-HAADF micrograph **(a)** and the corresponding EDX spectra **(b)-(g)** of the $Pd_{85}Ni_{10}Bi_5/C^{(I)}$ catalyst [3].

Table 43: TEM-EDX results of the $Pd_{85}Ni_{10}Bi_5/C^{(I)}$ catalyst [3].

EDX areas	3 elements	net counts	k-factor (Si)	rel. (wt.%)	wt.% (norm.)	at.%	rel. (at.%)
15	Pd-L	1203	2.651	1.000	82.85	82.29	1.000
	Ni-K	176	1.525	0.084	6.97	12.56	0.153
	Bi-L	61	6.425	0.123	10.18	5.15	0.063
16	Pd-L	1638	2.651	1.000	87.43	87.05	1.000
	Ni-K	165	1.525	0.058	5.07	9.15	0.105
	Bi-L	58	6.425	0.086	7.50	3.80	0.044
17	Pd-L	2308	2.651	1.000	82.11	83.59	1.000
	Ni-K	263	1.525	0.066	5.38	9.93	0.119
	Bi-L	145	6.425	0.152	12.50	6.48	0.078
18	Pd-L	2403	2.651	1.000	82.61	84.24	1.000
	Ni-K	256	1.525	0.061	5.06	9.36	0.111
	Bi-L	148	6.425	0.149	12.33	6.40	0.076
19	Pd-L	4096	2.651	1.000	80.96	82.83	1.000
	Ni-K	478	1.525	0.067	5.43	10.08	0.122
	Bi-L	284	6.425	0.168	13.60	7.09	0.086
20	Pd-L	2352	2.651	1.000	81.36	82.75	1.000
	Ni-K	288	1.525	0.070	5.73	10.57	0.128
	Bi-L	154	6.425	0.159	12.91	6.69	0.081

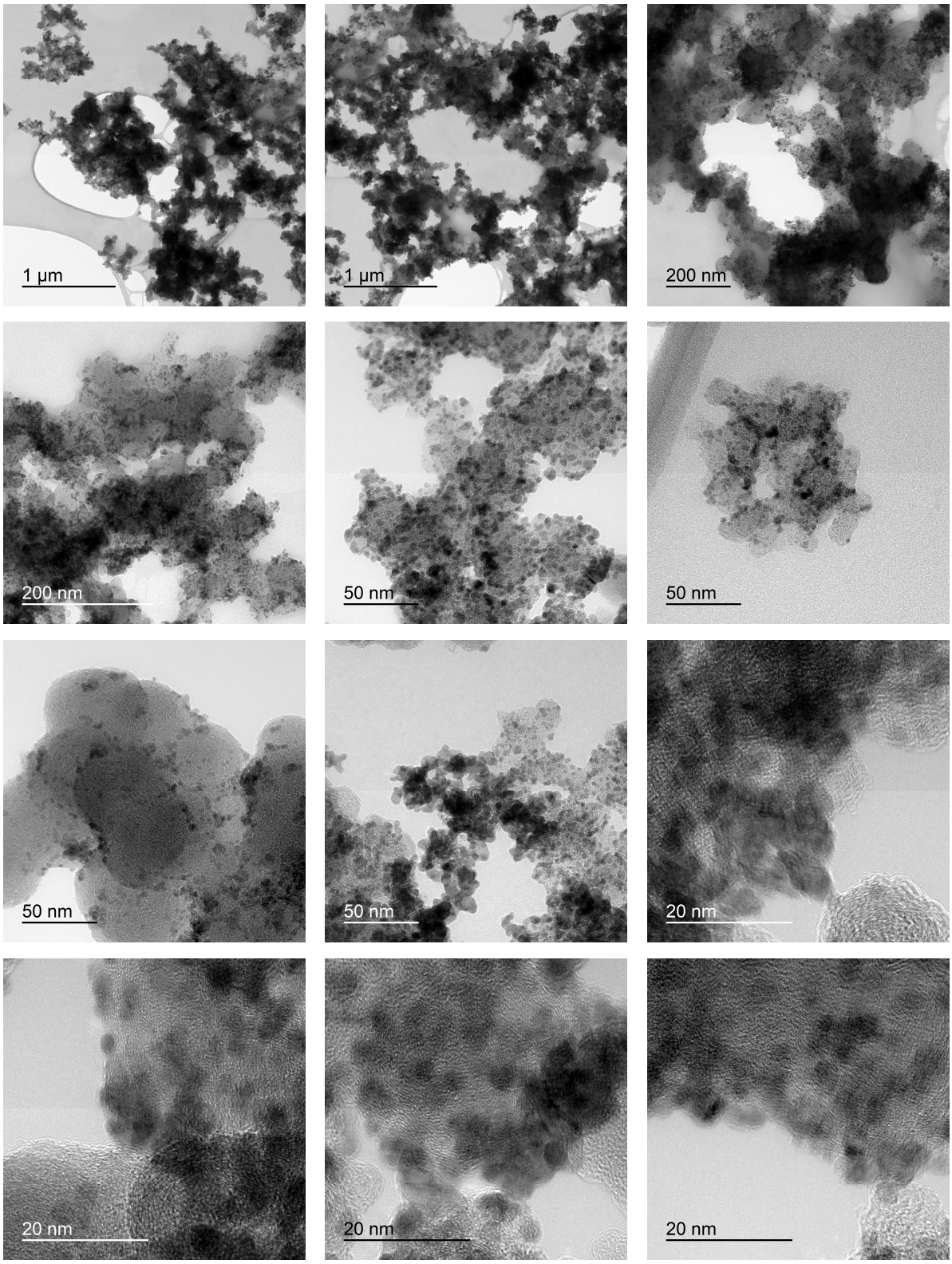


Figure 71: TEM micrographs with low and high magnifications of the $Pd_{85}Ni_{10}Bi_5/C^{(II)}$ catalyst [3].

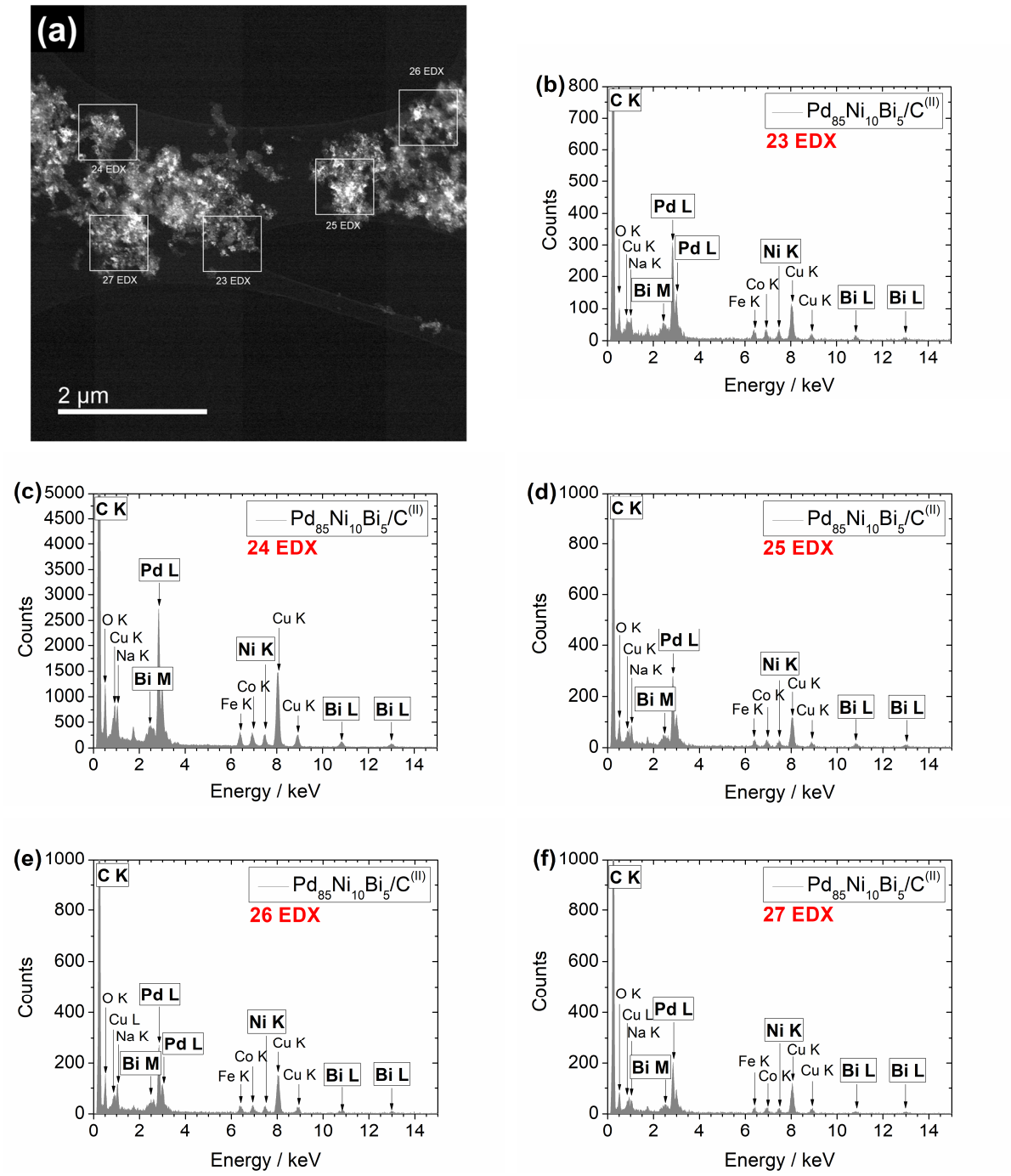


Figure 72: STEM-HAADF micrograph **(a)** and the corresponding EDX spectra **(b)-(f)** of the $Pd_{85}Ni_{10}Bi_5/C^{(II)}$ catalyst [3].

Table 44: TEM-EDX results of the $Pd_{85}Ni_{10}Bi_5/C^{(II)}$ catalyst [3].

EDX areas	3 elements	net counts	k-factor (Si)	rel. (wt.%)	wt.% (norm.)	at.%	rel. (at.%)
23	Pd-L	3344	2.651	1.000	84.48	85.09	1.000
	Ni-K	364	1.525	0.063	5.29	9.66	0.114
	Bi-L	167	6.425	0.121	10.23	5.24	0.062
24	Pd-L	29847	2.651	1.000	82.66	84.09	1.000
	Ni-K	3280	1.525	0.063	5.23	9.64	0.115
	Bi-L	1804	6.425	0.146	12.11	6.27	0.075
25	Pd-L	3265	2.651	1.000	82.59	84.62	1.000
	Ni-K	324	1.525	0.057	4.71	8.76	0.103
	Bi-L	207	6.425	0.154	12.69	6.62	0.078
26	Pd-L	3107	2.651	1.000	82.04	84.07	1.000
	Ni-K	323	1.525	0.060	4.91	9.12	0.108
	Bi-L	204	6.425	0.159	13.05	6.81	0.081
27	Pd-L	2196	2.651	1.000	83.67	84.77	1.000
	Ni-K	235	1.525	0.062	5.15%	9.46	0.112
	Bi-L	121	6.425	0.134	11.17%	5.76	0.068

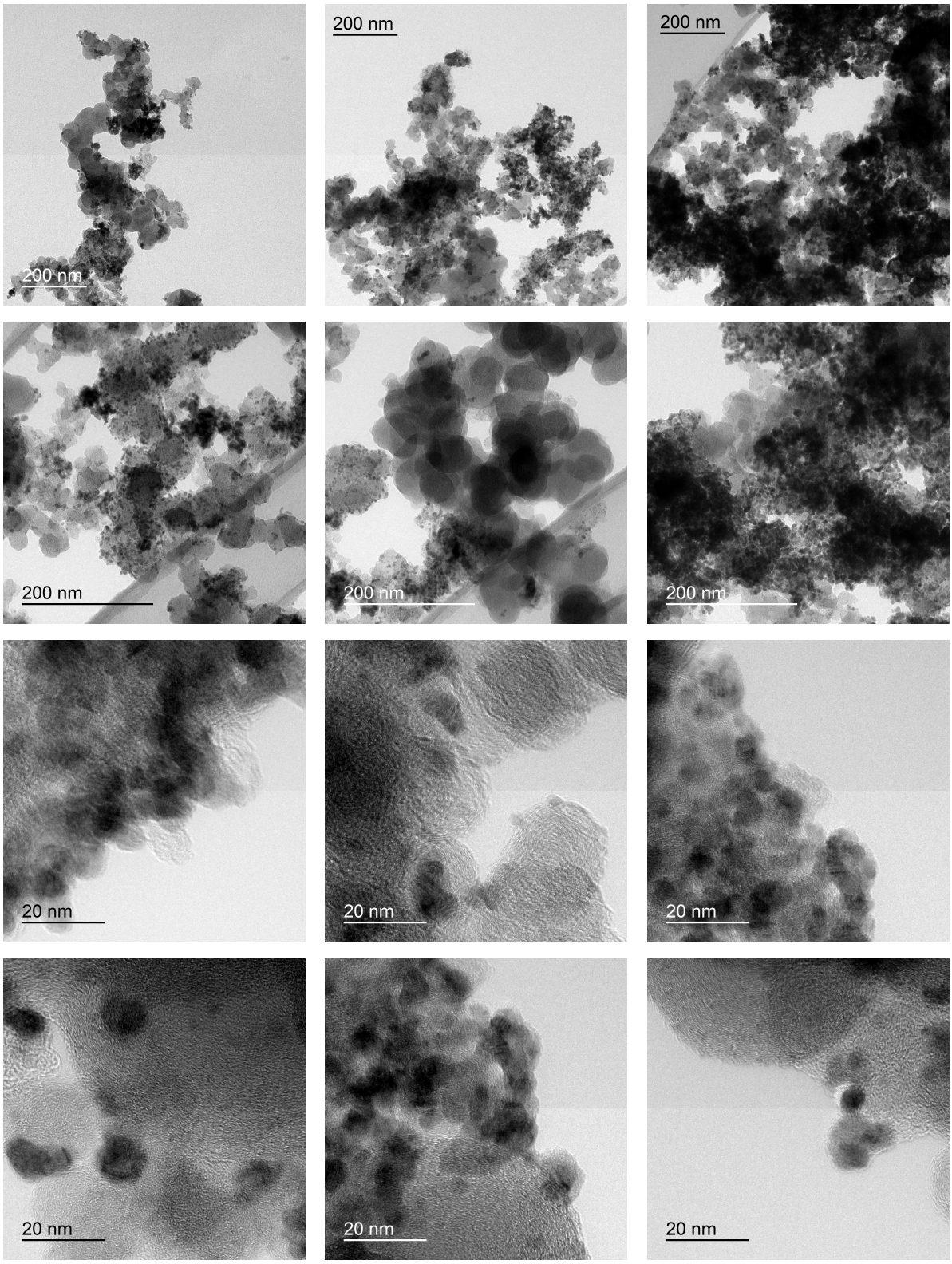


Figure 73: TEM micrographs with low and high magnifications of the $Pd_{85}Ni_{10}Bi_5/C^{(III)}$ catalyst [3].

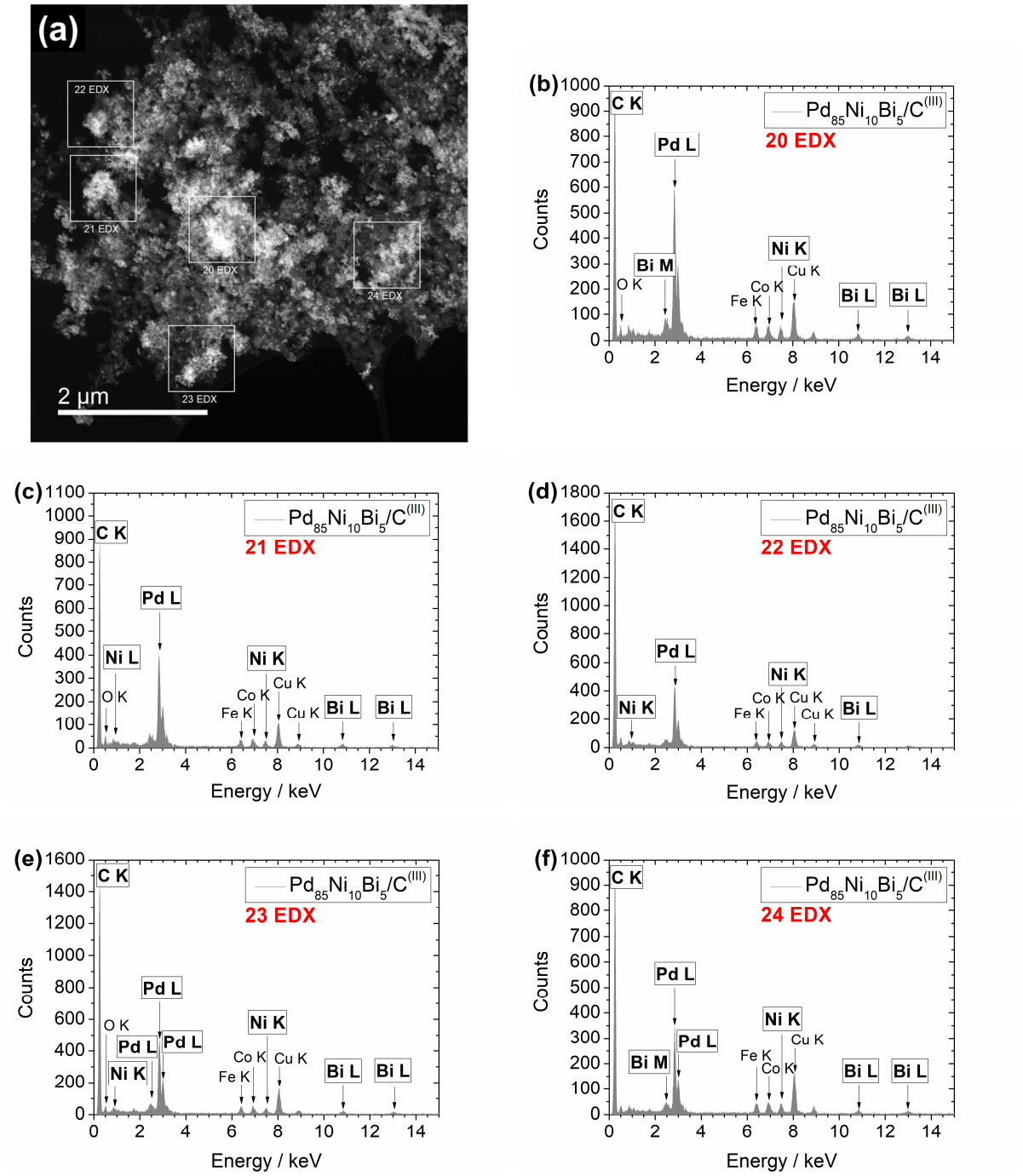


Figure 74: STEM-HAADF micrograph **(a)** and the corresponding EDX spectra **(b)-(f)** of the $Pd_{85}Ni_{10}Bi_5/C^{(III)}$ catalyst [3].

Table 45: TEM-EDX results of the $Pd_{85}Ni_{10}Bi_5/C^{(III)}$ catalyst [3].

EDX areas	3 elements	net counts	k-factor (Si)	rel. (wt.%)	wt.% (norm.)	at.%	rel. (at.%)
20	Pd-L	6631	2.651	1.000	85.21	86.29	1.000
	Ni-K	623	1.525	0.054	4.61	8.46	0.098
	Bi-L	327	6.425	0.120	10.18	5.25	0.061
21	Pd-L	4744	2.651	1.000	85.19	85.43	1.000
	Ni-K	519	1.525	0.063	5.36	9.75	0.114
	Bi-L	217	6.425	0.111	9.44	4.82	0.056
22	Pd-L	4663	2.651	1.000	83.38	84.38	1.000
	Ni-K	520	1.525	0.064	5.35	9.81	0.116
	Bi-L	260	6.425	0.135	11.27	5.81	0.069
23	Pd-L	5152	2.651	1.000	81.66	81.76	1.000
	Ni-K	747	1.525	0.083	6.81	12.36	0.151
	Bi-L	300	6.425	0.141	11.52	5.88	0.072
24	Pd-L	3359	2.651	1.000	78.84	79.31	1.000
	Ni-K	556	1.525	0.095	7.51	13.69	0.173
	Bi-L	240	6.425	0.173	13.65	6.99	0.088

XRD analysis

Table 46: XRD data (Rietveld refinement) of the commercial Pd/C catalyst [3].

Catalyst	Peak No.	Peak Pos. (° 2θ)	*d*-spacing (Å)	Rel. Int. (%)	FWHM (° 2θ)	h	k	l	Assignment
	1	24.756	3.593	1.3	2.414	0	0	2	Graphite(2H)_187640-ICSD
	2	27.303	3.264	0.1	1.970	1	1	1	NaCl_655785-ICSD
	3	31.640	2.826	1.4	1.970	0	0	2	NaCl_655785-ICSD
	4	39.246	2.294	0.1	2.414	0	1	0	Graphite(2H)_187640-ICSD
	5	40.057	2.249	100.0	1.143	1	1	1	Pd_64922-ICSD
	6	41.291	2.185	0.2	2.414	0	1	1	Graphite(2H)_187640-ICSD
	7	45.385	1.997	0.9	1.970	0	2	2	NaCl_655785-ICSD
	8	46.602	1.947	28.1	1.159	0	0	2	Pd_64922-ICSD
	9	46.986	1.932	0.1	2.414	0	1	2	Graphite(2H)_187640-ICSD
	10	50.847	1.794	0.1	2.414	0	0	4	Graphite(2H)_187640-ICSD
Pd/C comm	11	55.472	1.655	0.1	2.414	0	1	3	Graphite(2H)_187640-ICSD
	12	56.410	1.630	0.3	1.970	2	2	2	NaCl_655785-ICSD
	13	66.164	1.411	0.1	1.970	0	0	4	NaCl_655785-ICSD
	14	68.067	1.376	12.5	1.238	0	2	2	Pd_64922-ICSD
	15	71.202	1.323	0.1	2.414	1	1	0	Graphite(2H)_187640-ICSD
	16	75.230	1.262	0.3	1.970	0	2	4	NaCl_655785-ICSD
	17	76.709	1.241	0.1	2.414	1	1	2	Graphite(2H)_187640-ICSD
	18	82.052	1.174	10.7	1.321	1	1	3	Pd_64922-ICSD
	19	83.930	1.152	0.3	1.970	2	2	4	NaCl_655785-ICSD
	20	86.569	1.124	3.2	1.355	2	2	2	Pd_64922-ICSD
	21	92.705	1.065	0.1	2.414	1	1	4	Graphite(2H)_187640-ICSD

Table 47: XRD data (Rietveld refinement) of the $Pd_{85}Ni_{10}Bi_5/C^{(I)}$ catalyst [3].

Catalyst	Peak No.	Peak Pos. (° 2θ)	*d*-spacing (Å)	Rel. Int. (%)	FWHM (° 2θ)	h	k	l	Assignment
	1	25.038	3.554	8.2	3.162	0	0	2	Graphite(2H)_187640-ICSD
	2	39.821	2.262	100.0	2.550	1	1	1	Pd_64922-ICSD
	3	42.452	2.128	0.2	3.162	0	1	0	Graphite(2H)_187640-ICSD
	4	44.366	2.040	1.2	3.162	0	1	1	Graphite(2H)_187640-ICSD
	5	46.243	1.962	23.2	2.648	0	0	2	Pd_64922-ICSD
	6	49.755	1.831	0.3	3.162	0	1	2	Graphite(2H)_187640-ICSD
	7	50.943	1.791	0.6	3.162	0	0	4	Graphite(2H)_187640-ICSD
	8	57.893	1.592	0.4	3.162	0	1	3	Graphite(2H)_187640-ICSD
	9	67.256	1.391	11.7	3.095	0	2	2	Pd_64922-ICSD
	10	68.200	1.374	0.1	3.162	0	1	4	Graphite(2H)_187640-ICSD
$Pd_{85}Ni_{10}Bi_5/C^{(I)}$	11	77.267	1.234	0.4	3.162	1	1	0	Graphite(2H)_187640-ICSD
	12	80.055	1.198	0.1	3.162	0	0	6	Graphite(2H)_187640-ICSD
	13	80.458	1.193	0.1	3.162	0	1	5	Graphite(2H)_187640-ICSD
	14	80.883	1.188	10.5	3.520	1	1	3	Pd_64922-ICSD
	15	82.582	1.167	0.7	3.162	1	1	2	Graphite(2H)_187640-ICSD
	16	85.269	1.137	3.5	3.686	2	2	2	Pd_64922-ICSD
	17	92.147	1.070	0.0	3.162	0	2	0	Graphite(2H)_187640-ICSD
	18	93.455	1.058	0.1	3.162	0	2	1	Graphite(2H)_187640-ICSD
	19	94.881	1.046	0.0	3.162	0	1	6	Graphite(2H)_187640-ICSD
	20	97.390	1.025	0.0	3.162	0	2	2	Graphite(2H)_187640-ICSD
	21	98.307	1.018	0.5	3.162	1	1	4	Graphite(2H)_187640-ICSD
	22	25.038	3.554	8.2	3.162	0	0	2	Graphite(2H)_187640-ICSD

Table 48: XRD data (Rietveld refinement) of the $Pd_{85}Ni_{10}Bi_5/C^{(II)}$ catalyst [3].

Catalyst	Peak No.	Peak Pos. (° 2θ)	*d*-spacing (Å)	Rel. Int. (%)	FWHM (° 2θ)	h	k	l	Assignment
	1	24.815	3.585	6.5	2.336	0	0	2	Graphite(2H)_187640-ICSD
	2	38.458	2.339	0.3	2.336	0	1	0	Graphite(2H)_187640-ICSD
	3	39.570	2.276	100.0	2.660	1	1	1	Pd_64922-ICSD
	4	40.519	2.225	1.3	2.336	0	1	1	Graphite(2H)_187640-ICSD
	5	45.987	1.972	9.0	2.650	0	0	2	Pd_64922-ICSD
	6	46.244	1.962	0.3	2.336	0	1	2	Graphite(2H)_187640-ICSD
	7	50.720	1.798	0.5	2.336	0	0	4	Graphite(2H)_187640-ICSD
	8	54.737	1.676	0.4	2.336	0	1	3	Graphite(2H)_187640-ICSD
	9	65.324	1.427	0.1	2.336	0	1	4	Graphite(2H)_187640-ICSD
	10	66.981	1.396	2.7	2.601	0	2	2	Pd_64922-ICSD
$Pd_{85}Ni_{10}Bi_5/C^{(II)}$	11	69.409	1.353	0.4	2.336	1	1	0	Graphite(2H)_187640-ICSD
	12	74.906	1.267	0.7	2.336	1	1	2	Graphite(2H)_187640-ICSD
	13	77.754	1.227	0.1	2.336	0	1	5	Graphite(2H)_187640-ICSD
	14	79.831	1.200	0.1	2.336	0	0	6	Graphite(2H)_187640-ICSD
	15	80.594	1.191	1.5	2.547	1	1	3	Pd_64922-ICSD
	16	83.484	1.157	0.1	2.336	0	2	1	Graphite(2H)_187640-ICSD
	17	84.975	1.140	0.6	2.523	2	2	2	Pd_64922-ICSD
	18	87.417	1.115	0.0	2.336	0	2	2	Graphite(2H)_187640-ICSD
	19	90.761	1.082	0.4	2.336	1	1	4	Graphite(2H)_187640-ICSD
	20	92.221	1.069	0.0	2.336	0	1	6	Graphite(2H)_187640-ICSD
	21	93.953	1.054	0.1	2.336	0	2	3	Graphite(2H)_187640-ICSD

Table 49: XRD data (Rietveld refinement) of the $Pd_{85}Ni_{10}Bi_5/C^{(III)}$ catalyst [3].

Catalyst	Peak No.	Peak Pos. (° 2θ)	*d*-spacing (Å)	Rel. Int. (%)	FWHM (° 2θ)	h	k	l	Assignment
$Pd_{85}Ni_{10}Bi_5/C^{(III)}$	1	25.273	3.521	4.4	2.441	0	0	2	Graphite(2H)_187640-ICSD
	2	39.227	2.295	100.0	2.269	1	1	1	Pd_64922-ICSD
	3	42.086	2.145	0.1	2.441	0	1	0	Graphite(2H)_187640-ICSD
	4	44.033	2.055	0.7	2.441	0	1	1	Graphite(2H)_187640-ICSD
	5	45.518	1.991	22.8	2.258	0	0	2	Pd_64922-ICSD
	6	49.502	1.840	0.1	2.441	0	1	2	Graphite(2H)_187640-ICSD
	7	51.290	1.780	0.3	2.441	0	0	4	Graphite(2H)_187640-ICSD
	8	57.740	1.595	0.2	2.441	0	1	3	Graphite(2H)_187640-ICSD
	9	66.049	1.413	8.9	2.204	0	2	2	Pd_64922-ICSD
	10	68.150	1.375	0.0	2.441	0	1	4	Graphite(2H)_187640-ICSD
	11	76.368	1.246	0.2	2.441	1	1	0	Graphite(2H)_187640-ICSD
	12	79.302	1.207	6.6	2.144	1	1	3	Pd_64922-ICSD
	13	80.511	1.192	0.1	2.441	0	1	5	Graphite(2H)_187640-ICSD
	14	80.563	1.191	0.1	2.441	0	0	6	Graphite(2H)_187640-ICSD
	15	81.742	1.177	0.4	2.441	1	1	2	Graphite(2H)_187640-ICSD
	16	83.552	1.156	2.1	2.118	2	2	2	Pd_64922-ICSD
	17	90.941	1.081	0.0	2.441	0	2	0	Graphite(2H)_187640-ICSD
	18	92.258	1.069	0.1	2.441	0	2	1	Graphite(2H)_187640-ICSD
	19	95.048	1.044	0.0	2.441	0	1	6	Graphite(2H)_187640-ICSD
	20	95.997	1.037	0.1	2.251	0	2	3	Graphite(2H)_187640-ICSD
	21	96.216	1.035	0.0	2.441	0	2	2	Graphite(2H)_187640-ICSD
	22	97.592	1.024	0.3	2.441	1	1	4	Graphite(2H)_187640-ICSD

Table 50: XRD analysis of the commercial Pd/C catalyst – average crystallite size estimation according to Scherrer, assuming spherical crystallites with cubic crystal system at five diffraction peaks (peak pos.) including the determination of half-width (B_{obs}) and lattice parameter by profile fit and Rietveld refinement, respectively [3].

Catalyst	Peak No	$B_{obs.}$[a] (° 2θ)	$B_{std.}$[b] (° 2θ)	Peak pos.[c] (° 2θ)	$B_{struct.}$[d] (° 2θ)	Crystallite size (Å)	Crystallite size (nm)
Pd/C comm.	1	1.143	0.046	40.057	1.054	86	9
	2	1.159	0.048	46.602	1.342	87	9
	3	1.238	0.055	68.067	1.265	90	9
	4	1.321	0.060	82.052	1.290	93	9
	5	1.355	0.064	86.569	1.290	94	9
Lattice parameter: a = 3.890 Å							

[a]$B_{obs.}$: half width (full width half maximum FWHM, peak width) - obs. = observed; [b]B_{std}: device-related width, Derived from LaB_6 - std. = standard; [c]pos.: position; [d]$B_{struct.}$: Difference between $B_{obs.}$ and B_{std} - struct. = structural.

Table 51: XRD analysis of the $Pd_{85}Ni_{10}Bi_5/C^{(I)}$ catalyst – average crystallite size estimation according to Scherrer, assuming spherical crystallites with cubic crystal system at five diffraction peaks (peak pos.) including the determination of half-width (B_{obs}) and lattice parameter by profile fit and Rietveld refinement, respectively [3].

Catalyst	Peak No	$B_{obs.}$[a] (° 2θ)	$B_{std.}$[b] (° 2θ)	Peak pos.[c] (° 2θ)	$B_{struct.}$[d] (° 2θ)	Crystallite size (Å)	Crystallite size (nm)
$Pd_{85}Ni_{10}Bi_5/C^{(I)}$	1	2.550	0.046	39.821	2.504	38	4
	2	2.648	0.048	46.243	2.600	37	4
	3	3.095	0.055	67.256	3.040	35	3
	4	3.520	0.060	80.883	3.460	34	3
	5	3.686	0.064	85.269	3.622	33	3
Lattice parameter: a = 3.953 Å							

[a]$B_{obs.}$: half width (full width half maximum FWHM, peak width) - obs. = observed; [b]B_{std}: device-related width, Derived from LaB_6 - std. = standard; [c]pos.: position; [d]$B_{struct.}$: Difference between $B_{obs.}$ and B_{std} - struct. = structural.

Table 52: XRD analysis of the $Pd_{85}Ni_{10}Bi_5/C^{(II)}$ catalyst – average crystallite size estimation according to Scherrer assuming spherical crystallites with cubic crystal system at five diffraction peaks (peak pos.) including the determination of half-width *(B_{obs})* and lattice parameter by profile fit and Rietveld refinement, respectively [3].

Catalyst	Peak No	$B_{obs.}$[a] (° 2θ)	$B_{std.}$[b] (° 2θ)	Peak pos.[c] (° 2θ)	$B_{struct.}$[d] (° 2θ)	Crystallite size (Å)	Crystallite size (nm)
$Pd_{85}Ni_{10}Bi_5/C^{(II)}$	1	2.660	0.046	39.570	2.614	36	4
	2	2.650	0.048	45.987	2.602	37	4
	3	2.601	0.055	66.981	2.546	42	4
	4	2.547	0.060	80.594	2.487	47	5
	5	2.523	0.064	84.975	2.459	49	5
Lattice parameter: a = 3.957 Å							

[a]$B_{obs.}$: half width (full width half maximum FWHM, peak width) - obs. = observed; [b]B_{std}: device-related width, Derived from LaB_6 - std. = standard; [c]pos.: position; [d]$B_{struct.}$: Difference between $B_{obs.}$ and B_{std} - struct. = structural.

Table 53: XRD analysis of the $Pd_{85}Ni_{10}Bi_5/C^{(III)}$ catalyst – average crystallite size estimation according to Scherrer, assuming spherical crystallites with cubic crystal system at five diffraction peaks (peak pos.) including the determination of half-width (B_{obs}) and lattice parameter by profile fit and Rietveld refinement, respectively [3].

Catalyst	Peak No	$B_{obs.}$[a] (° 2θ)	$B_{std.}$[b] (° 2θ)	Peak pos.[c] (° 2θ)	$B_{struct.}$[d] (° 2θ)	Crystallite size (Å)	Crystallite size (nm)
$Pd_{85}Ni_{10}Bi_5/C^{(III)}$	1	2.269	0.046	39.227	2.223	42	4
	2	2.258	0.048	45.518	2.210	43	4
	3	2.204	0.055	66.049	2.149	49	5
	4	2.144	0.060	79.302	2.084	55	5
	5	2.118	0.064	83.552	2.054	58	6
Lattice parameter: a = 4.024 Å							

[a]$B_{obs.}$: half width (full width half maximum FWHM, peak width) - obs. = observed; [b]B_{std}: device-related width, Derived from LaB_6 - std. = standard; [c]pos.: position; [d]$B_{struct.}$: Difference between $B_{obs.}$ and B_{std} - struct. = structural.

XPS analysis

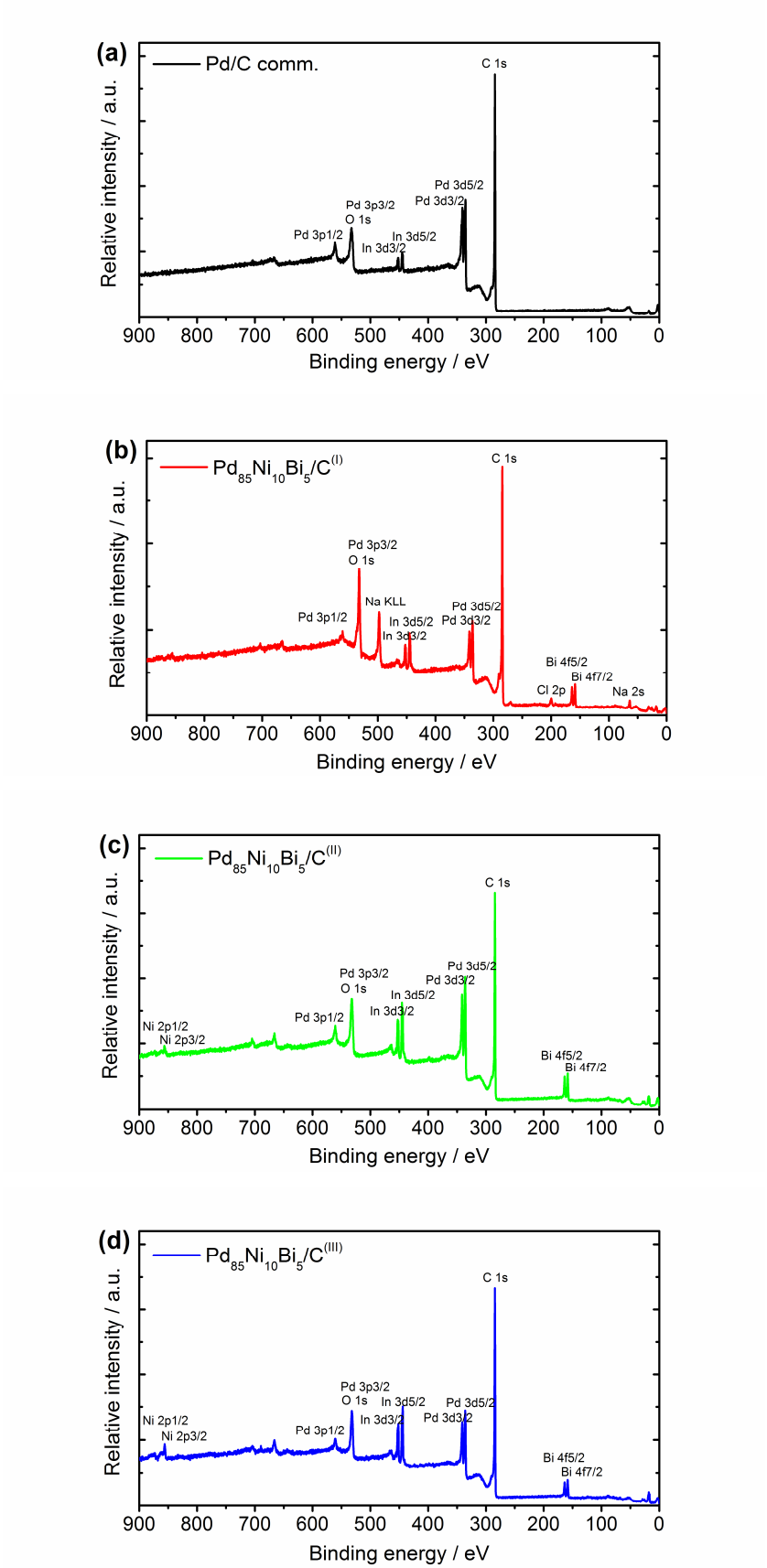


Figure 75: Survey XPS spectra of the **(a)** Pd/C comm., **(b)** $Pd_{85}Ni_{10}Bi_5/C^{(I)}$, **(c)** $Pd_{85}Ni_{10}Bi_5/C^{(II)}$ and **(d)** $Pd_{85}Ni_{10}Bi_5/C^{(III)}$ catalyst [3].

Table 54: XPS data (measured) of the commercial Pd/C catalyst [3].

Catalyst	Peak Name	Peak Pos. (eV)	Raw Area	Area/(RSF*T*MFP)[a]	At. Conc. (%)[b]
Pd/C comm.	C 1s	284.00	328619	328619	90.68
	Pd 3d	335.00	385754	24049.5	6.64
	Bi 4f	161.00	-171.275	-6.89792	0
	Ni 2p3/2	847.40	-325.222	-22.2603	0
	O 1s	534.53	28471	9717.07	2.68

[a]RSF: relative sensitivity factor, T: transmission factor, MFP: mean free path; [b]atomic concentration.

Table 55: XPS data (measured) of the $Pd_{85}Ni_{10}Bi_5/C^{(I)}$ catalyst [3].

Catalyst	Peak Name	Peak Pos. (eV)	Raw Area	Area/(RSF*T*MFP)[a]	At. Conc. (%)[b]
$Pd_{85}Ni_{10}Bi_5/C^{(I)}$	C 1s	284.00	270798	270798	89.65
	Pd 3d	335.60	175750	10957	3.63
	Bi 4f	158.00	46957.9	1891.18	0.63
	Ni 2p3/2	855.20	19169.4	1312.07	0.43
	O 1s	530.90	50070.4	17088.9	5.66

[a]RSF: relative sensitivity factor, T: transmission factor, MFP: mean free path; [b]atomic concentration.

Table 56: XPS data (measured) of the $Pd_{85}Ni_{10}Bi_5/C^{(II)}$ catalyst [3].

Catalyst	Peak Name	Peak Pos. (eV)	Raw Area	Area/(RSF*T*MFP)[a]	At. Conc. (%)[b]
$Pd_{85}Ni_{10}Bi_5/C^{(II)}$	C 1s	284.00	294509	294509	87.22
	Pd 3d	335.60	366470	22847.3	6.77
	Bi 4f	158.00	71298.9	2871.48	0.85
	Ni 2p3/2	856.20	32983.2	2257.57	0.67
	O 1s	529.85	44430.2	15163.9	4.49

[a]RSF: relative sensitivity factor, T: transmission factor, MFP: mean free path; [b]atomic concentration.

Table 57: XPS data (measured) of the $Pd_{85}Ni_{10}Bi_5/C^{(III)}$ catalyst [3].

Catalyst	Peak Name	Peak Pos. (eV)	Raw Area	Area/(RSF*T*MFP)[a]	At. Conc. (%)[b]
$Pd_{85}Ni_{10}Bi_5/C^{(III)}$	C 1s	283.95	292014	292014	90.41
	Pd 3d	335.35	231567	14436.9	4.47
	Bi 4f	158.15	51581.8	2077.4	0.64
	Ni 2p3/2	855.55	50236.4	3438.5	1.06
	O 1s	530.07	32338.7	11037.1	3.42

[a]RSF: relative sensitivity factor, T: transmission factor, MFP: mean free path; [b]atomic concentration.

Table 58: XPS results (fitted) of carbon supported Pd-based catalysts with the assignments of Pd 3d, Ni 2p and Bi 4f peaks including the determined metal contents obtained from measured data [3].

Catalyst	Pd 3d (eV)	Pd (at.%)	Assignment	Ni 2p (eV)	Ni (at.%)	Assignment	Bi 4f (eV)	Bi (at.%)	Assignment	Pd/ metal	Ni/ metal	Bi/ metal
Pd/C comm.	335.00 340.30	5.83	Pd^0	-	-	-	-	-	-	**100**	-	-
	336.76 342.06	1.15	PdO	-	-	-	-	-	-			
$Pd_{85}Ni_{10}Bi_5/C^{(I)}$	335.15 340.45	3.17	Pd^0	855.74 854.97	0.20	$Ni(OH)_2$	158.10 163.40	0.49	Bi^0	**77**	**9**	**13**
	336.53 341.83	0.88	PdO	857.74 860.53	0.02	$Ni(OH)_2$	159.50 164.80	0.16	Bi_2O_3			
				861.53 866.66	0.16	$Ni(OH)_2$						
$Pd_{85}Ni_{10}Bi_5/C^{(II)}$	335.15 340.45	6.23	Pd^0	855.80 855.03	0.35	$Ni(OH)_2$	158.02 163.32	0.63	Bi^0	**82**	**8**	**10**
	336.53 341.83	1.23	PdO	857.80 860.59	0.03	$Ni(OH)_2$	159.29 164.59	0.23	Bi_2O_3			
				861.59 866.66	0.28	$Ni(OH)_2$						
$Pd_{85}Ni_{10}Bi_5/C^{(III)}$	335.15 340.45	4.61	Pd^0	855.79 855.02	0.57	$Ni(OH)_2$	157.99 163.29	0.47	Bi^0	**72**	**17**	**10**
	336.53 341.83	0.27	PdO	857.79 860.58	0.04	$Ni(OH)_2$	159.33 164.63	0.17	Bi_2O_3			
				861.58 866.66	0.46	$Ni(OH)_2$						

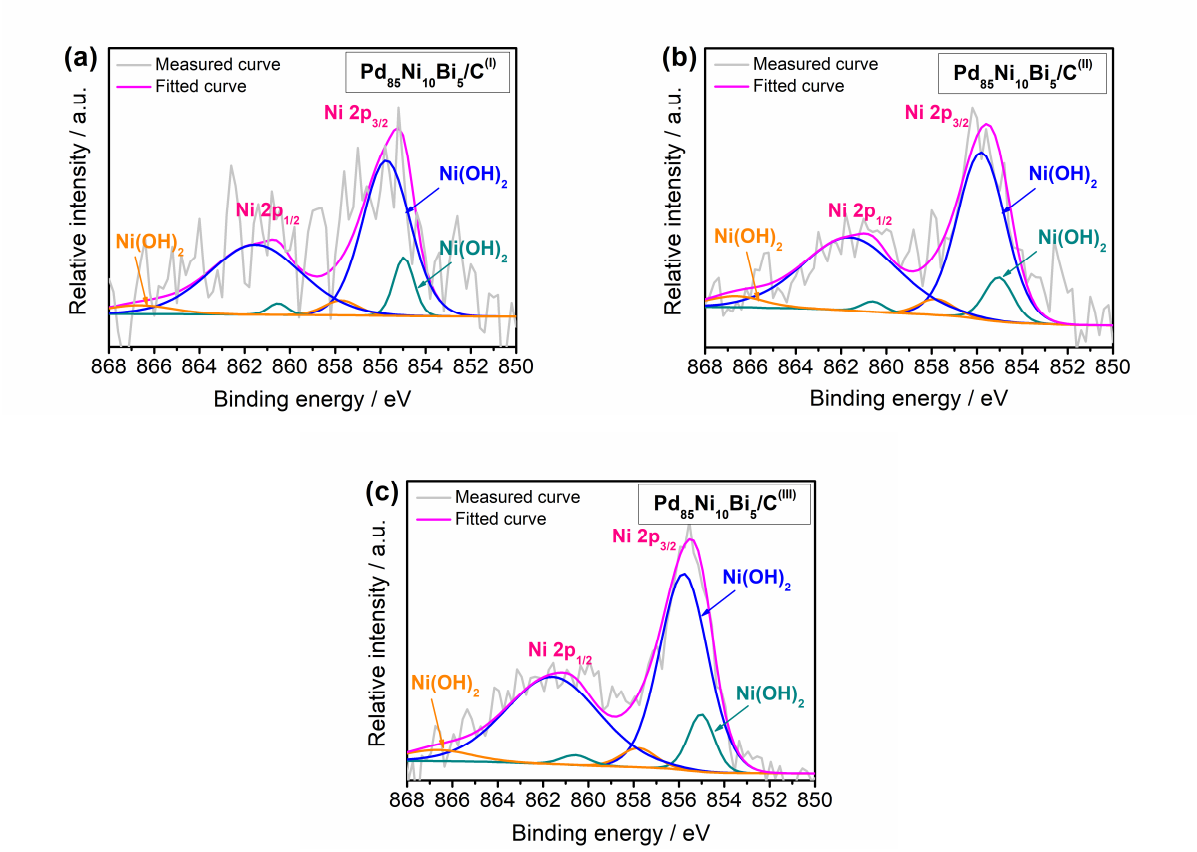


Figure 76: Ni 2p core level XPS spectra of the **(a)** $Pd_{85}Ni_{10}Bi_5/C^{(I)}$, **(b)** $Pd_{85}Ni_{10}Bi_5/C^{(II)}$ and **(c)** $Pd_{85}Ni_{10}Bi_5/C^{(III)}$ catalyst [3].

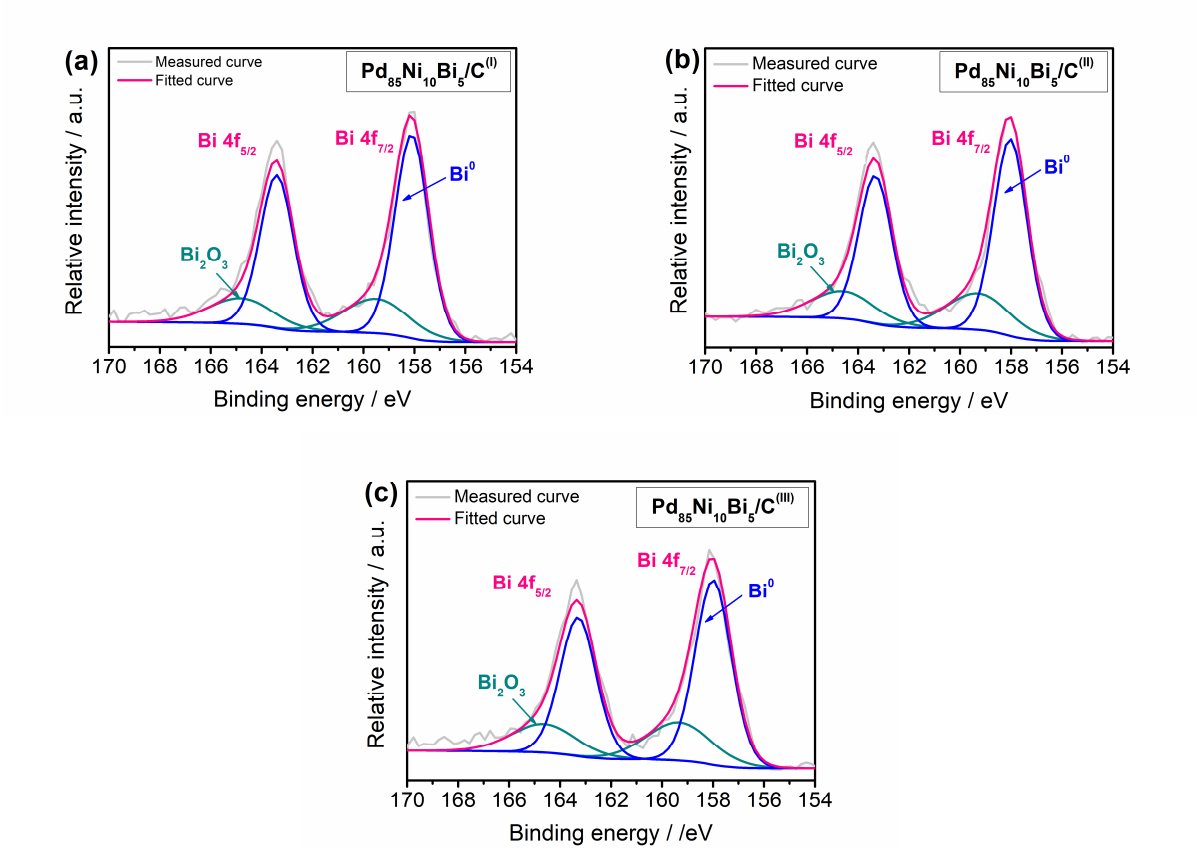


Figure 77: Bi 4f core level XPS spectra of the **(a)** $Pd_{85}Ni_{10}Bi_5/C^{(I)}$, **(b)** $Pd_{85}Ni_{10}Bi_5/C^{(II)}$ and **(c)** $Pd_{85}Ni_{10}Bi_5/C^{(III)}$ catalyst [3].

8.4.3 Electrochemical Characterization

CV analysis

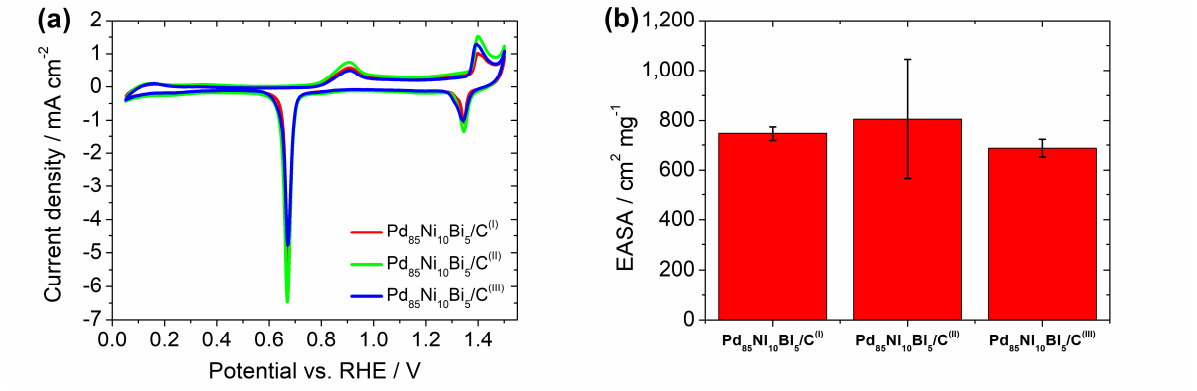


Figure 78: CVs of **(a)** $Pd_{85}Ni_{10}Bi_5/C$ catalysts in de-aerated 1.0 M KOH at 30 °C and with a scan rate of 10 $mV \cdot s^{-1}$ in the potential range of 0.05-1.5 V with **(b)** their resulting determined EASA [3].

Active layer thickness determination of the catalysts

The active layer thickness (ALT) of the catalysts (commercial Pd/C and $Pd_{85}Ni_{10}Bi_5/C^{(I)-(III)}$) on the glassy carbon (GC) of the rotating disk electrode (RDE) was calculated according to the equations below assuming a uniformly distributed layer [3].

- **Steps for calculation of the ALT from the commercial Pd/C catalyst** [3]**:**

$$m_{Pd} = \frac{m_{catalyst}}{V_{mixture}} \cdot V_{catalyst\ ink} \cdot 0.4 = \frac{0.0137\ g}{5\ mL} \cdot 0.01\ mL \cdot 0.4 = \mathbf{1.1 \cdot 10^{-5}\ g}$$

$$m_{Vulcan\ XC72} = \frac{m_{catalyst}}{V_{mixture}} \cdot V_{catalyst\ ink} \cdot 0.6 = \frac{0.0137\ g}{5\ mL} \cdot 0.01\ mL \cdot 0.6 = \mathbf{1.6 \cdot 10^{-5}\ g}$$

$$m_{Nafion\ 5\ wt.\%} = \frac{\rho_{Nafion\ 5\ wt.\%} \cdot V_{Nafion\ 5\ wt.\%} \cdot \frac{5}{100}}{\frac{V_{mixture}}{V_{catalyst\ ink}}} = \frac{0.94\ g \cdot cm^{-3} \cdot 0.023\ cm^3 \cdot \frac{5}{100}}{\frac{5\ mL}{0.01\ mL}} = \mathbf{2.2 \cdot 10^{-6}\ g}$$

$$\begin{aligned} \boldsymbol{ALT_{catalyst}} &= \frac{\frac{m_{Pd}}{\rho_{Pd}} + \frac{m_{Vulcan\ XC72}}{\rho_{Vulcan\ XC72}} + \frac{m_{Nafion\ 5\ wt.\%}}{\rho_{Nafion}}}{A_{GC}} \\ &= \frac{\frac{1.1 \cdot 10^{-5}\ g}{12.02\ g \cdot cm^{-3}} + \frac{1.6 \cdot 10^{-5}\ g}{0.264\ g \cdot cm^{-3}} + \frac{2.2 \cdot 10^{-6}\ g}{1.98\ g \cdot cm^{-3}}}{0.196\ cm^2} = \mathbf{0.000328\ cm} \\ &= \mathbf{3.3\ \mu m} \end{aligned} \quad (27)$$

- **Steps for calculation of the ALT from the $Pd_{85}Ni_{10}Bi_5/C^{(I)-(III)}$ catalysts** [3]**:**

$$m_{Pd} = \frac{m_{catalyst}}{V_{mixture}} \cdot V_{catalyst\ ink} \cdot 0.4 = \frac{0.0162\ g}{5\ mL} \cdot 0.01\ mL \cdot 0.4 = \mathbf{1.3 \cdot 10^{-5}\ g}$$

$$m_{Vulcan\ XC72R} = \frac{m_{catalyst}}{V_{mixture}} \cdot V_{catalyst\ ink} \cdot 0.6 = \frac{0.0162\ g}{5\ mL} \cdot 0.01\ mL \cdot 0.6 = \mathbf{1.9 \cdot 10^{-5}\ g}$$

$$m_{Nafion\ 5\ wt.\%} = \frac{\rho_{Nafion\ 5\ wt.\%} \cdot V_{Nafion\ 5\ wt.\%} \cdot \frac{5}{100}}{\frac{V_{mixture}}{V_{catalyst\ ink}}} = \frac{0.94\ g \cdot cm^{-3} \cdot 0.023\ cm^3 \cdot \frac{5}{100}}{\frac{5\ mL}{0.01\ mL}} = \mathbf{2.2 \cdot 10^{-6}\ g}$$

$$\begin{aligned} \boldsymbol{ALT_{catalyst}} &= \frac{\frac{m_{Pd}}{\rho_{Pd}} + \frac{m_{Vulcan\ XC72R}}{\rho_{Vulcan\ XC72R}} + \frac{m_{Nafion\ 5\ wt.\%}}{\rho_{Nafion}}}{A_{GC}} \\ &= \frac{\frac{1.3 \cdot 10^{-5}\ g}{12.02\ g \cdot cm^{-3}} + \frac{1.9 \cdot 10^{-5}\ g}{0.096\ g \cdot cm^{-3}} + \frac{2.2 \cdot 10^{-6}\ g}{1.98\ g \cdot cm^{-3}}}{0.196\ cm^2} = \mathbf{0.001044\ cm} \\ &= \mathbf{10.4\ \mu m} \end{aligned} \quad (28)$$

$ALT_{catalyst}$	Active layer thickness (= Pd + Nafion ionomer (5 wt.%, Quintech) as binder + Vulcan) of the catalyst used
$\frac{m_{catalyst}}{V_{mixture}}$	Catalyst ink: A certain amount of the catalyst ($m_{catalyst}$ = 13.7 mg for comm. Pd/C; $m_{catalyst}$ = 16.2 mg for $Pd_{85}Ni_{10}Bi_5/C^{(I-III)}$) in a mixture of 3477 µL 2-propanol, 1500 µL ultra-pure water and 23 µL Nafion ionomer solution ($V_{mixture}$ = 5 mL)
$V_{catalyst\ ink}$	10 µL of the catalyst ink was applied onto the GC disk to achieve the loading of 56 μg_{Pd} cm^{-2} for the catalyst used
$V_{Nafion\ 5\ wt.\%}$	23 µL (= 0.023 cm^3) of Nafion ionomer solution
$m_{Pd} = \frac{m_{catalyst}}{V_{mixture}} \cdot V_{catalyst\ ink} \cdot 0.4$	Mass of Pd (40 wt.% of the catalyst)
$m_{Vulcan} = \frac{m_{catalyst}}{V_{mixture}} \cdot V_{catalyst\ ink} \cdot 0.6$	Mass of Vulcan XC72 (60 wt.% of Pd/C) Mass of Vulcan XC72R (60 wt.% of $Pd_{85}Ni_{10}Bi_5/C^{(I-III)}$)
$m_{Nafion\ 5\ wt.\%} = \frac{\rho_{Nafion\ 5\ wt.\%} \cdot V_{Nafion\ 5\ wt.\%} \cdot \frac{5}{100}}{\frac{V_{mixture}}{V_{catalyst\ ink}}}$	Mass of Nafion ionomer
$V_{Pd} = \frac{m_{Pd}}{\rho_{Pd}}$	Volume of Pd
$V_{Vulcan} = \frac{m_{Vulcan}}{\rho_{Vulcan}}$	Volume of Vulcan XC72 (Pd/C) Volume of Vulcan XC72R ($Pd_{85}Ni_{10}Bi_5/C^{(I-III)}$)
$V_{Nafion\ 5\ wt.\%} = \frac{m_{Nafion\ 5\ wt.\%}}{\rho_{Nafion}}$	Volume of Nafion ionomer
$\rho_{Nafion\ 5wt.\%}$	Density of Nafion ionomer (0.94 g cm^{-3})
ρ_{Pd}	Density of Pd (Lit.: 12.02 g cm^{-3}) https://www.reade.com/products/palladium-pd-powder-shot-pellets-ingot
$\rho_{Vulcan\ XC72}$	Density of Vulcan XC72 (Lit.: 0.264 g cm^{-3}) https://fuelcellstore.com/fuel-cell-components/vulcan-xc72
$\rho_{Vulcan\ XC72R}$	Density of Vulcan XC72R (Lit.: 0.096 g cm^{-3}) https://fuelcellstore.com/fuel-cell-components/vulcan-xc-72r
ρ_{Nafion}	Density of Nafion (Lit.: 1.98 g cm^{-3}) http://www.nafionstore.com/Shared/Bulletins/N115-N117-N1110.pdf
A_{GC-RDE}	Area of the GC-RDE (Ø = 5 mm; 0.196 cm^2)

The thickness of the catalyst layer has an influence on mass transport and diffusion. It has previously been shown in a detailed study how the thickness of the catalyst affects electrochemical measurements [160]. The variation of the electrode thickness was outside the scope of this study [3].

9 Appendix B: Resulting Scientific Publications during the Doctoral Study

Web sites: **Research Gate**, **Google Scholar**, **ORCID**

9.1 Peer-Reviewed Articles

- **Cermenek, B**.; Genorio, B.; Winter, T.; Wolf, S.; Connell, J.A.; Roschger, M.; Letofsky-Papst, I.; Kienzl, N.; Bitschnau, B.; Hacker, V. Alkaline Ethanol Oxidation Reaction on Carbon Supported Ternary PdNiBi Nanocatalyst using Modified Instant Reduction Synthesis. *Electrocatalysis*, **2020**, *11*, 203–214. (as **corresponding author**)
  DOI: 10.1007/s12678-019-00577-8; **IF: 2.311**

- **Cermenek, B**.; Ranninger, J.; Feketeföldi, B.; Letofsky-Papst, I.; Kienzl, N.; Bitschnau, B.; Hacker, V. Novel highly active carbon supported ternary PdNiBi nanoparticles as anode catalyst for the alkaline direct ethanol fuel cell. *Nano Res.*, **2019**, *12*, 683–693. (as **corresponding author**)
  DOI: 10.1007/s12274-019-2277-z; **IF: 8.515**

- Chaiburi, C.; **Cermenek, B**.; Pichler, B.E.; Grimmer, C.; Hacker, V. Ethanol: Tolerant Oxygen Reduction Reaction Catalysts in Alkaline Media. *J. Electrochem. Energy Convers. Storage*, **2019**, *16*, 021004-1–021004-6.
  DOI: 10.1115/1.4041979; **IF: 1.515**

- Grimmer, I.; Zorn, P.J.; Weinberger, S.; Grimmer, C.; Pichler, B.E.; **Cermenek, B**.; Gebetsroither, F.; Schenk, A.; Mautner, F.-A.; Bitschnau, B.; Hacker, V. Ethanol tolerant precious metal free cathode catalyst for alkaline direct ethanol fuel cells. *Electrochim. Acta*, **2017**, *228*, 325–331.
  DOI: 10.1016/j.electacta.2017.01.087; **IF: 5.383**

- Weinberger, S.; Trattner, S.H.; **Cermenek, B**.; Schenk, A.; Grimmer, C.; Hacker, V. Generic tool for the simulation of electrochemical fuel cell monitoring techniques. *J. Energy Storage*, **2017**, *12*, 319–331.
  DOI: 10.1016/j.est.2017.05.010; **IF: 3.517**

- Chaiburi, C.; **Cermenek, B**.; Pichler, B.E.; Grimmer, C.; Schenk, A.; Hacker, V. Ethanol - Tolerant Pt-free Cathode Catalysts for the Alkaline Direct Ethanol Fuel Cell. *J. New Mater. Electrochem. Syst.*, **2017**, *19*, 199–207.
  DOI: 10.14447/jnmes.v19i4.282 ; **IF: 0.400**

- Feketeföldi, B.; **Cermenek, B**.; Spirk, C.; Schenk, A.; Grimmer, C.; Bodner, M.; Koller, M.; Ribitsch, V.; Hacker, V. Chitosan-Based Anion Exchange Membranes for Direct Ethanol Fuel Cells. *J. Membr. Sci. Technol.*, **2016**, *6*, 145. (as **corresponding author**)
  DOI: 10.4172/2155-9589.1000145; **IF: 1.18**

- Grimmer, C.; Grandi, M.; Zacharias, R.; **Cermenek, B**.; Weber, H.; Morais, C.; Napporn, T.W.; Weinberger, S.; Schenk, A.; Hacker, V. The electrooxidation of borohydride: A mechanistic study on palladium (Pd/C) applying RRDE, ^{11}B-NMR and FTIR. *Appl. Catal. B Environ.*, **2016**, *180*, 614–621.
  DOI: 10.1016/j.apcatb.2015.07.028; **IF: 14.229**

- Grimmer, C.; Zacharias, R.; Grandi, M.; Pichler, B.E.; Kaltenböck, I.; Gebetsroither, F.; Wagner, J.; **Cermenek, B**.; Weinberger, S.; Schenk, A.; Hacker, V. A membrane-free and practical mixed electrolyte direct borohydride fuel cell. *J. Electrochem. Soc.*, **2016**, *163*, F278–F283.
  DOI: 10.1149/2.1111603jes; **IF: 3.120**

- Grimmer, C.; Zacharias, R.; Grandi, M.; **Cermenek, B**.; Schenk, A.; Weinberger, S.; Mautner, F.-A.; Bitschnau, B.; Hacker, V. Carbon Supported Ruthenium as Anode Catalyst for Alkaline Direct Borohydride Fuel Cells. *J. Phys. Chem. C*, **2015**, *119*, 23839–23844.
  DOI: 10.1021/acs.jpcc.5b06862; **IF: 4.309**

- Bodner, M.; **Cermenek, B.**; Rami, M.; Hacker, V. The Effect of Platinum Electrocatalyst on Membrane Degradation in Polymer Electrolyte Fuel Cells. *Membranes*, **2015**, *5*, 888–902. (as **corresponding author**)
  DOI: 10.3390/membranes5040888; **IF: -**

- Ranacher, C.; Resel, R.; Moni, P.; **Cermenek, B.**; Hacker, V.; Coclite, A.M. Layered Nanostructures in Proton Conductive Polymers obtained by initiated Chemical Vapor Deposition. *Macromolecules* **2015**, *48*, 6177–6183.
  DOI: 10.1021/acs.macromol.5b01145; **IF: 5.997**

Note: Impact factor (IF) 2018 - accessed 28/02/2020

9.2 Lectures

- Kocher, K.; Wolf, S.; **Cermenek, B.**; Mayer, K.; Hacker, V. Polymer coated catalysts toward durable PEM fuel cells. *IEA AFC TCP Annex 31 Spring Meeting 2019*, Washington, United States, 01/05/19–03/05/19.

- **Cermenek, B.**; Malli, K.; Stark, A.; Hacker, V. Precious metal free electrocatalysts for regenerative alkaline fuel cells. *Université de Poitiers* **2019**, Poitiers, France, 27/03/19.

- **Cermenek, B.**; Hacker, V. Enhanced ethanol oxidation reaction in alkaline direct alcohol fuel cells. *International Symposium on Electrocatalysis: Recent Advances in Electro-c-talysis and Photoelectrocatalysis* **2018**, Szczyrk, Poland, 31/08/18.

- Schenk, A.; Grimmer, C.; Bodner, M.; **Cermenek, B.**; Hacker, V. DAFC, DBFC, HTPEM and AFC. *9th International Summer School on Advanced Studies of Polymer Electrolyte Fuel Cells* **2016**, Graz, Austria, 28/08/16–03/09/16.

- **Cermenek, B.**; Grimmer, C.; Hacker, V. Highly Efficient Anode Catalysts for Alkaline Direct Ethanol Fuel Cells. *IEA Implementing Agreements Annex 35 Meeting* **2016**, Messina, Italy, 01/04/16.

- **Cermenek, B.**; Grimmer, C.; Hacker, V. Power Generation of Liquid Fuels in Alkaline Direct Fuel Cells. *IEA AFC Implementing Agreements Annex 31 Meeting* **2016**, Messina, Italy, 31/03/16.

9.3 Book Chapters

- **Cermenek, B.**; Ranninger, J.; Hacker, V. Chapter 15 - Alkaline Direct Ethanol Fuel Cell. In *Ethanol: Science and Engineering*; Basile, A.; Iulianelli, A.; Dalena, F.; Veziroglu, N.T., Eds.*;* Elsevier Inc.: Amsterdam, **2019**; pp. 383–405.
  DOI: 10.1016/B978-0-12-811458-2.00015-8

- Schenk, A.; **Cermenek, B.**; Hacker, V. Chapter 5 - Other Polymer Electrolyte Fuel Cells. In *Fuel Cells and Hydrogen: From Fundamentals to Applied Research*; Hacker, V.; Mitsushima, S., Eds.*;* Elsevier Inc.: Amsterdam, **2018**; pp. 91–115.
  DOI: 10.1016/B978-0-12-811459-9.00005-0

9.4 Commissioned Reports

- **Cermenek, B.**; Hacker, V.; Feketeföldi, B.; Ribitsch, V. Pt-freie Katalysatorsysteme und ethanolbeständige Polysaccharid-Membranen für die alkalische DEFC. *End report*, **2017**.
- Hacker, V.; **Cermenek, B.** IEA AFC Annex 35: Brennstoffzellen für portable Anwendungen: Arbeitsperiode 2014-2017. *End report*, **2017**.
- Bodner, M.; Hofer, A.; **Cermenek, B.** Hacker, V. Green Cell - Neue Materialien für die alkalische Hochleistungs-Direkt-Ethanol-Brennstoffzelle. *End report*, **2014**.

9.5 Conference Contributions and Professional Articles

- Wolf, S.; Roschger, M.; **Cermenek B.**; Lemoine, C.; Hacker, V. Development and Characterization of Carbon Supported Ternary PdNiBi Anode Catalysts for the Alkaline Direct Ethanol Fuel Cell. *5th International Workshop on Hydrogen and Fuel Cells as part of the 12th International Summer School on Advanced Studies of Polymer Electrolyte Fuel Cells* **2019**, Yokohama, Japan, 26/08/19–31/08/19.
- Roschger, M.; Wolf, S.; **Cermenek, B.**; Genorio, B.; Hacker, V. Graphene Oxide Based Anode Catalysts for Alkaline Direct Ethanol Fuel Cells. *5th International Workshop on Hydrogen and Fuel Cells as part of the 12th International Summer School on Advanced Studies of Polymer Electrolyte Fuel Cells* **2019**, Yokohama, Japan, 26/08/19–31/08/19.
- Wolf, S.; **Cermenek, B.**; Roschger, M.; Hacker, V. Carbon Supported Ternary PdNiBi Electrocatalysts for Ethanol Oxidation Reaction in Alkaline Direct Ethanol Fuel Cells (ADEFCs). *Electrolysis and Fuel Cell Discussions* **2019**, La Grande Motte, France, 15/09/19–18/09/19.
- Hacker, V.; **Cermenek, B**. Enhanced ethanol oxidation reaction in alkaline direct alcohol fuel cells. in *International Symposium on Electrocatalysis - Book of Abstracts: Recent Advances in Electrocatalysis and Photoelectrocatalysis, Kulesza, P.; Adamczyk, L.; Szaniawska, I. (eds)* **2018**, Szczyrk , Poland, 29/08/18, pp. 40–41.
- Hacker, V.; Ranninger, J.; **Cermenek, B.**; Feketeföldi, B.; Spirk, C.; Hesse, J.; Ribitsch, V. Optimization of the Catalyst and Membrane Performance by addition of various Additives for the alkaline Direct Ethanol Fuel Cell. *Zenodo*, **2018**.
  DOI: 10.5281/zenodo.1491477; (as **corresponding author**)

- **Cermenek, B.**; Hacker, V. Ethanol to Power. in *Proceedings of 14th Minisymposium Chemical and Process Engineering and 5th Austrian Particle Forum, Samhaber, W. M.; Schneiderbauer, S.; Rezaei, M. (eds)* **2018**, 1st ed. Johannes Kepler University, Linz, Austria, 04/04/18–05/04/18.

- Ranninger, J.; **Cermenek, B.**; Hacker, V. Anode catalysts for the alkaline DEFC tested in a single cell using polybenzimidazole membrane. *3rd International Workshop on Hydrogen and Fuel Cells: as part of the 10th International Summer School on Advanced Studies of Polymer Electrolyte Fuel Cells* **2017**, Yokohama, Japan, 23/08/17, pp. 41–42.

- **Cermenek, B.**; Ranninger, J.; Grimmer, I.; Feketeföldi, B.; Spirk, C.; Hacker, V. Pt-free membrane electrode assemblies for the alkaline direct ethanol fuel cell. *26th ATC Industrial Inorganic Chemistry – Materials and Processes* **2017**, Frankfurt am Main, Germany, 23/02/17–24/02/17, pp. 40–40.

- **Cermenek, B.**; Ranninger, J.; Grimmer, I.; Feketeföldi, B.; Spirk, C.; Hacker, V. Pt-free electrocatalysts and chitosan-based anion exchange membranes for the low temperature ADEFC. *International Workshop on Ethanol Electro-oxidation (DECORE WORKSHOP)* **2016**, Florence, Italy, 05/12/16–07/12/16, pp. 28–28.

- Schenk, A.; Grimmer, C.; Bodner, M.; **Cermenek, B**.; Hacker, V. DAFC, DBFC, HTPEM and AFC. *9th International Summer School on Advanced Studies of Polymer Electrolyte Fuel Cells* **2016**, Graz, Austria, 28/08/16–03/09/16, pp. 139–149.

- Bodner, M.; **Cermenek, B.**; Rami, M.; Schenk, A.; Hacker, V. Membrane degradation mitigation by the presence of platinum electrocatalyst. *2nd International Workshop on Hydrogen and Fuel Cells: as part of the 9th International Summer School on Advanced Studies of Polymer Electrolyte Fuel Cells* **2016**, Graz, Austria, 31/08/16–31/08/16, pp. 34–35.

- Schenk, A.; Hammer, B.; Bodner, M.; **Cermenek, B.**; Hacker, V. The Austrian participation in the IEA Technology Collaboration Program on Advanced Fuel Cells. *2nd International Workshop on Hydrogen and Fuel Cells: as part of the 9th International Summer School on Advanced Studies of Polymer Electrolyte Fuel Cells* **2016**, Graz, Austria, 31/08/16–31/08/16, pp. 102–103.

- **Cermenek, B.**; Schenk, A.; Weinberger, S.; Grimmer, C.; Hacker, V. Sustainable and Economical Materials for the Alkaline Direct Ethanol Fuel Cell. *Workshop on Ion Exchange Membranes for Energy Applications – EMEA2016* **2016**; Bad Zwischenahn, Germany, 27/06/16–29/06/16.

- Chaiburi, C.; **Cermenek, B.**; Pichler, B.E.; Grimmer, C.; Hacker, V. Study on ethanol-tolerant electrocatalysts for oxygen reduction reaction in alkaline media. in *Proceedings of 12th Minisymposium Chemical and Process Engineering* **2016**, pp. 109–112. **DOI:** 10.3217/978-3-85125-456-3

- Kaltenböck, I.; Grimmer, C.; Pichler, B.E.; **Cermenek, B.**; Schenk, A.; Hacker, V. Non-precious cathode catalysts for direct liquid fuel cells. in *Proceedings of 12th Mini-symposium Chemical and Process Engineering* **2016**. pp. 75–78. **DOI:** 10.3217/978-3-85125-456-3

Cermenek, B.; Grimmer, I.; Raunicher, J.; Ranninger, J.; Hacker, V. Materialentwicklung für die ADEFC. *CEET Konkret*, **2016**, 28–29. **DOI:** 10.3217/978-3-85125-503-4

- Hacker, V.; **Cermenek, B.**; Grimmer, C. Direktverstromung von Ethanol. *Biobased future*, **2016**, *5*, 19–19.

- **Cermenek, B.**; Hacker, V. Hocheffiziente und langzeitstabile Pt-freie Elektrokatalysatoren für die alkalische Direkt-Ethanol Brennstoffzelle. *CEET Konkret*, **2015**, 38–39.

- **Cermenek, B.**; Feketeföldi, B.; Zacharias, R.; Ribitsch, V.; Hacker, V. Characterization of Platinum-free electrocatalysts and anion exchange membranes for direct ethanol fuel cell. in *Proceedings of 6th European Fuel Cell - Piero Lunghi Conference, Cigolotti, V.; Barchiesi, C.; Chianella, M. (eds)* **2015**, ENEA, Naples, Italy, 16/12/15–18/12/15, pp. 167–168.

- **Cermenek, B.**; Zacharias, R.; Grandi, M.; Grimmer, C.; Schenk, A.; Hacker, V. Palladium based electrocatalysts for ethanol oxidation reaction in alkaline medium. in *1st International Workshop on Hydrogen and Fuel Cells: as part of the 8th International Summer School on Advanced Studies of Polymer Electrolyte Fuel Cells* **2015**, Yokohama, Japan, 31/08/15–05/09/15, pp. 28–29.

- Weinberger, S.; **Cermenek, B**.; Hacker, V. Großsignalersatzschaltbilder zur Analyse von Polymerelektrolytmembran-Brennstoffzellen. in *Proceedings of the 11th Minisymposium Chemical and Process Engineering* **2015**, Vienna, Austria, 14/04/15–15/04/15, pp. 191–194.

9.6 Scientific Posters

- Wolf, S.; **Cermenek, B.**; Roschger, M.; Hacker, V. Carbon Supported Ternary PdNiBi Electrocatalysts for Ethanol Oxidation Reaction in Alkaline Direct Ethanol Fuel Cells (ADEFCs). *Electrolysis and Fuel Cell Discussions 2019*, **2019**, La Grande Motte, France, 15/09/19–18/09/19.

- Wolf, S.; Roschger, M.; **Cermenek, B.**; Lemoine, C.; Hacker, V. Development and Characterization of Carbon Supported Ternary PdNiBi Anode Catalysts for the Alkaline Direct Ethanol Fuel Cell. *5th International Workshop on Hydrogen and Fuel Cells: as part of the 12th International Summer School on Advanced Studies of Polymer Electrolyte Fuel Cells*, **2019**, Yokohama, Japan, 29/08/19.

- Roschger, M.; Wolf, S.; **Cermenek, B.**; Genorio, B.; Hacker, V. Graphene Oxide Based Anode Catalysts for Alkaline Direct Ethanol Fuel Cells. *5th International Workshop on Hydrogen and Fuel Cells: as part of the 12th International Summer School on Advanced Studies of Polymer Electrolyte Fuel Cells*, **2019**, Yokohama, Japan, 29/08/19.

- Hacker, V.; Ranninger, J.; **Cermenek, B**.; Feketeföldi, B.; Spirk, C.; Hesse, J.; Ribitsch, V. Optimization of the Catalyst and Membrane Performance by addition of various Additives for the alkaline Direct Ethanol Fuel Cell. *7th Transport Research Arena*, **2018**, Vienna, Austria, 19/04/18.

- **Cermenek, B.**; Hacker, V. Ethanol to Power. *14th Minisymposium Chemical and Process Engineering*, **2018**, Linz, Austria, 04/04/18.

- Ranninger, J.; **Cermenek, B.**; Hacker, V. Anode catalysts for the alkaline DEFC tested in a single cell using polybenzimidazole membrane. *3rd International Workshop on Hydrogen and Fuel Cells: as part of the 10th International Summer School on Advanced Studies of Polymer Electrolyte Fuel Cells*, **2017**, Yokohama, Japan, 23/08/17.

- **Cermenek, B.**; Ranninger, J.; Feketeföldi, B.; Spirk, C.; Ribitsch, V.; Hacker, V. Direct Ethanol Fuel Cell for Clean and Efficient Power. *Smart Energy Systems Week Austria*, **2017**, Graz, Austria, 15/05/17–19/05/17.

- Hacker, V.; Kocher, K.; Bender, C.E.A.; **Cermenek, B.**; Schenk, A. Membrane Electrode Assembly development for High Temperature Polymer Electrolyte Membrane Fuel Cell. *Smart Energy Systems Week Austria*, **2017,** Graz, Austria, 15/05/17–19/05/17.

- **Cermenek, B.**; Ranninger, J.; Grimmer, I.; Feketeföldi, B.; Spirk, C.; Hacker, V. Pt-free membrane electrode assemblies for the alkaline direct ethanol fuel cell. *26th ATC Industrial Inorganic Chemistry – Materials and Processes*, **2017**, Frankfurt am Main, Germany, 23/02/17–24/02/17.

- **Cermenek, B.**; Ranninger, J.; Grimmer, I.; Feketeföldi, B.; Spirk, C.; Hacker, V. Pt-free electrocatalysts and chitosan-based anion exchange membranes for the low temperature ADEFC. *International Workshop on Ethanol Electro-oxidation (DECORE WORKSHOP)*, **2016**, Florence, Italy, 05/12/16–07/12/16.

- Bodner, M.; **Cermenek, B.**; Rami, M.; Schenk, A.; Hacker, V. Membrane degradation mitigation by the presence of platinum electrocatalyst. *2nd International Workshop on Hydrogen and Fuel Cells: as part of the 9th International Summer School on Advanced Studies of Polymer Electrolyte Fuel Cells*, **2016**, Graz, Austria, 31/08/16–31/08/16.

- Schenk, A.; Hammer, B.; Bodner, M.; **Cermenek, B.**; Hacker, V. The Austrian Participation in the IEA Technology Collaboration Program on Advanced Fuel Cells. *2nd International Workshop on Hydrogen and Fuel Cells: as part of the 9th International Summer School on Advanced Studies of Polymer Electrolyte Fuel Cells*, **2016**, Graz, Austria, 31/08/16–31/08/16.

- Kaltenböck, I.; Zorn, P.J.; **Cermenek, B.**; Pichler, B.E.; Hacker, V. A passive, membraneless and platinum-free direct ethanol fuel cell. *67th Annual Meeting of the International Society of Electrochemistry*, **2016**, Den Haag, Netherlands, 21/08/16–26/08/16.

- **Cermenek, B.**; Schenk, A.; Weinberger, S.; Grimmer, C.; Hacker, V. Sustainable and Economical Materials for the Alkaline Direct Ethanol Fuel Cell. *Workshop on Ion Exchange Membranes for Energy Applications – EMEA2016*, **2016**, Bad Zwischenahn, Germany, 27/06/16–29/06/16.

- Chaiburi, C.; **Cermenek, B.**; Pichler, B.E.; Grimmer, C.; Hacker, V. Study on ethanol-tolerant electrocatalysts for oxygen reduction reaction in alkaline media. *12th Minisymposium Chemical and Process Engineering*, **2016**, Graz, Austria, 30/03/16–31/03/16.

- Kaltenböck, I.; Grimmer, C.; **Cermenek, B.**; Hacker, V. Non-precious cathode catalysts for direct liquid fuel cells. *12th Minisymposium Chemical and Process Engineering*, **2016**, Graz, Austria, 30/03/16–31/03/16.

- **Cermenek, B.**; Feketeföldi, B.; Zacharias, R.; Ribitsch, V.; Hacker, V. Characterization of Platinum-free electrocatalysts and anion exchange membranes for direct ethanol fuel cell. *6th European Fuel Cell - Piero Lunghi Conference*, **2015**, Naples, Italy, 16/12/15–18/12/15.

- **Cermenek, B.**; Zacharias, R.; Grandi, M.; Grimmer, C.; Schenk, A.; Hacker, V. Palladium based electrocatalysts for ethanol oxidation reaction in alkaline medium. *1st International Workshop on Hydrogen and Fuel Cells as part of the 8th International Summer School on Advanced Studies of Polymer Electrolyte Fuel Cells*, **2015**, Yokohama, Japan, 31/08/15–05/09/15.

10 Appendix C: Other Research Activities

10.1 Involvement in the Preparation of Accepted Proposals

- **WTZ Proposal AUSTRIA/FRANCE (OeAD GmbH)**
  - Call for Applications for joint projects in 2019–2020
  - Project title: Precious metal free electrocatalysts for regenerative alkaline fuel cells
  - Project partners:
    - Graz University of Technology (CEET, Fuel Cell and Hydrogen Systems Group)
    - University of Poitiers (Institute of Chemistry of Materials and Media of Poitiers IC2MP)
  - Submitted: 30/05/2018; Accepted: 23/11/2018
  - Project description (see Link here)

- **FWF Proposal**
  - International Cooperation Project (Joint Project – Lead Agency Procedure): Slovenian Research Agency (ARRS) – Austrian Science Fund (FWF)
  - Project title: GO DEFC – Graphene oxide based MEAs for the direct ethanol fuel cell
  - Project partners:
    - Graz University of Technology (CEET, Fuel Cell and Hydrogen Systems Group)
    - University of Maribor (Faculty of Electrical Engineering and Computer Science)
    - University of Ljubljana (Faculty of Chemistry and Chemical Technology)
  - Submitted: 20/12/2017; Accepted: 29/05/2018
  - Project description (see Link here)

- **WTZ Proposal AUSTRIA/SLOVENIA (OeAD GmbH)**
  - Call for Applications for joint projects in 2018–2019
  - Project title: Transfer of ex-situ measured properties to in-situ application of new high performance PEMFC electrocatalysts
  - Project partners:
    - Graz University of Technology (CEET, Fuel Cell and Hydrogen Systems Group)
    - University of Ljubljana (National Institute of Chemistry NIC)
  - Submitted: 31/05/2017; Accepted: 12/12/2017
  - Project description (see Link here)

10.2 Supervised Students

- **Thomas Winter** 2018, Vorgänge während der Herstellung von Pd-basierenden Katalysatoren für die Direkt-Ethanol-Brennstoffzelle, *Master project work*, Graz University of Technology, 10/2017–03/2018.

- **Johanna Ranninger** 2017, Development and Characterization of Pd-based Catalysts for the alkaline Direct Ethanol Fuel Cell, *Master's thesis*, Graz University of Technology, 11/2016–11/2017.

- **Johanna Ranninger** 2016, Polymetallic anode electrocatalysts for the alkaline direct ethanol fuel cell, *Project Laboratory*, Graz University of Technology, 30/05/16–24/06/16.

- **Julia Raunicher** 2016, Development of $Pd_{80}Ni_{20}$ electrocatalysts with different carbon support materials for the alkaline ethanol oxidation reaction, *Project Laboratory*, Graz University of Technology, 11/01/16–05/02/16.

- **Dominic Leipold** 2015, Electrocatalysts for Alkaline Ethanol Oxidation Reaction and Oxygen Reduction Reaction, *Project Laboratory*, Graz University of Technology, 06/07/15–31/07/15.

10.3 News and Stories

- **Event: „Von der Wissenschaft zur Innovation" - Ehrung der Erfinderinnen und Erfinder der Grazer Universitäten**
  - Location: Aula der Alten Universität Graz, Graz, Austria (see Link here).
  - **Honor as inventor** of the Graz University of Technology; Awarded date: 12/11/2019.
  - **Title** of the ínvention disclosure: ***"Katalysator für die alkalische Direkt-Ethanol-Brennstoffzelle (DEFC) / Catalyst for the alkaline direct ethanol fuel cell (DEFC)"***

- **Uni Webradio; Soundportal (in German):**
  - **Title: *Vom Studenten zum Forscher***
    „Hand aufs Herz – der Weg zum Abschluss des Studiums dauert wahrscheinlich noch ein paar Semester, jedoch hat sich sicherlich schon jedeR StudentIn einmal gedacht: „Ein Doktorat, das wär' doch was…". Wie genau läuft es aber bei einem Doktoratsstudium ab? Ein Doktorand der TU Graz erlaubt Einblicke."
  - Author: Christopher Kommetter; Date of publication: 31/10/2016; (see Link here).